THE PHYSICAL REVIEW

VOLUME 87 Second Series NUMBER 5

SEPTEMBER 1, 1952

Published for the
AMERICAN PHYSICAL SOCIETY
by the
AMERICAN INSTITUTE OF PHYSICS
Lancaster, Pa., and New York, N. Y.

THE PHYSICAL REVIEW

A journal of experimental and theoretical physics established by E. L. Nichols in 1893

Published by the American Institute of Physics for the

AMERICAN PHYSICAL SOCIETY

Officers

President

J. H. VAN VLECK
Harvard University
Cambridge, Massachusetts

Vice-President

ENRICO FERMI
Institute for Nuclear Studies
University of Chicago
Chicago 37, Illinois

Secretary

K. K. DARROW
Bell Telephone Laboratories
Office:
Columbia University
New York 27, New York

Treasurer

G. B. PEGRAM
Columbia University
New York 27, New York

Local Secretary for the Pacific Coast

J. KAPLAN
University of California at Los Angeles
Los Angeles, California

Managing Editor

S. A. GOUDSMIT
Brookhaven National Laboratory
Upton, Long Island
New York

BOARD OF EDITORS

Editor

S. A. GOUDSMIT

Assistant Editor

S. PASSMANOFF

Associate Editors

HARVEY BROOKS — M. GOLDHABER — W. P. ALLIS
R. F. CHRISTY — R. HOFSTADTER — F. G. BRICKWEDDE
C. L. CRITCHFIELD — A. W. LAWSON — W. B. FRETTER
M. DEUTSCH — A. PAIS — CONYERS HERRING
T. H. JOHNSON — R. SERBER — H. W. LEVERENZ
BRUNO ROSSI — C. H. TOWNES — ARNOLD NORDSIECK

Manuscripts for publication should be submitted to S. A. Goudsmit, Brookhaven National Laboratory, Upton, Long Island, New York. The authors' institutions are requested to pay a publication charge of $15 per page which, if honored, entitles them to 100 free reprints. Instructions will be sent with galley proofs.

Proof and all correspondence concerning papers in the process of publication should be addressed to the Publication Manager, American Institute of Physics, 57 East 55 Street, New York 22, New York.

Subscription Price

United States and Canada $30.00
Elsewhere $32.00

Back Numbers[1]

Yearly back number sets when complete year is available
Prior to 1949: $25.00
Thereafter: $30.00
Single copies: $3.00 each, prior to July, 1929;
$1.50 each, July, 1929–December, 1941;
$3.00 each, January, 1942–December, 1946;
$1.50 each, thereafter.
General index, 1893–1920: $4.00.

Subscriptions, renewals, and orders for back numbers should be addressed to the American Institute of Physics, 57 East 55 Street, New York 22, New York.

Changes of address in the case of members of the American Physical Society should be addressed to the Treasurer; in the case of other subscribers to the American Institute of Physics.

[1] For Series I inquire of Physics Department, Cornell University, Ithaca, New York.

The Physical Review is published semi-monthly at Prince and Lemon Streets, Lancaster, Pennsylvania.

Entered as second-class matter March 6, 1947, at the Post Office at Lancaster, Pennsylvania, under the Act of March 3, 1879.

Acceptance for mailing at special rate of postage provided for in paragraph (d-2), section 34.40, P. L. & R. of 1948, authorized January 27, 1950.

THE
PHYSICAL REVIEW

A journal of experimental and theoretical physics established by E. L. Nichols in 1893

SECOND SERIES, VOL. 87, NO. 5 SEPTEMBER 1, 1952

The $Cu^{63}(\gamma,n)Cu^{62}$ Cross Section*

V. E. KROHN, JR., AND E. F. SHRADER
Case Institute of Technology, Cleveland, Ohio
(Received May 16, 1952)

The cross section for the reaction $Cu^{63}(\gamma,n)Cu^{62}$ has been determined as a function of energy by the analysis of the x-ray activation curve. D_2O loaded emulsions and a pair spectrometer were used as monitors, and the results obtained are in good agreement with the results of recent measurements which depend upon the calculated response of r-meters.

I. INTRODUCTION

A NUMBER of workers have measured cross sections for gamma-ray reactions by analyzing x-ray activation curves. In most cases an r-meter or ionization chamber has been used as a monitor, and the monitor response as a function of photon energy has been determined by calculations.[1–4] In this way the absolute cross section as a function of photon energy has been determined for numerous reactions. Also, reactions have been used to monitor one another,[2–5] but the results (expecially the absolute measurements) remain dependent upon the calculated response of an r-meter or ionization chamber.

In order to obtain a result independent of ionization measurements we have monitored the activation curve for $Cu^{63}(\gamma,n)Cu^{62}$ with an 180° magnetic pair spectrometer operating at 10.3 Mev. As the absolute response of the spectrometer was not well known, three points on the activation curve were monitored with D_2O loaded emulsions. The theoretical cross section for photodisintegration of the deuteron[6] together with experimental determinations in good agreement with the theory[7] allow us to obtain an absolute cross section scale for the copper reaction with an uncertainty of ten percent.

II. EXPERIMENTAL

Reduction of the accidental background to a level sufficiently low for efficient operation of the pair spectrometer requires gamma-ray pulses of appreciably longer duration than are obtained when expansion is forced by pulses through the betatron expander coils. Using self-expansion, gamma-pulses of about 150-μsec duration are available from the Case betatron.[8] These pulses have a full width at half-max which corresponds to 0.8 Mev at 13 Mev and 0.3 Mev at 21 Mev. Unfortunately, the self-expanded beam was not available at energies above 21 Mev.

The desired energies were obtained by adjusting the betatron to superimpose a photomultiplier pulse from the gamma-ray output upon a marker pulse on an oscilloscope. The marker pulse was one which is ordinarily used as the trigger of a constant energy expansion system described elsewhere.[9] This system was calibrated at the thresholds of $Cu^{63}(\gamma,n)Cu^{62}$ and $C^{12}(\gamma,n)C^{11}$ and is accurate within ±0.2 Mev. In spite of the appreciable energy band resulting from self-expansion the data showed that errors in reproducing energies were less than 0.1 Mev.

All measurements were made within ½° of the center of the gamma-ray beam. Copper disks were aligned with the monitor (D_2O loaded plate or spectrometer radiator) and subtended approximately the same solid angle at the betatron target. When the spectrometer was used as the monitor, it was cycled to count accidental

* Work supported by the AEC.
[1] G. C. Baldwin and G. S. Klaiber, Phys. Rev. **73**, 1156 (1948).
[2] B. C. Diven and G. M. Almy, Phys. Rev. **80**, 407 (1950).
[3] L. Katz and A. G. W. Cameron, Can. J. Research **29**, 518 (1951).
[4] P. R. Byerly, Jr., and W. E. Stephens, Phys. Rev. **83**, 54 (1951).
[5] R. Sagane, Phys. Rev. **84**, 586 (1951).
[6] H. A. Bethe and C. Longmire, Phys. Rev. **77**, 647 (1950).
[7] J. H. Carver and D. H. Wilkinson, Nature **167**, 154 (1951).
[8] E. C. Gregg, Jr., Rev. Sci. Instr. **22**, 176 (1951).
[9] K. D. Broadbent and E. C. Gregg, Jr., Atomic Energy Commission Unclassified Report No. 1661 (1951).

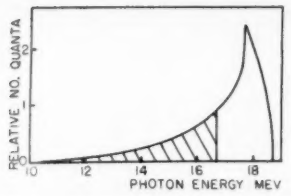

FIG. 1. Difference spectrum obtained by subtracting 17.7-Mev spectrum from 18.7-Mev spectrum after the two were normalized at 10.3 Mev. Results obtained from data taken at lower energies were used to calculate the contribution to the activation by the quanta corresponding to the shaded area of the figure. The remaining increase in activation was then attributed to the quanta corresponding to the remaining area under the difference spectrum.

background with a 0.05-μsec delay line in one channel during two minutes of each ten-minute run.

Exposures with the D_2O loaded emulsions acting as monitors varied from two to five minutes. A background was obtained from an H_2O loaded emulsion exposed with each D_2O loaded plate. Proton tracks resulting from gamma-rays of energy less than 6 Mev were eliminated from the data while gamma-rays of energy greater than 12 Mev were of little importance in determining gamma-ray intensities because of the poor statistics obtained from proton tracks corresponding to higher gamma-energies. Allowance was made for the escape of protons from the emulsions and for the absorption of some of the heavy water by the pure gelatin used as a base in the manufacture of the NTB plates. Although the plates used in this work were perpendicular to the gamma-ray beam, these corrections are similar to those used by the authors for plates exposed parallel to the beam.[10] The assumption that the gelatin in the emulsion and in the base absorb water in the ratio of their volumes led to agreement of the results from plates which had 4 percent of their gelatin in the base with the result from one plate which had 30 percent of its total gelatin in the base.

End-window counters calibrated with standard RaD+E and P^{32} sources were used to count the ten-minute positron activity of the copper. The usual corrections were made for the decay of the copper activity during and after the irradiations, and an extrapolation to zero thickness was used to correct the counting rate per Cu^{63} atom for self-scattering and self-absorption.

III. CALCULATIONS

The analysis of activation curves has been discussed at length in the literature,[8,9] so only a brief discription of our procedure will be given. For the spectra the total radiation formula of Schiff[11] was used rather than his zero angle formula. This was done because one effect of a target of appreciable thickness or of electrons going through the target more than once would be the scattering of electrons in the target through angles comparable with the intrinsic width of the bremsstrahlung. In fact, this scattering may be expected to reduce deviations from the thin target spectra as most electrons which have lost appreciable energy in the target will have been scattered through angles from which they cannot contribute to the radiation at the center of the beam. Fortunately, the zero angle and total radiation formulas of Schiff are so nearly identical that our choice of spectra had very little effect on our results.

Spectra were calculated for each datum point and normalized at 10.3 Mev, and each was subtracted from the spectrum following it in energy. The difference spectra obtained must account for the increase in yield between the corresponding points on the activation curve. After cross sections near the threshold had been determined they were used to predict the contribution to the activation by the lower energy gamma-rays present in the difference spectra at higher energies. In order to minimize oscillations in the cross section curve without smoothing the activation curve we avoided use of the predictions for energies above the highest gamma-ray energy present in the second preceding difference spectrum. Thus, with points on the activation curve spaced at approximately one-Mev intervals the points on the cross section curve represent averages over approximately two-Mev energy intervals. A typical difference spectrum is shown in Fig. 1.

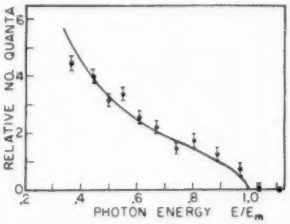

FIG. 2. Experimental and theoretical bremsstrahlung spectra normalized $E/E_m<0.6$.

IV. RESULTS

Experimental bremsstrahlung spectra were obtained from the D_2O loaded emulsions used in this work and in our study of the angular distribution of photoprotons from the deuteron.[10] The cross section for photodisintegration of the deuteron given by Bethe and Longmire[6] was used in the reduction of the data. The results from both experiments and for 14.0-, 16.7-, and 19.8-Mev bremsstrahlung have been combined and are presented in Fig. 2. The solid curve represents the Schiff total radiation spectrum for thin molybdenum targets. Actually, the Schiff spectra plotted in terms of E/E_m (where E is the quantum energy and E_m is the kinetic energy of the electrons producing the bremsstrahlung) differ for the three values of E_m. The curve

[10] V. E. Krohn, Jr., and E. F. Shrader, Phys. Rev. **86**, 391 (1952).
[11] L. I. Schiff, Phys. Rev. **83**, 252 (1951).

of Fig. 2 is a compromise which never differs from any of the three Schiff spectra by more than two percent. When the spectra were considered separately each was consistent with the combined result within the statistical error.

The activation curve for the reaction $Cu^{63}(\gamma,n)Cu^{62}$ is shown in Fig. 3, and the resulting cross section curve is presented in Fig. 4 along with the results of several recent investigations in which r-meters served as monitors. The shape of the smooth cross section curve was taken into account in the final calculation of the points of Fig. 4.

V. DISCUSSION

The experimental spectrum of Fig. 2 is in satisfactory agreement with the expression of Schiff, but with the

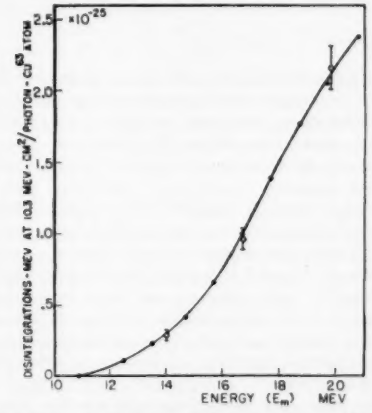

FIG. 3. The activation curve for the copper reaction. The solid points were obtained with the pair spectrometer serving as monitor and have been normalized to the open circles which were obtained from the results of runs monitored by D_2O loaded emulsions.

theory and experiment normalized for $E/E_m<0.6$ there is evidence of more quanta than the theory predicts at higher energies.

The result obtained for the $Cu^{63}(\gamma,n)Cu^{62}$ cross section is in good agreement with the other experimental results shown in Fig. 4. Our result is independent of

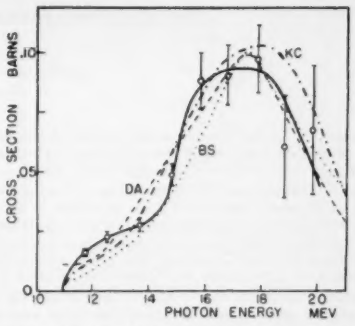

FIG. 4. Results obtained for the $Cu^{63}(\gamma,n)Cu^{62}$ cross section. Errors shown do not include the ten percent uncertainty in the absolute cross section scale. It should be noted that the combination of two adjacent points would reduce the error by a factor of 2 rather than the usual $\sqrt{2}$. The dotted curves are the results of: DA—Diven and Almy,[3] KC—Katz and Cameron,[3] and BS—Byerly and Stephens.[4]

the others to the extent that we have substituted the theoretical cross section for photodisintegration of the deuteron and the linear response of the pair spectrometer to 10.3-Mev photons for the calculated response of an r-meter. All the results of Fig. 4 have probably been affected in a similar way by errors in the theoretical spectrum. Johns *et al.*[12] have discussed the possible effect of such errors. In our case, the molybdenum ($Z=42$) target should reduce errors arising in the use of the Born approximation in bremsstrahlung theory. The cross section obtained in this work rises as the $\frac{3}{2}$ power of the energy above the threshold up to about 3 Mev above threshold, but one must remember that a detail of this sort will be affected by errors in the theoretical spectrum to a greater extent than the position of the resonance and the area under the cross section curve which Johns *et al.*[12] have shown to be relatively insensitive to the spectrum assumed.

We wish to thank Mr. H. N. Fisher and Mr. W. K. Bonsack who assisted in reading the track plates, Mr. W. H. Voelker and Mr. R. L. Stearns of the betatron crew, and Dr. L. L. Foldy for their interest in this experiment.

[12] Johns, Katz, Douglas, and Haslam, Phys. Rev. **80**, 1062 (1950).

The Electromagnetic Properties of Dirac Particles*

L. L. FOLDY
Case Institute of Technology, Cleveland, Ohio
(Received April 30, 1952)

A framework for describing those electromagnetic properties of Dirac (spin-$\frac{1}{2}$) particles which determine their behavior when moving with low momentum through weak, slowly varying, external electromagnetic fields is developed by finding the most general interaction terms which may be added to the Dirac equation for the particle subject to appropriate conditions. The interaction terms found form an infinite series involving arbitrarily high derivatives of the electromagnetic potentials evaluated at the position of the particle. The series of coefficients of these terms then characterize the properties to be described and can be interpreted as a series of moments of the charge and current distribution associated with the Dirac particle. The first coefficient represents the charge of the particle, the second its anomalous magnetic moment. The third is a measure of the spatial extent of the particle's charge distribution, and the corresponding term describes a direct interaction of the particle and the charge distribution responsible for the external electromagnetic field. Higher terms in the series describe direct interactions of the particle with various derivatives of the external charge and current distribution. The correct physical interpretation of the terms is examined by transforming to the Foldy-Wouthuysen (nonrelativistic) representation of the Dirac equation. The consistency of the framework developed with field theoretical results is discussed. Limitations of the characterization derived here and the possibilities of broadening the assumptions on which it is based are examined. The results are applied in the succeeding paper to the interpretation of the electromagnetic properties of nucleons with particular reference to the electron-neutron interaction.

INTRODUCTION

THE present paper represents an attempt to characterize those electromagnetic properties of Dirac (spin-$\frac{1}{2}$) particles which determine their behavior when moving with low momentum through weak, slowly varying, external (classically describable) electromagnetic fields. For this purpose we assume that the particle satisfies a Dirac equation with terms representing the interaction with the electromagnetic field. The nature of the interaction terms which are included is determined by the following restrictions:

(a) that the equation be Lorentz covariant and gauge invariant;
(b) that the interaction be linear in the electromagnetic potentials (the assumption of weak fields);
(c) that the terms do not vanish in the limit of vanishing momentum of the Dirac particle;
(d) that the charge and current distribution associated with the Dirac particle be sufficiently localized that its interaction with slowly varying electromagnetic fields may be expressed, through an expansion in "moments," in terms of the electromagnetic potentials and arbitrarily high derivatives of these potentials evaluated at the position of the particle.

It is found that an infinite series of interaction terms can be found satisfying these restrictions. The coefficients of these terms then characterize the electromagnetic properties of the particle which we set out to describe and represent "moments" of various order of the charge and current distribution associated with the Dirac particle. The first two coefficients can be identified with the charge and anomalous (intrinsic) magnetic moment of the particle. The next term represents a direct interaction between the Dirac particle and the charge distribution which produces the external electromagnetic field. In the case of the neutron, the coefficient of this term characterizes the "intrinsic" electron-neutron interaction, that is, the part of the electron-neutron interaction which is not associated with the anomalous magnetic moment of the neutron.[1] Higher terms in the series describe the interaction of the particle with various derivatives of the charge and current distribution responsible for the electromagnetic field.

While the characterization of the electromagnetic properties of a Dirac particle by the series of coefficients mentioned above is based on the assumption that the particle satisfies the Dirac equation, it is believed that this characterization actually has greater validity and applies under more general assumptions. The S-matrix formalism provides a more general domain in which this problem may be examined, and the author hopes to investigate this more general problem in the future.

Although from the point of view of Lorentz covariance it is convenient to deal with the problem posed above in the usual Dirac representation of the Dirac equation, the physical interpretation of the interaction terms is facilitated by passing to the Foldy-Wouthuysen (nonrelativistic) representation of the Dirac equation.[2] The coefficients defining the interaction take different forms in the two representations and in describing an electromagnetic property of a Dirac particle it is necessary to specify the representation which is being employed in order to avoid ambiguity. The confusion concerning the electron-neutron interaction stems primarily from a confusion of representations, and it is hoped that the discussion given below will clarify this point. The results derived herein are applied in the subsequent paper to an analysis of the significance of

* The research was supported by the AEC. Some of the results contained herein were presented at the Columbus, Ohio, meeting of the American Physical Society, March 20–22, 1952.

[1] L. L. Foldy, Phys. Rev. **83**, 688 (1951).
[2] L. L. Foldy and S. A. Wouthuysen, Phys. Rev. **78**, 29 (1950).

the experimental results on the electron-neutron interaction.

ELECTROMAGNETIC INTERACTIONS OF DIRAC PARTICLES

The Dirac equation for a free particle can be written in the form

$$H\psi=\{\beta mc^2+c\boldsymbol{\alpha}\cdot\mathbf{p}\}\psi=i\hbar\partial\psi/\partial t, \tag{1}$$

where $\mathbf{p}=-i\hbar\nabla$, $\mathbf{x}$ is the position vector of the particle, β and $\boldsymbol{\alpha}$ are the familiar Dirac matrices, and m, c, and $\hbar$ are, as usual, the rest mass of the particle, the velocity of light, and Planck's constant (divided by 2π), respectively. It is convenient for our purposes to write Eq. (1) in manifestly covariant form:

$$\gamma_\mu\partial\psi/\partial x_\mu+(mc/\hbar)\psi=0, \tag{2}$$

by the use of the relations

$$x_\mu=(\mathbf{x}, ict), \quad \gamma_\mu=(-i\beta\boldsymbol{\alpha}, \beta),$$

with the usual summation convention applying in expressions involving repeated Greek indices.

If the particle has a charge e and interacts with an electromagnetic field specified by the four-vector potential $A_\mu(x)$, then Eq. (2) must be modified to read

$$\gamma_\mu\partial\psi/\partial x_\mu+(mc/\hbar)\psi-i(e/\hbar c)\gamma_\mu A_\mu\psi=0. \tag{3}$$

Although the addition of this term appears to imply that the Dirac particle has only a point charge, it is well known that in its interactions the particle behaves as if it also had a magnetic moment of one Bohr magnetron. Pauli[3] showed that Eq. (3) can be still further modified so as to represent a particle having an arbitrary magnetic moment by adding to the left side the term $-(i\mu/\hbar c)\gamma_\mu\gamma_\nu(\partial A_\mu/\partial x_\nu-\partial A_\nu/\partial x_\mu)$, whereupon the particle behaves as if it had an "anomalous" moment μ in addition to its "normal" moment.

One may inquire as to the degree to which one can add further interaction terms to Eq. (3) without destroying its relativistic covariance and gauge invariance. One easily finds that a great variety of terms may be added. If one restricts oneself to such terms as satisfy the conditions specified in the introduction, namely, terms which are linear in the electromagnetic potentials, which depend on these potentials and their derivatives evaluated only at the position of the particle, and which do not vanish in the limit of vanishing momentum of the particle (quasi-static interactions) and hence do not involve derivatives of the wave function, then one can easily construct all possible terms. This calculation is given in the appendix; the result for the most general equation is[4]

$$\gamma_\mu\frac{\partial\psi}{\partial x_\mu}+\frac{mc}{\hbar}\psi-\frac{i}{\hbar c}\sum_{n=0}^{\infty}\Big[\epsilon_n\Box^n\gamma_\mu A_\mu+\mu_n\Box^n\gamma_\mu\gamma_\nu\Big(\frac{\partial A_\mu}{\partial x_\nu}-\frac{\partial A_\nu}{\partial x_\mu}\Big)\Big]\psi=0, \tag{4}$$

where $\Box$ stands for the d'Alembertian operator:

$$\Box=\partial^2/\partial x_\sigma\partial x_\sigma=\nabla^2-\partial^2/c^2\partial t^2.$$

The coefficients ϵ_n and μ_n are constants characterizing the interactions, of which ϵ_0 may immediately be identified as the electric charge of the Dirac particle and μ_0 as its anomalous magnetic moment. The higher terms in the series represent a direct interaction between the Dirac particle and the charge and current distribution which produces the external electromagnetic field as may be seen by employing the equations

$$\Box A_\mu=-4\pi j_\mu, \quad F_{\nu\mu}=\partial A_\mu/\partial x_\nu-\partial A_\nu/\partial x_\mu, \tag{5}$$

with

$$j_\mu=(\mathbf{j}, i\rho), \quad F_{\nu\mu}=(\mathbf{H}, i\mathbf{E}),$$

to rewrite Eq. (4) in the form

$$\gamma_\mu\frac{\partial\psi}{\partial x_\mu}+\frac{mc}{\hbar}\psi-\frac{i}{\hbar c}\Big\{\epsilon_0\gamma_\mu A_\mu+\mu_0\gamma_\mu\gamma_\nu F_{\nu\mu}-4\pi\sum_{n=1}^{\infty}\Big[\epsilon_n\Box^{n-1}\gamma_\mu j_\mu+\mu_n\Box^{n-1}\gamma_\mu\gamma_\nu\Big(\frac{\partial j_\mu}{\partial x_\nu}-\frac{\partial j_\nu}{\partial x_\mu}\Big)\Big]\Big\}\psi=0. \tag{6}$$

The remainder of this paper is concerned with a more direct physical interpretation of these interaction terms.

However, before proceeding with this aspect of the problem, we wish to comment briefly on the domain of validity of an equation of the type (4). It is very unlikely that there exist any real particles which satisfy an equation of this type rigorously. However, it is not necessary that the equation be satisfied rigorously for the characterization of the electromagnetic structure of the particle by the coefficients ϵ_n and μ_n to be valid. In fact we may assume that the interaction terms in (4) must be treated only by first-order perturbation theory (Born approximation) since we have limited ourselves to the case of terms linear in the electromagnetic field. In this case, Eq. (4) may be used to calculate the S-matrix in the Born approximation for the elastic scattering of the Dirac particle in an external electromagnetic field, and the elements of the S-matrix will then depend on the coefficients ϵ_n and μ_n in a definite way. Equation (4) may then be considered as reduced to playing the role of an equation which gives the same S-matrix for weak electromagnetic fields as will be yielded by some more elaborate and fundamental theory. That Eq. (4) can actually play such a role is demonstrated by the usual treatment of the problem of

[3] W. Pauli, Revs. Modern Phys. **13**, 203 (1941).

[4] That the meson theory expression for the modification of the convection current of a nucleon due to interaction with mesons can be put into the form of the term in ϵ_1 in Eq. (4) was pointed out to the author by Professor F. Villars in a private communication.

the modification of the interaction of a nucleon with an electromagnetic field due to the interaction of the nucleon with a meson field. In this case an equation of the form (4) can be written down with determined values of the coefficients which will yield the same result in the Born approximation for the elastic scattering part of the S-matrix as is yielded by the more fundamental methods of field theory. The characterization by the coefficients ϵ_n and μ_n of certain of the electromagnetic properties of a Dirac particle may thus have a domain of validity much wider than would be indicated by the basis on which it was derived. This is the reason for our earlier remark that it would be of interest to reinvestigate this problem directly from the point of view of the S-matrix and its invariance properties rather than from a wave equation.

PHYSICAL INTERPRETATION OF THE DIRAC EQUATION

The physical interpretation of the interaction terms contained in Eq. (4) requires considerable care; that this is the case can already be seen in the special case represented by Eq. (3), for an examination of this equation itself would lead one to the conclusion that the interaction of the Dirac particle with the electromagnetic field is simply that of a point electric charge. Actually, as mentioned above, it is well known that the Dirac particle described by this equation exhibits in its electromagnetic interactions not only the properties of a point charge but also more complex properties, ordinarily characteristic of a particle possessing an extended charge and current distribution, as, for example, a magnetic moment.

As has been demonstrated in a previous publication,[2] the electromagnetic properties of a Dirac particle may be exhibited in a very direct way by transforming the Dirac equation into a new representation in which states of positive and negative energy for the particle are separately represented by two-component wave functions. The unitary transformation which generates the new representation leads to the introduction of a new position operator (the Newton-Wigner position operator[8]) for the particle which can more readily be identified with the conventional position operator for a particle. The modification in form of the electromagnetic interaction of the particle can then be traced directly to the fact that the interaction in the new representation is expressed in terms of the electromagnetic potentials and their derivatives evaluated at this new position which is displaced by a finite distance from the Dirac position which occurs in the usual representation of the Dirac equation. Actually, in the presence of interaction, the generating function for the transformation to the new representation can only be obtained as a series expansion in powers of the Compton wavelength of the particle and consequently the Hamiltonian occurring in the new form of the Dirac equation is also obtained as a power series in the same parameter. Details of the transformation are given in the reference quoted and hence will not be discussed here. If the transformation is carried out on Eq. (3), the Dirac equation takes the form[6]

$$\left\{\beta mc^2+\frac{\beta}{2m}\left(\mathbf{p}-\frac{e}{c}\mathbf{A}\right)^2+e\varphi-\frac{e\hbar}{2mc}\beta\boldsymbol{\sigma}\cdot\mathbf{H}\right.$$
$$+\frac{e\hbar}{8m^2c^2}\left[\boldsymbol{\sigma}\cdot\left(\mathbf{p}-\frac{e}{c}\mathbf{A}\right)\times\mathbf{E}-\boldsymbol{\sigma}\cdot\mathbf{E}\times\left(\mathbf{p}-\frac{e}{c}\mathbf{A}\right)\right]$$
$$\left.-\frac{e\hbar^2}{8m^2c^2}\operatorname{div}\mathbf{E}+\cdots\right\}\psi=i\hbar\frac{\partial\psi}{\partial t}, \quad (7)$$

where we have retained terms to order $(\hbar/mc)^2$ relative to the rest energy of the particle. It will be noted that the electromagnetic interaction is now expressed in a relatively complicated way but that one may immediately recognize the physical significance of the various terms:

(a) The term

$$e\varphi-(e\beta/2mc)[(\mathbf{p}-e\mathbf{A}/c)\cdot\mathbf{A}+\mathbf{A}\cdot(\mathbf{p}-e\mathbf{A}/c)]$$

represents the interaction of a point charge e with the electromagnetic field.

(b) The term $-(e\hbar/2mc)\beta\boldsymbol{\sigma}\cdot\mathbf{H}$ expresses the interaction of a magnetic moment of one Bohr magneton with the magnetic field.

(c) The term

$$(e\hbar/8m^2c^2)[\boldsymbol{\sigma}\cdot(\mathbf{p}-e\mathbf{A}/c)\times\mathbf{E}-\boldsymbol{\sigma}\cdot\mathbf{E}\times(\mathbf{p}-e\mathbf{A}/c)]$$

represents the "spin-orbit" coupling associated with this magnetic moment; it arises from the fact that the motion of the magnetic moment gives rise to an electric moment for the particle which interacts with the electric field.

(d) The term $-(e\hbar^2/8m^2c^2)\operatorname{div}\mathbf{E}$ (the so-called "Darwin" term)[7] can be interpreted in the following way: if the charge of the particle is not concentrated at a point but is spread out over a small spherical volume, then the first-order correction to the point charge interaction is represented by this term. Since $\operatorname{div}\mathbf{E}=4\pi\rho$, where ρ is the density of charge giving rise to the external electromagnetic field, this term expresses a direct interaction of the Dirac particle with the charge distribution generating the external electromagnetic field.

(e) Higher order terms in the series which have not been written down describe interaction terms depending

[8] T. D. Newton and E. P. Wigner, Revs. Modern Phys. **21**, 400 (1949).

[6] The last section of the paper quoted in reference 2 contains a number of errors and misprints in its equations. The correct form of Eq. (36) of that reference is given in Eq. (7) of the present paper.

[7] C. G. Darwin, Proc. Roy. Soc. (London) **A118**, 654 (1928). The term we call the Darwin term is not identical with that introduced by Darwin in this reference. The difference is due to the fact that Darwin does not write his spin-orbit coupling term as a Hermitian operator.

on higher derivatives of the electromagnetic fields evaluated at the Newton-Wigner position of the particle. All such terms can be written as for (d) above directly in terms of the charge and current distributions which generate the external electromagnetic field. For example, the next term in the series is proportional to $\beta\boldsymbol{\sigma}\cdot\mathbf{curl}\mathbf{j}$, where $\mathbf{j}$ is the current density generating the external electromagnetic field.

The direct physical interpretation of the various terms occurring in the Hamiltonian is possible since the wave function for the Dirac particle in a state of definite energy is just the usual Pauli wave function with well-known properties.

We can then interpret physically the interaction terms in our more general equation (4) by transforming it into the same representation. The methods given in the reference quoted above are directly applicable here, and we only quote the result:

$$\left\{\beta mc^2+\frac{\beta p^2}{2m}+\sum_{n=0}^{\infty}\left[\left\{\epsilon_n+\frac{\hbar}{2mc}\mu_{n-1}+\frac{1}{2}\left(\frac{\hbar}{2mc}\right)^2\epsilon_{n-1}+\cdots\right\}\Box^n\varphi-\left\{\mu_n+\frac{\hbar}{2mc}\epsilon_n+\frac{1}{2}\left(\frac{\hbar}{2mc}\right)^2\mu_{n-1}+\cdots\right\}\Box^n\beta\boldsymbol{\sigma}\cdot\mathbf{H}\right]\right\}\psi=i\hbar\frac{\partial\psi}{\partial t}. \quad (8)$$

In writing down this equation we have again indicated explicitly only those terms which are of no higher order than $(\hbar/mc)^2$ relative to the rest energy term. Also, in view of the fact that we have omitted terms nonlinear in the electromagnetic field and interaction terms which vanish for vanishing momentum of the particle in Eq. (4), we have likewise omitted such terms in Eq. (8). This explains the absence of the point-current term and the spin-orbit coupling term (for example) in this last equation.

We can now analyze the physical significance of the various interaction terms in Eq. (8). It will be noted that they fall into two general classes—electric interactions and magnetic interactions. In particular, we may note:

(a) The term $\epsilon_0\varphi$ represents the usual point charge interaction of the particle with the scalar potential which allows us immediately to identify it with the electric charge of the particle.

(b) The term $\{\mu_0+(\hbar/2mc)\epsilon_0\}\beta\boldsymbol{\sigma}\cdot\mathbf{H}$ represents the interaction of a magnetic moment of magnitude $\mu_0+(\hbar/2mc)\epsilon_0$ with the magnetic field. Since $(\hbar/2mc)\epsilon_0$ represents just the normal moment for the particle, μ_0 can immediately be identified with the anomalous or "intrinsic" magnetic moment of the particle.

(c) The term $\{\epsilon_1+(\hbar/2mc)\mu_0+\frac{1}{2}(\hbar/2mc)^2\epsilon_0\}\Box\varphi$ has just the form of a "Darwin" term ($\Box\varphi=-\mathrm{div}\mathbf{E}=-4\pi\rho$) and so represents a direct interaction of the particle with the charge density of the sources of the electromagnetic field. It consists of three contributions, the part depending on $\frac{1}{2}(\hbar/2mc)^2\epsilon_0$, which is just the ordinary Darwin term, a contribution depending on $(\hbar/2mc)\mu_0$ and therefore arising from the anomalous magnetic moment, and an "intrinsic" part depending on ϵ_1. To have a name for this last quantity we shall call it the "intrinsic" Darwin coefficient for the particle. In the case of the neutron, it determines the "intrinsic" electron-neutron interaction, that is, the portion of this interaction not accounted for by the anomalous moment of the neutron.

(d) Further terms in the series have a character similar to the higher order terms described briefly in our earlier example. It will be noted that every coefficient ϵ_n or μ_n in the Dirac representation of the equation appears not only in the coefficient of the corresponding term in the Foldy-Wouthuysen representation but in the coefficients of all succeeding terms.

It is thus apparent that the same electromagnetic interaction which is described by the set of coefficients $\epsilon_0, \mu_0, \epsilon_1, \cdots$ in the Dirac representation is described by the alternate set of coefficients ϵ_0, $\mu_0+(\hbar/2mc)\epsilon_1$, $\epsilon_1+(\hbar/2mc)\mu_0+\frac{1}{2}(\hbar/2mc)^2\epsilon_0, \cdots$ in the Foldy-Wouthuysen representation. Although the latter coefficients have the more direct physical interpretation, it is presumed that the coefficients in the Dirac representation should be regarded as having the more fundamental significance. The important point, however, is that it is necessary to specify the representation of the Dirac equation to which one is referring in order to describe unambiguously the electromagnetic properties of a Dirac particle.

DISCUSSION

The development presented above may be considered to be a phenomenological description of certain electromagnetic properties of Dirac particles. In this sense it represents a framework into which may be fitted either empirical or theoretical values of the characterizing coefficients. Of course there is no binding reason why values of the coefficients determined empirically cannot be considered to be intrinsic properties of the particle which cannot be determined by any more fundamental theory, but this would represent a very unsatisfying conclusion. It is the general hope that the values are actually determined through the interactions of the particle with quantized fields; that the latter is very probably the true state of affairs is strongly suggested by the recent developments in the quantum electrodynamics of the electron. In spite of the fact that the rather unsatisfactory device of infinite renormalizations must be employed in this theory, one cannot ignore the fact that all observed electromagnetic properties of the electron find a correct quantitative prediction in terms of only two fundamental parameters, the observed charge and mass of this particle.

In view of the fact that we know at present more concerning the electromagnetic properties of the electron than any other particle, it is of interest to see if this knowledge can be fitted into the framework that we have constructed. Unfortunately, we encounter a rather unexpected difficulty. Examining the results of Schwinger,[8] for example, we find that there is no difficulty in identifying ϵ_0 immediately with the observed electric charge of the electron, $-|e|$, and further identifying the anomalous magnetic moment of the electron as

$$\mu_0 = -\frac{1}{2\pi}\frac{e^2}{\hbar c}\frac{|e|\hbar}{2mc} + \cdots$$

(where the dots represent further contributions of higher order in e). However, we encounter a problem with the intrinsic Darwin coefficient, for there is no finite quantity that can be identified with this coefficient. The quantity that would play this role in the expressions given by Schwinger is represented by a divergent integral. The "infrared catastrophe" involved in this result is known, however, to be canceled by an associated "infrared catastrophe" arising from the radiation of real photons by the electron in so far as the calculation of any result of physical significance is concerned. Why is our theory inadequate to deal with this problem? It is not difficult to find the answer when we examine the premises on which our description is derived. We have assumed that there exists some approximation in which the behavior of the particle can be described by our original Dirac equation, or at least that the elastic scattering part of the S-matrix may be computed from this equation. However, for an electron interacting with the quantized electromagnetic field whose quanta have zero rest mass, there exists no such elastic scattering part of the S-matrix. If the electron is scattered, however weakly, by an external electromagnetic field, it will of necessity radiate some low energy photons. This difficulty will therefore be present for any particle as well as for the electron when interaction with the quantized electromagnetic field is taken into account. We need not be too concerned over this failure of our formulation of the electromagnetic properties of Dirac particles, since the origin of the failure is well understood, and we have available in quantum electrodynamics the machinery for correcting this defect. In fact, an approximate repair of the theory may be made regarding a scattering in which the electron loses no more than some small part of its energy by radiation as an "elastic" scattering and then replacing the divergent integral which represents the intrinsic Darwin term by a finite integral by an appropriate modification of the lower limit in the original integral. On the other hand, we believe that we must not regard this inadequacy of our theory too lightly since it illustrates sufficient weakness in the foundation on which it rests to seriously limit its applicability.

We may expect that our theory may be more successful when coping with cases where the electromagnetic properties of the Dirac particle are determined principally by its interaction with a quantized field whose quanta have nonvanishing rest mass. Such a case is exemplified in the modification of the electromagnetic properties of nucleons through their interaction with a meson field. Since this problem is discussed in the following paper, we do not enter into details here but merely mention that recent calculations bear out this expectation, although calculated values are at great variance with the observed properties of nucleons. The important point, however, is that there is no difficulty in identifying in these calculations the characteristic coefficients which we have postulated in our formalism. This is sufficient to show that the division of the electron-neutron interaction into two contributions—one arising from the anomalous magnetic moment of the neutron and the other from an intrinsic Darwin coefficient—is justifiable in meson theory even though both of these contributions have a common origin.

Another point in regard to our description of the electromagnetic properties of Dirac particles worth some discussion is the question of the convergence of the series of interaction terms we have introduced into the Dirac equation. The convergence of the series depends, of course, on the nature of the external electromagnetic field and in particular on how rapidly it varies in space and time. One would expect that this series would be convergent for sufficiently slowly varying electromagnetic fields but that the convergence would cease when the fields varied appreciably over the charge and current distribution associated with the particle whose moments determine the values of our coefficients. It is reasonable to assume, however, that the values of the coefficients we have given may still determine the interaction with rapidly varying fields in the following manner: We consider the electromagnetic field to be expanded in a Fourier integral in space and time and deal with one Fourier component. The series of interaction terms then has the form of a power series expansion in the wave vector and frequency of this Fourier component and presumably this series will converge for sufficiently small values of these quantities. For larger values of the wave vector and frequency we may analytically continue the function represented by the series beyond the radius of convergence and assume that this represents the interaction for higher values of the wave vector and frequency. If the analytic continuation process can be extended over the whole complex plane for these variables, then the series of initial coefficients will characterize the interaction with electromagnetic fields of arbitrarily rapid variation.

We should mention also that if the coefficients ϵ_n and μ_n actually represent moments of the charge and

[8] J. Schwinger, Phys. Rev. **76**, 790 (1949).

current distribution associated with the particle, then these coefficients themselves can be finite only if this charge and current density ultimately fall off faster with distance from the particle than any inverse power of this distance. When this is not the case our representation obviously fails, for some coefficients in the series will then be infinite.

Our primary purpose in setting up the characterization of the electromagnetic properties of Dirac particles presented above has been to provide a framework for the interpretation of the experimental results on the electron-neutron interaction as given in the following paper. However, we regard our results as quite tentative and have emphasized the shortcomings of our characterization to indicate how urgently a more satisfactory characterization is needed.

APPENDIX

We consider the problem of constructing all possible Lorentz scalars formed from the Dirac matrices γ_μ and the four-vector A_μ of the electromagnetic potentials, and its derivatives, which are linear in A_μ. We employ a Lorentz gauge so that A_μ satisfies the equation

$$\partial A_\mu/\partial x_\mu=0. \tag{A-1}$$

We proceed by examining in succession invariants of the form

$$\gamma_\tau\cdots\gamma_\sigma\gamma_\nu\gamma_\mu\partial^n A_\mu/\partial x_\tau\cdots\partial x_\sigma\partial x_\nu.$$

The first of these containing one γ is $\gamma_\mu A_\mu$. The next containing two γ's is

$$\gamma_\nu\gamma_\mu\partial A_\mu/\partial x_\nu,$$

which we may transform by the use of the commutation relations of the γ's,

$$\gamma_\mu\gamma_\nu+\gamma_\nu\gamma_\mu=2\delta_{\mu\nu},$$

in the following way:

$$\begin{aligned}\gamma_\nu\gamma_\mu\partial A_\mu\partial x_\nu&=\tfrac{1}{2}(\gamma_\nu\gamma_\mu-\gamma_\mu\gamma_\nu+2\delta_{\mu\nu})\partial A_\mu/\partial x_\nu\\&=\tfrac{1}{2}\gamma_\nu\gamma_\mu(\partial A_\mu/\partial x_\nu-\partial A_\nu/\partial x_\mu).\end{aligned}$$

With three γ's we may form and reduce the invariant

$$\begin{aligned}&\gamma_\sigma\gamma_\nu\gamma_\mu\partial^2 A_\mu/\partial x_\sigma\partial x_\nu\\&\quad=\tfrac{1}{2}[\gamma_\sigma\gamma_\nu-\gamma_\nu\gamma_\sigma+2\delta_{\nu\sigma}]\gamma_\mu\partial^2 A_\mu/\partial x_\sigma\partial x_\nu\\&\quad=\gamma_\mu\partial^2 A_\mu/\partial x_\nu\partial x_\nu=\gamma_\mu\Box A_\mu.\end{aligned}$$

By continuation of this process one readily finds that the most general invariants which may be formed belong to one of the two classes:

$$\gamma_\mu\Box^n A_\mu,\quad \gamma_\nu\gamma_\mu\Box^n(\partial A_\mu/\partial x_\nu-\partial A_\nu/\partial x_\mu),$$

where n is any non-negative integer.

PHYSICAL REVIEW VOLUME 87, NUMBER 5 SEPTEMBER 1, 1952

The Electron-Neutron Interaction*

L. L. FOLDY
Case Institute of Technology, Cleveland, Ohio
(Received April 30, 1952)

The known electromagnetic properties of nucleons, assuming that the electron-neutron interaction is fundamentally of electromagnetic origin, are fitted into the phenomenological framework developed in the preceding paper and the results compared with predictions of weak coupling meson theories. The detailed comparison shows that the intrinsic electron-neutron interaction is somewhat smaller than predicted and it is suggested that even in the more favorable cases, the rough agreement as to order of magnitude may be largely due to a fortuitious cancellation of different contributions, which may easily be upset when higher order effects are included in the theory. Even apart from the detailed calculations, it is indicated that the observed intrinsic electron-neutron interaction is considerably smaller than order-of-magnitude expectations from general meson-theoretical principles. The results emphasize the importance of more accurate experimental determinations of the electron-neutron interaction, since a smaller value of the intrinsic interaction will either pose a very stringent test for any meson theory or require a critical re-evaluation of our present ideas regarding nucleonic structure. Some phenomena related to the electron-neutron interaction and the possibility that the intrinsic interaction may be nonelectromagnetic in origin are briefly discussed.

RECENT measurements of the magnitude of the electron-neutron interaction by Hughes[1] and by Hamermesh, Ringo, and Wattenberg,[2] when combined with previous measurements by Fermi and Marshall,[3] and by Havens, Rabi, and Rainwater,[4] now yield an experimental value for this quantity with an accuracy of the order of ten percent. While there appear prospects for a considerably more accurate determination of this interaction in the near future, it appears appropriate, nevertheless, to examine the available results in the

* This work was supported by the AEC. Some of the results contained herein were presented at the Columbus, Ohio, meeting of the American Physical Society, March 20–22, 1952. [Phys. Rev. 86, 646 (1952)].

[1] D. J. Hughes, New York meeting of the American Physical Society [Phys. Rev. 86, 606 (1952)].

[2] Hamermesh, Ringo, and Wattenberg, Phys. Rev. 85, 483 (1952).

[3] E. Fermi and L. Marshall, Phys. Rev. 72, 1139 (1947).

[4] Havens, Rainwater, and Rabi, Phys. Rev. 82, 345 (1951).

light of current notions concerning the origin of this interaction at the present time. Such an examination as given in this paper indicates the possibility of a rather severe conflict between these experimental results and current ideas which ascribe the electron-neutron interaction to the charge cloud of virtual mesons surrounding the neutron. The importance of further and more accurate measurements of the electron-neutron interaction is thus emphasized.

We begin with a summary of experimental results concerning the electromagnetic properties of nucleons and their characterization in the phenomenological scheme developed in the preceding paper. The results are then compared with expectations from meson theory and some of the difficulties discussed. Finally the possibility of a nonelectromagnetic origin of the electron-neutron interaction is considered and some other phenomena which bear on this question are briefly discussed.

At the present time we have experimental knowledge concerning four purely electromagnetic properties of nucleons, namely, (1) the charge on the proton $=|e|$ where e is the electronic charge, (2) the magnetic moment of the proton $=2.7896$ nuclear magnetons, (3) the magnetic moment of the neutron $=-1.9135$ nuclear magnetons, and (4) the electron-neutron interaction. The last quantity is a short range interaction between a neutron and an electron which is given (perhaps prematurely) an electromagnetic interpretation by considering it to be a direct interaction of the neutron with the charge density responsible for an electromagnetic field. The experimental determinations of this interaction have been executed only in the case where this charge density is that associated with electrons in atoms, hence the ascription of the name electron-neutron interaction. Its magnitude is usually specified by the convention of giving the magnitude of the potential which must extend over a spherical volume of radius equal to the classical electron radius e^2/mc^2 which will give the same scattering matrix element at low energies as does the actual interaction.[5] The experimental determinations of this potential V_0 are given in Table I together with their weighted mean. At present we have no information concerning the corresponding interaction for the proton.

TABLE I. Experimental determinations of the electron-neutron interaction V_0.

Investigators	V_0, ev
Fermi and Marshall	-300 ± 5000
Havens, Rabi, and Rainwater	-5300 ± 1000
Hughes	-4200 ± 700
Hammermesh, Ringo, and Wattenberg	-4100 ± 1000
Weighted mean	-4400 ± 400
Contribution of magnetic moment	-4080
Residual (intrinsic interaction)	-320 ± 400

[5] The use of the classical electron radius is very arbitrary and somewhat inappropriate, since this radius presumably has nothing to do with the actual range of the interaction. In fact, as will be clearer later, the Compton wavelength of the neutron would be a considerably more appropriate radius to employ.

We may note first by a comparison of these results with the phenomenological framework developed in the preceding paper[6] for characterizing electromagnetic properties of Dirac particles, that this framework is adequate for the description of experimental results. Thus for the proton we may immediately identify ϵ with the charge of the proton and μ_0 with the anomalous magnetic moment of the proton:

$$\epsilon_0{}^p=|e|, \quad \mu_0{}^p=1.7896|e|\hbar/2Mc.$$

We have no information concerning the values of the succeeding coefficients $\epsilon_1{}^p$, $\mu_1{}^p$, etc.

Correspondingly, we have for the neutron the identifications:

$$\epsilon_0{}^n=0; \quad \mu_0{}^n=-1.9135|e|\hbar/2Mc.$$

The electron-neutron interaction, however, allows us to obtain a rough value for the next coefficient $\epsilon_1{}^n$. To obtain this we note that the volume integral of the term in $\mathrm{div}\mathbf{E}=-\Box\varphi$ in Eq. (8) of the preceding paper, where $\mathbf{E}$ is the electric field due to an electron, may be immediately identified with V_0 multiplied by the volume over which it is assumed to exist:

$$\frac{4\pi}{3}\left(\frac{e^2}{mc^2}\right)^3 V_0=|e|\left\{\epsilon_1{}^n+\frac{\hbar}{2Mc}\mu_0{}^n+\frac{1}{2}\left(\frac{\hbar}{2Mc}\right)^2\epsilon_0{}^n\right\}.$$

The last term in the brackets on the right vanishes for the neutron, and the second term in the brackets, as shown in a previous publication,[7] accounts for -4080 ev of the observed potential V_0. The remainder -320 ± 400 ev then yields for $\epsilon_1{}^n$ the value

$$\epsilon_1{}^n=-(0.08\pm0.10)|e|(\hbar/Mc)^2.$$

Before discussing these results further we compare them with the predictions obtained from meson theory in the limit of weak coupling.[8] A direct comparison is made somewhat difficult by the fact that the meson theory results depend on the value of the coupling constant assumed. To circumvent this difficulty we have tabulated in Table II the values of the ratios $\epsilon_1{}^n/(\mu_0{}^n\hbar/2Mc)$ and $\mu_0{}^p/\mu_0{}^n$ which, in weak coupling theory, are independent of the choice of coupling constant. However, it must be remembered that this

[6] L. L. Foldy, Phys. Rev. **87**, 688 (1952) (preceding paper).

[7] L. L. Foldy, Phys. Rev. **83**, 688 (1951). The difference between the present value quoted for the contribution of the neutron's magnetic moment and that quoted in this reference (-3900 ev) is due simply to the use of very rough values for fundamental constants in the previous calculation. The present value should be correct to approximately 1 ev. See also G. Breit, Proc. Nat. Acad. Sci. U. S. **37**, 837 (1951).

[8] J. M. Luttinger, Phys. Rev. **74**, 893 (1948); M. Slotnick and W. Heitler, Phys. Rev. **75**, 1645 (1949); Helv. Phys. Acta **21**, 1645 (1949); K. M. Case, Phys. Rev. **76**, 1 (1949); S. M. Dancoff and S. D. Drell, Phys. Rev. **76**, 205 (1949); S. Borowitz and W. Kohn, Phys. Rev. **76**, 818 (1949); B. D. Fried (to be published).

will no longer be the case if higher order terms in the meson theory were retained. Calculations have been made for the neutral, charged, and symmetrical scalar and pseudoscalar theories. The calculations for the neutral theory have been omitted from Table II since they lead to zero neutron magnetic moment and zero electron-neutron interaction.

An examination of the table shows immediately that it is not possible to fit simultaneously the nucleon magnetic moments and the electron-neutron interaction to the observed results by any choice of the coupling constant in any of these theories. The best fit is provided by the charged pseudoscalar theory but this can hardly be taken as evidence for its validity. Of particular interest, however, is the sensitivity of the electron-neutron interaction to the type of meson theory. There is a difference of a factor of thirty between the results in the scalar and the pseudoscalar theories. The pseudoscalar result is somewhat smaller than one would expect on rough dimensional grounds and this suggests that its smallness is at least partly the result of an accidental cancellation. This conjecture appears to be substantiated by some calculations of the author of the value of the ratio $\epsilon_1{}^n/(\mu_0{}^n\hbar/2Mc)$ as a function of the ratio of meson to nucleon mass. These calculations indicate this quantity is positive for small mass ratio but becomes negative for larger mass ratios, and the result passes through zero not far from the experimental ratio of pi-meson to nucleon mass. This is an important point, since if we do have an accidental near cancellation in the pseudoscalar theory, it is likely to be upset when other effects (higher order corrections, for example) are included and the discrepancy with the experimental value thereby increased. The smallness of the observed intrinsic electron-neutron interaction would then be a very stringent test for any meson theory. In this connection, the discrepancy by a factor of one hundred (even apart from the discrepancy in sign) between the experimental value of $\epsilon_1{}^n/(\mu_0{}^n\hbar/2Mc)$ and that predicted by the scalar meson theory would seem to be a strong argument against this theory, since it indicates that either the meson charge cloud in this theory is far too extended or the region over which the currents that give rise to the anomalous moment are distributed is far too compact.[9]

The discrepancies between the experimental results and meson theory calculations is not too surprising in view of the other well-known deficiencies of meson theory. However, there is nevertheless a rather striking anomaly in the experimental results which can be stated in a manner which is independent of any direct reference to meson theory. We may see this by remembering that at the present time we know of only two electromagnetic interactions of the neutron (remembering that the neutron has no electric charge) which are

[9] This is due, of course, to the fact that in the scalar theory, the charge cloud is produced principally by the mesons, but the mesons do not contribute to the magnetic moment.

TABLE II. Comparison of experimental results on electromagnetic properties of nucleons with predictions of weak coupling meson theories.[a]

Theory	$\epsilon_1{}^n/(\mu_0{}^n\hbar/2Mc)$	$\mu_0{}^p/\mu_0{}^n$
Symmetrical pseudoscalar	0.318	−0.128
Charged psuedoscalar	0.318	−0.422
Symmetrical scalar	−9.05	0.627
Charged scalar	−9.05	0.088
Experimental	0.08±0.10	−0.935

[a] The theoretical values in this table have been compiled from the publications listed in reference 8.

measured by the two fundamental parameters: $\mu_0{}^n$ the magnetic moment of the neutron, and $\epsilon_1{}^n$ the intrinsic Darwin coefficient which measures the intrinsic electron-neutron interaction. The ratio of these two parameters $\epsilon_1{}^n/\mu_0{}^n$ is a quantity of the dimensions of a length and represents the only "electromagnetic radius" of the neutron of which we have present knowledge. The experimental ratio is $\epsilon_1{}^n/\mu_0{}^n=(0.04\pm0.05)\hbar/Mc$ and is, therefore, twenty-five times smaller than the "mechanical radius" of the neutron given by the neutron's Compton wavelength. This is certainly much smaller than would be expected from any *a priori* notions. This odd disparity can be demonstrated in another way: if we assume that q represents the effective distributed electric charge of the neutron and that the charge and current of the neutron are both spread over a spherical volume whose radius is of the order a, then we would expect

$$\epsilon_1{}^n\sim qa^2, \quad \mu_0{}^n\sim qa.$$

Solving these for q and a we find

$$a\sim\epsilon_1{}^n/\mu_0{}^n\sim0.04\hbar/Mc, \quad q\sim(\mu_0{}^n)^2/\epsilon_1{}^n\sim-25|e|,$$

which is a result quite out of line with current notions. If we assume that the effective distributed charge of the neutron is actually of the order of $-|e|$, then we must assume that the charge density of the neutron is spread over a region whose radius is of the order of 1/25 of the radius of the region over which the current density of the neutron is distributed.

The situation is not quite so dark as painted above, however, when we note that in the pseudoscalar meson theory we find also a small theoretical value for the ratio $\epsilon_1{}^n/\mu_0{}^n$, namely, $0.16\hbar/Mc$. An explanation for the smallness of this result may be formulated as follows: In the pseudoscalar theory, the emission of a negative meson by a neutron (which simultaneously is converted into a proton) is accompanied by a relatively large recoil of the proton. Hence, not only is the negative meson charge spread out over a finite volume, but so also is the positive proton charge. If the spatial spread of the two is nearly the same, the intrinsic electron-neutron interaction will be considerably reduced over its value when the recoil of the proton is neglected. Hence the smallness of the interaction in the pseudoscalar theory probably results from a cancellation

between the negative meson charge distribution and the positive proton charge distribution. This conjecture is substantiated by the fact that the intrinsic electron-neutron interaction changes sign when the meson mass becomes comparable with the nucleon mass, indicating that in this case because of the larger proton recoil, the proton charge is actually spread over a larger volume than the meson charge. Also in line with this explanation is the fact that in the scalar theory where the proton recoil is relatively smaller, the computed electron-neutron interaction is considerably larger than in the pseudoscalar theory. However, it should also be mentioned that the failure of the pseudoscalar meson theory to give approximately equal but opposite anomalous magnetic moments to the proton and neutron, as observed experimentally, seems also to be due to the large nucleon recoil effects;[10] this would suggest a difficulty in formulating a meson theory which simultaneously yields a small intrinsic electron-neutron interaction and approximately equal and opposite anomalous magnetic moments for the proton and neutron.

Our discussion above has been based on the assumption that the intrinsic electron-neutron interaction is essentially an electromagnetic interaction between the neutron and the charge density producing an external electromagnetic field. If this is a valid assumption, then the short range interaction of the neutron with an electron is not specific to the electron but would be present in the interaction of the neutron with any charged particle to the same magnitude but with a sign corresponding to an attraction between the neutron and negatively charged particles and repulsion between the neutron and positively charged particles. It is, in principle, possible to detect this interaction in the case of the neutron-proton interaction, but the presence of the large specifically nuclear interaction whose exact nature is not known makes this unfeasable at the present time.[11] The possibility of detecting a neutron-positron interaction or the interaction of a neutron and mu-mesons also appears very remote at the present time in view of the experimental difficulties. The interaction of the neutron and charged pi-mesons is also obscured, in this case by a strong meso-nucleonic interaction of nonelectromagnetic origin about which we also know very little. Hence, it is not likely that we may verify the assumption that the observed intrinsic electron-neutron interaction is fundamentally electromagnetic in nature in the near future. The detection of an intrinsic short range electron-proton interaction arising from a nonzero intrinsic Darwin coefficient for the proton is also possible, in principle, from its contribution to the Lamb shift in hydrogen, but some refinement of both the theory and the experimental determination of the Lamb shift is necessary before a quantitative result would be available. In this connection, we may also note that the electron-neutron interaction would be expected to contribute to a very slight difference in the Lamb shift in hydrogen and deuterium.

Before closing, it is of interest to consider the possibility of nonelectromagnetic contributions to the intrinsic electron-neutron interaction. Since this interaction can be formulated as a direct interaction between two incoming and two outgoing Dirac particles, one can express it in a manner analogous to beta-decay interactions—that is, as a Fermi-type coupling. It might even be expected that, in view of other evidence for the existence of a universal Fermi interaction between all fermions, such a Fermi interaction between neutrons and electrons should exist. If the entire intrinsic electron-neutron interaction were represented by a Fermi interaction, the corresponding coupling constant G_{e-n}, which has the dimensions erg-cm^3, can be directly identified with the observed volume integral of the electron-neutron interaction and, expressed in absolute units, would have the value

$$G_{e-n}=(5\pm 6)\times 10^{-47}\ \text{erg-cm}^3.$$

Comparing this with the Fermi constant for beta-decay $G_\beta=2.5\times 10^{-49}$ erg-cm^3 we see that the observed intrinsic electron-neutron interaction is, at most, two orders of magnitude greater than beta-decay interactions, and, in fact, the large error in the experimental results does not yet preclude the possibility of them being identical. If the last possibility were actually the case, then the intrinsic electron-neutron interaction would have a magnitude of only 1.6 ev.

We summarize with the observation that the intrinsic electron-neutron interaction is somewhat smaller than would be expected on the basis of semiquantitative conclusions obtained from meson theory. Its experimental determination is not yet sufficiently precise to indicate how much of a hurdle this fact represents for meson theory, and the need for more precise measurements is clearly indicated. Should the interaction turn out to be appreciably smaller than -300 ev, a real challenge will be presented to currently popular forms of meson theory, since it appears that only a rather unlikely accidental cancellation of contributions to the interaction would lead to a predicted interaction as small as this. In such an eventuality, a complete and critical re-evaluation of our current ideas concerning the structure of nucleons would be necessitated.

[10] K. M. Case, Phys. Rev. **76**, 1 (1949).
[11] See, however, J. Schwinger, Phys. Rev. **78**, 135 (1950).

The Gyromagnetic Ratios of the Ferromagnetic Elements

G. G. SCOTT
Research Laboratories Division, General Motors Corporation, Detroit, Michigan
(Received March 31, 1952)

The gyromagnetic ratios for the three ferromagnetic elements have been determined by means of a technique involving a sensitive torsional pendulum. The final values obtained, in terms of the mass-to-charge ratio of the electron, are: iron 1.028±0.001; cobalt 1.068±0.004; and nickel 1.078±0.002.

INTRODUCTION

THE values of the gyromagnetic ratios for the ferromagnetic elements given in this paper are the result of a very extensive investigation undertaken at the General Motors Research Laboratories during the past four years. The results for iron have already been reported, and the reader is referred to that paper[1] for a description of the apparatus and of the experimental techniques used.

The rods used for the three ferromagnetic elements were very nearly of the same dimensions (1.5 cm diameter and 22 cm long). In the case of both iron and nickel, these rods were of very high purity. A cobalt rod of high purity could not be obtained. Measurements for this material were made on two different rods; each of them contained about 1 percent nickel as an impurity.

TABLE I. Condensed data for the determination of the gyromagnetic ratio of nickel.

Date	Double amplitude change per reversal d (cm)	Element current i_e (amp)	Element magnetic moment M_e (amp cm²)	Period P (sec)	Azimuth positions	Gyromagnetic ratio (in terms of m/e for the electron)
1- 9-51	0.03708	0.01601	22289	26.647	*XY*	1.074
1-10-51	0.03722	0.01601	22284	26.652	*XY*	1.078
1-11-51	0.03687	0.01600	22272	26.650	*RS*	1.068
1-17-51	0.03691	0.01600	22237	26.654	*RS*	1.071
1-18-51	0.03720	0.01600	22265	26.651	*RS*	1.079
1-19-51	0.03738	0.01600	22255	26.650	*XY*	1.085
1-24-51	0.03736	0.01601	22268	26.645	*XY*	1.084
1-25-51	0.03671	0.01600	22263	26.642	*XY*	1.064
1-26-51	0.03676	0.01601	22247	26.643	*RS*	1.066
1-29-51	0.03766	0.01600	22241	26.645	*RS*	1.095
1-31-51	0.03729	0.01600	22261	26.645	*XY*	1.082
2- 2-51	0.03730	0.01600	22246	26.641	*XY*	1.083
2- 6-51	0.03751	0.01601	22261	26.647	*RS*	1.089
2- 7-51	0.03742	0.01601	22199	26.649	*RS*	1.089
2- 8-51	0.03699	0.01601	22193	26.640	*RS*	1.076
2- 9-51	0.03651	0.01601	22147	26.638	*XY*	1.063
2-12-51	0.01571	0.00861	9292	26.618	*XY*	1.078
2-13-51	0.01601	0.00861	9283	26.616	*RS*	1.103
2-14-51	0.01543	0.00861	9273	26.613	*XY*	1.059
					Average	1.078

Area summation of element winding $\Sigma A = 74858$ cm²
Moment of inertia for 16-milliampere runs $I = 206.89$ gram cm²
Moment of inertia for 8.6-milliampere runs $I = 206.75$ gram cm²
Note: 8.6-milliampere values weighted ½ because of the decreased accuracy obtained with this lower value of the element current.

[1] G. G. Scott, Phys. Rev. **82**, 542 (1951).

RESULTS ON NICKEL

The final readings to determine the gyromagnetic ratio of nickel were taken on 19 different days. The work each day consisted of four separate runs taken in two pairs. The first run of a pair would be at one particular azimuth position. The azimuth would then immediately be changed by 180° and the second run of the pair obtained. The second pair would be a repetition of the first pair, except that the small reversing switch located below the pendulum would be reversed. In each run the amplitude was first built up for 30 periods of the torsional pendulum system and then cut down for 30 periods. This was done by synchronously reversing the current in the gyromagnetic pendulum winding. From the amplitude readings taken during these runs the change in angular momentum corresponding to a given change in magnetic moment was computed and the gyromagnetic ratio thereby determined.

Table I gives a day-by-day summary of all the data taken to determine the gyromagnetic ratio of nickel. Table II gives a semiquantitative spectrographic analysis of the nickel rod.

For both nickel and cobalt the magnetic permeability is quite sensitive to temperature. Great care was therefore taken to allow for these temperature effects in determining magnetic moments. With 16 ma flowing in its winding, the nickel rod had a magnetic moment of 22,280 amp cm², and an increase of one degree Fahrenheit would cause an increase of 15 amp cm² in the magnetic moment.

These magnetic moments were ultimately determined by a series of measurements of values of the torque produced by the field of the 8-ft diameter north-south Helmholtz coil system.

RESULTS ON COBALT

In determining angular momentum changes in the cobalt specimens, nonuniformity of magnetization

TABLE II. Semiquantitative spectrographic analysis of impurities in the nickel rod used in gyromagnetic experiments.

Iron	0.003% to 0.03%
Cobalt	0.003 to 0.03
Silicon	0.03 to 0.3
Manganese	0.02 to 0.2
Antimony	0.003 to 0.03
Silver	0.001 to 0.01

TABLE III. Condensed data for the determination of the gyromagnetic ratio of cobalt (IN specimen).

Date	Double amplitude change per reversal d (cm)	Element current i_e (amp)	Element magnetic moment M_e (amp cm²)	Period P (sec)	Azimuth positions	Element switch positions	Gyromagnetic ratio[a] (in terms of m/e of the electron)
6- 6-51	0.07043	0.01601	42129	26.226	*XY*	AB	1.109
6-11-51	0.06975	0.01601	42252	26.331	*XY*	AB	1.090
6-14-51	0.03474	0.00901	21982	26.255	*RS*	AB	1.042
6-19-51	0.03486	0.00901	21984	26.262	*RS*	AB	1.045
6-20-51	0.02608	0.00701	16386	26.259	*RS*	AB	1.048
6-21-51	0.04937	0.01201	30724	26.270	*RS*	AB	1.061
6-25-51	0.04868	0.01201	30680	26.269	*RS*	AB	1.047
6-26-51	0.06777	0.01601	42256	26.285	*RS*	AB	1.059
6-27-51	0.06663	0.01601	42298	26.283	*RS*	AB	1.039
7- 3-51	0.03619	0.00901	22013	26.257	*XY*	AB	1.086
7- 5-51	0.03655	0.00901	21981	26.253	*XY*	AB	1.099
7- 6-51	0.05017	0.01201	30695	26.268	*XY*	AB	1.080
7- 9-51	0.05058	0.01201	30705	26.271	*XY*	AB	1.089
7-10-51	0.02730	0.00701	16413	26.259	*XY*	AB	1.098
					XYRS four azimuth average		1.071
10- 2-51	0.03584	0.00901	22196	26.821	*VWPQ*	A	1.061
10- 3-51	0.03537	0.00901	21957	26.810	*VWPQ*	B	1.059
10- 4-51	0.03536	0.00901	22054	26.821	*VWPQ*	A	1.053
10- 5-51	0.03489	0.00901	22015	26.808	*VWPQ*	B	1.041
10-10-51	0.03381	0.00901	21972	26.801	*VWPQ*	B	1.009
10-11-51	0.03649	0.00901	21959	26.790	*VWPQ*	A	1.095
					VWPQ four azimuth average		1.053
					Average for all eight azimuth positions		1.062

Area summation of element winding $\Sigma A = 74149$ cm²
Moment of inertia for first set $I = 204.49$ gram cm²
Moment of inertia for second set $I = 208.02$ gram cm²
Note: increase in moment of inertia for second set is caused by a design change in suspension support.

[a] Individual values include magnetic coupling errors.

caused a higher order of magnetic coupling error to become important. Because of this nonuniformity and because of very small magnetic gradients in the neutralized space, two 180° separated azimuth positions were no longer sufficient to eliminate magnetic coupling errors. It was found necessary to take readings at eight 45° spaced azimuth positions in order to eliminate magnetic coupling errors. Also readings at two positions of the small reversing switch located below the element were required in order to eliminate suspension effects.

TABLE IV. Condensed data for the determination of the gyromagnetic ratio of cobalt (GM specimen).

Date	Double amplitude change per reversal d (cm)	Element current i_e (amp)	Element magnetic moment M_e (amp cm²)	Period P (sec)	Azimuth positions	Element switch positions	Gyromagnetic ratio[a] (in terms of m/e of the electron)
7-18-51	0.04174	0.00901	23201	26.123	*RS*	AB	1.189
7-19-51	0.03547	0.00901	23191	26.121	*XY*	AB	1.001
7-24-51	0.03831	0.00902	23211	26.117	*XYRS*	A	1.085
7-26-51	0.03853	0.00901	23233	26.115	*XYRS*	B	1.091
					XYRS four azimuth average		1.092
9- 6-51	0.03635	0.00901	23125	26.045	*VWPQ*	A	1.063
9- 7-51	0.03605	0.00901	23095	26.037	*VWPQ*	B	1.056
9-11-51	0.03615	0.00901	23154	26.050	*VWPQ*	B	1.055
9-13-51	0.03622	0.00901	23165	26.046	*VWPQ*	A	1.057
					VWPQ four azimuth average		1.058
					Average for all eight azimuth positions		1.075

Area summation of element winding $\Sigma A = 84458$ cm²
Moment of inertia for first set $I = 202.90$ gram cm²
Moment of inertia for second set $I = 208.38$ gram cm²
Note: increase in moment of inertia for second set is caused by a design change in suspension support.

[a] Individual values include magnetic coupling errors.

TABLE V. Chemical analysis of impurities in the cobalt rods used in gyromagnetic experiments.

	International Nickel Company specimen	General Motors Research Laboratories specimen
Nickel	0.87%	0.93%
Iron	0.12	0.10
Silicon	0.26	0.10
Manganese	0.22	0.03
Aluminum	0.11	...
Carbon	0.02	...
Sulfur	0.01	...
Chromium	...	0.08
Cadmium	...	0.05

The mirror on the gyromagnetic pendulum system had four 90° spaced faces so that readings at four 90° azimuth positions could be readily obtained. To obtain readings at eight azimuth positions, the data were taken in two sets. In the second set this four-sided mirror was rotated 45° from the position it occupied for the first set. In the Tables azimuth positions X and Y are 180° apart. Positions R and S are likewise 180° apart and 90° removed from X and Y. In the second set, V and W are 180° apart, and P and Q are likewise 180° apart and 90° removed from V and W.

One of the two different rods used in working with cobalt was furnished by the International Nickel Company and is labeled IN in the Tables. The other rod was cast by the Metallurgical Department at the General Motors Research Laboratories. This second rod is labeled GM in the Tables.

A summary of all the data obtained on the IN cobalt rod is given in Table III. This information is tabulated in the order in which it was taken. Each azimuth set is averaged and the average of the two sets taken to determine the final value for the rod. A similar tabulation for the GM cobalt rod is given in Table IV, and a chemical analysis of the two rods is shown in Table V.

The difference between the two rods is probably caused by accidental error rather than to the effect of different amounts of impurities. In obtaining the average value for cobalt, the IN rod is weighted 3 to 2 for the GM rod because of the larger number of readings taken on the IN rod.

TABLE VI. Final values for the gyromagnetic ratios of the ferromagnetic elements expressed in terms of the mass-charge ratio of the electron (ρ) along with the corresponding Landé factors (g').

	ρ	g'
Iron	1.028±0.001	1.946
Cobalt	1.068±0.004	1.873
Nickel	1.078±0.002	1.855

The final value for cobalt is, therefore, $1.068m/e \pm 0.004$.

SUMMARY

In Table VI we have the final tabulation of the values measured in these experiments for the gyromagnetic ratios of the ferromagnetic elements, in terms of the mass-charge ratio of the electron. The corresponding Landé factors are also given in this table.

The author wishes to express his appreciation to Dr. C. F. Kettering for his continued interest in these experiments, and also to the various other members of the General Motors Research Laboratories whose cooperation made this work possible.

PHYSICAL REVIEW VOLUME 87, NUMBER 5 SEPTEMBER 1, 1952

Proton-Proton Scattering at 5 Mev by a Coincidence Method*

R. O. Bondelid,†‡ C. H. Braden,§ M. E. Battat,† and P. Bohlman
Physics Department, Washington University, St. Louis, Missouri

(Received October 1, 1951)

The scattering of 5-Mev protons by protons was examined by a coincidence method. Particular attention was given to the absolute value of the differential cross section at 45° in the laboratory system. The differential cross sections at other angles were determined relative to the cross section at 45°. The *S*-wave phase shift calculated from the observed cross section at 45° agrees, within the experimental error, with that from other experiments in this energy range. No indication of a *P*-wave effect was observed.

INTRODUCTION

PROTON–PROTON scattering at 5 Mev has been reported by two other workers,[1,2] one of them from this laboratory. In view of the fact that both of these results were obtained by the photographic plate technique, it appears to be desirable to report the results obtained by a totally different method. The method employed in the present work is similar to that described by Wilson and co-workers,[3] which uses two proportional counters placed at 90° with respect to one another and a hydrogenous foil used as a scattering medium. True scattering events are recorded by coincidence pulses between the two counters. Knowing the angle between the scattered and recoil particles makes it possible to predetermine the geometrical factors involved, except for the effect of multiple scattering.

APPARATUS

The apparatus used in the present experiment is basically the same as that described by Karr *et al.*[4] Minor circuit improvements were made and an oscillating foil holder was added. The purpose of the latter was to provide an automatic method of averaging over variations in foil thickness. The same definitions of defining and conjugate counter apply, i.e., the defining counter and defining slit are to be associated with the solid angle definition and resolution of the experiment. The conjugate counter and conjugate slit are to be associated with the particles conjugate to those entering the defining counter.

PROCEDURE AND CALCULATIONS

The only measurement of absolute cross section was made at an angle $\Theta=45°$ in the laboratory frame of reference. The scattering yield from seven foils was measured by observing no less than 10,000 scattering events from any one foil.[5] Variations in foil thickness

TABLE I. The letter in column 1 designates the foil. *A*, *B*, *C*, and E_2 were Nylon foils. B_2, *D*, and *E* were polyethylene-terephthalate foils. Column 2 shows the average number of hydrogen atoms per cm² and column 3 lists the laboratory cross section as determined from that foil. The correction for multiple scattering is not included in these figures.

Foil	$N\times10^{-19}$	$\sigma(45°)\times10^{24}$ cm² steradian^{-1}
A	3.293	0.268
B	2.785	0.259
B_2	1.921	0.262
C	2.907	0.261
D	1.816	0.274
E	1.682	0.273
E_2	2.957	0.262

$\sigma(45°)_{lab}=0.266\pm0.002\times10^{-24}$ cm² steradian^{-1}.

* Assisted by the joint program of the ONR and AEC.
† Now at Los Alamos Scientific Laboratory, Los Alamos, New Mexico.
‡ Now at Naval Research Laboratory, Washington, D. C.
§ Now at Georgia School of Technology, Atlanta, Georgia.
[1] R. E. Meagher, Phys. Rev. **78**, 667 (1950).
[2] K. B. Mather, Phys. Rev. **82**, 133 (1951).
[3] R. R. Wilson and E. C. Creutz, Phys. Rev. **71**, 339 (1947); R. R. Wilson, Phys. Rev. **71**, 384 (1947); and Wilson, Lofgran, Richardson, Wright, and Shankland, Phys. Rev. **72**, 1131 (1947).
[4] Karr, Bondelid, and Mather, Phys. Rev. **81**, 37 (1951).
[5] It was found that prolonged bombardment caused changes to occur in the foil. Hence, the seven foils used to determine the absolute cross section were not subjected to any previous bombardment and only the first observation of *Y* on any one foil was used to determine the absolute cross section. The relative cross sections were determined by making successive measurements at different angles during a period of foil stability. A foil was considered to be stable when no change was observed in the yield at a given angle as a function of bombardment time.

TABLE II. Relative yield (Y/n) as a function of laboratory angle.

Θ	$(Y/n)\times10^{3}$	% standard deviation
40	0.584	0.8
35	0.616	0.8
30	0.619	0.8
45	0.551	0.9
60	0.347	1.1
55	0.421	1.0
50	0.499	0.9
45	0.548	0.9
40	0.589	1.0

were averaged out by use of the foil holder mentioned previously. After the scattering yield Y was obtained, a section of the foil was removed and submitted to a chemist for weighing and chemical analysis.[4] The number of hydrogen atoms per cm² N was found from the percent hydrogen content obtained from chemical analysis averaged with the manufacturer's quotation of the hydrogen content and that deduced from the chemical formula. The number of incident protons n was measured by the current integrator.[4] The solid angle Ω is known.[4] The cross section can then be computed by means of the relation $\sigma(\Theta)=Y/n N\Omega$. Table I lists the results of the above determination.

The relative scattering cross sections between the angles $\Theta=30°$ and $\Theta=60°$ were obtained by the coincidence method using only one foil.[5] The procedure for obtaining the scattering yield is the same as that described above. For a given foil, the quantity $N\Omega$ is constant and can be obtained by inserting in the cross section formula the value of $\sigma(45°)$ from the absolute measurement and the value of Y/n from the relative measurement. This value of $N\Omega$ is then used in subsequent calculations of relative cross sections. This procedure serves to normalize the relative measurements to the absolute at 45°. The quantity Y/n, directly proportional to the cross section, was observed for the angles listed in Table II. These values of Y/n are not corrected for multiple scattering.

At defining angles less than 30° and greater than 60°, multiple scattering places prohibitive demands on the conjugate slit system geometry. Hence, to obtain a point at 65°, a single-counter integral bias curve method was used.[6] The ratio of Y/n at 65° to the normalizing value of Y/n at 45° was found to be 0.320/0.565. A check was made on the single-counter method by comparing single-counter and corrected coincidence data at 60° (see Appendix).

TABLE III. Laboratory cross sections.

Lab. angle Θ	30	35	40	45	50	55	60	65
$\sigma(\Theta)\times10^{24}$ cm²	0.332	0.314	0.289	0.268	0.246	0.214	0.189	0.152

[6] Because of natural symmetry about $\theta=90°$ (c.m.) ($\Theta=45°$ lab.), the cross section at 65° is equivalent to the cross section at 25°. The single-counter measurement is feasible at 65° and not at 25°, because at 65° it is easy to discriminate between the energy of the hydrogen-scattered protons and protons scattered by the carbon, nitrogen, and oxygen in the foil.

CORRECTIONS TO DATA

The corrections to the current integration and corrections arising from the coincidence circuit are discussed by Karr *et al.*[4] The multiple scattering corrections are discussed in the appendix.

The energy of the proton beam as determined by a photographic plate and a magnetic deflection method was 5.16±0.14 Mev. A correction was applied to this for the thickness of the scattering foils. The result is 5.14±0.14 Mev as the average incident energy.

EVALUATION OF ERRORS

Absolute point: The cross section formula is rearranged for purposes of computation as follows:

$$\sigma(\Theta)=\frac{1}{k}\frac{Y}{NV}\frac{1}{C}\frac{1}{\Omega},$$

where $\sigma(\Theta)$ = the laboratory cross section (cm²) per unit solid angle at an angle Θ; Y = the number of particles scattered into the defining counter between the angles Θ and $\Theta+d\Theta$; N = the number of scattering centers per cm²; C = integrating capacitance; V = the final voltage across C; Ω = the solid angle subtended at the defining counter aperture; and k = fundamental constant. The product CV is proportional to the number of incident particles. The error in (Y/NV) can be found from the seven foils used for the measurement of absolute cross section (see Table I). This turns out to be ±0.8 percent.[7] The error in the capacitance is determined from the values quoted by the Bureau of Standards and is taken to be ±1.1 percent. The error in the solid-angle measurement is found from the rms deviation of four independent checks (see Appendix). This error is ±0.8 percent. The error in the multiple

TABLE IV. Comparison of cross sections. The percent rms errors are indicated in parentheses.

θ	Meagher (4.96±0.08 Mev) $\sigma_{c.m.}$ (barns)	Mather (5.07±0.04 Mev) $\sigma_{c.m.}$ (barns)	This report (5.14±0.14 Mev) $\sigma_{c.m.}$ (barns)
50	0.929 (1.94)	0.921 (1.12)	0.899 (2.1)
60	0.962 (1.94)	0.949 (1.24)	0.947 (2.9)
70	0.988 (1.94)	0.957 (1.06)	0.946 (2.4)
80	0.993 (1.94)	0.958 (1.07)	0.950 (2.2)
90	0.996 (1.94)	0.99 (5.3)	0.948 (1.6)

[7] The error quoted in (Y/NV) does not contain any systematic errors in N. (Y/NV) should be the same for all foils, and hence the rms deviation of the seven readings is chosen as the random error in this result. Systematic errors in the determination of N are discussed in Sec. VII of reference 4, Karr *et al.* (Use the terms as defined in this section.) The uncertainty in s and m is small. If only the chemical analyses had been used in the determination of f, the error would be treated as wholly random. However, since the manufacturers data and the value deduced from chemical formula have been averaged into the value of f, a systematic error has been introduced in the value of Y/NV. N deduced from chemical analysis gives an average value of Y/NV less than one percent different from that obtained when N is deduced from all three values for f.

scattering correction is 0.2 percent at $\Theta=45°$. The error in $\sigma(45°)$ is then ± 1.6 percent as determined by standard methods of combining errors.

Relative points: Since all other points are normalized to the cross section at $\Theta=45°$, there is no relative error in the cross section at 45°. The relative points are obtained by dividing the Y/n at a given angle by the observation of Y/n at $\Theta=45°$. The relative cross section can then be expressed as

$$\sigma_{rel}(\Theta)=k'Y_\Theta C_{45}/Y_{45}C_\Theta,$$

where k' is a constant of proportionality. The capacitance is included to account for small variations in its value due to effects of variations in the charge and discharge times. The error in Y is taken to be the standard deviation of the number of counts observed. The error in multiple scattering correction is taken to be 10 percent. The errors in the relative cross sections for the indicated center-of-mass angles (θ) are

Angle θ	50	60	70	80	90
Percent error	2.1	2.9	2.4	2.2	0

TABLE V. Comparison of S-wave phase shifts. The average δ_a quoted by Meagher and Mather include more angles than indicated in this table.

θ	Meagher[a] (4.96±0.08 Mev) δ_a	Mather (5.07±0.04 Mev) δ_a	This paper[b] (5.14±0.14 Mev) δ_a
50	53.56	54.58±0.35	53.92±0.64
60	53.87	54.77±0.41	54.88±1.04
70	54.20	54.50±0.36	54.26±0.76
80	54.06	54.24±0.37	54.08±0.70
90	54.06	55.3 ±1.8	53.89±0.63
δ_a used to compute $f(E)$	Av. δ_a= 54.02±0.60	Av. δ_a=54.5±0.6	δ_a at 90°

[a] See reference 8.
[b] See footnote 7.

The error at 50° does not include the multiple scattering error since this is a single counter point.

RESULTS

The present work was done at an energy of 5.14±0.14 Mev as measured in the laboratory. The scattering cross sections as a function of angle were obtained relative to the cross section at 45°. The absolute cross section was measured at 45°. Table III shows the laboratory cross sections as a function of angle. All corrections are included. A comparison of the present data with the values obtained by Meagher[1] and Mather[2] is shown in Tables IV and V. The investigations of Meagher and Mather were more extensive with respect to the angular region studied, but for purposes of comparison, only the angles studied here are included. Except for the point at $\theta=90°$, it is to be noted that Mather's cross sections are slightly higher but that the phase shifts are in fair agreement. Mather places a high error on his point at 90°. The difference between Meagher's cross sections and the cross sections from this investigation

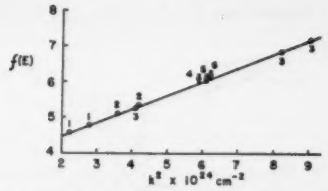

FIG. 1. Plot of the function $f(E)$ *versus* k^2. The various points are: (1) Herb, Kerst, Parkinson, and Plain, Phys. Rev. **55**, 247 (1939); (2) Blair, Freier, Lampi, Sleator, and Williams, Phys. Rev. **74**, 553 (1948); (3) J. Rouvina, Phys. Rev. **81**, 593 (1951); (4) R. E. Meagher, reference 1; (5) K. B. Mather, reference 2; (6) This investigation.

can be accounted for, within the experimental accuracy, by the difference in beam energy.

The plot of the straight line function $f(E)$ as defined by Jackson[8] is shown in Fig. 1. The value of the S-wave phase shift at 90° was used to compute the point contributed by this experiment because the cross sections at other angles are relative values. The relative data were analyzed according to the method of Jackson[8] for P-wave effects. The result of this calculation is shown in Fig. 2. Least-squares straight lines were calculated for the following two cases: Holding the point at 90° as fixed, results in a value for $\delta_1=-1.00°$. Not holding any point fixed, $\delta_1=-0.07°$ with intercept 54.2°. The only conclusion to draw from these data is that $\delta_1=0°$ $\pm 1.5°$.

The results indicate that there is good agreement between the photographic data and the coincidence data.[9]

It is a pleasure to acknowledge the helpful interest of Professors R. N. Varney, A. L. Hughes, and H. Primakoff. We are indebted to the cyclotron staff under the direction of Mr. A. A. Schulke and the staff of the shop under Mr. O. Retzloff.

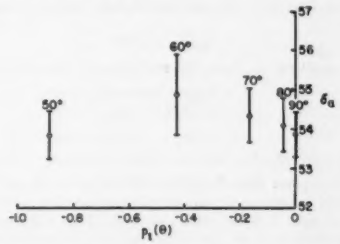

FIG. 2. Apparent S-wave phase shifts plotted against the function $P_1(\theta)$, calculated according to the method of Jackson (see reference 8).

[8] J. D. Jackson and J. M. Blatt, Revs. Modern Phys. **22**, 77 (1950).
[9] Coincidence-counter results published by Bondelid, Bohlman, and Mather, Phys. Rev. **76**, 865 (1949) are incorrect. A systematic error in the current integrator was discovered and eliminated. This error is not present in the results published subsequent to the aforementioned letter.

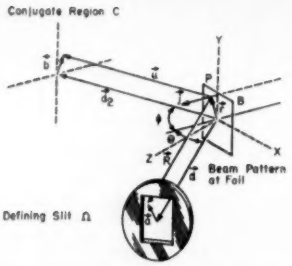

FIG. 3. Schematic of the equal-mass collision process.

APPENDIX

In order to determine the number of scattered particles Y by the coincidence technique, it is necessary to know where the scattered and recoil protons will be after the collision. The scattered and recoil proton paths are coplanar with the path of the incident proton and are separated by an angle of 90 degrees. The schematic collision process is shown in Fig. 3. The region B, the area of the foil within which scattering occurs, is determined by the size of the collimating slits. The exact borders of the region are influenced by the amount of slit-edge scattering and the variation in initial direction of the incident particles. The method of determining the dimensions of B is discussed by Karr *et al.*[4] The solid angle was redetermined and found to be $(1.126\pm0.009)\times10^{-4}$ steradian. This is the average result of the measurements of four persons working independently. Returning to Fig. 3, the axes are chosen so that Z is always perpendicular to the plane of the foil. During the experiment the foil was rotated so that Z always bisected the angle between $\mathbf{d}_1$ and $\mathbf{d}_2$. Assume that a scattering event occurs at the point P on the foil. Let $\mathbf{r}$ be the vector from the center of the scattering area to the point P. The vector from P to a point in Ω is called $\mathbf{R}$, while the vector from the center of Ω to this same point is represented by $\mathbf{a}$. The vector $\mathbf{u}$ is the vector of the conjugate proton, and $\mathbf{b}$ is the vector from the center of the conjugate region C to the terminus of $\mathbf{u}$. Let $\mathbf{j}$ be a unit vector in the direction of the incident particle. The laws of conservation of energy and momentum specify that $\mathbf{u}$ is perpendicular to $\mathbf{R}$, hence

$$(\mathbf{u}\cdot\mathbf{R})=0.$$

The same laws state that $\mathbf{u}$, $\mathbf{j}$, and $\mathbf{R}$ must lie in the same plane, hence

$$(\mathbf{j}\cdot[\mathbf{u}\times\mathbf{r}])=0.$$

These equations can, for a first approximation, be reduced to

$$b_x=[\tfrac{1}{2}(c_3-c_4)r_x-c_4a_2]/c_3,$$
$$b_y=(c_1+c_2)r_y-c_2a_y,$$

where

$$c_1=(J_x-J_z)d_{1x};\quad c_2=(J_x+J_z)d_{2x};\quad c_3=d_{1x};\quad c_4=d_{2x}.$$

These equations give the dimensions of the conjugate area C demanded by geometric considerations alone. The quantity b_y is the half height of the conjugate region and $b_x\sqrt{2}$ is the half-width. The dimensions of the conjugate region as a function of Θ are given in Table VI.

TABLE VI. Required geometrical dimensions of the conjugate slit

Θ	Width (mm)	Height (mm)
25	0.968	9.36
30	0.962	8.02
35	0.956	7.02
40	0.954	6.26
45	0.954	5.64
50	0.954	5.12
55	0.956	4.66
60	0.962	4.28
65	0.968	3.92

TABLE VII. Multiple scattering correction as a function of laboratory angle.

Θ	Percent correction
30	10.3
35	4.94
40	1.71
45	0.6
50	1.61
55	4.74
60	10.0

For the geometry employed in this experiment, the practical minimum limit for Θ was 30 degrees. In practice, the conjugate slit must be larger than indicated by geometrical considerations alone. Multiple scattering of the scattered and recoil particles in the foil causes the conjugate pattern to spread out over a much wider region. The method used for experimentally determining this spread is outlined: For a given angle, a conjugate-counter aperture was used which was approximately one degree wide.[10] The conjugate counter was then moved in one-degree steps on either side of the conjugate position and the number of true coincidence counts observed. The data were then expressed in the form of a histogram. From the histogram so obtained and the dimensions of the slit width used in obtaining the cross section data, a correction to account for any deficiency in slit width can be calculated. From the amount of horizontal spread and the geometrical slit height, a height correction can be obtained. The corrections to be applied to the various angles are listed in Table VII.

At all angles except $\Theta=45°$, the error in the multiple scattering correction due to variations in foil thickness and counting statistics is estimated to be 10 percent. The variation in the thicknesses of the seven foils used to determine $\sigma(\theta=90°)$ introduces a possible error of 30 percent in the multiple scattering correction at this point. However, since the correction is only 0.6 percent, the error this introduces into $\sigma(\theta=90°)$ is then 0.2 percent. Checks on the validity of the correction were made by applying the correction to data taken with conjugate slits of differing widths. The corrected data agreed within the estimated error of the correction. A further check was made by comparing single counter data with corrected coincidence data at $\Theta=60°$. The ratio of the relative yield of the corrected coincidence data to the single-counter data was found to be (0.185/0.187).

[10] It is convenient to express the slit width in terms of the number of degrees subtended, at the center of the chamber, by the slit.

Dirac's New Classical Theory of Electrons*

BANESH HOFFMANN
Queens College, Flushing, New York
(Received March 25, 1952)

Similarities are pointed out between Dirac's theory and certain equations belonging to the projective theory of relativity. The latter include an electromagnetic potential of fixed gauge and are such that if one reduces them to special relativity in the conventional way by taking g_{ab} to be Galilean, one can extract from them equations closely corresponding to those of Dirac's theory. However, it is shown that taking g_{ab} to be Galilean ignores quantities that may not be negligible relative to Dirac's gauge-fixing constant $k^2=m^2/e^2$; thus, effects arising from non-Galilean g_{ab} may be important in a theory of the type proposed by Dirac. When g_{ab} is not Galilean one apparently loses the central characteristic of Dirac's theory that all electric currents have m/e of electronic value. Equations of motion are still present, however. And since the gauge-fixed electromagnetic potential can be zero without contradicting the field equations, one need not postulate an ether for the reasons that arise from Dirac's theory.

I. INTRODUCTION

BECAUSE the Maxwell equations are linear they do not imply the equations of motion of charged particles in an electromagnetic field. When the Maxwell equations are brought into the general theory of relativity, however, the nonlinearity arising from the gravitational field is enough to insure that the equations of motion of charged particles are consequences of the field equations.[1]

In his new classical theory of electrons[2] Dirac introduces a much simpler nonlinearity into the Maxwell theory. Remaining within the framework of the special theory of relativity, he subjects the electromagnetic potential four vector A_μ to the quadratic condition

$$A_\mu A^\mu = k^2, \tag{D9}$$

where k is a constant; and he shows that if $k=m/e$, where m and e are, respectively, the mass and charge of the electron, one obtains a theory of the electromagnetic field that automatically contains the equations of motion of electronic currents. His field equations consist of the above condition (D9) and the set

$$\partial F_{\mu\nu}/\partial x^\nu = \lambda A_\mu, \tag{D11}$$

where

$$F_{\mu\nu}=\partial A_\nu/\partial x^\mu - \partial A_\mu/\partial x^\nu, \tag{D3}$$

and μ, ν have the range 0, 1, 2, 3, with the 0 referring to time.

One no longer has the customary freedom to add an arbitrary gradient to the electromagnetic potential A_μ; gauge invariance has been destroyed by the condition (D9).

II. COMPARISON WITH PROJECTIVE EQUATIONS

The fact that Dirac's theory contains five field equations for five field quantities is in itself enough to suggest that the theory may be related to the projective theory of relativity, which is an outgrowth of the five-dimensional theory of Kaluza and Klein. It turns out that there are further suggestive similarities between Dirac's equations and certain equations belonging to the projective theory that may not be without interest.

The projective equations in question are[3]

$$(R^{ab}-\tfrac{1}{2}g^{ab}R)-6N^2g^{ab}+2(g^{cd}\varphi^a{}_c\varphi^b{}_d+\tfrac{1}{4}g^{ab}\varphi^e{}_d\varphi^d{}_e) - 12N^2(\theta^a\theta^b-\tfrac{1}{2}g^{ab}\theta^c\theta_c)=0 \tag{I49}$$

and

$$\varphi^{ab}{}_{,b}+24N^2\theta^a=0, \tag{I50}$$

together with

$$\theta^a{}_{,a}=0, \tag{I51}$$

the last not being an independent equation but a consequence of (I50).

Here a, b, c, d have the range 1, 2, 3, 4, with 4 referring to time. The quantity N was regarded as a constant in I (it may be taken to be a parameter, but not a function). $R^{ab}-\frac{1}{2}g^{ab}R$ is the Einstein tensor formed from the metric g_{ab}. The commas in (I50), (I51) denote covariant derivatives with respect to this metric. The quantity θ_a is of particular interest. In the projective formalism there appear a projective scalar Φ and a projective vector having the five components $(\varphi_a, 1)$. Under a gauge transformation, the components φ_a acquire an added gradient while Φ becomes multiplied by a corresponding function such that the combination

$$\theta_a \equiv \varphi_a - (1/N)\partial \log\Phi/\partial x^a \tag{I40 and 41}$$

remains unaltered. Thus θ_a is an affine vector. And, although gauge transformations are part of the basic projective formalism, θ_a is gauge invariant and can correspond to the gauge-fixed A_μ of Dirac's theory.

* *Note added in proof.*—Since writing the present paper I have found a better treatment somewhat different from that given here. I hope to publish these results shortly.

[1] Einstein, Infeld, and Hoffmann, Ann. Math. **39**, 65 (1938); see pages 94–95. See also L. Infeld, Phys. Rev. **53**, 836 (1938), and Einstein and Infeld, Can. J. Math. **I**, 209 (1949).

[2] P. A. M. Dirac, Proc. Roy. Soc. (London) **A209**, 291 (1951). Equations belonging to Dirac's theory will here be labeled by a D followed by the number of the equation in Dirac's paper.

[3] B. Hoffmann, Phys. Rev. **72**, 458 (1947), hereinafter referred to as I. Equations from I are here labeled by I followed by their number in I. References to the previous literature are given in I.

The curl of θ_a is equal to that of φ_a, the quantity φ_{ab} being defined by[4]

$$\varphi_{ab}=\tfrac{1}{2}(\partial\varphi_a/\partial x^b-\partial\varphi_b/\partial x^a)=\tfrac{1}{2}(\partial\theta_a/\partial x^b-\partial\theta_b/\partial x^a). \quad (1)$$

If N is zero, the above equations reduce to the usual field equations of the general theory of relativity for gravitational and electromagnetic fields in the absence of matter. When N differs from zero they contain additional terms.

In comparing these equations with those of Dirac, one must allow not only for differences of notation but also for the fact that the present equations belong to the general theory of relativity while Dirac's are confined to the special theory.

The four equations (I50) are similar in structure to Dirac's equations (D11). Apart from notation, the main difference is that Dirac's λ is a field quantity while N is a constant, or at best a numerical parameter. This is offset by the fact that Dirac uses Galilean g_{ab} while, when gravitation is not neglected, the g_{ab} that enter (I50) are field quantities. Thus, if θ_a corresponds to Dirac's A_μ, the quantity corresponding to Dirac's A^μ is $g^{ab}\theta_b$.

Equation (I51) corresponds to Dirac's equation of continuity

$$\partial j_\mu/\partial x^\mu=0, \quad (D13)$$

which is a consequence of (D11) and the definition

$$j_\mu=-\lambda A_\mu. \quad (D12)$$

Consider now the set of ten equations (I49). To compare these with equations in Dirac's theory let us temporarily neglect gravitation.[5] The customary way to do this is to take Galilean g_{ab}. The Einstein tensor $R^{ab}-\frac{1}{2}g^{ab}R$ will then be zero. If we now multiply what remains of (I49) by g_{ab} and sum over a and b, the part containing the φ's goes to zero identically and we are left with

$$-12N^2-12N^2(\theta^a\theta_a-2\theta^a\theta_a)=0$$

or

$$\theta^a\theta_a=2, \quad (2)$$

which is of the same form[6] as Dirac's nonlinear condition (D9).

In (I49) and (I50) there are fourteen field quantities, g_{ab}, θ_a, satisfying fourteen field equations. If we wish to ignore gravitation, as Dirac does, we lose ten field quantities g_{ab} out of the original fourteen. The usual way to compensate for this loss is to ignore the ten field equations that correspond to (I49) in the general theory of relativity. But, for Galilean g_{ab}, the Eqs. (I49) imply Eq. (2). And if we wish to retain Eq. (2) as a field equation to go with the four field equations (I50) with Galilean g_{ab}, we shall have five field equations in all and shall therefore need an extra field quantity to go with the four field quantities θ_a. This suggests the possibility that Dirac's field quantity λ might be a substitute, within the framework of the special theory of relativity, for the ten gravitational potentials g_{ab} of the general theory of relativity and that his nonlinear relation (D9) might be a substitute for the ten nonlinear equations (I49). In this connection it should be noted that in the general theory of relativity the equations corresponding to (I49) determine the motion of charged particles (see reference 1), while (D9) performs a like function in Dirac's theory.

III. THE POSSIBILITY OF LOCALIZED ELECTRON BEAMS

In Dirac's theory the field quantity λ enters primarily because there are five field equations and only four electromagnetic potentials A_μ. So far as Dirac's discussion of the motion of electrons is concerned, his reasoning would be valid if λ were regarded as a parameter rather than a function of position. But there is the possibility that if λ were only a parameter one would be unable to represent localized electron beams; for Dirac's electron current four-vector is $-\lambda A_\mu$, and if λ were a parameter this would give electron current wherever A_μ differed from zero. By taking λ to be a function that is zero everywhere except in a small region, one can definitely localize the electron beam. Apparently, then, λ may not be replaced by a parameter. But this is not necessarily so. For if A_μ is the electromagnetic potential of the whole field, it will be large in the immediate vicinity of the electron beam, owing to the field of the electrons constituting the beam,[7] and it will be smaller away from the beam. Thus, if one takes λ to be not a function but a small constant, the current four-vector $-\lambda A_\mu$ will be negligible except in the vicinity of the electron beam and one will thus have in effect a localized electron beam despite the fact that λ is not a function.

In the projective equations here considered N cannot be a function of position. Thus, one must rely on the electromagnetic potential to localize the electron beam in the manner suggested above. This is not unreasonable physically, since if charge is an aspect of the electromagnetic field its motion and distribution can be expected to be determined by the electromagnetic field quantities θ_a.

In I the quantity N was regarded as large since the field equations were there interpreted as referring to mesons. If, in the light of Dirac's ideas, we now wish to interpret them as pertaining to electric charges we may no longer take N to be large. Instead we must take it to be small, so that the current four-vector, which is proportional to $N^2\theta^a$, will be negligible except at those places where θ^a is very large. That N must be small is also required by the fact that the centrally symmetric electrostatic field may not differ significantly from the Coulomb field for terrestrial distances.

[4] There is a misprint in (I7). The φ_{ba} there should be φ_{ab}.
[5] But see Sec. 4 later.
[6] We shall discuss the question of signs and units later.
[7] Compare K. J. Le Couteur, Nature **169**, 146 (1952).

IV. UNITS. THE EFFECTS OF THE GRAVITATIONAL TERMS

The special relativity equation (2) does not correspond to Dirac's Eq. (D9) if Dirac's k is to have the value m/e. This is because the terms involving φ_{ab} in (I49) must represent, in the proper units, the usual Maxwell stress-momentum-energy tensor of the general theory of relativity; thus we must have

$$\theta_a=(2\kappa)^{\frac{1}{2}}A_a, \tag{5}$$

where A_a is in Dirac's units and κ is the Einstein gravitational constant. Moreover, in order that the Maxwellian terms in (I49) shall have the correct sign one must take g_{ab} to have the signature $+++-$. Dirac uses $---+$.

Thus Dirac's Eq. (D9) with $k=m/e$ becomes, in the present notation,

$$\theta^a\theta_a=-2\kappa m^2/e^2, \tag{6}$$

and the quantity on the right is not only negative but also extremely small numerically compared with the 2 in Eq. (2).

We can easily change the 2 in Eq. (2) to any desired value. The field equations (I49), (I50), (I51), were obtained from the four-dimensional variational principle

$$\delta\int\{\bar{P}(G)^{\frac{1}{2}}/\Phi^3\}dx^1dx^2dx^3dx^4=0, \tag{I17}$$

which is the same as

$$\delta\int P(g)^{\frac{1}{2}}dx^1dx^2dx^3dx^4=0. \tag{I21}$$

Let us add to the integrand in (I17) or (I21) the term $12N^2\Lambda(g)^{\frac{1}{2}}$, where Λ is a constant. This introduces an extra term $6N^2\Lambda g^{ab}$ in the field equations (I49) without affecting (I50) or (I51). The new equations, replacing (I49), are accordingly

$$\begin{aligned}(R^{ab}-\tfrac{1}{2}g^{ab}R)+6N^2(1-\Lambda)g^{ab}\\ +2(g^{cd}\varphi^a{}_c\varphi^b{}_d+\tfrac{1}{4}g^{ab}\varphi^c{}_d\varphi^d{}_c)\\ -12N^2(\theta^a\theta^b-\tfrac{1}{2}g^{ab}\theta^c\theta_c)=0.\end{aligned} \tag{7}$$

On contracting these and neglecting gravitation as before, we now obtain, instead of Eq. (2), the equation

$$\theta^a\theta_a=-2(\Lambda-1), \tag{8}$$

and the constant on the right can be given any value.

However, it is not clear what this value should be since we may not neglect gravitation in the usual way by simply taking Galilean g_{ab}. For if we contract Eq. (7) without neglecting gravitation we obtain

$$R-12N^2\{\theta^a\theta_a+2(\Lambda-1)\}=0 \tag{9}$$

or

$$\theta^a\theta_a=-2(\Lambda-1)+R/12N^2. \tag{10}$$

The presence of the curvature scalar R gives these equations a different significance from that of Eq. (8). For example, unlike Eq. (8), they can be satisfied by $\theta_a=0$, so that no ether velocity is implied such as is envisaged by Dirac.[8]

Because the right-hand side of Eq. (10) is not necessarily a constant, we can no longer infer, as Dirac did from (D9), that the motion will correspond to that of charges with a given value of m/e. This central feature of Dirac's theory may thus be lost in the transition to the present projective equations. However, equations of motion still remain, since they are a consequence of the nonlinear field equations, and the projective equations may still be regarded as pertaining to electric, even if not necessarily to electronic, currents. Perhaps one should not expect the electronic value of m/e to appear in a nonquantized theory.

When θ_a is zero the curvature scalar R takes the constant value $24N^2(\Lambda-1)$, the quantities $2(\Lambda-1)$ and $R/12N^2$ in Eq. (10) being equal. Thus when θ_a differs from zero, the term $R/12N^2$ is not likely to be small compared with $2(\Lambda-1)$. For an electron, the pure number $2\kappa m^2/e^2$ in Eq. (6) is of the order of magnitude 10^{-41}. Thus, if N is of the order 10^{-8} cm^{-1}, the quantity $24N^2(\Lambda-1)$ would be of the order of magnitude of a cosmological constant and thus of the order of magnitude of the scalar curvature R in some of the equations considered in relativistic cosmology. While these estimates are tentative, they suggest that gravitational effects, or at least the non-Galilean effects associated with an over-all world-curvature, may not be negligible in a theory of electrons of the sort proposed by Dirac.

[8] P. A. M. Dirac, Nature **168**, 906 (1951).

Nuclear Scattering of 17-Mev Gamma-Rays

MARY BETH STEARNS*
Laboratory of Nuclear Studies, Cornell University, Ithaca, New York
(Received April 17, 1952)

The nuclear scattering of gamma-rays from the $Li^7(p,\gamma)Be^8$ reaction has been measured. The scatterers used were Bi, Pb, Sn, and Cu. The observed Z dependence of the elastically scattered gamma-rays varied as $Z^{2.5\pm0.5}$, while the inelastically scattered gamma-rays varied at a rate greater than $Z^{2.5\pm0.5}$. An appreciable amount of inelastic scattering was observed.

The elastic scattering results combined with previously measured integrated $\gamma-n$ cross sections of Cu are in agreement with a gamma-ray absorption curve centered around 17–18 Mev and having a width of 4–6 Mev.

I. INTRODUCTION

FROM the study of the internal conversion of gamma-radiation of naturally radioactive nuclei it has long been recognized that the intensities of dipole and quadrupole transitions for these gamma-rays are about equally strong. This result was at first surprising since quadrupole transitions should be about a factor of $(R/\lambda)^2$ weaker than dipole transitions. For even the heaviest nuclei and 1-Mev gamma-rays, this gives $(R/\lambda)^2 \sim 1/250$. Bethe[1] was able to explain this discrepancy by showing that the dipole transitions are greatly inhibited by correlations between the motions of the nucleons. Thus, these low energy gamma-rays do not have sufficient energy to disrupt the correlations between the nucleons and therefore the dipole transitions are seldom excited. However, in recent years, photoinduced reactions with gamma-rays of energies greater than 12 Mev have been observed and studied by many groups. In the energy region between 15 and 25 Mev, gamma-rays are absorbed strongly by all nuclei indicating that dipole transitions are involved. Here the gamma-rays seem to have enough energy to break up some of the correlations between the nucleons. From the investigations of these photoinduced processes it is therefore hoped to learn more about the type and behavior of the subunits in nuclei.

The photoinduced reactions consist of a nucleus first being excited by absorbing a photon and then decaying by the emission of one or more particles or gamma-rays. The reactions investigated up to the present time have been mainly those in which neutrons or protons are the particles emitted. A qualitative picture of the photoinduced reactions which agrees with the experimental results thus far is the following. The gamma-rays are absorbed in a dipole mode by a nucleon or small group of nucleons in the nucleus. This nucleon then usually interacts with the rest of the nucleons in the nucleus, producing a compound state. However, a small fraction of the time the excited nucleon escapes directly with no interactions, and therefore in these cases particles of high energies are emitted with dipole angular distributions. With this picture, the energy distribution of the emitted particle agrees with the statistical model distribution at low energies but possesses a high energy tail whose angular distribution is symmetrical with a maximum at 90°, as shown in several experiments.[2,3]

As a first attempt to explain the observed results theoretically, Goldhaber and Teller[4] assumed that the gamma-rays excite the whole nucleus into a dipole mode of vibration. This dipole vibration was pictured as a motion in the nucleus in which the bulk of the protons moved in one direction and the bulk of the neutrons in the opposite direction. They further assumed that the coupling between the dipole vibration and other modes of nuclear motion was weak and that only the levels near the first excited level of the dipole vibration were important. These assumptions then yield a one-level theory in which the absorption of gamma-rays is effectively due to the first excited level of a simple harmonic dipole vibration of the entire nucleus; however, this level may be broadened by coupling with other nuclear motions. Since their theory contains only one energy level, they predict that most of the scattered gamma-rays should be elastic and that the integrated cross section for the scattering of gamma-rays should be an appreciable fraction of the total absorption cross section.

More recently, Levinger and Bethe[5] showed that one obtains the same total absorption cross section as Goldhaber and Teller by using only the assumption of dipole absorption of the gamma-rays, without any assumptions about the modes of vibration of the nucleus. That is, one gets the same total cross sections whether the nucleus as a whole or a single nucleon or some subunit of the nucleus absorbs the gamma-rays. They also considered the effects of exchange forces, intrinsic range, and type of well of the $n-p$ potential

* Now at Nuclear Research Center, Carnegie Institute of Technology, Pittsburgh, Pennsylvania.

[1] H. A. Bethe, Revs. Modern Phys. **9**, 71 (1937), Secs. 87 to 90.

[2] B. C. Diven and G. M. Almy, Phys. Rev. **80**, 407 (1950).

[3] P. R. Byerly, Jr., and W. E. Stephens, Phys. Rev. **83**, 54 (1951); Curtis, Hornbostel, Lee, and Salant, Phys. Rev. **77**, 290 (1950); H. L. Poss, Phys. Rev. **79**, 539 (1950); M. E. Toms and W. E. Stephens, Phys. Rev. **82**, 709 (1951); D. H. Wilkinson and J. H. Carver, Phys. Rev. **83**, 466 (1951).

[4] M. Goldhaber and E. Teller, Phys. Rev. **74**, 1046 (1948). See also H. Steinwedel and J. H. D. Jensen, Z. Naturforsch. **5a**, 414 (1950).

[5] J. S. Levinger and H. A. Bethe, Phys. Rev. **78**, 115 (1950).

on the total absorption cross section. Since the Levinger-Bethe theory allows many energy levels, it predicts that there will be some inelastic scattering of gamma-rays. This theory, therefore, also predicts that the cross section for the inelastic scattering of gamma-rays will be smaller than predicted by the Goldhaber-Teller theory.

Courant[6] proposed a direct photodisintegration process, which hypothesized that the gamma-ray is absorbed by a nucleon in the nucleus and the nucleon is then emitted directly without the formation of an intermediate compound nucleus. This model would explain the particles which are emitted with higher energies than would be expected from a statistical model. It also agrees with the high energy particles having angular distributions with a maximum at 90° as is observed experimentally. Small amounts of this direct interaction also make plausible the high ratios of (γ, p) to (γ, n) yields which were obtained for moderately heavy nuclei and which were much too high to be accounted for by a statistical model.

The purpose of this experiment is, therefore, to gain more information about these photoinduced nuclear reactions by studying the nuclear scattering of gamma-rays. From the magnitude and Z dependence of the scattering one can learn more about the "resonance" properties and nuclear model needed to explain gamma-ray absorption. If appreciable inelastic scattering is observed, it indicates that the simple one-level model of the Goldhaber-Teller theory cannot be correct without modification.

Previously two experiments have been performed to detect the nuclear scattering of gamma-rays. The first, by Gaerttner and Yeater,[7] was done by attempting to detect the scattered gamma-rays of a 100-Mev betatron by producing pairs in a cloud chamber. The cloud chamber was placed such that the gamma-rays had to be scattered through an angle of 120° within a spread of 45°. They state that if the assumption is made that all their observed pairs are from nuclear scattering then "the scattering in C and Cu is less than 1 percent and 3 percent, respectively, of the total cross section for resonance absorption," as predicted by the Goldhaber-Teller theory. However, they point out that all the observed pairs can probably be accounted for by bremsstrahlung from the secondary electrons in the scatterers.

The other measurement of scattered gamma-rays was made by Dressel, Goldhaber, and Hanson.[8] They placed Pr foils at 90° and 145° to the gamma-ray beam of a 22-Mev betatron. Then, using Pb as the scatterer, they measured the activity produced due to the $Pr^{141}(\gamma, n)Pr^{140}$ reaction. Their final cross sections for Pb were: $(d\sigma/d\omega)_{90°}=1.1\pm0.6$ mb/sterad; $(d\sigma/d\omega)_{145°}=2.0\pm1.0$ mb/sterad.

[6] E. D. Courant, Phys. Rev. **82**, 703 (1951).
[7] E. R. Gaerttner and M. L. Yeater, Phys. Rev. **76**, 363 (1949).
[8] Dressel, Goldhaber, and Hanson, Phys. Rev. **77**, 754 (1950).

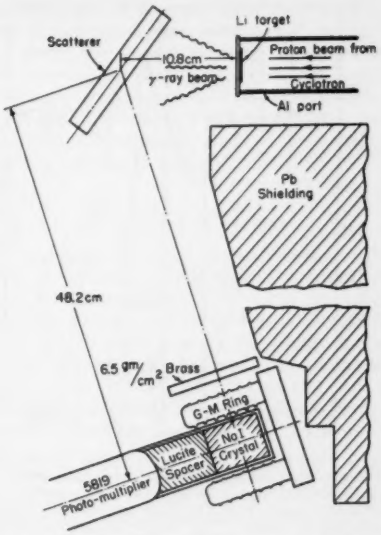

FIG. 1. Experimental arrangement of gamma-ray source, scatterer, and detector.

II. APPARATUS

The experimental arrangement used to study the scattering of gamma-rays is shown in Fig. 1.

The gamma-rays to be scattered were produced by bombarding a thick Li target with 700-kev protons from the Cornell cyclotron. The scatterers used were Bi, Pb, Sn, and Cu. Each element was molded into a block from cp grade stock and then machined to be 5×5 inches in area. The thicknesses were usually equal to the absorption mean free path of 17.6-Mev gamma-rays as measured by Walker.[9] Three Geiger counters were mounted above the source and used as monitors. Their counting rates throughout the experiment remained constant with respect to each other to within 2 percent.

The gamma-ray detector was a NaI(Tl) crystal which was in anticoincidence with a ring of Victoreen Geiger counters. The Geiger counters were staggered in position and thereby completely surrounded the crystal. They were all connected in parallel. The main function of the Geiger counters was to decrease the background due to cosmic rays. They reduced this background by factor of 8.5. The Geiger counters and anticoincidence arrangement also prevented detection of charged particles coming from the scatterer. However, this function was not very important since these particles were stopped by 6.5 g/cm² of brass placed between the detector and scatterer as shown in Fig. 1.

[9] R. L. Walker, Phys. Rev. **76**, 527 (1949).

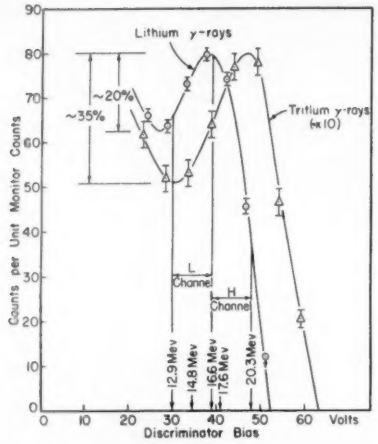

FIG. 2. Pulse-height distribution curves for Li and tritium gamma-rays. The pulse-height distribution curves were obtained by placing the NaI crystal directly in the beam and taking differential number—bias curves. The energy scale has been determined by assigning an energy of 17.6 Mev to the peak of the pulse-height distribution curve which would be obtained with monoenergetic gamma-rays of 17.6 Mev. The two indicated channels were those used for detection of the scattered gamma-rays.

The detector was shielded from the gamma-ray source as shown in Fig. 1.

The NaI(Tl) crystal was a cylinder 4 cm in diameter and 5 cm in height. Since the crystal was so large, it had a rather high efficiency (about $\frac{1}{3}$) for detecting gamma-rays in the energy region of around 16 Mev. By measuring the height of the pulses coming from the crystal, one could also obtain energy discrimination of the gamma-rays. The crystal was mounted by immersing it and a 5-cm Lucite spacer into mineral oil in a hollow Lucite cylinder. The hollow cylinder had all its inner surfaces lined with reflectors, a mirror cemented to the end opposite the phototube, and an Al foil along the inside wall. This assembly was then optically connected to the phototube window by a thick coating of Canada balsam.

The main factors that made this experiment more sensitive than previous experiments were the increase in efficiency of detection of the gamma-rays by the use of the NaI(Tl) crystal and the decrease in background obtained by having the Geiger counters in anticoincidence with the crystal.

The over-all electronic system, from the input at the phototube and through to the pulse-height discriminator and recording scalers, was checked for linearity many times throughout the experiment and was never found to deviate from linearity by more than 2 percent.

The discriminators were units of a multichannel discriminator, and the voltage intervals between them were fixed by batteries. The zero of the discriminator system was checked frequently while running and was never found to vary by more than 2 percent of the channel width. The channel widths were 9 volts.

The cosmic-ray background was measured about every other day while running and was constant within the statistics. The lithium pulse-height distribution was also taken throughout the experiment and remained the same over periods of days. The recording apparatus was always left on over night, with the counter high voltage off. This allowed one to determine if any pulses from the power line or elsewhere were being picked up.

The detection system was also checked to determine whether the anticoincidence circuit was causing any unusual behavior. This was done by counting with the crystal in the direct beam and with and without the Geiger counters on. Within the accuracy of the apparatus, the results under both conditions were the same.

III. AUXILIARY MEASUREMENTS

Characteristics of the Detector

The lithium gamma-ray pulse-height distribution was obtained by placing the NaI(Tl) crystal directly in the beam and taking differential number—bias curves. The result of these measurements is shown in Fig. 2. One sees that the crystal detector does not resolve the 14.8-Mev and 17.6-Mev lines of the lithium spectrum. The resolution of the crystal is poor because a large fraction of the time the pairs formed by the gamma-rays do not lose their full energy in the crystal. Two things can happen to cause this. Either the members of the pairs may not be completely stopped in the crystal but leave it before losing all their energy, or else they may emit bremsstrahlung and the created gamma-rays leave the crystal without interacting. One can qualitatively understand the observed distribution curve in Fig. 2, as a compound distribution of the 14.8-Mev and 17.6-Mev lines, if the response of the detector to monoenergetic gamma-rays is known. For this purpose a measurement was made of the pulse-height distribution of the 20-Mev monoenergetic gamma-rays obtained by bombarding tritium with 0.96-Mev protons. This is also shown in Fig. 2. To obtain the expected pulse-height distribution for the 14.8-Mev and 17 6-Mev lines from this measurement at 20 Mev, one has to assume that the shape of the distribution curve for monoenergetic gamma-rays does not vary with energy over the energy region from about 14 Mev to 20 Mev. This assumption is reasonable in view of the following facts. The resolution of the detector for ThC″ gamma-rays (2.62 Mev) was measured and found to be about 15 percent, while near 17 Mev it is 28 percent. Therefore, while the resolution of the detector does vary some with energy, it does not do so very rapidly. Thus, between 14–20 Mev it should be a reasonable assumption to suppose that it stays constant. If the separate lithium lines are therefore given shapes corresponding to that obtained from

the tritium pulse-height distributions and are then added together in the proper ratios, they reproduce very well the observed lithium pulse-height distribution shown in Fig. 2.

Energy sensitivity curves for the various channels can also be obtained using the monoenergetic gamma-ray pulse-height distribution. They are shown in Fig. 3. Again one has to assume that the shape of the distribution curve remains constant over the range of about 13–20 Mev. The energy sensitivity curve for a given discriminator setting is obtained by reflecting about its peak, the monoenergetic gamma-ray pulse-height distribution for that energy gamma-ray that has the peak of its distribution curve at the energy that corresponds to the discriminator setting. Therefore, to get the energy sensitivity of a channel with a finite width one must add up the sensitivity curves for all points in the energy range of the channel. The energy sensitivity curves, for each of the single channels used in the experiment, were obtained by adding the sensitivity curves for three equally spaced points in the channels. The energy sensitivity curve for both channels taken together was then obtained from the sensitivity curves of the two single channels. From these curves it is possible to obtain the effective range of gamma-ray energies for which each channel is sensitive.

Two separate runs of the whole experiment were made. In the first run the detector had a resolution of 33 percent, and only one energy channel was used. The energy biases for this channel were 12.9 Mev and 21.8 Mev, based on an energy scale which would correspond to assigning the energy of 17.6 Mev to the peak of the pulse-height distribution curve that would be obtained from a monoenergetic gamma-ray of 17.6 Mev. For this channel 90 percent of the area under the sensitivity curve below 17.6 Mev was due to gamma-rays of energies greater than 12.0 Mev. In the second run the detector had been remounted, and it now had a resolution of 28 percent; also two energy channels were used. The energy biases were 12.9 Mev and 16.6 Mev for the low energy channel (called the L channel) and 16.6 Mev and 20.3 Mev for the high energy channel (called the H channel). For the H channel 90 percent of the area under the sensitivity curve below 17.6 Mev was due to gamma-rays of energies greater than 14.4 Mev, while in the two channels taken together (called the HL channel) 90 percent of the area of sensitivity below 17.6 Mev was due to gamma-rays of energies greater than 12.3 Mev.

The average energies detected by the various channels depends on the spectrum of the gamma-rays incident on the crystal. If the energy spectrum of the incident gamma-rays is represented by a function $f(E)$ and the energy sensitivity of the channel is given by a function $S(E)$, then the average energy is given by

$$\bar{E} = \int_0^{17.6\ \text{Mev}} Ef(E)S(E)dE \Big/ \int_0^{17.6\ \text{Mev}} f(E)S(E)dE. \quad (1)$$

Since the spectra of the scattered gamma-rays are not known, the average energy of detection of the channels is in general not known. However, the spectrum is known when looking at the direct beam, and, therefore, the average energy for the various channels can be obtained for this condition. The average energies of detection for the direct beam, obtained in this manner, are 16.9 Mev for the H channel and 16.3 Mev for the L channel.

Identification of Particles

The experiment was run with 6.5 g/cm² of brass between the scatterer and detector. This caused electrons of 15 Mev to lose about 11 Mev in the brass. In this way electrons were prevented from producing pulses large enough to be recorded by the energy channels. Any other charged particles would also lose at least this much energy in the brass, and they also could not be recorded by the detection system. It can therefore be concluded that the counts from the scatterer were not due to charged particles.

It is true that there might be a small amount of conversion of some of the energy of the secondary electrons into gamma-rays in the brass. However, the number of gamma-rays that might be formed in this way is entirely negligible compared to the number that might be formed in the scatterer itself. Therefore, there is little advantage to be obtained by using a lower Z element, like Al, in

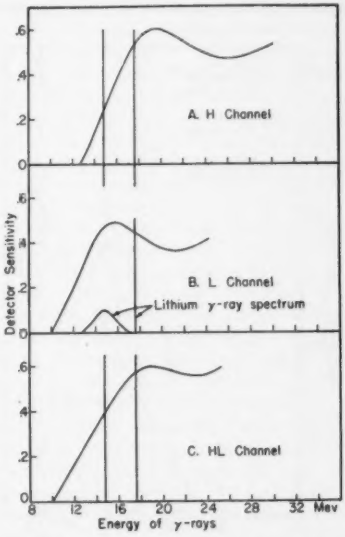

FIG. 3. Energy sensitivity curves for the various energy channels. In obtaining these curves the assumption is made that the shape of the pulse-height distribution curves for monoenergetic gamma-rays remains constant over the energy region from 13–20 Mev.

place of the brass. The brass has the advantage that it is much more compact. This bremsstrahlung production by the secondary electrons is considered later in more detail.

It would be extremely improbable for the gamma-rays to give rise to the emission of neutrons of sufficiently high energy to be detected by the crystal. At best the neutrons could be emitted with about 17 Mev minus their binding energy. Also the efficiency of the NaI(Tl) crystal for detecting neutrons is extremely small. But, to make certain that neutrons were not being detected, a run was made with a block of paraffin between the scatterer and detector. A thickness of paraffin of one mean-free-path for 12-Mev neutrons was used. If the counts were due to neutrons, the counting rate with the paraffin should have been reduced to 37 percent of the counting rate without the paraffin. However, if the counts were due to gamma-rays, the paraffin should have reduced the counting rate to 80 percent of that without the paraffin. Normalizing the counting rate without the paraffin to be 1.0 ± 0.15, the results were that with the paraffin in place the counting rate was 0.75 ± 0.12. This then indicates that the counts were due to gamma-rays and not neutrons.

To check further that the counts from the scatterer were due to gamma-rays, runs were made with a Pb absorber, of two mean-free-paths for 17-Mev gamma-rays, inserted between the scatterer and detector. If the counts were due to gamma-rays, this amount of Pb should have a transmission of 0.13. Taking the normalized counting rate without the Pb absorber equal to 1.0 ± 0.09, the counting rate with the Pb absorber was 0.11 ± 0.09. This agrees well with the expected transmission, making it quite certain that what were being detected by the crystal were scattered gamma-rays.

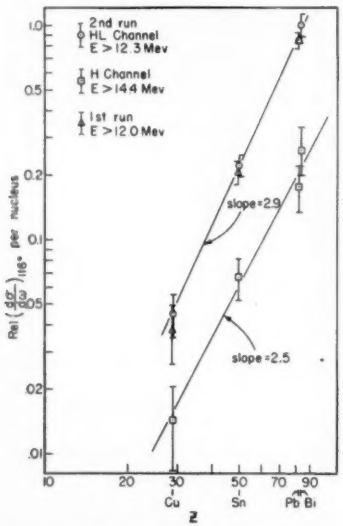

FIG. 4. Variation of the relative differential nuclear scattering cross section per nucleus as a function of Z. The average angle of scattering was $116°\pm17°$.

IV. GENERAL PROCEDURE

The scattering of gamma-rays was measured for four different nuclei: Bi, Pb, Sn, and Cu. From these measurements the variation of the differential cross section with Z was obtained. The scattering measurements were made by alternately taking runs with the scatterers in place and without them. The number of scattered gamma-rays was then obtained for each run by subtracting the backgrounds adjacent to each scatterer run. In this way the total scattering measurement for each type of nucleus was made up of several individual runs. These individual runs were then used to compute an rms error, i.e., the error determined by taking the deviation from the mean of the separate runs. The statistical standard deviation for the total scattering measurements was also computed. In all cases the rms error agreed very well with the statistical error. This gave a good check on the stability and internal consistency of the data. All errors quoted in the results are the larger of the rms error or the standard deviation.

To be sure that the scattering observed was not due to gamma-rays from bremsstrahlung caused by the secondary electrons in the scatterer, the scattered gamma-rays were measured at three angles for Pb and Sn.

By counting with the detector in the direct beam and with the same energy channels as when measuring scattered gamma-rays, measurements were obtained which, when combined with the scattered gamma-ray measurements, allowed the absolute differential cross section for the nuclear scattering of gamma-rays to be determined.

The magnitude of the proton beam throughout the experiment was about 90–100 μa when measuring scattered gamma-rays and about 20–25 μa when making measurements of the direct beam. A beam of 90–100 μa of 700-kev protons striking a thick lithium target yields about 10^7 gammas/sec. In the *HL* channel the counting rates for gamma-rays scattered through 116° were about as follows: Bi, 1.4 counts/min; Pb, 1.2 counts/min; Sn, 0.75 count/min; Cu, 0.35 count/min; cosmic-ray background, 0.8 count/min; and background with no scatterer, 1.6 counts/min. These are the counting rates for each scattering block. The scatters did not contain equal number of nuclei. The counting time per observation was about 35 minutes. At 116° a total scattering measurement was comprised of about eleven separate runs consisting of counting both with and without the scatterer in the beam.

V. RESULTS

Z Dependence

Figure 4 shows the Z dependence of the differential cross section per nucleus at an average angle of scattering of $116°\pm17°$. The average angle of scattering is determined from the measured angle (108°) by the application of three geometric weighting factors. The first factor weights the angles of scattering from different portions of the scatterer by the solid angle subtended at the source. This is a large correction since some portions of the scatter subtend about four times the solid angle that others subtend. The second correction comes about because the detector subtends different solid angles for different portions of the scatterer. The largest variation in detector solid angle for the various portions is only 25 percent; therefore, this correction is much smaller than the first correction. It is also in the opposite direction. The third correction is due to the variation in distance that the gamma-rays travel before and after being scattered in the different regions of the scatterer. This correction is also much smaller than the first correction and in the opposite direction. The greatest variation between various portions of the scatterer is about 25 percent.

For the second run the counting rates for the various elements have been taken relative to Bi which has been normalized to 1. For the first run Bi was not measured, and the counting rates have been taken relative to Pb which has been normalized to the same value it had in run 2. It is seen that the agreement between runs 1 and 2 is excellent. Run 2 was made with much more care and accuracy than run 1, and only it will be considered from now on. Both the counting rate for the H channel and the HL channel have been plotted. Since the H channel does not detect many gamma-rays below 14.5 Mev, the counts in this channel are essentially due to elastic scattering. The differential cross-section variation determined from only the H channel data goes as $Z^{2.0\pm0.5}$. The differential cross-section variation from the HL channel data goes as $Z^{2.9\pm0.3}$.

While one might expect such a rapid variation with Z, as $Z^{2.5}$, for elastic scattering (due to a Z^2 from coherence), it is at first surprising that the inelastic scattering should vary as strongly as $Z^{2.9}$ or greater. Thus, it might be suspected that some process other than nuclear scattering is contributing to the HL channel data. The bremsstrahlung process mentioned before would be expected to go as about Z^4 per nucleus (Z^2 for pair production, Z^2/A for Coulomb scattering and Z^2/A for the bremsstrahlung emission). Therefore, one suspects that the strong Z dependence of the both channel data may be due to the bremsstrahlung process. So angular distribution measurements were made to investigate the bremsstrahlung more thoroughly.

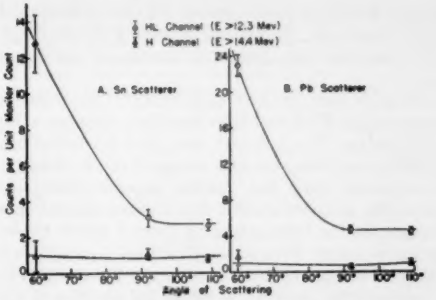

FIG. 5. Variation of the intensity of scattered gamma-rays from Pb and Sn as a function of the scattering angle. The data are plotted at the average bremsstrahlung angle of scattering. The line drawn through the H channel data corresponds to a $(1+\cos^2\theta)$ distribution.

Investigation of Possible Bremsstrahlung Contamination

The bremsstrahlung process comes about from the electrons and positrons, formed from pair production, being scattered through large angles and then emitting bremsstrahlung. To obtain information about the amount of bremsstrahlung present, measurements of the scattering were made at three angles for Pb and Sn. The three measured angles were 108°, 90°, and 62½°. The average angles of scattering are determined by applying the previously mentioned three correction factors and also another correction factor depending on the type of scattering which the electron or positron undergoes. Rough information about the type of scattering can be obtained by using the curves of Snyder and Scott.[10] By considering these curves we conclude the following. At the two larger angles measured (90° and 108°), Coulomb scattering is the most important type of scattering. For the 62½° angle of scattering the multiple (or plural) scattering is about three times the single Coulomb scattering for the Pb scatterer and about two times the single scattering for the Sn scatterer. Therefore, for the two larger angles, 90° and 108°, we apply a Coulomb scattering angular dependence factor to obtain the average bremsstrahlung angle of scattering, while for the 62½° angle of scattering we know only that the angular dependence varies more rapidly than the Coulomb scattering angular distribution. When the formerly described three geometric correction factors and the Coulomb weighting factor, $1/\sin^4(\theta/2)[1+\beta^2\sin^2(\theta/2)]$, are applied to the two larger angles, the 90° scattering angle becomes 92° and the 108° angle becomes 109°. For the smallest angle (62½°) we shall estimate the average angle of scattering to be around 60°.

In Fig. 5 the variation of the number of scattered gamma-rays with the average scattering angle is shown.

[10] H. S. Snyder and W. T. Scott, Phys. Rev. **76**, 220 (1949).

These yields have been corrected for the different solid angles subtended by different regions of the scatterer, etc. (the first three geometric corrections mentioned above).

It can be seen that for both Sn and Pb the number of counts in the H channel stays essentially the same at all three angles. This indicates that little bremstrahlung is being counted by the high energy channel. This is to be expected, since this channel measures essentially elastically scattered gamma-rays and any gamma-rays formed by the bremsstrahlung process would be degraded in energy. (The elastically scattered gamma-rays should have an angular distribution like $(1+\cos^2\theta)$. This variation, however, is within the statistics of the plotted points.)

The yield of scattered gamma-rays from the HL channel data rises rapidly as we go to smaller angles. (Since the inelastically scattered gamma-rays probably

TABLE I. Experimental values of quantities in Eq. (4).

Quantity	Bi	Pb	Sn	Cu	Units
n_H	13.3±3.4	8.9 ±2.2	7.9 ±2.0	4.1 ±1.8	counts / monitor count
n_{HL}	49.6±6.2	42.7±3.8	26.5±3.1	12.9±3.0	counts / monitor count
N	2.82×10^{23}	3.29×10^{22}	3.79×10^{22}	8.45×10^{23}	atoms/cm²
λ	1.07	1.49	3.04	3.26	cm

$t=0.80$ for 17-Mev gamma-rays.
$C_{HL}=(2.00\pm0.04)\times10^8$ counts/monitor count.
$C_H=(0.96\pm0.02)\times10^8$ counts/monitor count.
$f\Omega_1=0.482$ steradians (a standard deviation of 10 percent is estimated for this quantity).
$I_{0°}/I_{90°}=1.09$.[a]

[a] The 440-kev resonance has a width of about 12 kev, and the nonresonant tail from 440 kev to 700 kev has an intensity of 2 percent of the peak of the 440-kev resonance [see W. A. Fowler and C. C. Lauritsen, Phys. Rev. **76**, 314 (1949)]. Therefore, at 0° a 700-kev proton beam incident on a thick Li target produces radiation which is about 30 percent nonresonant and 70 percent resonant radiation. Since the nonresonant radiation is anisotropic the 0° and 90°, intensities are therefore unequal (see reference 11).

are emitted from a compound state of the nucleus, it is assumed that they are isotropic. Therefore, if all the HL channel data were the result of nuclear scattering, it would remain constant at all angles.) This rapid rise shows that, at least at small angles, there is a large amount of bremsstrahlung emitted from the scatterers. Assuming that the observed counts are due only to nuclear scattering and bremsstrahlung, we can calculate the amount of bremsstrahlung present for the largest angle of scattering. The results obtained from the 90° data show that the bremsstrahlung process contributes about 13±13 percent in the 116° nuclear scattering measurement. In addition, the calculations from the 60° data indicate that the bremsstrahlung process contributes less than about 10 percent in the 116° scattering measurement.

An estimate of the amount of bremsstrahlung in the 116° scattering data can also be obtained by calculating the absolute differential cross section of the bremsstrahlung process. Starting with a 17.6-Mev gamma-ray striking a Pb scatterer and considering energy losses due to ionization, a detailed calculation was made of the probability of obtaining an electron or positron of a given energy which had been singly Coulomb scattered through a given angle. Next the probability of the electron emitting a gamma-ray of energy sufficient to be recorded by the HL channel was calculated. An integration was then made over all possible energies of the electron or positron. The absolute differential cross section obtained in this way was $(d\sigma/d\omega)_{116°}\simeq0.02$ mb/sterad.

As will be seen later, a lower limit for the observed differential cross section for scattering from Pb is 1.2±0.2 mg/sterad. Hence, it is seen that the estimate of the cross section for the single scattering bremsstrahlung process is only 2 percent of the observed lower limit of the cross section for the scattering of gamma-rays. Calculations considering two ($54\frac{1}{2}$°) scatterings instead of a single scattering yield differential cross sections about twenty times smaller than that of the above calculation. Nevertheless, there may exist combinations of plural and multiple scatterings that have probabilities that are as large or larger than the single scattering probability. However, these processes are rare, and it is therefore probably safe to assume that the single scattering process gives a reasonable estimate of the scattering process.

Since the above calculation of the cross section for the bremsstrahlung process is probably on the high side or in any case it yields a result that is much smaller than the measured cross section, the amount of bremsstrahlung in the data for the HL channel will be assumed to be small and be neglected in the analysis. The bremsstrahlung in the high energy channel will be assumed to be zero.

Differential Cross Section of Nuclear Scattering

The absolute differential cross section for the nuclear scattering of gamma-rays can be determined by combining the scattering measurements with measurements of the direct beam. The direct beam measurements were obtained by simply placing the crystal at a known distance from the source in the direct beam and observing the number of counts per unit monitor count.

To assure that the phototube experienced the same fringe magnetic field from the cyclotron throughout all measurements, the crystal was kept at essentially the same location for detecting both scattered or direct gamma-rays. Therefore, for the direct beam measurements it was at about 90° to the incident proton beam. The crystal was also placed the same distance from the source for the direct beam measurements of scattered radiation. This assured that the detector subtended the same solid angle in both cases.

For the measurements with the crystal in the direct beam, the observed number of counts per unit monitor

count is given by

$$C = I_{90°} \epsilon A_2 / d^2, \tag{2}$$

where C is the number of counts per unit monitor count with the crystal in the direct beam, $I_{90°}$ is the number of gamma-rays emitted from the source per unit monitor count per unit solid angle at 90° to the proton beam, ϵ is the efficiency of the crystal for detecting gamma-rays, A_2 is the effective area of the crystal, and d is the distance from the center of the detector to the center of the source or also from the center of the scatterer to the center of the detector (=48.2 cm).

From the measurements of the scattered radiation, the observed number of counts per unit monitor count is given by

$$n = I_{0°} f \Omega_1 N (d\sigma/d\omega)_{116°} \lambda (\epsilon A_2 / d^2) t, \tag{3}$$

where n is the number of scattered gamma-rays counted by the detector per unit monitor count, N is the number of atoms per cm³ in the scatterer, $(d\sigma/d\omega)_{116°}$ is the differential scattering cross section for an average angle of 116°, λ is the mean-free-path for 17.6-Mev gamma-ray[9] (equal to the scatterer thickness), t is the transmission factor for 17-Mev gamma-rays going through the 6.5 g/cm² of brass between the scatterer and detector, Ω_1 is the solid angle subtended by the scatterer at the source, and f is the absorption correction factor for the scatterers due to the variation in distance which the gamma-rays travel before and after being scattered in different regions of the scatterer. By substituting (2) in (3), we obtain

$$(d\sigma/d\omega)_{116°} = [n/(N\lambda t C f \Omega_1)](I_{0°}/I_{90°}). \tag{4}$$

The values of the quantities to be used in Eq. (4) are given in Table I. Substituting the values for the various quantities into Eq. (4) yields the differential cross sections for the nuclear scattering of gamma-rays which are tabulated in Table II.

The efficiency used in these calculations is the efficiency for the detection of rather high energy gamma-rays, since it is obtained from the direct beam measurement. Owing to the fact that the energy sensitivity curves fall off very rapidly with decreasing energies (see Fig. 3), this efficiency is greater than the actual efficiency for detecting inelastically scattered gamma-rays. Therefore, the cross sections obtained from the HL channel data give only a lower limit for the scattering of the gamma-rays detected in this channel. As one can see from Fig. 3, the efficiency used probably does not differ from the actual efficiency by more than a factor of three. Therefore, the upper limits for the cross sections determined from the HL channel data are about three times the values listed in the above table.

The efficiency obtained from the direct beam measurement is, however, very nearly equal to the efficiency with which the elastically scattered gamma-rays are detected. Therefore, the cross sections obtained from the H channel data are correct. The errors given for these cross sections are standard deviations.

TABLE II. Differential cross sections for the nuclear scattering of the gamma-rays from the $Li^7(p,\gamma)Be^8$ reaction. For the H channel 90 percent of the scattered gamma-rays have energies greater than 14.4 Mev. For the HL channel 90 percent of the gamma-rays have energies greater than 12.3 Mev.

	$(d\sigma/d\omega)116°$ in mb/sterad		
Scatterer	H channel	HL channel	Estimates of accuracy of HL channel values
Bi	0.82 ±0.22	1.5	$+3.0$ -0.2
Pb	0.53±0.14	1.2	$+2.4$ -0.2
Sn	0.20 ±0.049	0.33	$+0.66$ -0.05
Cu	0.044±0.020	0.07	$+0.13$ -0.02

Inelastic Scattering

With the crystal in the direct beam, the ratio of counts in the high channel to those in the low channel was 0.93±0.03. The ratios observed for the scattered gamma-rays are given in Table III.

If the scattering were all elastic we should expect the ratio of counts in the high to low channels to be larger than 0.93 for the following three reasons: (1) The cross section for scattering probably has a maximum around 18–20 Mev and decreases at lower energies. Thus, the scattering of the higher energy gamma-rays is favored. (2) We know that the energy sensitivity curves fall off very rapidly at lower energies. Therefore, in the detection of the gamma-rays the higher energy gamma-rays are much favored over the lower energy gamma-rays. (3) The gamma-rays produced by 700-kev protons striking a thick lithium target have for the ratios of 17.6-Mev to 14.8-Mev gamma-rays values of 1.3 and 1.1, respectively, at 0° and 90° to the incident proton beam.[11] Therefore, the gamma-rays to be scattered have a slightly higher average energy than the directly measured gamma-rays. All three of these factors would then contribute to give more counts in the high channel than in the low channel. Therefore, to account for the large decrease in the high to low ratio of counts for the

TABLE III. Ratios of the number of counts in the H channel to those in the HL channel from the scattered gamma-rays.

	Scatterer			
	Bi	Pb	Sn	Cu
$\frac{H \text{ channel counts}}{HL \text{ channel counts}}$	0.37±0.11	0.26±0.07	0.43±0.12	0.46±0.23
Ratio for the direct beam = 0.93±0.03				

[11] M. B. Stearns and B. D. McDaniel, Phys. Rev. **82**, 450 (1951).

TABLE IV. Values of E_{max} obtained by comparing the experimental values for elastic scattering with the theoretical values derived under the assumption of a Rayleigh-type scattering of the gamma-rays. Two values of E_{max} are obtained, the lower by assuming the scattered gamma-rays have energy greater than the resonant energy and the higher by assuming the incident gamma-rays have energy less than the resonant energy. x is the fraction of attraction exchange force for the $n-p$ potential.

	$x=0$		$x=\frac{1}{2}$	
	Upper	Lower	Upper	Lower
Pb	$19.5^{+0.3}_{-0.2}$ Mev	$13.7^{+0.1}_{-0.3}$ Mev	$20.2^{+0.4}_{-0.3}$ Mev	$12.9^{+0.4}_{-0.5}$ Mev
Sn	$19.4^{+0.3}_{-0.2}$ Mev	13.7 ± 0.2 Mev	$20.1^{+0.4}_{-0.2}$ Mev	$13.1^{+0.2}_{-0.5}$ Mev
Cu	$19.7^{+0.7}_{-0.4}$ Mev	$13.5^{+0.3}_{-0.8}$ Mev	$20.5^{+1.0}_{-0.5}$ Mev	$12.6^{+0.6}_{-1.0}$ Mev

scattered radiation with respect to the direct radiation, it is concluded that there must be a considerable amount of inelastic scattering present.

VI. DISCUSSION OF RESULTS

Using gamma-rays with a 100-Mev bremsstrahlung spectrum, Gaerttner and Yeater[7] obtained a cross section for Cu (assuming a 5-Mev total resonance width) of, $(d\sigma/d\omega)_{116°}<0.4$ mb/sterad. The comparable measurement in this experiment yielded $(d\sigma/d\omega)_{116°}\geqslant 0.066\pm0.016$ mb/sterad, with an estimated upper limit of about 0.2 mb/sterad.

For the scattering of gamma-rays with a 22-Mev bremsstrahlung spectrum from Pb, Dressel *et al.*[8] obtained a value of $(d\sigma/d\omega)_{116°}\simeq 1.5\pm0.7$ mb/sterad. This experiment yielded a value of $(d\sigma/d\omega)_{116°}\geqslant 1.2\pm0.2$ mb/sterad with an upper limit of about 3.6 mb/sterad.

The elastic nuclear scattering can be considered from the point of view of two limiting cases. In the first case we assume that the absorption curve is due to a single energy level of small width and also that the energy of the incident gamma-ray is many widths of the absorption curve away from the resonant energy, i.e., that the scattering takes place on the tail of the resonance curve, ordinary Rayleigh scattering. For the second case we assume that the absorption curve is widened; owing to, for example, many overlapping energy levels. We also assume that the energy of the incident gamma-ray is within a half-width of the peak of the absorption curve. (This is the case of resonance fluorescence.)

Case 1. Making the assumptions given above for the first case, the expression for the elastic nuclear scattering of gamma-rays can be easily obtained from the Kramers and Heisenberg dispersion formula.[12] The expression obtained is

$$\sigma_{Th}=\frac{8\pi}{3}r_0^2\left(\frac{m}{M}\right)^2\left(\frac{E^2}{E_{max}^2-E^2}\right)^2\left(\frac{NZ}{A}(1+0.8x)\right)^2, \quad (5)$$

where r_0 is the classical radius of the electron, m is the mass of the electron, M is the mass of a nucleon, E is the energy of the gamma-ray, N is the number of neutrons in the scattering nucleus, Z is the number of protons in the scattering nucleus, A is the atomic number of the scattering nucleus, x is the fraction of attractive exchange force for the $n-p$ potential, and E_{max} is the energy at the maximum of the absorption excitation curve.

Since, if the value of x is assumed, E_{max} is the only adjustable parameter in Eq. (5), we can determine values of E_{max} by substituting the experimentally obtained elastic cross sections into this equation for σ_{Th}.

To obtain the total measured cross sections from the differential cross sections we must know the angular dependence of the cross sections. It is the same as the angular dependence for Thomson scattering, that is, a $(1+\cos^2\theta)$ dependence. Using this angular dependence, we get from the observed differential cross sections the following total elastic scattering cross sections: $\sigma_{Pb}=7.4\pm2.0$ mb, $\sigma_{Sn}=2.8\pm0.7$ mb, and $\sigma_{Cu}=0.62\pm0.28$ mb. Two values of x are assumed, $x=0$ and $x=\frac{1}{2}$. For the value $x=0$, the $n-p$ interactions are presumed to be due to only ordinary forces. While for the value $x=\frac{1}{2}$, the $n-p$ interactions are assumed to be due to half exchange and half ordinary forces. The value of $x=\frac{1}{2}$ for the attractive exchange force is in agreement with the Berkeley $n-p$ scattering experiments.[13] For each element, two values of E_{max} are obtained by substituting the observed cross sections into Eq. (5). These values of E_{max} are given in Table IV.

From $\gamma-n$, $\gamma-\alpha$, and $\gamma-p$ excitation curves we know that most of the maxima fall between 15 and 21 Mev; therefore, the higher energy, nearer 20 Mev, is probably the value to be considered. However, having $E_{max}\sim20$ Mev is in poor agreement with other evidence.[14] An integrated $\gamma-n$ cross section of about 0.9 Mev-barns, with $E_{max}\sim18$ Mev, has been observed for Cu.[2,15] The total integrated cross section predicted by Levinger and Bethe is $\sigma_T=0.94$ Mev-barns for $x=0$ or 1.3 Mev-barns for $x=\frac{1}{2}$. Therefore, if E_{max} were near 20 Mev, the gamma-ray absorption curve must continue increasing up to 20 Mev, and the total integrated cross section would become larger than the total oscillator strength permits. This then leads one to believe that the absorption of the gamma-rays may not be due purely to one single dipole level but may for some reason be due to a widened level. So let us now look at Case 2.

Case 2. In this case the assumption is made that the absorption curve is widened and that the incident gamma-ray energy is inside the width of the absorption

[12] W. Heitler, *Quantum Theory of Radiation* (Oxford University Press, London, 1944), second edition, p. 132.

[13] Hadley, Kelly, Leith, Segrè, Wiegand, and York, Phys. Rev. **75**, 351 (1949).

[14] P. Morrison (private communication).

[15] Johns, Katz, Douglas, and Haslam, Phys. Rev. **80**, 1062 (1950); Katz, Johns, Baker, Haslam, and Douglas, Phys. Rev. **82**, 271 (1951).

curve. In this case Eq. (5) becomes[16]

$$\sigma_{\mathrm{Th}}=\frac{2\pi}{3}r_0^2\left(\frac{m}{M}\right)^2\left[\frac{NZ}{A}(1+0.8x)\right]^2\frac{E^2}{(E_{\max}-E)^2+(\delta/2)^2},$$

where δ is the full width of the absorption curve.

For this case let us assume that $E_{\max}$ is around 17–18 Mev; than δ is the only adjustable parameter. Substituting the experimental cross section into Eq. (6) for σ_{Th} we get a width of $\delta\sim 4$ Mev for $x=0$ and a width of $\delta\sim 5.5$ Mev for $x=\frac{1}{2}$. The observed widths from $\gamma-n$ excitation curves are about 5 Mev. Therefore, it is seen that by using values of $E_{\max}$ around 17–18 Mev with the assumption of a broad resonance, this model gives good agreement with the observed $\gamma-n$ widths.

The data from this experiment, whether treated under Case 1 or Case 2, give no evidence that $E_{\max}$ has any dependence on Z.

The models used in the above two cases are the limiting cases of wide and narrow resonances. From the elastic scattering results alone, we are unable to distinguish between the two cases. However, the $\gamma-n$ results and the $\gamma-\gamma$ results obtained here would tend to favor a wide level theory with the maximum of the absorption curve around 17–18 Mev and a full width of from 4 to 6 Mev. Both of the models assumed above are one-level theories, and while they give qualitative agreement with the observed elastic scattering they are not very trustworthy quantitatively.

The large amount of inelastic scattering observed indicates that the Goldhaber-Teller model, of the nucleus vibrating as a whole in only one main mode, cannot be correct without modification. This is as expected, since this model is intentionally extreme and assumed primarily because it is easy to handle in calculations.

To interpret the high Z dependence of the inelastic scattering ($>Z^{2.9}$), let us consider the inelastic scattering process in two steps. In the first step the gamma-ray is absorbed by a group of nucleons in the nucleus. (This absorption process is roughly proportional to Z.) The energy of the gamma-ray then becomes shared among all the nucleons, forming a compound state of the nucleus. The second step is then the de-excitation of the compound nucleus. One would expect the decay of the compound nucleus to depend quite strongly on the number of nucleons in the nucleus. We can get a rough idea of this dependence if we know the energy level density at the various energies and the probability of the nucleus to emit a given energy gamma-ray. By multiplying these two quantities together and integrating over the energy region corresponding to the detected gamma-rays, we can obtain an estimate of the Z dependence for the emission of gamma-rays.

If one uses Weisskopf's expression for the energy level density,[17] $\omega\simeq C\exp[1.6(A-40)^{\frac{1}{2}}E]^{\frac{1}{2}}$, and assuming mainly dipole transitions, where the probability of emission of gamma-rays goes as $(E_\gamma)^3$, $(E_\gamma=17.6-E)$, one obtains

$$\sigma_{\mathrm{inel}}\sim\int_{E=0}^{E=5.3\ \mathrm{Mev}}(17.6-E)^3\exp[1.6(A-40)^{\frac{1}{2}}E]^{\frac{1}{2}}dE. \tag{7}$$

An upper limit of 5.3 Mev is used, since the HL channel detected gamma-rays greater than 12.3 Mev. If one evaluates this quantity, it is, of course, not a function of a single power of Z, but for the elements Cu, Sn, and Pb it varies roughly as Z^4. This then shows that considering the inelastic scattering as a dipole absorption of the gamma-rays followed by the formation and subsequent decay of a compound state of the nucleus leads to the inelastic scattering cross section being a strongly dependent function of Z ($\sim Z^5$ for this model). The above estimate of the variation with Z is very crude, since the statistical model is applied to energy levels in the region between 0 and 5.3 Mev where this model is not very suitable. Also it has been assumed that the gamma-ray transitions from the compound nucleus are due to only dipole transitions, which is probably not true for these high energy gamma-rays.

It is seen that the general results of the experiment can be qualitatively understood by using very simplified models of the nucleus. However, much more realistic and detailed calculations must be made, assuming various models for the subunits in the nucleus, before the experimental results are understood quantitatively.

It is a pleasure to thank Professors B. D. McDaniel and P. Morrison for their helpful discussions and suggestions throughout the course of this work. I also wish to thank Professor Bethe for several valuable discussions, and I am grateful to Dr. Robert S. Rochlin for the use of his tritium target.

[16] See, for example, reference 13, p. 38.

[17] See reference 2, p. 412.

The Disintegration of Oxygen and Nitrogen by 14.1-Mev Neutrons*

ALAN B. LILLIE
Rice Institute, Houston, Texas
(Received May 26, 1952)

Oxygen and nitrogen contained as a gas in a cloud chamber were bombarded by 14.1-Mev neutrons. From the disintegrations of these nuclei the following data have been collected: (*a*) the range-energy relations of C^{12} in the energy range 0–5 Mev, and the range-energy curve of B^{11} from 0–7 Mev; (*b*) the excited states of the nuclei C^{13}, B^{11}, N^{15}, and N^{14}; (*c*) the angular distributions of the alpha-particles emitted in the $O^{16}(n,\alpha)C^{13}$ and $N^{14}(n,\alpha)B^{11}$ reactions; (*d*) the cross sections for some of the reactions taking place.

I. INTRODUCTION

CLOUD-CHAMBER studies of disintegrations produced by neutrons have been made by several groups. Feather[1] in 1932 studied the $N^{14}(n,\alpha)B^{11}$ reaction; Bonner and Brubaker[2] in 1936 studied the same reaction and the $N^{14}(n,p)C^{14}$ and $N^{14}(n,2\alpha)Li^{7}$ reactions. These early investigations were limited by the lack of monoenergetic neutron sources. With the availability of tritium, the high energy 14.1-Mev neutrons from the $H^{3}(d,n)He^{4}$ reaction opened a new region of study to this older technique. The large cross section for this reaction, obtained with low deuteron energy, makes this a very strong source of monoenergetic neutrons. In addition, since the neutrons are fast and uncharged, their penetrability is high even for large values of angular momentum. For this reason a nuclear level possessing a large spin might be excited by these neutrons, while it might not be found in reactions using slower charged particles of low angular momentum. This present study makes use of these fast neutrons to study the disintegration of oxygen and nitrogen.

II. APPARATUS

The target was tritium absorbed in a zirconium film deposited on a tungsten disk $\frac{1}{2}$ in. in diameter by $\frac{1}{16}$ in. thick.[3] The deuterons were accelerated in the Rice Institute 200-kev Cockroft-Walton accelerator. The neutrons from the $H^{3}(d,n)He^{4}$ reaction entered the cloud chamber at 90° to the deuteron beam.

The cloud chamber was 15 cm in diameter by 8 cm deep and of light construction to minimize the scattering of neutrons. The center of the chamber was placed $28\frac{1}{2}$ cm from the center of the target and 95 cm from the floor, which was the nearest large scattering mass.

Tank oxygen and nitrogen having less than one percent impurities filled the cloud chamber to a pressure of one atmosphere. While the recoil protons from the hydrogen present are readily recognizable, disintegrations due to other impurities may not be distinguished from those due to oxygen or nitrogen. Water vapor was therefore used as the vapor in the cloud chamber so that the only nuclei present to more than one percent would be O^{16}, N^{14}, and H^{1}.

Stereoscopic pictures of the tracks in the cloud chamber were taken and after the film was processed, the images were reprojected through the same optical system. Measurements of track lengths and the angles that the tracks made with the neutrons' paths were made. In addition, the relative track densities in a fork (to aid in the identification of reactions) and the positions in the chamber were noted. All forks were measured provided that the plane of the fork was less than 50° to the horizontal. All recoil nuclei lying within a cone of 10° half-angle for oxygen and 15° half-angle for nitrogen were measured.

Measurements were made to see whether the plane of the fork passed through the target position. This plane would not normally pass through the target position if the disintegration were caused by a scattered neutron. The percentage of forks caused by scattered neutrons was found to be less than four percent.

III. RESULTS

A total of 1600 pictures were taken of disintegrations in oxygen and 2700 pictures of nitrogen. The number of forks (two-particle disintegrations) measured were 1200 in oxygen and 1800 in nitrogen. In the case of nitrogen, 256 tridents (three-particle disintegrations) were also measured. This latter is the disintegration of the nitrogen into two alpha-particles and a Li^{7} particle. Figures 1 and 2 show stereoscopic views of disintegrations in oxygen and nitrogen, respectively. In Fig. 1 are several examples of alpha-emission. In Fig. 2 are two cases of three-particle disintegrations, as well as a disintegration in which either a proton or deuteron or triton is emitted, crosses, and leaves the chamber. Some recoil nitrogen nuclei can be seen as very short heavy tracks. An example of alpha-emission is also seen here.

1. Range-Energy Relations

Sufficient numbers of forks for a study of range-energy relations were available from the reactions $O^{16}(n,\alpha)C^{13}$ and $N^{14}(n,\alpha)B^{11}$. The measured length of the heavy particle track in a fork was converted into the range in standard air by multiplying by the stopping power of the gas mixture calculated from the stopping

* This work was supported by the AEC program.
[1] N. Feather, Proc. Roy. Soc. (London) **A136**, 709 (1932).
[2] T. W. Bonner and W. M. Brubaker, Phys. Rev. **49**, 223 (1936).
[3] A. B. Lillie and J. P. Conner, Rev. Sci. Instr. **22**, 210 (1951).

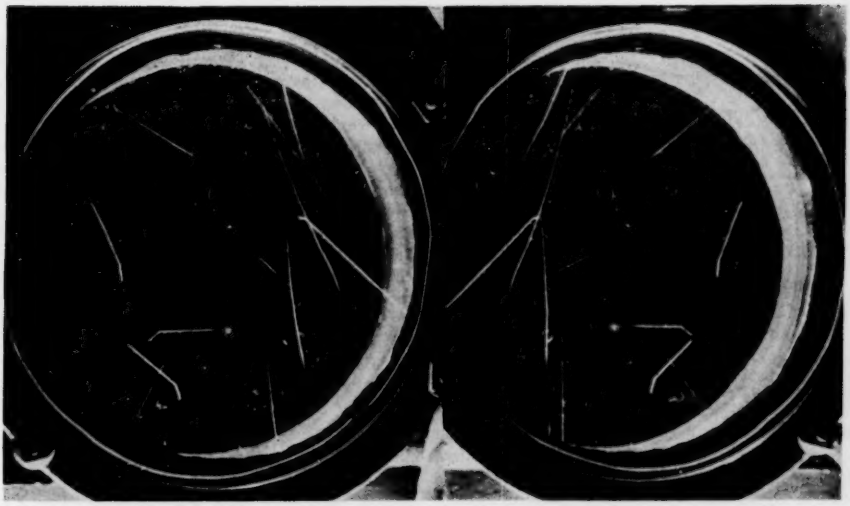

FIG. 1. Stereoscopic picture of disintegrations in oxygen. The neutrons enter from the top of the picture. Several examples of disintegration with alpha-emission can be noted.

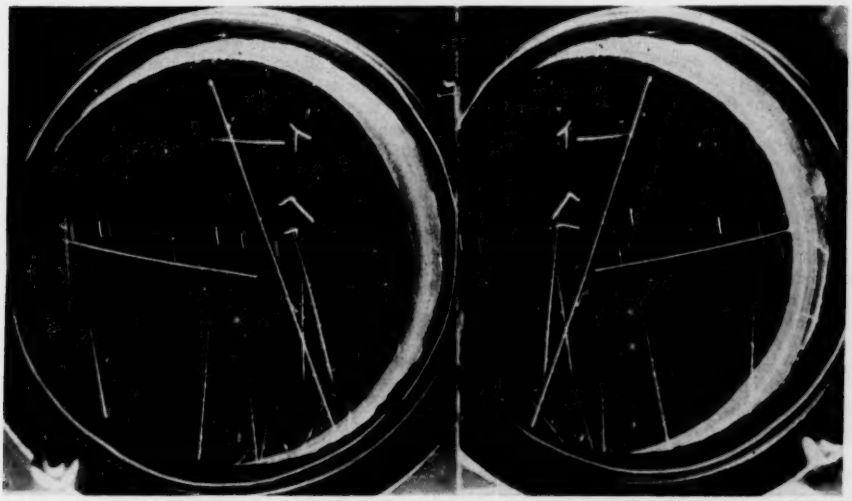

FIG. 2. Stereoscopic picture of disintegrations in nitrogen. The neutrons enter from the top of the picture. Two cases of three-particle disintegration can be seen, as well as a disintegration in which either a proton or deuteron or triton is emitted which crosses and leaves the chamber. Some recoil nitrogen nuclei identifiable as short heavy tracks and an example of alpha-emission are also seen.

powers given by Mano[4] for oxygen, nitrogen, and water. When the excitation energy distributions were plotted later, it was found that the groups were slightly too high in position. The stopping powers were increased by less than two percent to bring the ground level groups into their correct positions of zero excitation energy.

[4] G. Mano, J. phys. et radium **5**, 628 (1934).

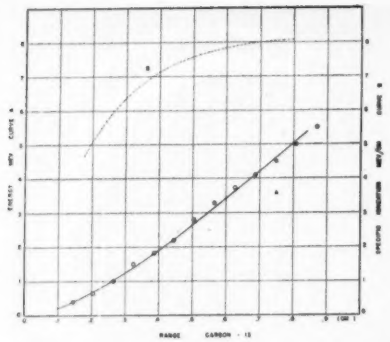

FIG. 3. Curve A: the range-energy curve for a C^{13} particle in air. Curve B: the specific ionization of a C^{13} particle in air as a function of the residual range. This curve is the slope of curve A.

The energy of the heavy particle is calculated by consideration of the momenta involved in the reaction, using the equation

$$M_R E_R = M_n E_n + M_\alpha E_\alpha - 2(M_n M_\alpha E_n E_\alpha)^{\frac{1}{2}} \cos\theta, \quad (1)$$

where M_R, M_n, M_α are the masses of the recoil particle, neutron, and alpha-particle, respectively; E_R, E_n, E_α are the energies of the recoil particle, neutron, and alpha-particle, respectively; and θ is the angle between the alpha-particle track and the neutron's path.

The energy of the alpha-particle is found from the range-energy curves of Bethe.[5] The angle θ is also measured, while the energy of the neutrons and all the mass values are known. The energy of the heavy particle can then be calculated.

The range straggling of the heavy particles, errors in the energies of the alphas, or errors in the angles θ of the alpha tracks contributed to give a considerable spread in range for a given particle energy. To determine the points on the range-energy curve the most probable value of energy for all track lengths in 0.05 cm intervals was plotted *versus* track length. The numbers of tracks in each such interval varied from about 20 to 85 for C^{13}, and from 20 to 100 for B^{11}, there being fewer tracks at high energy. A total of 300 forks for C^{13} and 800 forks for B^{11} were used in these determinations.

Curves A in Figs. 3 and 4 give these range-energy curves for C^{13} and B^{11}, respectively. Curves B in each figure show the specific ionization of the heavy particle as a function of the residual range.

A simple theory[6] indicates that an orbital electron will be lost or captured when the heavy particle has a velocity greater than or less than the effective velocity of that electron. The effective velocity v_{eff} of the most tightly bound electron can be calculated from its ionization potential I by the relation

$$v_{eff}^2 = 2I/m, \quad (2)$$

where m is the mass of the electron.[7] For carbon and boron these velocities are 13.1×10^8 cm/sec and 10.9×10^8 cm/sec, respectively. The energies of the C^{13} and B^{11} particles with these velocities are 11.7 Mev and 6.9 Mev, respectively. At these energies, when the most tightly bound electron is just lost, the specific ionization is expected to reach a maximum. The ranges for these maximum specific ionizations should be found at about 1.6 cm for C^{13} and at 1.1 cm for B^{11}. The experimental curves for the specific ionizations do not extend over these peaks although that for B^{11} appears to have reached a maximum. Higher particle energies would be necessary to locate the peaks accurately.

To synthesize the range-energy curve for a particle of charge Z and mass M in terms of the range-energy curve for a particle of charge Z_0 and mass M_0, both particles having the same velocity, the approximate relation is[6]

$$R_M(E) = \frac{M}{M_0}\left(\frac{Z_0}{Z}\right)^n R_{M0}\left(\frac{M_0}{M}E\right), \quad (3)$$

where E is the energy of the particle of mass M and n is a parameter dependent on the particles and energies concerned. For velocities of the particles large enough so that all orbital electrons are stripped off (e.g., protons or alphas in the Mev range), this equation is approximately true with $n=2$. The value of n for any two particles may be found by comparing their range-energy curves. The value of n for C^{13} particles and alpha-particles varies from 0.8 for a 0.5-Mev C^{13} particle to 1.0 for a 5-Mev C^{13} particle. For B^{11} particles and alpha-particles the value varies from 1.0 for a 0.5-Mev B^{11} particle to 1.2 for a 7-Mev B^{11} particle.

For C^{13} and B^{11} particles the value of n varies from 0.5 to 0.6 for the C^{13} energy range 0.5 Mev to 5 Mev.

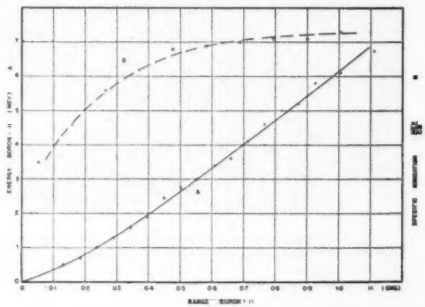

FIG. 4. Curve A: the range-energy curve for a B^{11} particle in air. Curve B: the specific ionization of a B^{11} particle in air as a function of the residual range. This curve is the slope of curve A.

[5] H. A. Bethe, Revs. Modern Phys. **22**, 213 (1950).

[6] N. Bohr, Kgl. Danske Videnskab. Selskab, Mat.-fys. Medd. **18**, No. 8 (1948).

[7] C. E. Moore, *Atomic Energy Levels*, National Bureau of Standards Circular No. 467 (1949), Vol. I.

Blackett,[8] studying O^{16} and N^{14} recoils, found a value of $\frac{1}{2}$ for n between these particles in a similar energy range. In the case where the recoils are much heavier than the atoms of the stopping gas, Bohr gives a theoretical value of $\frac{2}{3}$ for the charge dependence of the range of particles with the same velocity.

2. Calculation of the Energy of Excited States

When a disintegration is produced by a neutron, often the residual heavy nucleus is left excited. The excitation energy can be calculated by the relation

$$E_x = Q_0 + E_n(1 - M_n/M_R) - E_a(1 + M_a/M_R) + 2(M_n M_a E_n E_a)^{\frac{1}{2}}(\cos\theta)/M_R, \quad (4)$$

where Q_0 is the energy released in going to the ground level. The excitation energy is thus dependent on two measured quantities only, the angle θ and the alpha track length.

The number of forks in which a given excitation energy was found was plotted *versus* the excitation energy. Two conditions were applied to all disintegration forks used: (1) the range of the heavy particle in a disintegration was required to lie within 0.1 cm of the mean value of the range for that energy; (2) the computed angle of recoil of the heavy particle and the measured angle were required to agree within 10°.

TABLE I. Excitation energies for C^{13} from the $O^{16}(n,\alpha)C^{13}$ reaction and from the $C^{13}(d,p)C^{13}$ reaction.

Levels found here Mev	Levels found by Rotblat Mev
3.0	3.1
3.7	3.7
	3.9
	6.3
	6.9
	7.6
	7.9
	8.3

$O^{16}(n,\alpha)C^{13}$

From the mass value tables of Li, Whaling, Fowler, and Lauritsen[9] one finds the Q_0 for this reaction to be -2.2 Mev. With 14.1-Mev neutrons the maximum possible excitation of the residual C^{13} nucleus is 11.0 Mev. Owing to the low penetrability[10] of the alpha-particles when the C^{13} is left highly excited (0.3 at 8.2 Mev and 4×10^{-5} at 10.3 Mev excitation of the C^{13}), the cross section is reduced so that the reaction may not be observed in this region. Figure 5 gives the number of disintegration forks as a function of excitation energy of the residual C^{13} nucleus. Positions of levels as reported by Rotblat[11] are indicated by dotted lines.

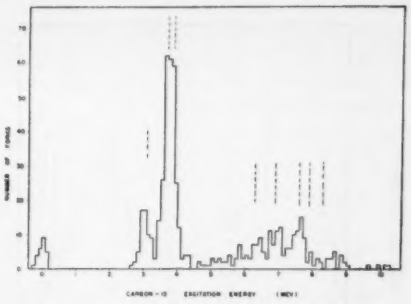

FIG. 5. The number of disintegrations in the $O^{16}(n,\alpha)C^{13}$ reaction as a function of the excitation energy of the residual C^{13} nucleus. The dotted lines indicate the positions of levels reported by Rotblat.

The first two levels at 3.0 Mev and 3.7 Mev agree with those of Rotblat at 3.1 Mev and 3.7 Mev, although there is no indication of a doublet at 3.7 Mev. Malm and Buechner,[12] studying the $N^{15}(d,\alpha)C^{13}$ reaction, have placed these levels at 3.083 and 3.677 Mev, respectively. No group is found corresponding to a level at 1 Mev as reported by others.[13,14] The higher levels have not been resolved.

Table I gives the levels found here and those reported by Rotblat.

Figures 6 and 7 show the angular distributions of the alpha-particles from the 3.0 Mev and 3.7 Mev levels, respectively. Each distribution has been fitted with a Legendre polynomial series, and this latter curve is shown by the smooth line. From the large orders of polynomials required for these fits (10 for the 3.0-Mev group and 8 for the 3.7-Mev group) one concludes that angular momenta of orders 5 and 4, respectively, are

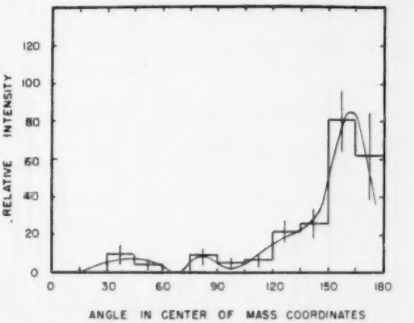

FIG. 6. The angular distribution in the center-of-mass system of alpha-particles emitted in the $O^{16}(n,\alpha)C^{13}$ reaction, which leave the C^{13} nucleus excited to 3.0 Mev. The solid curve is a Legendre polynomial series expansion of order 10 fitted to the histogram.

[8] P. M. S. Blackett, Proc. Roy. Soc. (London) **A134**, 669 (1932).
[9] Li, Whaling, Fowler, and Lauritsen, Phys. Rev. **83**, 512 (1951).
[10] Bloch, Hull, Broyles, Bouricius, Freeman, and Breit, Revs. Modern Phys. **23**, 147 (1951).
[11] J. Rotblat, Harwell Conference (1950).
[12] R. Malm and W. W. Buechner, Phys. Rev. **81**, 519 (1951).
[13] I. B. Berlman, Phys. Rev. **79**, 411 (1950).
[14] K. Boyer, Phys. Rev. **78**, 345 (1950).

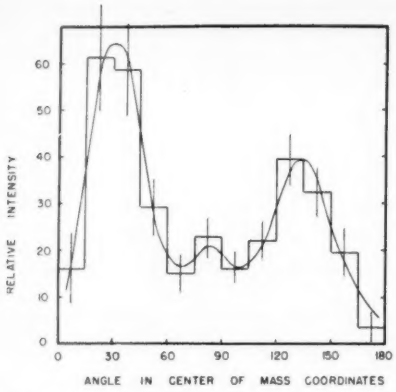

FIG. 7. The angular distribution in the center-of-mass system of alpha-particles emitted in the $O^{16}(n,\alpha)C^{13}$ reaction, which leave the C^{13} nucleus excited to 3.7 Mev. The solid curve is a Legendre polynomial series expansion of order 8 fitted to the histogram.

probably involved and that the compound states of O^{17} involved are states of high angular momentum.

The group at 3.7 Mev was divided into two parts, those with C^{13} excitations above 3.7 Mev and those with C^{13} excitations below. The angular distributions for these two groups were essentially the same, indicating that all the forks were probably due to one level and not to a doublet. The angular distribution for this level is similar in shape to those predicted by Butler's stripping theory, although there is apparently no reason for this.

$N^{14}(n,\alpha)B^{11}$

From the mass value tables, the Q_0 for the reaction $N^{14}(n,\alpha)B^{11}$ is found to be -0.2 Mev. The maximum excitation energy of the B^{11} nucleus possible with the 14.1-Mev neutrons is 12.9 Mev. Again, owing to the low penetrability of the alphas when the B^{11} is left highly excited, the reaction cross section may be expected to become small. Figure 8 shows the number of forks as a function of the excitation of the B^{11}. Known levels, as reported by Van Patter *et al.*[15] from a study of the reaction $B^{10}(d,p)B^{11}$, are indicated by arrows.

The level at 8.0 Mev, which was not found by Van Patter, may correspond to a level found at 7.82 Mev by Bateson[16] using the $B^{10}(d,p)B^{11}$ reaction and by Fulbright and Bush[17] who studied the inelastic scattering of protons.

In the region of excitation of the B^{11} from 8.3 Mev to 11.7 Mev, the penetrability of the alpha-particles drops a factor of 25 from 0.67 to 0.026, and few tracks are found above $9\frac{1}{2}$ Mev. At 11.8 Mev, however, a large group does appear, which is much more intense than the lower levels found.

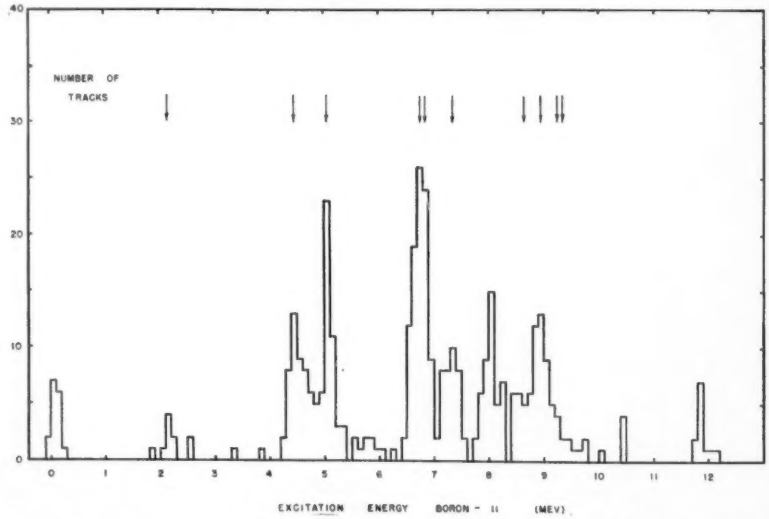

FIG. 8. The number of disintegrations in the $N^{14}(n,\alpha)B^{11}$ reaction as a function of the excitation energy of the residual B^{11} nucleus. The arrows indicate the positions of levels reported by Van Patter *et al.*

[15] Van Patter, Buechner, and Sperduto, Phys. Rev. **82**, 254 (1951).
[16] W. O. Bateson, Phys. Rev. **80**, 984 (1950).
[17] H. W. Fulbright and R. R. Bush, Phys. Rev. **74**, 1323 (1948).

Table II gives the levels as found here and those reported by Van Patter.

While a sufficient number of tracks to permit a detailed study of the angular distributions and hence the angular momenta involved was unavailable in these alpha-groups, it was felt that the distributions were worth tabulating. Table III gives these distributions, corrected for solid angle, for each group of alphas found in Fig. 8, listed according to the range of excitation energies in each group. Most of the distributions are not spherically symmetric, but there does not appear to be any particularly preferred direction for the maximum intensity.

TABLE II. Excitation energies for B^{11} found here from $N^{14}(n,\alpha)B^{11}$ reaction, and those found by Van Patter studying the $B^{10}(d,p)B^{11}$ reaction using magnetic analysis.

Levels found here Mev	Levels found by Van Patter Mev
2.1	2.138
4.4	4.459
5.0	5.034
6.7	6.758
	6.808
7.3	7.298
8.0	
8.5	8.568
8.9	8.926
	9.190
	9.276
11.8	

$O^{16}(n,p)N^{16}$ and $O^{16}(n,d)N^{15}$

The Q_0 for the reaction $O^{16}(n,d)N^{15}$ is -9.9 Mev. The Q_0 for the $O^{16}(n,p)N^{16}$ reaction is not accurately known. A value of this Q may be determined, however, by using the Q value -0.034 Mev for the $N^{15}(d,p)N^{16}$ reaction determined by Malm and Buechner,[18] assuming that this Q relates to the ground level transition and not to an excited state of N^{16}. This gives the Q_0 for the $O^{16}(n,p)N^{16}$ reaction equal to -9.9 Mev. Maximum excitations of the residual N^{15} and N^{16} nuclei of 3.3 Mev are possible in each case.

It is difficult to distinguish proton reactions from deuteron reactions, since the density of a proton track and the density of a deuteron track of the same range are approximately the same, and the other criteria used above were not decisive. The reactions were accordingly computed first as all being proton reactions and then as all being deuteron reactions. Four groups were found of which three could be assigned to known levels in one or the other of the two nuclei. Figure 9 shows three of these groups assigned to N^{16}. The fourth group was due to the ground level transition in the reaction $O^{16}(n,d)$-N^{15}. Dotted lines indicate the positions of known levels. The group at 1.7 Mev probably corresponds to the level at 1.6 Mev reported by Bleuler and Rossel.[19] The general spread near the ground level could be due to the level at 0.3 Mev reported by Wyly.[20]

[18] R. Malm and W. W. Buechner, Phys. Rev. **80**, 771 (1950).
[19] E. Bleuler and J. Rossel, Helv. Phys. Acta **20**, 445 (1947).

TABLE III. The number of alpha-particles emitted at different laboratory angles for the $N^{14}(n,\alpha)B^{11}$ reaction. These are tabulated according to groups as found in Fig. 8.

Group with B^{11} excitation energy	Angle of emission of α-particles (laboratory system) 0–30	30–60	60–90	90–120	120–150	150–180
−0.1 to 0.2	0	0	1	6	13	9
4.3 to 4.6	0	14	13	7	8	14
4.7 to 5.1	20	10	8	8	15	10
6.5 to 6.9	10	17	27	25	34	14
7.1 to 7.4	3	8	10	16	4	0
7.8 to 8.2	15	5	6	13	23	16
8.4 to 9.4	15	29	22	16	7	5
10.4	0	1	1	1	2	0
11.7 to 12.1	10	3	3	0	5	0

Assigning the groups to certain reactions is not purely arbitrary. One factor considered is whether a group agrees with the position of a known level in one nucleus but does not agree with any level in the other nucleus. This was the case with three of the four groups found. Two agree with known levels in N^{16} (ground level and 1.6-Mev level), and one agrees with the ground level of the N^{15}. In general, if a group due to one reaction is misinterpreted as being due to the other reaction, the group on the excitation energy histogram will be smeared out. Thus, the group shown at 2.6 Mev for N^{16} and which has a spread of 0.7 Mev had a spread of 2 Mev when computed as being due to the n–d reaction. Also, this group did not correspond to a known level in either nucleus—there being no known levels in N^{15} up to 5.3 Mev. This might, of course, be a high-spin state of excited N^{15} which had not been found by reactions involving slower charged particles. Finally, the group near the ground level of N^{16}, when computed as due to the n–d reaction, led to negative excitation energies which are impossible.

Table IV lists the levels found here together with those reported elsewhere.

$N^{14}(n,p)C^{14}$, $N^{14}(n,d)C^{13}$, $N^{14}(n,t)C^{12}$

The disintegration of N^{14} gives rise to three reactions with the emission of hydrogen nuclei: $N^{14}(n,p)C^{14}+0.6$

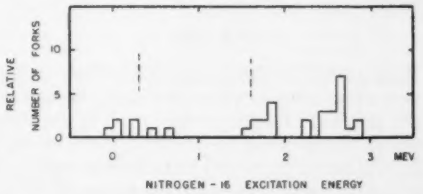

FIG. 9. The number of disintegrations in the $O^{16}(n,p)N^{16}$ reaction as a function of the excitation energy of the residual N^{16} nucleus. The dotted lines indicate the positions of levels reported by Wyly at 0.3 Mev and by Bleuler and Rossel at 1.6 Mev.

[20] L. D. Wyly, Phys. Rev. **76**, 316 (1949).

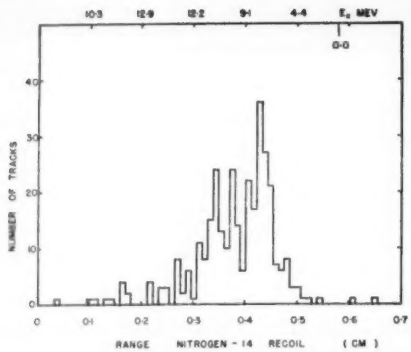

FIG. 10. The number of recoil N^{14} nuclei struck by 14.1-Mev neutrons as a function of the range of the recoil nuclei. All recoil nuclei measured lay within a cone of 15° half-angle with respect to the neutron's path. The scale at the top is the calculated excitation energy of the recoil.

Mev, $N^{14}(n,d)C^{13}-5.3$ Mev, and $N^{14}(n,t)C^{12}-4.0$ Mev. The last of these reactions will not likely be measured, however, since tritons leaving the C^{12} in the 4.5-Mev or ground levels are too energetic and will not be stopped in the chamber. On the other hand, a group from the next higher known level at 9.7 Mev is not energetically possible. Only if there were an intermediate level would the tritons actually stop in the chamber. The protons and deuterons emitted have long ranges and also will not be stopped in the chamber in some cases. However, the protons can stop in the chamber when the C^{14} is left excited above $9\frac{1}{2}$ Mev (13.8-Mev excitation is possible), and the deuterons can stop in the chamber if the C^{13} is left excited above $1\frac{1}{2}$ Mev (7.9-Mev excitation is possible).

Since the proton, deuteron, and triton reactions cannot be distinguished from each other by the appearance of the tracks, all these hydrogen reactions were computed first as n–p and then as n–d reactions. Groups could be seen in each case but were not entirely resolved. As a result, the positive identification of the reactions was not possible here as in the n–p and n–d reactions in O^{16}.

3. Recoils

When a neutron strikes an oxygen or nitrogen nucleus it may be scattered elastically or inelastically, and the event observed as a short heavy recoil in the cloud chamber. By measuring the length of the recoil track (and thus getting its energy) and the recoil angle from the neutron's path, the excitation energy of the recoiling particle can be determined. Figure 10 shows the number of nitrogen recoils in the forward direction *versus* the range of the recoil. The top scale is the corresponding excitation energy. In a collision process

$$E_x=-(M_n+M_R)E_R/M_n+2(M_RE_nE_R/M_n)^{\frac{1}{2}}, \quad (5)$$

where the recoil is at zero degrees to the neutron's path, and E_x is the excitation energy of the recoil particle. The energy E_R of the recoil can be derived from the track length by using Eq. (3) and by comparing with the range-energy curve of C^{13} of Fig. 3.

For elastic scattering of the neutron through 180°,

$$E_R=4M_RM_n(M_R+M_n)^{-2}E_n. \quad (6)$$

With 14.1-Mev neutrons, this gives $E_R=3.5$ Mev. The range of the recoil with this energy, using Eq. (3) with $n=0.5$, is $R=0.58$ cm.

The track lengths to be measured are very short, and the relative errors are large. It can be seen, however, that the number of elastically scattered neutrons is very small with respect to the number of inelastically scattered neutrons for recoils lying less than 15° from the neutron's path.

Similar results were found for oxygen recoils although the number of tracks involved was smaller.

TABLE IV. Excitation energies for N^{16} found here from the $O^{16}(n,p)N^{16}$ reaction, and levels reported elsewhere.

Levels found here Mev	Levels reported elsewhere Mev
0.3?	0.3[a]
1.7	1.6[b]
2.6	

[a] See reference 20.
[b] See reference 19.

4. Cross Sections

To compute the value of the cross section for a reaction, the number of times the reaction occurs is compared to the number of recoil protons occurring in the same number of pictures. Since the relative number of oxygen (or nitrogen) and hydrogen nuclei present are known and since the neutron flux is the same for all reactions, the ratio of the cross section for this reaction to that for n–p scattering can be determined. A value of 0.675 barns[21] for the n–p scattering was used.

In the disintegration of oxygen the cross section for alpha-emission is 310 millibarns. The cross sections for proton emission and deuteron emission are 35 and 15 millibarns.

In the disintegration of nitrogen the cross section for alpha-emission is 100 millibarns. Since it is difficult to distinguish between proton, deuteron, and triton tracks, these reactions have been grouped together with a total cross section of 100 millibarns. The cross section for the disintegration of the nitrogen into Li^7 and two alpha-particles is 15 millibarns.

[21] R. K. Adair, Revs. Modern Phys. **22**, 249 (1950).

Gyromagnetic Ratios of Iron, Cobalt, and Many Binary Alloys of Iron, Cobalt, and Nickel

S. J. BARNETT, *University of California, Los Angeles, California, and California Institute of Technology, Pasadena, California*

AND

G. S. KENNY,* *California Institute of Technology, Pasadena, California*

(Received January 14, 1952)

Gyromagnetic ratios for iron, cobalt, and many binary alloys of iron, cobalt, and nickel were determined by measurements on the Einstein-de Haas effect much as made in the Norman Bridge Laboratory previously. Improvements were made in the method of eliminating large quadrature torques, in the method of reducing disturbances due to the vibrations of the building, in the method of frequency control, in the design of the square wave commutator, and in the design of the rotors. For each series of binary alloys the gyromagnetic ratio was found to vary linearly, or nearly linearly, with the concentration. For the small number of these materials studied in the Norman Bridge Laboratory previously there is good agreement between the new results and the older, both those obtained by the Barnett effect and those obtained by the Einstein-de Haas effect. For the three series of alloys the ranges of $\rho e/m$ are approximately as follows: iron-cobalt, 1.03 to 1.08 or 1.09; iron-nickel, 1.03 to 1.05; and nickel-cobalt, 1.05 to 1.08 or 1.09.

I. INTRODUCTION

THIS paper is a sequel of a series of articles on the Barnett[1,2] and Einstein-deHaas[3–5] gyromagnetic effects published by one of us in earlier years. The principal object of the new work was to make, by means of the Einstein-de Haas effect, as nearly complete an investigation as practicable, in the time at our disposal, of the gyromagnetic ratios of the binary alloys of the three principal ferromagnetic elements, of which only a few were studied in the earlier work (see Table I) and of which almost none have been studied by others. A few new measurements were made on iron and cobalt, chiefly as a check on the other work.

II. EARLIER WORK IN THE NORMAN BRIDGE LABORATORY

It will be conducive to brevity in the discussion of this new work to refer in the text for details to some of the earlier papers, and by the numbers affixed to their titles given below:

I. Researches on the rotation of permalloy and soft iron by magnetization and the nature of the elementary magnet, Proc. Am. Acad. Arts Sci. **66**, 273 (1931).

II. The rotation of cobalt and nickel by magnetization and the gyromagnetic ratios of their magnetic elements, Proc. Am. Acad. Arts Sci. **69**, 119 (1924).

III. Gyromagnetic and electron inertia effects, Revs. Modern Phys. **7**, 129 (1935).

IV. Gyromagnetic ratios for ferromagnetic substances; new determinations and a new discussion of earlier determinations, Proc. Am. Acad. Arts Sci **73**, 401 (1940).

V. New researches on magnetization by rotation and the gyromagnetic ratios of ferromagnetic substances, Proc. Am. Acad. Arts Sci. **75**, 109 (1944). See also Phys. Rev. **66**, 224 (1944).

VI. Magnetization and rotation, Am. J. Phys. **16**, 140 (1948).

The gyromagnetic ratios as obtained previously in the Bridge Laboratory from the Einstein-de Haas effect in iron, nickel, cobalt, and their alloys, and published in IV, are collected in Table I.

These values of ρ are in substantial agreement with those obtained from measurements on the Barnett effect. See IV, V, and VI.

III. RESULTS OBTAINED IN OTHER LABORATORIES

The nearly identical values for iron, given above, are also in close agreement with all measurements made elsewhere on this material (see IV) (or the ferrites)[6] in recent years, and comparable with them in the precision claimed, with one exception: A. J. P. Meyer[7] has recently obtained for ρ about $1.00\times m/e$ from a small number of measurements on iron, nickel, and a few Co–Ni–Fe alloys. For one alloy (Fe_3Ni) his result is $0.966\times m/e$. His observations on nickel are the only recent ones made outside the Bridge Laboratory.†

* Now at George Fox College, Newberg, Oregon.

[1] S. J. Barnett, Phys. Rev. **6**, 239 (1915).

[2] S. J. Barnett and L. J. H. Barnett, Proc. Am. Acad. Arts Sci. **60**, 125 (1925); S. J. Barnett, **75**, 109 (1944).

[3] A. Einstein and W. J. de Haas, Verhandl. deut. physik Ges. **17**, 152 (1915); A. Einstein, Verhandl. deut. physik Ges. **17**, 203 (1915).

[4] W. J. de Haas, Proc. Amsterdam Acad. Sci. **18**, 1280 (1916); A. Einstein, Verhandl. deut. physik Ges. **18**, 17 (1916).

[5] See especially S. J. Barnett, Proc. Am. Acad. Arts Sci. **73**, 401 (1940).

[6] D. P. Raychaudhuri, Indian J. Phys. **9**, 383 (1935).

[7] A. J. P. Meyer, Ann. phys. **6**, 171 (1951).

† *Note added in proof by senior author.*—Two erroneous statements made in Meyer's papers should be corrected here, *viz:* (1) That I had recently acknowledged a systematic error of 1 percent in my gyromagnetic ratios on account of results obtained by Major Webber and myself on the torsion modulus of German silver wire [see S. J. Barnett and D. S. Webber, Phys. Rev. **71**, 896 (1947)]. These results have nothing at all to do with my own gyromagnetic experiments, but they bring the results obtained long ago by Messrs. Sucksmith and Bates I percent closer to mine. (2) That I had found a variation in the gyromagnetic ratio of pure iron in samples of different origin. Within the limits of the experimental error all specimens of pure, or nearly pure, iron give the same value. In some of the earlier work there was a discrepancy between ρ for a specimen of electrolytic iron obtained from the Barnett effect and ρ for nearly identical material obtained from the same effect; but this was long ago traced to a defect in a coil used with electrolytic iron in the experiments on the Barnett effect.

TABLE I.[a] Values of $\rho e/m$ from paper IV, Table 43, Einstein-de Haas effect.

Armco iron	1.032	Hopkinson's alloy (75% Fe, 24½% Ni)	1.024
Honda iron	1.032[b]	Permalloy (Ca 80% Ni, 20% Fe)	1.047
Yensen electrolytic iron	1.034	Cobalt (99.9% Co)	1.090
Cold rolled steel	1.039	Cu-cobalt (92.4% Co)	1.082
Nickel	1.052	Cobalt-iron (34% Co)	1.026
Hipernik (50% Fe, 50% Ni)	1.052	Cobalt-nickel (54% Co)	1.077

[a] *Note added in proof by the senior author.*—The referee on this paper suggested to the Editors that it might be well to include in this table, in addition to the *gyromagnetic ratios*, the so-called *g'* values recently introduced into the literature by certain authors interested in microresonance. To this I made to the Editors on March 5 the following reply, which I hope will help to clarify the situation:

I have always thought it far better to use the term *gyromagnetic ratio*, defined as the ratio of the angular momentum of the element to its magnetic moment, a simple physical quantity, than the terms "*g*-factor," "Landé splitting factor," etc.; and also I do not like to encourage those physicists who write as if the microresonance experiments were not gyromagnetic experiments—or as if there were anything strange in the gyromagnetic ratio (for the same substance) being different under different circumstances. All the experiments have the same dynamical basis, and there is no reason why the relative contributions of electron and orbit should not differ in different cases (as they appear to do).

[b] In the table of IV, 1.023 is incorrectly printed for this number.

Special mention should be made of a very elaborate and precise investigation on pure iron by G. G. Scott,[5] who gives as his final value $\rho e/m = 1.0278 \pm 0.0014$, in close agreement with the values quoted in Table I for pure and nearly pure iron. His values for 1948 are in even closer agreement (1.031 and 1.028) with the table.

IV. METHODS USED IN THE NEW WORK

Methods used in the new work and details of theory are essentially identical with those described in I, p. 302; II, pp. 403–404; III, p. 30; and IV, p. 3, with certain modifications (mostly of a minor character) described below. A very brief discussion follows:

The rotor C, Fig. 1, rigidly attached to a double-faced mirror E and a small permanent magnet F with axis normal to the mirrors, is magnetized by a fixed solenoid B fed by a storage battery V through a square wave commutator W running at the natural frequency of the rotor. The alternations of the magnetization produce a gyromagnetic torque g upon the rotor.

Also the changing magnetization of C produces a current in the induction solenoid A and the torque coil HH, which, acting on F, alters the amplitude and phase of the vibration according to the value of the adjustable conductance $X = 1/R$ of the circuit.

The quadrature coil GG, fed by a battery P through a square wave commutator Q, produces on F a torque, whose phase and magnitude are adjustable until it is in, or nearly in, quadrature with the gyromagnetic torque g. The two commutators are mounted on the same shaft. Mutual inductance compensators $A'B'$, $H'H'$, $G'G'$ reduce to zero the mutual inductances between the different circuits.

Observations are made in a region neutral, or nearly neutral, magnetically. The conductance $X_0+\delta X_0$ of the secondary circuit at which the resonance amplitude is a minimum is determined by measuring accurately the amplitudes A_1 and A_2 (=approximately A_1), respectively, for $X=0$ and $X=X_2$ [=approximately $2(X_0+\delta X_0)$]; by measuring approximately A_0 the minimum amplitude for X=approximately $X_0+\delta X_0$; and by substituting in the formula

$$X_0+\delta X_0=\frac{X_2(A_1^2-A_0^2)^{\frac{1}{2}}}{(A_1^2-A_0^2)^{\frac{1}{2}}+(A_2^2-A_0^2)^{\frac{1}{2}}},$$

which become

$$X_0+\delta X_0=X_2A_1/(A_1+A_2)$$

when $A_0=0$.

X_0 is the conductance at which the amplitude would vanish if there were no extraneous torques; and δX_0, the error due to such torques, is eliminated by making observations for both directions I and II of the asymmetry reversing switch U in the magnetizing circuit, and for two azimuths, NPE and NPW, differing by 180°, of the rotor and permanent magnet attached to it. The mean value of δX_0 for these four arrangements is zero, and the gyromagnetic ratio is determined from the equation

$$-\rho=X_0\Gamma_0\gamma_0m_0,$$

where Γ_0 and γ_0 are the constants of the torque coil and induction solenoid, respectively, and m_0 is the moment of the permanent magnet. Under good conditions the use of the quadrature coil made A_0 negligible.

In calculating the results the simpler formula was always used first. This sufficed for the final calculation in nearly all cases because of the smallness of A_0/A_1 and $|(A_0-A_2)|/A_1$. In the few cases in which appreciable error resulted from the use of the simple formula, the longer formula was used for the final calculation.

V. PRINCIPAL SOURCES OF ERROR

Most of the sources of error and the methods of eliminating or avoiding them have been discussed in references I, II, and IV. Only a brief discussion will be given here. The principal disturbing torques may be divided into three groups: (1) torques due to the residual earth's field, (2) torques due to the action of the fixed magnetizing coil on the vibrating system, and (3) torques due to magnetostriction.

(1) The horizontal component of the residual earth's field acting on the horizontal component of the magnetic moment of the rotor (h) will produce a torque about a vertical axis. If the horizontal component of the mag-

[5] G. G. Scott, Phys. Rev. **82**, 542 (1951).

netic moment h is in phase with the vertical component μ which produces the gyromagnetic torque, this disturbing torque will be in quadrature with the gyromagnetic torque and cause no error. If h is not exactly in phase with μ, this disturbing torque will have in-phase components which would increase or decrease the observed value for the gyromagnetic ratio. If the suspended system is turned through 180° about its axis, the torque will be unaltered in magnitude but will be reversed in sign and will be eliminated, provided the residual field remains constant.

(2) If the field of the magnetizing solenoid is not strictly vertical, it will produce a torque about a horizontal axis by acting on the horizontal component of the permanent magnetism of the rotor. This torque also is reversed in sign by changing the azimuth 180°. There is a similar torque on the fixed magnets of the magnet-mirror holder. In this work the magnets of the magnet-mirror holder were much stronger than in the earlier work, about 5.5 emu instead of some 0.7 emu. The stronger magnets gave certain advantages discussed later, but they increased the effects of the torques due to the magnetizing solenoid. Since square waves were supplied to the magnetizing solenoid, the magnetic moment of the rotor was nearly in phase with the fundamaental of the square wave. Hence the fundamental of the square wave was nearly in quadrature with the gyromagnetic torque, which is proportional to the rate of change of the magnetic moment. So any torque on the magnets due to the magnetizing solenoid would be largely a quadrature torque. The principal quadrature torques were due to magnetostriction (see below) and the residual earth's field. No certain effects due to the torque on the permanent magnets were observed. In any event, the torque is reversed in sign but not in magnitude when the suspended system is turned 180° in azimuth, and the effect is thus eliminated. Great care was taken to insure straightness of the suspended system. The action of the magnetizing current on the alternating magnetization of the rotor produces a double-frequency torque which is without effect except in the case of asymmetry. In this case it is eliminated along with magnetostriction. [See (3) below.]

(3) Longitudinal magnetostriction was large in most of the alloys investigated. The vertical motions produced by magnetostriction may be partly converted into axial vibrations because of asymmetries present in rotor and wave form. Since the change in length due to magnetostriction is independent of the direction of magnetization, the frequency of the effect will be twice that of the magnetizing current and thus not in resonance. However, if the two half-cycles of the magnetizing current are dissimilar, the difference between the two effects will have the frequency of the magnetizing current and may have any phase relation to the gyromagnetic torque. The effect may be eliminated by a reversing switch in the magnetizing circuit which interchanges the half-cycles of current producing a particular direction of magnetization.

The quadrature torque usually reversed its phase while retaining nearly the same amplitude when the asymmetry reversing switch was thrown, indicating that most of the quadrature torque was due to magnetostriction.

VI. ELIMINATION OF QUADRATURE TORQUES

The presence of torques in quadrature with the gyromagnetic torque flattens the vibration amplitude *vs* conductance curve and makes the precise determination of the value of $X_0 \pm \delta X_0$ difficult. To eliminate such torques, a quadrature coil was first used by de Haas. One of us used a quadrature coil in his earlier work on nickel and cobalt (see II) and in some of the later work. Like de Haas he obtained the current for the quadrature coil from the current supply for the magnetizing solenoid. If the magnetic moment of the rotor is exactly in phase with this current, the gyromagnetic torque is in quadrature with the magnetizing current. The emf across a nearly noninductive resistance in the magnetizing circuit was used to supply the quadrature coils. Since the resistance in the quadrature circuit was high and the inductance small, the current in this circuit was assumed to be in phase with the magnetizing current. Various time lags, however, may still be present on account of hysteresis, eddy currents within the material, and other effects. If such a time lag is present, the torque of the quadrature coils on the magnets will not be strictly in quadrature with the gyromagnetic torque and will produce in-phase effects. It was sometimes practicable to eliminate these effects by determining the apparent values of ρ for several values of the applied quadrature torque, and by interpolation or extrapolation to zero quadrature torque. This was not always possible, however, and it appeared desirable to supply the quadrature coils from a source with arbitrary phase angle with respect to the magnetizing current.

In preparation for the present investigation a double set of commutators was prepared (see I for details of

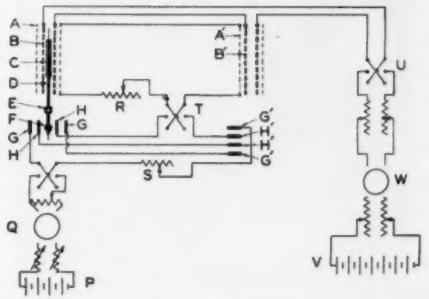

FIG. 1. Primary, secondary, and quadrature circuits.

design, also XII below), mounted on the same shaft to give two square waves of exactly the same frequency (Fig. 2). They were so constructed that one set could be rotated to an arbitrary position with respect to the other, and the position was indicated on an accurately made scale and vernier. The two sets of commutator segments were supplied from independent banks of lead storage cells. Both commutators were driven on the same shaft by a ½-horse power dc motor whose frequency was accurately controlled by a method referred to below. This apparatus gave two square waves having identical frequencies but arbitrary phases and independent amplitudes. These will be designated as the *main square wave* (which was supplied to the magnetizing helix) and the *quadrature wave*.

Let the fundamental of the main square wave (current) be given by

$$I = I_0 \cos(\omega t + \alpha),$$

and the fundamental of the magnetic moment of the rotor by

$$\mu = \mu_0 \cos\omega t.$$

The gyromagnetic torque then is given by

$$G = -\rho d\mu/dt = \mu\rho\omega \sin\omega t.$$

The phase angle α was unknown and varied from rotor to rotor. To make effective use of the new quadrature supply it was necessary to determine the phase angle α or the phase of the first harmonic of quadrature wave with respect to the gyromagnetic torque. This was done by making use of the current in the secondary circuit.

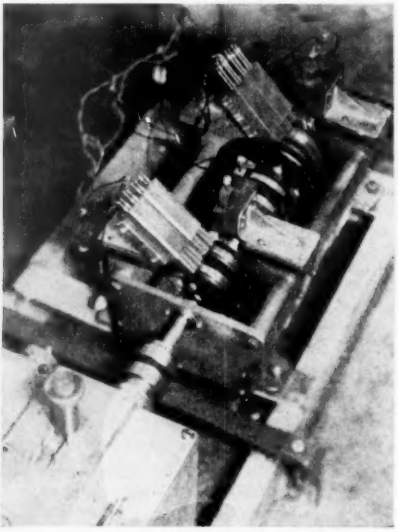

FIG. 2. Main and quadrature square wave commutators.

The first harmonic of the current in the secondary circuit is given by

$$i = -(\gamma/R)d\mu/dt = -(\gamma\omega\mu_0/R) \sin\omega t,$$

and is in phase with the gyromagnetic torque because of the negligible reactance of the secondary circuit.[9] The current in the secondary circuit was quite different in form from the quadrature wave (a square wave) (see Figs. 8–11); and the problem was to determine the phase angle between the fundamentals of the waves in these circuits.

To measure this angle a phase adjuster was constructed as follows: Two sets of coaxial coils were constructed, wound on a single Bakelite tube (Fig. 3). An Alnico magnet with its axis horizontal and a mirror were suspended midway between these by a piano wire suspension of adjustable length. The piano wire suspension passed through a No. 0 Brown and Sharpe pin vise and out the top. The hollow handle was threaded with a 5–40 tap to a depth of some 1½ inches. The piano wire passed through a hole in a special brass screw inserted in the pin vise. A collar around the wire above the brass screw was used to fix its length. With this arrangement it was possible to tune the system to the natural frequency of the rotor to within 1 part in 2500. The inductance of the inner set of coils was 15 millihenrys, the outer set 12 millihenrys. Usually each set was connected in series with 4000 to 6000 ohms resistance. When in use, the flat topped waves from the quadrature commutators were supplied to the outer set of coils, the current from the secondary circuit was supplied to the inner set of coils.

The main square wave was first tuned to the natural frequency of the rotor; then the magnet-mirror system of the phase-meter was tuned to the frequency of the main square wave by adjusting the length of the suspension. By adjusting the resistance and phase of the quadrature circuit it was possible to tune the system to a minimum amplitude of vibration. The quadrature wave was then 180° out of phase with the fundamental of the current in the secondary circuit. Rotation of the quadrature commutator 90° from this position put the first harmonic of the quadrature wave in quadrature with the first harmonic of the current in the secondary circuit and thus with the gyromagnetic torque. With care, the null position could be determined to within $\pm\frac{1}{4}$ degree, but was usually determined only to within $\pm\frac{1}{2}$ degree.

The settings for quadrature were constant (to within 1°) for one rotor for a period of several days, and appeared to change only as the brushes gradually wore down. The settings varied from rotor to rotor, however, by angles up to 7°, according to the effects of hysteresis,

[9] The frequency used was about 10 cycles per second, the inductance of the secondary circuit less than 0.05 henry, resistance 10,000 ohms or more. The reactance $\omega L/R$ then is 3×10^{-4} radian.

eddy currents, and other factors on the forms of the waves they produce in the secondary circuit. (See Figs. 7–11.)

The phase adjuster made it possible to set the fundamental of the quadrature wave in almost exact quadrature with the gyromagnetic torque, and thus the quadrature torques could be eliminated without introducing in-phase components.‡

VII. TORQUE AND QUADRATURE COILS

The torque and quadrature coils were used in part of the earlier work and were designated torque and quadrature system *E*. (See page 410, reference IV for a diagram.) The constant of the torque coil was measured again and found to be unchanged from its original value of 1009.6 emu. The mutual inductance between the torque and quadrature coils was again compensated by connecting a duplicate set of coils in such a way that the mutual inductance of the second set was opposed to that of the main set. Tests showed the residual mutual inductance to be entirely negligible.

VIII. INDUCTION SOLENOID AND FIXED MAGNETIZING COILS

The induction solenoid and fixed magnetizing coils also had been used in the earlier work (see IV, Sec. 12, last paragraph). Their mutual inductance was compensated as before by that of a duplicate set of coils. The balance was adjusted by moving the magnetizing coil of the compensator axially with respect to the induction solenoid. When the coils were adjusted properly, the residual mutual inductance was less than 0.02 percent of that of either set alone. The magnetic intensity applied to the rotor in all measurements was about 50 gausses. The insulation between primary and secondary circuits was exceedingly high.

IX. MAGNET-MIRROR HOLDER

The magnet-mirror holder used was the one designated as No. 7 in reference IV. The steel magnets previously used were replaced by magnets made from "Cunife" kindly presented by the General Electric Company. The moment of these magnets was about 5.3 emu instead of the 0.6 to 0.8 emu of the spring steel magnets previously used. This increased moment made the magnetic moment itself much easier to measure. No control magnet was necessary to increase the sensitivity of the magnetometer. The current in the torque coils was reduced in the same ratio as the increase in magnetic moment. Thus, any direct effect of the magnetic field of the torque coil on the rotor was reduced. The increased resistance in the secondary circuit decreased the already negligible time lag between the current in the secondary circuit and the gyromagnetic torque.

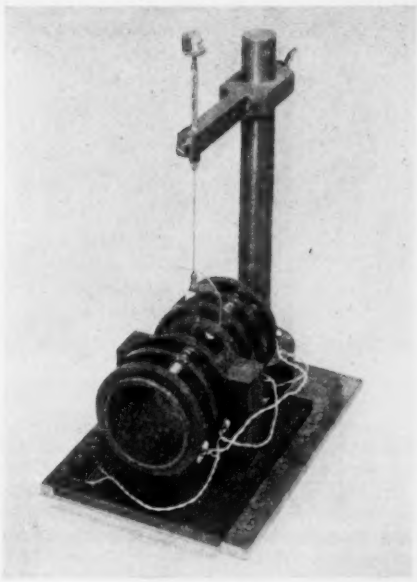

FIG. 3. The phase adjuster.

X. ROTOR AND SUSPENSION CONSTRUCTION

All of the rotors were of the standard short type, unwound, and were constructed on the antimagnetostriction principle described in references II and IV, but with improvements, as indicated in Fig. 4. The upper and lower suspensions were made of No. 30 German silver wire 6.9 cm long and 5 cm long, respectively. Since the rotors were of nearly identical construction, the same upper and lower suspensions could be used for all of them. Their resonance frequencies were all near 11 cycles per second.

XI. THE VIBRATION-FREE MOUNTING

The vibrations in the building due to traffic outside and people and equipment in other parts of the labora-

‡ If Q designates the amplitude of the quadrature torque which has to be annulled, and G that of the gyromagnetic torque, then the fractional error in ρ due to the angular error $\Delta\theta$ in setting the quadrature circle correctly is

$$\delta\rho/\rho = \sin\Delta\theta \cdot (Q/G).$$

If C designates the constant of the quadrature coil, I the amplitude of the current which traverses it when the quadrature torque is annulled, and A'_0 the amplitude of the quadrature vibration produced by Q, we may write

$$\delta\rho/\rho = \sin\Delta\theta \cdot (CIm_0/\rho\omega\mu) = \sin\Delta\theta \cdot (A'_0/A_1).$$

The absolute sign of $\Delta\theta$, whose magnitude will be assumed to be one-half degree, or 1/115 radian, is of course not known, but the relative signs for all the constituents NPE_I, NPE_{II}, NPW_I, NPW_{II} of each set are known from the directions of the emf and the directions of the quadrature current switch. Thus $\overline{\delta\rho/\rho}$ can be obtained for each set. This quantitity proved to be entirely negligible for every *rotor;* and indeed for every *set* but three, where it reached about one part in a thousand, it is entirely negligible.

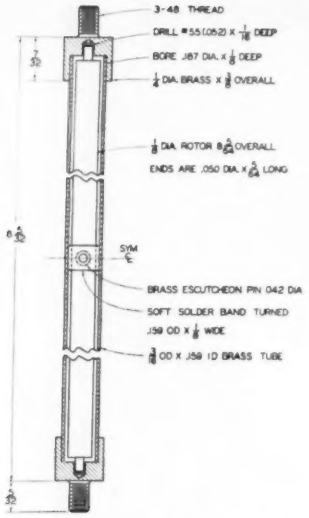
3-48 THREAD
DRILL #55 (.052) X 1/16 DEEP
BORE .187 DIA. X 1/8 DEEP
1/4 DIA. BRASS X 3/8 OVERALL
1/8 DIA. ROTOR 8 3/4 OVERALL
ENDS ARE .050 DIA. X 1/4 LONG
6 1/4
SYM
BRASS ESCUTCHEON PIN .042 DIA
SOFT SOLDER BAND TURNED
.359 OD X 1/8 WIDE
1/8 OD X .359 ID BRASS TUBE

FIG. 4. Construction of the improved type of rotor. All lengths are in inches.

tory disturbed the moving system and made it necessary to protect it from the vibrations. As the vibration free support used in the earlier investigations was in use, it was necessary to construct a new support.

A modification of the form developed by Becker[10] was adopted (see Figs. 5 and 6). The necessity of using nonmagnetic material in the apparatus caused difficulties. The greatest freedom from vibrations is obtained when the suspended system has a low natural frequency. Loading the suspension to increase the mass caused the rods to buckle before the period was sufficiently long to give good protection from vibration. In order to get rid of vibrations, the marble slab (15 in.×30 in.×2½ in.) on which the sensitive apparatus rested was suspended from the ceiling by 8 brass springs 44 in. long (before extension) about 1 in. o.d., made from 0.128 in. brass spring wire. In use, the springs were extended to 62 inches, making the period for vertical oscillations about 1.4 seconds. To provide for damping, the springs were wrapped with flat gum-rubber strips 2 inches wide. The high internal friction of the rubber and friction between the rubber and the springs damped the vertical oscillations very effectively. To remove the asymmetry in Becker's system two similar pendulums, arranged symmetrically, were used instead of one.

Horizontal vibrations were a much more serious source of disturbance than vertical oscillations, and it was necessary to suppress their effects as much as possible. As is well known, internal damping is much superior to external damping in obtaining freedom from vibrations.

The vibrations of the system in a horizontal direction, or oscillations about a vertical axis, were damped by pendulums of the type developed by Becker mentioned previously. Figure 6 shows the top of one of the pendulums. The two arms at right angles to each other carry pistons which dissipate the energy of oscillation of the pendulum by friction with heavy oil. The pendulum was supported by a wire instead of a pivot. At small amplitudes of vibration the friction at the pivot increased greatly so the pendulums did not swing but moved with the apparatus and provided no damping. The wire support, however, does not have increased friction for small amplitudes and the pendulums remained effective.[11] It was necessary to tune the pendulums by adjusting the lengths until the pendulum period was nearly equal to that of the suspended system. The pendulum hobs weighed about 3.8 kg each; their length in proper adjustment was about 170 cm. The half time for horizontal vibrations was 14 seconds, for vertical motions about 30 seconds.

The freedom from mechanical disturbances was sufficient to permit work not requiring precise annullment of the earth's magnetic field to be done at any time of day or night except late afternoon, when traffic was too heavy.

XII. SQUARE WAVES, COMMUTATORS, BRUSHES, AND FREQUENCY CONTROL

The square waves of electromotive force which supplied the current in the magnetizing coil and the quadrature coils at the natural frequency of vibration of the rotor were obtained much as in the earlier investigations, but with several improvements. The Wenner system of speed control was modified to great advantage by placing the resistor which was automatically short-circuited in the armature circuit instead of in the field circuit. This change greatly strengthened the control.

The 3-hp motor used in the previous investigations required too much current for the present battery bank in the Norman Bridge Laboratory and was replaced by a ½-hp motor. One gear box was used instead of two.

Although the motor ran at the same average frequency as the tuning fork, it tended to hunt and thus produced changes in the phase of the square wave, which affected the amplitude of the vibrating rotor in the main experiment. To increase the inertia, a flywheel, 1 foot in diameter and 65 pounds in weight, was constructed and connected rigidly to the motor shaft. It was mounted in ball bearings and carefully aligned so that it added little to the load on the motor after the system reached its final speed. The voltage of the current supplied to the motor was stabilized by a set of 20 6-volt lead storage batteries across the line.

[10] H. E. R. Becker, Z. Tech. Physik **21**, 195 (1940).

[11] This improvement in the apparatus was suggested to us by Mr. Sheldon J. Brown.

The commutator construction has been discussed in the earlier papers and in VI above (see Fig. 2). New brushes and brush-holders were constructed. Two independent brushes pressed on each commutator at an angle of 45° with the surface, so that the frictional drag would tend to pull the brushes into closer contact. The pair of brushes insured more nearly uniform contact since it was unlikely that both would miss contact at the same time. Much less force was required to give satisfactory contact, the power input to the motor was reduced by one-third, and the reduced load made the speed control much easier. After all the changes mentioned were made the square waves and frequency control were quite satisfactory.

XIII. NEUTRALIZATION OF THE EARTH'S MAGNETIC FIELD

The three components of the earth's magnetic intensity were neutralized by the three Helmholtz coils shown in Fig. 5, much as in the earlier investigations. The currents for the three sets of coils were furnished by three independent banks of lead storage batteries.

The proper compensating currents were determined from the nullification of the electromotive force induced in a small rotating coil mounted inside a Lucite cylinder and driven by an air stream. The voltage induced in the coil was read by a vacuum tube voltmeter. The sensitivity was sufficient to compensate the field intensity to 1 part in 5000, but the earth's field fluctuations were much larger than this. The compensating currents

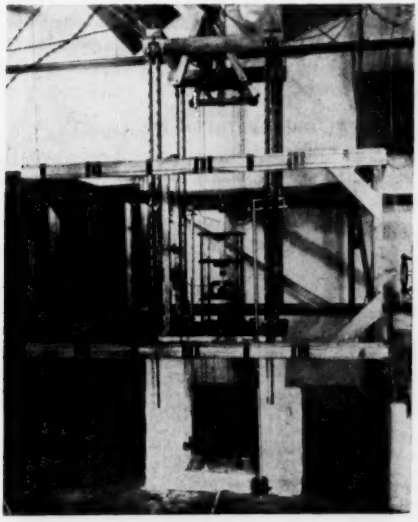

FIG. 5. The coils for neutralizing the earth's magnetic field, the antivibration equipment, the coils in which the rotor was suspended, the torque and quadrature coils, etc.

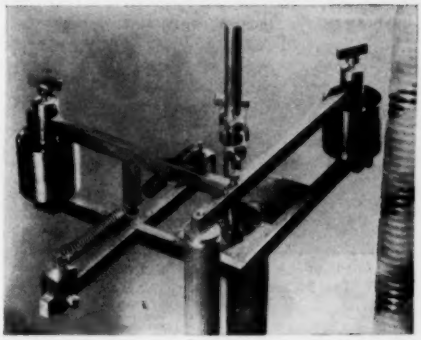

FIG. 6. Details of devices for annulling horizontal and vertical vibrations.

for the north-south and vertical components were determined to 1 part in 1000, that of the small east-west component to 1 part in 250.

In order to make this calibration, it was necessary to remove and again replace the magnetizing and induction solenoids, a time-consuming operation. It was also necessary to have the rotor in place several hours before the measurements began (see below). Thus it was impossible to make a direct measurement of the compensating currents immediately before beginning a run. The difficulty was avoided, as in the earlier work, by making supplementary measurements with an earth inductor and a Hibbert magnetic standard.

There were only slight changes in the vertical component over a period of months. Also, slight changes in the vertical intensity produce no effect on the observed value of the gyromagnetic ratio. The compensating currents were left the same for both azimuths of the rotor. Except in the cases of two rotors which were unsymmetrical and had very large horizontal moments, the residual earth's field introduced no serious difficulties.

XIV. DETERMINATION OF CONSTANTS

The constants of the torque coil Γ_0 and the induction solenoid γ_0, the resistance $R_0 = 1/X_0$ of the secondary circuit, and the moment of the magnets m_0 which enter into the fundamental equation for ρ, *viz.*,

$$-\rho = X_0 \gamma_0 \Gamma_0 m_0,$$

must be accurately known. The constants of the torque coil and induction solenoid were measured with precision in the earlier work and were checked for this work. The moment m_0 of the magnet was measured bi-monthly by the magnetometer method described in I. The moment changed by only 0.1 percent per month, and the value for any particular night was found from the curve.

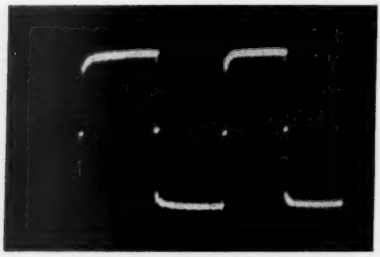

FIG. 7. Current in primary coil *vs* time for Bell Telephone iron rotor.

The resistance R_0 was 8500 ohms or more, 124 ohms in the coils and leads, the rest in the resistance boxes. The standard resistance boxes were checked carefully and found to be accurate to 0.1 percent or better for the high resistance used. Below 40 ohms, the resistances were good to only 0.5 percent or 1 percent, but this error was a negligible contribution to the total resistance. Thus the total resistance of the induction circuit was known to an accuracy of at least 0.1 percent.

XV. OSCILLOGRAMS

For one of the rotors Fig. 7 shows the current in the primary circuit. The commutator gaps are visible as dots. Figures 8–11 show the electromotive forces in the secondary circuit due to the rotor *F* (41 percent Ni, 60 percent Fe), the rotor *A* (15 percent Ni, 85 percent Co) and an iron rotor, respectively. The primary current was the same for each of these four rotors. The differences in shape show how the first harmonic of this wave form (which is essentially the same as the gyromagnetic torque on the rotor) may be shifted in phase by several degrees from exact quadrature with the fundamental of the magnetizing current. The differences in form are caused by the differences in the properties

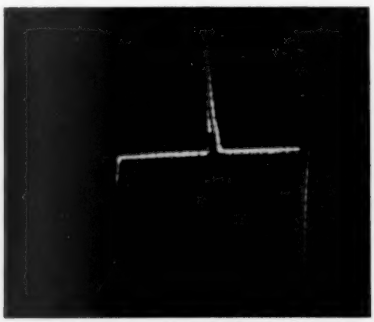

FIG. 8. Secondary emf *vs* time for 41 percent Ni 60 percent Fe rotor.

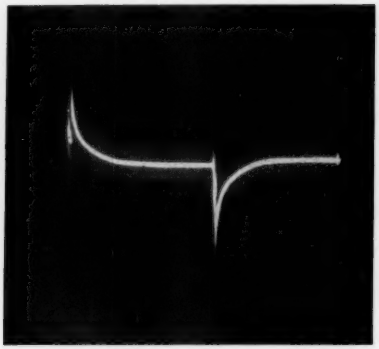

FIG. 9. Secondary emf *vs* time for 15 percent Ni 85 percent Co rotor.

of the materials. Most of the lag in iron appears to be due to eddy currents since the decay is exponential. Ideally, one should want to have a very sharp peak and no lag to reduce the influence of the in-phase components of the disturbing torques. Figure 11 is for the same material as Fig. 8. The peak is shown broadened to illustrate its double nature. With mechanical commutators, the current first falls to zero when the brush passes over the gap and then rises to a maximum in the opposite direction. The first part of the double peak is due to the change in magnetization when the current falls to zero, the second part is caused by the change in magnetization when the current rises to a maximum in the opposite direction. The change is so rapid that the rising part of the curve does not appear, but the decay is clearly visible.

XVI. OBSERVATIONAL PROCEDURE

In order to insure the necessary stable conditions before beginning observations, the motor driving the

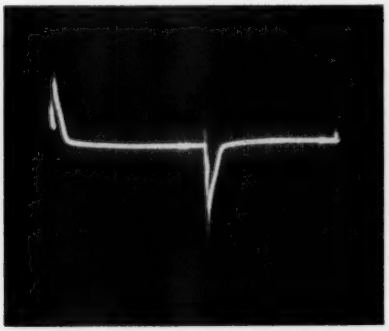

FIG. 10. Secondary emf *vs* time for electrolytic iron rotor.

TABLE II. Composition of Bell Telephone cobalt-iron alloys.

Percent Cobalt	Percent Manganese	Percent Iron	Percent Silicon	Percent Carbon
10.17	0.31	89.41	0.01	
20.04	0.47	79.22	Nil	
30.19	0.45	69.37	Nil	
40.09	0.44	59.44	Nil	
50.11	0.47	49.18	0.01	
59.82	0.58	39.45	0.01	
69.62	0.39	29.80	0.01	
79.36	0.48	20.18	0.01	
89.78	0.63	9.56	0.03	
98.90	0.63	0.18	0.09	0.20

commutators, the tuning fork, and the rotor current were all turned on for at least four hours before observations began. After the motor was brought under the frequency control, the frequency was adjusted until the rotor amplitude was a maximum. Then the resistances of the secondary circuit and the quadrature circuit which gave minimum amplitude (see discussion of method above) were determined for both positions of the asymmetry reversing switch. The measurements then proceeded as described in detail in IV.

Most of the measurements were made after midnight; some were made in the evening before midnight, and a few were attempted in the daytime. On a few occasions two complete sets of observations were made in one night. Work was made impossible on a few nights by magnetic storms, but the conditions between 1:00 A.M. and 4:30 A.M. were usually very good.

XVII. OBSERVATIONS AND RESULTS

A. Cobalt-Iron Alloys

Through the kindness of the Bell Telephone Laboratories, a series of iron-cobalt alloys was obtained. The analysis provided with the alloys is given in Table II. The samples were all annealed for one-half hour at 900°C after swaging.

1. *10 percent cobalt-iron rotor.*—This rotor had a very large horizontal magnetic moment which made measurements impossible. Repairs to the rotor were not completed in time for this work.

2. *20 percent cobalt-iron rotor.*—(See Table III.) The band of light on the scale was crossed by faint lines, indicating that the effects of magnetostriction were not completely eliminated by the complex rotor construction (see I, p. 332). The pattern was steady, but it was necessary to use the quadrature coil.

TABLE III. 20 percent cobalt-iron rotor. Double amplitude 3.1–3.8 cm.

Date	T	Obs	NPE I	NPE II	NPW I	NPW II	pe/m
1940							
June 5	nt	1	1.016	1.025	0.989	1.032	1.016
6	nt	1	0.974	1.093	0.992	1.091	1.030
7	day	½	0.983	1.057	0.944	1.032	1.004
7	eve	½	0.964	1.093	0.959	1.087	1.026
10	nt	1	0.904	1.103	0.903	1.104	1.004
14	nt	1	1.021	1.089	0.954	1.107	1.042

The weighted mean is $pe/m = 1.021 \pm 0.013$.

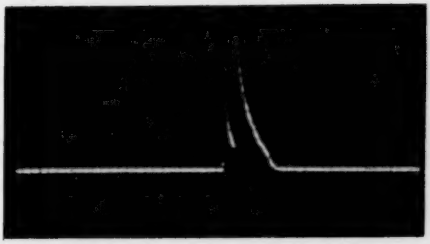

FIG. 11. Secondary emf *vs* time for 41 percent Ni—60 percent Fe rotor of Fig. 8, but with a different time scale.

3. *30 percent cobalt-iron rotor.*—(See Table IV.) As first constructed, this rotor had a large horizontal magnetic moment and the effects of magnetostriction were very evident. The rotor was remade, in an attempt to make it more nearly symmetrical. It then behaved quite well, although the I, II asymmetry was larger than usual. The quadrature coil was used. The rotor was inverted for the observation of July 27.

4. *40 percent cobalt-iron rotor.*—This rotor broke during construction and could not be repaired or replaced.

5. *50 percent cobalt-iron rotor.*—(See Table V.) All observations on this rotor were made during the daytime or early evening. It had a rather small horizontal magnetic moment, however, and the observations were fairly good. The quadrature coil was used.

6. *60 percent cobalt-iron rotor.*—(See Table VI.) The earth's magnetic field was unsteady through this series of observations, but the small horizontal moment of the rotor reduced the effects of the fluctuations. Quadrature torques were small. The quadrature coil was used.

7. *70 percent cobalt-iron rotor.*—(See Table VII.) The earth's magnetic field was steady during this series. The quadrature coil was used.

8. *80 percent cobalt-iron rotor.*—(See Table VIII.) This rotor had a large magnetic moment and gave large amplitudes. The quadrature coil was used.

9. *90 percent cobalt-iron rotor.*—(See Table IX.) This rotor was very good. The quadrature coil was used.

TABLE IV. 30 percent cobalt-iron rotor. Double amplitude 4.4–5.6 cm.

Date	T	Obs	NPE I	NPE II	NPW I	NPW II	pe/m
1950							
July 22	eve	½	1.141	0.921	1.113	0.902	1.019
24	nt	1	1.158	0.968	1.127	0.923	1.044
27	nt	1	0.645	1.443	0.669	1.408	1.041

The weighted mean is 1.038 ± 0.007.

TABLE V. 50 percent cobalt-iron rotor. Double amplitude 2.7–3.3 cm.

Date	T	Obs	NPE I	NPE II	NPW I	NPW II	$\rho e/m$
1950							
Mar. 14	day	½	1.126	1.010	1.054	1.029	1.054
16	day	½	1.160	1.053	1.085	1.054	1.088
16	eve	½	1.163	1.032	1.079	0.068	1.061

The mean of these results is 1.068 ± 0.013.

10. *Cobalt rotor.*—(See Table X.) This rotor was exceptionally good. Quadrature torques were small and the amplitude very stable. The quadrature coil was used.

B. Cobalt-Nickel Alloys

Measurements of the gyromagnetic ratio were made on three cobalt-nickel alloys. The alloys were obtained from the General Electric Company, to which we are much indebted for them. They were deoxidized with 0.2 percent aluminum, 0.2 percent silicon, and 0.5 percent manganese. The percentages are by addition; the alloys were not analyzed. We are much indebted to Dr. Duwez of the Metallurgical Laboratory for annealing all these rotors. They were annealed in hydrogen for 4 hours at 1350°C.

TABLE VI. 60 percent cobalt-iron rotor. Double amplitude 3.3–4.2 cm.

Date	T	Obs	NPE I	NPE II	NPW I	NPW II	$\rho e/m$
1950							
Aug. 6	nt	1	1.086	1.046	1.031	0.977	1.035
7	eve	1	1.075	1.083	1.033	1.009	1.050
7	nt	1	1.105	1.065	1.019	0.993	1.046
8	nt	1	1.076	1.095	0.994	1.013	1.045
8	nt	1	1.103	1.074	1.022	1.007	1.052

From these observations the mean value of $\rho e/m$ is 1.046 ± 0.004.

1. *20 percent cobalt-nickel rotor.*—(See Table XI.) The band of light on the scale was crossed by lines showing that the effects of magnetostriction were present. The pattern was steady. After 3 runs which were rejected because of large asymmetries and poor magnetic conditions, four good sets of measurements were obtained. The quadrature coil was used.

TABLE VII. 70 percent cobalt-iron rotor. Double amplitude 3.0–3.8 cm.

Date	T	Obs	NPE I	NPE II	NPW I	NPW II	$\rho e/m$
1950							
Aug. 1	eve	1	1.087	1.049	0.998	1.046	1.045
4	eve	1	1.016	1.075	1.085	1.061	1.059
5	nt	1	1.052	1.077	1.025	1.062	1.054
5	nt	1	1.012	1.074	1.076	1.105	1.066

The mean of these results is $\rho e/m = 1.056 \pm 0.007$.

TABLE VIII. 80 percent cobalt-iron rotor. Double amplitude 4.7–7.0 cm.

Date	T	Obs	NPE I	NPE II	NPW I	NPW II	$\rho e/m$
1950							
Mar. 20	nt	½	1.249	0.945	1.185	0.962	1.085
22	eve	1	1.159	1.012	1.060	1.079	1.077
23	day	1	1.195	1.028	1.091	1.036	1.088

The weighted mean for these observations is $\rho e/m = 1.083 \pm 0.005$.

2. *40 percent cobalt-nickel rotor.*—(See Table XII.) Quadrature torques were small. The quadrature coil was used.

3. *70 percent cobalt-nickel rotor.*—There were enormous effects from magnetostriction in this rotor. Measurements were not attempted.

4. *85 percent cobalt-nickel rotor.*—(See Table XIII.) This rotor gave rather small amplitudes, but very steady readings. Quadrature effects were small. The quadrature coil was used.

TABLE IX. 90 percent cobalt-iron rotor. Double amplitude 3.6–4.4 cm.

Date	T	Obs	NPE I	NPE II	NPW I	NPW II	$\rho e/m$
1950							
April 6	day	½	1.117	1.124	1.044	1.067	1.088
7	nt	1	1.126	1.110	1.062	1.064	1.091
8	nt	1	1.116	1.100	1.053	1.062	1.083
11	nt	1	1.100	1.096	1.059	1.067	1.081

The weighted mean of these results is $\rho e/m = 1.086 \pm 0.004$.

C. Nickel-Iron Alloys

Measurements of gyromagnetic ratios were made on 4 nickel-iron alloys obtained from the General Electric Company, to which we desire to express our thanks. The alloys were deoxidized with 0.2 percent silicon and 0.2 percent aluminum. The percentages listed are by addition. We desire to express our thanks also to Dr. Duwez, who annealed these rotors in the same manner in which the Co−Ni rotors were annealed.

1. *15 percent nickel-iron rotor.*—(See Table XIV.) Quadrature torques were so small with this rotor that the quadrature coil was not used.

TABLE X. Cobalt rotor. Double amplitude 2.0–2.2 cm.

Date	T	Obs	NPE I	NPE II	NPW I	NPW II	$\rho e/m$
1950							
June 27	nt	1	1.067	1.110	1.084	1.019	1.070
28	nt	1	1.059	1.102	1.099	1.040	1.075
30	eve	½	1.088	1.089	1.084	1.053	1.078
July 1	eve	1	1.101	1.075	1.049	1.097	1.081

The weighted mean of these results is $\rho e/m = 1.076 \pm 0.004$. (On the curves of Figs. 12 and 13 this point is placed one-tenth percent too low.)

TABLE XI. 20 percent cobalt-nickel rotor. Double amplitude 1.7–2.4 cm.

Date	T	Obs	NPE I	NPE II	NPW I	NPW II	pe/m
1950							
Aug. 16	eve	1	0.970	1.132	1.046	1.091	1.060
16	nt	1	0.953	1.133	1.046	1.096	1.057
17	nt	1	0.927	1.172	1.068	1.097	1.066
17	nt	1	0.967	1.135	1.025	1.079	1.052

The mean of these results is $pe/m = 1.059 \pm 0.005$.

2. *40 percent nickel-iron rotor.*—(See Table XV.) At small amplitudes, the band of light on the scale was crossed by faint lines, indicating small effects from magnetostriction were present. Quadrature torques were very small and the quadrature coil was not used.

3. *65 percent nickel-iron rotor.*—(See Table XVI.) One measurement was rejected because of very unstable conditions. Two good measurements were obtained. The rotor was very nearly symmetrical. The quadrature coil was used.

4. *90 percent nickel-iron rotor.*—(See Table XVII.) The earth's magnetic field was not very steady during this series of measurements. The rotor was very true mechanically. The quadrature coil was used.

TABLE XII. 40 percent cobalt-nickel rotor. Double amplitude 2.6–3.6 cm.

Date	T	Obs	NPE I	NPE II	NPW I	NPW II	pe/m
1950							
Aug. 22	nt	½	0.975	1.189	0.964	1.159	1.072
	nt	½	0.959	1.247	0.909	1.172	1.072
	nt	½	1.085	1.118	1.034	1.097	1.083
	nt	1	1.121	1.090	1.072	1.073	1.089

The weighted mean of the results is $pe/m = 1.080 \pm 0.008$.

D. Iron Rotors

Gyromagnetic ratios were measured for two pure iron rotors. The material for one was obtained from Westinghouse, that for the other was obtained from the Bell Telephone Laboratories.

1. *Westinghouse rotor.*—(See Table XVIII.) This rotor was reconstructed from the same material used in earlier researches on the Einstein-de Haas effect, and was cut out from a rod used in Columbus and Washington on the Barnett effect. In the process of reconstruction the rotor broke in the middle but was welded togther again. The quadrature coil was used.

TABLE XIII. 85 percent cobalt-nickel rotor. Double amplitude 1.1–1.3 cm.

Date	T	Obs	NPE I	NPE II	NPW I	NPW II	pe/m
1950							
Aug. 26	nt	1	1.036	1.162	1.096	1.031	1.081
26	nt	1	1.031	1.184	1.098	1.030	1.080
27	nt	1	1.051	1.153	1.102	1.025	1.083
27	nt	1	1.032	1.184	1.106	1.010	1.083

The mean of these observations gives $pe/m = 1.082 \pm 0.001$.

TABLE XIV. 15 percent nickel-iron rotor. Double amplitude 3.1–3.4 cm.

Date	T	Obs	NPE I	NPE II	NPW I	NPW II	pe/m
1950							
Aug. 30	nt	1	1.075	1.014	1.041	0.983	1.028
Sept. 1	nt	1	1.086	1.018	0.999	1.032	1.034
	nt	1	1.057	1.057	1.011	1.027	1.038

The mean of these results is $pe/m = 1.033 \pm 0.004$.

2. *Bell Telephone rotor.*—(See Table XIX.) Quadrature effects were small, but the quadrature coil was used.

The mean value for pure iron is 1.037 ± 0.003.

XVIII. CONCLUSIONS

Figures 12, 13, and 14 show the gyromagnetic ratio plotted against the concentration for each of the three series of alloys. The solid circles represent the values obtained in the present investigation; the open circles, values obtained in the Norman Bridge Laboratory in the course of earlier measurements on a few of the same materials, or closely related materials, by the Einstein-de Haas effect; and the squares, values obtained in the same laboratory in the course of measurements by the Barnett effect. The open circle values are considered the most precise. All are in excellent agreement in view of the difficulties involved.

The average errors for all the new rotors are given immediately after the tables. The average for all new

TABLE XV. 40 percent nickel-iron rotor. Double amplitude 4.6–5.2 cm.

Date	T	Obs	NPE I	NPE II	NPW I	NPW II	pe/m
1950							
Sept. 8	nt	1	1.016	1.070	1.056	0.989	1.033
	nt	1	1.077	1.011	1.061	0.983	1.035
	nt	1	1.072	1.018	1.082	0.972	1.038

The mean of these results is $pe/m = 1.035 \pm 0.002$.

TABLE XVI. 65 percent nickel-iron rotor. Double amplitude 2.4–3.2 cm.

Date	T	Obs	NPE I	NPE II	NPW I	NPW II	pe/m
1950							
Sept. 14	nt	1	0.917	1.205	1.037	1.041	1.050
15	nt	1	1.000	1.112	0.999	1.074	1.046

The mean from these observations is $pe/m = 1.048 \pm 0.002$.

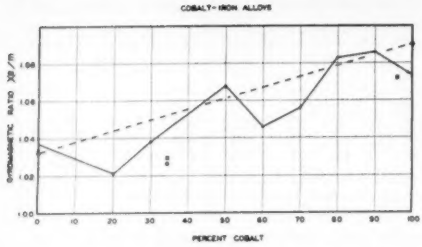

FIG. 12. Results for cobalt-iron alloys.

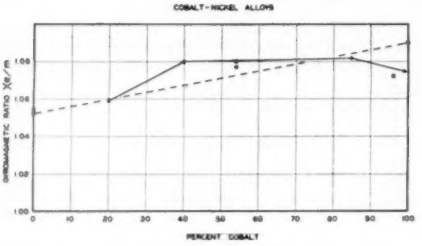

FIG. 13. Results for cobalt-nickel alloys.

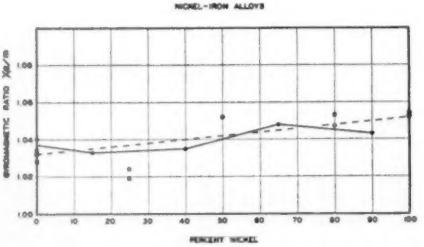

FIG. 14. Results for nickel-iron alloys.

rotors is 0.006±0.004. The errors range from 0.001 for Bell Telephone iron and 85 percent cobalt-nickel, to 0.018 for 90 percent nickel-iron.

The most important characteristic of each of the curves is the general increase which it shows in the value of ρ with increasing concentration of the element which has the larger gyromagnetic ratio. The linear or nearly linear relation[12] between the gyromagnetic ratio and the concentration is unmistakable.

TABLE XVII. 90 percent nickel-iron rotor. Double amplitude 2.3–3.1 cm.

Date	T	Obs	NPE I	NPE II	NPW I	NPW II	$\rho e/m$
1950							
Sept. 2	nt	1	1.015	1.062	0.897	1.139	1.028
4	nt	1	0.949	1.124	0.873	1.148	1.024
4	nt	1	0.987	1.156	0.888	1.154	1.047
5	nt	1	0.989	1.172	0.882	1.195	1.060
7	nt	1	0.970	1.135	0.939	1.182	1.056

The mean from these observations is $\rho e/m = 1.043 \pm 0.018$.

TABLE XVIII. Westinghouse pure iron rotor. Double amplitude 3.0–3.9 cm.

Date	T	Obs	NPE I	NPE II	NPW I	NPW II	$\rho e/m$
1950							
July 5	eve	½	1.027	1.025	1.024	1.043	1.030
6	eve	1	1.055	1.058	1.015	1.044	1.043
7	nt	1	1.068	1.073	1.005	1.030	1.044
11	nt	1	1.078	1.060	1.014	1.021	1.043

The mean for these observations is $\rho e/m = 1.040 \pm 0.005$.

TABLE XIX. Bell Telephone pure iron rotor. Double amplitude 3.5–4.8 cm.

Date	T	Obs	NPE I	NPE II	NPW I	NPW II	$\rho e/m$
1950							
July 12	nt	½	1.030	1.073	1.002	1.034	1.035
15	nt	1	1.017	1.070	1.000	1.041	1.032
20	nt	1	0.974	1.042	1.030	1.097	1.035

The mean of these results is $\rho e/m = 1.034 \pm 0.001$.

XIX. SPECIAL ACKNOWLEDGMENTS

For important help in this work we are indebted to many others, a number of whom are mentioned in the text. We have to thank the Carnegie Institution of Washington for the use of much of the fixed equipment and the U. S. Navy for support in all parts of the work. The experiments have been made in the Norman Bridge Laboratory of the California Institute of Technology.

[12] In a note in the Comptes Rendus [S. J. Barnett, Compt. rend. **231**, 761 (1950)], in the French translation, the gyromagnetic ratio in the case of each series was said to increase linearly with the concentration. The original had linearly or nearly linearly, as above.

The 7.4-Mev State of Li^7

MURRAY PESHKIN AND A. J. F. SIEGERT
Northwestern University, Evanston, Illinois

(Received May 5, 1952)

Blair and Holland have reported preliminary measurements of the cross section for the $Li^6(n,\alpha)$ reaction as a function of the neutron energy. Roberts *et al.* have measured the angular distribution of the tritons for a neutron energy of 270 kev. Assuming that the nonresonance part of the cross section is due entirely to s-neutrons and that there is no accidental degeneracy of the resonance state, this state is shown to have spin $\frac{3}{2}$.* Experiments which might test the assumptions are discussed.

1. INTRODUCTION

THE compound state of Li^7 formed in the $Li^6(n,\alpha)$ reaction at resonance is of interest because the shell model leads to a spin of 5/2 for this state, while the model of Inglis[1] permits 3/2. Connected with the interpretation of this reaction is the question whether the radius of the Li^6 nucleus is of normal size ($\sim 1.4A^{\frac{1}{3}} \times 10^{-13}$ cm) or whether it is abnormally large, as might be expected if it consists, roughly speaking, of an alpha-particle and a deuteron.

The absorption cross section measurements of Blair and Holland[2] show a resonance maximum of 3.1 barns, 2.5 barns of which is actually due to the resonance, at 250 kev with width at half-maximum about 100 kev. We understand from Dr. Holland that these results are regarded as preliminary and that the absolute calibration may be in error by as much as 20 percent. Roberts and co-workers[3] have measured the angular distribution $I(\theta)$ of the tritons at 270 kev and found (in the c.m. system)

$$I(\theta) = 103 + 83\cos\theta + 192\cos^2\theta. \qquad (1)$$

Roberts' relative coefficients are estimated to be accurate to about 20 percent.

We propose to show that the combined results of Roberts and of Blair and Holland are, within their present uncertainties, compatible with the simplest possible assumptions about the $Li^6(n,\alpha)$ reaction. We assume that the nonresonance part of the cross section at 270 kev is due to s-neutrons alone and that there is no accidental degeneracy of the compound state. Then we will show that the data are compatible with, and only with, spin 3/2 for the compound state. Only a small improvement of the data is needed to clarify the situation appreciably. In particular, if it turns out that the total cross section is really as high as the present most probable value and that our first assumption is confirmed by new measurements of the angular distribution, then the compound state must be degenerate.[4]

2. PRELIMINARY REMARKS

Our first assumption implies that the nuclear radius r of Li^6 is smaller than $\lambda = (1/2\pi) \times$(neutron wavelength) $= 0.95 \times 10^{-12}$ cm at 250 kev. The existence of the $\cos\theta$-term requires that at least one odd and one even component of the incident neutron wave are absorbed, so that the excited Li^7 nucleus does not have definite parity. The resonant part must now be due to the p-wave. Higher odd angular momenta are excluded by the large height and width of the resonance. The neutron width Γ_n is in fact limited[5] by

$$\Gamma_n \leqq (3\hbar^2/mr\lambda)T_l = 1500T_l \text{ kev}, \qquad (2)$$

where m is the neutron mass and the factors T_l depend only on r/λ, rising for f-neutrons from $T_3 = 1/225000$ for $r/\lambda = 0.3$ to $T_3 = 1/275$ when $r/\lambda = 1$. For higher angular momenta T_l decreases rapidly with increasing l. Even if $r/\lambda = 1$ (which would actually contradict our assumption of s-waves only for the nonresonance absorption), we would thus have $\Gamma_n \leqq 4.1$ kev, while the actual width is 100 kev, so that not even several closely spaced f-neutron resonances could account for the observed line width. If, contrary to the usual situation in this energy range, the absorption width $\Gamma_a \gg \Gamma_n$ so that Γ_a would be the total width, Γ_n/Γ_a would have to be less than 0.04 for f-neutrons and the cross section would be limited to much less than one barn. These considerations strengthen the observation of Roberts that no $\cos^4\theta$-term appears in the angular distribution.[6]

Since the ground state of Li^6 has angular momentum 1, this limits us to the possibilities of one or more p-neutron resonances or to compound nuclei of total angular momentum 1/2, 3/2, and 5/2. The state $J = 1/2$ will lead to a triton distribution without a $\cos^2\theta$-term and can therefore be excluded unless it is nearly degenerate with a state of $J = 3/2$ or 5/2.

---

* *Footnote added in proof:*—Dr. Roberts has recently informed us that his preliminary result may require revision. Any effect of this revision on our conclusions will be seen by substituting the revised coefficients into our equations (12) and (16).

[1] D. R. Inglis, Phys. Rev. **85**, 492 (1952). We wish to thank Dr. Inglis for several enlightening discussions on this point.

[2] J. M. Blair and R. E. Holland (to be published). See R. K. Adair, Revs. Modern Phys. **22**, 249 (1950) for preliminary data.

[3] Roberts, Darlington, and Haugsnes, Phys. Rev. **82**, 299 (1951). We are indebted to Dr. Roberts for supplying us with his corrected data prior to publication.

[4] One such case is calculated in the Appendix.

[5] E. P. Wigner, Am. J. Phys. **17**, 99 (1949).

[6] By virtue of a theorem derived by E. Eisner and R. G. Sachs, Phys. Rev. **72**, 680 (1947) and L. Wolfenstein and R. G. Sachs, Phys. Rev. **73**, 528 (1948).

The total absorption cross section is limited by the inequality,[7]

$$\sigma_a \leqq \tfrac{1}{6}(2J+1)\pi\lambda^2; \tag{3}$$

i.e., $\sigma_a \leqq 2.12$ barns for $J=3/2$ and $\sigma_a \leqq 3.07$ barns for $J=5/2$. To compare these figures to the measured values we must subtract the nonresonance part of the experimental cross section and multiply the result by 13.3 to correct for the abundance of Li^6. This corrected experimental value is about 2.5 barns, which is consistent with either spin value within the uncertainty of the calibration. To obtain further information we must calculate the angular distribution.[8]

3. CALCULATIONS

We denote by X_{jm} $(j=1/2,\ 3/2)$ the spin wave functions of the combined neutron and Li^6 spins, and by $Y_{00}{}^N+AY_{10}{}^N$ the s and p parts of the orbital wave function of the incident neutron wave. Those "outside" wave functions of Li^6 and n which are contained in the incident plane wave are denoted by

$$u_{jm} \equiv X_{jm}(Y_{00}{}^N+AY_{10}{}^N). \tag{4}$$

Of all outside wave functions having orbital angular momentum 0 or 1, we form linear combinations $\phi_{Jm}{}^{(e)}$, $\varphi_{Jm}{}^{(0)}$, $\phi_{Jm}{}^{(0)}$ of definite angular momentum J. The superscripts indicate the parity and $\varphi_{Jm}{}^{(0)}$ and $\phi_{Jm}{}^{(0)}$ contain the spin functions X_{1m} and X_{0m}, respectively. For the wave functions of even parity $l=0$, so that $J=j$ and there is no ambiguity:

$$u_{1m} = \phi_{1m}{}^{(e)} + A\sum_{J=\frac{1}{2}}^{\frac{1}{2}} C_J{}^{(\frac{1}{2})}\varphi_{Jm}{}^{(0)}, \tag{5}$$

$$u_{0m} = \phi_{0m}{}^{(e)} + A\sum_{J=\frac{1}{2}}^{\frac{1}{2}} C_{Jm}{}^{(\frac{1}{2})}\phi_{Jm}{}^{(0)}, \tag{6}$$

where $C_J{}^{(\frac{1}{2})}$ and $C_{Jm}{}^{(\frac{1}{2})}$ are known coefficients.[9] In this form the incident wave functions can be tied in with "inside" wave functions of the excited nucleus Li^7. Through these, they will be coupled to "outside" T, α-wave functions $\psi_{Jm}{}^{(0)}$ and $\psi_{Jm}{}^{(e)}$ with unknown coefficients $p^{(j)}$ and $q_J{}^{(j)}$ which depend on J, j and parity, but not upon m:

$$u_{1m} \to p^{(\frac{1}{2})}\psi_{1m}{}^{(e)} + \sum_{J=\frac{1}{2}}^{\frac{1}{2}} q_J{}^{(\frac{1}{2})}C_J{}^{(\frac{1}{2})}\psi_{Jm}{}^{(0)}, \tag{7}$$

$$u_{0m} \to p^{(\frac{1}{2})}\psi_{0m}{}^{(e)} + \sum_{J=\frac{1}{2}}^{\frac{1}{2}} q_J{}^{(\frac{1}{2})}C_{Jm}{}^{(\frac{1}{2})}\psi_{Jm}{}^{(0)}. \tag{8}$$

Apart from the improbable event of an accidental degeneracy or near degeneracy, the coefficients $q_J{}^{(j)}$ vanish except for one value of J. We shall, therefore, proceed with the alternatives $J=3/2$ or $5/2$, since $J=1/2$ could not yield a $\cos^2\theta$-term in the angular distribution.

The functions $\psi_{Jm}{}^{(0)}$ and $\psi_{Jm}{}^{(e)}$ must be expressed as linear combinations $\chi_\pm{}^T Y_{lm'}$ where $\chi_\pm{}^T$ is the spin wave function of the triton and $Y_{lm'}$ is the orbital wave function for the T, α-wave. There is no excited bound state for either triton or α-particle, and the ground states are even $1/2$ and even 0, respectively.

Case I: $J=5/2$.

Using the abrreviations $p^{(\frac{1}{2})}=a$, $p^{(\frac{1}{2})}=b$, and $q_1{}^{(\frac{1}{2})}=\sigma$, we obtain

$$u_{0m} \to b\delta_{m\frac{1}{2}}Y_{00}\chi_+{}^T, \tag{9}$$

$$u_{1m} \to \left[a\left(\frac{5-2m}{10}\right)^{\frac{1}{2}}Y_{2,m-\frac{1}{2}} + \sigma\left(\frac{25-4m^2}{40}\right)^{\frac{1}{2}}\left(\frac{7-2m}{14}\right)^{\frac{1}{2}}Y_{3,m-\frac{1}{2}}\right]\chi_+{}^T, \tag{10}$$

where we have written the $C_{Jm}{}^{(j)}$ explicitly and omitted the terms with $\chi_-{}^T$. The intensity I is equal to the sum of the absolute squares of the coefficients of $\chi_+{}^T$, summed over j and m:

$$I(\theta) = |a|^2+\tfrac{1}{2}|b|^2+(3/10)|\sigma|^2 + (3/\sqrt{10})(a^*\sigma+a\sigma^*)\cos\theta+\tfrac{3}{8}|\sigma|^2\cos^2\theta. \tag{11}$$

By comparing Eq. (11) with Roberts' experimental results we have $|\sigma|^2=320$, $|a|^2+\frac{1}{2}|b|^2=7$. From this we obtain the ratio of the resonance part of the total absorption cross section $[(3/10)|\sigma|^2+\frac{1}{3}\times\frac{3}{8}|\sigma|^2]$ to the nonresonance part $[|a|^2+\frac{1}{2}|b|^2]$ as

$$\tfrac{1}{2}|\sigma|^2/(|a|^2+\tfrac{1}{2}|b|^2)=23. \tag{12}$$

The data of Blair and Holland, however, give this ratio as about 3. The coefficient of $\cos\theta$ in Eq. (1) must on the same basis be smaller in magnitude than

$$(3/10^{\frac{1}{2}})2(320)^{\frac{1}{2}}7^{\frac{1}{2}}=90,$$

which is not in contradiction with present data.

Case II: $J=3/2$.

Using $p^{(\frac{1}{2})}=a$, $p^{(\frac{1}{2})}=b$, $q_1{}^{(\frac{1}{2})}=\rho$, and $q_0{}^{(\frac{1}{2})}=\tau$ and again writing only the terms in $\chi_+{}^T$, we have

$$u_{0m} \to \left[b\delta_{m\frac{1}{2}}Y_{00}+\tau\left(\frac{3+2m}{6}\right)^{\frac{1}{2}}Y_{1,m-\frac{1}{2}}\right]\chi_+{}^T, \tag{13}$$

$$u_{1m} \to \left[a\left(\frac{5-2m}{10}\right)^{\frac{1}{2}}Y_{2,m-\frac{1}{2}} + \rho\frac{2m}{(15)^{\frac{1}{2}}}\left(\frac{3+2m}{6}\right)^{\frac{1}{2}}Y_{1,m-\frac{1}{2}}\right]\chi_+{}^T. \tag{14}$$

[7] Freshbach, Peaslee, and Weisskopf, Phys. Rev. **71**, 145 (1947).

[8] Although the general problem of angular distributions has been calculated by J. M. Blatt and L. C. Biedenharn [Phys. Rev. **82**, 123 (1951) and preliminary mimeographed publication], it is more convenient in our case to write down the wave functions explicitly.

[9] B. L. v. d. Waerden, *Die gruppentheoretische Methode in der Quantenmechanik* (Verlag Julius Springer, Berlin, Germany, 1932), p. 70. Our normalization is different, however.

This yields for the intensity $I(\theta)$

$$I(\theta)=|a|^2+\tfrac{1}{2}|b|^2+(\tfrac{1}{4}|\tau|^2+(7/15)|\rho|^2)+\left(\frac{a^*\rho+a\rho^*}{(15)^{\frac{1}{2}}}+\frac{b^*\tau+b\tau^*}{(2)^{\frac{1}{2}}}\right)\cos\theta+(\tfrac{3}{4}|\tau|^2-\tfrac{3}{8}|\rho|^2)\cos^2\theta. \quad (15)$$

If we compare with Eq. (1), we get $|\tau|^2=256+(8/15)|\rho|^2$ from the $\cos^2\theta$ term and

$$|a|^2+\tfrac{1}{2}|b|^2=103-[\tfrac{1}{4}|\tau|^2+(7/15)|\rho|^2]$$

from the constant term. The ratio of resonance to nonresonance part of the total absorption is

$$(\tfrac{1}{2}|\tau|^2+\tfrac{1}{3}|\rho|^2)/(|a|^2+\tfrac{1}{2}|b|^2)=(128+\tfrac{3}{5}|\rho|^2)/(39-\tfrac{3}{8}|\rho|^2). \quad (16)$$

This is in agreement with Blair and Holland's data if ρ is assumed to be zero. Because of the unknown phase relations we have for the $\cos\theta$-term in Eq. (15) only an inequality, which is satisfied by, e.g., $\rho=0$ and any $|a|^2<29$.

4. DISCUSSION

Assuming first that the assumptions underlying our calculations are correct, we note that our main conclusions are not very sensitive to possible experimental inaccuracies. In order to make spin 5/2 possible, for instance, we must assume either that the measurement of the ratio of resonance to nonresonance cross section is too small by about a factor 6 or that in Roberts' measurement the ratio of the $\cos^2\theta$-term to the constant term is too large by about 45 percent. Roberts' ratio is estimated to be correct within twenty percent. While there is some doubt about the calibration in the experiment of Blair and Holland, the experimental error cannot account for a factor six in the *ratio* of resonance to nonresonance cross section. Furthermore, the nonresonance cross section is in fair agreement with the extrapolated $1/v$ law and to have a ratio of 23 would require a resonance peak higher than the maximum possible for p-neutrons.

The truth of our assumptions should be clarified by certain further experiments. An improvement of the total cross section measurement to 10 percent could rule out a nondegenerate state of spin 3/2 if it turns out that the resonance cross section exceeds 2.12 barns. If Roberts' angular distribution measurements at 100 kev, now in progress, show too large an angle dependence, our first assumption is wrong. It may then still be possible to determine the spin of the compound nucleus by an extension of our calculations to include d-neutrons. As yet, there is no indication of a term in $\cos^4\theta$ up to 400 kev.

The unlikely possibility of an accidental near degeneracy can of course never be excluded by considerations of this type. We have in fact treated in the Appendix the case of a 1/2, 5/2 degeneracy and found that even this combination is compatible with all the data.

APPENDIX

For the combined 1/2 and 5/2 states we use Eqs. (7) and (8) with the abbreviations $p^{(1)}=a$, $p^{(\frac{1}{2})}=b$, $q_{\frac{1}{2}}{}^{(\frac{1}{2})}=\xi$, $q_{\frac{1}{2}}{}^{(\frac{3}{2})}=\eta$, and $q_{\frac{1}{2}}{}^{(1)}=\sigma$, and obtain

$$u_{\frac{1}{2}m}\rightarrow[b\delta_{m\frac{1}{2}}Y_{00}+\xi 2m(3-2m)^{\frac{1}{2}}Y_{1,m-\frac{1}{2}}]\chi_+{}^T, \quad (17)$$

$$u_{\frac{1}{2}m}\rightarrow\left[a\left(\frac{5-2m}{10}\right)^{\frac{1}{2}}Y_{2,m-\frac{1}{2}}+\eta(9-4m^2)^{\frac{1}{2}}(3-2m)^{\frac{1}{2}}Y_{1,m-\frac{1}{2}}+\sigma\left(\frac{25-4m^2}{40}\right)^{\frac{1}{2}}\left(\frac{7-2m}{14}\right)^{\frac{1}{2}}Y_{3,m-\frac{1}{2}}\right]\chi_+{}^T, \quad (18)$$

and consequently,

$$I(\theta)=|a|^2+\tfrac{1}{2}|b|^2+(3/10)|\sigma|^2+3|\xi|^2+24|\eta|^2-6(3/20)^{\frac{1}{2}}(\sigma^*\eta+\sigma\eta^*)+[(3/10^{\frac{1}{2}})(a^*\sigma+a\sigma^*)+(3/2)^{\frac{1}{2}}(b^*\xi+b\xi^*)+2\sqrt{6}(a^*\eta+a\eta^*)]\cos\theta+[\tfrac{3}{8}|\sigma|^2+18(3/20)^{\frac{1}{2}}(\sigma^*\eta+\sigma\eta^*)]\cos^2\theta. \quad (19)$$

The ratio of resonance to nonresonance cross section is then

$$\text{Res./nonres.}=(\tfrac{1}{2}|\sigma|^2+3|\xi|^2+24|\eta|^2)/(|a|^2+\tfrac{1}{2}|b|^2)=Z/(167-Z), \quad (20)$$

where

$$Z=\tfrac{1}{2}|\sigma|^2+3|\xi|^2+24|\eta|^2. \quad (21)$$

To obtain a resonance to nonresonance ratio of 3 we must have $Z=125$. This must be compatible with an inequality obtained from

$$18(3/20)^{\frac{1}{2}}(\sigma^*\eta+\sigma\eta^*)=192-\tfrac{3}{8}|\sigma|^2, \quad (22)$$

as

$$36(3/20)^{\frac{1}{2}}|\sigma||\eta|\geqq|192-\tfrac{3}{8}|\sigma|^2| \quad (23)$$

or

$$|192-\tfrac{3}{8}|\sigma|^2|\leqq[(125-\tfrac{1}{2}|\sigma|^2)/24]^{\frac{1}{2}}. \quad (24)$$

This inequality is fulfilled for, e.g., $|\sigma|=13$. To explain all the present data with a 1/2, 5/2 degeneracy it is, therefore, sufficient to assume that the 1/2 state contributes one third of the measured resonance cross section, which is in agreement with Eq. (3).

The Angular and Lateral Distribution Functions for the Nucleon Component of the Cosmic Radiation

H. MESSEL AND H. S. GREEN
University of Adelaide, Adelaide, South Australia
(Received February 28, 1952)

A method is developed, whereby the angular and radial distribution functions for the nucleon component of the cosmic radiation in the atmosphere may be obtained in terms of the moments of the distributions. Essentially the method consists of an expansion of the unknown distribution functions in a series of derivatives of the Dirac delta-function, whose coefficients are identified with the angular and radial moments. The method gives results identical with those obtained by a more tedious procedure, and is of general applicability in reconstructing distribution functions when only their moments are known.

The angular and radial distribution functions are found for various initial conditions and numerical results given for the case of an integral primary proton power law spectrum with exponent $\gamma=1.1$. Variation of atmospheric density with height is taken into account. Using a form of the differential cross section for nucleon-nucleon collisions, $R+S'\cos^2\bar{\theta}$ in the center-of-mass frame of reference, predicted by most field theoretic treatments, it is shown that the calculated results are in disagreement by an order of magnitude with experimental data. The various assumptions on which our theory is based (power law, homogeneous form of total cross section, etc.) are then critically examined. It is concluded that the theory can be reconciled with experiment only when the number of scattered particles decreases exponentially from the direction of motion of the incident particle in the laboratory frame of reference. Using this result, the new angular and radial distribution functions are then calculated and found to be given at sea level essentially by $\exp\{-166U(1-C)\}$ and $\exp\{-3.72U^{\frac{1}{2}}r\}$, respectively, for particles of energy greater than U Bev, where C is the cosine of the angle with the shower axis and r is the distance in kilometers from the shower axis. The half-value of the radial distribution occurs at a distance of 92 meters from the shower axis.

I. INTRODUCTION

A SHORT time ago the authors[1,2] made a theoretical determination of the mean square angular deviation and mean square distance of the nucleons in extensive air showers from the shower axis. The numerical results were of considerable interest in showing the horizontal and vertical development of air showers in consequence of a given differential cross section for nucleon-nucleon collisions and a given energy spectrum for the primary particles. It might be hoped further that comparison with the experimental data would provide valuable information on the nuclear differential cross sections at very high energies.

From the quantitative point of view, the lateral spread derived from a general type of cross section was surprisingly large, indicating that either the corresponding distribution function must possess a long "tail" or that some unknown physical factor comes into play. We were not able at the time to confirm the existence of a tail quantitatively and were thus led to consider the problem of the determination of the angular and lateral distribution functions for the nucleon component of the cosmic radiation.

So far as we are aware, this problem has not been considered before, although Molière[3–5] has considered the corresponding problem for the soft component. His result were later verified by Cocconi *et al.*[6] within the experimental error and within 200 meters of the shower axis. This was remarkable, in view of the physical hypotheses on which Molière's theory was based. For, at the time, it was not known that the soft component was secondary to the nucleon component of the cosmic radiation, being produced continuously throughout the atmosphere by decay of the neutral π-mesons evolved in nuclear collisions. Furthermore, Molière's results were calculated only for the cascade maximum in an atmosphere of constant density; and it would be very coincidental if this procedure should yield even approximately correct results. For our treatment of the corresponding nucleon problem has shown that the development of showers in media of constant and variable density has very different characteristics.

Molière's calculations were based on Landau's equation,[7] as were also those of other authors[8–10] who attempted to evaluate the higher moments of the angular and radial distributions for the soft component. Landau's equation, however, neglects the fourth and higher even moments of the angular distribution for the individual processes concerned; it will therefore give correctly only the mean square angular and lateral deviation of the shower particles from the trajectory of the generating primary. It might be hoped that the error for the higher moments would be small; but our experience with the corresponding nucleon problem lends no support to this hope. Molière was evidently aware of the difficulty when he recently[11] made a detailed calculation with the limited objective of obtaining the mean square angular and radial deviations.

[1] H. S. Green and H. Messel, Phys. Rev. **85**, 678 (1952).
[2] H. S. Green and H. Messel, Proc. Phys. Soc. (London) (to be published).
[3] G. Molière, Naturwiss. **30**, 87 (1942).
[4] G. Molière and W. Heisenberg, *Cosmic Radiation* (Dover Publications, New York, 1946).
[5] G. Molière, Phys. Rev. **77**, 715 (1949).
[6] Cocconi, Cocconi Tongiorgi, and Griesen, Phys. Rev. **76**, 1020 (1949).
[7] L. Landau, J. Phys. (U.S.S.R.) **3**, 237 (1940).
[8] A. Borsellino, Nuovo cimento **7**, No. 4, 700 (1950).
[9] L. Eyges and S. Fernbach, Phys. Rev. **82**, 23 (1951).
[10] Nordheim, Osborne, and Blatt, Proc. Echo Lake Symposium (1949).
[11] G. Molière, Z. Physik **125**, 250 (1948).

Experimental work on the subject has been performed by Cocconi *et al.*,[6] Greisen *et al.*,[12] and also by the Russian school,[13–15] which extended measurements to distances of the order of 1 km. Although the latter obtained a radial distribution varying as $r^{-2.6}$ with the distance r from the shower axis, which would imply an infinite mean square distance from it, their distribution agrees roughly with the earlier determinations in having an apparent half-width of about 150 meters.

Since the method which we shall adopt requires a detailed mathematical analysis, a mathematical introduction follows. The calculations are embodied in the second half of the paper, and a nonmathematical discussion of the results obtained will be found at the end.

II. MATHEMATICAL INTRODUCTION

The use of the δ-function has been well established in quantum mechanics[16] and pulse theory; however, the rigor of the mathematical procedures in which it is used has sometimes been questioned, and we therefore state at the outset the unambiguous meaning of an equation of the type.

$$f(x)=w(x)\sum a_k(x)\delta^{(k)}(x), \tag{1}$$

where x is an arbitrary variable and the superscript represents the number of differentiations with respect to x. The functions $a_k(x)$ must be regular at $x=0$, but $w(x)$ may have any kind of singularity. If $q(x)$ is an arbitrary function, regular at $x=0$, then (1) is equivalent to the assertion

$$\int_{-a}^{b} dx q(x)f(x)/w(x)=\sum(-1)^k q_k{}^{(k)}(0), \qquad q_k(x)=q(x)a_k(x), \tag{2}$$

where a and b are any positive numbers less than the radius of convergence of the power series

$$q(x)=\sum_{k=0}^{\infty} q^{(k)}(0)x^k/k!.$$

Now

$$\int_{-a}^{b} q(x)f(x)dx=\sum_{k=0}^{\infty} q^{(k)}(0)\int_{-a}^{b} x^k f(x)dx/k!. \tag{3}$$

Hence, using the equivalence of (1) and (2) for the special case $w(x)=1$, one has

$$f(x)=\sum_{k=0}^{\infty}(-1)^k f_{(k)}\delta^{(k)}(x)/k!, \tag{4}$$

$$f_{(k)}=\int_{-a}^{b} x^k f(x)dx. \tag{5}$$

Thus any integrable function $f(x)$ can be expanded as a series of derivatives of the δ-function, with coefficients which are proportional to the moments (5) of the function $f(x)$, within a certain range of the variable.

This result is easily extended to functions of any number of variables. For example,

$$f(r_1, r_2, C)=\sum_{l,m,n=0}^{\infty}\frac{(-1)^{l+m+n}2^{-n}}{l!m!n!}f_{(l,m,n)} \times\delta^{(l)}(r_1)\delta^{(m)}(r_2)\delta^{(n)}(1-C), \tag{6}$$

where

$$f_{(l,m,n)}=2^n\int\int\int f(r_1, r_2, C)r_1{}^l r_2{}^m(1-C)^n dr_1 dr_2 dC. \tag{7}$$

We shall require the value of

$$\int_0^{2\pi} f(r\cos\Psi, r\sin\Psi, C)d\Psi=f(r, C), \tag{8}$$

where the function f is defined by (6). It is clear from (8) that $f(r, C)$ must be an even function of r; hence, by an analog of (4),

$$f(r, C)=\sum_{l,n=0}^{\infty}\frac{(-1)^{l+n}2^{-n}}{l!n!}f_{(l,n)}\delta^{(l)}(r^2)\delta^{(n)}(1-C), \tag{9}$$

where

$$\begin{aligned} f_{(l,n)}&=2^n\int\int\int f(r\cos\Psi, r\sin\Psi, C) \times r^{2l}(1-C)^n d(r^2)dCd\Psi \\ &=2^{n+1}\int\int\int f(r_1, r_2, C)(r_1{}^2+r_2{}^2)^l \times(1-C)^n dr_1 dr_2 dC \\ &=2\sum_{k=0}^{l}\binom{l}{k}f_{(2k,\,2l-2k,\,n)}, \end{aligned} \tag{10}$$

according to (7). Substituting (10) into (9), one has

$$f(r, C)=2\sum_{l,m,n=0}^{\infty}\frac{(-1)^{l+m+n}2^{-n}}{l!m!n!}f_{(2l,\,2m,\,n)} \times\delta^{(l+m)}(r^2)\delta^{(n)}(1-C). \tag{11}$$

Returning to (4) we examine the question of reconstructing the function $f(x)$ from a knowledge of the moments, if $f_{(k)}$ has a singularity at $x=0$, let $w(x)$ be a "weight function" with a singularity of the same type; and let

$$f(x)=w(x)\sum f_n S_n(x), \tag{12}$$

[12] Greisen, Walker, and Walker, Phys. Rev. **80**, 535 (1950).
[13] Eidus, Alymova, and Videnskii, Dokl. Akad. Nauk. (U.S.S.R.) **75**, 669 (1950).
[14] Vernov, Grigorov, and Charaklchyan, Izv. Akad. Nauk. (U.S.S.R.) Ser. Fiz; **14** (No. 1) 51, (1950).
[15] Eidus, Blinova, Videnskii, and Suvorov, Dokl. Akad. Nauk. (U.S.S.R.) **74**, 477 (1950).
[16] P. A. M. Dirac, *The Principles of Quantum Mechanics* (Clarendon Press, Oxford, 1947), third edition.

where $S_n(x)$ is a set of polynomials defined by

$$S_n(x)=\begin{vmatrix} w_{(0)} & w_{(1)} & \cdots & w_{(n)} \\ w_{(1)} & w_{(2)} & \cdots & w_{(n+1)} \\ \cdot & \cdot & \cdot & \cdot \\ w_{(n-1)} & w_{(n)} & \cdots & w_{(2n-1)} \\ 1 & x & \cdots & x^n \end{vmatrix}, \tag{13}$$

and

$$w_{(k)}=\int w(x)x^k dx. \tag{14}$$

The polynomials satisfy the orthogonality relations

$$\int w(x)S_m(x)S_n(x)dx=N_m\delta_{m,n}, \tag{15}$$

where the normality constants are given by

$$N_n=\Delta_n\Delta_{n-1},$$

$$\Delta_n=\begin{vmatrix} w_{(0)} & w_{(1)} & \cdots & w_{(n)} \\ w_{(1)} & w_{(2)} & \cdots & w_{(n+1)} \\ \cdot & \cdot & \cdot & \cdot \\ w_{(n)} & w_{(n+1)} & \cdots & w_{(2n)} \end{vmatrix}. \tag{16}$$

Then the f_n in (12) are given by

$$N_n f_n=\int f(x)S_n(x)dx$$

$$=\begin{vmatrix} w_{(0)} & w_{(1)} & \cdots & w_{(n)} \\ w_{(1)} & w_{(2)} & \cdots & w_{(n+1)} \\ \cdot & \cdot & \cdot & \cdot \\ w_{(n-1)} & w_{(n)} & \cdots & w_{(2n-1)} \\ f_{(0)} & f_{(1)} & \cdots & f_{(n)} \end{vmatrix}. \tag{17}$$

Thus the function $f(x)$ has been expanded in a series of orthogonal polynomials, the coefficients of which are linear combinations of its moments.

This development may be used to verify the formula (4). For, replacing $f(x)$ by $\delta^{(k)}(x)$ in the above argument, one has

$$\delta^{(k)}(x)=w(x)(-1)^k k!\sum_{l=0}^{k}\Delta_{l(k)}S_l(x)/N_l, \tag{18}$$

where $\Delta_{l(k)}$ is the minor of $w(k+l)$ in the last row or column of the determinant Δ_l. Substituting this result in (4), one obtains again (12) with the coefficients f_n given by (17).

We now state a series of formulas involving δ-functions which will be required in the subsequent work. Let O and Q represent the differential operators

$$O\equiv\frac{d}{dC}(1-C^2)\frac{d}{dC},\quad Q\equiv\frac{\partial}{\partial C}(1-C^2)\frac{\partial}{\partial C}+\frac{1}{1-C^2}\frac{\partial^2}{\partial\beta^2}, \tag{19}$$

of the Legendre and associated Legendre functions, respectively. If $b(C)$ is a regular function of C, then

$$b(C)\delta^{(k)}(1-C)=\sum_{l=0}^{k}\binom{k}{l}b^{(l)}(1)\delta^{(k-l)}(1-C), \tag{20}$$

$$O\delta^{(k)}(1-C)=-k(k+1)\delta^{(k)}(1-C)-2(k+1)\delta^{(k+1)}(1-C), \tag{21}$$

$$O(O+1.2)(O+2.3)\cdots\{O+l(l-1)\}\delta(1-C)=(-2)^l l!\delta^{(l)}(1-C). \tag{22}$$

Also, if $S=(1-C^2)^{\frac{1}{2}}$,

$$Q\{(S\cos\beta)\delta^{(1)}(1-C)\}=-2S\cos\beta\delta^{(2)}(1-C), \tag{23}$$

$$Q\{\cos^2\beta\delta(1-C)\}=-\delta^{(1)}(1-C)-\tfrac{1}{2}\delta(1-C)\cos 2\beta. \tag{24}$$

These formulas may all be tested by the rules of integration given at the beginning of this section.

III. HIGHER ANGULAR MOMENTS FOR NUCLEON-NUCLEON COLLISIONS

The differential probability that a nucleon of energy U, dU should be scattered inelastically at an angle of cosine c, dc to the direction of motion of the incident nucleon of energy U_0 is taken to be

$$W(U_0, U, c)dUdc=UF(U_0, U)y\{U(1-c)\}dUdc$$
$$\{c_0\approx 1-U^{-1},\ F(U_0, U)=20U_0^{-5}U(U-U_0)^3\} \tag{25}$$

for $c\geqq c_0$. For relativistic reasons it is impossible for a nucleon to be scattered through an angle greater than $\cos^{-1}c_0$ in a nucleon-nucleon collision.

If we adopt the form of $W(U_0, U, c)$ determined in our previous paper[17] by assuming that in the center-of-mass coordinates the differential cross section is of the form $R(\bar{U})+S'(\bar{U})\cos^2\bar{\theta}$, then $y(x)=6x(1-x)$. We shall see, however, at a later stage in our work, that this choice is incompatible with experimental data.

The nth angular moment of $W(U_0, U, c)$ defined by (25) is

$$W_{(n)}=2^n\int_{c_0}^{1}W(U_0, U, c)(1-c)^n dc$$

$$=(2/U)^n\int_0^1 F(U_0, U)y(x)x^n dx$$

$$=(2/U)^n F(U_0, U)y_{(n)}. \tag{26}$$

IV. ANGULAR MOMENTS FOR NUCLEON-NUCLEUS COLLISIONS

In a previous paper[18,19] the authors derived the mean square angle of emission of nucleons resulting from nucleon-nucleus collisions, for both light and heavy ele-

[17] H. S. Green and H. Messel, Proc. Phys. Soc. (London) **A64**, 1083 (1951).
[18] H. Messel and H. S. Green, Phys. Rev. **83**, 1279 (1951).
[19] H. Messel and H. S. Green, Proc. Phys. Soc. (London), **A65**, 245 (1952).

ments. The method is to consider the development of a nucleon cascade in homogeneous nuclear matter, finally averaging over all possible paths through the nucleus, assumed to be spherical in shape. At the energies considered interference effects are negligible.

For our present purpose, it will be necessary to determine the higher moments of the angular distribution of particles emitted from the nucleus. The probability $\nu(U, C, z)dUdC$ of finding a nucleon at depth z (measured in the direction of motion of the incident particle) in homogeneous nuclear matter, with energy U, dU and direction of motion making an angle of cosine C, dC with that of the incident particle satisfies the integro-differential equation

$$C\frac{\partial \nu}{\partial z}(U, C)+\nu(U, C)=2\int_U^\infty dU'\int_{c_0}^1 dc\int_0^{2\pi}\frac{d\omega}{2\pi}\times\nu(U', C')W(U', U, c), \quad (27)$$

$$C'=Cc+Ss\cos\omega, \quad S=(1-C^2)^{\frac{1}{2}}, \quad s=(1-c^2)^{\frac{1}{2}}.$$

The integrand can be developed as a series of differentia coefficients of $\nu(U', C)$, in the following way. Expand $\nu(U', C')$ as a series of Legendre polynomials, thus:

$$\nu(U', C')=\sum_{k=0}^{\infty}(k+\tfrac{1}{2})\nu_k(U')P_k(C'). \quad (28)$$

Then making use of the addition theorem for Legendre polynomials, one has

$$\int_{c_0}^1 dc\int_0^{2\pi}\frac{d\omega}{2\pi}\nu(U', C')W(U', U, c)$$

$$=\sum_{k=0}^{\infty}(k+\tfrac{1}{2})\nu_k(U')P_k(C)\int_{c_0}^1 P_k(c)W(U', U, c)dc$$

$$=\sum_{k=0}^{\infty}(k+\tfrac{1}{2})\nu_k(U')P_k(C)\sum_{l=0}^{k}\frac{(k+l)!}{(k-l)!}\frac{(-4)^{-l}}{(l!)^2}W_{(l)} \quad (29)$$

by expanding $P_k(c)$ in powers of $(1-c)$ and substituting from (26). Interchanging the order of the summations and using the property $k(k+1)P_k(C)=OP_k(C)$, where O is the operator defined in (19), one obtains

$$\int_{c_0}^1 dc\int_0^{2\pi}\frac{d\omega}{2\pi}\nu(U', C')W(U', U, c)$$

$$=\sum_{l=0}^{\infty}O(O+1.2)\cdots\{O+l(l-1)\}\nu(U', C)4^{-l}(l!)^{-2}W_{(l)}. \quad (30)$$

Substituting for $W_{(l)}$ from (26) and inserting in (30) one has

$$C\frac{\partial \nu}{\partial z}(U, C)+\nu(U, C)=2\int_U^\infty dU'F(U', U)\sum_{l=0}^{\infty}\frac{(2U)^{-l}}{(l!)^2}y_{(l)}\times O(O+2)\cdots\{O+l(l-1)\}\nu(U', C). \quad (31)$$

Thus the equation satisfied by the Mellin transform

$$\nu(v, C)=\int_0^\infty dUU^v\nu(U, C) \quad (32)$$

is then

$$C\frac{\partial \nu(v)}{\partial z}+\alpha(v)\nu(v)=\sum_{l=1}^{\infty}\frac{2^{-l}}{(l!)^2}y_{(l)}O(O+2)\cdots\times\{O+l(l-1)\}\nu(v-l)W(v-l), \quad (33)$$

where

$$\alpha(v)=1-W(v),$$

$$W(v)=2\int_0^\infty dU(U/U')^vF(U', U) \quad (34)$$

$$=240\{(v+2)(v+3)(v+4)(v+5)\}^{-1}.$$

The initial conditions to be applied to these equations are

$$\nu(U, C, z=0)=\delta(U-U_0)\delta(1-C),$$
$$\nu(v, C, z=0)=U_0^v\delta(1-C). \quad (35)$$

Equation (33) can be conveniently handled by taking the Laplace transform with respect to z:

$$\bar{\nu}(v, C, \lambda)=\int_0^\infty e^{-\lambda z}\nu(v, C, z)dz. \quad (36)$$

Equation (33) then becomes

$$\{\lambda C+\alpha(v)\}\bar{\nu}(v)=U_0^v\delta(1-C)+\sum_{l=1}^{\infty}2^{-l}(l!)^{-2}y_{(l)}O(O+2)\cdots\times\{O+l(l-1)\}\bar{\nu}(v-l)W(v-l). \quad (37)$$

The solution of (37), in the form of a series of derivatives of $\delta(1-C)$, can now be obtained by an iterative procedure:

$$\bar{\nu}(v)=\sum_{l=0}^{\infty}(-2)^l l!A_v^l\delta^{(l)}(1-C), \quad (38)$$

where

$$A_v^l=U_0^{v-l}\{\lambda+\alpha(v-l)\}^{-1}\sum{}'\prod_{i=1}^{l}\alpha_{v-(a_1+\cdots+a_{i-1})}^{a_i},$$
$$\alpha_v^l=y_{(l)}W(v-l)2^{-l}(l!)^{-2}\{\lambda+\alpha(v)\}^{-1}, \quad l=1, 2, \text{etc.} \quad (39)$$

The formulas (21) and (22) have been used to simplify the result (38), terms differing from those given by a factor U_0^{-1} having been neglected in the high energy approximation. In (39) the summation $\sum'$ is applied to all different products for which

$$a_1+a_2+\cdots+a_l=1. \tag{40}$$

The a's may take positive integral values, including zero and $a^0=1$.

Using (4) with $x=2(1-C)$, $a=b=1$, the value of the transform of the lth angular moment may be immediately inferred from (38):

$$\bar{\nu}_{(l)}(v,\lambda)=4^l(l!)^2A_v{}^l. \tag{41}$$

To obtain the lth moment itself, for the distribution of particles within the nucleus, one simply takes an inverse Laplace-Mellin transform.

The distribution of particles emitted by the nucleus is given by

$$n(U,C)=2D^{-2}\int_0^D \nu(U,C,z)z\,dz, \tag{42}$$

where D is the average number of collisions suffered by a nucleon in a diametrical passage through the nucleus; and the moments of this distribution are therefore

$$n_{(l)}(U)=2D^{-2}\int_0^D z\,dz\frac{1}{2\pi i}\int_{v_0-i\infty}^{v_0+i\infty}U^{-(v+1)}dv \cdot\frac{1}{2\pi i}\int_{\lambda_0-i\infty}^{\lambda_0+i\infty}e^{\lambda z}d\lambda\,\bar{\nu}_{(l)}(v,\lambda). \tag{43}$$

For large values of l, this expression is of the order $2^l y_{(l)}$.

V. THE ANGULAR AND LATERAL SPREAD OF THE ATMOSPHERIC NUCLEON CASCADE

We have previously[1,2] developed a method for obtaining the mean square angle made with, and the mean square distance from, the shower axis of the nucleon component of extensive air showers. We set up a vector equation for the probability $f(\mathbf{p},\mathbf{r},t)\bar{d}\mathbf{p}d\mathbf{r}$ of finding a nucleon with momentum $\mathbf{p}$, $\bar{d}\mathbf{p}(=dp_1dp_2dp_3/2\pi p^2)$, at height t, and with a radius vector $\mathbf{r}$, $d\mathbf{r}$ measured normal to the shower axis. The height t and the two components of $\mathbf{r}$ are measured in cm, the three components (normal to and along the shower axis) of $\mathbf{p}$ in units of Mc, where M is the proton mass and c the velocity of light. Then, at ultrarelativistic energies, the scalar magnitude of $\mathbf{p}$ is the energy U, measured in proton mass units.

Let $\delta(t)$ be the density of the atmosphere at height t; then the probability that a nucleon will traverse the layer between height τ and height $t<\tau$, without colliding with an air nucleus, is

$$\exp-\{\theta(t)-\theta(\tau)\}/C_1,$$

where

$$\theta(t)=\frac{1}{75}\int_t^\infty\delta(\tau)d\tau, \tag{44}$$

and C_1 is the angle between the vector $\mathbf{p}$ and the vertical. The phase-space distribution function f satisfies the partial integro-differential equation

$$-\frac{1}{\theta'(t)}\left\{\frac{p_3}{U}\frac{\partial f}{\partial u}+\frac{p_1}{U}\frac{\partial f}{\partial r_1}+\frac{p_2}{U}\frac{\partial f}{\partial r_2}\right\}+f =\int f(\mathbf{p}',\mathbf{r},t)n(\mathbf{p}',\mathbf{p})\bar{d}\mathbf{p}', \tag{45}$$

where u is the distance measured along the shower axis, so $t=uC_2$ where C_2 is the angle made by the shower axis with the vertical. The arguments $\mathbf{p}'$, $\mathbf{p}$ of $n(\mathbf{p}',\mathbf{p})$ are equivalent to those

$$[U=|\mathbf{p}|,\ U'=|\mathbf{p}'|,\ C=\mathbf{p}\cdot\mathbf{p}'/UU']$$

of the previous section, and $\bar{d}\mathbf{p}'=dp_1'dp_2'dp_3'/2\pi p'^2$.

Henceforth C will represent the cosine of the angle between the vector $\mathbf{p}$ and the shower axis, and Ψ the angle between the component of $\mathbf{p}$ normal to the shower axis and the radius vector $\mathbf{r}$. Then, replacing the variable $\mathbf{p}$ by U,C; $\mathbf{p}'$ by U',C'; and $\mathbf{r}$ by r, Ψ, (45) becomes

$$\frac{1}{\theta'(t)}\left\{C\frac{\partial f}{\partial u}-S\cos\Psi\frac{\partial f}{\partial r}+\frac{S\sin\Psi}{r}\frac{\partial f}{\partial\Psi}\right\}+f =\int_U^\infty dU'\int_{-1}^1 dC'\int_0^{2\pi}\frac{d\Psi'}{2\pi}f(U',C',\Psi',r,t) \times n\{U',U,CC'+SS'\cos(\Psi-\Psi')\}, \tag{46}$$

where $C=-P_3/U$, $S=(1-C^2)^{\frac{1}{2}}$, and $S'=(1-C'^2)^{\frac{1}{2}}$.

The solution of this equation will now be obtained in the form (6) of Sec. 2, which, with the aid of (12) will enable us to construct the angular and radial distribution functions for the nucleon component of extensive air showers.

The integral on the right-hand side of (46) is first developed in a series of differential coefficients of $f(U',C,\Psi)$ with respect to C and Ψ, in a manner precisely analogous to that of the previous section. If P is the associated Legendre operator, defined by

$$P\equiv\frac{\partial}{\partial C}S^2\frac{\partial}{\partial C}+\frac{1}{S^2}\frac{\partial^2}{\partial\Psi^2}, \tag{47}$$

one has

$$\int_{-1}^1 dC'\int_0^{2\pi}\frac{d\Psi'}{2\pi}f(U',C',\Psi') \times n\{U',U,CC'+SS'\cos(\Psi-\Psi')\} =\sum_{l=0}^\infty 4^{-l}(l!)^{-2}P(P+1.2)\cdots\{P+l(l-1)\} \times f(U',C,\Psi)n_{(l)}(U',U), \tag{48}$$

where

$$n_{(l)}(U', U)=2^l\int_{-1}^{1} n(U', U, c)(1-c)^l dc \qquad (49)$$

is the same function as in (43). Defining the Mellin transform $f(v, C, \Psi)$ of $f(U, C, \Psi)$ by

$$f(v, C, \Psi)=\int_0^\infty U^v dU f(U, C, \Psi), \qquad (50)$$

(46) reduces to

$$C_2C\frac{\partial f(v)}{\partial\theta}-\frac{S}{\theta'(t)}\cos\Psi\frac{\partial f(v)}{\partial r}+\frac{S}{\theta'(t)}\frac{\sin\Psi}{r}\frac{\partial f(v)}{\partial\Psi}+h(v)f(v)$$
$$=\sum_{l=1}^{\infty}4^{-l}(l!)^{-2}n_{(l)}(v)P(P+2)\cdots$$
$$\times\{P+l(l-1)\}f(v-l), \qquad (51)$$

where

$$n_{(l)}(v)=U'^l\int_0^\infty (U/U')^v n_{(l)}(U', U)dU, \qquad (52)$$

and

$$h(v)=1-n_{(0)}(v). \qquad (53)$$

Equation (51) may be simplified by introducing the further transform

$$g(v, K, \beta)=\int_0^{2\pi}d\Psi\int_0^\infty r dr$$
$$\times\exp\{iKr\cos(\Psi-\beta)\}f(v, r, \Psi), \qquad (54)$$

of which the inverse is

$$f(v, r, \Psi)=(2\pi)^{-2}\int_0^{2\pi}d\beta\int_0^\infty KdK$$
$$\times\exp\{-iKr\cos(\Psi-\beta)\}g(v, K, \beta). \qquad (55)$$

Then one has

$$C_2C\frac{\partial g(v)}{\partial\theta}-iKS\cos\beta g(v)/\theta'(t)+h(v)g(v)$$
$$=\sum_{l=1}^{\infty}4^{-l}(l!)^{-2}n_{(l)}(v)Q(Q+2)\cdots$$
$$\times\{Q+l(l-1)\}g(v-l), \qquad (56)$$

where Q is the operator defined in (19). The initial conditions of the preceding equations are

$$f(U, C, r, \theta=0)=\delta(U-U_0)\delta(1-C)\delta(r)/2\pi r,$$
$$f(v, C, r, \theta=0)=U_0^v\delta(1-C)\delta(r)/2\pi r, \qquad (57)$$
$$g(v, \theta=0)=U_0^v\delta(1-C).$$

On the left-hand side of (56) we may set $C=1$, with the neglect of terms differing by an order U_0^{-1} in comparison with those retained.

In an isothermal atmosphere with surface pressure p_0 and surface density δ_0,

$$\theta(t)=(p_0/75g)\exp(-g\delta_0 t/p_0),$$
$$\theta'(t)=-g\delta_0\theta(t)/p_0, \qquad (58)$$

where g is the acceleration due to gravity. The ratio p_0/δ_0, according to the gas laws, is directly proportional to the absolute temperature. Since the denominator θ' in (56) depends on θ, this equation, unlike (33), cannot be solved by Laplace transforms. We therefore adopt the following almost equivalent iteration procedure.

An initial value $g_0(v)$ of $g(v)$ is derived by neglecting the right-hand side of (56) and solving the resultant equation with the help of (57):

$$g_0(v)=U_0^v\exp\{-h(v)\theta/C_2\}\delta(1-C). \qquad (59)$$

This value is now substituted in the right-hand side of (56) and the resultant equation solved in order to determine the second iteration value $g_1(v)$ of $g(v)$:

$$g_1(v)=g_0(v)+\exp[-h(v)\theta/C_2]$$
$$\times\sum_{l=1}^{\infty}U_0^{v-l}(-2)^{-l}(l!)^{-1}n_{(l)}(v)\delta^{(l)}(1-C)$$
$$\times\int_0^\theta\exp[\{h(v)-h(v-l)\}\lambda/C_2$$
$$+iKS\cos\beta\{l(\lambda)-l(\theta)\}]d\lambda, \qquad (60)$$

with the help of (22) and setting $l(\theta)=-\int^\theta d\Theta(\lambda)/\theta'(\lambda)$. In the integrand of (60) one now expands the factor

$$\exp[iKS\cos\beta\{l(\lambda)-l(\theta)\}]$$
$$=\sum_{m=0}^{\infty}(m!)^{-1}[iKS\cos\beta\{l(\lambda)-l(\theta)\}]^m. \qquad (61)$$

Since $S^{2l+1}\delta^{(l)}(1-C)=0$, terms with $m>2l$ will vanish in (60). The terms with $m=1, 2, 3, \cdots, (2l-1)$ correspond to mixed angular-radial moments of no interest for our present purpose; we therefore consider only the terms with $m=0$ and $m=2l$, which correspond to pure angular and radial moments, respectively. Thus

$$g_1(v)=g_0(v)+\exp\{-h(v)\theta/C_2\}$$
$$\times\sum_{l=1}^{\infty}U_0^{v-l}n_{(l)}(v)(l!)^{-1}2^{-l}\Big[(-1)^l\delta^{(l)}(1-C)$$
$$\times\int_0^\theta\exp[\{h(v)-h(v-l)\}\lambda/C_2]d\lambda$$
$$+(KS\cos\beta)^{2l}(2l!)^{-1}\delta^{(l)}(1-C)$$
$$\cdot\int_0^\theta\exp[\{h(v)-h(v-l)\}\lambda/C_2]$$
$$\times\{l(\lambda)-l(\theta)\}^{2l}d\lambda+\text{other terms}\Big]. \qquad (62)$$

By repeating the iteration procedure one can obtain a better approximation for $g(v)$; we have verified numerically that the corrections so obtained are negligible, for the radial moments, though in the case of the angular moments they may amount to 50 percent of the value of terms so far obtained. We shall not reproduce the elementary but tedious calculations here. Substituting

$$S^{2l}\delta^{(l)}(1-C)=(-2)^l l!P_l(1)=(-2)^l l!, \quad (63)$$

and taking the inverse transform defined by (55), we find

$$\begin{aligned}f(v,r,\Psi)&=U_0{}^v\exp\{-h(v)\theta/C_2\}\delta(1-C)\delta(r_1)\delta(r_2)\\&+\exp\{-h(v)\theta/C_2\}\sum_{l=1}^{\infty}U_0{}^{v-l}n_{(l)}(v)\\&\Big[(-2)^{-l}(l!)^{-1}\delta^{(l)}(1-C)\delta(r_1)\delta(r_2)\\&\int_0^{\theta}\exp[\{h(v)-h(v-l)\}\lambda/C_2]d\lambda\\&+(2l!)^{-1}\delta(1-C)\delta^{(2l)}(r_1)\delta(r_2)\\&\times\int_0^{\theta}\exp[\{h(v)-h(v-l)\}\lambda/C_2]\\&\times\{l(\lambda)-l(\theta)\}^{2l}d\lambda+\text{other terms}\Big], \quad (64)\end{aligned}$$

where $r_1=r\cos\Psi$ and $r_2=r\sin\Psi$. By comparing (64) with (6) one infers the following values for $f_{(l,m,n)}(r)$:

$$\begin{aligned}f_{(0,0,l)}(v)&=U_0{}^{v-l}n_{(l)}(v)\exp\{-h(v)\theta/C_2\}\\&\times\int_0^{\theta}\exp[\{h(v)-h(v-l)\}\lambda/C_2]d\lambda, \quad (65)\end{aligned}$$

$$\begin{aligned}f_{(2l,0,0)}(v)&=U_0{}^{v-l}n_{(l)}(v)\exp\{-h(v)\theta/C_2\}\\&\times\int_0^{\theta}\exp[\{h(v)-h(v-l)\}\lambda/C_2]\{l(\lambda)-l(\theta)\}^{2l}d\lambda\\&=U_0{}^{v-l}(2l)!\left(\frac{g\delta_0}{p_0}\right)^{-2l}\frac{n_{(l)}(v)\exp\{-h(v)\theta/C_2\}}{h(v)-h(v-l)}\\&\times\sum_{k=1}^{\infty}\frac{\{h(v)-h(v-l)\}^k}{k^{2l}k!}\left(\frac{\theta}{C_2}\right)^k. \quad (66)\end{aligned}$$

For a single particle of energy U_0, incident at an angle with the vertical whose cosine is C_2 at the top of the atmosphere, the angular and radial moments relative to the shower axis are given by

$$f_{(l,m,n)}(U_0,U)=\frac{1}{2\pi i}\int_{v_0-i\infty}^{v_0+i\infty}f_{(l,m,n)}(v)U^{-(v+1)}dv. \quad (67)$$

For a differential power-law spectrum whose exponent is $\gamma+1$, the corresponding moments are

$$\gamma U_c{}^{-\gamma}\int_{U_c}^{\infty}(U_c/U_0)^{\gamma+1}f_{(l,m,n)}(U_0,U)dU_0.$$

For the corresponding integral power-law spectrum, one has

$$\begin{aligned}F_{(l,m,n)}(U)&=\gamma U_c{}^{-\gamma}\int_U^{\infty}dU\int_{U_c}^{\infty}dU'(U_c/U')^{\gamma+1}\\&\times f_{(l,m,n)}(U',U). \quad (68)\end{aligned}$$

On substituting (65), (66), and (67) one obtains

$$\begin{aligned}F_{(0,0,l)}(U)&=\frac{U^{-l}}{2\pi i}\int_{v_0-i\infty}^{v_0+i\infty}\left(\frac{U_c}{U}\right)^v\\&\times\frac{n_{(l)}(v+l)[\exp\{-h(v)\theta/C_2\}-\exp\{-h(v+l)\theta/C_2\}]}{\{h(v+l)-h(v)\}}\\&\times\frac{\gamma dv}{(\gamma-v)(v+l)} \quad (69)\end{aligned}$$

apart from corrections arising from the advanced stages of the iteration procedure, and

$$\begin{aligned}F_{(2l,0,0)}(U)&=\frac{U^{-l}}{2\pi i}\int_{v_0-i\infty}^{v_0+i\infty}\left(\frac{U_c}{U}\right)^v(2l)!\left(\frac{g\delta_0}{p_0}\right)^{-2l}\\&\times\frac{n_{(l)}(v+l)\exp\{-h(v+l)\theta/C_2\}}{h(v+l)-h(v)}\\&\times\sum_{k=1}^{\infty}\frac{\{h(v+l)-h(v)\}^k}{(C_2k)^{2l}k!}\left(\frac{\theta}{C_2}\right)^k\frac{\gamma dv}{(\gamma-v)(v+l)}. \quad (70)\end{aligned}$$

The correction terms for (70) have been evaluated and amount to only 2 percent at small atmospheric depths, rising to 7 percent at sea level.

For energies greater than the geomagnetic cut-off energy U_c, the complex integrals of (69) and (70) are easily evaluated by the method of residues, the integrands having a simple pole at $v=\gamma$ in the right-hand half-plane. Thus

$$\begin{aligned}F_{(0,0,l)}(U)&=\frac{\gamma U^{-l}}{\gamma+l}(U_c/U)^{\gamma}n_{(l)}(\gamma+l)\\&\times\frac{[\exp\{-h(\gamma)\theta/C_2\}-\exp\{-h(\gamma+l)\theta/C_2\}]}{\{h(\gamma+l)-h(\gamma)\}}, \quad (71)\end{aligned}$$

and

$$\begin{aligned}F_{(2l,0,0)}(U)&=\frac{\gamma U^{-l}}{\gamma+l}(U_c/U)^{\gamma}n_{(l)}(\gamma+l)(2l)!\\&\times\left(\frac{g\delta_0}{p_0}\right)^{-2l}\frac{\exp\{-h(\gamma+l)\theta/C_2\}}{h(\gamma+l)-h(\gamma)}\\&\times\sum_{k=1}^{\infty}\frac{\{h(\gamma+l)-h(\gamma)\}^k}{(C_2k)^{2l}k!}\left(\frac{\theta}{C_2}\right)^k, \quad (72)\end{aligned}$$

apart from the correction terms.

TABLE I. The first few moments of the angular and radial distribution functions relative to the shower axis. $C_2=1$ and $\gamma=1.1$ θ is measured in units of the interaction free path.

	$\theta=2$	$\theta=6$	$\theta=13.7$
$F_{(0,0,0)}$	0.303	2.79×10^{-2}	2.83×10^{-4}
$F_{(0,0,1)}$	$0.186y_{(1)}$	$3.64\times10^{-2}y_{(1)}$	$4.92\times10^{-4}y_{(1)}$
$F_{(0,0,2)}$	$0.221y_{(2)}+0.243y_{(1)}^2$	$[4.11y_{(2)}+6.64y_{(1)}^2]\times10^{-2}$	$[4.25y_{(2)}+11.4y_{(1)}^2]\times10^{-4}$
$F_{(2,0,0)}$	$20.0y_{(1)}$	$2.74y_{(1)}$	$1.70\times10^{-2}y_{(1)}$
$F_{(4,0,0)}$	$[2.76y_{(2)}+2.17y_{(1)}^2]\times10^4$	$[3.15y_{(2)}+2.47y_{(1)}^2]\times10^2$	$13.6y_{(2)}+10.7y_{(1)}^2$
$F_{(6,0,0)}$	$[4.17y_{(3)}+19.3y_{(1)}y_{(2)}]\times10^7$	$[4.15y_{(3)}+19.2y_{(1)}y_{(2)}]\times10^4$	$[1.35y_{(3)}+6.24y_{(1)}y_{(2)}]\times10^6$

VI. RECONSTRUCTION OF THE DISTRIBUTION FUNCTIONS

It is convenient to reconstruct the radial and angular distribution functions before averaging over all angles of inclination to the shower axis. This requires only a correct application of the theory given in Sec. 2.

The most important step in this procedure is the identification of the proper weight-function $w(x)$ in (12). For this purpose, a knowledge of only the lower moments is useless; and an arbitrary choice will most likely give a divergent series. Indeed, if the function $f(x)$ has a singularity at $x=0$, and $w(x)$ has not a singularity of the same type, the series (12) is inevitably divergent. To identify $w(x)$ correctly without knowledge of the type of singularity involved, one must know the asymptotic behavior of the moment $f_{(n)}$ as $n\to\infty$. This may then be compared with the corresponding behavior of the moments of the function

$$w(x)=\exp(-Bx^A),$$

which gives

$$w_{(l)}=A^{-1}B^{-(l+1)/A}\Gamma\{(l+1)/A\}.$$

Now the right-hand side of (71) varies asymptotically as $U^{-l}n_{(l)}(\gamma+l)$, or $(2/U)^l y_{(l)}$, as defined in (26); also the right-hand side of (72) varies as $(2/U)^l y_{(l)}\times(g\delta_0/p_0)^{-2l}(2l)!$. For a rational form of $y(x)$, such as $6x(1-x)$ (which we used in our previous work[1,2]) or $(\epsilon+\frac{1}{2})\{(\epsilon+x)(1+\epsilon-x)\ln(1+\epsilon)/\epsilon\}^{-1}$ (which would correspond to a Fermi-type[20] distribution), the factor $y_{(l)}$ is a rational function of l and may be omitted. Then the angular distribution has no singularity, and the radial distribution function, regarded as a function of r^2, has a branch point of the type $\exp(-Br)$, at $r^2=0$. For $y(x)=e^{-\beta x}$, $y_{(l)}$ varies as β^{-l}, so the type of singularity is unchanged, though the value of B is altered. When the numerical values of a limited number (n) of lower moments are available, the most practical procedure is to terminate the series (12) at the $(n-1)$th term and fix B to give correctly the value of the nth moment. (This requires the numerical solution of an algebraic equation of the nth degree.)

We have evaluated the first few moments of both the angular and radial distribution functions relative to the shower axis, given by (71) and (72), together with corrections arising from advanced stages of the iteration procedure. For the power law corresponding to $\gamma=1.1$ and for $C_2=1$ we obtained the results given in Table I, where θ is measured in units of the interaction mean free path. We have used these values to reconstruct the angular and radial distribution functions, but find that, once the weight function has been determined in the manner described above, the series (12) converges so rapidly for small values of the argument that for practical purposes it suffices to consider only the first term. Thus the value of B may be obtained sufficiently accurately from the numerical values of the mean squares. The angular distribution function is

$$\Theta(U,C,\theta/C_2)=2[F^2_{(0,0,0)}/F_{(0,0,1)}]\times\exp\{-2F_{(0,0,0)}(1-C)/F_{(0,0,1)}\},\quad(73)$$

and the radial distribution function is

$$R(U,r,\theta/C_2)=6[F^3_{(0,0,0)}/F_{(2,0,0)}]\times\exp\{-[6F_{(0,0,0)}/F_{(2,0,0)}]^{\frac{1}{2}}r\}.\quad(74)$$

The numerical values of the $F_{(l,m,n)}$ given above are for a spectrum of particles incident vertically at the top of the atmosphere. Actually, the incident angular distribution is almost isotropic. If $\Theta(U,C,\theta)$ is the angular distribution function,

$$\Theta(U,C,\theta)=\int_U^\infty dU\int\int f(U,C,\Psi,r,\theta)rdrd\Psi\quad(75)$$

calculated for an incident power law spectrum, and $C_2=1$, the corresponding distribution function for other values of C_2 is $\Theta(U,C,\theta/C_2)$, where C is still the angle made with the shower axis. If C_1 is the angle which the track of a particle makes with the vertical, one has

$$C_1=CC_2+SS_2\cos\chi,\quad(76)$$

where χ is the polar angle with respect to the shower axis. Thus the $2l$th moment of the angular distribution with respect to the vertical is

$$2^l\int_0^{2\pi}\frac{d\chi}{2\pi}\int_{-1}^1 dC\Theta(U,C,\theta/C_2)\{1-(CC_2+SS_2\cos\chi)\}^l$$

for a shower axis making an angle C_2 with the vertical, and

$$2^l\int_0^1 dC_2\int_0^{2\pi}\frac{d\chi}{2\pi}\int_{-1}^1 dC\Theta(U,C,\theta/C_2)\times\{1-(CC_2+SS_2\cos\chi)\}^l\quad(77)$$

[20] E. Fermi, Phys. Rev. **81**, 683 (1951).

for an incident isotropic distribution. The average number of particles with energy greater than $U>U_c$ at depth θ, averaged over all incident particles, is obtained by setting $l=0$:

$$\int_0^1 F_{(0,0,0)}(U,\theta;C_2)dC_2=\left(\frac{U_c}{U}\right)^\gamma\int_0^1 e^{-h(\gamma)\theta/C_2}dC_2$$
$$\approx\left(\frac{U_c}{U}\right)^\gamma\frac{\exp\{-h(\gamma)\theta\}}{h(\gamma)\theta} \quad (78)$$

for all except small atmospheric depths. Similarly the second moment is

$$\int_0^1\{F_{(0,0,1)}(U,\theta;C_2)+2(1-C_2)F_{(0,0,0)}(U,\theta;C_2)\}dC_2$$

with the omission of a factor $C\approx 1$ in the second term, which reduces to

$$\left(\frac{U_c}{U}\right)^\gamma\int_0^1\left[\frac{2y_{(1)}W(\gamma)}{U\{\alpha(\gamma+1)-\alpha(\gamma)\}}\frac{\gamma}{(\gamma+1)}\right.$$
$$\left.\times\{e^{-h(\gamma)\theta/C_2}-e^{-h(\gamma+1)\theta/C_2}\}+2(1-C_2)e^{-h(\gamma)\theta/C_2}\right]dC_2. \quad (79)$$

The first term does not differ much from

$$\left(\frac{U_c}{U}\right)^\gamma\frac{2y_{(1)}W(\gamma)\gamma}{U\{\alpha(\gamma+1)-\alpha(\gamma)\}(\gamma+1)}\frac{\exp\{-h(\gamma)\theta\}}{h(\gamma)\theta}$$
$$\times\left\{1-\frac{h(\gamma)\exp\{h(\gamma)-h(\gamma+1)\}\theta}{h(\gamma+1)}\right\};$$

since $h(\gamma)/h(\gamma+1)=0.749$, with $\gamma=1.1$, it gives a contribution to the mean square angle very nearly the same as for vertically incident particles at the top of the atmosphere. The second term gives an energy-independent contribution $2\{\theta h(\gamma)\}^{-1}$ to the mean square angle, owing to the persistence of the initial incident distribution.

To obtain the actual radial distribution from that —$R(U,r,\theta)$ say—calculated for $C_2=1$, one replaces r by $r(\cos^2\chi+C_2^2\sin^2\chi)^{\frac{1}{2}}$ and θ by θ/C_2 and integrates over C_2 and χ. The radial moments of this distribution function do not differ radically from those already calculated, owing to the fact that few incident particles inclined at more than a few degrees to the vertical generate showers which penetrate to a great depth in the atmosphere.

VII. DISCUSSION

The angular distribution function, relative to the shower axis, of the nucleon component of the cosmic radiation is given very nearly by

$$\Theta(U,C,\theta/C_2)=F_{(0,0,0)}B_e\exp\{-B_e(1-C)\}, \quad (80)$$

which expresses the differential probability of finding a particle with energy greater than U (measured in Bev) at an angle with the shower axis whose cosine is C; θ is the atmospheric depth in units of the interaction mean free path, and C_2 is the angle made by the shower axis with the vertical. Values of B_e for an integral proton primary power-law spectrum of exponent $\gamma=1.1$, and for $C_2=1$ are given below in terms of the mean square angular deviation $y_{(1)}$ is a nucleon-nucleon collision.

The corresponding radial distribution function is given by

$$R(U,r,\theta/C_2)=F_{(0,0,0)}B_r^2\exp(-B_r r), \quad (81)$$

where r is the normal distance from the shower axis. We find the following values of B_e and B_r:

	$\theta=2$	$\theta=6$	$\theta=13.7$
B_e	$3.26U/y_{(1)}$	$1.53U/y_{(1)}$	$1.15U/y_{(1)}$
B_r	$0.301U^{\frac{1}{2}}/y_{(1)}^{\frac{1}{2}}$	$0.246U^{\frac{1}{2}}/y_{(1)}^{\frac{1}{2}}$	$0.310U^{\frac{1}{2}}/y_{(1)}^{\frac{1}{2}}$.

(82)

We have shown[17,18] that, if the cross section for nucleon-nucleon collisions is a quadratic function of the cosine of the scattering angle, in the center-of-mass system of reference, $y_{(1)}=\frac{1}{2}$; this was assumed in our previous calculation of the mean square values of $\{2(1-C)\}^{\frac{1}{2}}$ and r.[1,2] It will be seen from (82) that the value of B_r varies with the depth and has a minimum value at an atmospheric depth of about 450 g/cm². When B_r has this minimum value, the spread of a shower attains its maximum extent, as we concluded from our evaluation of the mean square distance from the shower axis, referred to above. On the other hand, the large quantitative values for the mean square distance corresponding to $y_{(1)}=\frac{1}{2}$ could be reconciled with the experimental indications[6,12–15] only on the hypothesis that the distribution possessed a long "tail." The function $\exp(-B_r)$ has a tail, but actually one would require a radial dependence at least like $\exp(-B_r'r^{\frac{1}{2}})$ to account numerically for the experimental results. Thus there remained a discrepancy of an order of magnitude affecting the value of $y_{(1)}$ or one of the physical assumptions on which the theory was based.

Setting aside for the moment the assumed form of differential cross section for nucleon-nucleon collisions, the assumptions on which our results are based will now be examined. It has been supposed throughout that the energies of the particles considered are in the ultra-relativistic range, at a lowest estimate greater than 3 Bev. The results for an "atmosphere" of constant density would be very different from those for an isothermal atmosphere which we have obtained. In the isothermal atmosphere, the density decreases exponentially with height; it is the nearest practicable realization of the physical reality.

We have assumed that the exponent γ of the primary power-law spectrum has the value 1.1, and the numerical results depend quite sensitively on this assumption. Indeed, the results can be brought into agreement with experiment, but only by assuming a value as low

as 0.7 for γ. The existing experimental evidence[21] for the very high energies which are important for extensive air showers, however, suggests that, if anything, the value of γ should exceed that which we have assumed. For a given differential cross section, the only way to decrease the mean lateral spread is to increase the number of highly energetic particles throughout the atmosphere; and this conclusion is independent of the type of incident primary spectrum adopted. It is therefore possible, but unlikely, that this particular physical assumption made is the seat of the difficulty, and the reason for the discrepancy must be sought for in the form of cross section adopted.

The results obtained are not much affected by the form of the total cross section $F(U_0, U)$ adopted. They may be improved only by increasing the proportion of energy taken up by the nucleon component at the expense of the mesons. Our choice of $F(U_0, U)$, given in (25), allows, on the average, an energy loss of 33 percent to the meson or mesons in a nucleon-nucleon collision; but even if this loss were completely eliminated, the mean spread would not be sufficiently decreased. Here again, the conclusion is not affected by the functional form, homogeneous or inhomogeneous, of $F(U_0, U)$ adopted. We therefore conclude that the differential cross section adopted previously was at fault.

For relativistic reasons, the particles scattered in a nucleon-nucleon collision must be contained within a cone of semivertical angle $(2U^{-1})^{\frac{1}{2}}$; the particles near the periphery of this cone correspond to backward-scattered particles in the center-of-mass frame of reference, and have low energies in the laboratory frame which contribute little to the propagation of extensive air showers. It is therefore the distribution of particles in the neighborhood of the axis of the cone, i.e., in the forward direction, which is important. Any slowly varying function, such as that adopted by Fermi[20] or ourselves,[17,18] cannot be correct. We therefore arrive at the somewhat surprising conclusion that a cross section of the form $R+S'\cos^2\theta$ in the center-of-mass frame—as predicted by most field theories—cannot be correct and that there must be an exponential decrease in the number of scattered particles from the forward direction. We therefore substitute in (25) the function

$$y\{U(1-C)\}=\beta(1-e^{-\beta})^{-1}\exp\{-\beta U(1-C)\}, \quad (83)$$

which gives

$$y_{(1)}=\beta^{-1}(1-e^{-\beta})^{-1}\int_0^{\beta} e^{-x}x^1dx. \quad (84)$$

To reconcile results with experiment, it is necessary to take $\beta\approx 144$. Then

$$y_{(1)}=\beta^{-1}=1/144. \quad (85)$$

At sea level, this gives a half-value distance of 92 m, for the radial distribution of particles with energy greater than 4 Bev as found by Cocconi.[6] At a distance of 1 km the density is approximately 5×10^{-4} times that at the shower axis, which is in sufficient agreement with the Russian factor of 4×10^{-4}.

Recently the angular distribution of penetrating particles with respect to the shower axis at an atmospheric depth of 700 g/cm^2 has been measured by Branch;[22] the experimental half-value is at $2\frac{1}{2}\pm\frac{1}{2}$ degrees, compared with our calculated value of 2°32′. We conclude that all the experimental data are adequately explained by assuming a cross section of the form (83) with $\beta=144$.

A method for the determination of the absorption mean free path[23,24,25] depends on the measurement of the angular distribution of high energy penetrating particles with the vertical, neglecting the scattering due to any collisions which they may have suffered in their passage through the atmosphere. This amounts to neglecting the first of the two terms in Eq. (79). If the value of β were as small as one might expect *a priori*, this procedure would not be justified. However, with the value of β given by (83), the angular deviation from the shower axis due to scattering is negligible compared with the energy independent angular deviation from the vertical which results from the persistence of the incident distribution at the top of the atmosphere.

The preceding results are for an absorber with varying density. A similar treatment may, however, be applied to an absorber with constant density. We shall in the near future present results in this case as well.

[21] H. V. Neher, *Progress in Cosmic-Ray Physics* (North-Holland Publishing Company, Amsterdam, 1952).

[22] M. Branch, Phys. Rev. **84**, 147 (1951).
[23] W. D. Walker, Phys. Rev. **77**, 686 (1950).
[24] T. G. Stinchcomb, Phys. Rev. **83**, 422 (1951).
[25] M. B. Gottlieb, Phys. Rev. **82**, 349 (1951).

Moments of the Angular Distribution for High Energy Nuclear Collisions

B. A. CHARTRES AND H. MESSEL
University of Adelaide, Adelaide, South Australia

(Received May 16, 1952)

Detailed results for the mean square angle of scattering of nucleons in high energy nucleon-nucleus collisions are presented using the accurate expressions previously determined by Messel and Green. Curves are given both for light and heavy elements. Confirmation of the results presented would provide valuable information on the differential cross section for nucleon-nucleon collisions.

1. INTRODUCTION

DURING a calculation of the angular and radial distribution functions for the nucleon component of the cosmic radiation in the atmosphere, Messel and Green[1-3] were led to consider the problem of determining the angular moments of scattered nucleons in high energy nuclear collisions.

The preliminary results of this calculation were reported in reference 2 and in the first approximation in reference 3. In 2 and 3 a differential cross section for nucleon-nucleon collisions of the form $R+S'\cos^2\bar{\theta}$ in the center-of-mass frame of reference was used, where R and S' were functions of the energy only, and $\bar{\theta}$ the scattering angle in the center-of-mass frame. This form of cross section was taken from the predictions of field theories. Messel and Green[1] have since shown that a differential cross section of this form is incompatible with experimental observations on the radial spread of the nucleon component of the cosmic radiation, and that theory could only be reconciled with experiment when the number of scattered particles decreases exponentially from the direction of motion of the incident nucleon in the laboratory frame. The purpose of this paper is to present results for the mean square angle of scatter of nucleons resulting from high energy nuclear encounters in light and heavy elements, using the accurate expression for the second moment and the new differential cross section taken from 1. These results should prove to be of considerable value in interpreting high energy collisions observed in photographic plate work.

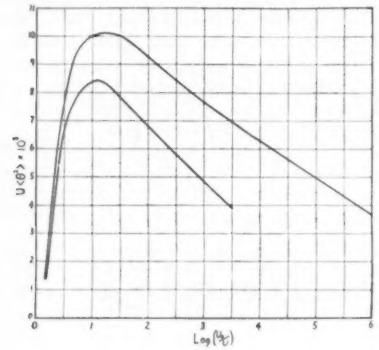

FIG. 1. A plot of $U\langle\theta^2(U_0, U)\rangle\times10^2$ against the logarithm of the ratio of the primary energy U_0 and the energy U above which particles are emitted from a nucleus. The energies are measured in proton mass units. $\langle\theta^2(U_0, U)\rangle$ gives the mean square angle of emission in radians squared of nucleons resulting from a nucleon-nucleus collision. The upper curve is valid for the heavy elements silver and bromine, the lower curve for the light nuclei carbon, oxygen, and nitrogen.

2. FUNDAMENTAL EQUATIONS AND SOLUTIONS

The probability $\nu(U, C, z)dUdC$ of finding a nucleon at a depth z (measured in the direction of motion of the incident particle) in homogeneous nuclear matter, with energy U, dU and direction of motion making an angle of cosine C, dC with that of the incident particle satisfies the integro-differential equation

$$C\frac{\partial\nu}{\partial z}(U, C)+\nu(U, C) = 2\int_U^\infty dU'\int_{c_0}^1 dc\int_0^{2\pi}\frac{d\omega}{2\pi}\nu(U', C')W(U', U, c), \quad (1)$$

$C'=Cc+Ss\cos\omega$, $S=(1-C^2)^{\frac{1}{2}}$, $s=(1-c^2)^{\frac{1}{2}}$, $c_0=1-1/U$,

where

$$W(U_0, U, c)dUdc=UG(U_0, U)y\{U(1-c)\}dUdc \quad (2)$$

is the differential cross section for nucleon-nucleon collisions and

$$y\{U(1-c)\}=144(1-e^{-144})^{-1}\exp\{-144U(1-c)\}, \quad (3)$$

$$G(U_0, U)=20U_0^{-5}U(U_0-U)^3. \quad (4)$$

All energies are measured in proton mass units ($\sim$1 Bev), and U_0 is the primary energy. The nth moment of $W(U_0, U, c)$ is defined by

$$W_{(n)}=2^n\int_{c_0}^1 W(U_0, U, c)(1-c)^n dc = (2/U)^n\int_0^1 G(U_0, U)y(x)x^n dx = (2/U)^n G(U_0, U)y_{(n)}, \quad (5)$$

[1] H. Messel and H. S. Green, Phys. Rev. **87**, 738 (1952).
[2] H. Messel and H. S. Green, Phys. Rev. **83**, 1279 (1951).
[3] H. Messel and H. S. Green, Proc. Phys. Soc. (London) **A65** 245 (1952).

and the lth moment of $\nu(U, C, z)$ by

$$\nu_{(l)}(U, z)=2^l\int_{-1}^{1}(1-C)^l\nu(U, C, z)dC. \quad (6)$$

Using the initial condition,

$$\nu(U, C, z=0)=\delta(U_0-U)\delta(1-C), \quad (7)$$

Messel and Green[1] have shown that the accurate expression for $\nu_{(l)}(U, z)$ is given by

$$U_0\nu_{(l)}(U, z)=(2\pi i)^{-2}\int_{v_0-i\infty}^{v_0+i\infty}dv\int_{p_0-i\infty}^{p_0+i\infty}dp \times(U_0/U)^{v+1}e^{pz}4^l(l!)^2A_v^l, \quad (8)$$

where

$$A_v^l=U_0^{-l}\{p+\alpha(v-l)\}^{-l} \times\sum{}'\prod_{i=1}^{l}\alpha^{a_i}{}_{v-(a_1+\cdots+a_{i-1})}, \quad (9)$$

$$\alpha_v^l=y_{(l)}W(v-l)2^{-l}(l!)^{-2}\{p+\alpha(v)\}^{-1}, l=1, 2, \text{etc.}$$

$$\alpha(v)=1-240\{(v+2)(v+3)(v+4)(v+5)\}^{-1}, \quad (10)$$

$$W(v)=1-\alpha(v). \quad (11)$$

The summation $\sum'$ in (9) is applied to all different products for which $a_1+a_2+\cdots+a_l=l$. The a's may take the positive integral values, including zero and $\alpha^0=1$.

The distribution of particles emitted by a nucleus may be obtained from $\nu(U, C, z)$ by applying the averaging operator $\mathbf{N}(D_A)=\int_0^{D_A}2zdz/D_A{}^2$ to it. D_A is the average number of collisions suffered by a nucleon on making a diametrical passage through a nucleus of atomic weight A. Thus

$$n(U, C)=\mathbf{N}(D_A)\nu(U, C, z), \quad (12)$$

and the lth moments of this nuclear distribution function are given in

$$n_{(l)}(U)=\mathbf{N}(D_A)\nu_{(l)}(U, z). \quad (13)$$

If we consider only those emitted particles whose energies are in excess of U, we have

$$N(U, C)=\int_{U}^{U_0}n(U', C)dU', \quad (14)$$

and for the lth moments of $N(U, C)$,

$$N_{(l)}(U)=\mathbf{N}(D_A)(2\pi i)^{-2}\int_{v_0-i\infty}^{v_0+i\infty}dv/v\int_{p_0-i\infty}^{p_0+1\infty}dp \times(U_0/U)^ve^{pz}4^l(l!)^2A_v^l. \quad (15)$$

3. RESULTS

The mean square angle of scatter of nucleons with energies $>U$, resulting from a nucleon-nucleus collision, is given by

$$\langle\theta^2\rangle=N_{(1)}(U)/N_{(0)}(U), \quad (16)$$

where, from (15),

$$N_{(0)}(U)=(2\pi i)^{-1}\int_{v_0-i\infty}^{v_0+i\infty}(U_0/U)^v\{1-h(v)\}dv/v, \quad (17)$$

$$N_{(1)}(U)=(2\pi iU_0)^{-1}\int_{v_0-i\infty}^{v_0+i\infty}(U_0/U)^v2y_{(1)}W(v-1) \times\{\alpha(v)-\alpha(v-1)\}^{-1}\{h(v)-h(v-1)\}dv/v, \quad (18)$$

and

$$h(v)=1-2[1-\{1+D_A\alpha(v)\}\exp\{-D_A\alpha(v)\}] \times\{D_A\alpha(v)\}^{-2}. \quad (19)$$

In Fig. 1 we have given the results of a calculation for $\langle\theta^2\rangle$ defined by (16). The values of $U\langle\theta^2\rangle$ for the light elements carbon, nitrogen, and oxygen ($D_A=3.7$) and the heavy elements silver and bromine ($D_A=6.8$) are plotted against $\log(U_0/U)$. The qualitative behavior of the curves is similar to that already discussed in reference 2. Quantitatively, however, there is little similarity in the values obtained, the values of $\langle\theta^2\rangle$ are now smaller by an order of magnitude than those previously obtained.

It should be pointed out that the values of $\langle\theta^2\rangle$ are independent of the theory of meson production employed for nucleon-nucleon collisions. They are equally valid on the plural and multiple hypotheses of meson production. If, however, one assumes that the mesons are produced according to the plural theory, then the values of $\langle\theta^2\rangle$ for mesons would be very close to those we have given for the nucleons.

Messel and Green[1] have pointed out that the differential cross section given by (2), (3), and (4) is quite different from what had hitherto been expected. It imposes upon the scattering angle a condition more stringent than that obtained from relativistic transformations. Strong support for their conclusions is given by the recent results of Branch,[4] who found during an experiment on the angular distribution of penetrating particles, with respect to the shower axis, a mean angle of only 2½ degrees. Further quantitative experimental verification of our results would therefore provide very valuable confirmation of the differential cross section and at the same time allow these results to be used with confidence in interpreting high energy nuclear phenomena.

[4] G. M. Branch, Phys. Rev. **84**, 147 (1951).

Radiative Correction to the Angular Distribution of Nuclear Recoils from Electron Scattering*

L. I. SCHIFF
Stanford University, Stanford, California
(Received May 23, 1952)

A calculation is made of the cross section for the recoil of nuclei from electron scattering when the angle of recoil is specified but the recoil energy is not. The influence of radiation is taken into account. Use is made of the calculation by Drell in the following paper to gauge the accuracy of the computed cross section for light nuclei; the fractional error is believed to be substantially smaller than the ratio of the recoil nucleus velocity to the velocity of light.

EXPERIMENTS on the scattering of high energy electrons from nuclei can provide information from which the distribution of electric charge within the nuclei can be determined. The interpretation of such experimental data is simplest when a separation into elastic and inelastic (radiative) processes can be made. This is the case, for example, when the experiment is performed by measuring the distribution of the recoil nuclei with respect to angle and energy. In a particular experimental arrangement now being employed in this laboratory,[1] the recoil nuclei are to be recorded by a photographic emulsion. It is then convenient to measure the angle of each nuclear recoil; however, it is difficult to get reasonable statistics on the distribution of recoil energies, except that to be measured they must exceed a minimum value that is determined by the geometrical arrangement of the emulsions and their wrappings. The theoretical results on elastic electron-nuclear scattering can be compared with such experimental data only if a correction is applied that takes into account the emission of photons.

This paper presents an estimate of the radiative correction that is required. The following three approximations are made:

(1) The Bethe-Heitler differential bremsstrahlung cross section[2] is used as the starting point (Born approximation).

(2) The dominant contribution to the bremsstrahlung cross section arises from events in which both the scattered electron and the photon emerge within an angle of order mc^2/E_0 of the incident electron direction, where m is the electron mass and E_0 its initial energy. But in order for the recoil nucleus to be observed as such, its momentum must be large in comparison with mc (about 100 times as large for a proton that recoils with 1.5-Mev kinetic energy).[3] Thus, either the scattered electron or the photon, or both, must make an angle with the incident electron direction that is large in comparison with mc^2/E_0, for those processes of interest here. This means that screening of the nucleus by atomic electrons can be ignored; on the other hand, the nuclear form factor is important, and information concerning the nuclear charge distribution can be obtained from such an experiment. An important simplification in carrying through the integrations over photon energy and angle can then be achieved by noticing that in such cases the photon has a marked tendency to emerge with direction close to that of either the incident electron or the scattered electron. This makes it easy to find the leading term in the radiative correction, which is in error only by a factor in a logarithm. This factor can then be determined by "calibrating" the resulting formula against Schwinger's expression for nearly elastic scattering with emission of very low energy photons.[4]

(3) The effect of the finite recoil velocity of the nucleus on the cross section is neglected. Thus, what is found is the momentum distribution of the recoil nuclei under the assumption that they are infinitely massive. In the following paper, Drell[5] calculates the effect of nuclear recoil on the bremsstrahlung cross section through terms of first order in the recoil velocity. This calculation shows that the tendency of the photon to emerge in line with the incident or the scattered electron is not nearly as marked in the correction terms as in the Bethe-Heitler formula. Because of this, only the argument, and not the coefficient, of the logarithm mentioned in the preceding paragraph is affected. Unfortunately, this uncertainty cannot be "calibrated" out, since Schwinger's formula[4] also fails to take account of recoil.

The Bethe-Heitler differential bremsstrahlung cross section is[2]

$$\frac{Z^2e^4}{2\pi 137}\frac{dk}{k}\frac{p}{p_0}\frac{\sin\theta_0 d\theta_0 \sin\theta d\theta d\phi}{q^4}$$
$$\times\left\{\frac{p_0^2\sin^2\theta_0(4E^2-q^2)}{(E_0-p_0\cos\theta_0)^2}+\frac{p^2\sin^2\theta(4E_0^2-q^2)}{(E-p\cos\theta)^2}\right.$$
$$-\frac{2p_0p\sin\theta_0\sin\theta\cos\phi(4E_0E-q^2+2k^2)}{(E_0-p_0\cos\theta_0)(E-p\cos\theta)}$$
$$\left.+\frac{2k^2(p_0^2\sin^2\theta_0+p^2\sin^2\theta)}{(E_0-p_0\cos\theta_0)(E-p\cos\theta)}\right\}, \quad (1)$$

* Assisted by the joint program of ONR and AEC.

[1] Private communication from W. K. H. Panofsky.

[2] W. Heitler, *The Quantum Theory of Radiation* (Oxford University Press, London, 1944), second edition, p. 164.

[3] For this reason, the numerical results of Jost, Luttinger, and Slotnick, Phys. Rev. **80**, 189 (1950), on nuclear recoils from pair production are not useful in the present connection.

[4] J. Schwinger, Phys. Rev. **75**, 899 (1949).

[5] S. D. Drell, following article, Phys. Rev. **87**, 753 (1952).

where E_0, p_0 are the energy and momentum (expressed in energy units) of the incident electron, E, p those of the scattered electron, k the energy of the emitted photon, θ_0 the angle between photon and incident electron, θ the angle between photon and scattered electron, ϕ the angle between the planes in which θ_0 and θ lie, and q is the momentum (expressed in energy units) transferred to the nucleus of charge Ze. If the nucleus has a finite size, Eq. (1) and all the other expression for cross sections given below must be multiplied by a nuclear form factor that is a function of q. The momentum transfer is given by

$$q^2=p_0^2+p^2+k^2-2p_0k\cos\theta_0+2pk\cos\theta -2p_0p(\cos\theta_0\cos\theta+\sin\theta_0\sin\theta\cos\phi).$$

In principle, we wish to integrate Eq. (1) over all the domains of the four variables θ_0, θ, ϕ, and k except for that one combination that corresponds to a particular value of the angle between the momentum transfer vector and the incident electron direction. In practice, we notice that since we are only interested in the case $q\gg\mu\equiv mc^2$, the differential cross section is largest when one or the other of the quantities $(E_0-p_0\cos\theta)$, $(E-p\cos\theta)$ is small, that is, when either θ_0 or θ is small; they cannot both be small at once since then q would also be small. The approximation is then made of selecting just two regions from the whole domain of multiple integration and neglecting the rest. In one of these, θ_0 is assumed to be small, and the integration is carried over it with all other variables taking the values they would have if θ_0 were zero; in the other, θ is substituted for θ_0, and the same procedure is followed. The leading terms contain multiplicative factors of order $\ln(E_0/\mu)$ or $\ln(E/\mu)$, and only these terms are retained (extreme relativistic region). Since some of the neglected terms would alter the arguments of the logarithms, no attempt is made to obtain this logarithmic factor correctly. Instead, the quantity $\ln(E_0/\mu)$ is used symbolically to denote the result of any integration that would diverge logarithmically if μ were made to vanish, and an estimate of its value is made later. The integration over k extends down to some minimum value k_m, which also appears as the maximum photon energy in the correction owing to radiation of very low energy photons.[4] Finally, the experimental arrangement is such that q must exceed a minimum value q_m, which is assumed here to be independent of recoil angle, although this is not an important restriction.

Inspection of Eq. (1) shows that the leading terms arise from integration of the first term in curly brackets for small θ_0, the second term for small θ, and the first and second parts of the fourth term for small θ and θ_0, respectively. For the small θ_0 contributions, we can put $q\cong 2E\sin\frac{1}{2}\theta$ and $\gamma\cong\frac{1}{2}(\pi-\theta)$, where γ is the nuclear recoil angle. For the small θ contributions, we can put $q\cong 2E_0\sin\frac{1}{2}\theta_0$ and $\gamma\cong\frac{1}{2}(\pi-\theta_0)$. Integration over θ_0 and ϕ of those terms that are important for small θ_0 yields

$$\frac{Z^2e^4}{137}\frac{dk}{k}\frac{E}{E_0}\frac{\sin\theta d\theta}{q^4}\left\{4(4E^2-q^2)+\frac{4k^2E\sin^2\theta}{E_0(1-\cos\theta)}\right\}\ln\left(\frac{E_0}{\mu}\right) =\frac{2Z^2e^4}{137}\frac{dk}{k}\tan^3\gamma d\gamma\left(\frac{E_0^2+E^2}{E_0^2E^2}\right)\ln\left(\frac{E_0}{\mu}\right), \quad (2)$$

where γ has been substituted for θ and q, and μ has been neglected everywhere except in the logarithm. Similarly, integration over θ and ϕ of those terms that are important for small θ yields

$$\frac{2Z^2e^4}{137}\frac{dk}{k}\tan^3\gamma d\gamma\left(\frac{E_0^2+E^2}{E_0^4}\right)\ln\left(\frac{E_0}{\mu}\right). \quad (3)$$

Since q must be greater than q_m, Eq. (2) is valid only for $\gamma<\gamma_m$, where $\cos\gamma_m=q_m/2E=q_m/2(E_0-k)$, and Eq. (3) is valid only for $\gamma<\gamma_m$, where now $\cos\gamma_m=q_m/2E_0$.

The integration of Eq. (2) over k extends from k_m only up to $E_0-(q_m/2\cos\gamma)$, since for larger values of k, q is less than q_m. Equation (3) is to be integrated over k from k_m to E_0. The result from Eq. (2) is

$$\frac{2Z^2e^4}{137}\ln\left(\frac{E_0}{\mu}\right)\tan^3\gamma d\gamma\left\{2\ln\left(\frac{E_0}{k_m}\right) +\ln\left(x+\frac{1}{x}-2\right)+x-1\right\}, \quad x\equiv 2E_0\cos\gamma/q_m,$$

where terms that vanish as k_m becomes zero are neglected. Similarly, from Eq. (3) we get

$$\frac{2Z^2e^4}{137}\ln\left(\frac{E_0}{\mu}\right)\tan^3\gamma d\gamma\left\{2\ln\left(\frac{E_0}{k_m}\right)-\tfrac{3}{2}\right\}.$$

The sum of these represents the cross section for scattering in which the nucleus recoils into $d\gamma$ and a photon of energy greater than k_m is emitted:

$$\frac{8Z^2e^4}{137}\ln\left(\frac{E_0}{\mu}\right)\tan^3\gamma d\gamma\left\{\ln\left(\frac{E_0}{k_m}\right) +\tfrac{1}{4}\ln\left(x+\frac{1}{x}-2\right)+\frac{x}{4}-\tfrac{3}{8}\right\}. \quad (4)$$

In the same notation, the Mott-Rutherford formula for elastic Coulomb scattering is[6]

$$(2\pi Z^2e^4/E_0^2)\tan^3\gamma d\gamma. \quad (5)$$

The correction to this, owing to emission of very low energy photons, consists in multiplication by the factor

[6] N. F. Mott and H. S. W. Massey, *The Theory of Atomic Collisions* (Oxford University Press, London, 1949), second edition, p. 80.

TABLE I. Fractional radiative correction Δ to the Mott-Rutherford formula.

E_0 (Mev)	γ	$-\delta$ (%)	Eq. (4)/Eq. (5) (%)	Δ (%)
100	0°	−10.7	18.4	7.7
100	45°	− 9.7	15.0	5.3
200	0°	−11.9	27.9	16.0
200	45°	−10.9	17.7	6.8

$(1-\delta)$, where[4]

$$\delta=\frac{4}{137\pi}\left\{\left[\ln\left(\frac{2E_0\cos\gamma}{\mu}\right)-\tfrac{1}{2}\right]\left[\ln\left(\frac{E_0}{k_m}\right)-\frac{13}{12}\right]+\frac{17}{72}+\phi(\pi-2\gamma)\right\}. \quad (6)$$

Here the function $\phi(\theta)$ is given by Eqs. (10) and (11) of reference 4; for $\gamma=0$, $\phi(\pi)=\pi^2/24$, and for $\gamma=\pi/4$, $\phi(\pi/2)=0.292$. The fractional correction to the Mott-Rutherford formula, owing to emission of both low and high energy photons, should now be Eq. (4) divided by Eq. (5), minus δ as given by Eq. (6). When this combination is formed, the quantity k_m, which is an artificial boundary between the very low energy photons and those of higher energy, should cancel out. It is apparent that this cancellation occurs if the symbolic factor $\ln(E_0/\mu)$ in Eq. (4) is set equal to $\{\ln[(2E_0\cos\gamma)/\mu]-\frac{1}{2}\}$, and this is a plausible substitution to make. We therefore adopt this "calibration" factor and obtain finally for the fractional radiative correction to the Mott-Rutherford formula

$$\Delta=\frac{4}{137\pi}\left\{\left[\ln\left(\frac{2E_0\cos\gamma}{\mu}\right)-\tfrac{1}{2}\right]\times\left[\tfrac{1}{4}\ln\left(x+\frac{1}{x}-2\right)+\frac{x}{4}+\frac{11}{24}\right]-\frac{17}{72}-\phi(\pi-2\gamma)\right\},$$

$$x\equiv 2E_0\cos\gamma/q_m. \quad (7)$$

For heavy nuclei, the most important approximation made in this calculation is the use of the Born approximation, and little can be done about that at the present time.[7] For light nuclei, the most important approximation is the third of those mentioned near the beginning of this paper. Now Drell's calculation[5] shows that the recoil corrections are of order β times those terms in Eq. (1) that are neglected in arriving at the first logarithm in Eq. (4), where β is the ratio of the recoil nucleus velocity to the velocity of light. This means that the error in Eq. (4) itself is substantially smaller than β. On the other hand, Rosenbluth[5] has shown that the recoil correction to the Mott-Rutherford formula (5) is of order β. Thus, if we assume, as appears reasonable, that the Schwinger correction to the cross section [product of Eqs. (5) and (6)] has the same accuracy as Eq. (4), then the net radiative correction to the cross section [product of Eqs. (5) and (7)] should also have the same superior accuracy as Eq. (4). This means that the net radiative correction to the cross section may be added to Rosenbluth's elastic scattering cross section to obtain a result that can be compared with the experimental cross section. The comparison will be expected to yield a nuclear form factor that is in error by a factor considerably smaller than β.

In order to get an idea of the order of magnitude of the radiative correction factor, values of Δ (in percent) are given in Table I for four combinations of values of E_0 and γ, with $q_m=100\ mc^2$, which corresponds to a proton recoiling with a minimum of 1.5 Mev kinetic energy. The table also lists the breakdown of the Δ values into $-\delta$ and the ratio of Eq. (4) to Eq. (5), when k_m is arbitrarily chosen to be $E_0/20$; the values of Δ given by Eq. (7) are, of course, independent of the choice of k_m. As might be expected, the emission of all photons makes the observed cross section in each case larger than would be calculated on the basis of elastic scattering.

The correlation of the emitted photon direction with that of either the incident or the scattered electron when the momentum transfer is large might be subject to direct experimental verification. The analogous result in pair production by gamma-rays is that either the electron or the positron tends to emerge close to the direction of the incident photon when the momentum transfer is large.

[7] *Note added in proof:*—Recent calculations of L. C. Maximon and H. A. Bethe [Phys. Rev. (to be published)] extend Eq. (1) beyond the Born approximation.

[5] M. N. Rosenbluth, Phys. Rev. **79**, 615 (1950).

Recoil Correction to Bremsstrahlung Cross Section*

S. D. DRELL
Stanford University, Stanford, California
(Received May 23, 1952)

A correction to the Bethe-Heitler differential cross section for bremsstrahlung (or pair production) due to the recoil of the source of the Coulomb field (proton) is derived. Terms of order v/c, where v is the recoil velocity of the scattering center, are studied. They are shown not to contribute in the analysis of electron-proton scattering given by Schiff in the preceding paper.

I. DISCUSSION AND RESULTS

BETHE and Heitler[1] have calculated differential and total cross sections for the emission of bremsstrahlung by an electron scattered in a static Coulomb field. They have also obtained formulas for the closely related process of pair production by a gamma-ray in a static Coulomb field.

This paper derives a correction to the Bethe-Heitler differential cross sections due to the recoil of the source of the Coulomb field (proton) during the interaction. The recoil terms are reduced relative to the leading terms of the B-H formulas by a factor $q/Mc \cong v/c$, where c is the velocity of light, and M, q, and v are, respectively, the mass, recoil momentum, and recoil velocity of the scattering center. Thus, the recoil correction may be appreciable in the case of radiative scattering of energetic electrons by protons.[2]

This calculation is motivated by an experiment of Panofsky[3] now in progress at Stanford and by an analysis of this experiment given by Schiff in the preceding paper.[4] In this experiment electrons of several hundred Mev energy are scattered, and the recoil protons are detected with photographic plates. The sum of the nonradiative (elastic) and radiative electron-proton scattering cross sections is measured as a function of the recoil proton angular distribution for proton recoils of all energies greater then a minimum value that we take here to be 1.5 Mev.[5] Lower energy recoils are not detected, so that the experiment discriminates in favor of high momentum proton recoils ($>100\ mc$).

Large momentum transfer to the recoil proton requires the scattered electron or the photon, or both, to make an angle with the direction of the incident electron that is large compared with mc^2/E_0, where E_0 is the initial electron energy. Then, as pointed out in S, the photon exhibits a strong preference to emerge in the direction of either the incident or scattered electron. Utilizing the strong directional correlation of the photon to simplify the formulas, Schiff has integrated the B-H differential bremsstrahlung cross section to obtain a correction to the Mott-Rutherford[6] formula for elastic Coulomb scattering. Joining this result with the Schwinger[7] correction (for the emission of soft quanta and the reactive effect of virtual quanta), he thereby obtains a fractional radiative correction to the Mott-Rutherford formula [See Eq. (7) of S]. For incident electrons of 200 Mev and for proton recoils at 45° with the incident direction, the fractional increase of the Mott-Rutherford formula amounts to[4] 6.8 percent. This breaks down into larger individual corrections of $+17.7$ percent for emission of quanta with energy greater than 10 Mev, and of -10.9 percent for softer and virtual quanta.

We are thus motivated to investigate recoil corrections. Both the B-H formula, which serves as the starting point for Schiff's calculation, and the Schwinger correction are derived for an electron scattered in a static Coulomb potential. The Mott-Rutherford cross section for scattering of electrons of energy E_0 through an angle θ in the Coulomb field of charge Ze is

$$\sigma d\Omega = (Ze^2/2E_0)^2 \cot^2\tfrac{1}{2}\theta \csc^2\tfrac{1}{2}\theta d\Omega. \quad (1)$$

To order $E_0/M(<1)$, this cross section is reduced by a factor

$$(1-2(E_0/M)\sin^2\tfrac{1}{2}\theta), \quad (2)$$

if the proton recoil is included in the calculation of electron-proton elastic scattering.[8] For large momentum transfer (large angle scattering) the above recoil factor amounts to an appreciable reduction in the differential cross section ($\sim$20 percent for $E_0=200$ Mev).

We here study the analogous recoil correction to the B-H formula. A complete investigation of the elastic plus radiative electron-proton scattering cross section requires calculation of the recoil correction to the Schwinger formula also. We do not perform that calculation in this work. The motivation to consider

* Assisted by the joint program of the ONR and the AEC.

[1] H. Bethe and W. Heitler, Proc. Roy. Soc. (London) **146**, 83 (1934), referred to here as B-H. See W. Heitler, *The Quantum Theory of Radiation* (Oxford University Press, London, 1944), second edition, page 161, for further discussion and for references to earlier literature.

[2] We confine remarks here to the bremsstrahlung process. For application to pair production by high energy gamma-rays one need only transcribe the notation in the manner explicitly given on page 196 of Heitler's book (reference 1).

[3] Private communication from W. K. H. Panofsky.

[4] L. I. Schiff, preceding article, Phys. Rev. **87**, 750 (1952), referred to here as S.

[5] Energy analysis of the recoil proton tracks would require more labor for reasonable statistics than is now feasible.

[6] N. F. Mott and H. S. W. Massey, *The Theory of Atomic Collisions* (Oxford University Press, London, 1949), second edition, p. 80.

[7] J. Schwinger, Phys. Rev. **75**, 899 (1949).

[8] M. N. Rosenbluth, Phys. Rev. **79**, 615 (1950).

the bremsstrahlung recoil correction primarily and separately is twofold: (1) As seen in S, the radiative is the larger of the two correction terms to the Mott-Rutherford formula, and therefore, a recoil correction to it is expected to be, percentage-wise, more significant in the final result. (2) The matrix elements are of order e^3 for the radiative process, whereas, for the Schwinger correction, they are of order e^4, and correspondingly more difficult to calculate.

To summarize briefly the results of this work, we derive a correction of order (q/Mc) to the B-H differential cross section for bremsstralung in electron-proton scattering. As in Rosenbluth's work,[8,9] magnetic moment contributions to the cross section are reduced in the order of $(q/Mc)^2$. Correction terms of order (q/Mc) result from both dynamical and kinematical considerations. The two Feynman graphs in Fig. 1 represent emission of the bremsstralung gamma-ray by the electron before and after scattering. In the limit of infinite proton mass, these graphs yield the B-H cross section. Terms of order (q/Mc) resulting from these two graphs will be seen in the following to result solely from the kinematical equations of momentum and energy conservation. That is, to order (q/Mc), the proton and electron interact only through their static Coulomb fields, for the processes depicted in Fig. 1. In calculating the analogous two Feynman graphs for proton emission of the bremsstrahlung gamma-ray (Fig. 2), we directly use the kinematics for $M\to\infty$. This is because the matrix element for proton emission of the gamma-ray is reduced in the order (q/Mc) compared with the corresponding matrix element for electron emission of the gamma-ray. Contributions from these graphs of Fig. 2 comprise the dynamical correction to the B-H formula.

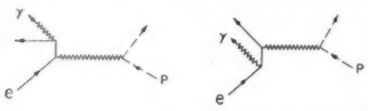

FIG. 1. Diagrams for the inelastic scattering of an electron and a proton with emission of the bremsstrahlung photon by the electron.

In developing the recoil correction to S we use only the dynamical correction to the B-H formula. The kinematical conservation equations for scattering in a fixed Coulomb field must be used in joining the formulas given here with the Schwinger formula,[7] which has been derived for infinitely massive nuclei. The final results obtained here support the qualitative validity of the no recoil analysis given in S. This may be understood as follows. It is shown in S that the photon is emitted within an angle $\sim mc^2/E_0$ of the incident or scattered electron direction. The terms of order (q/Mc), given below, that arise because of the dynamical part of the recoil contribution, correlate the electron and photon directions much less strongly and are effectively masked by the peaked distribution obtained by Schiff.

II. CALCULATION

Calculation of the matrix elements is "straightforward but tedious." The Feynman-Dyson methods are used. We exhibit here just the square of the matrix element to order (q/Mc), summed over final electron spin and photon polarization, and averaged over initial spin. Choosing the proton to be initially at rest in the laboratory frame, and with the notation

$\hbar=c=1$;
$\mathbf{k}$, k = emitted photon momentum, energy;
$\mathbf{p}_0$, E_0 = initial electron momentum, energy;
$\mathbf{p}$, E = scattered electron momentum, energy;
$\mathbf{q}=\mathbf{p}_0-\mathbf{p}-\mathbf{k}$ = momentum transferred to the proton;
Ze = proton charge;

we obtain

$$\langle|\text{M.E.}|^2\rangle_{\text{Av}}=(2\pi)^4(Z^2e^6/k^3E_0E)\left[\frac{1}{q^4}\left\{\frac{(\mathbf{k}\times\mathbf{p})^2}{(kE-\mathbf{k}\cdot\mathbf{p})^2}[4E_0^2-q^2(1+2E_0/M)]+\frac{(\mathbf{k}\times\mathbf{p}_0)^2}{(kE_0-\mathbf{k}\cdot\mathbf{p}_0)^2}[4E^2-q^2(1-2E/M)]\right.\right.$$
$$\left.+2\frac{k^2(\mathbf{k}\times\mathbf{p})^2+k^2(\mathbf{k}\times\mathbf{p}_0)^2-(4E_0E+2k^2-q^2\{1-k/M\})\mathbf{k}\times\mathbf{p}\cdot\mathbf{k}\times\mathbf{p}_0}{(kE-\mathbf{k}\cdot\mathbf{p})(kE_0-\mathbf{k}\cdot\mathbf{p}_0)}\right\}$$
$$-\frac{2Z}{Mkq^2[(\mathbf{p}-\mathbf{p}_0)^2-k^2]}\left\{\mathbf{k}\times\mathbf{q}\cdot\mathbf{k}\times\mathbf{p}_0\left(1-\frac{2EE_0-kE+2m^2+2\mathbf{p}\cdot\mathbf{p}_0-\mathbf{k}\cdot\mathbf{p}}{(kE_0-\mathbf{k}\cdot\mathbf{p}_0)}\right)\right.$$
$$+\mathbf{k}\times\mathbf{q}\cdot\mathbf{k}\times\mathbf{p}\left(1+\frac{2EE_0+kE_0+2m^2+2\mathbf{p}_0\cdot\mathbf{p}+\mathbf{k}\cdot\mathbf{p}_0}{(kE-\mathbf{k}\cdot\mathbf{p})}\right)$$
$$-\frac{2k}{(kE_0-\mathbf{k}\cdot\mathbf{p}_0)}(2E(m^2k^2-EE_0k^2+\mathbf{k}\cdot\mathbf{p}\mathbf{k}\cdot\mathbf{p}_0)-(k^2E_0\mathbf{p}\cdot\mathbf{q}-E\mathbf{k}\cdot\mathbf{p}_0\mathbf{k}\cdot\mathbf{q}))$$
$$\left.\left.+\frac{2k}{(kE-\mathbf{k}\cdot\mathbf{p})}(2E_0(m^2k^2-E_0Ek^2+\mathbf{k}\cdot\mathbf{p}_0\mathbf{k}\cdot\mathbf{p})+(k^2E\mathbf{p}_0\cdot\mathbf{q}-E_0\mathbf{k}\cdot\mathbf{p}\mathbf{k}\cdot\mathbf{q}))\right\}\right]. \quad (3)$$

[9] Use of Pauli terms to represent the anomalous magnetic moment of the proton seems justified on the basis of Rosenbluth's calculation (reference 8) for not too high bombarding energies (~200 Mev).

Formula (3) is seen to reduce directly to the B-H formula[1] for $M\to\infty$. The terms of order E/M, E_0/M and k/M in the first bracket comprise the kinematical correction due to recoil; the dynamical correction is contained in the second bracket. After this calculation was performed, a paper by Rzewuski[10] which contains part of formula (3) was discovered. Rzewuski considers the instantaneous Coulomb interaction between two Dirac electrons and calculates a cross section for their radiative collision with neglect of exclusion principle interference effects. His result contains the kinematical corrections to the B-H formula plus a dynamical correction resulting from the nonretarded part of the particles' interaction. To order (q/Mc), it differs from formula (3) above in two respects: (1) The energy denominator $[(\mathbf{p}-\mathbf{p}_0)^2-k^2]$ for the second set of terms appears without the retardation correction as $(\mathbf{p}-\mathbf{p}_0)^2$. (2) The last two lines of Eq. (3), expressing the possibility for proton pair formation in the intermediate (virtual) state, are not present. It is of interest to speculate that these last two terms might give definite information concerning existence of the negative proton at some future date when precision coincidence experiments on high energy electron-proton bremsstrahlung (or high energy pair production in the field of a proton) become feasible.

In order to convert Eq. (3) to a cross section we need to calculate the transition rate and divide by the incident electron flux. The result is

$$d\sigma=2\pi(E_0/p_0)\langle|\,\text{M.E.}\,|^2\rangle_{\text{Av}}\rho_f,$$

where ρ_f denotes the final state sum for the three outgoing particles—the recoil proton, the scattered electron, and the bremsstrahlung photon. It is given by $d^3k d^3p d^3q$, where four of these nine dimensions are collapsed by the four relations of energy-momentum conservation:

$$\mathbf{p}_0=\mathbf{p}+\mathbf{q}+\mathbf{k},$$
$$E_{p0}=E_p+(q^2/2M)+k.$$

The density ρ_f may be expressed in variables appropriate to the experimental situation considered. In terms of recoil proton variables and the photon angular distribution, we have, for example,

$$\rho f=k^2E_p q^2 dq d\Omega_k d\Omega_q/(kE_p-\mathbf{k}\cdot\mathbf{p}).$$

We consider now the contribution of the dynamical correction to the B-H formula [second set of terms in Eq. (3)] to the calculation given in S. It is simply verified by direct computation[11] that these correction terms do not correlate the direction of the emitted photon very strongly with the direction of the incident or scattered electron. Thus, in the last line of Eq. (3) the multiplier of $1/(kE-\mathbf{k}\cdot\mathbf{p})\approx 2/kp\theta^2$, according to Schiff's approximation in the limit $\theta\to 0$ (i.e., for the photon emitted in the direction of the scattered electron), vanishes with θ. To leading order, therefore, these recoil terms do not contribute.

To conclude, we calculate a leading order recoil correction to the Bethe-Heitler differential cross section for bremsstrahlung.[2] This correction does not contribute in the analysis of electron-proton scattering (elastic and radiative) given in the preceding paper by Schiff.[4]

FIG. 2. Diagrams for the inelastic scattering of an electron and a proton with emission of the bremsstrahlung photon by the proton.

[10] J. Rzewuski, Acta Phys. Polon. **IX**, 121 (1947–48).

[11] The kinematics for $M\to\infty$ are used since the magnitude of the correction terms is already reduced by the factor (q/Mc).

Gamma-Neutron Reactions in Fluorine

R. J. Horsley, R. N. H. Haslam, and H. E. Johns
Department of Physics, University of Saskatchewan, Saskatoon, Saskatchewan, Canada
(Received May 26, 1952)

The cross-sectional curves for the reactions $F^{19}(\gamma, n)F^{18}$ and $F^{19}(\gamma, 2n)F^{17}$ have been determined by measurement of the induced positron activities. The (γ, n) cross-sectional curve rises almost vertically from the threshold to a value of about 2 mb, remains constant for about 3 Mev, and then increases again to a maximum value of 3.48 mb at 20 Mev. The $(\gamma, 2n)$ cross-sectional curve has a peak value of 0.66 mb at about 26 Mev. The integrated cross sections for the (γ, n) and $(\gamma, 2n)$ reactions are 0.039 and 0.0024 Mev-barns, respectively. However, the $(\gamma, 2n)$ reaction is evaluated only up to its peak position at 26 Mev. A new value of 60 ± 1 seconds is reported for the F^{17} activity.

INTRODUCTION

As part of a general program of measuring the photonuclear reactions in elements of low atomic number, the cross sections for the two reactions $F^{19}(\gamma, n)F^{18}$ and $F^{19}(\gamma, 2n)F^{17}$ have been measured as functions of photon energy by detecting the residual position activities in F^{18} and F^{17}. This latter reaction is the first $(\gamma, 2n)$ cross-sectional curve determined in this laboratory using the photon difference method.[1]

EXPERIMENTAL PROCEDURE

For the reaction $F^{19}(\gamma, n)F^{18}$, the experimental procedure was similar to that previously reported.[2,3] One-gram samples of LiF powder were radiated in a small cadmium thimble which approximated in size the sensitive volume of a Victoreen 100 r chamber. The dose was monitored by a Victoreen 100 r chamber placed in the center of a 8-cm cube of Lucite. The cadmium thimble filled with LiF powder was radiated in this same position. The 112-minute F^{18} activity was then counted in a fixed geometry. A delay of about 15 minutes was allowed between the end of irradiation and the start of counting to allow the short-lived activities to die away. Although the LiF powder was reagent grade, a 2-minute activity was detected which was attributed to the presence of oxygen as an impurity.

For the reaction $F^{19}(\gamma, 2n)F^{17}$, the procedure was changed. The two-minute activity mentioned above made it impossible to use this same material to measure the shorter-lived F^{17} positron activity. Pure LiF crystals 2 cm×2 cm×2 mm were used in which no interfering activity was observed. The $F^{19}(\gamma, n)F^{18}$ activity was used to monitor the $F^{19}(\gamma, 2n)F^{17}$ reaction similar

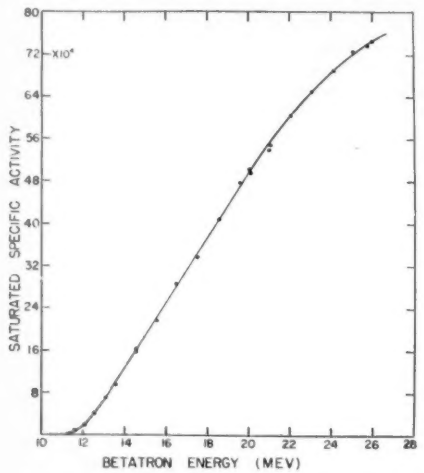

FIG. 1. Saturated specific activity in disintegrations per gram per 100 r as a function of maximum betatron energy for the reaction $F^{19}(\gamma, n)F^{18}$. Corrections for geometry, etc., have been applied.

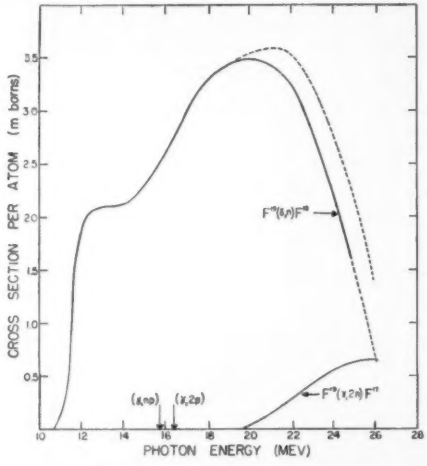

FIG. 2. Cross section vs energy curves for the reactions $F^{19}(\gamma, n)F^{18}$ and $F^{19}(\gamma, 2n)F^{17}$. The dotted line indicates the sum of the two reactions. The (γ, np) and $(\gamma, 2p)$ calculated thresholds are marked.

[1] L. Katz and A. G. W. Cameron, Can. J. Phys. **29**, 518 (1951).
[2] Johns, Horsley, Haslam, and Quinton, Phys. Rev. **84**, 856 (1951).
[3] Horsley, Haslam, and Johns, Can. J. Phys. **30**, 159 (1952).

to the method previously reported for the $Cu^{65}(\gamma, n)Cu^{64}$ reaction.[4] The counting equipment was placed close to the betatron in order that little time would be lost between the end of irradiation and the start of counting. With this arrangement it was possible to start counting 20 seconds after the end of the irradiation. Because of the 12-second neutron-induced F^{20} activity there was no advantage in starting to count sooner.

RESULTS

$F^{19}(\gamma, n)F^{18}$

Figure 1 shows the saturated specific activity curve for the $F^{19}(\gamma, n)F^{18}$ reaction per gram of parent isotope at a dosage rate of 100 r per minute. Corrections for self-absorption, back-scattering, and geometry have been applied. Normalization against the $Cu^{63}(\gamma, n)Cu^{62}$ reaction[4,5] was carried out at 23.5 Mev. The neutron yield at 22 Mev is 1.14×10^6 neutrons/mole/r as compared to the value 1.6×10^5 reported by Price and Kerst.[6]

The cross-sectional curve was determined by the photon difference method[1] and is shown in Fig. 2. This curve rises almost vertically from the calculated threshold at 10.7 Mev to a value of about 2 mb at 12 Mev, remains almost constant for about 3 Mev, and then increases again to a peak value of 3.48 mb at 20 Mev. The pertinent information obtained from this curve is shown in Table I.

TABLE I. Information obtained from the $F^{19}(\gamma, n)F^{18}$ and $F^{19}(\gamma, 2n)F^{17}$ cross-sectional curves.

Reaction	$F^{19}(\gamma, n)F^{18}$	$F^{19}(\gamma, 2n)F^{17}$
Peak position	20 Mev	26 Mev
Peak cross section	3.48 mb	0.66 mb
Width at half-maximum	12.9 Mev	—
Integrated cross section (to 26 Mev)	0.039 Mev-barns	0.0024 Mev-barns

The ratio of the $F^{19}(\gamma, n)F^{18}$ and $Cu^{63}(\gamma, n)Cu^{62}$ cross-sectional values has been determined by Wäffler and Hirzel,[7] with lithium gamma-radiation. Using the $Cu^{63}(\gamma, n)Cu^{62}$ cross-sectional results[4,5] previously determined in this laboratory and weighting our cross-sectional values according to the percentage of 17.6- and 14.5-Mev photons in lithium gamma-radiation, our value of 0.030 for this ratio is in satisfactory agreement with the value of 0.025 as reported by Wäffler and Hirzel.

$F^{19}(\gamma, 2n)F^{17}$

Many determinations were made of the F^{17} half-life using the LiF crystals. The average value obtained for this half-life is 60 ± 1 seconds, which is lower than the value of 66 seconds reported by Brown and Perez-Mendez.[8] A sample decay curve is reproduced in Fig. 3. In addition to the 112-minute F^{18} activity and the 60-second F^{17} activity, there is shown the 12-second F^{20} neutron-induced activity.

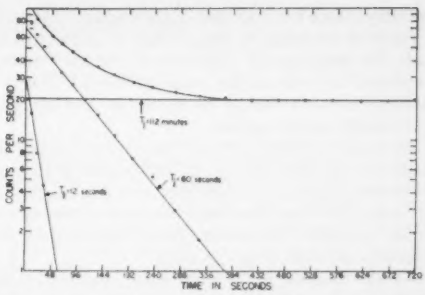

FIG. 3. A sample decay curve using pure LiF crystals, showing the F^{18} 112-minute activity, the F^{17} 60-second activity, and the neutron-induced 12-second F^{20} activity.

Figure 4 shows the saturated specific activity curve for the reaction $F^{19}(\gamma, 2n)F^{17}$. Normalization against the $Cu^{63}(\gamma, n)Cu^{62}$ reaction was carried out at 24.5 Mev. Because of the difficulty in procuring sufficiently thin LiF crystals to determine a self-absorption curve, the self-absorption correction was obtained indirectly. Recent work[9] done in this laboratory indicates that the self-absorption and self-scattering of samples of the same area but of different materials are the same to a first order of approximation, provided that the thicknesses of the samples, expressed in terms of the fraction of the range of their emitted β-particles, are equal. A sample of copper and one of fluorine of the same area were irradiated simultaneously and counted in the same

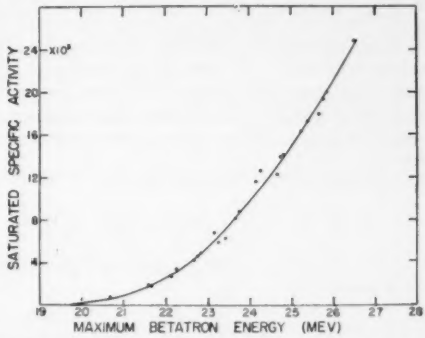

FIG. 4. Saturated specific activity in disintegrations per gram per 100 r as a function of maximum betatron energy for the reaction $F^{19}(\gamma, 2n)F^{17}$.

[4] Johns, Katz, Douglas, and Haslam, Phys. Rev. **80**, 1062 (1950).
[5] Haslam, Johns, and Horsley, Phys. Rev. **82**, 270 (1951).
[6] G. A. Price and D. W. Kerst, Phys. Rev. **77**, 806 (1950).
[7] H. Wäffler and O. Hirzel, Helv. Phys. Acta **21**, 200 (1948).
[8] H. Brown and V. Perez-Mendez, Phys. Rev. **75**, 1286 (1949).
[9] R. Baker, Master's thesis, University of Saskatchewan (1952).

geometry. Since the thickness of the copper (expressed in terms of the range of the 2.9 Mev β^+ particle) was made the same as the thickness of the LiF crystal (expressed in terms of the range of the 2.1 Mev β^+ particle), only corrections for saturation and isotopic abundances need be applied.

The cross-sectional curve for the $(\gamma, 2n)$ reaction in fluorine is shown in Fig. 2. It rises smoothly from a calculated threshold at 19.4 Mev to a peak value of 0.66 mb at 26 Mev. The integrated cross section up to 26 Mev is 0.0024 Mev-barns. Table I contains the information obtained from this curve.

A rough estimate of the total $(\gamma, 2n)$ integrated cross section can be obtained if we assume that the $(\gamma, 2n)$ cross-sectional curve is symmetrical about its peak position at 26 Mev. This assumption is questionable, since we have no information concerning the shape of the latter part of the curve and how far it may extend. The above assumption leads to a value of 0.0048 Mev-barns for the total integrated cross section, and the ratio of the (γ, n) to the $(\gamma, 2n)$ integrated cross section is then about 8 to 1. Perlman and Friedlander[10] report that the ratio of the (γ, n) and $(\gamma, 2n)$ yields at 50 and 100 Mev bremsstrahlung energies are 18.7 and 12.3, respectively. The large difference in their results can hardly be explained in terms of the variation in shape of the bremsstrahlung spectrum in the region of importance for the (γ, n) and $(\gamma, 2n)$ reactions for maximum betatron energies of 50 and 100 Mev.

DISCUSSION

The shape of the (γ, n) cross-sectional curve differs somewhat from the usual resonance type of curve obtained for photonuclear reactions. The small step in the first part of the curve cannot be explained satisfactorily in terms of competing reactions since the thresholds for any possible competing reactions lie at too high energies. A possible exception is the $F^{19}(\gamma, p)O^{18}$ reaction which has a calculated threshold of 7.8 Mev. Although the "effective" threshold for this reaction may be 2 or 3 Mev higher because of the barrier effect, it is doubtful if it would come in strongly enough at an energy of 12 or 13 Mev to account for the observed distortion of the curve. A somewhat similar behavior of the cross-sectional curves for the reactions $O^{16}(\gamma, n)O^{15}$ and $N^{14}(\gamma, n)N^{13}$ was tentatively explained in terms of the absorption mechanism.[2,3] It was suggested that the initial portion might be due in large part to electric quadrupole and magnetic dipole absorption, while the subsequent rapid rise might be attributed to increased electric dipole absorption. A similar explanation may hold in this case.

However, an alternative explanation may be provided by work in progress in this laboratory. It has been found that there are sharp breaks in the $O^{16}(\gamma, n)O^{15}$ and $C^{12}(\gamma, n)C^{11}$ activation curves which may be explained as being due to strong absorption levels in the initial nucleus.[11] A variation in the density and strength of F^{19} levels in the critical region may well account for the observed cross-sectional shape. A careful investigation of levels in F^{19} is planned.

The turning over of the (γ, n) cross-sectional curve above 20 Mev cannot be attributed to the competing $(\gamma, 2n)$ reaction since the sum of these two cross-sectional curves also turns over. This is shown by the dotted line in Fig. 2. The effect of the (γ, np) and $(\gamma, 2p)$ reactions are not known, but it seems probable that the magnitude of these cross sections would be insufficient to account to any appreciable extent for the rapid falling off of the sum of the (γ, n) and $(\gamma, 2n)$ cross-sectional curves. The decreased cross section is thus thought to be due to a falling off in the photon absorption cross section at energies above 22 Mev.

CONCLUSIONS

The shape of the $F^{19}(\gamma, n)F^{18}$ cross-sectional curve cannot be explained satisfactorily in terms of any competing processes including the measured $F^{19}(\gamma, 2n)F^{17}$ reaction. The anomalous shape of the first part of the curve as well as the turning over of the curve at 21 Mev must be explained in terms of the mechanism of gamma-ray absorption which at present is being investigated.

The authors appreciate the financial assistance of the National Research Council of Canada and the National Cancer Institute. One of the authors (R.J.H.) is indebted to the National Research Council for a studentship.

[10] M. L. Perlman and G. Friedlander, Phys. Rev. **74**, 442 (1948).

[11] Haslam, Katz, Horsley, Cameron, and Montalbetti, Phys. Rev. **87**, 196 (1952).

Cascade Theories with Ionization Loss

H. MESSEL AND R. B. POTTS
University of Adelaide, Adelaide, South Australia
(Received April 29, 1952)

Analytical solutions have previously been given for the number distribution functions and for the general moments of the electron-photon and nucleon cascades neglecting ionization losses (approximation *A*). Solutions are now given for the moments of the electron-photon and proton-neutron cascades taking into account energy loss, via ionization, by electrons and protons (approximation *B*). The diffusion equations for the differential moment functions, which yield the required factorial moments by a simple integration over the energy variables, are transformed by Laplace-Mellin transforms to matrix recurrence relations, the general solution of which is obtained in the form of power series. From these series, solutions for the moments in a form suitable for numerical calculations are obtained by a generalization of the method used by Bhabha and Chakrabarty for the first moments of the electron-photon cascade and by Messel in the proton-neutron cascade. To a first approximation, the solutions for the moments in approximation *B* are expressed as a correction factor multiplying the solutions obtained in approximation *A*.

1. INTRODUCTION

ANALYTICAL solutions have recently[1-5] been given for the fluctuation problems arising in nucleon and electron-photon cascade theories in approximation *A* (neglecting ionization loss). In the above references, analytical expressions were obtained for the general number distribution functions as well as for their factorial moments. It is the purpose of the present paper to give solutions for the (n,m)th factorial moments of the electron-photon and nucleon cascades when energy loss by ionization is accounted for (approximation *B*). In this case it is necessary to distinguish the protons and neutrons in the nucleon cascade, and to emphasize this the cascade will be called the "proton-neutron" cascade.

The method used in this paper is the following:—The diffusion equation for the differential moment function is solved in series form. From this probability function the (n,m)th factorial moments are obtained by a simple integration over the energy variables. In a manner similar to that used by Bhabha and Chakrabarty[6,7] and Messel[8,9] for the first moments in electron-photon and proton-neutron cascade theory, respectively, the series solution for the moments is transformed to a new series, the first term of which gives an approximate formula for the moments in a form suitable for numerical calculations.

The general results, not unexpectedly, are exceedingly complicated. The amount of work required to compute the second moments is not prohibitive providing one has the aid of an electronic brain. A program is at present being set up for such a calculation.

2. THE ELECTRON-PHOTON CASCADE

(a) The Diffusion Equations

Using the same notation as previously,[5] we let $q_{n,m}{}^{(j)}(E_0; E_1, \cdots, E_n; E_{n+1}, \cdots, E_{n+m}; x)$ be the differential moment function expressing the probability that after a depth of x cascade units a primary (j) of energy E_0 has given rise to n electrons with energies in the ranges E_k, dE_k, $k=1, \cdots, n$ in any order, to m photons with energies in the ranges E_{n+l}, dE_{n+l}, $l=1, \cdots m$ in any order, and to any numbers of electrons and photons with arbitrary energies. For $j=1$, the primary is an electron, for $j=2$, a photon. It is assumed that the electrons suffer a constant energy loss β by ionization. For the cross sections, the well-known Bethe-Heitler expressions in the full-screening approximation will be used: $w^{(1)}(E_k, E_l)$ for bremsstrahlung, $w^{(2)}(E_k, E_l)$ for pair production, and $\alpha^{(1)}$ and $\alpha^{(2)}$ for the corresponding total cross sections.

The last-collision diffusion equation[4] satisfied by $q_{n,m}{}^{(j)}$ is

$$\left(\frac{\partial}{\partial x}+n\alpha^{(1)}+m\alpha^{(2)}\right)q_{n,m}{}^{(j)}(E_0; E_1, \cdots, E_n; E_{n+1}, \cdots, E_{n+m}; x)$$
$$=\sum_{C_1^n}\sum_{C_1^m} q_{n,m-1}{}^{(j)}(E_0; E_1', \cdots, E_{n-1}', E_n'+E_{n+m}'; E_{n+1}', \cdots, E_{n+m-1}'; x)w^{(1)}(E_n', E_{n+m}')$$
$$+\sum_{C_2^n} q_{n-2,m+1}{}^{(j)}(E_0; E_1', \cdots, E_{n-2}'; E_{n+1}, \cdots, E_{n+m}, E_{n-1}'+E_n'; x)w^{(2)}(E_{n-1}', E_n')$$

(continued on next page)

[1] H. Messel, Proc. Phys. Soc. (London) **A65**, 465 (1952).
[2] H. Messel and J. W. Gardner, Phys. Rev. **84**, 1256 (1951).
[3] H. Messel and R. B. Potts, Proc. Phys. Soc. (London) **A65**, 473 (1952).
[4] H. Messel and R. B. Potts, Proc. Phys. Soc. (London) (to be published).
[5] H. Messel and R. B. Potts, Phys. Rev. **86**, 847 (1952).
[6] H. J. Bhabha and S. K. Chakrabarty, Proc. Roy. Soc. (London) **A181**, 267 (1943).
[7] H. J. Bhabha and S. K. Chakrabarty, Phys. Rev. **74**, 1352 (1948).
[8] H. Messel, Phys. Rev. **83**, 21 (1951).
[9] H. Messel, Phys. Rev. **83**, 26 (1951).

$$+\sum_{C_1^n}\int_0^\infty q_{n-1,\,m+1}{}^{(j)}(E_0; E_1', \cdots, E_{n-1}'; E_{n+1}, \cdots, E_{n+m}, U; x)2w^{(2)}(U-E_n', E_n')dU$$

$$+\sum_{C_1^m}\int_0^\infty q_{n,\,m}{}^{(j)}(E_0; E_1', \cdots, E_{n-1}', U; E_{n+1}, \cdots, E_{n+m}; x)w^{(1)}(E_n', U-E_n')dU$$

$$+\sum_{C_1^m}\int_0^\infty q_{n+1,\,m-1}{}^{(j)}(E_0; E_1, \cdots, E_n, U; E_{n+1}', \cdots, E_{n+m-1}'; x)w^{(1)}(U-E_{n+m}'E_{n+m}')dU$$

$$+\beta\sum_{k=1}^{n}\frac{\partial}{\partial E_k}q_{n,\,m}{}^{(j)}(E_0; E_1, \cdots, E_n; E_{n+1}, \cdots, E_{n+m}; x). \quad (1)$$

This equation, apart from the last term which expresses a shift in energy due to ionization loss by electrons, is the last-collision diffusion equation for the differential moment function in approximation A.[5] The reader is referred to this paper for definitions of the notation used in (1) and subsequently.

If the Laplace-Mellin transform $Q_{n,\,m}{}^{(j)}$ and the Mellin transform $W^{(j)}$ are defined by

$$Q_{n,\,m}{}^{(j)}(s_1, \cdots, s_n; s_{n+1}, \cdots, s_{n+m}; \lambda)=\int_0^\infty dE_1\cdots\int_0^\infty dE_{n+m}\int_0^\infty dx(E_1/E_0)^{s_1}\cdots(E_{n+m}/E_0)^{s_{n+m}}e^{-\lambda x}q_{n,\,m}{}^{(j)} \quad (2)$$

and

$$W^{(j)}(s_1, s_2)=\int_0^\infty\left(\frac{E_1}{E_1+E_2}\right)^{s_1}\left(\frac{E_2}{E_1+E_2}\right)^{s_2}w^{(j)}(E_1, E_2)dE_2, \quad (3)$$

then (1) may be transformed to

$$\begin{aligned}(\lambda+n\alpha^{(1)}+m\alpha^{(2)})Q_{n,\,m}{}^{(j)}-\delta_{n+j,\,2}\delta_{m+1,\,j}\\
=\sum_{C_1^n}\sum_{C_1^m}Q_{n,\,m-1}{}^{(j)}(s_1', \cdots, s_{n-1}', s_n'+s_{n+m}'; s_{n+1}', \cdots, s_{n+m-1}'; \lambda)W^{(1)}(s_n', s_{n+m}')\\
+\sum_{C_1^n}Q_{n-2,\,m+1}{}^{(j)}(s_1', \cdots, s_{n-2}'; s_{n+1}, \cdots, s_{n+m}, s_{n-1}'+s_n'; \lambda)W^{(2)}(s_{n-1}', s_n')\\
+\sum_{C_1^n}Q_{n-1,\,m+1}{}^{(j)}(s_1', \cdots, s_{n-1}'; s_{n+1}, \cdots, s_{n+m}, s_n'; \lambda)2W^{(2)}(s_n', 0)\\
+\sum_{C_1^n}Q_{n,\,m}{}^{(j)}(s_1, \cdots, s_n; s_{n+1}, \cdots, s_{n+m}; \lambda)W^{(1)}(s_n', 0)\\
+\sum_{C_1^m}Q_{n+1,\,m-1}{}^{(j)}(s_1, \cdots, s_n, s_{n+m}'; s_{n+1}', \cdots, s_{n+m-1}'; \lambda)W^{(1)}(0, s_{n+m}')\\
-(\beta/E_0)\sum_{C_1^n}s_nQ_{n,\,m}{}^{(j)}(s_1, \cdots, s_{n-1}, s_n-1; s_{n+1}, \cdots, s_{n+m}; \lambda). \quad (4)\end{aligned}$$

This equation may be transformed into the matrix equations*

$$[\lambda\mathbf{E}_1+\mathbf{A}_1(s_1)]\mathbf{Q}_1(s_1; \lambda)=\mathbf{E}_1-(\beta/E_0)\mathbf{S}_1(s_1)\mathbf{Q}_1(s_1-1; \lambda) \quad (5)$$

and

$$\begin{aligned}[\lambda\mathbf{E}_N+\sum_{r=1}^{N}\mathbf{A}_N(s_r)]\mathbf{Q}_N(s_1, \cdots, s_N; \lambda)\\
=\sum_{C_2^N}\mathbf{W}_{N-1}(s_{N-1}, s_N)\mathbf{Q}_{N-1}(s_1, \cdots, s_{N-2}, s_{N-1}+s_N; \lambda)\\
-(\beta/E_0)\sum_{C_1^N}\mathbf{S}_N(s_N)\mathbf{Q}_N(s_1, \cdots, s_{N-1}, s_N-1; \lambda),\\
N>1. \quad (6)\end{aligned}$$

* For definitions of $A_n(s_r)$ see Eqs. (22) and (23) of reference 5. The notation is as used in reference 5 with the addition that $\mathbf{S}_N(s_r)$ is the direct product of $N2\times2$ matrices:

$$\mathbf{S}_N(s_r)=\mathbf{E}_1\times\cdots\times\underset{r\text{th factor}}{\begin{bmatrix}s_r & 0\\ 0 & 0\end{bmatrix}}\times\cdots\times\mathbf{E}_1. \quad (7)$$

(b) Series Solution for $q_{n,\,m}{}^{(j)}$

The Eqs. (5) and (6) are matrix recurrence relations, the solution of which may be obtained in the form of a power series in (β/E_0). Although this series itself cannot be used directly because of its slow convergence, it is shown in a later section that it may be transformed to give rapidly convergent results.

If

$$Q_{n,m}{}^{(j)}=\sum_{a=0}^{\infty}(-\beta/E_0)^a Q_{n,m,a}{}^{(j)}, \tag{8}$$

$$\mathbf{Q}_N=\sum_{a=0}^{\infty}(-\beta/E_0)^a \mathbf{Q}_{N,a}, \quad N=n+m, \tag{9}$$

then from (5) and (6)

$$\mathbf{Q}_{1,a}(s_1;\lambda)=[\lambda\mathbf{E}_1+\mathbf{A}_1(s_1)]^{-1}\mathbf{S}_1(s_1)\mathbf{Q}_{1,a-1}(s_1-1;\lambda) \tag{10}$$

and

$$\begin{aligned}\mathbf{Q}_{N,a}&(s_1,\cdots,s_N;\lambda)\\ &=\sum_{C_2{}^N}[\lambda\mathbf{E}_N+\sum_{r=1}^{N}\mathbf{A}_N(s_r)]^{-1}\mathbf{W}_{N-1}(s_{N-1},s_N)\\ &\quad\times\mathbf{Q}_{N-1,a}(s_1,\cdots,s_{N-2},s_{N-1}+s_N;\lambda)\\ &\quad+\sum_{C_1{}^N}[\lambda\mathbf{E}_N+\sum_{r=1}^{N}\mathbf{A}_N(s_r)]^{-1}\mathbf{S}_N(s_N)\\ &\quad\times\mathbf{Q}_{N,a-1}(s_1,\cdots,s_{N-1},s_N-1;\lambda), \quad N>1.\end{aligned} \tag{11}$$

For $a=0$, the solution in approximation A is obtained, namely,[5]

$$\begin{aligned}\mathbf{Q}_{N,0}=\Big\{\prod_{d=N-1}^{1}\sum_{C_2{}^{d+1}}&[\lambda\mathbf{E}_{d+1}+\mathbf{A}_{d+1}(s_1)+\cdots\\ &+\mathbf{A}_{d+1}(s_d)+\mathbf{A}_{d+1}(s_{d+1}+\cdots+s_N)]^{-1}\\ &\times\mathbf{W}_d(s_d,s_{d+1},+\cdots+s_N)\Big\}\\ &\times[\lambda\mathbf{E}_1+\mathbf{A}_1(s_1+\cdots+s_N)]^{-1}.\end{aligned} \tag{12}$$

To solve (10) and (11) is by no means an easy task because of the recurrence on N and also on a. The general solution given below may be verified by induction:

$$\mathbf{Q}_{N,a}=\Big\{\prod_{e=a-1}^{0}\sum_{b(e)=0}^{b(e+1)}\Big\{\prod_{d(e)=b(e+1)}^{b(e)+1}\Big\}\Sigma'\,\mathbf{F}_{d(e)}\Big\}\Sigma''\,\mathbf{G}_{b(e)}\Big\}\times\mathbf{Q}_{b(0)+1,0}, \tag{13a}$$

where

$$\begin{aligned}\mathbf{F}_{d(e)}=[\lambda\mathbf{E}_{d(e)+1}&+\mathbf{A}_{d(e)+1}(s_1)+\cdots+\mathbf{A}_{d(e)+1}(s_{d(e)})\\ &+\mathbf{A}_{d(e)+1}(s_{d(e)+1}+\cdots+s_N-a+1+e)]^{-1}\\ &\times\mathbf{W}_{d(e)}(s_{d(e)},s_{d(e)+1}+\cdots+s_N-a+1+e);\end{aligned} \tag{13b}$$

$$\begin{aligned}\mathbf{G}_{b(e)}=[\lambda\mathbf{E}_{b(e)+1}&+\mathbf{A}_{b(e)+1}(s_1)+\cdots+A_{b(e)+1}(s_{b(e)})\\ &+\mathbf{A}_{b(e)+1}(s_{b(e)+1}+\cdots+s_N-a+1+e)]^{-1}\\ &\times\mathbf{S}_{b(e)+1}(s_{b(e)+1}+\cdots+s_N-a+1+e);\end{aligned} \tag{13c}$$

$\mathbf{Q}_{b(0)+1,0}=\mathbf{Q}_{b(0)+1,0}(s_1,\cdots,s_{b(0)},s_{b(0)+1}+\cdots+s_N-a)$, which is given by (12);

$\Sigma'=\sum_{C_{d(e)+1}}$ signifies summation over all choices of $s_{d(e)}, s_{d(e)+1}+\cdots+s_N-a+1+e$ from $s_1,\cdots,s_{d(e)}, s_{d(e)+1}+\cdots+s_N-a+1+e$;

$\Sigma''=\sum_{C_{b(e)+1}}$ signifies summation over all choices of $s_{b(e)+1}+\cdots+s_N-a+1+e$ from $s_1,\cdots,s_{b(e)}, s_{b(e)+1}+\cdots+s_N-a+1+e$; and $b(a)=N-1$.

The order in which the summations and products in (13a) are to be carried out is as follows: first $\prod_e$, then $\sum_{b(e)}$ from the left, next $\prod_{d(e)}$ and finally $\sum_C$ from the right.† To illustrate the notation and result, a simple case will be discussed in a later section.

Equations (13), (9), and (8) determine the solution for $Q_{n,m}{}^{(j)}$. Taking an inverse Laplace-Mellin transform yields

$$\begin{aligned}q_{n,m}{}^{(j)}&(E_0;E_1,\cdots,E_n;E_{n+1},\cdots,E_{n+m};x)\\ &=I_{n+m}E_0{}^{-(n+m)}(E_0/E_1)^{s_1+1}\cdots\\ &\quad\times(E_0/E_{n+m})^{s_{n+m}+1}\sum_{a=0}^{\infty}(-\beta/E_0)^a\mathfrak{Q}_{n,m,a}{}^{(j)},\end{aligned} \tag{14}$$

with I_{n+m} defined as the operator

$$I_{n+m}=1/(2\pi i)^{n+m}\int_{u_1-i\infty}^{u_1+i\infty}ds_1\cdots\int_{u_{n+m}-i\infty}^{u_{n+m}+i\infty}ds_{n+m}, \tag{15}$$

and

$$\begin{aligned}\mathfrak{Q}_{n,m,a}{}^{(j)}&(s_1,\cdots,s_n;s_{n+1},\cdots,s_{n+m};x)\\ &=(2\pi i)^{-1}\int_{\lambda_0-i\infty}^{\lambda_0+i\infty}e^{\lambda x}Q_{n,m,a}{}^{(j)}\\ &\quad\times(s_1,\cdots,s_n;s_{n+1},\cdots,s_{n+m};\lambda)d\lambda\end{aligned} \tag{16}$$

In carrying out the inverse Laplace transform (16), it is convenient to express the inverse matrices appearing in (13) as partial fractions. This can be simply done by using the following result in the theory of resolvents:[10] If $\mathbf{M}$ is a matrix of order p with non-degenerate eigenvalues λ_r, then

$$[\lambda\mathbf{E}+\mathbf{M}]^{-1}=\sum_{r=1}^{p}\frac{1}{\lambda+\lambda_r}\prod_{\substack{k\\ k\neq r}}\frac{[\lambda_k\mathbf{E}-\mathbf{M}]}{\lambda_k-\lambda_r}. \tag{17}$$

The eigenvalues of the matrices appearing in (13) may be easily obtained. For example, consider the matrix

$$\sum_{r=1}^{N}\mathbf{A}_N(s_r),$$

where $\mathbf{A}_N(s_r)$ is the direct product of N matrices of

† The summation Σ_C refers to Σ' and Σ''. Furthermore, $b(e)$ and $d(e)$ are dummy variables.

[10] Frazer, Duncan, and Collar, *Elementary Matrices* (Cambridge University Press, London, England, 1938).

order 2^s

$$\mathbf{A}_N(s_r)=\mathbf{E}_1\times\cdots\times\underbrace{\begin{bmatrix}A_1(s_r) & A_2(s_r)\\ A_3(s_r) & A_4(s_r)\end{bmatrix}}_{r\text{th factor}}\times\cdots\times\mathbf{E}_1. \quad (18)$$

The N matrices $\mathbf{A}_N(s_r)$, $r=1, \cdots, N$, form a set of commuting matrices, and hence the eigen values of their sum are the sums of the eigenvalues of each. If the eigenvalues of the 2×2 matrix

$$\begin{bmatrix}A_1(s_r) & A_2(s_r)\\ A_3(s_r) & A_4(s_r)\end{bmatrix}$$

are $\lambda_1(s_r)$ and $\lambda_2(s_r)$, then the eigenvalues of the direct product $\mathbf{A}_n(s_r)$, being the products of the eigenvalues of the factors, are $\lambda_1(s_r)$ or $\lambda_2(s_r)$ according to whether, in the 2^N binary numbers $s_1s_2\cdots s_N$ with digits 1 and 2, the rth digit is a 1 or 2. Hence the eigenvalues of

$$\sum_{r=1}^{N}\mathbf{A}_N(s_r)$$

are

$$\lambda_1(s_1)+\lambda_1(s_2)+\cdots+\lambda_1(s_{N-1})+\lambda_1(s_N),$$

$$\lambda_1(s_1)+\lambda_1(s_2)+\cdots+\lambda_1(s_{N-1})+\lambda_2(s_N),$$

etc., which may be read off from the binary numbers

$$\begin{matrix}1 & 1 & \cdots & 1 & 1\\ 1 & 1 & \cdots & 1 & 2,\end{matrix}$$

etc. A table of numerical values for $\lambda_1(s)$ and $\lambda_2(s)$ has already been given by Janossy and Messel.[11]

The solution for the (n, m)th factorial moments, derived from the $q_{n,m}{}^{(j)}$, will be given after the differential moment function for the proton-neutron cascade has been determined.

3. THE PROTON-NEUTRON CASCADE IN A FINITE ABSORBER

(a) Preliminaries

The analytical solution for the moments of the nucleon cascade in approximation A has been given by Messel and Potts.[3] Some of their results required for the present work are quoted below.

If $y_N(E_0; E_1, \cdots, E_N; \theta)$ is the differential moment function for nucleons, then the Laplace-Mellin transform of the diffusion equation for y_N is

$$\{\lambda+h(s_1)\}Y_1(s_1;\lambda)=1, \quad (19)$$

$$\{\lambda+\sum_{r=1}^{N}h(s_r)\}Y_N(s_1,\cdots,s_N;\lambda)$$

$$=\sum_{k=2}^{N}\sum_{(k)}B_k(s_1',\cdots,s_k')Y_{N-k+1}$$

$$\times(s_{k+1}',\cdots,s_N',s_1'+\cdots+s_k';\lambda), \quad N>1, \quad (20)$$

where

(a) Y_N is the Laplace-Mellin transform of y_N as in Eq. (2).

(b) $B_N(s_1, \cdots, s_N)$ is the N-fold Mellin transform of the distribution function $b_N(E_0; E_1, \cdots, E_N)$ giving the probability that a primary nucleon of energy E_0 collides with a nucleus giving rise to N nucleons with energies E_k, dE_k and any number of nucleons with arbitrary energies.

(c) $h(s)=1-B_1(s)$.

(d) $\sum_{(k)}$ signifies summation over all compositions of $s_1, \cdots, s_N$ into the two groups $s_1', \cdots, s_k'$ and $s_{k+1}', \cdots, s_N'$.

The solution of (19) and (20) is

$$Y_N(s_1,\cdots,s_N;\lambda)$$

$$=\sum_{c(N-1)}\{\prod_{d=1}^{t}\sum{}'(\lambda+h(s_1)+\cdots+h(s_{q(d)})$$

$$+h(s_{q(d)+1}+\cdots+s_N))^{-1}B_{c(d)+1}$$

$$\times(s_{q(d-1)+1},\cdots,s_{q(d)},s_{q(d)+1}+\cdots+s_N)\}$$

$$\times\{\lambda+h(s_1+\cdots+s_N)\}^{-1}, \quad (21)$$

where $\sum_{c(N-1)}$ signifies summation over the 2^{N-2} compositions of $N-1$, c being the composition $c(1)$, $c(2)$, $\cdots$, $c(t)$, with $q(d)=c(1)+\cdots+c(d)$; and $\sum'$ signifies summation over all combinations of the $q(d)+1$ symbols $s_1, \cdots, s_{q(d)}, s_{q(d)+1}+\cdots+s_N$ taken $c(d)+1$ at a time.

(b) The Diffusion Equations in Approximation B

The diffusion equations for the differential moment functions appearing in a proton-neutron cascade theory are derived in a manner analogous to that used for the electron-photon case. Let $y_{n,m}{}^{(j)}(E_0; E_1, \cdots, E_n; E_{n+1}, \cdots, E_{n+m}; \theta)$ be the differential moment function expressing the probability that after a depth θ (measured in interaction mean free paths) in dispersed matter a primary (j) of energy E_0 has given rise to n protons in the energy ranges E_k, dE_k, $k=1, \cdots, n$ in any order, to m neutrons with energies in the ranges E_{n+l}, dE_{n+l}, $l=1, \cdots, m$ in any order, and to any numbers of protons and neutrons with arbitrary energies. For $j=1$, the primary is a proton, for $j=2$, a neutron. Furthermore, we take $b_{n,m}{}^{(j)}(E_0; E_1, \cdots, E_n; E_{n+1}, \cdots, E_{n+m})$ as the corresponding differential moment function for nucleon-nucleus collisions. Assuming that protons suffer a constant energy loss β by ionization, the last-collision diffusion equation satisfied by $y_{n,m}{}^{(j)}$ is

[11] L. Janossy and H. Messel, Proc. Roy. Irish Acad. **A54**, 245 (1951).

$$(\partial/\partial\theta+n+m)y_{n,m}{}^{(j)}(E_0; E_1, \cdots, E_n; E_{n+1}, \cdots, E_{n+m}; \theta)$$

$$=\sum_{\substack{k=0\\k+l>0}}^{n}\sum_{l=0}^{m}\sum_{(k)}\sum_{(l)}\int_0^\infty\{b_{k,l}{}^{(1)}(U; E_1', \cdots, E_k'; E_{n+1}', \cdots, E_{n+l}')y_{n-k+1,\,m-l}{}^{(j)}$$

$$\times(E_0; E_{k+1}', \cdots, E_n', U; E_{n+l+1}', \cdots, E_{n+m}'; \theta)+b_{k,l}{}^{(2)}(U; E_1', \cdots, E_k'; E_{n+1}', \cdots, E_{n+l}')y_{n-k,\,m-l+1}{}^{(j)}$$

$$\times(E_0; E_{k+1}', \cdots, E_n'; E_{n+l+1}', \cdots, E_{n+m}', U; \theta)\}dU+\beta\sum_{k=1}^{n}\frac{\partial}{\partial E_k}y_{n,m}{}^{(j)}(E_0; E_1, \cdots, E_n; E_{n+1}, \cdots, E_{n+m}; \theta). \quad (22)$$

If we define the Laplace-Mellin transforms of $y_{n,m}{}^{(j)}$ and $b_{n,m}{}^{(j)}$ as

$$Y_{n,m}{}^{(j)}(s_1, \cdots, s_n; s_{n+1}, \cdots, s_{n+m}; \lambda)=\int_0^\infty dE_1\cdots\int_0^\infty dE_{n+m}\int_0^\infty d\theta(E_1/E_0)^{s_1}\cdots$$

$$\times(E_{n+m}/E_0)^{s_{n+m}}e^{-\lambda\theta}y_{n,m}{}^{(j)}B_{n,m}{}^{(j)}(s_1, \cdots, s_n; s_{n+1}, \cdots, s_{n+m}) \quad (23)$$

$$=\int_0^\infty dE_1\cdots\int_0^\infty dE_{n+m}(E_1/E_0)^{s_1}\cdots(E_{n+m}/E_0)^{s_{n+m}}b_{n,m}{}^{(j)}, \quad (24)$$

then the Laplace-Mellin transform of (22) is

$$(\lambda+n+m)Y_{n,m}{}^{(j)}(s_1, \cdots, s_n; s_{n+1}, \cdots, s_{n+m}; \lambda)-\delta_{n+j,\,0}\,\delta_{n+l,\,0}$$

$$=\sum_{k=0}^{n}\sum_{l=0}^{m}\sum_{(k)}\sum_{(l)}\{B_{k,l}{}^{(1)}(s_1', \cdots, s_k'; s_{n+1}', \cdots, s_{n+l}')Y_{n-k+1,\,m-l}{}^{(j)}(s_{k+1}', \cdots, s_n', s_1'+\cdots+s_k'$$

$$+s_{n+1}'+\cdots+s_{n+l}'; s_{n+l+1}', \cdots, s_{n+m}'; \lambda)+B_{k,l}{}^{(2)}(s_1', \cdots, s_k'; s_{n+1}', \cdots, s_{n+l}')$$

$$\times Y_{n-k,\,m-l+1}{}^{(j)}(s_{k+1}', \cdots, s_n'; s_{n+l+1}', \cdots, s_{n+m}', s_1'+\cdots+s_k'+s_{n+1}'+\cdots+s_{n+l}'; \lambda)\}$$

$$-(\beta/E_0)\sum_{C_1^n}s_nY_{n,m}{}^{(j)}(s_1, \cdots, s_{n-1}, s_n-1; s_{n+1}, \cdots, s_{n+m}; \lambda). \quad (25)$$

Just as the transformed diffusion equation for the electron-photon cascade was written in the matrix form, (5) and (6), so (25) may be written

$$[\lambda\mathbf{E}_1+\mathbf{h}_1(s_1)]\mathbf{Y}_1(s_1; \lambda)=\mathbf{E}_1-(\beta/E_0)\mathbf{S}_1(s_1)\mathbf{Y}_1(s_1-1; \lambda), \quad (26)$$

$$[\lambda\mathbf{E}_N+\sum_{r=1}^{N}\mathbf{h}_N(s_r)]\mathbf{Y}_N(s_1, \cdots, s_N; \lambda)=\sum_{k=2}^{N}\sum_{(k)}\mathbf{B}_{N,k}(s_1', \cdots, s_k')\mathbf{Y}_{N-k+1}(s_{k+1}', \cdots, s_N', s_1'+\cdots+s_k'; \lambda)$$

$$-(\beta/E_0)\sum_{C_1^N}\mathbf{S}_N(s_N)\mathbf{Y}_N(s_1, \cdots, s_{N-1}, s_N-1; \lambda), \quad N>1. \quad (27)$$

The matrix $\mathbf{h}_N(s_r)$ is the direct product of N 2×2 matrices:

$$\mathbf{h}_N(s_r)=\mathbf{E}_1\times\cdots\times\underset{r\text{th factor}}{\mathbf{h}(s_r)}\times\cdots\times\mathbf{E}_1, \quad (28)$$

where $\mathbf{h}(s)$ is defined as

$$\mathbf{h}(s)=\begin{bmatrix}1-B_{1,0}{}^{(1)}(s) & -B_{1,0}{}^{(2)}(s)\\ -B_{0,1}{}^{(1)}(s) & 1-B_{0,1}{}^{(2)}(s)\end{bmatrix}. \quad (29)$$

The matrix $\mathbf{Y}_N$ is a $2^N\times2$ matrix the columns of which correspond to $Y^{(1)}$ and $Y^{(2)}$, and the rows are ordered by the binary numbers $s_1\cdots s_N$ with digits 1, 2 in the same way as $\mathbf{Q}_N$ was formed for the electron-photon cascade.[5] The matrix $\mathbf{B}_{N,k}(s_1, \cdots, s_k)$ is a $2^N\times2^{N-k+1}$ matrix in which the rows are ordered by the binary numbers $s_1\cdots s_N$. The nonzero elements are arranged according to the following rule: if in the binary number $s_1\cdots s_N$ it occurs that $s_1'=s_2'=\cdots=s_r'=1$, and $s_{r+1}'=s_{r+2}'=\cdots=s_k'=2$, then all the elements of the row are zero except for the terms $B_{r,k-r}{}^{(1)}(s_1', \cdots, s_r'; s_{r+1}', \cdots, s_k')$ and $B_{r,k-r}{}^{(2)}(s_1', \cdots, s_r'; s_{r+1}', \cdots, s_k')$, which are placed in the first odd-numbered and first even-numbered columns, respectively, in which these terms have not already appeared. For example,

$$\mathbf{B}_{2,2}(s_1, s_2)=\begin{Bmatrix}B_{2,0}{}^{(1)}(s_1, s_2) & B_{2,0}{}^{(2)}(s_1, s_2)\\ B_{1,1}{}^{(1)}(s_1; s_2) & B_{1,1}{}^{(2)}(s_1; s_2)\\ B_{1,1}{}^{(1)}(s_2; s_1) & B_{1,1}{}^{(2)}(s_2; s_1)\\ B_{0,2}{}^{(1)}(s_1, s_2) & B_{0,2}{}^{(2)}(s_1, s_2)\end{Bmatrix}, \quad (30a)$$

$$\mathbf{B}_{2,2}(s_1,s_2)=\begin{Bmatrix} B_{2,0}^{(1)}(s_1,s_2) & B_{2,0}^{(2)}(s_1,s_2) & 0 & 0 \\ 0 & 0 & B_{2,0}^{(1)}(s_1,s_2) & B_{2,0}^{(2)}(s_1,s_2) \\ B_{1,1}^{(1)}(s_1;s_2) & B_{1,1}^{(2)}(s_1;s_2) & 0 & 0 \\ 0 & 0 & B_{1,1}^{(1)}(s_1;s_2) & B_{1,1}^{(2)}(s_1;s_2) \\ B_{1,1}^{(1)}(s_2;s_1) & B_{1,1}^{(2)}(s_2;s_1) & 0 & 0 \\ 0 & 0 & B_{1,1}^{(1)}(s_2;s_1) & B_{1,1}^{(2)}(s_2;s_1) \\ B_{0,2}^{(1)}(s_1,s_2) & B_{0,2}^{(2)}(s_1,s_2) & 0 & 0 \\ 0 & 0 & B_{0,2}^{(1)}(s_1,s_2) & B_{0,2}^{(2)}(s_1,s_2) \end{Bmatrix}. \tag{30b}$$

(c) Solution for $y_{n,m}^{(j)}$, $\beta=0$

If we set $\beta=0$ in Eqs. (26) and (27) and write $\mathbf{Y}_{N,0}$ for $\mathbf{Y}_N$ in this case, we get

$$[\lambda\mathbf{E}_1+\mathbf{h}_1(s_1)]\mathbf{Y}_{1,0}(s_1;\lambda)=\mathbf{E}_1, \tag{31}$$

$$[\lambda\mathbf{E}_N+\sum_{r=1}^{N}\mathbf{h}_N(s_r)]\mathbf{Y}_{N,0}(s_1,\cdots,s_N;\lambda)$$

$$=\sum_{k=2}^{N}\sum_{(k)}\mathbf{B}_{N,k}(s_1',\cdots,s_k')\mathbf{Y}_{N,0}(s_{k+1}',\cdots,\times s_N',s_1'+\cdots+s_k';\lambda),\quad N>1. \tag{32}$$

These are the transforms of the last-collision diffusion equation for the proton-neutron cascade in approximation A. Their solution is

$$\mathbf{Y}_{N,0}(s_1,\cdots,s_N;\lambda)$$

$$=\sum_{c(N-1)}\{\prod_{d=1}^{1}\sum{}'[\lambda\mathbf{E}_{q(d)+1}+\mathbf{h}_{q(d)+1}(s_1)+\cdots+\mathbf{h}_{q(d)+1}(s_{q(d)})+\mathbf{h}_{q(d)+1}(s_{q(d)+1}+\cdots+s_N)]^{-1}\times\mathbf{B}_{q(d)+1,\,c(d)+1}(s_{q(d-1)+1},\cdots,s_{q(d)},s_{q(d)+1}+\cdots+s_N)\}[\lambda\mathbf{E}_1+\mathbf{h}_1(s_1+\cdots+s_N)]^{-1}, \tag{33}$$

with the same notation as in (21). The solution for $y_{n,m}^{(j)}$, $\beta=0$, is

$$y_{n,m,0}^{(j)}=I_{n+m}E_0^{-(n+m)}(E_0/E_1)^{s_1+1}\cdots\times(E_0/E_{n+m})^{s_{n+m}+1}\mathfrak{Y}_{n,m,0}^{(j)}, \tag{34}$$

where $\mathfrak{Y}_{n,m,0}^{(j)}$ is the inverse Laplace transform of $Y_{n,m,0}^{(j)}$ as given by (33).

The matrix Eqs. (31), (32), and their solution (33) for the proton-neutron cascade in approximation A are very similar in form to Eqs. (19), (20), and their solution (21) for the nucleon cascade in which the protons are not distinguished from the neutrons. It is the power of the matrix method that the matrices alone keep the protons separated from the neutrons. Once the equations for the proton-neutron cascade have been written in matrix form the difference between the protons and neutrons is hidden. Even the "trees" used to describe the solution for the nucleon cascade[3] can be used as they stand for the proton-neutron cascade in approximation A.

This matrix method is a general one and has already been applied by us[5] in electron-photon cascade theory in approximation A. Here again the matrices alone take account of the differences between the electrons and photons and the different cross sections for *bremsstrahlung* and pair production. In matrix notation the equations and solutions become analogous to those for the proton-neutron cascade in homogeneous nuclear matter, in which just one type of particle cascades by collisions with single particles of the same type.

(d) Series Solution for $y_{n,m}^{(j)}$, $\beta\neq0$

Equations (26) and (27) are matrix recurrence relations, the solution of which may be obtained in a manner similar to that used in Sec. 2(b) for $q_{n,m}^{(j)}$. Set

$$Y_{n,m}^{(j)}=\sum_{a=0}^{\infty}(-\beta/E_0)^a Y_{n,m,a}^{(j)}, \tag{35}$$

and hence

$$\mathbf{Y}_N=\sum_{a=0}^{\infty}(-\beta/E_0)^a\mathbf{Y}_{N,a}. \tag{36}$$

From (26) and (27),

$$\mathbf{Y}_{1,a}(s_1;\lambda)=[\lambda\mathbf{E}_1+\mathbf{h}_1(s_1)]^{-1}\mathbf{S}_1(s_1)\mathbf{Y}_{1,a-1}(s_1-1;\lambda) \tag{37}$$

and

$$\mathbf{Y}_{N,a}(s_1,\cdots,s_N;\lambda)$$

$$=\sum_{k=2}^{N}\sum_{(k)}[\lambda\mathbf{E}_N+\sum_{r=1}^{N}\mathbf{h}_N(s_r)]^{-1}\mathbf{B}_{N,k}(s_1',\cdots,s_k')\times\mathbf{Y}_{N-k+1,a}(s_{k+1}',\cdots,s_N',s_1'+\cdots+s_k';\lambda)+\sum_{c_1^N}[\lambda\mathbf{E}_N+\sum_{r=1}^{N}\mathbf{h}_N(s_r)]^{-1}\mathbf{S}_N(s_N)\mathbf{Y}_{N,a-1}\times(s_1,\cdots,s_{N-1},s_N-1;\lambda),\quad N>1. \tag{38}$$

For $a=0$, we obtain the solution for the proton-neutron cascade in approximation A as given by (33). The general solution for $\mathbf{Y}_{N,a}$ is [compare Eq. (13)],

$$\mathbf{Y}_{N,a}=\{\prod_{s=a-1}^{0}\sum_{b(s)=0}^{b(s+1)}\{\sum{}'\prod_{d=1}^{1}\sum{}''\mathbf{H}_d\}\sum{}'''\mathbf{G}_{b(s)}\}\mathbf{Y}_{b(0)+1,0}, \tag{39}$$

where

$$\mathbf{H}_d=[\lambda\mathbf{E}_{q(d)+b(s)+1}+\mathbf{h}_{q(d)+b(s)+1}(s_1)+\cdots+\mathbf{h}_{q(d)+b(s)+1}(s_{q(d)+b(s)})+h_{q(d)+b(s)+1}\times(s_{q(d)+b(s)+1}+\cdots+s_N-a+1+e)]^{-1}\times\mathbf{B}_{q(d)+b(s)+1,\,c(d)+1}(s_{q(d-1)+b(s)+1},\cdots,\times s_{q(d)+b(s)},s_{q(d)+b(s)+1}+\cdots+s_N-a+1+e). \tag{40}$$

$\mathbf{G}_{b(e)}$ is as given by (13b) with the matrix $\mathbf{A}_k(s_r)$ replaced by $\mathbf{h}_k(s_r)$.

$\mathbf{Y}_{b(0)+1,0}=\mathbf{Y}_{b(0)+1,0}(s_1, \cdots, s_{b(0)}, s_{b(0)+1}+\cdots+s_N-a; \lambda)$ as given by (33).

$\sum'=\sum_{c}\prod_{b(e+1)-b(e)}$ signifies summation over all compositions of $\{b(e+1)-b(e)\}$, c being the composition $c(1), c(2), \cdots, c(t)$ with $q(d)=c(1)+\cdots+c(d)$.

$\sum''=\sum_{C_{c(d)+1,c(d)+(e)+1}}$ signifies summation over all choices of $s_{q(d)+b(e)}$, $s_{q(d)+b(e)+1}+\cdots+s_N-a+1+e$ from $s_1, \cdots, s_{q(d)+b(e)}$, $s_{q(d)+b(e)+1}+\cdots+s_N-a+1+e$, and

$\sum'''=\sum_{C_{b(e)+1}}$ signifies summation over all choices of $s_{b(e)+1}+\cdots+s_N-a+1+e$ from $s_1, \cdots, s_{b(e)}$, $s_{b(e)+1}+\cdots+s_N-a+1+e$.

The order in which the summations and products in (39) are to be carried out is as follows: first $\prod_e$, then $\sum_{b(e)}$ from the left, next $\sum'$, then $\prod_d$ and $\sum_c$ from the right.

Inverting the Mellin transform we obtain the solution for $y_{n,m}^{(j)}$ in the form

$$y_{n,m}^{(j)}(E_0; E_1, \cdots, E_n; E_{n+1}, \cdots, E_{n+m}; \theta) = I_{n+m}E_0^{-(n+m)}(E_0/E_1)^{s_1+1}\cdots(E_0/E_{n+m})^{s_{n+m}+1} \times\sum_{a=0}^{\infty}(-\beta/E_0)^a\mathfrak{Y}_{n,m,a}^{(j)}, \quad (41)$$

where

$$\mathfrak{Y}_{n,m,a}^{(j)}(\theta)=\frac{1}{2\pi i}\int_{\lambda_0-i\infty}^{\lambda_0+i\infty}e^{\lambda\theta}Y_{n,m,a}^{(j)}(\lambda)d\lambda.$$

The same method as described in Sec. 2(b) may be used to perform this inverse Laplace transformation.

4. SOLUTIONS FOR THE (n, m)th FACTORIAL MOMENTS $T_{n,m}^{(j)}$

If $T_{n,m}^{(j)}(E_0; E, \beta; x)$ is the (n, m)th factorial moment of the distribution function $\varphi_{n,m}^{(j)}$ giving the probability of finding specified numbers of electrons and photons above a given energy E and an arbitrary number of electrons and photons with energies less than E, then[4,5]

$$T_{n,m}^{(j)}(E_0; E, \beta; x)=\sum_{a=0}^{\infty}\sum_{b=0}^{\infty}\frac{(n+a)!}{a!}\frac{(m+b)!}{b!} \times\varphi_{n+a,m+b}^{(j)}(E_0; E, \beta; x), \quad (42)$$

by definition. The solution for $T_{n,m}^{(j)}$ is obtained immediately by making use of the relation[4]

$$T_{n,m}^{(j)}(E_0; E, \beta; x)=\int_E^{\infty}dE_1\cdots\int_E^{\infty}dE_{n+m}f_{n,m}^{(j)}; \quad (43)$$

hence from (13),

$$T_{n,m}^{(j)}(E_0; E, \beta; x) = I_{n+m}(E_0/E)^{s_1+\cdots+s_{n+m}}\sum_{a=0}^{\infty}(-\beta/E_0)^a \times\Omega_{n,m,a}^{(j)}(s_1, \cdots, s_n; s_{n+1}, \cdots, \times s_{n+m}; x)/s_1\cdots s_{n+m}. \quad (44)$$

An identical set of relations holds between the (n, m)th factorial moments and $y_{n,m}^{(j)}$ for the proton-neutron cascade. Thus,

$$T_{n,m}^{(j)}(E_0; E, \beta; \theta)=\int_E^{\infty}dE_1\cdots\int_E^{\infty}dE_{n+m}y_{n,m}^{(j)}(\theta) \quad (45)$$

and, using (39),

$$T_{n,m}^{(j)}(E_0; E, \beta; \theta) = I_{n+m}(E_0/E)^{s_1+\cdots+s_{n+m}}\sum_{a=0}^{\infty}(-\beta/E_0)^a \times\mathfrak{Y}_{n,m,a}(s_1, \cdots, s_n; s_{n+1}, \cdots, \times s_{n+m}; \theta)/s_1\cdots s_{n+m}. \quad (46)$$

The solutions (44) and (46) for the (n, m)th factorial moments are of little value for computational purposes because of their slow convergence. They may, however, be transformed into a series which is rapidly converging. The method is a generalization of that used by Bhabha and Chakrabarty[6,7] and Messel[8,9] for the electron-photon and proton-neutron cascades, respectively. The Bhabha-Chakrabarty method has been severely criticised,[12,13] but Messel[14] has pointed out that these criticisms were inapplicable and that the Bhabha-Chakrabarty method of solving for the first moments in approximation B is the best available and gives the most reliable results.

The following development will be carried through for just the electron-photon cascade; an identical treatment may be given for the proton-neutron case.

By writing $s_k+a/(n+m)$ for s_k in (44) and by suitably changing the contour of integration, we obtain

$$T_{n,m}^{(j)}(E_0; E, \beta; x) = I_{n+m}\sum_{a=0}^{\infty}(E_0/E)^{s_1+\cdots+s_{n+m}+a}(-\beta/E_0)^a \times\left\{\left(s_1+\frac{a}{n+m}\right)\cdots\left(s_{n+m}+\frac{a}{n+m}\right)\right\}^{-1} \times\Omega_{n,m,a}\left(s_1+\frac{a}{n+m}, \cdots, s_n+\frac{a}{n+m}; \times s_{n+1}+\frac{a}{n+m}, \cdots, s_{n+m}+\frac{a}{n+m}; x\right). \quad (47)$$

For E we write $\{(E+\beta g)-\beta g\}$, where

$$g=g_{n,m}^{(j)}(s_1, \cdots, s_n; s_{n+1}, \cdots, s_{n+m}; x) \quad (47a)$$

is as yet an arbitrary function, to be determined at a later stage. Thus

$$(1/E)^{s_1+\cdots+s_{n+m}+a}=\sum_{b=0}^{\infty}\frac{\Gamma(s_1+\cdots+s_{n+m}+a+b+1)}{b!\Gamma(s_1+\cdots+s_{n+m}+a+1)} \times(\beta g)^b(E+\beta g)^{-(s_1+\cdots+s_{n+m}+a+b)}. \quad (48)$$

[12] I. E. Tamm and S. Belenky, Phys. Rev. **70**, 660 (1946).
[13] H. S. Snyder, Phys. Rev. **76**, 1563 (1949).
[14] H. Messel, Phys. Rev. **82**, 259 (1951).

By introducing (48) into (47) and setting $b=c-a$ we get

$$T_{n,m}^{(j)}(E_0; E, \beta; x) = I_{n+m}\sum_{c=0}^{\infty}\left(\frac{E_0}{E+\beta g}\right)^{s_1+\cdots+s_{n+m}}\left(\frac{\beta}{E+\beta g}\right)^{c} \times\frac{\Gamma(s_1+\cdots+s_{n+m}+c+1)}{\Gamma(s_1+\cdots+s_{n+m}+1)} f_{n,m,c}^{(j)}, \quad (49)$$

where

$$f_{n,m,c}^{(j)}(s_1, \cdots, s_n; s_{n+1}, \cdots, s_{n+m}; x) = \sum_{a=0}^{c}\frac{(-1)^a g^{c-a}}{(c-a)!}\frac{\Gamma(s_1+\cdots+s_{n+m}+1)}{\Gamma(s_1+\cdots+s_{n+m}+a+1)} \cdot\left\{\left(s_1+\frac{a}{n+m}\right)\cdots\left(s_{n+m}+\frac{a}{n+m}\right)\right\}^{-1} \times\Omega_{n,m,a}^{(j)}\left(s_1+\frac{a}{n+m}, \cdots; \cdots, \times s_{n+m}+\frac{a}{n+m}; x\right). \quad (50)$$

In particular,

$$f_{n,m,0}^{(j)} = \Omega_{n,m}^{(j)}(s_1, \cdots, s_n; \times s_{n+1}, \cdots, s_{n+m}; x)/s_1\cdots s_{n+m}. \quad (51)$$

The function g is so chosen that $f_{n,m,1}^{(j)}=0$, i.e.,

$$g_{n,m}^{(j)}(s_1, \cdots, s_n; s_{n+1}, \cdots, s_{n+m}; x) = \{s_1 s_2\cdots s_{n+m}\}(s_1+\cdots+s_{n+m})^{-1} \times\{s_1+(n+m)^{-1}\}^{-1}\cdots\{s_{n+m}+(n+m)^{-1}\}^{-1} \times\Omega_{n,m,1}^{(j)}\left(s_1+\frac{1}{n+m}, \cdots; \cdots, s_{n+m}+\frac{1}{n+m}; x\right) \times\{\Omega_{n,m,0}^{(j)}(s_1, \cdots, s_n; s_{n+1}, \cdots, s_{n+m}; x)\}^{-1}. \quad (52)$$

The general series solution (49) for the factorial moments may now be used for numerical work in the case of small n and m. For $E\approx\beta$ and $E_0\gg\beta$ the following formula gives approximate results for the moments

$$T_{n,m}^{(j)}(E_0; E, \beta; x) \approx[E/(E+\beta g)]^{s_1+\cdots+s_{n+m}} T_{n,m}^{(j)}(E_0; E, \beta=0; x), \quad (53)$$

where $[E/(E+\beta g)]^{s_1+\cdots+s_{n+m}}$ is a correction factor multiplying $T_{n,m}^{(j)}(\beta=0)$, the solution for the moments in approximation A.[6-9]

This completes the solution for the (n, m)th factorial moments in approximation B, both for the electron-photon and proton-neutron cascades. Together with the results presented,[1-5] it constitutes a complete analytical solution of the fluctuation problems arising in electron-photon and proton-neutron cascade theory. It is true that the solutions obtained in approximation A were exceedingly complex and that those just presented were more complex still; however, this is not surprising when one appreciates the complexity of the problems solved. It should be recalled that the solution of the cascade fluctuation problem demands a mathematical representation of every possible event, with suitable weight factors, which may take place in building up the cascade. When one further realizes that in many large air showers one often deals with millions of particles, the results are not unduly complicated. One may wonder what possibility there is of using the solutions presented for computational purposes. Numerical results for the 1st moments in both approximation A and B are easily obtained and have been given for instance by Janossy and Messel,[11] Bhabha and Chakrabarty,[6,7] and Messel.[8,9] The second moments in approximation A have also been calculated, both for the electron-photon and nucleon cascades (see Janossy and Messel[15] and Messel[16]); in approximation B results using (53) will be given in a subsequent publication. With the aid of an electronic brain it is proposed to calculate the third moments as well and then to use the first three moments to reconstruct the appropriate distribution functions (see Green and Messel[17]). This at present appears to be a more satisfactory method of attack than attempting to evaluate directly the analytical solutions given for the distribution functions.

In the next section we will give a simple example of the matrix method used in this paper.

5. THE FIRST MOMENTS OF THE ELECTRON-PHOTON CASCADE

To give a simple example of the Laplace transform and matrix method used in this paper, the g functions and expressions for the first moments of the electron-photon cascade will be derived.

To obtain the g function defined by (52) we require $\mathbf{Q}_{1,0}$ and $\mathbf{Q}_{1,1}$. From (12),

$$\mathbf{Q}_{1,0}(s; \lambda) = [\lambda\mathbf{E}_1+\mathbf{A}_1(s)]^{-1}, \quad (54)$$

where

$$\mathbf{A}_1(s) = \begin{bmatrix} A_1(s) & A_2(s) \\ A_3(s) & A_4 \end{bmatrix}. \quad (55)$$

Hence

$$\mathbf{Q}_{1,0}(s; \lambda) = \{(\lambda+\lambda_1(s))(\lambda_2(s)-\lambda_1(s))\}^{-1} \times[\lambda_2(s)\mathbf{E}_1-\mathbf{A}_1(s)] +\{(\lambda+\lambda_2(s))(\lambda_1(s)-\lambda_2(s))\}^{-1} \times[\lambda_1(s)\mathbf{E}_1-A_1(s)], \quad (56)$$

where $\lambda_1(s)$ and $\lambda_2(s)$ are the eigenvalues of $\mathbf{A}_1(s)$.

[15] L. Janossy and H. Messel, Proc. Phys. Soc. (London) **A63**, 1101 (1950).

[16] H. Messel, *Progress in Cosmic Ray Physics* (North Holland Publishing Company, Amsterdam, 1952), Vol. 2.

[17] H. S. Green and H. Messel, Proc. Cambridge Phil. Soc. (to be published).

An inverse Laplace transform of (56) yields

$$\mathfrak{Q}_{1,0}(s;x)=\begin{bmatrix}\mathfrak{Q}_{1,0,0}{}^{(1)}(s;x) & \mathfrak{Q}_{1,0,0}{}^{(2)}(s;x)\\ \mathfrak{Q}_{0,1,0}{}^{(1)}(s;x) & \mathfrak{Q}_{0,1,0}{}^{(2)}(s;x)\end{bmatrix}$$
$$=\frac{e^{-\lambda_1(s)x}}{\lambda_2(s)-\lambda_1(s)}\begin{bmatrix}\lambda_2(s)-A_1(s) & -A_2(s)\\ -A_3(s) & \lambda_2(s)-A_4\end{bmatrix}$$
$$+\frac{e^{-\lambda_2(s)x}}{\lambda_1(s)-\lambda_2(s)}\begin{bmatrix}\lambda_1(s)-A_1(s) & -A_2(s)\\ -A_3(s) & \lambda_1(s)-A_4\end{bmatrix}. \quad (57)$$

From (13),

$$\mathbf{Q}_{1,1}(s;\lambda)=[\lambda\mathbf{E}_1+\mathbf{A}_1(s)]^{-1}\mathbf{S}_1(s)[\lambda\mathbf{E}_1+\mathbf{A}_1(s-1)]^{-1}, \quad (58)$$

$$\mathbf{Q}_{1,1}(s;\lambda)=s\{(\lambda+\lambda_1(s))(\lambda+\lambda_2(s))$$
$$\times(\lambda+\lambda_1(s-1))(\lambda+\lambda_2(s-1))\}^{-1}$$
$$\times\begin{bmatrix}(\lambda+A_4)^2 & -A_2(s-1)(\lambda+A_4)\\ -A_3(s)(\lambda+A_4) & A_3(s)A_2(s-1)\end{bmatrix}. \quad (59)$$

Taking the inverse Laplace transform of (59) we find

$$\mathfrak{Q}_{1,1}(s;x)=\begin{bmatrix}\mathfrak{Q}_{1,0,1}{}^{(1)}(s;x) & \mathfrak{Q}_{1,0,1}{}^{(2)}(s;x)\\ \mathfrak{Q}_{0,1,1}{}^{(1)}(s;x) & \mathfrak{Q}_{0,1,1}{}^{(2)}(s;x)\end{bmatrix}$$
$$=\frac{se^{-\lambda_1(s)x}}{\{\lambda_2(s)-\lambda_1(s)\}\{\lambda_1(s-1)-\lambda_1(s)\}\{\lambda_2(s-1)-\lambda_1(s)\}}\begin{bmatrix}\{\lambda_1(s)-A_4\}^2 & A_2(s-1)\{\lambda_1(s)-A_4\}\\ A_3(s)\{\lambda_1(s)-A_4\} & A_3(s)A_2(s-1)\end{bmatrix}$$
$$+\frac{se^{-\lambda_2(s)x}}{\{\lambda_1(s)-\lambda_2(s)\}\{\lambda_1(s-1)-\lambda_2(s)\}\{\lambda_2(s-1)-\lambda_2(s)\}}\begin{bmatrix}\{\lambda_2(s)-A_4\}^2 & A_2(s-1)\{\lambda_2(s)-A_4\}\\ A_3(s)\{\lambda_2(s)-A_4\} & A_3(s)A_2(s-1)\end{bmatrix} \quad (60)$$
$$+\frac{se^{-\lambda_1(s-1)x}}{\{\lambda_1(s)-\lambda_1(s-1)\}\{\lambda_2(s)-\lambda_1(s-1)\}\{\lambda_2(s-1)-\lambda_1(s-1)\}}$$
$$\times\begin{bmatrix}\{\lambda_1(s-1)-A_4\}^2 & A_2(s-1)\{\lambda_1(s-1)-A_4\}\\ A_3(s)\{\lambda_1(s-1)-A_4\} & A_3(s)A_2(s-1)\end{bmatrix}$$
$$+\frac{se^{-\lambda_2(s-1)x}}{\{\lambda_1(s)-\lambda_2(s-1)\}\{\lambda_2(s)-\lambda_2(s-1)\}\{\lambda_1(s-1)-\lambda_2(s-1)\}}$$
$$\times\begin{bmatrix}\{\lambda_2(s-1)-A_4\}^2 & A_2(s-1)\{\lambda_2(s-1)-A_4\}\\ A_3(s)\{\lambda_2(s-1)-A_4\} & A_3(s)A_2(s-1)\end{bmatrix}.$$

Formula (52) now gives the values of $g_{1,0}{}^{(1)}$, $g_{1,0}{}^{(2)}$, $g_{0,1}{}^{(1)}$, and $g_{0,1}{}^{(2)}$. The result for $g_{1,0}{}^{(1)}$ agrees with that obtained previously by Bhabha and Chakrabarty[6] in a different manner. The result (60) enables one to calculate $T_{n,m}{}^{(j)}(E_0;E,\beta;x)$ using (53). To obtain a more accurate value for $T_{n,m}{}^{(j)}$ one must use (49) and (50); for instance, to carry the approximation (53) one stage further it is necessary to evaluate $f_{n,m,2}{}^{(j)}$ and hence $\mathfrak{Q}_{1,2}(s;x)$. From (13),

$$\mathbf{Q}_{1,2}(s;\lambda)=[\lambda\mathbf{E}_1+A_1(s)]^{-1}\mathbf{S}_1(s)[\lambda\mathbf{E}_1+\mathbf{A}_1(s-1)]^{-1}$$
$$\times\mathbf{S}_1(s-1)[\lambda\mathbf{E}_1+\mathbf{A}_1(s-2)], \quad (61)$$

and hence, taking the inverse Laplace transform, we find

$$\mathfrak{Q}_{1,2}(s;x)=\begin{bmatrix}\mathfrak{Q}_{1,0,2}{}^{(1)}(s;x) & \mathfrak{Q}_{1,0,2}{}^{(2)}(s;x)\\ \mathfrak{Q}_{0,1,2}{}^{(1)}(s;x) & \mathfrak{Q}_{0,1,2}{}^{(2)}(s;x)\end{bmatrix}$$
$$=s(s-1)\sum_{i=1}^{6}\{A_4-\gamma_i(s)\}e^{-\gamma_i(s)x}$$
$$\times\{\prod_{i\neq k}(\gamma_k(s)-\gamma_i(s))\}^{-1}$$
$$\times\begin{bmatrix}(\gamma_i(s)-A_4)^2 & A_2(s-2)(\gamma_i(s)-A_4)\\ A_3(s)(\gamma_i(s)-A_4) & A_3(s)A_2(s-2)\end{bmatrix}, \quad (62)$$

where

$$\gamma_1(s)=\lambda_1(s),\quad \gamma_2(s)=\lambda_1(s-1),\quad \gamma_3(s)=\lambda_1(s-2),$$
$$\gamma_4(s)=\lambda_2(s),\quad \gamma_5(s)=\lambda_2(s-1)\text{ and }\gamma_6(s)=\lambda_2(s-2).$$

As mentioned previously, the second moments with numerical calculations will be discussed in a separate paper.

Scattering of Electrons from Point Singularities in Metals*

D. L. DEXTER
Department of Physics, University of Illinois, Urbana, Illinois
(Received May 23, 1952)

Mott's calculations on the scattering of electrons from substitutional impurity atoms are extended to include the scattering from interstitial atoms and vacancies; the effects of lattice distortions around the singularities are taken into account. It is found that the lattice distortions do not change the order of magnitude of the calculated resistivity in most cases of practical interest, but may in some cases make a difference of a factor of three or more for substitutional atoms of the same valence as the replaced atoms. It is concluded that the resistance change due to a dissociated vacancy-interstitial pair in a monovalent metal of atomic number Z is about equal to or somewhat larger than that due to two divalent substitutional atoms of atomic number $Z+1$. Changes in the temperature-dependent part of the resistivity as a result of lattice distortions are found to be of the same order, at room temperature, as the changes in the residual resistivity due to the lattice distortions.

I. INTRODUCTION

THE scattering of electrons in solids by isolated point singularities, such as impurity atoms, has received attention in connection with the theory[1,2,2a] of the change in electrical conductivities of metals upon alloying and with the theory[3] of mobilities in semiconductors. Previous theoretical work[1,2] on the scattering of electrons in metals has taken account of the scattering arising from (1) the screened Coulomb potential associated with the substitutional atom of valence differing from that of the replaced atom, and (2) the difference in the average potential within the atomic polyhedron of the substitutional atom from that within the replaced atom, in the case that the impurity atom and the atoms of the mother lattice are of the same valence. Calculations based on these effects lead to semiquantitative agreement with experimental results on the electrical resistance of dilute solid solutions. In cases where one might expect good agreement between theory and experiment, namely, for the monovalent metals, the ratio of the observed resistance change to that calculated by the Thomas-Fermi method for effect (1) above is of the order of 1/7; Mott has attributed this discrepancy to errors inherent in the Thomas-Fermi method.

Interest in the general problem of scattering of electrons by singularities in metals has been revived because of the potentialities[4] of resistance measurements for the study of radiation damage to structural materials. One of the primary problems in the study of radiation damage[5] is the determination of the number of interstitial atoms and vacancies, produced as a result of irradiation with energetic particles, as a function of temperature, atomic number, crystal structure, and any other experimental parameters. It is clear that resistance measurements represent a powerful tool in such investigations, once the scattering cross sections of the singularities are known.

In the lattice surrounding point singularities there will, in general, exist elastic distortions, i.e., deviations from perfect periodicity, which give rise to scattering potentials in addition to those mentioned above. The scattering arising from this source has previously been neglected, and neither the magnitude nor the sign of the effect on the resistance has been determined. It is intuitively reasonable to assume that the effect of the elastic distortions on the resistance will be small compared with that of the screened Coulomb potential of a substitutional impurity atom of different valence but of about the same size as the atom it replaces; however, in connection with the interest in measurements of radiation damage, it is not obvious that the effect will be negligible for an interstitial atom or vacancy, around which the atomic displacements may be large. The purpose of this note is to examine the effects of the lattice distortions on the electrical resistance for the several interesting cases of vacancies, interstitial atoms, and substitutional impurities, and, in particular, to see if it is possible to explain by distortion effects the existing discrepancies between theoretical and experimental resistivities of substitutional alloys, so that the scattering from vacancies and interstitials can be calculated by the same methods.

II. CALCULATION OF THE SCATTERING MATRIX ELEMENT

According to Matthiessen's rule, we may treat the scattering from the singularities independently of the purely thermal effects; in the early part of this work, therefore, we shall completely ignore interactions with lattice vibrations, and the resistance we shall calculate is the change in residual resistance of a lattice upon the introduction of point singularities. With the above cus-

* Research supported by the ONR and AEC.
[1] N. F. Mott, Proc. Cambridge Phil. Soc. **32**, 281 (1936).
[2] N. F. Mott and H. Jones, *Properties of Metals and Alloys* (Oxford University Press, London, 1936), Chap. VII.
[2a] K. Huang, Proc. Phys. Soc. (London) **60**, 161 (1948).
[3] E. Conwell and V. F. Weisskopf, Phys. Rev. **77**, 388 (1950); G. L. Pearson and J. Bardeen, Phys. Rev. **75**, 865 (1949) and references contained therein.
[4] Henderson, Cooper, and Marx, Phys. Rev. **86**, 642 (1952) and Marx, Koehler, and Wert, Phys. Rev. **86**, 643 (1952). The writer is indebted to Professor Koehler for discussions of these experiments before publication.
[5] F. Seitz, Disc. Faraday Soc. **5**, 271 (1949).

tomary simplification, our problem reduces to the calculation of the matrix elements of the perturbation Hamiltonian for an electron in a stationary distorted lattice. We shall make the further simplification that the imperfections scatter independently, i.e., that all interference terms vanish; this assumption is certainly valid for sufficiently dilute solid solutions but may lead to small errors in the radiation damage problem if an appreciable fraction of the interstitial atoms are within one or two atomic distances of vacancies.

The perturbation Hamiltonian may be approximated by

$$H(\mathbf{r})=\sum_j{}' v_j(\mathbf{r}-\mathbf{R}_j-\mathbf{U}_j)-\sum_j v_j(\mathbf{r}-\mathbf{R}_j), \quad (1)$$

where $-v_j/e$ is the potential due to the jth nucleus and its surrounding cloud of electrons. $\mathbf{R}_j$ is the equilibrium position of the jth atom in the undistorted crystal, and $\mathbf{U}_j$ is its displacement as a result of the presence of the singularity. The second summation above represents the potential energy of an electron in the undistorted lattice, and thus all the v_j's in this sum are identical. The prime on the first summation symbol serves to remind us that we have added, subtracted, or exchanged an atom in the lattice; in the first or second event the summation is carried out over one extra or one less atom than in the second summation, and in the third event the v_j's are no longer all identical. Keeping only the first two terms in the expansion

$$v_j(\mathbf{r}-\mathbf{R}_j-\mathbf{U}_j)=v_j(\mathbf{r}-\mathbf{R}_j)-\mathbf{U}_j\cdot\nabla v_j(\mathbf{r}-\mathbf{R}_j)+\cdots, \quad (2)$$

we may write Eq. (1) as

$$H(\mathbf{r})=W(\mathbf{r})+w(\mathbf{r}), \quad (3)$$

where

$$W(\mathbf{r})\cong-\sum_j{}' \mathbf{U}_j\cdot\nabla v(\mathbf{r}-\mathbf{R}_j), \quad (4)$$

and $w(\mathbf{r})$ is as defined below. The reason for this separation will immediately become clear. The prime on the summation symbol in Eq. (4) now has the definite meaning that the singularity is excluded from the sum; i.e., the contributions to $H(\mathbf{r})$ which arise from a region of the crystal of the order of an atomic volume in size centered about the vacancy, interstitial atom or impurity atom, are to be taken account of in $w(\mathbf{r})$. In Eq. (4) the potential of the normal lattice atoms of valence z is denoted simply by $-v/e$, and the potential of an impurity atom of valence Z (which may or may not equal z) will be denoted below by $-V/e$. With these understandings in mind, we may express the function $w(\mathbf{r})$ for the four cases of interest as:

1. interstitial lattice atom: $w_1(\mathbf{r})=v(\mathbf{r})$;
2. vacancy: $w_2(\mathbf{r})=-v(\mathbf{r})$;
3. substitutional impurity: $w_3(\mathbf{r})=V(\mathbf{r})-v(\mathbf{r})$;
4. interstitial impurity: $w_4(\mathbf{r})=V(\mathbf{r})$. (5)

Here we have made the assumption that the potential due to an atom in an interstitial position is the same as for that atom in a normal lattice site. The extent to which this assumption is justified will be considered in Sec. IV.

We now compute the matrix elements of the above perturbation Hamiltonians between two electronic plane wave states characterized by the propagation vectors $\mathbf{k}$ and $\mathbf{k}'$. The matrix elements we require are

$$\langle\mathbf{k}'|H|\mathbf{k}\rangle=\Omega^{-1}\int\exp(-i\mathbf{k}'\cdot\mathbf{r})[W(\mathbf{r})+w(\mathbf{r})]\times\exp(i\mathbf{k}\cdot\mathbf{r})d\tau=M(\boldsymbol{\kappa})+m(\boldsymbol{\kappa}), \quad (6)$$

where

$$M(\boldsymbol{\kappa})=-\Omega^{-1}\int\exp(-i\boldsymbol{\kappa}\cdot\mathbf{r})\sum_j{}'\mathbf{U}_j\cdot\nabla v(\mathbf{r}-\mathbf{R}_j)d\tau, \quad (7)$$

$$m(\boldsymbol{\kappa})=\Omega^{-1}\int\exp(-i\boldsymbol{\kappa}\cdot\mathbf{r})w(\mathbf{r})d\tau. \quad (8)$$

Ω is the volume of the metal, and $\boldsymbol{\kappa}\equiv\mathbf{k}'-\mathbf{k}$. The matrix element $m(\boldsymbol{\kappa})$ is the contribution evaluated by Mott,[1] and $M(\boldsymbol{\kappa})$ is that which takes account of the distortion of the lattice.

We may estimate the value of $M(\boldsymbol{\kappa})$ in the following way. Let us consider the spherical singularity to be at the center of a large sphere; then according to the theory of elasticity for a homogeneous isotropic medium, the displacement of the lattice at a point $\mathbf{r}$, measured from the center of the spherical imperfection, is proportional to $\mathbf{r}/r^3$ for $r>r_0$, where r_0 is the radius of the imperfection.[6] Letting $\mathbf{U}_j=A\mathbf{R}_j/R_j^3$, and approximating[2] $v(\mathbf{r})$ by $-ze^2\exp(-q\mathbf{r})/r$, we obtain

$$M(\boldsymbol{\kappa})=\frac{4\pi ize^2A}{\Omega(\kappa^2+q^2)}\sum_j{}'\frac{\mathbf{R}_j\cdot\boldsymbol{\kappa}\exp(-i\boldsymbol{\kappa}\cdot\mathbf{R}_j)}{R_j^3}. \quad (9)$$

The integral in Eq. (7) has been evaluated by interchanging the order of summation and integration, transforming the variable of integration from $\mathbf{r}$ to $\mathbf{r}-\mathbf{R}_j$ and integrating by parts.

For purposes of qualitative discussion we may use the approximation of smeared-out positive charge and replace the summation in Eq. (9) by an integration, obtaining

$$M(\boldsymbol{\kappa})=\frac{16\pi^2ze^2A}{\Omega(\kappa^2+q^2)\Delta}\frac{\sin\kappa r_0}{\kappa r_0}, \quad (9')$$

where Δ is the atomic volume, and r_0 has the somewhat ambiguous meaning of the inner cut-off radius for the contribution to the matrix element from the elastic distortions of the smeared-out medium. This approximation is a rather poor one, but it will serve to show in what cases the distortion effects are unimportant. The

[6] We are neglecting a term in the displacement which is proportional to $\mathbf{r}$. The effects of this term on the resistance are discussed in Sec. IV.

more accurate expression Eq. (9) can be used in specific cases where Eq. (9′) shows the lattice distortion to be significant. The use of Eq. (9) is made more difficult by the fact that the matrix element depends upon the direction of κ in a complicated way, and the Boltzmann transport equation which must be solved for the resistivity has been treated in a simple way[2] only on the assumption that the scattering matrix element is independent of the direction of κ. In a more accurate analysis, therefore, where Eq. (9) is used, it appears necessary, in order to avoid the considerable computational difficulties associated with the solution of the transport equation in its general form, to perform the indicated summation for a number of directions of κ and to replace the resulting complicated function by a function of $|\kappa|$ alone which represents a suitable average over direction; such a function would be expected to be a better approximation than that indicated by Eq. (9′), but it is not as suitable for a general discussion since it depends on the details of the crystal structure and the type of singularity.

An approximate evaluation of Eq. (7), equivalent to Eq. (9′) but exhibiting another feature of the potential, may be performed in the following way. Let us replace the summation in Eq. (4) by an integration before interchanging the order of integration and summation, and obtain

$$W(\mathbf{r})=\Delta^{-1}\int_{r_0}\mathbf{U}(\mathbf{R})\cdot\nabla_{\mathbf{R}}v(\mathbf{r}-\mathbf{R})d\tau_{\mathbf{R}}, \tag{10}$$

where the integration is carried out over all space outside a sphere of radius r_0, and the subscript $\mathbf{R}$ on the Nabla operator denotes differentiation with respect to the integration variable. Making use of the vector identity for the divergence of a product $v\mathbf{U}$, we transform Eq. (10) into

$$W(\mathbf{r})=\Delta^{-1}\int_{r_0}\nabla_{\mathbf{R}}\cdot(v\mathbf{U})-v\nabla_{\mathbf{R}}\cdot\mathbf{U}d\tau_{\mathbf{R}}. \tag{11}$$

According to a well-known theorem of vector calculus, the divergence of $R^n\mathbf{R}$ is equal to $(n+3)R^n$; thus, since $\mathbf{U}(\mathbf{R})$ is proportional to $R^{-3}\mathbf{R}$, the divergence of $\mathbf{U}$ vanishes. It should be pointed out that, since $\nabla\cdot\mathbf{U}$ is proportional to the density change, the density in an infinite, continuous, isotropic medium remains unchanged when a spherically symmetric distortion is introduced. That is, any transfer of material to or from the spherical imperfection is associated with the surface at infinity. In spite of the absence of density changes, however, the potential $W(\mathbf{r})$ and the matrix element $M(\kappa)$ do not vanish, as can easily be seen by transforming the first term on the right side of Eq. (11) by the divergence theorem and inserting it in Eq. (7). Interchanging the order of the integrations and evaluating directly, we obtain the result given in Eq. (9′).

The above result for the total perturbation Hamiltonian, $w(\mathbf{r})+\Delta^{-1}\int\nabla_{\mathbf{R}}\cdot(v\mathbf{U})d\tau_{\mathbf{R}}$, should be compared with the corresponding expression[7] for the scattering of electrons by edge-type dislocations. In the latter case the term $\nabla\cdot\mathbf{U}$ does not vanish, and the term $\Delta^{-1}\int\nabla\cdot(v\mathbf{U})$ cancels the term, corresponding to $w(\mathbf{r})$, which arises from the missing plane of atoms. The physical difference in the two situations is that, whereas in the present calculation there exists a real discontinuity at the singularity, across the plane of missing atoms, on the other hand, the discontinuity in atomic displacement gives rise only to a fictitious discontinuity in the lattice; that is, the lattice is in register across the missing plane of atoms.

Mott has approximated[1] $w(\mathbf{r})$ for case 3 by

$$\begin{aligned} w_3(\mathbf{r})&=-(Z-z)e^2\exp(-qr)/r+(E_Z-E_z)\delta_{Zz}, && r<R_0\\ &=-(Z-z)e^2\exp(-qr)/r, && r>R_0 \end{aligned} \tag{12}$$

where δ_{zZ} is the Kronecker delta, and R_0 the radius of the equivalent sphere of the lattice atoms. E_z is the energy of the lowest electronic state in the conduction band of the pure lattice, and E_Z is the lowest energy for an electron about the impurity atom, which is compressed or distended to fill a volume corresponding to its present position in the foreign lattice. A term proportional to (E_Z-E_z) should also be included for substitutional atoms of different valence, of course, although its contribution will be small for atoms of about the same atomic number because of the similarity of the electronic wave functions. For a pair such as Hg in Ag the effect of this term may be as large as the valence term, so we shall use Eq. (12) without the Kronecker delta in order to allow for the effect, at least formally, in all cases. For the other three cases, (1), (2), and (4), $w(\mathbf{r})$ is taken to be $-e^2\exp(-qr)/r$ multiplied by the appropriate quantity z, $-z$ and Z, respectively, plus a term corresponding to that just discussed which takes account of the change in average potential in the region of the singularity. The matrix elements $m(\kappa)$ [Eq. (8)] are readily evaluated, and the following results are obtained:

$$\begin{aligned} m_1(\kappa)&=\frac{-4\pi ze^2}{\Omega(\kappa^2+q^2)}+\frac{\Delta_1 E}{\Omega}4\pi R_0^3 f(\kappa R_0),\\ m_2(\kappa)&=\frac{4\pi ze^2}{\Omega(\kappa^2+q^2)}+\frac{\Delta_2 E}{\Omega}4\pi R_0^3 f(\kappa R_0),\\ m_3(\kappa)&=\frac{-4\pi(Z-z)e^2}{\Omega(\kappa^2+q^2)}+\frac{(E_Z-E_z)}{\Omega}4\pi R_0^3 f(\kappa R_0),\\ m_4(\kappa)&=\frac{-4\pi Ze^2}{\Omega(\kappa^2+q^2)}+\frac{\Delta_4 E}{\Omega}4\pi R_0^3 f(\kappa R_0), \end{aligned} \tag{13}$$

where $f(y)=(\sin y-y\cos y)/y^3$.

[7] D. L. Dexter, Phys. Rev. **86**, 447 (1952).

III. CALCULATION OF RESIDUAL RESISTANCE

The calculation of the resistivity from the Boltzmann transport equation proceeds in the manner described in reference 2; the change in the residual resistivity upon the introduction of N randomly spaced identical point singularities is found to be

$$\Delta\rho=\frac{z^2e^2m^{*2}N}{6\pi\hbar^3n^2}\int_0^\pi d\theta(1-\cos\theta)\times\sin\theta\frac{\Omega^2k^4}{\pi^2z^2e^4}|M(\kappa)+m(\kappa)|^2, \quad (14)$$

where the matrix elements are assumed to depend only on θ, the angle between $\mathbf{k}$ and $\mathbf{k}'$, and n is the density of free electrons in the pure lattice. We have now to consider only those values for $\mathbf{k}$ and $\mathbf{k}'$ which lie along the Fermi surface, so that $|\mathbf{k}|=|\mathbf{k}'|$ and $\kappa=|\mathbf{k}'-\mathbf{k}=2k\sin\frac{1}{2}\theta$. After making the substitution $x=\sin\frac{1}{2}\theta$, we insert the expressions for $m_1(\kappa)$ and $M(\kappa)$, Eqs. (13) and (9′), and obtain for the resistivity change associated with the addition of N interstitial lattice atoms the value

$$\Delta\rho_1=\frac{4z^2e^2m^{*2}N}{3\pi\hbar^3n^2}\int_0^1 x^3dx\left[\frac{-1}{a^2+x^2}+\Delta_1E\frac{(2kR_0)^2f(2kR_0x)}{(ze^2/R_0)}+\frac{4\pi A_1}{\Delta(a^2+x^2)}\frac{\sin2kr_0x}{2kr_0x}\right]^2. \quad (15)$$

The parameter a is defined as $q/2k$ and is of the order unity for the monovalent metals. To obtain the resistivity change associated with the presence of vacancies, substitutional atoms, and interstitial impurity atoms, it is necessary to replace the square-bracketed quantity above by the expressions

$$\left[\frac{1}{a^2+x^2}+\Delta_2E\frac{(2kR_0)^2f(2kR_0x)}{(ze^2/R_0)}+\frac{4\pi A_2}{\Delta(a^2+x^2)}\frac{\sin2kr_0x}{2kr_0x}\right]^2,$$

$$\left[-\left(\frac{Z}{z}-1\right)\Big/(a^2+x^2)+(E_Z-E_z)(2kR_0)^2\frac{f(2kR_0x)}{(ze^2/R_0)}+\frac{4\pi A_3}{\Delta(a^2+x^2)}\frac{\sin2kr_0x}{2kr_0x}\right]^2,$$

$$\left[-\frac{Z}{z(a^2+x^2)}+\Delta_4E\frac{(2kR_0)f(2kR_0x)}{(ze^2/R_0)}+\frac{4\pi A_4}{\Delta(a^2+x^2)}\frac{\sin2kr_0x}{2kr_0x}\right]^2,$$

respectively.

Before evaluating Eq. (15) let us investigate the magnitudes of the dimensionless parameters a^2, $2kR_0$, and $2kr_0$. According to the Thomas-Fermi approximation,[8] q^2 is equal to $(4m^*e^2/\hbar^2)(3n/\pi)^{\frac{1}{3}}$, so that $a^2\equiv q^2/4k^2$ is $m^*e^2/[\pi\hbar^2(3\pi^2n)^{\frac{1}{3}}]$, where we have made use of the relation $k^3=3\pi^2n$. Evaluating a^2 for copper with the use of specific heat data,[9] we set $m^*=1.47m_e$ and $n=0.85\times10^{23}$ cm^{-3}, so that a^2 becomes 0.65. Experimental resistance measurements indicate, however, that a^2 is of the order 1.5 for the monovalent metals. Such a discrepancy is to be expected from the Thomas-Fermi approximation.[2]

We now recall that r_0 is the inner cut-off radius for the contribution from the lattice distortions; thus r_0 must be determined in any particular case from the sizes of the atoms and the cavities available to them, and from the elastic constants of the medium. However, in most cases of practical interest r_0 will be of the order of R_0, the radius of the equivalent sphere for the lattice atoms. Using this value for r_0 in the present qualitative discussion, we find $2kr_0$ is equal to $2(3\pi^2n)^{\frac{1}{3}}(3n_{eff}/4\pi n)^{\frac{1}{3}}=3.84(n_{eff})^{\frac{1}{3}}$, where n_{eff} is the effective number of free electrons per atom, or about unity for the monovalent metals.

Equation (15) and the corresponding expressions for the other types of singularities can easily be integrated numerically in any particular case, once the values of the parameters are known. Since we are at the moment primarily interested in the corrections to the resistivity due to the effects of the lattice distortions, let us perform the following approximate evaluation of Eq. (15) in order to compare the contribution from the lattice distortions with the largest contribution from the other sources. In most cases where the shielded Coulomb effect exists, it represents the largest contribution to the resistance; consequently we shall compare the distortion scattering with the shielded Coulomb scattering in all cases but that of the substitutional atom of valence $Z=z$. Thus the following Eqs. (16-1), (16-2), and (16-3) are not to be considered evaluations of the resistance, but rather as expressions to indicate the relative importance of the lattice distortions. Leaving out the term proportional to Δ_1E, an approximate evaluation of Eq. (15), valid only for $4\pi A_1/\Delta$ less than unity, is found to be

$$\Delta\rho_1=\frac{2z^2e^2m^{*2}N}{3\pi\hbar^3n^2}\left(\ln\frac{a^2+1}{a^2}-\frac{1}{a^2+1}\right)[1-\eta(r_0)4\pi A_1/\Delta]. \quad (16\text{-}1)$$

The first term in the square brackets arises from the shielded Coulomb potential of the interstitial lattice atom, and the second from the lattice distortions. The corresponding expressions for vacancies and interstitial foreign atoms are

$$\Delta\rho_3=\rho_N[1+\eta(r_0)4\pi A_2/\Delta],$$
$$\Delta\rho_4=\rho_N[(Z/z)^2-(Z/z)\eta(r_0)4\pi A_4/\Delta], \quad (16\text{-}2)$$

[8] Reference 2, p. 87.

[9] F. Seitz, *Modern Theory of Solids* (McGraw-Hill Book Company, Inc., New York, 1940), Chap. IV.

respectively, where we have written ρ_N for the quantity

$$\rho_N=\frac{2z^2e^2m^{*2}N}{3\pi\hbar^3n^2}\left(\ln\frac{a^2+1}{a^2}-\frac{1}{a^2+1}\right). \quad (17)$$

η is unfortunately a rapidly varying function of r_0, being about 0.1 for $2kr_0$ equal to 3.84, i.e., for $r_0=R_0$, about 0.5 for r_0 equal to 4/5 R_0, and about -0.1 for $r_0=1.15R_0$. Because of this rapid variation of η with r_0, it is necessary to attempt to fix the proper value for r_0 from comparison with the summation in Eq. (9). It appears that for the vacancy or substitutional atom r_0 should be chosen somewhat larger than R_0, so that η is in the range 0.1 to -0.2. For the interstitial atom r_0 should be about R_0, so that η is of the order 0 to 0.2.

For the case of the substitutional atom of valence different from that of the lattice atoms the comparable resistivity change is

$$\Delta\rho_3=\rho_N[(Z/z-1)^2-(Z/z-1)\eta(r_0)4\pi A_3/\Delta]; \quad (16\text{–}3)$$

if the valences are the same, however, $\Delta\rho_3'$ becomes

$$\Delta\rho_3'=\frac{2z^2e^2m^{*2}N}{3\pi\hbar^3n^2}\left\{\frac{2(E_Z-E_s)^2(2kR_0)^4}{(ze^2/R_0)^2}\times\left[\int_0^1 f^2(2kR_0x)x^2dx+2\frac{(ze^2/R_0)(4\pi A_3'/\Delta)}{(E_Z-E_s)(2kR_0)^2}\times\int_0^1 f(2kR_0x)\frac{\sin 2kr_0x}{2kr_0x}\frac{x^3dx}{a^2+x^2}\right]\right\}, \quad (18)$$

on the assumption that the coefficient of the second integral is small in comparison with unity. The first integral has been evaluated numerically by Mott[1] for r_0 equal to the radius of the equivalent sphere of the lattice atoms, i.e., for $2kr_0$ equal to 3.84; he found the value of the first integral to be 4.0×10^{-3}. Using this same value for r_0 and evaluating the second integral numerically also, we find that it is equal to 3×10^{-3} for a^2 equal to 1.5. The above values for these integrals are typical of those for the monovalent metals; if a^2 is larger than 1.5, the second integral is somewhat smaller than the value quoted [by approximately the ratio $2/(a^2+0.5)$], and if r_0 is larger than the radius of the equivalent sphere for the lattice atoms, the second integral, corresponding to the lattice distortions, is reduced in about the same way as is η.

Equation (18) becomes, on inserting the above numerical results for the integrals,

$$\Delta\rho_3'=\frac{2z^2e^2m^{*2}N}{3\pi\hbar^3n^2}\left\{\frac{1.74(E_Z-E_s)^2}{(ze^2/R_0)^2}\times\left[1+\frac{0.10(4\pi A_3'/\Delta)(ze^2/R_0)}{(E_Z-E_s)}\right]\right\}. \quad (16\text{–}3')$$

From the Eqs. (16) we can now see the sign of the effects of the lattice distortions on the calculated resistance. In the expressions for $\Delta\rho_1$, $\Delta\rho_2$, and $\Delta\rho_4$ the signs of the A's are positive, negative, and positive, respectively; that is, the lattice is pushed out around an interstitial atom and relaxes around a vacancy. In these three cases, therefore [see Eqs. (16–1), (16–2), and (16–4)], the resistance is reduced by the inclusion of the effects of the lattice distortions, as long as η is positive. This conclusion is reasonable physically on the basis that in each case the relaxation of the lattice around the singularity tends to smooth out the perturbing potential. When η is negative, on the other hand, the scattering is increased by the distortion. This situation corresponds to a reinforcement of the scattered wave, even though the potential is of the opposite sign from the shielded Coulomb potential, because of the difference in phase of the electron wave in the regions where the two potentials are most effective.

In the calculation of $\Delta\rho_3$ [see Eq. (16–3)], the lattice distortions may either reduce or increase the resistance. For example, if a relatively small, light atom of valence higher than that of the lattice atoms is in a substitutional position, the distortions will further increase the magnitude of the scattering potential near the singularity and thus increase the resistance (for $\eta>0$). Similarly, for $\Delta\rho_3'$ [see Eq. (16–3′)] the distortions may either increase or decrease the calculated resistance; the effect of a heavier atom of the same valence will be to expand the lattice, but the electronic energy difference depends on the details of the wave functions, and E_Z-E_s may be negative, as for Au in Cu, or positive, as for Ag in Cu. In addition to these effects the sign of η may result either in a reduction or increase in the calculated resistance as a result of the distortions.

We have now to discuss the magnitudes of the parameters A; we shall first consider A_3, which characterizes the displacements around a vacancy. The relaxation around a vacancy has been estimated by Huntington and Seitz,[10] and by Huntington,[11] for the f.c.c. lattice of copper, and by Dienes[12] for copper and for the b.c.c. lattice of sodium. Huntington and Seitz[10] found that the nearest neighbors in Cu are displaced inward by an amount $\sim2\times10^{-2}\lambda$, where λ is the nearest neighbor distance. Thus A_2 is $-2\times10^{-2}\lambda^3$, and, since $1/\Delta=\sqrt{2}/\lambda^3$ in a f.c.c. crystal, $4\pi A_2/\Delta=-0.35$. In the accompanying more accurate treatment Huntington[11] estimated the inward displacement in Cu to be less than or equal to about $1\times10^{-2}\lambda$, and Dienes calculated $2\times10^{-2}\lambda$ for Cu and something less than this for the b.c.c. lattice of Na. For a displacement of $\sim2\times10^{-2}\lambda$ the correction to the resistance [see Eq. (16–2)] is of the order 5 percent.

It seems reasonable to assume, with regard to the estimates of the corrections to $\Delta\rho_3$ and $\Delta\rho_3'$, that the inward displacements are somewhat less around any

[10] H. B. Huntington and F. Seitz, Phys. Rev. **61**, 315 (1942).
[11] H. B. Huntington, Phys. Rev. **61**, 325 (1942).
[12] J. Dienes, AEC Report NAA-SR-144 (1951).

small substitutional impurity atom than they are around a vacancy. The relative correction to $\Delta\rho_3$ for the substitution of a smaller atom is thus, less than or of the order, $0.05/(-1+Z/z)$. The magnitude of the relative correction to $\Delta\rho_3'$ is $\gtrsim 0.02(ze^2/R_0)/(E_Z-E_z)$. For $E_Z-E_z\sim 2$ ev ($E_Z-E_z\sim 2$ ev for the case of copper in gold[9]), $z=1$, and $r_0=1.59$A (for gold), the correction is about 0.1.

The remaining situations, those of interstitial atoms and of substitutional atoms which are larger than the lattice atoms they replace, are all associated with a distension of the lattice. We can immediately restrict ourselves further, in the case of interstitial impurity atoms, to those which are smaller than the lattice atoms, since larger ones will not go into solid solution in interstitial positions; in the event that a large impurity is knocked from a normal lattice site into an interstitial position in the course, say, of nuclear bombardment, the lattice will tend to rearrange itself to exchange the positions of the large interstitial impurity and of a lattice atom.

Let us consider on the basis of the theory of elasticity for a continuous isotropic medium the problem of a spherical cavity, initially of radius R_1, into which we forcibly insert a sphere of material, initially of radius R_2, too large for the cavity.[13] We may obtain two values for A, depending on the two sets of boundary conditions we may impose at the periphery of the cavity. If we assume that the sphere is compressible, with about the same elastic constants as those of the medium, we obtain

$$A_c=\frac{R_1^3(R_2-R_1)}{R_1+2R_2/[1+3\nu/(1-2\nu)]}\sim\frac{R_1^3(R_2-R_1)}{R_1+R_2/2}, \quad (19)$$

where ν is Poisson's ratio. If we assume that the sphere is incompressible, on the other hand, we obtain

$$A_i=R_1^2(R_2-R_1). \quad (20)$$

In the case of the large, heavy substitutional atom the second boundary condition is probably the better, whereas for an interstitial lattice atom it is probably correct to consider the atom as being partially compressible. The two expressions (19) and (20) differ by about a factor of two for several of the interesting cases.

We shall associate with R_2 the radius of the atom, that is, one half of the nearest neighbor spacing λ in a pure crystal of that material, not the radius of the equivalent sphere. Discussing first the case of the substitutional atom, we see that it is not clear what length should be used for the radius R_1. R_1 cannot properly be taken to be the radius of the equivalent sphere for the displaced lattice atom, since such an assumption would allow no lattice distortion unless the impurity atom were at least 10 percent larger in diameter than the lattice atom it replaces. However, if we take R_1 to be half the nearest neighbor separation of the lattice, we are exaggerating the distortion inasmuch as we are not allowing the impurity atom to take advantage of the effectively larger radius of the cavity in directions other than directly toward the nearest neighbors. Nevertheless, we shall use $\lambda/2$ as the cavity radius for an approximate evaluation of $4\pi A_i/\Delta$ (thus exaggerating the distortion effects); we find for the f.c.c. lattice the value $4\pi A_i/\Delta=2.2(-1+\lambda'/\lambda)$, and for the b.c.c. lattice $4\pi A_i/\Delta=2.0(-1+\lambda'/\lambda)$. Thus [see Eq. (16–3)], the lattice distortions associated with the presence of a substitutional atom of 50 percent larger radius than that of the replaced atom would give rise to scattering of about 1/10 the magnitude of that from the shielded Coulomb potential from an atom of twice as high a valence as the lattice atoms. However, according to the Hume-Rothery rule, it is difficult experimentally to put an appreciable amount of impurity into a metal if the radius of the impurity atom is more than about 15 percent larger than that of the lattice atoms. For a divalent impurity in a monovalent lattice, consequently, the maximum correction to the shielded Coulomb scattering is of the order of or less than 5 percent. For a monovalent atom in a divalent lattice, though, the correction can become 10 percent, and for a divalent impurity in a trivalent lattice about 15 percent. These last corrections are too large to be ignored in careful interpretations of experimental results. Unfortunately, the separation of the effects of distortions is made difficult by the circumstance that as the impurity atom increases in size, thus increasing the effects of lattice distortions, so also increases the effects associated with the difference in the cores, about which relatively little is known theoretically; we have so far ignored these effects except for substitutional impurities of the same valence as the lattice atoms, but they are in fact sizable for atoms of much different atomic number, and furthermore are in some cases of opposite sign from those of lattice distortions. This point will be discussed further in the next section.

The distortion correction arising from a substitutional atom of the same valence as the lattice atoms likewise shows a dependence on the valence. For example, a gold atom has a radius 13 percent larger than that of a copper atom, and, according to the above model, i.e., Eq. (20), produces displacements in a copper lattice characterized by $4\pi A_i'/\Delta=0.28$. Taking $r_0(\mathrm{Cu})=1.41\times10^{-8}$ cm and $E_Z-E_z=-3$ ev,[1] we find [see Eq. (16–3′)] that the resistance may be changed about 5 percent by the lattice distortions from the value calculated on the basis of the inner potential alone. Divalent atoms with these relative sizes and with the same value for E_Z-E_z would result in a correction of 10 percent.

For discussion of the displacements of the lattice surrounding an interstitial atom we could, if necessary, use Eq. (19) and attempt to fix the radius of the interstitial hole from geometric arguments; however, our result would be extremely dependent on our assumptions because of the smallness of the cavity in compari-

[13] N. F. Mott and F. R. N. Nabarro, Proc. Phys. Soc. (London) 52, 86 (1940).

son with the interstitial atom. Fortunately we need not rely on the elastic theory of a continuous medium for the solution of this atomic problem, since the displacements of the nearest atoms have been estimated on an atomistic basis. Huntington and Seitz[10] have found a displacement of about 0.10 $a/2$ for the face-centered atoms in Cu (a=cube edge length), and Dienes[12] calculated 0.09 $a/2$ in Cu, and 0.30 $a/2$ for the displacement of the nearest atoms, those in body-centered positions, in sodium, on the assumption that the center of the cavity is located in the center of one face of the unit cell. These displacements lead to values for A of 0.1 $(a/2)^3$ in Cu and 0.3 $(a/2)^3$ in Na, so that $4\pi A_1/\Delta \sim 0.6$ in Cu and ~ 0.9 in Na. Thus, the scattering from the lattice distortions around interstitial atoms is of the order 1/10 that from the shielded Coulomb potential for a divalent impurity in Cu or Na.

IV. DISCUSSION OF RESULTS

In reviewing the above calculations with the intent of examining their validity, we recall that we have assumed potentials of the form $e\exp(-qr)/r$ for the various nuclei and their surrounding electrons (except for the substitutional atom of the same valence as the lattice atoms, in which case we added a square-well potential to take account of the difference in average potential throughout the atomic volume). Let us examine this assumption more closely to see what effect it has had on our results. We can be fairly confident of its approximate validity as applied to the evaluation of the Hamiltonian $W(\mathbf{r})$ [Eq. (4)] and the matrix element $M(\kappa)$ [Eq. (9)], which are both related to the effects of the lattice distortions, since the primary effect of the small displacement of a lattice atom can be described in terms of the motion of its shielded nuclear charge alone.[14] That this is so can be understood from the fact that the density of the lattice outside the imperfection is unchanged, so that no change occurs in the average potential of the unit cell. Of course, if the volume of the inner core is not small as compared with that of the equivalent atomic sphere, the "effective nuclear charge" may be larger than e times the valence of the atom; we shall ignore this possible effect, temporarily, and shall consider the only serious error in our evaluation of $M(\kappa)$ to arise from our value of the shielding constant q as calculated from the Thomas-Fermi approximation. We may evaluate the shielding constant experimentally from the resistance change associated with the addition of small amounts of substitutional impurity atoms of adjacent atomic number, for which the effects of lattice distortions and different electronic energies should be small. In the following it will be assumed that this has been done, so that for every metal our shielded Coulomb potential is correct. Thus we expect the relative magnitudes of the distortion effects as calculated above to be qualitatively correct, namely, of the order of or less than 10 percent; hence it is not possible to explain by these distortion effects the relatively large discrepancies between calculated and measured resistivities for solid solutions.

We have, however, introduced serious errors in our choices of potentials associated with the singularities themselves, whenever we have neglected the electronic energy difference, $E_Z - E_z$, throughout the region occupied by the singularity. That is, as pointed out earlier, Eqs. (16–1), (16–2), and (16–3) are not even approximately valid in absolute value. It is clear from the experimental data[15] that the effect of the ΔE term is large, and in some cases, e.g., for the substitution of Ag in Au, as large as the shielded Coulomb scattering from an atom of one higher valence (see Table I.) Terms of the above type, i.e., the ΔE terms, can easily be carried along in the scattering matrix elements, as was done up until the approximate evaluations of Eqs. (16). They have not been included in Eqs. (16) for the purpose of exhibiting explicitly the magnitude of the effects associated with lattice distortions.

In the remaining discussion we shall explicitly restrict ourselves to consideration of those metals to which the application of free-electron theory may be expected to be semiquantitatively correct, that is, to the alkali and noble metals. Let us now consider to what extent we are able to make quantitative predictions of resistance measurements. We have found that the lattice distortions around all the types of singularities treated give rise to corrections in the calculated resistance of the order of 5 or 10 percent. Experimentally we can measure the shielding constant q with much higher accuracy than we can calculate it, but it seems unlikely that even with adjacent metals in the periodic table we can eliminate all the effects but valence with an accuracy better than 5 or 10 percent. That is, even using experimentally demined values for q it is improbable that we can calculate resistances to within 10 percent, and it thus appears that distortion effects are of secondary importance.

It is interesting to note, however, that the lattice distortions play another role which in some cases is a very important one and may even lead to a difference of a factor of three or more in the calculated resistance. Consider, for example, the resistance associated with the additions of Cu to Ag. Mott[1] has estimated the term $E_Z - E_z$ for Cu in Ag from Wigner-Seitz calculations of the energy of the lowest electronic state as a function of the radius of the equivalent sphere and has calculated, neglecting all distortion effects, a resistance about one third that observed experimentally. Mott assumed, for the equivalent sphere radius of the Cu atom, the normal radius of the equivalent sphere for a silver atom in a pure silver lattice ando btained an energy difference $E_{Cu} - E_{Ag} = -0.5$ ev. Since the Cu atom is 13 percent smaller in radius than the Ag atom it replaces,

[14] J. Bardeen, Phys. Rev. **52**, 688 (1937), Table I; J. Bardeen and W. Shockley, Phys. Rev. **80**, 72 (1950).

[15] References to most of the pertinent data can be found in reference 2 and in E. Grüneisen, Ergeb. exakt. Naturwiss. **21**, 50 (1945).

we would expect some relaxation of the lattice, leading to an effective radius for the equivalent sphere for Cu somewhat smaller than that assumed by Mott. A displacement of the nearest neighbors equal to one fourth that calculated[10–12] around a vacancy, that is, $5\times10^{-3}\lambda$, would lead to a reduction of 3 percent for the radius of the equivalent sphere. Using this reduced radius, we find an energy difference -0.8 ev from the Wigner-Seitz energy calculations, thus leading to agreement with experiment. The displacement of $5\times10^{-3}\lambda$ was of course chosen *ad hoc*, but it is not an unreasonably large value, and the above example demonstrates how lattice distortions may have a large effect in cases where the energy curve for the impurity has a steep slope at the equivalent sphere radius of the lattice atoms, and where the energy difference is small. For Ag in Cu, on the other hand, the above effect is a small one, since the energy curve for Ag has a broad minimum between the sphere radii for Cu and Ag. When a shielded Coulomb term is present, as for a divalent impurity, the above effect likewise will be a relatively small one if the square well adds to the valence effect (as for Hg in Cu), since a square well of the order 2 ev deep is required to give rise to the resistance associated with a single charge, and the energy shifts according to the above mechanism can be only of the order of a few tenths of an ev. If the square well tends to cancel the valence term, as is the case, for example, with Cd in Cu, the above distortion effect could in principle be important, although in practice the writer does not know of an alloy for which it makes a significant contribution.

Throughout the foregoing discussion it has been assumed that the effective nuclear charge for all the monovalent metals is e. That this is a valid assumption for resistance calculations is indicated by the goodness of the agreement of Bardeen's calculations of resistance in the monovalent metals with the measured values, and in particular by the circumstance that his results for Au are no worse than for Cu although an effective nuclear charge of e was assumed for both metals. Another argument supporting this conclusion derives from measurements of the resistivity of solid solutions of the monovalent metals, such as Cu in Ag. If the effective nuclear charges of any of these metals were different from e, certainly gold would be expected to have one of the largest because of its large inner core, and conversely, copper would be expected to have the smallest (of the noble metals) because of its relatively small core; furthermore, one would expect to find a relatively large difference in their effective charges because of the large difference in their core sizes. Stating this again in a slightly different way, unless the effective charges are all close to e, it seems difficult to understand how they can all be equal. But the smallness of the experimental resistivities of dilute monovalent alloys and the close agreement[1] with experiment of most of these resistivities calculated with the square well potentials as described above show that the differences in the effective nuclear charges must be small compared with e; therefore, we conclude that they are all closely equal to e. A third argument in support of this conclusion is based on the measured resistivities of Cu, Ag, and Au containing divalent, trivalent, and tetravalent impurities.[16] These measurements show that the scattering from the impurities of valence Z is approximately proportional to $(Z-1)^2$. If the effective nuclear charge of Au were appreciably larger than that for Cu, for example, one would expect large discrepancies in this proportionality, and in particular, one would expect to find a negative slope in a plot of resistivity change in Au *versus* $(Z-1)^2$ for the impurity series Cu, Zn, Ga, Ge. The consistency of these data with the interpretation on the basis of the valence effect is a strong indication that the effective nuclear charges for the noble metals are all very close to e.

TABLE I. Measured resistivity change (see reference 16) in micro-ohm cm of the metal s upon the addition of one atomic percent of the element Z.

in s / Z Percent of Z	Au Measured value	Ag Measured value	Cu Measured value	Cu Reduced value
Hg	0.41	0.79	1.00	1.13
Cd	0.64	0.38	0.21	0.24
Zn	0.96	0.62	0.34	0.38
Au	...	0.38	0.55	
Ag	0.38	...	0.14	
Cu	0.48	0.07	...	

The measurements of Linde[16] shown in Table I provide an excellent test for our understanding of the resistivities of dilute substitutional alloy; if these data can be interpreted on the basis of the electronic energy dffierence, the valence, and the distortion effects, one might hope to be able to compute in the same way the resistance change in a monovalent metal upon the introduction of vacancies and interstitials. The resistivity changes in Cu, Ag, and Au (in micro-ohm cm) upon the introduction of one atomic percent of monovalent or divalent impurities are shown in the first three columns. According to Eqs. (16–3) and (17) the resistivity change is approximately proportional to $n^{-\frac{1}{3}}$, as may be seen by expanding the logarithm in Eq. (17). Thus in the fourth column we have multiplied the value for Cu by the ratio of the atomic radii for Ag and Au to that for Cu, in order to make the values for Cu directly comparable with those for Ag and Au. The most striking feature to notice is that for the addition of those elements for which we expect only valence effects to be important, i.e., for Hg in Au, Cd in Ag, and Zn in Cu, the resistivity changes are indeed very similar, 0.41, 0.38, and 0.38 $\mu\Omega$ cm, respectively. This result indicates that the dependence of the Thomas-Fermi shielding constant q on density is correct, and also indicates that such effects as the association of vacancies with the

[16] J. O. Linde, Ann. Physik (5) **15**, 239 (1932).

divalent impurity atoms are unimportant for an interpretation of these data.

Most of these data for Cu, Ag, Au in Cu, Ag, and Au can be interpreted on the basis of the square well potential, as Mott has shown.[1] It should be pointed out, however, that the resistivity changes of Cu in Au and of Ag in Au are not consistent with the square well potential. That is, if the electronic energy for Cu is 0.8 ev lower than that for Ag, as indicated by the Wigner-Seitz calculations and by the measured resistivity change for Cu in Ag, then the height of the square well for Cu in Au should be 0.8 ev less than for Ag in Au (1.9 ev as measured by resistivity change), or should be 1.1 ev instead of the measured 2.1 ev; stating this again in a slightly different way, accepting the measured resistivities for Cu in Ag and for Ag in Au, we would predict a resistivity change of 0.126 $\mu\Omega$ cm rather than the observed change of 0.485 $\mu\Omega$ cm for Cu in Au. Distortion effects cannot significantly improve this discrepancy, nor is it possible to construct a reasonable, internally consistent set of effective nuclear charges and square wells that will explain all of these results, even if we wished to change the effective nuclear charges. Thus it appears that the details of the wave functions and potentials are important for interpreting some of these resistance data.

Similarly the data for Hg, Cd, and Zn in Cu, Ag, and Au cannot be satisfactorily understood on the basis of valence, square well, and distortion effects. For example, one can explain Zn in Ag giving rise to a larger resistivity change than Zn in Cu, but one cannot explain the even larger change for Zn in Au; the result for Cd in Cu is understandable, but not that for Cd in Au. Again it is not possible to interpret all of the data in a reasonable way by assigning different effective nuclear charges to the various atoms.

Our conclusions from all of the above arguments are that the valence and effective nuclear charge effects alone are fairly well understood, and that the rough approximation of a square-well potential is not sufficient to account for the specific potentials and wave functions in most of these simple systems. Consequently, we do not believe that it is reasonable to expect to be able to compute the scattering from vacancies and interstitials on the same approximations. Nevertheless, since the valence effect does seem to be constant from one metal to the next and since there is relatively little spread in the measured resistivity changes for divalent impurities, it seems safe to choose a value in this range for the addition of vacancies and interstitials to the lattice. The writer's estimate of the resistivity change in Cu, Ag, and Au per atomic percent of imperfection is ~ 0.4 $\mu\Omega$ cm for vacancies and ~ 0.6 $\mu\Omega$ cm for interstitials. These values are probably good to within a factor of two.

To make more precise statements than the above concerning the scattering from interstitials and vacancies seems a formidable problem involving a self-consistent calculation for the potential and displacements near the singularity, a calculation in which modifications to the d shell probably are important. Until better approximations are likewise made for the electronic wave functions and for the solution of the Boltzmann transport equation and until more is known about the "effective number of free electrons per atom" and the electronic effective mass, it is questionable if such a calculation is warranted.

We have now to discuss the previously neglected effects arising from the uniform dilation of the lattice. In Sec. II we assumed displacements of the form $\mathbf{U}=A\mathbf{r}/r^3$ instead of the general form $A\mathbf{r}/r^3+B\mathbf{r}$. The second term is responsible for a uniform density change throughout the metal, and will lead to a change in resistivity just as does the application of a hydrostatic pressure. The latter effect can be qualitatively accounted for[17] in most cases on the basis of the change in amplitudes of the lattice vibrations associated with the strengthened atomic forces in the compressed metal. Thus the density change gives rise to a temperature dependent resistance change which should not be treated on the same basis as the changes in the residual resistance discussed above. At constant temperature, however, the change in the measured resistivity of a sample after the introduction of point singularities will depend not only on the factors discussed in Secs. II–IV, but also on the density change of the material associated with the parameter B. Furthermore, in an interpretation of experimental resistance measurements, it must be borne in mind that the dimensions of the sample also change, both because of the B term and also the A term, and thus the resistivity of the material would have changed even if the measured resistance remained constant. The correction to the resistivity because of this last effect is in all cases small compared with those previously discussed.

We may obtain an estimate of the magnitude of the density change effect from the following considerations. Suppose that a metallic sphere, initially of radius R, has introduced into it a number N identical singularities. Then the density D is changed by an amount

$$\delta D \cong -DN\nabla\cdot\mathbf{U}=-3BDN, \tag{21}$$

where B is given by $2A(1-2\nu)/R^3(1+\nu)$. Now the change in resistivity $\delta\rho$ is given by

$$\frac{\delta\rho}{\rho}=\frac{d(\log\rho)}{d(\log D)}\frac{\delta D}{D}$$

$$=-\frac{d(\log\rho)}{d(\log D)}\frac{2N\Delta}{\Omega}\left(\frac{1-2\nu}{1+\nu}\right)\left(\frac{4\pi A}{\Delta}\right), \tag{22}$$

or about $(3/2)(4\pi A/\Delta)f$, where f is the number of singularities per lattice atom, and where we have made use of the observed[17] resistivity dependence on density,

[17] See, for example, reference 2, p. 271.

namely, $d(\log\rho)/d(\log D)\sim -3$ for most metals. Since we found above that $4\pi A/\Delta$ is of the order of or less than 2/3, the fractional resistivity change associated with the change in density is of the order of or less than one percent in the presence of one percent singularities. This change is small ($\sim 1/10$) compared with the residual resistance change arising from the shielded Coulomb term or the electronic energy difference term discussed above, and of about the same magnitude as that associated with the lattice distortions, i.e., the A term.

In conclusion, mention should be made of the implications of the foregoing to studies of densities of imperfections in metals. For example, in Seitz's[18] discussion of the generation of vacancies by moving dislocations, he used a scattering cross section of vacancies for electrons 25 times larger than the estimate given above and obtained a very conservative value for the density of vacancies in Cu at liquid air temperatures. His estimate was based on the measured[19] resistivity change in Cu after straining by about 10 percent at liquid air temperatures, namely, 0.019 $\mu\Omega$ cm, and on the assumption that all or most of the resistivity change is associated with the presence of vacancies. His result for the concentration of vacancies under these conditions of 1.6×10^{18} cm^{-3} would become, if the present estimate for the vacancy cross section is correct, equal to 4×10^{19} cm^{-3}. Since the energy required to create a vacancy is about 1 ev, this concentration of vacancies represents a storage of about 4×10^{19} ev/cm^3 and since the energy expended in straining the lattice by 10 percent is 7.5×10^{19} ev/cm^3, these arguments would suggest that at least half of the energy of cold work is stored at liquid air temperatures.[20]

It is of interest to inquire if the low temperature data are consistent with the hypothesis that dislocations are predominantly responsible for the resistivity change in Cu. If the resistivity change per line cm of edge-type dislocation[7] is 1.7×10^{-14} $\mu\Omega$ cm and the energy stored[21] per cm is 1.6×10^5 ev, the resistivity change per unit stored energy is 1.06×10^{-22} $\mu\Omega$ cm per ev. This value is to be compared with 4.7×10^{-22} $\mu\Omega$ cm per ev for vacancies. That is, for a given amount of stored energy, vacancies have about 4 times as large an effect on the resistivity as do edge-type dislocations. Thus even if all the energy expended in cold work at low temperatures were stored in the form of dislocations, the resistivity change would be only about half of that observed. A similar result is found for the room temperature data, namely, that it does not seem possible to explain all of the observed resistivity change associated with cold-working on the basis of scattering from dislocations alone.[7] If many vacancies are produced by moving dislocations, as suggested by Seitz,[18] it seems possible that at room temperatures they are able to clump together into cavities of the type recently proposed by Blin and Guinier[22] as a result of small-angle x-ray scattering experiments, and that an interpretation of room temperature data on cold-worked specimens also may be based on vacancy effects.

V. SUMMARY

We have estimated the contributions to the electrical resistance arising from distortions of the lattice around vacancies, interstitials, and substitutional impurity atoms, and have shown that the scattering associated with distortion of the lattice outside of the imperfection itself leads to a correction sufficiently small, of the order 5 or 10 percent, to be neglected in all practical calculations capable of being performed at present. The reasons for the smallness of the correction are: (1) the smallness of $4\pi A/\Delta$, that is, the smallness of the distortion, and (2) the smallness of η because of the effective cancellation of the scattered wave associated with the rapid variation of its phase in the regions where the distortion is sizeable. We conclude that accurate interpretations of resistance measurements cannot be expected on the basis of the effects discussed by Mott for substitutional impurities, i.e., the valence and the energy difference effects, and that in many cases a difficult self-consistent calculation is required for both the displacements and potential near the singularity. The resistivity change in Au, Ag, and Cu associated with one atomic percent of vacancy-interstitial pairs is estimated to be about 1 micro-ohm cm. A brief discussion of deviations from Matthiessen's rule shows that such effects are small ($\lesssim 1/10$) compared with valence effects.

The writer is indebted to Professor J. S. Koehler for interesting discussions of his radiation damage experiments, to Dr. J. D. Eshelby for helpful conversations about the effects of surface stresses in elastic theory, to Dr. Peter Gibbs for a useful suggestion regarding the summation in Eq. (9), and to Professors F. Seitz and J. Bardeen for their kind interest in this work.

[18] F. Seitz, Phil. Mag. Supplement **1**, 43 (1952).
[19] J. Molenaar and W. H. Aarts, Nature **166**, 690 (1950).
[20] Energy storage measurements by G. I. Taylor and H. Quinney [Proc. Roy. Soc. (London) **143**, 307 (1934); **163**, 157 (1937)]; B. Welber [Phys. Rev. **87**, 211 (1952)]; and H. Kanzaki [J. Phys. Soc. Japan **6**, 456 (1951)] indicate that the energy stored during cold-working at room temperature is only about 3 percent of the expended energy, thus suggesting considerable annealing below room temperature, in agreement with the experiments of Molenaar and Aarts (see reference 19), Koehler (see reference 4) and others.
[21] J. S. Koehler, Phys. Rev. **60**, 397 (1941).
[22] J. Blin and A. Guinier, Compt. rend. **233**, 1288 (1951).

The Scattering of Elementary Particles by Complex Nuclei—A Generalization of the Impulse Approximation

GEOFFREY F. CHEW,
Physics Department, University of Illinois, Urbana, Illinois

AND

M. L. GOLDBERGER,
Institute for Nuclear Studies and Physics Department, University of Chicago, Chicago, Illinois

(Received May 19, 1952)

By a systematic iteration procedure it is shown how the problem of the scattering of an elementary particle by a complex nucleus (or any many-particle target system) can be expressed in terms of two-body operators. The results are related to the previous work of Chew and Wick on the impulse approximation, with special attention given to multiple scattering effects which have heretofore not been formulated in a rigorous way. An explicit formula for the double scattering terms is presented.

I. INTRODUCTION

IN a recent paper,[1] hereafter referred to as I.A., Chew and Wick have presented a tentative analysis of the problem of the scattering of elementary particles by complex nuclei. They discuss the nature of the errors involved in treating such problems by the so-called "impulse approximation" introduced earlier by Chew.[2] The basic idea of this method may be stated as an attempt to represent the scattering amplitude from a complex nucleus as a superposition of scattering amplitudes from "free" nucleons which have the same momentum distribution as the initially bound nucleons. The assumptions under which the approximation is valid were stated to be the following: (I) The incident particle interacts only with one single nucleon at a time. (II) The amplitude of the incident wave is not appreciably diminished in crossing the nucleus. (III) The binding force has a negligible effect during the interval of strong interaction. Of these three assumptions, only (III) was discussed quantitatively in I.A. and even so, the mathematical treatment was based on a variational method which appeared unnecessarily devious. Shortly after the paper was submitted, Ashkin and Wick[3] succeeded in making a straightforward treatment of (III) for the case of the scattering by a single bound nucleon. The purpose of the present paper is to present a formal solution to the complete problem of expressing the scattering from a complex nucleus in terms of two particle operators. Our results include those of Ashkin and Wick as a special case and also permit a systematic discussion of assumptions (I) and (II).

II. FORMULATION AND SOLUTION OF THE PROBLEM

The problem is that of the scattering of a particle by a complex nucleus. The total Hamiltonian is (following the notation of I.A.)

$$H=H_0+V, \tag{1}$$

with

$$H_0=K+U. \tag{2}$$

K is the total kinetic energy operator, U the nuclear potential energy, and V is the total interaction between the nucleus and incoming particle. We shall suppose V to be of the form

$$V=\sum_{k=1}^{N} V_k, \tag{3}$$

where V_k is the interaction potential between the projectile and the kth nucleon. H_0 is the "unperturbed" Hamiltonian in terms of which the initial and final nucleus plus free particle states are classified. (We shall not be concerned here with the so-called pick-up processes in which the incident particle forms a bound state with one of the target nucleons). By adopting the formalism of Lippmann and Schwinger,[4] the exact solution of our problem may be expressed in terms of either of two state functions $\Psi_a^{(+)}$, $\Psi_b^{(-)}$ which satisfy the integral equations

$$\Psi_a^{(+)}=\Phi_a+\frac{1}{E_a+i\eta-H_0}V\Psi_a^{(+)}, \tag{4a}$$

$$\Psi_b^{(-)}=\Phi_b+\frac{1}{E_b-i\eta-H_0}V\Psi_b^{(-)}, \tag{4b}$$

where the Φ_a and Φ_b are eigenfunctions of H_0 belonging to the same energy E, the total energy of the system. In terms of these functions, the matrix elements of the operator T, the square of which is essentially the transition probability of interest, may be written as

$$T_{ba}=(\Phi_b, V\Psi_a^{(+)})=(\Psi_b^{(-)}, V\Phi_a), \tag{5}$$

with $E_a=E_b=E$.

We now replace the fundamental Eqs. (4) by operator

[1] G. F. Chew and G. C. Wick, Phys. Rev. **85**, 636 (1952).
[2] G. F. Chew, Phys. Rev. **80**, 196 (1950).
[3] J. Ashkin and G. C. Wick, Phys. Rev. **85**, 686 (1952).
[4] B. Lippmann and J. Schwinger, Phys. Rev. **79**, 481 (1950).

equations. Define two operators $\Omega^{(+)}$ and $\Omega^{(-)}$ by

$$\Omega^{(+)}\Phi_a=\Psi_a^{(+)}, \tag{6a}$$

$$\Omega^{(-)\dagger}\Phi_b=\Psi_b^{(-)}, \tag{6b}$$

where † means Hermitian adjoint. (We here deviate from the notation of I.A. where the symbol Ω is used to represent the operator designated in this paper by $\omega^{(+)}$.) The Φ are assumed to be a complete set so that (6) defines the operators $\Omega^{(\pm)}$. They satisfy the equations

$$\Omega^{(+)}=1+\frac{1}{E_a+i\eta-H_0}V\Omega^{(+)}, \tag{7a}$$

$$\Omega^{(-)}=1+\Omega^{(-)}V\frac{1}{E_b+i\eta-H_0}, \tag{7b}$$

so long as $\Omega^{(+)}$ is always going to operate on Φ_a to the right and $\Omega^{(-)}$ on Φ_b* to the left. The operator Eqs. (7) may actually be freed of all reference to the states Φ_a and Φ_b by writing them as

$$\Omega^{(+)}=1-i\int_{-\infty}^{0}dx e^{\eta x}e^{iH_0x}V\Omega^{(+)}e^{-iH_0x}, \tag{8a}$$

$$\Omega^{(-)}=1-i\int_{-\infty}^{0}dx e^{\eta x}e^{-iH_0x}\Omega^{(-)}Ve^{iH_0x}. \tag{8b}$$

We shall continue, however, to use the forms given by (7) since there is no loss in generality.

In terms of $\Omega^{(\pm)}$ we may write expressions for operators $T^{(+)}$ and $T^{(-)}$ which have equal matrix elements between states Φ_a and Φ_b of the same energy and are both equal to the operator defined by Eq. (5) in such a case. We define

$$T^{(+)}=V\Omega^{(+)}, \tag{9a}$$

$$T^{(-)}=\Omega^{(-)}V. \tag{9b}$$

In the Appendix it is shown that, except for the time reversal unitary transformation, $\Omega^{(-)}$ is the transpose of $\Omega^{(+)}$ and $T^{(-)}$ is the transpose of $T^{(+)}$. Thus, it is really only necessary to write equations for the (+) operators. However, because the properties of the time reversal unitary transformation are familiar to only a small number of people, we have elected to write out the two equations in most cases.

The fundamental step of our development and the first original contribution of this paper is the recognition of the fact that the Eqs. (7) can be written in the form

$$\Omega^{(+)}=1+\frac{1}{E_a+i\eta-H_0-V}V, \tag{10a}$$

$$\Omega^{(-)}=1+V\frac{1}{E_b+i\eta-H_0-V}, \tag{10b}$$

as one may verify by expanding in powers of V and comparing with the iteration solution of Eqs. (7), or by operating on (10a), say with $(E_a+i\eta-H_0)^{-1}V$ and observing that the equation which results after some manipulation is just the first of Eqs. (7). It is clear that (10a) and (10b) may also be written

$$\Omega^{(+)}=1-i\int_{-\infty}^{0}dx e^{\eta x}e^{i(H_0+V)x}Ve^{-iH_0x}, \tag{11a}$$

$$\Omega^{(-)}=1-i\int_{-\infty}^{0}dx e^{\eta x}e^{-iH_0x}Ve^{i(H_0+V)x}. \tag{11b}$$

The physical meaning of the operators $\Omega^{(+)}$ and $\Omega^{(-)}$ is most clearly seen in the formalism of Ashkin and Wick,[3] who do not eliminate the time as we have done here. They show, for example, that if the system is in the state Φ_a "before" the collision, $\Omega^{(+)}$ is the operator which transforms Φ_a into the state $\Psi_b^{(+)}$ which exists "during" the collision. It is perhaps unfortunate that in the formalism used here, which deals with a stationary state of the system, the concept of collision time is obscure. The advantage of the stationary state approach, of course, is that one avoids the introduction of wave packets.

The forms of Eqs. (10) and (11) are such that we may easily develop an expansion of $\Omega^{(\pm)}$ (or $T^{(\pm)}$, using Eq. (9)) in powers of U. Such an expansion for the single scatterer problem was the object in I.A. and in the work of Wick and Ashkin.[3] The procedure of keeping only the zeroth-order terms of these expansions (terms independent of U) is quite properly referred to as the impulse approximation, since it corresponds to neglecting the effect of the binding field during the collision. However, when more than one target scatterer is present, as is always the case in a complex nucleus, the evaluation of these zeroth-order terms still requires solution of a many-body problem. We need to make a further approximation in order to obtain a workable formula, and the systematic formulation of this further approximation will be the second essential contribution of this paper.

The formal expression for the operator $T^{(+)}$ is

$$T^{(+)}=V+V\frac{1}{E_a+i\eta-H_0-V}V. \tag{12}$$

This expression, while exact and representing the formal solution of the complete problem, is of course not easily evaluable. We proceed then to rewrite (12) in a form suitable under certain conditions to an approximate evaluation. First we introduce the two particle scattering matrices $t_k^{(+)}$ and $t_k^{(-)}$ for the kth nucleon, defined by

$$(t_k^{(+)})_{mn}=(\chi_m, V_k\psi_{n,k}^{(+)}), \tag{13a}$$

$$(t_k^{(-)})_{mn}=(\psi_{m,k}^{(-)}, V_k\chi_n), \tag{13b}$$

where the ψ's are solutions of the equations

$$\psi_{l,k}^{(\pm)}=\chi_l+\frac{1}{E_l\pm i\eta-K}V_k\psi_{l,k}^{(\pm)}. \tag{14}$$

The χ's are eigenfunctions of K, and E_l is the eigenvalue of K belonging to χ_l. It is essential to differentiate between $t_k^{(+)}$ and $t_k^{(-)}$ since we require their matrix elements between states of unequal energy. We also introduce the analogs of Eqs. (9) and (10):

$$t_k^{(+)}=V_k\omega_k^{(+)}, \tag{15a}$$

$$t_k^{(-)}=\omega_k^{(-)}V_k, \tag{15b}$$

where

$$\omega_k^{(+)}=1+\frac{1}{E_l+i\eta-K-V_k}V_k, \tag{16a}$$

$$\omega_k^{(-)}=1+V_k\frac{1}{E_l+i\eta-K-V_k}. \tag{16b}$$

The validity of (16) requires $\omega_k^{(+)}$ to be operating to the right on χ_l and $\omega_k^{(-)}$ to be operating to the left on χ_l^*.

At this point a fundamental identity is to be derived. Let the symbol $B^{(+)}$ represent any operator of the form

$$B^{(+)}=\frac{1}{E_a+i\eta-H_0-V}A, \tag{17}$$

where A is an arbitrary operator. Let $b_k^{(+)}$ represent a corresponding operator,

$$b_k^{(+)}=\frac{1}{E_l+i\eta-K-V_k}A. \tag{18}$$

The relation between (17) and (18) is as follows:

$$B^{(+)}=b_k^{(+)}+(1/E_a+i\eta-H_0-V)\times\{[U, b_k^{(+)}]+(V-V_k)b_k^{(+)}\}. \tag{19a}$$

This identity is proved by the technique introduced in I.A., Eqs. (25) to (28). The method consists of writing $\Phi_a=\sum_l\chi_l(\chi_l, \Phi_a)$ and using the operator relation $(P-Q)^{-1}-P^{-1}=(P-Q)^{-1}QP^{-1}$, together with $H_0\Phi_a=E_a\Phi_a$. There also exists, of course, a relation corresponding to (19a) for $(-)$ type operators, $B^{(-)}=A(E_b+i\eta-H_0-V)^{-1}$:

$$B^{(-)}=b_k^{(-)}+\{[b_k^{(-)}, U]+b_k^{(-)}(V-V_k)\}1/(E_b+i\eta-H_0-V). \tag{19b}$$

It is important to notice that the identities (19a) and (19b) can be used over and over again in a kind of iteration procedure.

To make a first application of our identities, let us rewrite Eq. (12) as

$$T^{(+)}=\sum_{k=1}^{N}\left\{V_k+V\frac{1}{E_a+i\eta-H_0-V}V_k\right\}. \tag{20}$$

We can apply (19a) to obtain

$$\frac{1}{E_a+i\eta-H_0-V}V_k=(\omega_k^{(+)}-1)+\frac{1}{E_a+i\eta-H_0-V}\times\{[U, \omega_k^{(+)}]+(V-V_k)(\omega_k^{(+)}-1)\},$$

which when substituted into (20) with a slight rearrangement of terms, yields

$$T^{(+)}=\sum_{k=1}^{N}\left\{t_k^{(+)}+V\frac{1}{E_a+i\eta-H_0-V}[U, \omega_k^{(+)}]+\left[1+V\frac{1}{E_a+i\eta-H_0-V}\right](V-V_k)(\omega_k^{(+)}-1)\right\}. \tag{21}$$

The importance of breaking up $T^{(+)}$ in this way is that often the part, $\sum_k t_k^{(+)}$, is much larger than the remaining two parts, and the operator, $t_k^{(+)}$, is relatively tractable, depending only on the kth target particle and the incident particle. An adequate and workable approximation in many cases is thus obtained by evaluating $\sum_k t_k^{(+)}$ exactly and either neglecting completely the last two parts of (21) or approximating them by further iteration as shown below.

The significance of the last two terms is suggested by the observation that in general when U vanishes, the term containing $[U, \omega_k^{(+)}]$ vanishes, while the other remains. On the other hand, when there is only a single target particle, the term containing $(V-V_k)(\omega_k^{(+)}-1)$ vanishes, independently of U. The connection with the arguments given in I.A. is, therefore, as follows: The term proportional to $[U, \omega_k^{(+)}]$ represents the error associated with assumption III, the impulse assumption. The term proportional to $(V-V_k)(\omega_k^{(+)}-1)$ combines the error due to assumptions I and II. We might call this either the multiple scattering error or the opacity error, neither name being perfect. One thing is clear at this point. The name "impulse approximation," which has been given to the procedure of neglecting *both* the last two parts of (21), is misleading, since it suggests that multiple scattering effects are not omitted.

III. THE ERROR CAUSED BY THE IMPULSE ASSUMPTION

By making use of (10b), (7b), and (9b) one sees that, for transitions to states Φ_b of the same energy as $\Phi_a(E_b=E_a=E)$, the second part of (21) is the same as the expression derived in I.A. for a single target particle:

$$V\frac{1}{E+i\eta-H_0-V}[U, \omega_k^{(+)}]=[\Omega^{(-)}-1][U, \omega_k^{(+)}]=T^{(-)}\frac{1}{E+i\eta-H_0}[U, \omega_k^{(+)}]. \tag{22}$$

A first approximation to (22) is obtained by application of (19b):

$$V\frac{1}{E+i\eta-H_0-V}=\sum_k V_k\frac{1}{E+i\eta-H_0-V}=\sum_k(\omega_k^{(-)}-1)+\sum_k\{[\omega_k^{(-)}, U]+(\omega_k^{(-)}-1)(V-V_k)\}\frac{1}{E+i\eta-H_0-V}. \tag{23}$$

Regarding this as the second step of an iteration procedure, it is consistent to keep only the term $\sum_k(\omega_k^{(-)}-1)$ if the iteration is converging rapidly. Thus (22) is approximated by

$$\sum_k\sum_{k'}(\omega_{k'}^{(-)}-1)[U,\omega_k^{(+)}]$$
$$=\sum_k\sum_{k'}t_{k'}^{(-)}\frac{1}{E_l+i\eta-K}[U,\omega_k^{(+)}]. \quad (24)$$

The statements made in I.A. as to the conditions under which this error is small need no modification here. It should be noted that the result of Wick and Ashkin[3] corresponds to the original form of this term given in (21), i.e., the form which is valid for all matrix elements of $T^{(+)}$ and which may be expressed without reference to Φ_a as

$$-iV\int_{-\infty}^{0}dx e^{\eta x}e^{i(H_0+V)x}[U,\omega_k^{(+)}]e^{-iH_0x}. \quad (25)$$

IV. THE MULTIPLE SCATTERING ERROR

The third term of (21) can also be written in a variety of ways for transitions which conserve the energy, since

$$1+V\frac{1}{E+i\eta-H_0-V}=\Omega^{(-)}=T^{(-)}V^{-1}. \quad (26)$$

Thus, a possible form for the multiple scattering term in (21) is

$$\sum_{k=1}^{N}T^{(-)}V^{-1}(V-V_k)(\omega_k^{(+)}-1).$$

The following qualitative interpretation may be given this expression: The factor $(\omega_k^{(+)}-1)$ represents the outgoing wave from the kth nucleon. If the interaction between the incident particle and the individual nucleons is of short range in configuration space, then the dimensionless operator $V^{-1}(V-V_k)$ is localized at the positions of all the nucleons except the kth. Thus, the contribution of the kth term to the sum is proportional to the amplitude of the outgoing wave from the kth nucleon, evaluated at the positions of all the other nucleons. This is precisely the situation surmised on an intuitive basis in I.A. We have no reason to change the rough qualitative estimates made in that paper of the multiple scattering, but we can now give a formula suitable to quantitative calculation in the general case.

To obtain this formula, we carry out for the multiple scattering part of (21) the rearrangement (23) and again keep only the term $\sum_k(\omega_k^{(-)}-1)$. Thus, the multiple scattering term in first approximation is

$$[1+\sum_{k'}(\omega_{k'}^{(-)}-1)]\sum_k(V-V_k)(\omega_k^{(+)}-1). \quad (27)$$

Noticing that $\sum_k(V-V_k)(\omega_k^{(+)}-1)$ may be written $\sum\sum_{k\neq k''}V_{k''}(\omega_k^{(+)}-1)$, and remembering (15b), it is possible to re-express (27) as

$$\sum_{k'}\sum_{\neq k}t_{k'}^{(-)}(\omega_k^{(+)}-1)$$
$$+\sum_{k''}\sum_{\neq k'}\sum_{\neq k}(\omega_{k'}^{(-)}-1)V_{k''}(\omega_k^{(+)}-1). \quad (28)$$

The first part of (28) clearly represents double scattering, and this is, of course, very plausible as a next approximation to the single scattering terms $\sum_k t_k^{(+)}$. The second part of (28) involves three particles and should be neglected unless higher order terms are also kept in (23). Thus the final result for the first-order multiple scattering (double scattering) is

$$\sum_{k'}\sum_{\neq k}t_{k'}^{(-)}(\omega_k^{(+)}-1)$$
$$=\sum_{k'}\sum_{\neq k}t_{k'}^{(-)}\frac{1}{E_l+i\eta-K}t_k^{(+)}. \quad (29a)$$

It is worth recalling here a fact pointed out in I.A. We might just as well have begun by rearranging $T^{(-)}$ as $T^{(+)}$ and would then have arrived at $\sum_k t_k^{(-)}$ as a first approximation, with the double scattering term

$$\sum_{k'}\sum_{\neq k}(\omega_k^{(-)}-1)t_{k'}^{(+)} \quad (29b)$$

and the impulse correction term

$$\sum_k\sum_{k'}[\omega_k^{(-)},U](\omega_{k'}^{(+)}-1). \quad (30)$$

The two alternate forms are essentially the transposes of each other, and Blatt[5] has pointed out that if one wishes explicitly to maintain the property of detailed reversibility one should take the mean of the two. Actually, as shown by Ashkin and Wick,[3] the difference between the two is less than the residual error in the approximation.

APPENDIX

The material to be presented in this Appendix[6] is not intended to be an exhaustive discussion of the subject of time reversal but rather only to clarify the remarks made above. We assume that the Hamiltonian of our system may be written as $H=H_0+V$. If a system described by a state vector $\Psi(t)$ which satisfies the time dependent Schoedinger equation,

$$i\partial\Psi(t)/\partial t=H\Psi(t), \quad (A1)$$

is to be invariant under time reversal, then the state vector $\Psi(-t)$, which evidently satisfies

$$-i\partial\Psi(-t)/\partial t=H\Psi(-t), \quad (A2)$$

must be a possible solution of Eq. (A1). The appearance of the minus sign in (A2) suggests looking for the connection in the complex conjugate of (A1) [the state vectors $\Psi^*(t)$ must be regarded as being on an equal footing with the $\Psi(t)$], namely,

$$-i\partial\Psi^*(t)/\partial t=H^*\Psi^*(t). \quad (A3)$$

If then

$$\Psi(-t)=R\Psi^*(t), \quad (A4)$$

[5] J. M. Blatt, private communication.
[6] The notation employed here is largely based on unpublished notes of lectures given by J. Schwinger at Harvard in 1948.

where R is a unitary time independent operator which has the property

$$R^{-1}HR=R^{\dagger}HR=H^{*}, \tag{A5}$$

Eq. (A2) becomes equivalent to (A3) and thus to (A1). We see then that the condition for invariance under time reversal is the existence of the operator R.

We now apply the results just derived to our problem. Specifically, we introduce "time reversed" states according to the definition

$$\Phi_{-b}=R\Phi_{b}^{*}, \tag{A6}$$

where Φ_{-b} is the time reversed state corresponding to Φ_b. [For the simple case of a particle without spin, R is unity and if $\Phi_b=\exp(i\mathbf{k}\cdot\mathbf{r})$, $\Phi_{-b}=\exp(-i\mathbf{k}\cdot\mathbf{r})$ which evidently corresponds to a wave traveling in the opposite direction and hence with reversed velocity.] From our explicit equation for $\Omega^{(+)}$, namely,

$$\Omega^{(+)}=1+\frac{1}{E+i\eta-H}V, \tag{A7}$$

one finds using (A5)

$$R^{\dagger}\Omega^{(+)}R=1+\frac{1}{E+i\eta-H^{*}}V^{*}=\Omega^{(-)T}, \tag{A8}$$

where we have assumed H_0 and V are hermitian and used the result

$$\Omega^{(-)}=1+V\frac{1}{E+i\eta-H}. \tag{A9}$$

This proves the remark made in the text following Eq. (9). Written more explicitly, Eq. (A8) furnishes the information

$$(\Phi_b, \Omega^{(-)}\Phi_a)=(\Phi_{-a}, \Omega^{(+)}\Phi_{-b}). \tag{A10}$$

As a further illustration of the interconnection between the various operators $T^{(\pm)}$ and state vectors $\Psi^{(\pm)}$ we note the following results:

$$\begin{aligned}\Psi_{-a}^{(+)}&=R\Psi_a^{(+)*}=\Omega^{(-)\dagger}\Phi_{-a},\\ \Psi_{-b}^{(-)}&=R\Psi_b^{(-)*}=\Omega^{(+)}\Phi_{-b}.\end{aligned} \tag{A11}$$

These express the not unexpected interchange of incoming and outgoing scattered waves. With (A11) it is easy to show that the usual form of the reciprocity law[4]

$$(\Psi_b^{(-)}, V\Phi_a)=(\Phi_b, V\Psi_a^{(+)}) \tag{A12}$$

takes on the form

$$(\Phi_{-a}, V\Omega^{(+)}\Phi_{-b})=(\Phi_b, V\Omega^{(+)}\Phi_a) \tag{A13}$$

or, in terms of $T^{(+)}=V\Omega^{(+)}$,

$$T_{-a,-b}^{(+)}=T_{b,a}^{(+)}. \tag{A14}$$

PHYSICAL REVIEW VOLUME 87, NUMBER 5 SEPTEMBER 1, 1952

An Application of the Cellular Method to Silicon*

D. K. HOLMES†
Carnegie Institute of Technology, Pittsburgh, Pennsylvania
(Received January 28, 1952)

The calculations of Kimball and Mullaney applying the cellular method to elemental silicon are extended to a higher approximation. Although the energy gap is decreased through use of a larger number of harmonics, the values obtained are still much higher than that given by experiment. The proposal of Pearson, Haynes, and Shockley that the highest point of the filled band and the lowest point of the conduction band do not occur at the center of the zone may have a bearing on the results, since the calculations reported here are performed for zero wave number. The effective mass of the conduction electrons is determined under the assumption that the lowest point lies at the center of the zone.

INTRODUCTION

THE pure silicon crystal has the diamond type lattice and an experimentally known excitation energy as a semiconductor of 1.12 ev.[1] Kimball[2] obtained a solution for the band structure of diamond by use of the cellular method and Mullaney[3] adapted the diamond solution to silicon. Essentially the same method is used in part I of this paper to determine the lowest energy limit of the conduction band and the highest limit of the filled band, each for several possible values of the lattice spacing (under the assumption that the band limits occur at the center of the brillouin zone in a reduced scheme). The principal difference from previous work is in the choice of boundary conditions to be used in the fitting. In part II the functions obtained in part I are used to determine the effective mass for the conduction electrons.

The work reported here was performed in 1949 when it seemed likely that the top of the filled band and the bottom of the empty band did occur at the center of the brillouin zone. Pearson, Haynes, and Shockley have presented evidence[4] that these points may actually lie elsewhere in the brillouin zone. In spite of this, the calculations seem worth presenting briefly for their general value in connection with the properties of silicon.

I. THE BAND LIMITS

The total one electron eigenfunction may be expressed as[5]

$$\psi=\sum_l A_l[\sum_m C_{lm}Y_l^m(\phi,\theta)]R_l(E,r), \tag{1}$$

* Presented in partial fulfillment of the requirements for the degree of Doctor of Science to the Department of Physics of the Carnegie Institute of Technology, Pittsburgh, Pennsylvania.

† Now at the Oak Ridge National Laboratory, Oak Ridge, Tennessee.

[1] H. C. Torrey and C. A. Whitmer, *Crystal Rectifiers* (McGraw-Hill Book Company, Inc., New York, 1948), p. 64.

[2] G. E. Kimball, J. Chem. Phys. **3**, 560 (1935).

[3] J. F. Mullaney, Phys. Rev. **66**, 326 (1944).

[4] Pearson, Haynes, and Shockley, Phys. Rev. **78**, 295 (1950).

[5] F. C. VonderLage and H. A. Bethe, Phys. Rev. **71**, 612 (1947).

where the Y_l^m are surface spherical harmonics and the R_l are solutions of the radial Schrödinger equation for the free silicon atom. If the C_{lm} are obtained explicitly leaving the A_l undetermined, the total ψ may be fitted at the surface of the lattice cell for only a particular value of the energy, which appears as a parameter in the R_l. The angular parts may be constructed by noting that in the work of both Kimball and Mullaney the following conclusions are reached:

(1) At the bottom of the conduction band the wave functions are s-type about each nucleus and change sign upon inversion through the center of symmetry midway between adjacent nuclei.
(2) At the top of the filled band they are correspondingly p-type and even.

Thus it would be expected,[6] if these conclusions are actually acceptable, that the characteristic polynomials for the conduction band belong to the Γ_1 representation of the tetrahedral rotation group which expresses the symmetry of the silicon lattice, while the polynomials for the filled band would belong to the Γ_4 representation. Since the contribution of the higher harmonics is presumably small, only the first three characteristic polynomials were used in the total ψ for the conduction band, and only the first two for the filled band; these polynomials are listed below:

$$\Gamma_1: \quad 1, \quad xyz, \quad x^2y^2+y^2z^2+x^2z^2-\tfrac{1}{3}(x^4+y^4+z^4); \quad (2a)$$

$$\Gamma_4: \quad x, \quad yz. \quad (2b)$$

In order to fit the total wave functions of (1) so that they are continuous and have the periodicity and symmetry of the lattice, the appropriate number of boundary conditions must be chosen on the surface of the unit cell of the lattice. Figure 1 shows the polyhedron formed by passing bisecting planes perpendicularly through the lines joining a given silicon atom to its nearest and next-nearest neighbors. Since there are two atoms per unit cell in the silicon crystal, the surface of the unit cell is made up of two such polyhedra coinciding in a hexagonal face but rotated 60° with respect to each other about the line joining the two atoms of the unit cell. At equivalent points of the two polyhedra of the unit cell the Γ_1 wave function is equal-valued but has opposite signs in the two polyhedra; the Γ_4 wave functions for the two polyhedra pass into each other upon inversion in the midpoint of the common hexagonal face. The boundary conditions are applied at points of special symmetry, "a," "b," "c," and "d" of Fig. 1. Point "a" lies midway between two nearest neighbors at an experimentally determined distance of 2.22 Bohr radii from each atom of the unit cell. At "a" the total wave function with the symmetry of Γ_1 should have a node, while the total wave function belonging to Γ_4 should have a vanishing radial derivative. The vertices of four translationally equivalent polyhedra coincide at "b"; at this point the Γ_1 function may be expected to have a vanishing radial derivative, while the Γ_4 function itself should be zero. The third boundary condition needed for the Γ_1 wave function is obtained by noting that points "c" and "d" exchange symmetries on passage between the two polyhedra, so that the wave function at point "c" must be the negative of that at point "d." The following, then, are the boundary condition equations:

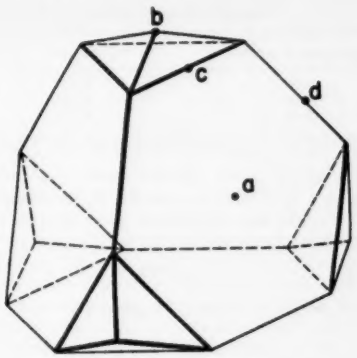

FIG. 1. The cellular polyhedron for silicon.

$$\Gamma_1: \quad \psi(a)=0, \quad (d\psi/dr)_{(b)}=0, \quad \psi(c)=-\psi(d). \quad (3)$$

$$\Gamma_4: \quad (d\psi/dr)_{(a)}=0, \quad \psi(b)=0. \quad (4)$$

When the ψ's of Eq. (1) containing the polynomials of Eq. (2) are substituted into Eqs. (3) and (4) there result two systems of equations for the A_l for the two cases, Γ_1 and Γ_4.[7] The determinantal equations which are the conditions for the solubility of the equations in the A_l are satisfied only when the R_l going with a particular energy are used. The eigenenergy was obtained for several lattice spacings with the results given in Table I.

Thus the energy gap as calculated for the center of the zone is much greater than 1.12 ev, the experimental value; however, as mentioned above, recent evidence[4] indicates that the smallest band separation may correspond to other than zero wave number.

TABLE I. Band-limit energies and excitation energies.

Internuclear separation (Bohr radii)	E (conduction band) (Rydberg units)	E (filled band) (Rydberg units)	Excitation energy (electron volts)
4.44	0.314	−0.424	9.983
4.66	0.159	...	...
4.88	0.057	−0.465	7.068
5.48	−0.091	−0.448	4.834

II. THE EFFECTIVE MASS

The one-electron wave functions which were fitted to the silicon lattice in the preceding work may be used in

[6] D. H. Ewing and F. Seitz, Phys. Rev. **50**, 760 (1936).

[7] The values of the radial wave functions R_l were obtained directly from reference 3 or by numerical integration using the effective potential given in reference 3.

TABLE II. The ratio m^*/m.

Internuclear separation	m^*/m
4.44	0.223
4.80	0.186
5.00	0.164

a determination of the effective mass of an electron occupying a level near the bottom of the conduction band.[8] We take the one-electron wave function going with wave number $\mathbf{k}$ in the form

$$\psi_k = \chi_k e^{i(\mathbf{k}\cdot\mathbf{r})}, \tag{5}$$

as usual, so that ψ of Eq. (1) is given by

$$\psi = \chi_0. \tag{6}$$

The differential equation satisfied by χ_k which is obtained by substituting the form (5) into the Schrödinger equation satisfied by ψ_k, is

$$-\frac{\hbar^2}{2m}\nabla^2\chi_k - \frac{i\hbar^2}{m}(\mathbf{k}\cdot\nabla\chi_k) + V\chi_k = \left(E_k - \frac{\hbar^2k^2}{2m}\right)\chi_k \cong E_0\chi_k. \tag{7}$$

For small $k = |\mathbf{k}|$ we assume

$$\chi_k = \chi_0 + ik\chi', \tag{8}$$

where $ik\chi'$ is a small perturbation on χ_0, and substitute into Eq. (7), obtaining (with the neglect of second-order terms)

$$-(\hbar^2/2m)\nabla^2\chi' - (\hbar^2/km)(\mathbf{k}\cdot\nabla\chi_0) + V\chi' = E_0\chi'. \tag{9}$$

The total solution of (9) may be taken in the form

$$\chi' = -[(\mathbf{k}\cdot\mathbf{r})/k]\chi_0 + \chi'', \tag{10}$$

where χ'' satisfies

$$-(\hbar^2/2m)\nabla^2\chi'' + V\chi'' = E_0\chi''. \tag{11}$$

Since χ' and therefore χ'', have the symmetry of $\nabla\chi_0$, i.e., the Γ_4 symmetry, an expansion of the type of Eq. (1) may be made for χ'' using the radial functions going with E_0 and the angular harmonics given in (2b). The boundary conditions of Eq. (4) may be applied to χ'' to determine the coefficients of the two terms in the expansion. With this definite form for χ'', χ' is completely specified by Eq. (10) and, thus, χ_k is completely specified by Eq. (8). The energy E_k going with χ_k may now be obtained from

$$E_k = c^2\int \chi_k^* e^{-i(\mathbf{k}\cdot\mathbf{r})}\left(-\frac{\hbar^2}{2m}\nabla^2 + V\right)\chi_k e^{i(\mathbf{k}\cdot\mathbf{r})}d\tau, \tag{12}$$

where the following normalization condition is to be imposed on χ_k:

$$c^2\int \chi_k^*\chi_k d\tau = 1. \tag{13}$$

The integrals in both (12) and (13) are to be taken over the unit cell. When the explicit form for χ_k along with the differential equations satisfied by χ_0, χ', and χ'' are used in Eqs. (12) and (13) (and higher order terms neglected) the following form for E_k results:

$$E_k = E_0 + \frac{\hbar^2k^2}{2m} + \frac{c^2\hbar^2k^2}{m}\int \chi_0\frac{\partial\chi'}{\partial x}d\tau. \tag{14}$$

Here the $\mathbf{k}$ vector has been arbitrarily chosen in the x direction for numerical computation, since, to the approximation used here, the direction chosen at the center of the zone is not significant. If E_k is expressed in the usual form,

$$E_k = E_0 + \hbar^2k^2/2m^*, \tag{15}$$

then m^*, the effective electron mass, takes the form

$$m^* = m\left[1 + \frac{2\int \chi_0(\partial\chi'/\partial x)d\tau}{\int \chi_0^2 d\tau + k^2\int \chi'^2 d\tau}\right]^{-1}, \tag{16}$$

with all integrals, again, to be taken over the unit cell.

The integrals in (16) were performed numerically for three values of the lattice spacing with the results for the ratio of m^* to m given in Table II.

A value of m^*/m of 0.67 has been reported by Pearson and Bardeen,[9] but it is not certain at this time that the calculated values have immediate bearing on the values obtained by Pearson and Bardeen.

[8] This work follows that of J. Bardeen, J. Chem. Phys. **6**, 367 (1938).

[9] G. L. Pearson and J. Bardeen, Phys. Rev. **75**, 865 (1949).

Thermal Neutron Absorption Cross Section of Deuterium

LOUIS KAPLAN, G. R. RINGO, AND K. E. WILZBACH
Argonne National Laboratory, Chicago, Illinois
(Received May 16, 1952)

The absorption cross section of deuterium for 2200-m/sec neutrons has been related to that of boron by intercomparison with lithium. A value of 0.57±0.01 millibarn for deuterium, based on a measured value of 755 barns for boron, has been obtained.

I. INTRODUCTION

THE absorption cross section of deuterium has been reported[1] to be $0.46\pm0.11\times10^{-27}$ cm² for 2200-m/sec neutrons. This value is based on a measurement of the diffusion length in heavy water and the assumption that the absorption in oxygen is negligible. Since this quantity has considerable theoretical interest[2,3] and practical importance, the determination of a more accurate value has been undertaken. The method used is essentially a refinement of one devised by Langsdorf[4] in 1943. The production of tritium from deuterium by neutron irradiation is compared with that from lithium; the neutron absorption of the lithium is in turn compared with that of a boron standard. Since these comparisons can be made with high precision, the calculated cross section of deuterium is as reliable as that of the boron standard.

II. EXPERIMENTAL PROCEDURE

Reagent grade lithium sulfate, dried to constant weight at 210°, was dissolved in specially purified heavy water, 99.57 percent D, to give a solution containing 0.937 gram atom of lithium per liter. The total cross section of this lithium solution was determined by comparison with standard boron solutions in a danger coefficient measurement[5] in the Argonne graphite reactor. The boron standards were prepared by diluting a heavy water solution of boric anhydride, the absorption cross section of which had been determined[6] by neutron transmission measurements.

TABLE I. Tritium formation in heavy water and lithium.

Content of ampoule	Shield	Tritium 10^{14} amp mmol^{-1}	$10^6\,\sigma_D/\sigma_{Li}$
D_2O	Cd	0.100	
D_2O	Cd	0.089	
D_2O	none	7.74±0.05	
D_2O	none	7.60±0.02	
Li_2SO_4 0.001871N	none	23.76±0.02	8.05
Li_2SO_4 0.003734N	none	40.07±0.04	7.98

One-gram samples of the heavy water and of two dilutions of the lithium sulfate solution in heavy water were weighed into quartz ampoules fitted with break seals. The ampoules were cooled in liquid nitrogen, evacuated, and sealed off. Two heavy water samples and the lithium solutions were irradiated in the vertical thimble of the Argonne heavy water reactor. Two ampoules of heavy water were wrapped in cadmium foil and similarly irradiated. Several days after removal from the pile each ampoule was opened on the vacuum line, the noncondensable gas was collected, the water was distilled, and aliquots of the distillate were converted to hydrogen by reaction with heated zinc. The tritium content of each hydrogen sample was determined by measurement, with a vibrating reed electrometer, of the current in an ionization chamber filled to atmospheric pressure with hydrogen.

III. RESULTS AND DISCUSSION

Analyses of the irradiated samples are presented in Table I. The recorded specific activities include the tritium found in the noncondensable gas; in no sample did this account for more than 0.6 percent of the total tritium. The ratio of the atomic cross sections for tritium production is calculated from the formula

$$\sigma_D/\sigma_{Li}=T_D N_{Li}/(T_{Li}-T_D)N_D,$$

where T_D and T_{Li} are the concentrations of tritium found in the heavy water and in the lithium solution, respectively, N_{Li} is the normality of the lithium solution at 25°, and N_D, the gram atoms of deuterium per liter of the heavy water, is 110.77 at 25°. No correction is made for the production of tritium by fast neutron capture since the tritium found in the cadmium-shielded samples can be accounted for by thermalization of epi-cadmium neutrons in the heavy water. The mean value of the ratio 8.02×10^{-6} is probably accurate to ±1.5 percent.

The absorption of the boron standard corresponds to a cross section[6] of 755±5 barns per atom for 2200-m/sec neutrons. From the danger coefficient measurement, the ratio of the cross section of lithium to that of the boron is 0.0941±0.0006, after a small correction for the absorption[7] by sulfur. These values give a total absorption cross section of 71.0±0.7 barns for lithium. This is essentially equal to the cross section for tritium

[1] Sargent, Cavanagh, and Niemi, Can. J. Research **A25**, 134 (1947).
[2] E. H. S. Burhop and H. S. W. Massey, Proc. Roy. Soc. (London) **A192**, 156 (1947).
[3] N. Austern, Phys. Rev. **83**, 672 (1951); **85**, 147 (1952).
[4] A. Langsdorf, private communication.
[5] Anderson, Fermi, Wattenberg, Weil, and Zinn, Phys. Rev. **72**, 16 (1947).
[6] G. R. Ringo (to be published).
[7] *Nuclear Data*, National Bureau of Standards Circular No. 499 (1950), p. 28.

production by the (n,α) reaction, since the (n,γ) cross section[8] of Li^7 is only 0.03 barn and that[9] of Li^6 in the natural element is less than 0.1 barn. Since boron, lithium, and deuterium are all $1/v$ absorbers, the cross section of deuterium for 2200-m/sec neutrons can be calculated to be 0.57 ± 0.01 millibarn.

[8] See reference 7, p. 4.
[9] B. Hamermesh and V. Hummel, Argonne National Laboratory (private communication).

PHYSICAL REVIEW VOLUME 87, NUMBER 5 SEPTEMBER 1, 1952

Resonance in Collision Processes*

O. OLDENBERG
Lyman Laboratory of Physics, Harvard University, Cambridge, Massachusetts
(Received May 13, 1952)

The limitations are investigated under which "resonance" provides certain collision processes with preferred probability. In impacts of the second kind, resonance strongly affects the transfer of electronic into electronic energy or into a small amount of vibrational energy, possibly the transfer of vibration into vibration, certainly not the transfer of vibration into rotation. Resonance is not effective in the transfer of energy of atomic recombination into electronic energy and, in general, resonance is not effective in processes in which nuclei change positions by appreciable amounts.

I. INTRODUCTION

IN certain cases impacts of the second kind show a preferred probability which Franck has attributed to "resonance." A similar preference due to "resonance" has been claimed for numerous other processes, in some instances with, in others without justification. In particular, certain theories of the afterglow of nitrogen, that is, of "active nitrogen," encounter difficulties by over-emphasizing the principle of resonance which actually applies only to a limited group of processes. The present paper proposes to examine the limits within which this principle is valid.

II. RESONANCE

We consider collision processes in which energy is transferred from one quantized energy level to another in atoms or molecules. Impacts of the second kind are an important type. In certain instances a particularly large probability for the transfer of energy has been observed. Franck[1] described such cases by adopting the principle that the cross section of the process is large *if no energy or only little energy is changed into translation or received from translation.* A striking example of this condition, which is called "resonance," is given by the observation of Beutler and Josephy[2] that excited mercury atoms Hg′ transfer energy to Na atoms with a pronounced preference to the Na level with an energy closest to that of Hg′. Fluorescence of Na provides another example. When one of the D lines of Na is separately excited, the other D line appears, depending upon the pressure, presumably excited by impacts of the second kind. Manley and Duffendack[3] observed resonance in the simultaneous ionization and excitation of magnesium atoms caused by impacts of the second kind with metastable or ionized neon atoms.

The corresponding effect in the energy transfer from an atom, argon, to a diatomic molecule, hydrogen, was observed by Lyman and later interpreted by Dieke and Hopfield.[4] A hypothetical, more extreme process illustrating such cases is the excitation of the O_2 molecule, for which the potential curves are well explored. While the energy of dissociation of O_2 is 5.08 ev, the molecule readily absorbs light of greater energy in a continuous range leading to excited molecules in a state of such compression that the molecule immediately dissociates. There is little doubt that the O_2 molecule may receive the same amount of energy by an impact of the second kind from an atom endowed with, say, 6 ev energy of excitation. Again a preferred probability due to resonance is expected to govern this transfer of electronic energy, irrespective of the fact that ultimately the free atoms produced are given energy of translation.

Mott and Massey[5] discuss the theory of the resonance effect and conclude that the sharpest resonance is expected for transfer of excitation involving optically allowed transitions in both systems.

An additional rule governing the probabilities of impacts of the second kind, derived by Wigner[6] on the

* This work is connected with experimental research supported by the ONR.
[1] J. Franck and P. Jordan, *Anregung von Quantensprüngen durch Stösse* (Springer, Berlin, 1926), p. 226.
[2] H. Beutler and B. Josephy, Z. Physik **53**, 747 (1929). See H. Beutler, Z. Physik **50**, 581 (1928).
[3] J. H. Manley and O. S. Duffendack, Phys. Rev. **47**, 56 (1935).
[4] T. Lyman, *Spectroscopy of the Extreme Ultraviolet* (Longmans Green, New York, 1928), second edition, p. 91; G. H. Dieke and J. J. Hopfield, Phys. Rev. **30**, 414 (1927).
[5] N. F. Mott and H. S. W. Massey, *The Theory of Atomic Collisions* (Clarendon Press, Oxford, 1949), second edition, p. 284. See P. M. Morse and E. C. G. Stueckelberg, Ann. Physik **9**, 579 (1931).
[6] E. Wigner, Gött. Nachr. 375 (1927). For the experimental confirmation, see A. C. G. Mitchell and M. W. Zemansky, *Resonance Radiation and Excited Atoms* (The Macmillan Company, New York, 1934), p. 69.

basis of quantum mechanics, claims a preference for a transfer in which the total resultant electronic spin of the colliding partners remains unchanged.

A process closely related to a collision of the second kind is charge transfer, for example, $He^+ + A \rightarrow He + A^+$. Mott and Massey point out that here again the effective cross section is largest in the case of resonance; that is, if the two partners have nearly equal energies of ionization.[7]

The examples referred to above are concerned with the transition of *electronic* into *electronic* energy. For the conversion of *electronic* energy of Hg into a *vibrational* quantum in various molecules, Zemansky[8] found relations which again are well described by resonance (although with an exception).

Less clear-cut is the problem of the transfer of energy of *vibration* to *vibration*. We compare this process with the excitation of vibration by electron impact. The application of the primitive picture of a fast electron hitting a diatomic molecule along the internuclear line leads to the prediction that the electron, because of its relatively small mass, simply bounces back without exciting vibration. Experiment, however, shows that an electron of a few volts energy is able to excite a vibrational quantum in H_2 or N_2.[9] For this process Franck[10] suggested a special picture in which the impinging electron is supposed to hit the molecule not along its internuclear line but in its equatorial plane. While the electron is crossing the molecule, it affects the internuclear force and so starts the vibration of the molecule. When the electron leaves the molecule, it may happen that the nuclei have just the positions and velocities which enable them to continue the vibration, the energy being supplied by the kinetic energy of the impinging electron.[11] A similar picture may be applied to the transfer of a vibrational quantum from one molecule to that of another. When the field surrounding a vibrating molecule interacts with a nonvibrating molecule, a transfer of a quantum may occur. It is plausible to assume that such a transfer takes place with a larger cross section between polar than between nonpolar molecules. Eucken systematically investigated such transfer processes by measuring the dispersion of sound. From numerous observations he inferred the general rule that a transfer is probable between molecules such as Cl_2 and CO_2 which are able to react chemically, although the transfer does not constitute a chemical reaction.[12]

III. NON-RESONANCE

It appears that Franck's principle of resonance, requiring a minimum production of energy of translation, is over-emphasized in papers on other types of collisions, in particular triple collisions. This criticism applies to theories of active nitrogen and will now be illustrated by examples.

It is generally agreed that active nitrogen consists of atomic nitrogen which upon recombining liberates sufficient energy to excite atoms and molecules. The first process to be considered is the recombination of two N atoms which in a triple collision give their energy to a molecule N_2:

$$N + N + N_2 \rightarrow N_2 + N_2'.$$

A theory of active nitrogen claims that resonance gives preference to a process in which the total energy of recombination (using the value 7.373 ev) is converted into electronic energy of the third body exciting its level $B^3\Pi_g$, $v=0$ (energy 7.36 ev). However, one cannot simply apply the theory of Mott and Massey to this triple collision process since the theory applies only to the transfer of *electronic* energy in a two-body collision. There is, however, another theory which demonstrates how readily vibration and translation may be produced in a triple collision. This is the theory of Eyring, Polanyi,[13] and their collaborators describing the triple collision by potential surfaces. It is true that this theory applies only to a simplified case, the approach along a straight line of three atoms, two of which form a molecule in a triple collision. The potential surface shows two valleys between which a transition can be made over a saddle point (representing the activated state). Any transition made by the reacting system is visualized as the free, frictionless motion under gravity of a mass point sliding on the surface. For a triple collision this picture leads to the conclusion that the energy of recombination can well be partly transformed into vibration and translation. This conclusion contradicts the principle of resonance.

When the third body is a diatomic molecule such as N_2, approaching in any direction, the situation is much too complicated to be represented by potential surfaces. Nevertheless, it seems safe to draw the same conclusion that the ready generation of vibrational and translational energy excludes the occurrence of resonance. Since energy of recombination is identical with a limiting case of vibrational energy, the recombination of two atoms in a triple collision rather resembles the

[7] An example is given by an observation of W. Hanle and K. Larché on ionized mercury, Physik. Z. **33**, 884 (1932).

[8] M. Zemansky, Phys. Rev. **36**, 919 (1936). For the theory see L. Nordheim, Z. Physik **36**, 496, 1926; H. Kallmann and F. London, Z. physik Chem. (B) **2**, 207 (1929); K. J. Laidler, J. Chem. Phys. **10**, 34 and 43 (1942).

[9] W. Harries, Z. Physik **42**, 26 (1927); H. Ramien, Z. Physik **70**, 353 (1931).

[10] J. Franck and P. Jordan, *Anregung von Quantensprüngen durch Stösse* (Springer, Berlin, 1926), p. 255.

[11] The theory given by Mott and Massey (reference 5) does not include this case, since it presupposes that the impinging particle hits along the internuclear line.

[12] For reference see O. Oldenberg and A. A. Frost, Chem. Revs. **20**, 99(1937); N. F. Mott and H. S. W. Massey, *The Theory of Atomic Collisions* (Clarendon Press, Oxford, 1949), second edition, p. 292.

[13] Glasstone, Laidler, and Eyring, *The Theory of Rate Processes* (McGraw-Hill Book Company, Inc., New York, 1941), p. 106, Fig. 25.

collision between a highly vibrating molecule and any other molecule. It appears likely that the collision dissipates the mechanical energy, which before the collision is all concentrated in one degree of freedom, distributing it over the various degrees of freedom available—vibrational, rotational, translational and, possibly, electronic. This concept is incompatible with resonance.

This theoretical argument, which implies lack of resonance in atomic recombination, is confirmed by Mohler's[14] observation that the sodium spectrum when excited in active hydrogen by the recombination of two atoms, shows only the D lines and not the higher lines, although resonance between the energy of recombination and the excitation of the atom would bring out several higher lines of the principal series. This observation contrasts with the pronounced resonance discussed above, which is evident in the sodium spectrum when excited by impacts of the second kind with *excited mercury*. The lack of resonance in the same type of triple collision is again evident in the excitation of Hg by active nitrogen, that is, presumably by a pair of recombining N atoms. Here, according to Okubo and Hamada and Bay and Steiner,[15] nearly the total energy of recombination may be transferred to the Hg atoms, but the highest spectral lines produced show only very low intensities, contrary to the prediction of resonance theory. It seems safe to conclude that resonance does not govern the transfer of energy from a recombining pair of atoms to a third body.

Even a physicist who insists on resonance has little reason to predict that the conversion of the energy of recombination of N+N into electronic energy of N_2 will occur with high probability, because this process would imply that the *total* energy of recombination of N+N is transferred to the third body. The colliding pair has many quantized vibrational levels at its disposal to which it may go while making available only a *fraction* of the recombination energy. The energy change from a pair of separate atoms to a nonvibrating molecule has no particular distinction in the large number of possible vibrational transitions, except that it is listed in tables as the energy of recombination of N+N. Therefore, even the argument based on resonance would not lead to a preference for transferring the total recombination energy at once.

Whereas the case just discussed is so complicated that potential curves cannot be drawn, the much simpler case of charge neutralization has been discussed in detail by Bates.[16] Bates found that in the process

$$O^-+N_2^+\rightarrow O'+N_2',$$

excited levels are produced such that a considerable share of the total energy available is transferred into energy of *translation*. Thus resonance is not effective in this process.

It is of interest to apply the same argument to simple chemical reactions. High probability by resonance is claimed[17] for the exchange reaction,

$$NO+O(^1S)\rightarrow N+O_2,$$

when both products, N and O_2, show certain electronic excitation. However, such reactions are well visualized by potential energy surfaces[18] which show that translation and vibration may readily be produced, thus excluding resonance.

In a chemical reaction, such as the one just mentioned, resonance would imply that the initial partners have the same energy as the final partners; in other words, that the reaction is neither exothermic nor endothermic. There is no chemical evidence in favor of such reactions. On the other hand, there is evidence that a reaction of this type requires an energy of activation. Therefore, reading the reaction in the reverse sense, it is not to be expected that an N atom is able to break up the O_2 structure except when aided by energy of activation, which again would violate the principle of resonance.

Another example is given by the reaction recently suggested by Bates,

$$H+O_3\rightarrow OH(v=9)+O_2,$$

which energetically explains the appearance of OH with a maximum of 9 vibrational quanta. This reaction is of great interest because it explains Meinel's[19] discovery of the corresponding vibrational spectrum in the night glow. Our present argument leads only to the conclusion that $v=9$ is presumably not preferred by resonance but is the maximum obtainable value of vibrational energy stored in the OH radical. However, it would be surprising if in the chemical rearrangement described the total energy available were to go into one degree of freedom, that is, into vibration of OH.

An exchange between *vibrational* and *rotational* energy was studied by Rieke[20] in the spectrum emitted from HgH molecules. He explained the high rotation evident in the spectrum by the original excitation of vibration (governed by the Franck-Condon rule) and the subsequent transfer in collisions of vibrational into rotational energy. In this process the conservation law requires that the angular momentum of the rotation produced by balanced by the angular momentum of the separating particles. Hence here again translational energy is necessarily generated.

Tentatively the results may be summarized as follows: Resonance is important in the transfer of

[14] F. L. Mohler, Phys. Rev. **29**, 419 (1927).
[15] J. Okubo and H. Hamada, Phil. Mag. **5**, 375 (1928); Z. Bay and W. Steiner, Z. Physik Ch. B, **9**, 106 (1930).
[16] Proceedings of the Conference on Ionospheric Physics at Pennsylvania State College (Pennsylvania State College, 1950) p. 12 BB.
[17] J. Kaplan (unpublished).
[18] Reference 13, Fig. 24, p. 105.
[19] A. B. Meinel, Astrophys. J. **112**, 120 (1950).
[20] F. F. Rieke, J. Chem. Phys. **4**, 513 (1936). See N. D. Smith, Phys. Rev. **49**, 345 (1936).

electronic into electronic energy ($Hg'+Na$) and of electronic energy into a small amount of vibration ($Hg'+$various molecules). Possibly resonance is important in the transfer of vibration into vibration, but is certainly not important in the transfer of vibration into rotation. The energy of recombination of a colliding pair like $N+N$ is not readily transferred by resonance to electronic excitation of a third body but more probably is distributed over the various degrees of freedom of the collision complex. Furthermore, in exchange reactions resonance is not effective.

In general, resonance is ineffective in collision processes in which nuclei change positions by appreciable amounts.

PHYSICAL REVIEW VOLUME 87, NUMBER 5 SEPTEMBER 1, 1952

Generation of Color Center Precursors in Alkali Halides by Electrolysis

MICHAEL HACSKAYLO AND GERHART GROETZINGER
Lewis Laboratory, National Advisory Committee for Aeronautics, Cleveland, Ohio
(Received April 3, 1952)

Two types of imperfections (designated as color center precursors) are created in NaCl crystals when they are subjected to electrolysis. Both of these types are present in a crystal not colored by the electrolysis and lead upon irradiation by x-rays to the development of temporary color centers in much larger numbers than are ordinarily produced and to permanent centers in about the same numbers as result when a crystal is directly colored by electrolysis. In crystals colored directly by electrolysis, only the former type of precursor is present. The properties of crystals containing precursors and of those containing color centers derived from precursors have been studied and compared with those of crystals in the other previously known states. A proposal regarding the nature of the second type of precursor is presented.

I. INTRODUCTION

THE fact that it is possible to produce color centers in ionic crystals is of special interest in the field of solid state physics for essentially two reasons. First, they represent themselves a type of imperfection that is relatively easy to study. Second, it is possible to draw conclusions regarding other types of imperfections through their influence on the tendency of color centers to be formed under the proper circumstances.

Essentially three ways of producing color centers in alkali halides have been reported: irradiation of the crystal with x-rays; exposure of the heated crystal to alkali metal vapors; and electrolysis of the heated crystal (by the use of a pointed cathode and a flat anode). While irradiation with x-rays leads to color centers that are bleached out upon application of light of wavelengths corresponding to one of their absorption bands, the other two methods of coloring lead to permanent color centers which cannot be destroyed by irradiation with light.[1] The formation of color centers is accompanied by changes in other physical properties; for example, it has been reported that the density of CaF_2 decreases upon coloration by electrolysis[2] and the density of KCl decreases upon coloration by irradiation with x-rays.[3] An excess of alkali metal after additive coloring has been observed in NaCl[4] and in KCl.[5]

On the other hand, the extent to which nonpermanent color centers are produced is affected if a crystal undergoes plastic flow before irradiation.[6] Moderate amounts of plastic flow increase the extent to which the crystal is colored by such treatment while large amounts lead to a diminution of the colorability.

We have found that when a crystal is subjected to electrolysis in such a fashion that no coloration is produced, the nature of the color center formation resulting from irradiation by x-rays is altered in the following way. First, the number of nonpermanent color centers is appreciably increased compared to that occurring in a normal crystal irradiated under the same conditions. Second, in addition, permanent color centers are formed, an effect which does not occur when a normal crystal is exposed to x-rays.

It seems reasonable to suppose that this change in the susceptibility for the formation of the two types of color centers is indicative of the presence of new imperfections in the crystal. Reserving for the time being any attempt to specify the nature of these imperfections, we will designate them as color center precursors.[7] There are evidently two types of such precursors, the first kind leading to nonpermanent, the second kind to permanent color centers. The precursors leading to the permanent color centers are metastable in the sense that they persist when the crystal is subjected to heat

[1] See, e.g., P. W. Pohl, Physik. Z. **39**, 36 (1938); N. F. Mott and R. W. Gurney, *Electronic Processes in Ionic Crystals* (Oxford University Press, London, 1940); F. Seitz, Revs. Modern Phys. **18**, 384 (1946).
[2] E. Mollwo, Gött. Nach. No. **6**, 79 (1934).
[3] Estermann, Leivo, and Stern, Phys. Rev. **75**, 627 (1949).
[4] A. L. Hughes, Revs. Modern Phys. **8**, 294 (1936).
[5] A. B. Scott and L. P. Bupp, Phys. Rev. **79**, 34 (1950).
[6] K. Przibram, Z. Physik **41**, 833 (1927); Burstein, Smith, and Davisson, Phys. Rev. **86**, 615 (1952); for a complete account of the older work see, e.g., F. Seitz, Phys. Rev. **80**, 241 (1950).
[7] Strictly speaking, the vacancy pairs associated with the production of color centers in ordinary crystals are also precursors. We prefer to reserve this term in the present paper, however, for the precursors generated by electrolysis.

or light in the visible region but are irreversibly converted to color centers when the crystal is exposed to irradiation of sufficiently short wavelengths. Consequently, a crystal containing such precursors can be considered to be in a metastable state.

The object of this investigation was to study the properties of crystals containing precursors and crystals containing color centers derived from precursors. In order to carry out this program, measurements of the absorption spectrum, the density, and chemical composition were performed on such crystals. For the purposes of comparison, similar measurements were performed on crystals colored by irradiation with x-rays in the normal state and by the pointed cathode method, in which cases some results reported in previous investigations were checked and supplemented.

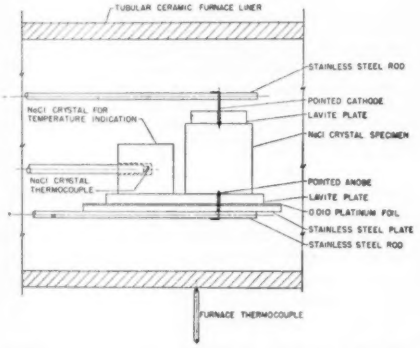

FIG. 1. Arrangement for subjecting crystals to electrolysis at elevated temperatures. In case a flat anode is desired, the lower lavite plate and the pointed anode are removed so that the crystal rests on the platinum foil.

II. EXPERIMENTAL PROCEDURE

The NaCl crystals used in these experiments were obtained from the Harshaw Chemical Company. In order to subject the crystals to electrolysis they were mounted in a Globar furnace in the way shown in Fig. 1. Two stainless steel rods served as the support for the crystal assembly and as part of the electrical circuit supplying the current for the electrolysis. The two electrodes making contact with the crystal were of nichrome wire filed to sharp points at the ends. In case a flat anode was preferred, the lower pointed electrode and lavite plate were removed so that the crystal made contact with the platinum foil. Current was supplied by a 360-volt battery with a 13,000-ohm resistor and a recording ammeter in series with the crystal. In all cases the furnace was brought up to a steady temperature before the crystals were inserted, the exterior of the ceramic tube being kept at 875°C. In order to determine the temperature of the electrolyzed crystal inside the furnace, a second crystal containing a thermocouple connected to a Brown recording potentiometer was mounted close to the first crystal.

For the irradiations with x-rays, a Machlett A.E.G. 50 beryllium window tube was used which was operated at a voltage of 50 kv and a current of 30 ma. During the irradiation the crystals were kept in a dried helium atmosphere, the beryllium window being a part of the container in which the helium gas was kept at a slight positive pressure.

As a general rule, the crystals used were freshly cleaved on all sides at the last possible moment before the start of an experiment.

The absorption spectra of the NaCl crystals were obtained with a Beckman spectrophotometer model DU which permitted measurements in the spectral range of 210–1000 mμ. To provide the sensitivity necessary for the determination of the absorption of very densely colored crystals, the phototube of the spectrophotometer was replaced with a dry ice cooled type 5819 photomultiplier tube used in conjunction with a scale of 4096 counter. Since it was impossible to measure with this system both the intensity of the light incident upon the crystal and that transmitted by it, the following indirect procedure was used. First, the light intensity of the source was adjusted so that with the colored crystal in place the counting rate was about three times background. Next, the crystal was replaced by a gray filter (exposed and developed photographic film) of sufficient density that the resulting counting rate of the detector was still below saturation. The ratio of the two counting rates equaled the ratio of the transmission coefficients of the crystal and the filter. Finally, the transmission coefficient of the filter was measured in the usual fashion with a diminished source intensity. The transmission coefficient of the crystal is, of course, the product of the ratio of the coefficients and the coefficient of the filter.

Density measurements were made by the suspension method.[8] Twelve or so pieces of crystal were measured together, half of which were specimens which had been subjected to the particular treatment under investigation and the other half, control specimens that had not been treated but came from adjacent parts of the same crystal. The pieces, which were of different size in order to distinguish the two groups, were introduced into a 200-ml graduated cylinder filled with about 30 ml of the suspension liquid. This cylinder was kept almost completely immersed in a 60-gallon water bath. To make the measurement, the temperature of the bath was slowly raised until all the crystals in the suspension liquid were at the bottom of the graduated cylinder. Heating of the bath was then discontinued, and it was cooled at a rate of approximately 0.01°C per minute by means of manually controlled cooling coils. The

[8] D. A. Hutchison and H. L. Johnston, J. Am. Chem. Soc. **62**, 3169 (1940); Phys. Rev. **62**, 32 (1942); D. A. Hutchison, Phys. Rev. **66**, 144 (1944); J. Chem. Phys. **10**, 383 (1945); H. L. Johnston and D. A. Hutchison, J. Chem. Phys. **8**, 869 (1940).

temperature at which each of the crystals first cleared a brass wire mesh placed near the bottom of the cylinder was recorded. It was found that introducing this mesh improved the reproducibility of the results.

The suspension liquid used for the density determination of NaCl was ethylene bromide.[9] The density of the ethylene bromide used in this experiment was determined in this laboratory to be 2.17820 g/cm³ at 20°C[10] which is close to the value of 2.17955 g/cm³ at 20°C obtained by Anderson.[11] In view of the fact that it would have been rather cumbersome to determine its density at another temperature with the equipment at hand, use was made of the volume thermal expansion coefficient of the liquid following from the measurement of Anderson. These measurements show that the density is a linear function of the temperature between 18° and 20°C, the thermal coefficient of expansion α being equal to 9.41×10^{-4}/°C. The thermal expansion coefficient β of NaCl can hardly depend to a great extent on the treatment to which the crystals were subjected, and therefore, the usual value[12] of 1.21×10^{-4}/°C was used in our computations. The difference in the density $\Delta\rho$ between two specimens is then given by the relation

$$\Delta\rho = -\rho_0(\alpha-\beta)\Delta T,$$

where ρ_0 is the density of the normal crystal at the suspension temperature and ΔT the difference between the suspension temperatures. The crystals used had approximate dimensions of $0.3\times0.3\times0.08$ cm and $0.2\times0.4\times0.08$ cm. Before they were immersed in the suspension liquid they were out-gassed at a temperature of 100°C for twenty minutes.

To determine the amount of free sodium, samples of crystals were dissolved in water and the hydrogen ion concentration was measured using a Beckman pH meter model 50. Before dissolving the crystals in the triply distilled water, the surface layers were cleaved off to remove any contaminants and, in the case of the crystals that had been subject to electrolysis, the portions that had not carried any of the current were cleaved off. Any excess alkali present formed the corresponding hydroxide upon solution, with a resulting increase in pH which measured the departure from the stoichiometric ratio. A similar quantitative estimate of any excess halogen present could not be made.

III. RESULTS

A. Production of the Metastable State

There are essentially two ways of producing crystals in the metastable state. In the first place, the color cloud in an electrolytically colored crystal can be removed either by reversing the polarity of the current before the cloud has spread from the cathode all the way to the anode or by continuing the flow of current in the same direction after the cloud has reached the anode.[13] Crystals treated in this manner were found to be in the metastable state. The second method consists of subjecting the crystals to electrolysis in such a fashion that no coloration is produced. The exact circumstances leading to this condition are not completely understood, but if the crystal is treated in essentially the normal fashion, such a result is often obtained with the pointed cathode and flat anode and, still more frequently, with two pointed electrodes. Since the second method is the more convenient one, it was used in most of our work.

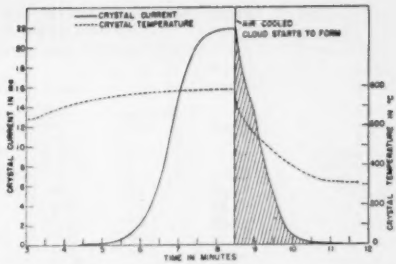

FIG. 2. Crystal temperature and electrolytical current as a function of the time at which the crystal was introduced and removed from a furnace at a temperature of 875°C.

Figure 2 shows the typical behavior of the electrolytic current through a crystal heated in the furnace. Two pointed electrodes were used in the way described above. The dashed curve in connection with the right-hand scale shows the temperature of the crystal as a function of the time after it was inserted into the

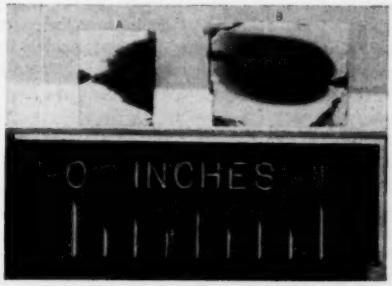

FIG. 3. NaCl crystals containing a region originally in the metastable state by electrolysis after coloration of x-rays and subsequent bleaching of nonpermanent centers. Left crystal: metastable state was obtained by a pointed cathode and a flat anode. Crystal to the right: by a pointed cathode and a pointed anode.

[9] Obtained from Ethyl Corporation of America.

[10] We are indebted to Dr. P. Wise for making these measurements.

[11] B. W. Anderson, Gemmologist **9**, 141 (1940).

[12] *Handbook of Chemistry and Physics* (Chemical Rubber Publishing Company, Cleveland, 1949), p. 516.

[13] O. Stasiv, Gött. Nach. **50**, 387 (1933).

TABLE I. Relative differences $\Delta\rho/\bar{\rho}_0$ of the densities with respect to the average density of the untreated NaCl crystals $\bar{\rho}_0$ at approximately 26°C.

Column	1	2	3		4		5	6	7
Color	Uncolored		Nonpermanently colored		Permanently and nonpermanently colored			Permanently colored	
State	Normal	Metastable state	Irradiation in normal state		Irradiated in metastable state		Irradiated after colored by electrolysis	Electrolytically colored	Bleached after irradiation in metastable state
Radiation time on each side of crystal			(a) 21 hours 21 hours	(b) 28 hours 66 hours	(a) 20 hours 22 hours	(b) 24 hours 65 hours	48 hours 68 hours		
$-\Delta\rho/\bar{\rho}_0\times10^5$	3.70	5.55	4.56	9.98	22.5	46.9	32.3	6.15	4.53
	2.94	3.91	3.74	9.12	20.8	46.9	31.5	6.15	3.65
	0.36	1.42	3.74	8.30	19.2	41.7	24.1	5.33	2.94
	−2.90	4.99	3.74	7.48	15.1	35.3	23.3	4.47	2.18
	−2.90	1.68	3.74	7.48	13.5	27.5	21.7	7.78	1.26
	0.40	0.00	2.92			45.2		7.78	
	−0.40	4.99	7.05			44.3		5.30	
	−0.40	2.49	6.24			41.7		1.16	
	−0.40	0.80	6.24			39.6		1.16	
	−0.40		5.42			39.1		0.34	
$[-\Delta\rho/\bar{\rho}_0\times10^5]_{\text{av}}$	0.00	2.9	4.7	8.4	18	41	27	4.6	2.9
Corrected $[-\Delta\rho/\bar{\rho}_0\times10^5]_{\text{av}}$	0.00	4.4	4.7	8.4	27	61	27	4.6	4.4

furnace. The current reaches a constant value after the temperature of the crystal becomes steady and drops rapidly after the assembly holding the two crystals is removed from the furnace. If a flat anode is used in connection with a pointed cathode the time dependence of the current and temperature is similar. The coloration started in most cases only at the time at which the crystal was removed from the furnace. In some crystals, coloration did not occur at all; in others it started at times at which the temperature was still increasing or already constant.

Figure 3 shows two crystals that had been colored by irradiation after having been brought into the metastable state and then heated to remove the temporary centers. The outside region is completely clear, but the part of the crystal in which the electrolysis occurred is colored. In case of crystal *A*, a pointed cathode and a flat anode, and in the case of crystal *B*, two pointed electrodes were used. Owing to the pressure, the pointed electrodes somewhat penetrated the crystals while they were at the elevated temperatures. The indentation marks can be seen in the figure.

B. Density of the Crystals

Crystals, which had undergone electrolysis without showing any coloration, were subjected to density measurements. In order to get more uniform results, parts of the region of each crystal that was believed to contain no precursors were cleaved off. It was possible to estimate the extent of this region since the color clouds that result after irradiation all have approximately the same shape (see Fig. 3).

The average density $\bar{\rho}_0$ of normal NaCl crystals was found to be 2.16472 at 20°C compared to the accepted value of 2.163 g/cm³.[14] The first column of Table I contains the deviations $\Delta\rho_0$ of the densities of the individual control pieces from their average density $\bar{\rho}_0$. Column 2 shows the deviations $\Delta\rho=\rho-\bar{\rho}_0$ of the densities ρ of crystals that had been subjected to electrolysis but were uncolored. The densities of these crystals were measured simultaneously with those of the crystals referred to in column 1. The values listed in the other columns are based on comparisons between the crystals in question and a group of control crystals measured simultaneously. The spread of the densities of these latter is not included, but it was in every case of the same order as the spread listed in column 1. Columns 3(a) and 3(b) refer to crystals, originally in the normal state, which were nonpermanently colored with x-rays. Columns 4(a), 4(b), and 5 refer to crystals in which permanent and nonpermanent color centers were present simultaneously. These crystals had either been irradiated with x-rays in the metastable state or else irradiated with x-rays after permanent color centers had been produced by the pointed cathode method. Columns 6 and 7 refer to permanently colored crystals which in the one case were colored by the pointed cathode method and in the other irradiated by x-rays while in the metastable state and then heated to bleach out the nonpermanent color centers. It is evident that the spread in the values $\Delta\rho/\bar{\rho}_0$ for the crystals subjected to electrolysis exceeds the spread due to errors of the density measurements (column 1). This is at least partly due to the fact that the volume affected by the electrolysis varies among samples.

Corrections to the results obtained had to be made in the case of crystals containing precursors because of the fact that these were not distributed uniformly throughout the sample. In the case where the density measurement was made before the sample was irradiated, the correction was achieved by dividing the measured value by a number equal to the proportion

[14] *International Critical Tables* (McGraw-Hill Book Company, Inc., New York, 1929).

of the crystal containing such precursors. This in turn was found by irradiating the sample with x-rays after the density measurement and then bleaching out the temporary centers. The appropriately corrected value is recorded in the last line of Table I.

Even though these measurements may not have too great an accuracy, the following results are quite obvious: (1) As has been observed by other investigators, crystals irradiated with x-rays show a decrease in the density. (2) Crystals in the colorless metastable state show a lower density than normal crystals. (3) Crystals with permanent color centers obtained either directly by electrolysis or indirectly by bleaching out the nonpermanent color centers after irradiation in the metastable state have approximately the same density as crystals in the colorless metastable state. (4) Crystals that have been subjected to electrolysis and then irradiated by x-rays show a decrease of density which exceeds that produced by irradiation in the normal state by a factor of 5 or 6 regardless of whether they are colored before being irradiated.

C. Deviation from Stoichiometric Ratio

Table II shows the results of the pH measurements.[15] These measurements were made within two days after the treatment of the crystal. Crystals having the weight given in column 2 were dissolved in 10 cc of triply distilled water. The slight change of the pH resulting was found to be approximately the same for untreated crystals, crystals in the metastable state, and crystals that had been colored by x-rays either in the normal or in the metastable state. Some of the crystals that had been colored by electrolysis did, however, display a significant increase of the pH. It was found that these crystals always exhibited minute dendritic patterns having a general direction from the cathode to the anode. This pattern might have been due to an electrical breakdown which led to a deposition of sodium inside the crystal. Except for such cases, there is probably no significant excess of negative vacancies over the positive ones.

TABLE II. Hydrogen ion concentration of NaCl crystals in different states dissolved in triply distilled water

State of crystal	Weight of crystal in grams	pH Triply distilled water	pH Crystal dissolved in 10 ml of water
Normal	0.1095	6.01	6.15
	0.1109	5.91	5.98
Metastable state	0.1282	6.15	6.20
	0.1690	6.19	6.25
Irradiated in normal state	0.1128	5.97	6.10
	0.1081	5.95	6.09
Irradiated in metastable state	0.0640	5.88	6.42
	0.1010	5.95	6.50
Electrolytically colored (dendritic patterns)	0.1305	6.11	8.50
	0.1047	6.18	9.01
Electrolytically colored (no dendritic patterns)	0.0290	6.08	8.72
	0.1590	6.05	6.20
	0.1110	6.01	6.40
	0.0265	6.15	6.20
Irradiated in metastable state, then bleached	0.1220	6.04	6.25
	0.0640	5.95	6.30

[15] We are grateful to Mr. Dumas A. Otterson for performing the pH measurements.

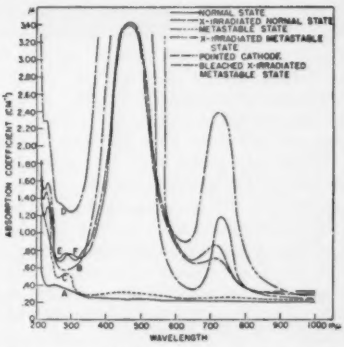

FIG. 4. Apparent optical absorption of NaCl crystals: (A) normal state; (B) x-irradiated normal state; (C) metastable state; (D) x-irradiated metastable state; (E) pointed cathode coloration; and (F) bleached x-irradiated metastable state.

D. Optical Absorption of the Crystals

Figure 4 shows the optical absorption spectra of crystals in all the states considered here (except for the irradiated electrolytically colored ones), arranged as follows: curves *A* and *B* refer to the normal and irradiated normal state, respectively; curves *C* and *D*, to the metastable and irradiated metastable states; and curves *E* and *F*, to the electrolytically colored and the bleached irradiated metastable. It may be noted that all the crystals that were subjected at some point to electrolysis (see curves *C* through *F*) show a pair of bands at 226 mμ and 285 mμ in the ultraviolet.[16]

In order to obtain curves *E* and *F* two crystals were selected which showed a relatively light coloration.[17] Unfortunately, the optical densities of crystals irradiated in the normal and metastable states to saturation were too high (curves *B* and *D*) to permit measurements over the whole range of the *F* band. However, some idea of their relative densities may be obtained from

[16] These two bands in the ultraviolet are not apparent in the absorption spectra obtained by J. P. Molnar [Ph.D. thesis, M.I.T. (1940)] for NaCl crystals colored by the pointed cathode method. Molnar was using a somewhat different condition during the electrolysis (". . . temperature from 550° to 650°C, a potential of up to 900 volts . . ."). He reports the appearance of a "yellow surface stain" which has been observed in this laboratory on only two occasions. Burstein *et al.* (see reference 6) report, however, the appearance of absorption bands at 240 mμ and 340 mμ in KCl crystals, which have been subjected to plastic deformation before irradiation with x-rays.

[17] On the other hand, crystals in which density measurements were performed were not selected in any way. The conditions during electrolysis that influence the resulting optical density are unknown.

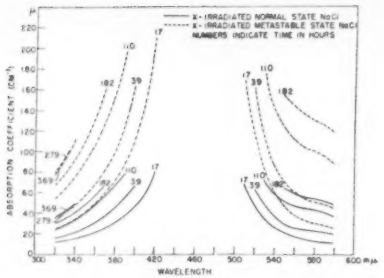

FIG. 5. Optical absorption of NaCl crystals x-irradiated in the normal state (solid curves) and metastable state (dashed curves). The curves were corrected for background.

Fig. 5, which shows the optical absorption spectra of two crystals in the normal and metastable state, respectively, at different times of irradiation. The greater sensitivity to radiation of the latter crystal is quite evident from the figure. Figure 6, which is based on the same experiment, shows the optical absorption at several different wavelengths as a function of time and clearly demonstrates the trend toward saturation.

E. Discussion

The fact that no significant change of the hydrogen ion concentration associated with the various treatments of the NaCl crystal can be detected proves that the number of negative vacancies per cm³, N^-, in no case exceeds the number of positive vacancies per cm³, N^+. If one assumes that N^+ and N^- are actually equal, the observed change in the density $\Delta\rho$, compared to that of the normal state, can be related to the number of missing atoms of either sign of electric charge irrespective of their arrangement in the form of single vacancies, pairs of vacancies, etc., by the equation

$$N^+ = N^- = (N/M)\Delta\rho,$$

where N is the Loschmidt number, M the molecular weight, and $\Delta\rho$ the change of density given in the last line of Table I. Table III gives the values of $N^-(=N^+)$ thus found.

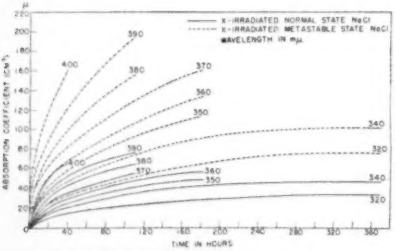

FIG. 6. Saturation of optical absorption of the x-irradiated normal state (solid curves) and metastable state (dashed curves) as a function of time. The curves were corrected for background.

It should be noted here that the values listed in column 2 refer to a crystal containing both the permanent and the nonpermanent color centers.

In the course of our experiments, we encountered essentially seven different states of the NaCl crystal as given in Table I. It seems apparent that the permanent centers associated with the states given in columns 6 and 7 are identical.

We have no explanation for the unusually high concentration of the nonpermanent centers resulting upon irradiating a crystal in the metastable state and shall, therefore, exclude them from consideration in the following. The discussion will be based on the usual concept that the basic entities connected with color centers are electrons trapped in negative vacancies and holes in the filled electron band trapped in positive vacancies.

In the normal state there are no isolated vacancies, but rather the equilibrium number of pairs of positive and negative vacancies; all the electrons are situated in filled bands. When such a crystal is irradiated, there is created temporarily a situation in which some of the electrons have been raised into one of the previously empty conduction bands leaving an equal number of holes. Color centers are formed when one of the electrons is trapped in a negative vacancy; and consequently, a hole, in a positive vacancy. This diminishes the number of free vacancy pairs, and therefore, new pairs enter from the surface in order to preserve equilibrium. This accounts for the decrease in density. A vacancy that has trapped an electron or a hole is no longer as tightly bound to the other member of its pair. The distance between such a vacancy and its mate therefore increases, but the two vacancies in question do not separate entirely. Consequently, if the electron or hole is removed from the vacancy owing to excitation by light or heat, the two vacancies may recombine to form a normal pair. Correspondingly, the electron recombines with a hole, thus returning to the filled band. This accounts for the process of bleaching. A crystal in the metastable state contains, in addition to vacancy pairs, also isolated positive and negative vacancies in approximately equal numbers. This accounts for the fact that such a crystal has a low density but the normal stoichiometric ratio. Because of the electrostatic forces involved, these vacancies are almost immobile, and therefore, the metastable state persists at high temperatures. When a crystal in the metastable state is irradiated, on the one hand, the same process occurs as in the case of a normal crystal. In addition, a certain number of the electrons or holes produced are

TABLE III. Concentration of negative vacancies for various states.

Metastable state	Saturation x-irradiation of metastable state	Pointed cathode coloration	Saturation x-irradiation normal state
9.6×10^{17} cm^{-3}	12.3×10^{18} cm^{-3}	1×10^{18} cm^{-3}	1.8×10^{18} cm^{-3}

trapped by the isolated vacancies. Since the bleaching process described above, which is based on the recombination of vacancy pairs, is not available for the case of isolated vacancies, color centers involving such vacancies are permanent.

In terms of the above scheme, the following mechanism for the phenomena associated with electrolysis may be advanced. Under the influence of an electric field at elevated temperatures, the negative ions start to move toward the anode producing an excess of negative vacancies near the cathode, and conversely, the positive ions move toward the cathode producing positive vacancies near the anode. In order that the crystal be locally neutral, it is necessary that there be introduced at the cathode electrons equal in number to the excess negative vacancies and similarly holes in the electron band equal to the number of positive vacancies introduced at the anode. In general, the electrons and holes will be trapped in the vacancies, thus leading to color centers which spread from the cathode toward the anode. It is quite clear that the spreading reverses itself if the polarity of the field is reversed at any stage. If the direction of the field remains unchanged, the nature of the process changes when the positive vacancies in which holes have been trapped arrive at the cathode. When this happens, the condition of the electric neutrality is satisfied if electrons entering from the cathode combine with the holes trapped in the positive vacancies. This allows the newly created negative vacancies to be formed free of electrons, i.e., as color center precursors. As the negative vacancies containing the electrons diffuse toward the anode they are replaced by these precursors and in this fashion the color cloud is swept out toward the anode. The above discussion does not take into account the inhomogeneity of the electric field produced by the pointed cathode and also fails to explain the direct production of precursors and the increased susceptibility of a crystal in the metastable state for the production of nonpermanent centers.

We are greatly indebted to Dr. Philip Schwed for valuable discussions and suggestions.

PHYSICAL REVIEW VOLUME 87, NUMBER 5 SEPTEMBER 1, 1952

Motion of Gaseous Ions in a Strong Electric Field. II

GREGORY H. WANNIER
Bell Telephone Laboratories, Murray Hill, New Jersey
(Received May 8, 1952)

This paper continues an earlier one on the same subject. Its object is to elucidate the nature of the random motion of an ion about its drift. In Sec. F it is shown that this motion can be described as a diffusion with a diffusion tensor axially symmetric about the field. If the mean free time between the collisions of an ion with molecules is independent of speed, then explicit expressions may be deprived for the two diffusion coefficients; these expressions are written down without proof in Sec. G; they are connected with the mobility by a natural extension of the Einstein relation. In Sec. H, the longitudinal diffusion coefficient is computed numerically for the hard sphere model, high field, and mass ratio 1; the method of computation is the same as in Sec. D. Finally, it is shown in Sec. I how approximate formulas of wider validity can be inferred from the ones obtained.

IN the first paper of this series[11] the problem of the motion of ions through a gas was formulated under the assumption that the electric field was too large to be treated as a perturbation, as is often done. This problem was solved in the sense that the values of some simple velocity averages were worked out precisely while no attempt was made to write down the entire velocity distribution function. I believe that this type of approach will yield most answers of experimental interest. The actual formulation was restricted, however, to uniform ion densities. In this paper the problem of nonuniform densities will be tackled in the same spirit.

F. CHARACTER OF THE RANDOM MOTION OF IONS

It is intuitively reasonable to suppose that the drift velocity of ions is their most important property from the point of view of observation and that the random motion about this mean value is essentially a diffusion process. It will now be shown that this view is correct, provided the medium is thought of as anisotropic with the field direction as symmetry axis.

In order to prove this we modify Eq. (6) by assuming f to be a density in phase space, depending on space and time as well as velocity. If we adopt the notations

$$\partial/\partial\mathbf{r} \quad \text{and} \quad \partial/\partial\mathbf{c}$$

for the gradients in ordinary and velocity space, this formula reads

$$\partial f(\mathbf{c},\mathbf{r},t)/\partial t+\mathbf{a}\cdot\partial f(\mathbf{c},\mathbf{r},t)/\partial\mathbf{c}+\mathbf{c}\cdot\partial f(\mathbf{c},\mathbf{r},t)/\partial\mathbf{r}$$
$$=\int\int\{M(\mathbf{C}')f(\mathbf{c}',\mathbf{r},t)-M(\mathbf{C})f(\mathbf{c},\mathbf{r},t)\}\times\frac{1}{\tau(\gamma)}d\Pi_c d\mathbf{C}. \quad (64)$$

[11] Gregory H. Wannier, Phys. Rev. **83**, 281 (1951). The two papers will be treated as forming together a single unit.

We now make the assumption that we deal with a distribution decaying at a constant small relative rate in some spatial direction. In zero approximation this distribution will displace itself with the drift velocity $\langle \mathbf{c} \rangle$. But in addition to this drift current there will be a current induced by the gradient which we propose to compute. We thus write the particle density $n(\mathbf{r}, t)$ in coordinate space in the form

$$n(\mathbf{r}, t) = n_0 \exp[\mathbf{k} \cdot (\mathbf{r} - \langle \mathbf{c} \rangle t)] \tag{65}$$

and the density in phase space

$$f(\mathbf{c}, \mathbf{r}, t) = n(\mathbf{r}, t)\{f(\mathbf{c}) + f^*(\mathbf{c})\}. \tag{66}$$

In this expression $f(\mathbf{c})$ is the normalized unperturbed velocity distribution which results from Eq. (6). $f^*(\mathbf{c})$ is a correction to $f(\mathbf{c})$ which is caused by the presence of the density gradient. It follows from the definition of the problem that $f^*(\mathbf{c})$ makes no net contribution to the density, that is, that

$$\int f^*(\mathbf{c}) d\mathbf{c} = 0. \tag{67}$$

It will make a contribution to the current, however. The total current density $\mathbf{j}_t$ is given in terms of $f(\mathbf{c}, \mathbf{r}, t)$ by the formula

$$\mathbf{j}_t = \int f(\mathbf{c}, \mathbf{r}, t) \mathbf{c} d\mathbf{c}, \tag{68}$$

which upon substitution of (66) decomposes in two parts, stemming from $f(c)$ and $f^*(\mathbf{c})$, respectively. The first part just equals the product of density and drift velocity and thus is the expected drift current. The new current $\mathbf{j}$ induced by the density gradient thus arises from $f^*(\mathbf{c})$ and equals

$$\mathbf{j} = n(\mathbf{r}, t) \int f^*(\mathbf{c}, t) \mathbf{c} d\mathbf{c}. \tag{69}$$

In order to justify the assumptions (65) and (66) and, incidentally, to determine $f^*(\mathbf{c})$, these expressions must be substituted back into (64). After simplification with (6), the following equation results:

$$\mathbf{a} \cdot \frac{\partial f^*(\mathbf{c})}{\partial \mathbf{c}} + \int\int \{M(\mathbf{C}) f^*(\mathbf{c}) - M(\mathbf{C}') f^*(\mathbf{c}')\} \frac{d\mathbf{\Pi}_c d\mathbf{C}}{\tau(\gamma)} = -\mathbf{k} \cdot (\mathbf{c} - \langle \mathbf{c} \rangle)\{f(\mathbf{c}) + f^*(\mathbf{c})\}. \tag{70}$$

This is an equation in velocity space only; the disappearance of the coordinates and the time proves the compatibility with (64) of the assumptions made in (65) and (66). In solving Eq. (70) we observe that our interest is only in diffusion, that is, the current resulting from a concentration gradient when treated in first-order perturbation. In this case both $\mathbf{k}$ and $f^*(\mathbf{c})$ are to be treated as small, and their product in (70) is to be neglected. The equation then becomes

$$\mathbf{a} \cdot \frac{\partial f^*(\mathbf{c})}{\partial \mathbf{c}} + \int\int \{M(\mathbf{C}) f^*(\mathbf{c}) - M(\mathbf{C}') f^*(\mathbf{c}')\} \frac{d\mathbf{\Pi}_c d\mathbf{C}}{\tau(\gamma)} = -\mathbf{k} \cdot (\mathbf{c} - \langle \mathbf{c} \rangle) f(\mathbf{c}). \tag{71}$$

The homogeneous prototype of this inhomogeneous equation is (6); arbitrary amounts of $f(\mathbf{c})$ could thus be added to a particular solution of (71) were it not for the orthogonality condition (67) which makes the solution definite.

The existence of the diffusion phenomenon follows easily from Eq. (71). $f^*(\mathbf{c})$ is a linear function of the three components k_x, k_y, and k_z with coefficients which do not depend on the density or its gradient, but only on the unperturbed velocity distribution $f(\mathbf{c})$; furthermore, the first two of these coefficients are equal. Hence, from (69) $\mathbf{j}$ comes out as a linear function of the three quantities $n(\mathbf{r}, t)k_x$, $n(\mathbf{r}, t)k_y$, $n(\mathbf{r}, t)k_z$; these are the components of the density gradient as is evident from (65); in addition, the multipliers of the first two components are equal. We may write therefore

$$\mathbf{j} = -(\mathfrak{D}) \partial n / \partial \mathbf{r}, \tag{72}$$

where $(\mathfrak{D})$ is a tensor which is axially symmetric about the field direction; its two components, which we shall call the longitudinal diffusion coefficient $D_{||}$ and the transverse coefficient $D_\perp$, are computed entirely from the unperturbed velocity distribution $f(\mathbf{c})$. It is to be noted, however, that they contain the acting electric field as a parameter.

G. DIFFUSION FOR CONSTANT MEAN FREE TIME; GENERALIZED EINSTEIN RELATION

It is not surprising, in view of the successes achieved earlier, that explicit expressions can be derived for the two diffusion coefficients if the model of Secs. C and E. is adopted. The derivations, which proceed most easily by the classical method of Maxwell[12] rather than that of Sec. B, will be given in BSTJ.[4] The final result is

$$j_i = -\left[\frac{m+M}{M} \frac{\tau}{\langle 1 - \cos\chi \rangle} \{\langle c_i c_k \rangle - \langle c_i \rangle \langle c_k \rangle\}\right] \frac{\partial n}{\partial x_k}. \tag{73}$$

Here tensorial notation has been employed in order to exhibit the tensor character of the square bracket, which, from (72), is just the diffusion tensor. If we substitute the explicit expressions (60), (62), and (63) for the velocity averages in (73), we get

$$D_{||} = \frac{(m+M)\tau kT}{mM\langle 1 - \cos\chi \rangle} + \frac{(m+M)^3 a^2 \tau^3 \langle 2m(1-\cos\chi)^2 + M \sin^2\chi \rangle}{mM^2 \langle 1 - \cos\chi \rangle^2 \langle 4m(1-\cos\chi) + 3M \sin^2\chi \rangle}, \tag{74}$$

[12] J. C. Maxwell, *Collected Papers* (Cambridge University Press, London, 1890), Vol. II, p. 40.

$$D_\perp=\frac{(m+M)\tau kT}{mM\langle 1-\cos\chi\rangle}+\frac{(m+M)^4a^2\tau^3\langle\sin^2\chi\rangle}{mM^2\langle 1-\cos\chi\rangle^3\langle 4m(1-\cos\chi)+3M\sin^2\chi\rangle}. \quad (75)$$

Special formulations for the isotropic model are obviously derivable from these. The formulas valid for the polarization force result by applying to them (30) and (31).

Equation (73) may be thought of as the natural extension of the Einstein relation to strong fields. This can be made explicit by writing it in the form

$$D_n/\text{mobility}=2\times(\text{mean random energy along } n)/e, \quad (76)$$

where n stands for one of the principal directions of the diffusion tensor. Equation (76) embraces both (73) and the Einstein relation. This means it is valid (a) for all interactions at low field and (b) for the mean free time case at all fields. An occasion to examine its validity beyond this range will present itself in the next section.

H. LONGITUDINAL DIFFUSION FOR THE CASE OF SECTION D

Diffusion offers a good test case to substantiate the claim made in Sec. D, namely, that specific quantities of experimental interest can be derived from the Boltzmann equation without working out the entire velocity distribution. Longitudinal diffusion was picked for computation, partly because its symmetry permits the use of the restricted expansion (11) rather than a more general expression, and partly because it looks as though the quantity is accessible to experimental measurement.[13]

For such a calculation the inhomogeneous equivalent of the equation system (17) is needed. This system is derived by following step by step the derivation of Sec. B, starting out from (71) which differs from (6) only in its inhomogeneous term. Skipping intermediate formulations corresponding to Eqs. (7), (8), and (14) we pass directly to the inhomogeneous form of the Eqs. (17), which reads

$$\begin{aligned}&a\nu(s+\nu+1)\{c^{s-1}P_{\nu-1}(\cos\vartheta)\}+a(\nu+1)(s-\nu)\\&\times\{c^{s-1}P_{\nu+1}(\cos\vartheta)\}-(2\nu+1)(1-I_{s,\nu})\\&\times\{c^sP_\nu(\cos\vartheta)/\tau(c)\}=k[\nu\langle c^{s+1}P_{\nu-1}(\cos\vartheta)\rangle\\&+(\nu+1)\langle c^{s+1}P_{\nu+1}(\cos\vartheta)\rangle-(2\nu+1)\langle c\cos\vartheta\rangle\\&\times\langle c^sP_\nu\cos\vartheta)\rangle]. \quad (77)\end{aligned}$$

Here the curly brackets represent averages over $f^*(\mathbf{c})$, that is, corrections to the angular brackets which are caused by the density gradient. Equation (77) permit addition of an arbitrary amount of the pointed brackets to these curly ones, because the former satisfy the homogeneous equations (17). This indeterminacy is removed by (67).

Just as in Part I we do not have to solve the equation system (77) completely in order to find the value of the longitudinal diffusion coefficient. As previously, this is trivially true for the case of constant mean free time. Here Eq. (77) with $s=\nu=1$ yields the answer directly. We find, using (16),

$$-3\frac{M\langle 1-\cos\chi\rangle}{(M+m)\tau}\{c_z\}=k\cdot 3[\langle c_z{}^2\rangle-\langle c_z\rangle^2].$$

Because of (65), (69), and (72) this is the longitudinal part of (73) which is thus derived.

The computation of $D_{||}$ from (77) for other models demands the use of the method of Sec. D. The case of special interest is the hard sphere model for equal masses. Let us specialize the system (77) for this case. We render the velocity dimensionless by adopting (37); we abbreviate further

$$\langle w^sP_\nu(\cos\vartheta)\rangle=\langle s,\nu\rangle \quad (78)$$

and

$$\{w^sP_\nu(\cos\vartheta)\}=k\lambda\{s,\nu\}. \quad (79)$$

The extra complication in the definition of the curly brackets symbols is such that all external parameters disappear from the equation system (77), which now reads

$$\begin{aligned}&\nu(s+\nu+1)\{s-1,\nu-1\}+(\nu+1)(s-\nu)\{s-1,\nu+1\}\\&-(2\nu+1)(1-I_{s,\nu})\{s+1,\nu\}=\nu\langle s+1,\nu-1\rangle\\&+(\nu+1)\langle s+1,\nu+1\rangle-(2\nu+1)\langle 1,1\rangle\langle s,\nu\rangle. \quad (80)\end{aligned}$$

Equation (80) forms a system of linear relations among the curly bracket symbols. Their interconnection is the same as the one shown in Fig. 4; hence the procedure for solving the system is identical with the one in Sec. D. The normalization condition is replaced by (67), which reads in the present notation

$$\{0,0\}=0. \quad (81)$$

In the place of (38), (39), and (40) we find

$$\begin{aligned}\{4,0\}=&-(5/3)\langle 4,1\rangle+(5/3)\langle 1,1\rangle\langle 3,0\rangle\\&-(10/3)\langle 2,0\rangle-(20/3)\langle 2,0\rangle+10\langle 1,1\rangle^2. \quad (82a)\end{aligned}$$

$$\begin{aligned}112\{3,0\}-3\{7,0\}=&4\langle 7,1\rangle-4\langle 1,1\rangle\langle 6,0\rangle\\&+(56/5)\langle 5,0\rangle+(112/5)\langle 5,2\rangle-(168/5)\langle 1,1\rangle\langle 4,1\rangle\\&-(1344/25)\langle 3,1\rangle+(1344/25)\langle 3,3\rangle\\&+(448/5)\langle 1,1\rangle\langle 2,0\rangle-(448/5)\langle 1,1\rangle\langle 2,2\rangle. \quad (83a)\end{aligned}$$

$$\begin{aligned}54\{2,0\}-(295/28)\{6,0\}+&(17/165)\{10,0\}\\=&-(17/135)\langle 10,1\rangle+(17/135)\langle 1,1\rangle\langle 9,0\rangle\\&-(17/36)\langle 8,0\rangle-(17/18)\langle 8,2\rangle+(17/12)\langle 1,1\rangle\langle 7,1\rangle\\&+6\langle 6,1\rangle-(21/5)\langle 6,3\rangle-(44/5)\langle 1,1\rangle\langle 5,0\rangle\\&+7\langle 1,1\rangle\langle 5,2\rangle+(54/5)\langle 4,0\rangle+(108/7)\langle 4,2\rangle\\&-(288/35)\langle 4,4\rangle-(162/5)\langle 1,1\rangle\langle 3,1\rangle\\&+(72/5)\langle 1,1\rangle\langle 3,3\rangle. \quad (84a)\end{aligned}$$

[13] The measurements of J. A. Hornbeck, Phys. Rev. **83**, 374 (1951), give a fluctuation in the mean drift which shows up in Fig. 5 for instance, by a rounding off of the vertical drop. One would expect this to be due to longitudinal diffusion of the ions.

The knowledge of the unperturbed velocity averages required by these equations is rather more extensive than was anticipated in Part I. Most of them are derivable from (41) and the coefficients following; for some the accuracy so obtained is insufficient because of cancellations in the equation system (17); these were obtained by extrapolation. The resultant numbers will be published in BSTJ.[4] Upon substitution the equations become

$$\{4,0\}=-10.494, \tag{82b}$$

$$112\{3,0\}-3\{7,0\}=647.8, \tag{83b}$$

$$54\{2,0\}-(295/28)\{6,0\}+(17/165)\{10,0\}=-566.4. \tag{84b}$$

The following step could perhaps be improved. We know in a general way that the diffusion correction to the velocity distribution is some sort of p-type function. What is needed, however, in this method is the correction to $h_0(w)$; beyond the knowledge implicit in (81), we know very little about it. In view of this ignorance the form (41) was adopted for this correction, with new undetermined coefficients p, q, r, s. This is undoubtedly a poor choice and explains the slower convergence observed here than in (42), (44), and (46). To start with the zero order is completely lost, because (81) yields a zero coefficient. We find in first order, using (81) and (82), $p^{(1)}=4.8842$, $q^{(1)}=-4.2689$, $r^{(1)}=s^{(1)}=0$; in second order, using (81), (82), and (83), $p^{(2)}=-10.542$, $q^{(2)}=+14.993$, $r^{(2)}=-4.408$, $s^{(2)}=0$; in the third order, using (81), (82), (83), and (84), $p^{(3)}=-0.8710$, $q^{(3)}=+1.1754$, $r^{(3)}=+1.0140$, $s^{(3)}=-0.5809$. The longitudinal diffusion coefficient results from these numbers by the use of (65), (69), and (72). With the notation of (79) the formula becomes

$$D_{||}=-a^{\frac{1}{2}}\lambda^{\frac{1}{2}}\{1,1\}. \tag{85}$$

The average $\{1,1\}$, in turn, is reducible to $\{3,0\}$ by the appropriate equation (80). We find

$$\{1,1\}^{(1)}=-0.3695, \tag{86a}$$

$$\{1,1\}^{(2)}=-0.2075, \tag{86b}$$

$$\{1,1\}^{(3)}=-0.2198. \tag{86c}$$

This extrapolates with reasonable certainty to

$$D_{||}=0.22a^{\frac{1}{2}}\lambda^{\frac{1}{2}}. \tag{87}$$

To gain an appreciation of this result we can compare it with the guess that would have resulted from (76). The mobility concept is ambiguous for all but the cases discussed then. It would seem that the appropriate concept here is the differential mobility because comparison is made between a small density gradient and a small change in the applied field. Thus, we would interpret (78) to mean

$$D_{||}\approx\frac{\partial\langle c_z\rangle}{\partial a}[\langle c_z^2\rangle-\langle c_z\rangle^2], \tag{88a}$$

which, with (37), (43), and (47), becomes

$$D_{||}\approx 0.26a^{\frac{1}{2}}\lambda^{\frac{1}{2}}. \tag{88b}$$

The error of formula (76) is thus 18 percent, when compared to (87).

I. CONCLUDING REMARKS; GENERALIZED RELATIONSHIPS

The purpose of these two articles was to develop the theory of ionic motion sufficiently well so that the presence of a strong electric field is no longer felt to be an insuperable obstacle to the use of kinetic theory. Explicit formulas, such as (43) and (87), were worked out when the experimental situation seemed to indicate the need for it.[5,12] For a wider and less rigorous use, estimates, such as (21) and (76), were presented. In addition, there is in the formulas for constant mean free time information which yields to judicious treatment. For example, if we desire to know the drift velocity of an ion for the hard sphere model and high field, but arbitrary mass ratio, then we can start from (18) replacing the mean free time by a mean free path

$$\langle c_z\rangle\approx[(M+m)/M](a\lambda/c).$$

As usual in kinetic theory we interpret the c in the denominator as a root mean square value; then we can substitute from (21) and get the final formula

$$\langle c_z\rangle\approx(M+m)^{\frac{1}{2}}m^{\frac{1}{2}}M^{-\frac{1}{2}}a^{\frac{1}{2}}\lambda^{\frac{1}{2}}. \tag{89}$$

For ions in the parent gas this expression differs from (43) by only 4 percent. For electrons (89) checks the result of Druyvesteyn[2] to within 12 percent. Finally, for heavy ions in a light gas, where the answer can be worked out rigorously also,[4] Eq. (89) is exact. Thus, it qualifies as a reliable approximate formula.

Because of a shortage of space, certain proofs and topics have been omitted from these two articles. A more extensive account is to appear shortly in the *Bell System Technical Journal*.[4]

These two articles owe their existence to the stimulation of Dr. J. A. Hornbeck of this laboratory. In the course of his experiments he perceived the gap in the existing theory which this study is intended to fill.

J. ERRATA IN PAPER I[11]

The definition of $I_{s,p}$ given in Eq. (16) does not agree with the verbal statement on the page preceding. A factor $(M+m)^s/2Mm$ has to be added to the verbal definition of $I_{s,p}$.

In the formula lying between (19) and (20) a factor $\langle 1-\cos\chi\rangle$ has been omitted in the denominator.

In formula (32) the second M should be an N.

In formula (63) the factor M^3 in the denominator should read M.

A Search for New Superconducting Compounds

B. T. MATTHIAS* AND J. K. HULM
Institute for the Study of Metals, University of Chicago, Chicago, Illinois
(Received May 12, 1952)

In an effort to throw new light on the electronic and structural conditions necessary for superconducting behavior, a magnetic test for superconductivity was applied to about ninety binary and ternary compounds at temperatures down to 1.28°K. The new superconductors Mo_2N, MoN, Mo_2B, NbB, $SrBi_3$, and $BaBi_3$ were discovered, and the superconductivity of TiN, ZrN, VN, Mo_2C, MoC, and W_2C, reported by previous investigators using the inconclusive electrical resistance test, was confirmed magnetically. No trace of superconductivity was observed in any one of the several ionic, covalent, or semiconducting compounds examined or in nine borides with boron content greater than 50 atomic percent. The results are discussed in relation to crystal structure and the periodic table.

I. INTRODUCTION

THE study of superconducting compounds began over twenty years ago when, following the discovery at Leiden and at Toronto that superconductivity occurs in many alloys and intermetallic compounds as well as in pure metals, Meissner and his co-workers[1–4] found that certain compounds of metals with nonmetallic elements such as nitrogen, carbon, and sulphur also become superconducting at solid hydrogen or liquid helium temperatures. One of the most interesting results disclosed by this work was that in some compounds, such as CuS, superconducting behavior was induced by the introduction of the nonmetal, since by itself the metallic element was known to remain normal down to the lowest temperatures of measurement. Although he tested quite a large number of binary compounds for superconductivity, Meissner unfortunately employed the electrical resistance method of measurement, which has since been shown to give ambiguous results in the case of impure specimens.[5] More recently a number of compounds have been tested by Justi and his co-workers[6] and by Horn and Ziegler,[7] while in the related field of intermetallic compounds of nonsuperconducting elements the early work of de Haas, von Aubel, and Voogd[8] on gold-bismuth has been extended by Alekseyevsky[9,10] and Reynolds and Lane.[11] The situation has remained far from satisfactory, however, in view of the large number of interesting compounds that have not been examined at low temperatures and owing to uncertainties regarding the extent to which the early experiments were affected by impurities and by deviations from stoichiometric composition. These difficulties led us some time ago to commence a new experimental survey of intermetallic and semimetallic compounds, the object being to remove some of the ambiguities of the earlier work and if possible to throw new light on the chemical and structural conditions governing the occurrence of superconductivity. While it seems unlikely that these conditions will be throughly understood until the quite well-established magnetic, electrical, and thermal properties of an "ideal" superconductor receive a satisfactory fundamental explanation, nevertheless, it is probable that both the chemical and physical objectives would be brought somewhat nearer if one knew the full range of types of solid and crystal lattices in which superconductivity is possible. Although our experiments have so far by no means completely answered the latter question, the results for about ninety compounds indicate certain solid types as unfavorable to superconductivity and also give a number of new superconductors which seem to be worth describing at the present time. Under the latter heading we shall discuss superconducting compounds of boron, carbon, and nitrogen with certain transition metals, some of which have already been briefly described,[12] and also some new intermetallic compounds of bismuth.

II. EXPERIMENTAL DETAILS

A. Method

The determination of superconducting behavior through the disappearance of the electrical resistance of a specimen suffers from the disadvantage that a small filament of superconducting impurity may short-circuit the bulk of the specimen and produce a large but spurious effect.[5,13,14] This difficulty may be to some

* Now at Bell Telephone Laboratories, Murray Hill, New Jersey.

[1] W. Meissner, Z. Physik **58**, 570 (1930).
[2] W. Meissner and H. Franz, Z. Physik **65**, 30 (1930).
[3] Meissner, Franz, and Westerhoff, Z. Physik **75**, 521 (1932).
[4] W. Meissner, Wien-Harms Handbuch der Exp. Physik **11**, 2 (Akad. Verlagsgesellschaft m.b.H., Leipzig, 1935).
[5] D. Shoenberg, Nature **159**, 303 (1947).
[6] Aschermann, Friederich, Justi, and Kramer, Physik. Z. **42**, 349 (1941).
[7] F. H. Horn and W. T. Ziegler, J. Am. Chem. Soc. **69**, 2762 (1947).
[8] de Haas, van Aubel, and Voogd, Leiden Comm. No. 197a and 197c (1929).
[9] N. Alekseyevsky, J. Phys. (U.S.S.R.) **9**, 350 (1945).
[10] N. Alekseyevsky, J. Exptl. Theor. Phys. **18**, 101 (1948); **19**, 671 (1949) and **20**, 863 (1950).
[11] J. M. Reynolds and C. T. Lane, Phys. Rev. **79**, 405 (1950).
[12] J. K. Hulm and B. T. Matthias, Phys. Rev. **82**, 273 (1951).
[13] This appears to have been the case, for example, in some of the early work on carbides. Ziegler and Young (see reference 14) recently found that certain carbides exhibit normal magnetic behavior in temperature ranges where superconducting resistance transitions had previously been reported by Meissner and Franz (see reference 2 and Sec. III D). Electrical resistance data must

extent overcome by measuring the change in magnetic induction of the specimen due to a given change in a small, externally applied magnetic field, or, in other words, determining the initial permeability of the specimen. Since a small, applied magnetic field cannot produce an appreciable induced field at a depth greater than about 10^{-5} cm, the penetration depth, below the surface of a homogeneous superconducting body, the initial permeability of such a body with linear dimensions large compared to 10^{-5} cm is essentially zero. The extent to which the permeability of an inhomogeneous

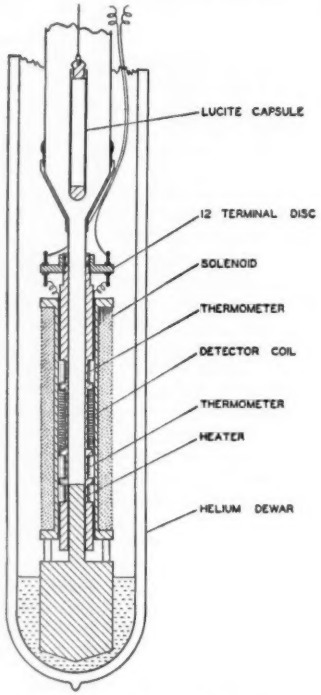

FIG. 1. Magnetic permeability apparatus.

specimen containing some superconducting regions differs from zero may give a rough idea of the volume of flux-linkable space or normal matter present, and with the aid of x-ray and chemical analysis the superconducting phase can often be identified unambiguously, in spite of the presence of considerable impurity. This is certainly possible for solid, superconducting grains in a normal matrix, but presents difficulties for normal grains in a superconducting matrix, since isolated normal regions may be completely screened from the applied field and contribute nothing to the total induction. That is to say, the effective permeability may differ appreciably from unity in spite of the presence of a relatively small volume of superconducting material, providing that this material is distributed in a "sponge-like" structure so as to sheath a large amount of normal material to a depth greater than the penetration depth. Such behavior has, in fact, been reported by Hudson[15] for tin-germanium alloys and has been experienced for certain compounds studied in the present work, as will be mentioned in the detailed discussion of experimental results. For the time being it will be remarked that although a consideration of impurities is important in the magnetic test as well as in the electrical test for superconductivity, in practice the permeability seems to be less sensitive to impurities than the resistance, presumably because closed superconducting sheaths are formed less readily than superconducting filaments. The magnetic method has the additional advantage that it is applicable to any state of physical aggregation, whereas solid rods, which are often difficult to fabricate, are necessary for satisfactory resistance measurements.

B. Magnetic Apparatus

Our particular system was designed to allow rapid testing of a fairly large number of specimens. Each sample, either in the form of a solid rod, or as a powder packed into a thin-walled cylindrical Lucite capsule, or sealed within a glass tube containing an atmosphere of helium gas in the case of materials unstable in air, was attached to the end of a Nylon fishing line and lowered into the arrangement shown schematically in Fig. 1. The sample was guided by a metal funnel into an 8-mm diameter Lucite tube on the outside of which was wound a detector coil, a heater coil, and two resistance thermometers. The detector coil consisted of 1000 turns of 40-gauge Formex-insulated copper wire wound in 3 layers on the Lucite tube, and changes in the induction of the specimen could be measured by observing the throw of a critically damped, high sensitivity galvanometer connected in series with the coil. In order to minimize the flux that leaked between the coil winding and the specimen material, the gap between these, including both Lucite and clearance space, was rarely allowed to exceed 0.07 mm. A magnetic field of a few oersteds could be applied to the specimen by a small solenoid which fitted closely around the specimen and detector coil. The whole arrangement was located in a liquid helium Dewar flask which was in turn surrounded by a liquid nitrogen flask and formed part of a conventional helium cryostat not shown in Fig. 1.

undoubtedly be treated with caution, and we hope to check magnetically all the important earlier results based solely on resistance measurements.

[14] W. T. Ziegler and R. A. Young, Report of the International Low Temperature Conference, Oxford, England, August, 1951.

[15] R. P. Hudson, Phys. Rev. **79**, 883 (1950).

C. Measuring Technique

For measurements below 4.2°K the detector system was completely immersed in liquid helium, and temperatures down to 1.28°K could be attained using a 45-liters-per-second pump suitably connected to the cryostat. Temperatures were obtained from the vapor pressure of the helium bath, using the 1949 International Scale.[16] Any one of six specimens could be lowered into the detector coil at a given temperature by means of six winches situated in the helium gas at the top of the cryostat. The winches were operated from the outside by driving rods packed with Teflon and were observed through a clear Lucite plate sealed into the top of the cryostat. To facilitate testing of more than six specimens down to 1.28°K, the entire winch assembly could easily be removed and new specimens quickly attached to the Nylon lines. The whole procedure of admitting helium gas to the cryostat to increase the pressure up to atmospheric value, changing specimens, and pumping down to 1.28°K again could be accomplished in a few minutes and with the loss of only a small quantity of liquid helium, probably because the main bulk of the bath did not have time to warm above the lambda-temperature. In this manner as many as 24 specimens were dealt with for one shot of liquid helium in the cryostat.

For measurements above 4.2°K the liquid helium level was allowed to fall below the detector coil and manganin heater coil, as shown in Fig. 1, whereupon the specimen temperature could be raised slowly by regulating the pumping speed and heater current. Temperatures were measured by two 1000-ohm, noninductive, constantan resistance thermometers which had a sensitivity of about 1 ohm per degree and which were located one above and one below the detector coil. These thermometers were calibrated in the liquid hydrogen and liquid helium ranges, and temperatures in the intermediate range were obtained by interpolation. Since a difference of a few tenths of a degree usually existed between the two thermometers in the 4.2° to 10°K range, specimen temperatures in this range were known to little better than 0.5°K.

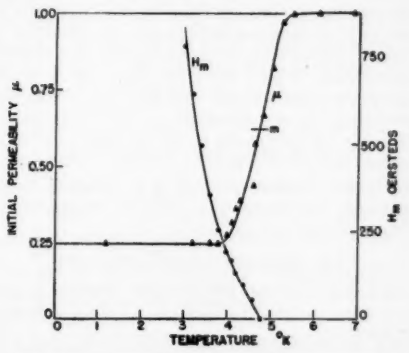

FIG. 2. Temperature variation of initial permeability μ and midpoint field H_m for Mo_3B specimen.

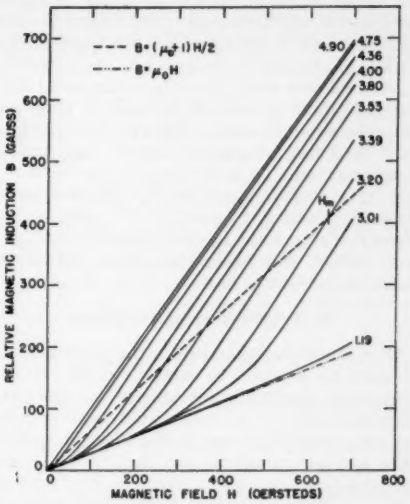

FIG. 3. Magnetic induction—magnetic field curves at various temperatures, Mo_3B specimen.

The usual procedure was to observe the galvanometer throw produced by switching off a field of about 10 oersteds, which is considerably less than the limiting critical field for most superconductors with transition temperatures above 1°K. During the "on" period the solenoid current was stabilized with a potentiometer circuit, so that by measuring the galvanometer throw for unit permeability before lowering the specimen into the coil, initial permeabilities close to unity could be determined with about 0.2 percent absolute accuracy and traces of superconducting behavior could readily be observed. The variation of permeability with temperature for most of the superconducting powder samples was of the type shown in Fig. 2, with the transition spread out over an appreciable range. The transition temperature was estimated in such cases from the midpoint m corresponding to a permeability of $(\mu_0+1)/2$, where $\mu \to \mu_0$ as $T \to 0$.

The initial permeability data were supplemented in a few cases by measurements at various temperatures of magnetic induction—magnetic field curves for field strengths up to 700 oersteds, using a large, external solenoid. These magnetic field transitions were also of the spread-out type shown in Fig. 3, where the term "relative magnetic induction" denotes the fact that all induction values were referred to the same zero, ignoring the contribution of frozen-in flux. Measurements

[16] H. van Dijk and D. Shoenberg, Nature **164**, 151 (1949).

based on the virgin magnetic state showed the latter contribution to be quite large in some cases. Defining the field H_m (not to be confused with the critical field H_c) as the field at which B attains a value $(\mu_0+1)H_m/2$, one may expect the curve of H_m *versus* T to intersect the temperature axis at the temperature of the midpoint m of the initial permeability curve. Since this was found to be true for several typical specimens (e.g., Fig. 2), we frequently used the H_m data alone to estimate the transition temperature. It should be mentioned that H_m was occasionally a linear function of T^2 over quite a wide temperature range, indicating a simple proportionality to H_c.

D. Preparations and Analyses

Most of the specimens were either readily available or could be prepared by methods similar to those described by previous investigators, which need not be discussed in detail. To mention a few essential points, the compounds $SrBi_3$ and $BaBi_3$, of which only the latter had been previously described,[17] were prepared by heating the appropriate mixtures in a controlled helium atmosphere at about 650°C. Both compounds formed as bright, silvery cubes which, however, were rapidly attacked by moist air at room temperature. For superconducting tests the crystals were packed tightly into thin-walled glass tubes which were filled with helium gas at atmospheric pressure before sealing off.

Several of the group 6A nitride specimens were prepared by passing ammonia gas over the heated metal, but in the case of molybdenum and tungsten a much faster reaction was obtained by ammoniating the metallic oxides at about 700°C, a method that does not seem to have been previously reported. Attempts to prepare WN by this method were unsuccessful, no samples being obtained with a nitrogen content appreciably greater than that of W_2N.

Most of the remaining intermetallic compounds and the borides and carbides were prepared using a vacuum induction furnace in which temperatures up to about 2100°C could easily be obtained. In recent work some of the more refractory compounds were prepared by melting the appropriate mixtures in a helium arc furnace.

X-ray powder diffraction patterns were taken in all cases where the structure or composition of a specimen were in doubt, while spectrographic analyses were performed for a few samples where the source of a trace of superconducting behavior could not be identified from the other information available. Where structural data are discussed without explicit reference to original papers, the information was obtained from Wyckoff's tables.[18]

Attention may be drawn to one case in which the x-ray results were of special interest, namely, molybdenum carbide, which was prepared in the arc furnace. Our pattern was in good agreement with the γ-phase pattern of Sykes, Kent, and Tucker,[19] except for a slight increase of all interplanar spacings. The latter effect appears to have been due to the fact that about 52 atomic percent of carbon was deliberately employed in our specimen to suppress the β-phase, Mo_2C, whereas the γ-phase studied by Sykes *et al.* probably contained only 50 atomic percent of carbon. Our x-ray data for MoC show no evidence for the presence of Mo_2C and strengthen the view that the structure of the γ-phase is more complex than the hexagonal arrangement (isomorphous with WC) suggested by Tutiya.[20]

III. RESULTS AND DISCUSSION

A. Compounds of Borderline Elements

It is well known that the twenty-one superconducting elements lie in two distinct regions of the periodic system, within groups 3A to 8A and groups 2B to 4B, respectively, and also that the known superconducting compounds, such as CuS and MoC, formed entirely from nonsuperconducting elements, contain at least one component lying immediately next to one of these two superconducting regions. On the hypothesis that the latter phenomenon springs partially from the fact that such "borderline" elements require the least drastic modification of their electronic character to produce superconducting behavior, we tested several compounds containing one or occasionally two of these elements. Although a large number of the compounds of Table I contain borderline elements in the superconducting sense, and in some cases show pronounced metallic character, they gave no evidence of superconducting behavior down to 1.28°K.

TABLE I. Compounds of borderline elements and semiconducting compounds nonsuperconducting down to 1.28°K (present work).

Copper	CuP, CuSi, Cu_3As,[a] Cu_3Sb, $CuBr_2$, Cu_2Mg, $CuMg_2$, CuSe,[a,b] Cu_2O,[c] CuO[a,d]
Silver	Ag_2O, Ag_2S,[c,d] Ag_2Se,[c] Ag_2Te,[c] Ag_2Be, Ag_2Bi, AgMg
Antimony	SbS_3, SbK, Sb_2Cr, Sb_3Ce, SbBi, SbCuMg
Oxides	MoO_2,[a] UO_2,[c] CoO,[c] NiO,[c] Mn_2O_3, V_2O_3, Ti_2O_3,[a] Rh_2O_3
Sulphides	MoS_2,[c] PbS,[a,c] SnS, CeS, Ce_2S_4, NiS
Others	MoP, SiC,[c] SiFe, PbTe,[a,c] NiAs[a]

[a] Previously tested by Meissner, Franz, and Westerhoff [Ann. Physik 17, 593 (1933)] down to 1.3°K.
[b] Isomorphous with CuS [International Union of Crystallography, Structure Reports, II. N. V. A. Dosthoeks Uitgevers MIJ Utrecht (1951)].
[c] Known semiconductors [F. Seitz, *Modern Theory of Solids* (McGraw-Hill Book Company, Inc., New York, 1940)].
[d] Previously tested by McLennan, Allen, and Wilhelm [Phil. Mag. 10, 500 (1930)] down to 1.9°K.

B. Semiconducting Compounds

It is difficult to say with certainty from the available data that a substance which has a resistance-tempera-

[17] E. Grube and A. Dietrich, Z. Elektrochem. 44, 755 (1938).

[18] R. W. G. Wyckoff, *Crystal Structures* (Interscience Publishers, New York, 1951), Vol. I.

[19] Sykes, Kent, and Tucker, Trans. Am. Inst. Mining Met. Engrs. 117, 173 (1935).

[20] H. Tutiya, Bull. Inst. Phys. Chem. Research (Tokyo) 11, 121 (1932).

ture curve of the type characterizing semiconduction[21] cannot undergo a superconducting transition at sufficiently low temperatures. This seems likely, of course, on any free-electron theories such as those proposed recently by Fröhlich[22] and Bardeen,[23] and we certainly found no evidence of superconducting behavior in the dozen or so semiconducting compounds listed in Table I. In the case of PbS and PbTe we support the recent conclusions of Hudson[24] that these compounds show normal magnetic behavior at liquid helium temperatures, so that the electrical resistance transition in the neighborhood of 4°K reported for PbS, PbSe, and PbTe by Darby, Hatton, and Rollin[25] was very probably due to filamentous superconducting impurities. Since the experiments of Meissner and his co-workers[4] and the present authors provide negative results for a fairly typical group of ionic and covalent substances, it seems likely at present that metallic bonding is an essential prerequisite for superconducting behavior.

C. Bismuth Compounds

Although bismuth correctly belongs to the class of borderline elements to which reference has already been made, its compounds offer such a markedly different picture from those of other members of the class that it seems best to discuss them separately. Despite the fact that bismuth itself behaves normally down to 0.05°K,[26] it combines with nine other nonsuperconducting metals to form ten distinct superconducting compounds. The available data on these compounds, including results of the present work, are given in Table II.

In view of Alekseyevsky's discovery that $CaBi_3$ becomes superconducting at about 1.7°K, it seemed worthwhile to investigate other compounds of bismuth with alkaline earth metals. We observed superconducting behavior in $SrBi_3$ and $BaBi_3$, obtaining isothermal magnetic field transitions which were of the gradual type described in Sec. II C. Since the half-value field H_m was a linear function of T^2 for both compounds over the whole superconducting range, the results may be expressed in the form

$$SrBi_3,\ H_m = 530\ (1-T^2/31.6)\ \text{oersteds},$$

$$BaBi_3,\ H_m = 740\ (1-T^2/32.4)\ \text{oersteds}.$$

The transition temperatures 5.62°K ($SrBi_3$) and 5.69°K ($BaBi_3$), which are the highest ones known for bismuth compounds, replace slightly different, earlier values[27] derived from initial permeability-temperature curves.

Its position in the periodic system and conformity to the $(8-N)$ coordination rule[28] indicates that bismuth lies in the border region between metallic and nonmetallic behavior. Its electrical and magnetic properties[29] point to a nearly filled Brillouin zone and to a conduction electron-to-atom ratio considerably less than one, so that in the formation of superconducting compounds of bismuth the function of the other metal may be mainly to increase the effective number of conduction electrons per atom. From another point of view, Meissner[4] suggested that the superconducting behavior of Au_2Bi and certain lead-bismuth alloys springs from the cubic coordination of bismuth in these solids. Examining this idea in the light of recent evidence, we note that of the six superconducting bismuthides for which structural data are available,[18,30] four (Au_2Bi, KBi_2, $SrBi_3$ and $BaBi_3$) are cubic and two (LiBi, NaBi) are body-centered tetragonal. Against this, the four nonsuperconductors of known symmetry are the two cubic compounds, CeBi and CuMgBi, and the two hexagonal compounds, MnBi and Mg_3Bi_2. The paramagnetic influence of cerium may inhibit superconductivity in the first case, but if the cubic structure hypothesis is correct, there seems to be no obvious explanation for the normal behavior of CuMgBi. It is also difficult to understand why, despite the close chemical resemblance between antimony and bismuth, none of the compounds formed by antimony and other nonsuperconducting elements are known to exhibit superconducting behavior in the liquid helium range,

TABLE II. Superconducting and nonsuperconducting compounds of bismuth with normal metals, including results of previous work (see references). Transition temperature or lowest temperature of measurement in parenthesis.

Superconducting		
LiBi (2.47°)[a]	$CaBi_3$ (1.7°)[b]	Au_2Bi (1.8°)[d]
NaBi (2.22°)[b]	$SrBi_3$ (5.62°)	$RhBi_2$ (2.2°)[b]
KBi_2 (3.6°)[c]	$BaBi_3$ (5.69°)	$RhBi_4$ (2.75°)[b]
		$NiBi_3$ (3.6°)[b]

Nonsuperconducting
CeBi, MoBi, SbBi, $CeBi_2$, $GeBi_2$, Ag−Bi, CuMgBi, Mg_3Bi_2, MnBi (1.28°)
$PtBi_2$ (1.8°),[b] $CrBi_2$ (1.57°),[b] Se_2Bi_3 (1.3°),[e] Te_2Bi_3 (1.3°)[e].

[a] L. Guttman and J. W. Stout, Proceedings of the Low Temperature Conference, National Bureau of Standards, March (1951).
[b] See reference 10.
[c] See reference 11.
[d] See reference 8.
[e] Meissner, Franz and Westerhoff, Ann. Physik **17**, 593 (1933).

[21] W. Shockley, *Electrons and Holes in Semiconductors* (D. Van Nostrand Company, Inc., New York, 1950).
[22] H. Fröhlich, Phys. Rev. **79**, 845 (1950).
[23] J. Bardeen, Phys. Rev. **80**, 567 (1950).
[24] R. P. Hudson, Proceedings of the Low Temperature Conference, National Bureau of Standards, Washington, March (1951).
[25] Darby, Hatton, and Rollin, Proc. Phys. Soc. (London) **63**, 1181 (1950).
[26] N. Kurti and F. Simon, Proc. Roy. Soc. (London) **A151**, 610 (1935).
[27] B. T. Matthias and J. K. Hulm, Proceedings of the Low Temperature Conference, National Bureau of Standards, March (1951).
[28] W. Hume-Rothery, *The Structure of Metals and Alloys* (Institute of Metals, London, 1936).
[29] N. F. Mott and H. Jones, *The Theory of the Properties of Metals and Alloys* (Oxford Press, London, 1936).
[30] M. Hansen, *Der Aufbau der Zweistofflegierungen* (J. Springer, Berlin, 1936).

TABLE III. Superconducting nitrides, carbides, and borides, including compounds (denoted *) for which earlier resistance data have been checked magnetically.

TiN (4.86°)[a, b, *]	Mo_2N (5.0°)	Mo_2C (2.78°)[a, *]
ZrN (9.05°)[a, b, *]	MoN (12.0°)	W_2C (2.74°)[d, *]
VN (7.5°)[a, b, *]	MoC (9.26°)[a, *]	Mo_2B (4.74°)
NbN (14.7°)[b, c]	NbC (10.3°)[a]	NbB (8.25°)

[a] See reference 2.
[b] See reference 34.
[c] See reference 7.
[d] See reference 38.

although six of these compounds were tested in the present work (Table I) and five by Alekseyevsky.[10]

D. Interstitial Compounds of the Transition Metals

Most of the transition metals form compounds of the type Me_2X, MeX, or MeX_2 or slightly more complex formulas in which the arrangement of the metal atoms Me approximates a face-centered cubic or hexagonal close-packed lattice with the small "metalloid" atoms, X, either hydrogen, boron, carbon, nitrogen, or oxygen in the interstices of the lattice. The structures of many of these compounds have been investigated by Hägg[31] and Kiessling,[32] while Moers[33] found that in several cases the electrical resistivity is similar both in magnitude and temperature variation to that of a typical moderately pure metal. A review of the experiments of Meissner,[4] Ziegler and Young,[14] and the present authors indicates that reliable evidence of superconducting behavior now exists for the nitrides, carbides, and borides listed in Table III.

On the other hand, we observed that the nitrides, carbides, and borides listed in Table IV behave normally down to 1.28°K. Oxides and hydrides will be omitted from the present discussion, since hardly any progress has been made in studying superconductivity in these compounds.

Nitrides

The superconducting behavior of the NaCl-structure mononitrides TiN, ZrN, VN, and NbN was confirmed[34] and a new mononitride, hexagonal MoN, was found to become superconducting at about 12.0°K; this value is not only the second highest transition temperature at present known but is also remarkable in view of the fact that although the metallic constituents of the first four nitrides mentioned above are themselves known to be superconducting, molybdenum metal remains normal down to 0.05°K.[35] Such behavior is not reproduced by the group 6A element immediately above molybdenum, since we found both chromium and NaCl-structure CrN to behave normally down to 1.28°K. The sudden drop in superconducting transition temperature which accompanies an increase in atomic number from 23 (V) to 24 (Cr)[36] evidently occurs, therefore, in the mononitrides as well as in the pure metals. In view of the antiferromagnetic nature of the body-centered cubic lattice proposed by Zener,[37] it may be that the disappearance of superconducting behavior with increasing atomic number is due, in the metallic case, to increased antiferromagnetic coupling. This explanation hardly seems applicable to the nitrides, however, since in both VN and CrN the metal atoms form a face-centered cubic lattice which is apparently unfavorable to antiferromagnetism.

Of the lower nitrides known to exist, we tested Mo_2N and W_2N, both of which have an NaCl type of structure with half of the interstitial positions vacant.[31] While Mo_2N became superconducting at about 5.0°K, W_2N remained normal down to 1.28°K. Although the mononitride of tungsten would be of considerable interest, this compound could not be prepared (Sec. II D).

TABLE IV. Nitrides, carbides, and borides nonsuperconducting down to 1.28°K (present work only).

Group 5A	Nb_2B_4, NbB_2, TaB, Ta_3B_4, TaB_2.
Group 6A	CrN, Cr_3C_2, CrB, CrB_2, MoB (tetragonal) MoB (orthorhombic), Mo_2B_5, W_2N, WC, WB, W_2B_5.
Others	BN, B_4C, RhC, RhB, PtB, IrB, CeC_2, TiB_2, BaB_6.

Carbides

From resistance measurements, Meissner and Franz[2] reported that the monocarbides ZrC, NbC, TaC, MoC, and WC exhibit superconducting transitions in the ranges 4.07°–3.35°, 10.5°–10.1°, 9.5°–9.3°, 7.8°–7.6°, and 4.2°–2.5°K, respectively. Recently, however, Ziegler and Young[14] tested ZrC, TaC, and WC magnetically and found no evidence of superconducting behavior down to 1.8°K. In view of the greater reliability of the magnetic method, it seems quite likely that the early results were spurious ones caused by superconducting impurities, probably either free metal or metallic nitrides.

We tested pure samples of WC and MoC, observing that the former remained normal down to 1.28°K, in agreement with Ziegler and Young, while the latter became superconducting at 9.26°K (see Fig. 4), not too far from the transition range found by Meissner and Franz. The transition temperature of our MoC sample may be somewhat higher than that of exactly stoichio-

[31] G. Hägg, Z. Phys. Chem. B **6**, 221 (1929); **7**, 339 (1930); **8**, 455 (1930); **12**, 33 (1931).
[32] R. Kiessling, Acta Chem. Scand. **1**, 893 (1947); **3**, 90 and 595 (1949); **4**, 146, and 209 (1950).
[33] K. Moers, Z. anorg. Chem. **198**, 262 (1931).
[34] G. Hardy and J. K. Hulm, Magnetic data for pure samples (to be published in detail shortly).
[35] E. Mendoza and J. G. Thomas, Report of the International Low Temperature Conference, Oxford, England, August (1951).
[36] It has recently been found that the addition of a few percent of Cr to V greatly decreases the transition temperature, less than 20 atom percent Cr probably being adequate to completely suppress superconducting behavior. Details will be published shortly.
[37] C. Zener, Phys. Rev. **81**, 440 (1951); **85**, 324 (1952).

metric MoC, owing to the slight excess of carbon, which, as already mentioned, was used to prevent the formation of Mo_2C. The possibility that the superconducting behavior was due to molybdenum nitride impurities is ruled out by the complete absence of nitride lines from the x-ray pattern. Until NbC has been tested magnetically, we conclude that MoC remains the only monocarbide unambiguously known to be superconducting.

We also tested nitride-free specimens of the hexagonal lower carbides Mo_2C and W_2C, both of which became superconducting at 2.78°K and 2.74°K, respectively, in quite good agreement with resistance transitions observed in the ranges 3.2°K–2.4°K for Mo_2C by Meissner and Franz[2] and 3.5°K–2.05°K for W_2C by McLennan, Allen, and Wilhelm.[38] Both our samples gave sharp x-ray patterns which were very similar to those obtained by Westgren and Phragmen[39] and Becker[40] and which indicated that the only impurity was a small trace of WC in the tungsten compound. Since tungsten monocarbide remains normal down to 1.28°K, its presence was of no importance.

Borides

By x-ray studies of the transition metal borides, Kiessling[32,41] found that with increasing boron content the boron atoms form successively into chains, nets, and three-dimensional frameworks, presumably through the formation of covalent bonds. In this respect the borides differ markedly from other interstitial compounds such as carbides and nitrides, among which Cr_3C_2 seems to be the only example of chain structure formation by the "metalloid" atoms. Kiessling suggested that boride formation is accompanied by a transfer of electrons from the boron chains to the metal atoms, but Pauling[42] contends that at least a fraction of an electron per atom is transferred in the opposite direction. Whichever direction the transfer, if any, takes place in, there is undoubtedly a change in metallic character with increasing boron content, a change which appears from our results to be increasingly unfavorable to superconductivity.

Commencing at the low boron content end of the range, there are several hemiborides with a tetragonal lattice of the $CuAl_2$ type containing boron atoms that are essentially isolated within groups of metal atoms. In this class we have so far tested only Mo_2B, which became superconducting at about 4.74°K (Figs. 2, 3). The x-ray pattern for this sample gave no evidence of the presence of superconducting impurities such as carbides or nitrides of molybdenum.

Among the monoborides Kiessling described three different types of lattice which have two common features: first, the occurrence of separate boron chains; and second, the arrangement of the metal atoms in a very distorted close-packed hexagonal lattice. The orthorhombic type represented by FeB, CoB, and MnB was not examined, but we tested all known examples of the other two types, *viz.*, orthorhombic CrB, NbB, TaB, and MoB and tetragonal MoB and WB. The only one of these compounds to exhibit superconducting behavior above 1.28°K was NbB, with a transition temperature of 8.25°K. In a previous paper[12] we reported a somewhat lower transition temperature, 6.0°K for NbB, which appears, however, to have been due to several percent of dissolved impurity, mainly molybdenum; furthermore, the superconducting transition

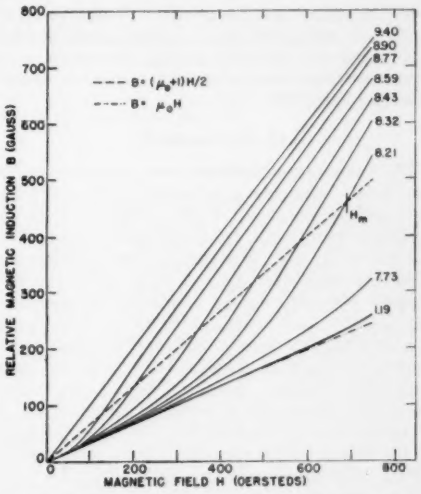

FIG. 4. Magnetic induction—magnetic field curves at various temperatures, MoC specimen.

reported at 4.4°K for MoB is now known to have been due to small amounts of Mo_2B impurity.[43]

Meissner and his co-workers[3] described resistance

[38] McLennan, Allen, and Wilhelm, Trans. Roy. Soc. (Canada) **25**, Sec. 3, 1 (1931).
[39] A. Westgren and G. Phragmen, Z. anorg. Chem. **156**, 31 (1926).
[40] K. Becker, Z. Physik **51**, 481 (1928).
[41] R. Kiessling, J. Electrochem. Soc. **98**, 166 (1951).
[42] L. Pauling, J. Electrochem. Soc. **98**, 518 (1951).

[43] Our early samples were powders prepared in the induction furnace. The molybdenum boride sample was mainly tetragonal MoB but contained small amounts of Mo_2B. Since flux was excluded from about 70 percent of the volume of the sample below 4.4°K, the superconducting behavior was attributed to MoB. However, Ziegler and Young failed to confirm our result, and the question was reopened by preparing an MoB sample entirely free of Mo_2B (by melting molybdenum with 52 atomic percent of boron in the arc furnace) and also a pure Mo_2B sample. As already mentioned, the Mo_2B sample became superconducting at 4.8°K, whereas the MoB sample, containing both the tetragonal form and a metastable orthorhombic form described by R. Steinitz [J. Metals 4, 148 (1952)] remained normal down to 1.28°K. We conclude, therefore, that the behavior of the earlier molybdenum boride sample was due to Mo_2B impurities distributed so as to envelop a good deal of normal matter in a flux-excluding sheath. The danger of ignoring small amounts of impurity, even in magnetic measurements, is well brought out.

tests on the monoborides of titanium, zirconium, and hafnium which disclosed a transition in the range 3.8°–2.8°K for "ZrB." However, considerable doubt is cast on these results by the structure work of Kiessling, according to which "ZrB" does not exist and TiB tends to decompose into titanium and TiB_2 at room temperature. We found the hexagonal compound TiB_2 to behave normally down to 1.28°K, while Ziegler and Young observe normal behavior in TiB_x, ZrB_2, and ThB_2 down to 1.8°K.

Other monoborides were disclosed by the recent work of Buddery and Welch[44] on the combination of boron with the platinum group of metals, but no structural data are yet available for these compounds. We tested sintered samples of the approximate compositions PtB, RhB, and IrB down to 1.28°K, without observing superconducting behavior. Finally, no superconductors were found with a boron content appreciably greater than 50 atomic percent, presumably owing to the dominant covalent character of boron in such cases (see Table IV).

IV. CONCLUSION

The known superconductors now comprise twenty-one metallic elements, a large number of alloys and intermetallic compounds which contain at least one superconducting metal, ten intermetallic compounds of bismuth with other nonsuperconducting metals and about thirteen distinct compounds of metals with nonmetallic elements, mainly interstitial compounds of boron, carbon, and nitrogen with metals of the transition groups. The present experiments revealed new superconducting bismuthides and new interstitial superconductors, without, however, yielding new superconducting compounds of radically different types, all of which tends to support the view, based primarily on the behavior of the elements, that the superconducting phenomenon requires metallic bonding of a rather special character, so far known mainly by its localization in the periodic system.[45] Perhaps the most interesting new evidence on this character is provided by the interstitial compounds, of which the known superconductors comprise six nitrides, four carbides, and two borides, possibly indicating a decrease in superconducting tendency with decrease in the number of electrons of the "metalloid" atom. There are, unfortunately, structure differences within the interstitial series which complicate this effect.

Although the role of crystal structure remains indefinite, we regard it as a significant fact that among the superconducting elements the transition takes place below 1°K for eight of the ten close-packed hexagonal metals and above 1°K for all of the eight cubic and tetragonal metals. This apparent tendency for transition temperatures to be lower for a hexagonal lattice than for a cubic lattice is borne out by the behavior of the nitrides, where in TiN and ZrN, for example, the metal atoms form a face-centered cubic lattice and the transition temperatures lie well above those of the close-packed hexagonal parent metals. Similarly, in the monoborides where the metal atoms form a very distorted close-packed hexagonal lattice, only NbB is known to be superconducting above 1.3°K; even in this case the transition temperature (8.25°K) is lower than that of the cubic parent metal Nb (9.3°K) or the cubic nitride NbN (14.7°K). Finally, in agreement with the above trend, mostly cubic or tetragonal symmetry has so far been found among the bismuth compounds known to be superconducting above 1°K.

Considerations of the above type could perhaps be placed on a more quantitative basis if the effects of crystal structure changes could be distinguished clearly from effects due purely to variations in the conduction electron-to-atom ratio in the normal solid. Although in a sense these two factors are inseparable, since the behavior of the conduction electrons is determined largely by the containing lattice, nevertheless, some hope is offered by the possibility of varying the number of conduction electrons per atom over a considerable range within a given type of structure. The extensively studied group *B* superconductors provide little opportunity in this respect, owing to the diversity of their crystal structures and their lack of interstitial compounds. A much more fruitful situation exists for the group A superconducting metals, however, since body-centered cubic, solid solution alloys are formed by the superconductors vanadium, niobium, and tantalum with up to about 80 atomic percent of their group 4A neighbors and over the complete range with their group 6A neighbors. Furthermore, the majority of the monoxides, mononitrides, and monocarbides of these metals belong to the simple NaCl lattice and presumably form wide range solid solutions among themselves. It is hoped that experiments that are now in progress on the magnetic and electrical properties of such alloys of the transition metals and their interstitial compounds will lead to a deeper understanding of the critical electronic conditions producing superconductivity.

It is a pleasure to thank Professor E. A. Long for help in the design and construction of the helium cryostat and Mr. G. Hardy for assisting in the later experiments.

[44] J. H. Buddery and A. J. E. Welch, Nature **167**, 362 (1951).

[45] *Note added in proof:*—$CoSi_2$, recently found to be superconducting by one of us (B. T. Matthias, Phys. Rev. **87**, 380 (1952), seems to be exceptional from this point of view.

A Soluble Problem in Energy Bands*

J. C. SLATER†
Brookhaven National Laboratory, Upton, New York
(Received April 30, 1952)

The problem of an electron moving in a periodic simple cubic potential of the form $\cos x+\cos y+\cos z$ is investigated, with particular attention to the nature of the wave functions, Wannier functions, degeneracy of overlapping bands, etc. It is well known that this problem is separable, leading to Mathieu's equation for the functions of x, y, and z. This equation can be solved, making use of the Fourier expansion of the wave function (the momentum eigenfunction). Solutions are set up, for a number of interatomic distances. The momentum eigenfunctions are similar to Hermite functions for the tightly-bound levels but very different for free-electron-like levels. Those for the levels near the top of the potential barrier, corresponding to the valence and conduction bands of a real crystal, are very complicated; we illustrate their properties by means of a test of the completeness relation for orthogonal functions. It is proved that the Wannier function is the Fourier transform of the momentum eigenfunction, and special cases are discussed. The effect of various perturbations on the one-dimensional problem is considered. It is shown that the usual assumption made in band theory, connecting the width of the gap introduced by a perturbation with the matrix component of the perturbative potential, is not generally justified. The case of a perturbation of double periodicity is taken up, and it is shown that this results in a spreading out of the Wannier function, which sometimes has large contributions on many atoms. In the two- and three-dimensional cases, the interesting feature is the degeneracy between overlapping bands, for example, between the different components of a p or a d band. These are discussed in detail. For the unperturbed Mathieu case, the energy surfaces cut without interaction, but almost any reasonable perturbation will cause them to interact, resulting in perturbed bands of great complication, which will not cut each other, though they may adhere at certain points of crystal symmetry, as can also be proved by group theory. The Wannier functions in these cases become combinations of the Wannier functions of the unperturbed problem, located on many different atoms, and possessing the rotational symmetry of the crystal, which the unperturbed Wannier functions do not have. The type of perturbation is also taken up which would convert the simple cubic potential of the unperturbed problem into a face-centered or body-centered structure.

ONE of the important parts of the quantum theory of solids is the solution of Schrödinger's equation for an electron moving in a periodic potential. Everyone is familiar with the two limiting approximate methods which have proved useful for this problem: the bound-electron or atomic approximation appropriate for the tightly-bound atomic electrons whose wave functions hardly overlap, and the free-electron approximation appropriate for electrons moving so fast that their wave functions are not far from plane waves. Everyone is also familiar with the fact that the general properties of energy bands, arising merely from the periodicity of the potential, and the mathematics associated with Floquet's theorem are valid independent of any approximation and hold equally for both of the limiting methods mentioned above. Unfortunately, however, there is every reason for thinking that the electrons which we are most interested in—the valence and conduction electrons in crystals—have wave functions of a type intermediate between the range of validity of the two approximations, and probably not representable very well by either method. Both methods, of course, have been used to describe these wave functions, as has also the cellular method. Nevertheless, it would add greatly to our confidence if we had a problem, not too far from the realities of the crystal lattice, in which we could follow through rigorously between the regions in which the two limiting approximations are applicable and see what really happens in the intermediate case.

Fortunately such a problem exists: the potential energy of the general form $-\cos x-\cos y-\cos z$. This has minima at the points of a simple cubic lattice, $x=2\pi n_x$, $y=2\pi n_y$, $z=2\pi n_z$, where n_x, n_y, n_z are integers. Around each minimum, the potential energy can be expanded in power series, representing a three-dimensional linear oscillator for small amplitudes; around the origin it has the value $-3+r^2/2\cdots$, where $r^2=x^2+y^2+z^2$. Thus the wave functions of tightly-bound states will be like the solutions of the three-dimensional oscillator problem and can be written in terms of Hermite functions. On the other hand, the high energy levels of the problem are like plane waves. The great virtue of this potential is that, being the sum of a function of x, a function of y, and a function of z, the problem is separable, and the corresponding one-dimensional problem is Mathieu's equation, which has been the subject of much attention by the mathematicians.

It is, of course, nothing new to realize this situation. Brillouin[1] used this problem in some of his earliest work on the theory of energy bands. Morse[2] recognized its value very early and used it for study of electron diffraction; MacColl,[3] working recently on the same problem by similar methods, seems unaware of Morse's earlier work. As an illustration of a recent application of the method, we may mention the work of Statz[4] on surface states. Nevertheless, there is a good deal more information to be extracted from the problem than has been found so far, and the writer has examined particularly the nature of the intermediate cases between the free and bound states, with results to be described in the present paper. This work has been considerably

* Research carried on under the AEC.
† On leave from Massachusetts Institute of Technology, Cambridge, Massachusetts.

[1] L. Brillouin, J. phys. et radium **1**, 377 (1930).
[2] P. M. Morse, Phys. Rev. **35**, 1310 (1930).
[3] L. A. MacColl, Bell System Tech. J. **30**, 888 (1951).
[4] H. Statz, Z. Naturforsch. **5a**, 534 (1950).

simplified and facilitated by the recent appearance[5] of a very important tabulation of some of the numerical properties of the Mathieu functions; though we shall see that some of the things most needed for the present study are not tabulated and have had to be computed.

We make a study of the one-, two-, and three-dimensional cases; the one-dimensional case because it is obviously simplest, and the foundation of the others; the two-dimensional case because it presents many of the complicating features of the three-dimensional case, and yet can be visualized and shown graphically much more easily; and the three-dimensional case for the obvious reason that it most closely resembles a real crystal. We consider not only the separable Mathieu problem, but also modifications of it resulting from introducing other Fourier components of potential as perturbations, resulting in potentials closer to those met in real crystals. We make much use of the Wannier functions, and particularly of their Fourier transforms, which we show, by extension of existing theorems, to be identical with the momentum eigenfunctions. In connection with this, we throw light on such previously puzzling questions as the nature of the Wannier functions in a case of overlapping bands.

As for specific results of direct value in the theory of energy bands, it is perhaps best merely to say that the material presented here should be very valuable to one trying to set up methods of approximating the solution of the periodic potential problem in real crystals; and in particular, it shows that our misgivings are justified, that the real wave functions of the valence and conduction electrons must be rather widely different from the approximate functions set up by either of the two limiting processes, so that we must be much more on our guard against the use of these procedures than most writers have been in the past.

1. ENERGY BANDS FOR THE ONE-DIMENSIONAL MATHIEU PROBLEM

For convenience in intercomparison, we shall describe the potential energy of an electron in a crystal in the same notation used in an earlier reference by the writer.[6] In this case, we set up a set of vectors $\mathbf{Q}_j$ from the origin to points corresponding to the origin in the jth unit cell of the crystal; $\mathbf{Q}_j$ will be expressible as a linear combination of three fundamental vectors $\mathbf{Q}_1$, $\mathbf{Q}_2$, $\mathbf{Q}_3$, with integral coefficients. For a simple cubic lattice, these fundamental vectors are of magnitude Q_0, and point along the three coordinate axes. Then we set up a set of vectors $\mathbf{P}_i$, in a momentum space (proportional to a reciprocal space), by the equations

$$\mathbf{P}_i \cdot \mathbf{Q}_j = h\delta_{ij}, \tag{1}$$

where h is Planck's constant, and δ_{ij} the Kronecker symbol. Thus the vectors $\mathbf{P}_i$ can be written as linear combinations of three fundamental vectors $\mathbf{P}_1$, $\mathbf{P}_2$, $\mathbf{P}_3$, with integral coefficients; in the simple cubic lattice, these vectors are all of magnitude h/Q_0 and are along the three coordinate axes. Then we can express any periodic potential energy U which repeats in each unit cell according to the Fourier expansion

$$U(\mathbf{r}) = \sum (\mathbf{P}_i) W(\mathbf{P}_i) \exp[(-2\pi i/h)(\mathbf{P}_i \cdot \mathbf{r})], \tag{2}$$

where $\mathbf{r}$ is the radius vector to any point of the lattice. The periodicity, according to which $U(\mathbf{r}+\mathbf{Q}_j) = U(\mathbf{r})$, follows at once from (1) and (2). To insure having a real potential, we must have $W(-\mathbf{P}_i) = W(\mathbf{P}_i)^*$.

The general case of a simple cubic structure could then be expressed in the form

$$U(\mathbf{r}) = \sum (lmn) W(lmn) \times \exp[(-2\pi i/Q_0)(lx+my+nz)], \tag{3}$$

where x, y, z are the components of $\mathbf{r}$, and $W(lmn)$ represents the Fourier coefficient associated with the point in momentum space with the coordinate lP_0, mP_0, nP_0. The simplified case which we can handle by our Mathieu method is that for which the only non-vanishing components are for l, m, $n = 0$ (a constant potential), and for the combinations (± 100), (0 ± 10), (00 ± 1). We may then write

$$U(\mathbf{r}) = W_0 - 2W_1 (\cos 2\pi x/Q_0 + \cos 2\pi y/Q_0 + \cos 2\pi z/Q_0), \tag{4}$$

where $W_0 = W(0, 0, 0)$, and where we have chosen $W(\pm 1, 0, 0)$, $W(0, \pm 1, 0)$, $W(0, 0, \pm 1)$ all to be equal, real, and equal to $-W_1$, where W_1 is positive; the negative sign has the effect of putting a minimum of potential at the origin. We shall find it convenient to choose W_0 so that the potential energy is zero at the potential minima, such as the origin; that is, we let

$$W_0 = 6W_1, \tag{5}$$

so that

$$U(\mathbf{r}) = 2W_1[(1-\cos 2\pi x/Q_0) + (1-\cos 2\pi y/Q_0) + (1-\cos 2\pi z/Q_0)]. \tag{6}$$

Schrödinger's equation is then

$$-(h^2/8\pi^2 m)\nabla^2 u + U(\mathbf{r})u = Eu. \tag{7}$$

We can at once separate variables; if $u = u_x(x)u_y(y)u_z(z)$, corresponding to the energy $E = E_x + E_y + E_z$, we have

$$-(h^2/8\pi^2 m)[d^2u_x(x)/dx^2] + 2W_1(1-\cos 2\pi x/Q_0)u_x(x) = E_x u_x(x). \tag{8}$$

This is Mathieu's equation. We wish to introduce dimensionless variables, to simplify notation. In doing

FIG. 1. Parabolic and sinusoidal potentials for two Q_0's, one twice the other. Note how the barrier height varies as Q_0^2.

[5] *Tables Relating to Mathieu Functions*, U. S. National Bureau of Standards (Columbia University Press, New York, 1951).
[6] J. C. Slater, Revs. Modern Phys. **6**, 209 (1934).

so, we shall try to make our equation resemble forms already existing in the literature. Unfortunately, there are many different notations in use. However, we gain a certain connection with other notations if we let

$$w=\pi x/Q_0, \quad s=32mQ_0^2W_1/h^2,$$
$$\epsilon=(2m/W_1)^{\frac{1}{2}}(Q_0E/h), \quad a=\epsilon s^{\frac{1}{2}}-s/2. \tag{9}$$

In terms of these quantities, we may express (8) in the alternative forms

$$-d^2u/dw^2+\tfrac{1}{2}s(1-\cos 2w)u=\epsilon s^{\frac{1}{2}}u, \tag{10}$$

$$d^2u/dw^2+(a+\tfrac{1}{2}s\cos 2w)u=0. \tag{11}$$

The form (11) is identical with Eq. (2.01) of reference 5, except that that equation has a minus sign instead of plus for the term $\frac{1}{2}s\cos 2w$; that is, the form in reference 5 corresponds to having the minima of potential at the points $w=\pm\pi/2, \pm 3\pi/2, \cdots$, instead of at $w=0, \pm\pi, \pm 2\pi, \cdots$, as we have in (10) and (11). On page xvii of reference 5 are given the rules for changing the sign of s, so that the many useful formulas of that reference are immediately applicable without change of notation.

Before going further, it is worth while making connection between our problem and a real case of energy bands in a crystal. The potential energy of Eq. (8) can be expanded about one of its minima (for instance, the minimum at $x=0$) as a quadratic, $W_1(2\pi x/Q_0)^2$. If we retained only this term, Eq. (8) would become the equation of a linear oscillator, with natural frequency ν_0, given by the relation

$$W_1(2\pi/Q_0)^2=2\pi^2m\nu_0^2. \tag{12}$$

By familiar methods, this linear oscillator would have wave functions

$$u_n=\exp(-z^2/2)H_n(z),$$
$$H_n(z)=(-1)^n\exp(z^2)d^n\exp(-z^2)/dz^n, \tag{13}$$
$$z=s^{\frac{1}{2}}w=s^{\frac{1}{2}}\pi x/Q_0,$$

corresponding to the energy

$$E_n=(n+\tfrac{1}{2})h\nu_0, \quad \epsilon_n=2n+1. \tag{14}$$

Thus we see that ϵ measures the energy, in units $h\nu_0/2$. We see furthermore that, since the charge density u_n^2 of the ground state of the oscillator falls to $1/e$ of its maximum value when z [of Eq. (13)] equals 1, the quantity s may be interpreted according to the equation

$$s^{\frac{1}{2}}=w_0^{-1}=Q_0/\pi x_0, \tag{15}$$

where w_0, x_0 represent the values of these quantities for which the charge density of the ground state of the oscillator will have fallen to $1/e$ of its maximum value. We may now visualize a situation in which "atoms" with a quadratic potential $2\pi^2m\nu_0^2x^2$ are located at the lattice points $x=0, \pm Q_0, \pm 2Q_0$, etc. The sinusoidal potential energy $m\nu_0^2Q_0^2(1-\cos 2\pi x/Q_0)$ reduces properly to these "atomic" potentials near each atomic position, but joins smoothly from one to the next, with

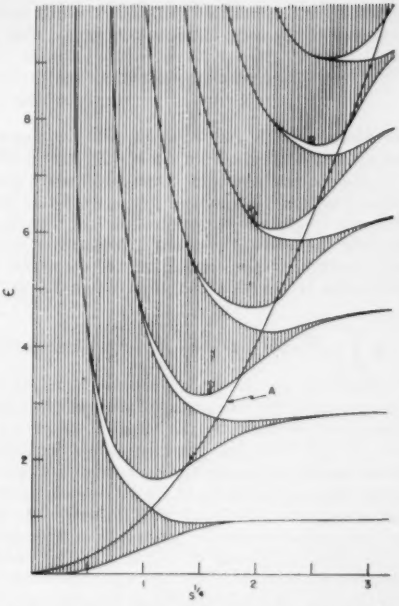

FIG. 2. Energy bands ϵ as function of lattice energy $s^{\frac{1}{2}}$, one-dimensional Mathieu problem. Curve A represents the height of the potential barrier between atoms.

a potential maximum between atoms. We picture ν_0, and x_0, which equals $(2\pi)^{-1}(h/m\nu_0)^{\frac{1}{2}}$, or the properties of an individual "atom," as staying constant while Q_0, or the lattice spacing, is changed. We see from Fig. 1 how it is that the height of the maximum (given by $4W_1=2m\nu_0^2Q_0^2$) increases as the lattice spacing increases at constant ν_0. And we see from (15) that, keeping x_0 fixed, the quantity Q_0 is equal to $\pi x_0 s^{\frac{1}{2}}$. Hence, if we wish to indicate the splitting of the energy bands as a function of Q_0, the lattice spacing, we can use $s^{\frac{1}{2}}$ as a dimensionless measure of the lattice spacing.

We can now use the results of reference 5 to give Fig. 2, showing the widths of the energy bands and energy gaps of the one-dimensional problem as a function of lattice spacing. We plot ϵ as a function of $s^{\frac{1}{2}}$, in accordance with the discussion of the preceding paragraph. The curves are taken out to $s=100$, the limiting value given in reference 5. There are many interesting features of these energy bands. In the first place, for large enough values of Q_0, where the bands become indefinitely narrow and the wave functions become atomic and do not overlap appreciably, the energies approach the values $\epsilon_n=2n+1$ of the linear oscillator. As the interatomic distance decreases, there is a depression of the energy levels, which sets in before they start to broaden. It is not hard to find the origin of this

depression. We remember that the potential energy [expressed in the dimensionless form of Eq. (10)] is

$$\tfrac{1}{2}s(1-\cos 2w)=\tfrac{1}{2}s[(2w)^2/2-(2w)^4/24+\cdots] \\ =s(w^2-w^4/3+\cdots).$$

The terms $-sw^4/3$ and following terms represent a perturbation applied to the linear oscillator problem. It is just the mean value of these perturbative energy terms over the unperturbed linear oscillator wave functions which are responsible for the depression. Thus, for example, let us take the ground state, whose wave function is proportional to $\exp(-s^{\frac{1}{2}}w^2/2)$. The mean value of $-sw^4/3$ over this wave function is

$$-\tfrac{1}{3}s\int_{-\infty}^{\infty}w^4\exp(-s^{\frac{1}{2}}w^2)dw\Big/\int_{-\infty}^{\infty}\exp(-s^{\frac{1}{2}}w^2)dw=-\tfrac{1}{4}.$$

Thus we expect that the energy of the ground state, for large s, will be given by the equation, $\epsilon s^{\frac{1}{2}}=s^{\frac{1}{2}}-\frac{1}{4}$, or $\epsilon=1-1/(4s^{\frac{1}{2}})$. This gives correctly the first two terms of the asymptotic expression for the energy as a function of s for large s, given in Eq. (2.35), reference 5, which for this case gives $\epsilon=1-1/(4s^{\frac{1}{2}})-1/(16s)-\cdots$. We shall see later, when we take up the two- and three-dimensional cases, that terms of this sort in the potential represent the crystalline field, the departure of the true potential from the linear-oscillator approximation, and having a cubic symmetry, arising from the approach of neighboring atoms. And we shall see that the cubic field, in the three-dimensional case, can remove the degeneracy arising from the spherical symmetry, just as the crystalline field removes the degeneracy of certain atomic states in problems of magnetic ions in crystals.

As the atoms approach more and more closely, in Fig. 2, the energy levels begin to broaden into bands, in the familiar way, the energy gaps disappearing as the interatomic distance goes to zero. We should expect that the broadening of a level would begin to be large when the barrier is lowered enough so that this level is at the top of the barrier; those levels below the barrier will be relatively sharp; those above will be broadened into bands with narrow gaps between. From Eq. (10), the top of the barrier comes for $\epsilon s^{\frac{1}{2}}=s$, $\epsilon=s^{\frac{1}{2}}$. We draw in Fig. 2 the parabola $\epsilon=s^{\frac{1}{2}}=(s^{\frac{1}{2}})^2$, marked A, and we see that it does roughly divide the figure into two regions, that below the parabola corresponding to the levels below the barrier, which are only slightly broadened, and that above corresponding to the levels above the barrier, which are very broad, with very narrow gaps. It is interesting to compare the relation of this curve A to the broadening of the bands, and the corresponding curve A in Fig. 9 of reference 6, where similar curves are drawn for the energy bands in a sodium crystal, as computed by the cellular method. The general resemblance is very strong.

2. WAVE FUNCTIONS, MOMENTUM EIGENFUNCTIONS, WANNIER FUNCTIONS, AND ENERGIES FOR THE ONE-DIMENSIONAL MATHIEU PROBLEM

The material concerning Mathieu functions given in reference 5 consists of numerical tables, and approximate formulas, for the wave functions and energies connected with the edges of the bands, for values of s up to 100, and for the lowest 15 bands. No information is given about the intermediate values between the edges of the bands, so that we cannot plot a curve of energy as a function of momentum directly from the results of that reference. We shall next therefore describe the method used for computing these quantities and show how these have been used in the present work to find the behavior of the bands.

The method used to discuss the Mathieu equation is to compute the momentum eigenfunction, or Fourier representation of the wave function; the reason why Mathieu's equation is so important is the unique simplicity of the difference equation governing the momentum eigenfunction. In reference 6, Sec. 20 ff, the momentum eigenfunction $v(p_x,\ p_y,\ p_z)$ is introduced. For convenience we describe the principal properties of this function; we state our results for the general three-dimensional problem and then specialize for our one-dimensional case. We start by considering a lattice of points in the momentum space, consisting of all the vectors $\mathbf{p}$ which can be made from a given $\mathbf{p}_0$ by adding any one of the vectors $\mathbf{P}_i$ described in Eq. (1). We know that a wave function $u(\mathbf{r})$ can be written as a sum of plane waves $\exp[(2\pi i/h)(\mathbf{p}_0+\mathbf{P}_i)\cdot\mathbf{r}]$, associated with some particular $\mathbf{p}_0$; for such a sum is the product of the plane wave $\exp[(2\pi i/h)\mathbf{p}_0\cdot\mathbf{r}]$ and a periodic function with the periodicity of the lattice. We can associate the Fourier coefficient connected with the wave of momentum $\mathbf{p}_0+\mathbf{P}_i$ with the point $\mathbf{p}_0+\mathbf{P}_i$ in momentum space. Let the Fourier coefficient be called $v(\mathbf{p}_0+\mathbf{P}_i)$. That is, we can write

$$u_{n,\,\mathbf{p}0}(\mathbf{r})=\sum(\mathbf{P}_i)v_n(\mathbf{p}_0+\mathbf{P}_i) \\ \times\exp[(2\pi i/h)(\mathbf{p}_0+\mathbf{P}_i)\cdot\mathbf{r}]. \quad (16)$$

The function $u_{n,\,\mathbf{p}0}(\mathbf{r})$ of course is to be associated with the particular $\mathbf{p}_0$, or rather with the lattice of points $\mathbf{p}_0+\mathbf{P}_i$; a different wave function is associated with each point of a unit cell in the momentum space. And of course we have different wave functions associated with the various energy bands, indicated by the subscript n on u and v. It is immaterial for most purposes whether we choose $\mathbf{p}_0$ to be in the central unit cell of momentum space or not, though we shall generally do so.

We now notice that a single wave function out of an energy band, associated with a given $\mathbf{p}_0$, defines the function v only at a discrete lattice of points in $\mathbf{p}$ space. However, the set of u's associated with an energy band, and all $\mathbf{p}_0$'s, defines this function at all points of $\mathbf{p}$ space. In other words, for each energy band, there is a single function $v(\mathbf{p})$ which gives complete information about

all the wave functions of this band. Before writing down the equation determining $v(\mathbf{p})$, the equivalent of Schrödinger's equation in momentum space, we may state some of the properties of $v(\mathbf{p})$. First, it is normalized, in the following sense: if $u(\mathbf{r})$ is normalized so that the average value of its product with its conjugate is unity, $v(\mathbf{p})$ will be normalized so that the sum of the quantity v^*v for all points of a single lattice of points equals unity.[7] Furthermore, there is an orthogonality relation between v's associated with different bands; we may write the normalization and orthogonality relations in the form

$$\sum(\mathbf{P}_i)v_m^*(\mathbf{p}_0+\mathbf{P}_i)v_n(\mathbf{p}_0+\mathbf{P}_i)=\delta_{mn}, \tag{17}$$

where the subscript denotes the band. There is another orthogonality and normalization condition (see reference 6, Sec. 22),

$$\sum(n)v_n^*(\mathbf{p}_0+\mathbf{P}_i)v_n(\mathbf{p}_0+\mathbf{P}_j)=\delta_{ij}, \tag{18}$$

whose special case for $i=j$ gives the very important completeness relation, which we shall use later: the sum of the squares of the absolute values of all the momentum eigenfunctions associated with all bands, at a given point of momentum space, equals unity. There is in addition a relation inverse to (16), expressing v in terms of u:

$$v_n(\mathbf{p})=(1/\Omega)\int u_{n,\mathbf{p}}(\mathbf{r})\exp[(-2\pi i/h)(\mathbf{p}\cdot\mathbf{r})]dxdydz, \tag{19}$$

where the integration is to be taken over a unit cell, Ω is the volume of the cell, and $\mathbf{p}$ equals one of the vectors $\mathbf{p}_0+\mathbf{P}_i$ associated with the lattice of points for which $u(\mathbf{r})$ is a wave function.

These relations are all discussed in reference 6. There is a further relation, of great importance, not given in that reference: $v(\mathbf{p})$ is the Fourier integral transform of the Wannier function,[8] a function which had not been proposed at the time reference 6 was written. Let us discuss this important theorem.

Wannier showed that there existed a function $a(\mathbf{r}-\mathbf{Q}_j)$, localized in the neighborhood of the $\mathbf{Q}_j$'th cell, such that we can write the wave function $u_{n,\mathbf{p}}(\mathbf{r})$ associated with a given momentum vector $\mathbf{p}$ by the equation

$$u_{n,\mathbf{p}}(\mathbf{r})=(\Omega)^{\frac{1}{2}}\sum(\mathbf{Q}_j)\exp[(2\pi i/h)(\mathbf{p}\cdot\mathbf{Q}_j)]a_n(\mathbf{r}-\mathbf{Q}_j). \tag{20}$$

That is, we can make a combination of a's in each cell, multiplied by an appropriate modulating factor, just as Bloch[9] proposed to do approximately using atomic orbitals. Here Ω is the volume of the unit cell, as before, and the factor $(\Omega)^{\frac{1}{2}}$ insures that if the a's are normalized to unity, the u's will be normalized on the average, as we have assumed earlier. Wannier, furthermore, showed howto set up the functions a. In our present normalization, his formula is

$$a_n(\mathbf{r}-\mathbf{Q}_j)=\frac{(\Omega)^{\frac{1}{2}}}{h^3}\int u_{n,\mathbf{p}}(\mathbf{r})\times\exp[(-2\pi i/h)(\mathbf{p}\cdot\mathbf{Q}_j)]dp_xdp_ydp_z, \tag{21}$$

where the integration is to be taken over a single unit cell in momentum space. He proved that the a's so set up are orthogonal, in the sense that

$$\int a_n^*(\mathbf{r}-\mathbf{Q}_j)a_n(\mathbf{r}-\mathbf{Q}_k)d\tau=\delta_{jk}.$$

Now let us express $u_{n,\mathbf{p}}(\mathbf{r})$ in terms of $v_n(\mathbf{p})$, by Eq. (16). Then (21) becomes

$$a_n(\mathbf{r}-\mathbf{Q}_j)=\frac{(\Omega)^{\frac{1}{2}}}{h^3}\sum(\mathbf{P}_i)\int v_n(\mathbf{p}+\mathbf{P}_i)\times\exp[(2\pi i/h)(\mathbf{p}+\mathbf{P}_i)\cdot(\mathbf{r}-\mathbf{Q}_j)]dp_xdp_ydp_z, \tag{22}$$

where we have used Eq. (1), and where still the integration is over a unit cell in momentum space. The combination, however, of integrating the $\mathbf{p}$'s over unit cell, and summing over $\mathbf{P}_i$, amounts to integrating over all momentum space. Thus

$$a_n(\mathbf{r}-\mathbf{Q}_j)=\frac{(\Omega)^{\frac{1}{2}}}{h^3}\int v_n(\mathbf{p})\times\exp[(2\pi i/h)\mathbf{p}\cdot(\mathbf{r}-\mathbf{Q}_j)]dp_xdp_ydp_z, \tag{23}$$

where now the integration is over all $\mathbf{p}$'s. This expresses a as the Fourier integral transform of v. Similarly we can express the inverse transformation. We use Eq. (19) to express $v_n(\mathbf{p})$ in terms of $u_{n,\mathbf{p}}(\mathbf{r})$, and (20) to express $u_{n,\mathbf{p}}(\mathbf{r})$ in terms of the a's. Here in a similar way we have an integration over a unit cell in coordinate space, coupled with a summation over all cells, amounting to an integration over all space. In this way we arrive at the result

$$v_n(\mathbf{p})=(\Omega)^{-\frac{1}{2}}\int a_n(\mathbf{r})\exp[(-2\pi i/h)(\mathbf{p}\cdot\mathbf{r})]dxdydz. \tag{24}$$

We note that in (23) where the integral is extended over all $\mathbf{p}$'s the integrand falls off for large $\mathbf{p}$'s, on account of the behavior of $v(\mathbf{p})$, just as the integrand in (24) falls off for large x's on account of the nature of a. From the results of this paragraph, we see that a very practical way to find a Wannier function is to find the momentum eigenfunction $v_n(\mathbf{p})$ and then its Fourier transform.

We have now examined the properties of the momentum eigenfunction $v(\mathbf{p})$, and we are ready to write down

[7] This normalization determines $v(\mathbf{p})$ at a lattice of points uniquely, except for an arbitrary phase factor. This factor must be properly chosen, for each lattice of points, to secure continuity of the function $v(\mathbf{p})$. Ordinarily the phase can be chosen by a requirement that $v(\mathbf{p})$ be real, or pure imaginary, leaving only a sign to be determined.

[8] G. Wannier, Phys. Rev. **52**, 191 (1937).

[9] F. Bloch, Z. Physik **52**, 555 (1928).

the equation it satisfies. From reference 5, Secs. 20 and 21, we see that the equivalent of Schrödinger's equation for w is the set of difference equations

$$[(p_x^2+p_y^2+p_z^2)/2m]v(\mathbf{p}) + \sum(\mathbf{P}_i)W(\mathbf{P}_i)v(\mathbf{p}+\mathbf{P}_i)=Ev(\mathbf{p}). \quad (25)$$

These equations, of course, may be considered as derived by the usual perturbation methods of quantum mechanics, in the process of expanding the correct wave function $u_p(\mathbf{r})$ of the problem, in a series of plane waves, which form a complete orthogonal set. The quantity $(p_x^2+p_y^2+p_z^2)/2m+W(0)$ is the diagonal matrix component of energy, associated with the wave of momentum $\mathbf{p}$, and $W(\mathbf{P}_i)$ is the nondiagonal matrix component of energy between the waves of momentum $\mathbf{p}$ and of $\mathbf{p}+\mathbf{P}_i$. Equation (25) will lead to a secular equation of the ordinary sort for the determination of the energy E.

We may now specialize for the one-dimensional Mathieu problem in which the W's have been given already. We have

$$(p^2/2m+2W_1-E)v(\mathbf{p}) - W_1[v(\mathbf{p}+\mathbf{P}_0)+v(\mathbf{p}-\mathbf{P}_0)]=0. \quad (26)$$

Here again let us introduce dimensionless quantities. It is convenient to introduce

$$g=2p/P_0=2pQ_0/h, \quad (27)$$

where as before $P_0=Q_0/h$. Then, using the abbreviation (9), Eq. (26) becomes

$$(g^2+\tfrac{1}{2}s-\epsilon s^{\frac{1}{2}})v(g)-\tfrac{1}{4}s[v(g+2)+v(g-2)]=0. \quad (28)$$

This forms a very simple difference equation for the v's. For preliminary orientation, we may observe that if $v(g)$ varies only slowly with g, this difference equation can be replaced by a differential equation. For then we should have approximately $[v(g+2)-v(g)]/2=dv/dg$ computed for $g+1$; $[v(g)-v(g-2)]/2=dv/dg$ for $g-1$; and $\{[v(g+2)-v(g)]-[v(g)-v(g-2)]\}/4\sim d^2v/dg^2$. Hence Eq. (28) is approximately equivalent to

$$-sd^2v(g)/dg^2+(g^2-\epsilon s^{\frac{1}{2}})v(g)=0. \quad (29)$$

This would be a Schrödinger-type equation for a particle in a parabolic potential, proportional to g^2. Thus its solutions would be proportional to

$$v_n=\exp(-z^2/2)H_n(z), \quad z=s^{-\frac{1}{4}}g, \quad (30)$$

corresponding to the same energy $\epsilon_n=2n+1$ as in (14). We shall find later that for the low energy levels, which are hardly broadened at all, it actually is true that $v(g)$ varies only slowly with g, so that (30) gives the correct solution for the momentum eigenfunction. We could have predicted in advance that this would be the case. For in this case the problem is essentially the linear oscillator problem, its coordinate wave functions are Hermite functions for the various atoms, the atoms overlap so little that the Wannier functions are equivalent to the atomic functions, and we know that the Fourier transforms of the Hermite functions of x are Hermite functions of p, or of g, just as we have found in Eq. (30).[10]

The situation is completely different, however, for the high energy levels, the free-electron-like solutions of (28). The extreme case would be one in which only one of the quantities $v(g')$ was different from zero. This would be found only when the energy was so great that s could be neglected compared to ϵ. Then we should have $(g^2-\epsilon s^{\frac{1}{2}})v(g)=0$, so that we should have only one equation, for the nonvanishing component $v(g')$, which would then determine the energy by the equation $\epsilon s^{\frac{1}{2}}=g'^2$, the free-electron value. The important intermediate cases of electrons which are partly free correspond to cases where the v's vary very rapidly from one value of g to the next value, but where, nevertheless, many components are different from zero. For these cases we must use numerical methods to solve Eq. (28).

One simple numerical method will immediately occur to the reader. From (28) we can immediately solve for $v(g+2)$ in terms of $v(g)$ and $v(g-2)$, or alternatively for $v(g-2)$ in terms of $v(g)$ and $v(g+2)$. Thus if we know E, and two successive entries in the table of v's, we can compute the next entry, and so on indefinitely. This is just like the standard method of numerical integration of a differential equation, which we replace approximately by a difference equation; only here the process is exact. We know that if we start with two arbitrary successive entries in the table, and an arbitrary E, and integrate both ways to $\pm\infty$, the function $v(g)$ will in general become exponentially infinite. We can always choose the ratio of the two initial successive entries so as to make it go to zero exponentially in one direction, but then it will still go infinite in the other direction. If the energy is properly chosen, it will go to zero both at $+\infty$ and $-\infty$. This determines the energy values. Instead of integrating from a finite point out to infinity, we can reverse the procedure, if we can estimate the limiting behavior of the function for large positive and negative g's, corresponding to the exponentially decreasing functions. We can then integrate in from infinity in both directions, toward $g=0$, for a given energy. In general we shall find that the integrations from the two limits do not match when they join; that is, we can determine the ratio of two successive entries (say $v(g_0)/v(g_0+2)$) from the integrations from both $+\infty$ and $-\infty$ and can then try various energy parameters until these ratios agree. This determines both the momentum eigenfunctions (which of course must then be normalized) and the energy, and it is an entirely practical method of calculation.

A slight modification of this method, however, the method of continued fractions, is essentially equivalent

[10] Oddly enough, these simple relations between Mathieu functions and the Hermite functions, and the theta-functions and their derivatives which arise when we make Bloch-type linear combinations of them, do not seem to be widely recognized, though my colleague Professor P. M. Morse informs me that he is familiar with them and will discuss them in a forthcoming book.

but more convenient in practice, and it is the method ordinarily used. This method operates with the ratios of successive v's, rather than with their differences. Thus let

$$G_g = v(g)/v(g-2). \tag{31}$$

Then [using the abbreviation a given in Eq. (9)], Eq. (28) becomes

$$(g^2-a) - \tfrac{1}{4}s(G_{g+2}+1/G_g) = 0. \tag{32}$$

If we let

$$V_g = (4/s)(g^2-a), \tag{33}$$

this is

$$V_g - G_{g+2} - 1/G_g = 0, \tag{34}$$

which we can solve in the form

$$G_g = (V_g - G_{g+2})^{-1}. \tag{35}$$

This is a very convenient equation to use for integrating in from $+\infty$. For a large positive g, the quantity V_g becomes very large. On the other hand, since we are looking for a solution falling off exponentially with increasing g, the ratio G_g or G_{g+2} will be very small. Thus G_{g+2} will be negligible compared to V_g for large enough g, and we can commence an inward integration by letting $G_g = V_g^{-1}$, for some particular large g. Then we have $G_{g-2} = (V_{g-2} - G_g)^{-1}$, etc., and we can continue integrating inward very easily. Here as before we assume an energy, integrate inward until we get to an entry near $g=0$. We set up an equivalent expression for integrating in from $-\infty$, continue to the same point, and see if the two solutions join smoothly. If they do not, we modify the energy until they do.

Once we know the energy, the actual numerical work involved in the calculation, using a desk computer, is very small. It is in this way that the calculations in reference 5 were performed; but these were done only for the edges of energy bands, corresponding to integral values of the g's. We have made similar calculations, to be described in the next sections, for a number of non-integral g's, enough to determine the general form of the continuous function $v(g)$ for the various energy bands, for several values of s. In the actual calculations, it is a great help to know in advance the approximate energy; if this is known, we can merely calculate for several energy values in that neighborhood, and interpolate until we get the correct energy, for which the ratio G calculated by integration for both directions agrees. In estimating the energy, the results of reference 5 are of great value. For the tightly bound bands, for which the band width is small, and the energies at the edges of the bands are given in reference 5, an interpolation between the values given there gives a very accurate preliminary value for the energy. For the higher energies, for which there is not much deviation from the free-electron energy, there is a series representation of the energy as a function of g which is quite accurate, except very close to the edges of the band (where the values are already given in reference 5). This series is given in Eq. (2.34) of reference 5, though for a slightly different purpose; it comes originally from Mathieu. It is

$$a = \epsilon s^{\frac{1}{2}} - s/2 = g^2 + \frac{s^2}{32(g^2-1)} + \frac{(5g^2+7)s^4}{8192(g^2-1)^3(g^2-4)} + \frac{(9g^4+58g^2+29)s^6}{262144(g^2-1)^5(g^2-4)(g^2-9)} + \cdots. \tag{36}$$

Clearly, as g approaches an integer (the edge of a band), the later terms of the series become infinite; nevertheless, the earlier terms give a very good approximation to the energy, even rather close to the edge of the band.

It is perhaps worth while indicating how Eq. (36) is derived, since it throws considerable light on the nature of the Mathieu problem. Let us start with a free-electron approximation, in which the solution is approximately $\exp(ig_0 w)$, for some particular g_0, for which we should have $a = g_0^2$. We then set up the series

$$u_{g_0}(w) = \sum(n) v(g_0+2n) \exp[i(g_0+2n)w], \tag{37}$$

equivalent to (16) but expressed in dimensionless form. We now postulate that we can set up a solution for small s's in which each successive v, going away from $v(g_0)$ in either direction, is smaller by a power of s. That is, if we set $v(g_0)=1$ (for an unnormalized function), we assume that $v(g_0 \pm 2)$ are of order s, $v(g_0 \pm 4)$ of order s^2, etc. Further we assume that a can be expanded in a series in s, of the nature of (36). We then inset these assumptions into Eq. (28), using that equation to work outward in both directions from g_0. We find that at each step we have enough equations to determine coefficients up to an additional power of s, so that the process actually can be carried through step by step. When we do this, we not only arrive at Eq. (36), for the energy, but also at the following frequently useful

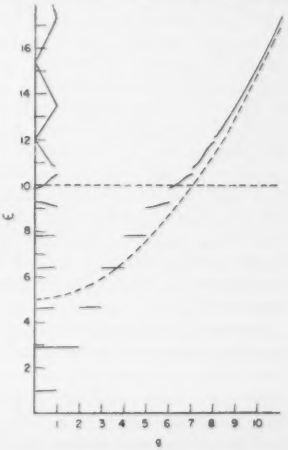

FIG. 3. Energy ϵ as function of momentum g, in dimensionless units, for the case $s=100$. Parabola shows energy of free electron in mean potential.

equations for the (unnormalized) momentum eigenfunction:

$$v(g_0)=1,$$

$$v(g_0\pm 2)=\frac{\pm s}{16(g_0\pm 1)}\pm\frac{(g_0^2\pm 4g_0+7)s^3}{8192(g_0\pm 1)^3(g_0\pm 2)(g_0\mp 1)}\pm\frac{(g_0^6\pm 5g_0^5+8g_0^4\pm 8g_0^3+47g_0^2\mp 13g_0+232)s^5}{3{,}145{,}728(g_0\pm 1)^5(g_0\pm 2)(g_0\pm 3)(g_0\mp 1)^3(g_0\mp 2)}\pm\cdots,$$

$$v(g_0\pm 4)=\frac{s^2}{512(g_0\pm 1)(g_0\pm 2)}+\frac{(g_0^3\pm 7g_0^2+20g_0\pm 20)s^4}{196{,}608(g_0\pm 1)^3(g_0\pm 2)^2(g_0\pm 3)(g_0\mp 1)}+\cdots,$$

$$v(g_0\pm 6)=\pm\frac{s^3}{24{,}576(g_0\pm 1)(g_0\pm 2)(g_0\pm 3)}\pm\cdots,$$

$$v(g_0\pm 8)=\frac{s^4}{2^{16}(4!)(g_0\pm 1)(g_0\pm 2)(g_0\pm 3)(g_0\pm 4)}+\cdots,$$

. . . . . .

$$v(g_0\pm 2n)=(\pm 1)^n\frac{s^n}{2^{4n}(n!)(g_0\pm 1)(g_0\pm 2)\cdots(g_0\pm n)}\pm\cdots. \tag{38}$$

We now see from (38) why our series representation fails near the edges of the energy bands. As g_0 approaches an integer, say a positive integer, the v's for negative g's will become large. As an example, let g_0 approach 3; then $v(g_0-2)$ will have a factor g_0-3 in the denominator of its third term, $v(g_0-4)$ in the second term, and $v(g_0-6)$ and all successive v's in its first term. The meaning of this is of course clear from our knowledge of Bragg reflection. We know that as g_0 approaches 3, for instance, there will come in another component, $v(-3)$, equal just at the edge of the band to $v(3)$. In other words, near the edge of the band, we are not justified in assuming that the v's fall off as successively higher powers of s; $v(-g_0)$ will be equal to $v(g_0)$, and a series which attempts to expand $v(-g_0)$ as a series starting with a term in s^{g_0} cannot be expected to converge.

Just at the edge of the band, however, a different procedure is possible. There we know that the component $v(-g)$ must be equal or opposite to $v(g)$, depending on whether the function is even or odd. We can then set up the assumption that the v's for positive g's fall off as we assumed above, but combine this with the condition that $v(g)$ be an even or odd function of g, so that we do not continue the integration to negative g's. In this case we find quite different series, similar to (36) and (37) but of course differing for each g_0 and not involving g_0 explicitly. These formulas, for the energy, are given in Eqs. (2.24)$\cdots$(2.33) of reference 5; similar formulas can be set up for the momentum eigenfunctions as well.

By use of a combination of the approximate formulas discussed above, and the numerical solution using (35), it is not hard to arrive at a good understanding of the energy and wave functions arising from Mathieu's equation for any value of s and as a function of g. We shall give in the next section some typical examples of the results, paying particular attention to the change in properties of the solutions as we go from the low, bound states to the higher states resembling free electrons.

3. NUMERICAL EXAMPLES FOR THE ONE-DIMENSIONAL CASE

Calculations have been made for $s=1$, 16, and 100, or $s^{\frac{1}{2}}$ (which we remember is proportional to the interatomic distance) equal to 1, 2, and 3.16. This gives a good range of properties. We remember that the top of the barrier comes from $\epsilon=s^{\frac{1}{2}}$ and that the energy levels of the corresponding linear oscillator problem are given by $\epsilon=2n+1$. Thus for $s=1$, the lowest level of the oscillator will lie just at the top of the barrier, so that even that lowest level is greatly broadened; for $s=16$, the energy levels for $n=0$ and $n=1$, corresponding to $\epsilon=1$ and 3, will lie below the barrier, which has a height of 4 units; for $s=100$, the lowest five levels, for $\epsilon=1$, 3, 5, 7, 9, will all lie below the barrier at $\epsilon=10$ (actually, since the energies are depressed as compared to those of the linear oscillator case, six energy levels come below the barrier in this case). In some ways the case $s=100$ is the most informing of the three, since in this the change from the properties of the bound states to the free states is more gradual, and we have very typical examples of the limiting sorts of states. Consequently we shall describe this case of $s=100$ first.

In Fig. 3, we show the energy as a function of g, for the various energy bands for $s=100$. We plot this in two ways. First, we plot it according to a free electron correspondence; that is, each energy band is plotted in the unit cell where it would be located if the barrier height were to be reduced to zero. Secondly, we plot the whole thing in the central cell of momentum space. We show the top of the barrier, at $\epsilon=10$; and we plot a parabola, whose equation is $\epsilon s^{\frac{1}{2}}=g^2+s/2$, giving the

energy of a free electron in the mean potential. There are many interesting features to be derived from this figure. Perhaps the first and most striking one is the very rapid way in which the bands become broadened as we go from the levels below the barrier, where they are quite narrow, to those above the barrier, where very soon the energy gaps almost disappear.

Next, we may consider how closely the energy approximates the atomic values for the lower bands, the free-electron values for the higher ones. We recall that the atomic levels would lie at $\epsilon = 1, 3, 5, 7, 9$; we actually find them at approximately 0.97, 2.87, 4.65, 6.30, 7.79, 9.09. These depressions compared to the free atom case, as was mentioned in Sec. 1, arise because the sinusoidal potential energy is really lower than the parabolic potential describing the free atom, and the depression in energy is approximately the average of this reduction in potential energy, averaged over the unperturbed wave function. The comparison with the free-electron energy $\epsilon s^{\frac{1}{2}} = g^2 + s/2$ is informing. We observe that the tightly bound levels lie below the parabola; the wave functions are concentrated near the potential minima, so that there is a decrease of potential energy as compared to the average through the crystal. For the higher bound states, on the contrary, and for the free electron states, the energy is higher than the parabola; and when we examine the wave functions, we find that at least for the free electron states the wave functions tend to be more concentrated around the potential maxima than the minima, giving a potential energy greater than the average through the crystal. At first sight this seems peculiar; but when we consider it more closely we see that it is not. For an electron whose energy is considerably above the top of the barrier, we can use the WKB approximation with good accuracy. We then of course find that the amplitude of the wave function is greater in regions of low velocity, and this is precisely at the potential maxima. A simple WKB approximation of this sort gives a good value for the excess of $\epsilon s^{\frac{1}{2}}$ over the parabola $g^2 + s/2$ [given analytically in Eq. (36)], for the states of high energy. This phenomenon, by which the wave functions in the lower free electron states tend to concentrate near the potential maxima, of course has its analog in real crystals, where for instance in the conduction bands of ordinary metals the wave functions tend to be large in the region between atomic centers, being less concentrated near the nuclei. From Fig. 3, and its interpretation in terms of the WKB method, we may anticipate that this effect will be less marked for really fast electrons, in energy bands far above the barrier.

Now that we have considered the energy, we may examine the behavior of the momentum eigenfunction $v(g)$, for the case $s = 100$. The values for integral values of g are given in reference 5, though the normalization must be changed to agree with our present conventions; they have been computed for half-integral values for a number of bands. These values are given in Table I.[11] The functions are plotted in Figs. 4 and 5. While the details are not completely obvious from the integral and half-integral values of Table I, they were made clear by comparison with the cases of $s = 1$ and $s = 16$, for which more points were computed, and by calculations for quarter-integral values for some of the more complicated cases. It is clear from examination of Figs. 4 and 5 that the curves have an extraordinary complexity, which needs a careful interpretation.

In the first place, the momentum eigenfunctions of the five or six lowest bands look very much like the first five or six Hermite functions, as we should expect from Eq. (30). These are the atomic levels; the Wannier functions are rather close to the atomic functions of the linear oscillator, and consequently the momentum eigenfunctions are similar to Hermite functions. But as soon as we go above these levels, the simplicity vanishes, and no real simplicity of any other sort appears, even as high as the fifteenth band, not shown in Fig. 5, but similar to the eleventh band. Even that high, there is no resemblance to a real free electron case, in which one component only of the wave function would be large. There is one interesting feature which comes in with these higher bands, however: the momentum eigenfunction is large for an interval of unity along g (say from g equal to an even integer out to the next odd integer) but is practically zero in the next interval of unity; the same thing repeats itself for negative g's, all momentum eigenfunctions being either even or odd functions of g, as we readily find out. This alternation has the effect that the solution is almost precisely a traveling rather than a standing wave. Thus in Fig. 6 we show such a momentum eigenfunction, and the lattice of points corresponding to two values of g, one (labeled 1) corresponding to a number between 0 and 1 plus an even integer, one (labeled 2) to a number between 0 and -1 plus an even integer; that is, remembering that the central Brillouin zone for this problem consists of the range of g from -1 to 1, the first lattice corresponds to a point in the right half of this central zone, the second lattice to a point in the left half. We now observe that for the first lattice, the only Fourier contributions of any significance come from negative g's, so that this represents a progressive wave in one direction; for the other lattice the only Fourier components come for positive g's. As the lattice of points approaches the edge of a band, however, (for instance as the lattice approaches the numbers $\cdots -5, -3, -1, 1, 3, 5, \cdots$) each point will lie in an almost vertical transition section of the curve, and there will, on account of the symmetry of the $v(g)$ curve, be equal contributions from positive and negative g's. This is the standing wave arising from Bragg reflection, and

[11] We shall later find it more convenient to regard the momentum eigenfunctions for the even-numbered states to be pure imaginary, for this leads to real Wannier functions. These imaginary functions are i times the functions given in Table I and in Figs. 4 and 5.

TABLE I. $v(g)$ for $s=100$. Note that *1st*, *3d*, and odd-numbered bands have functions $v(g)$ which are even functions of g, while *2d*, 4th, and even-numbered bands have odd $v(g)$s.

g	Band 1	Band 2	Band 3	Band 4	Band 5	Band 6	Band 7
0.0	0.60775	0.00000	−0.46792	0.00000	0.47293	0.00000	−0.42290
0.5	0.59953	0.14453	−0.43431	−0.20659	0.40506	0.31047	−0.33629
1.0	0.57557	0.27666	−0.33910	−0.36670	0.21296	0.46428	−0.09001
1.5	0.53785	0.38586	−0.19797	−0.44809	−0.03886	0.47987	0.20969
2.0	0.48932	0.46488	−0.03296	−0.43738	−0.26270	0.28905	0.41424
2.5	0.43356	0.51053	0.13245	−0.34293	−0.40968	−0.02519	0.47618
3.0	0.37428	0.52360	0.27778	−0.19121	−0.44350	−0.26093	0.28443
3.5	0.31496	0.50823	0.38859	−0.01436	−0.36452	−0.43031	−0.07452
4.0	0.25848	0.47074	0.45800	0.15722	−0.22225	−0.43706	−0.32233
4.5	0.20700	0.41838	0.48608	0.29885	−0.04978	−0.27952	−0.52050
5.0	0.16186	0.35826	0.47823	0.39702	0.12521	−0.14021	−0.43338
5.5	0.12365	0.29649	0.44312	0.44851	0.26749	0.01142	−0.09342
6.0	0.09233	0.23774	0.39061	0.45633	0.36765	0.16201	0.01092
6.5	0.06744	0.18507	0.32974	0.42989	0.42507	0.25191	0.16892
7.0	0.04821	0.14011	0.26780	0.38235	0.42816	0.34533	0.23568
7.5	0.03375	0.10331	0.21000	0.32427	0.42507	0.42545	0.15291
8.0	0.02315	0.07430	0.15950	0.26285	0.34276	0.39947	0.31666
8.5	0.01558	0.05217	0.11763	0.20455	0.29326	0.29060	0.45990
9.0	0.01027	0.03581	0.08437	0.15411	0.23337	0.26383	0.37679
9.5	0.00665	0.02405	0.05895	0.11281	0.17356	0.25164	0.12409
10.0	0.00423	0.01581	0.04020	0.08003	0.12860	0.19270	0.17938
10.5	0.00264	0.01019	0.02679	0.05510	0.09483	0.11376	0.21771
11.0	0.00162	0.00644	0.01745	0.03706	0.06600	0.08682	0.15614
11.5	0.00098	0.00399	0.01114	0.02441	0.04331	0.07236	0.04076
12.0	0.00058	0.00243	0.00696	0.01569	0.02860	0.04912	0.04945
12.5	9.00034	0.00146	0.00427	0.00983	0.01889	0.02546	0.05404
13.0	0.00020	0.00086	0.00257	0.00605	0.01198	0.01729	0.03540
13.5	0.00011	0.00050	0.00152	0.00356	0.00715	0.01308	0.00800
14.0			0.00088	0.00217	0.00432	0.00812	0.00859
14.5			0.00050	0.00126	0.00264	0.00382	0.00868
15.0					0.00152	0.00235	0.00529

the range of g values over which the curve is changing abruptly from one value to another is precisely the range where Bragg reflection is important, a narrower and narrower range as the energy gaps get narrower. There is no physical significance in the fact that the lattice of points in the right half of the central Brillouin zone, in Fig. 6, correspond to negative g's, and vice versa; this is because we are dealing with an even-numbered band, with odd momentum eigenfunction. In an odd-numbered band the situation would be reversed, points in the right half of the central Brillouin zone corresponding to positive g's.

We see, then, that this very sharp alternation of $v(g)$ between large and practically vanishing values in successive integral ranges of g is a necessary feature of the free electron wave functions; in the low-lying bands, where it is not found, the wave functions correspond almost exactly to standing waves, which is another way of saying that they carry practically no current. The momentum eigenfunction corresponding to a completely free electron would have just one integral range of g, for positive g's, for which it would be different from zero; there it would be equal to unity, and in the corresponding range of negative g's it would equal ± 1 depending on whether we were dealing with an even or odd state. We may now ask why it is that even the 15th band of our problem $s=100$ is so far from a free electron state; why are there a number of successive intervals of g where $v(g)$ is large? The answer is just what we have already mentioned in a preceding paragraph: the WKB method indicates that there will be a very considerable variation of amplitude, and also of effective wavelength,

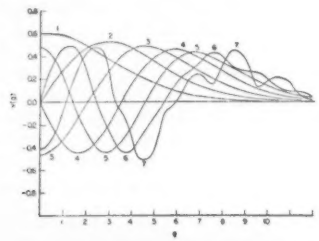

FIG. 4. Momentum eigenfunctions $v(g)$, for $s=100$, first seven bands.

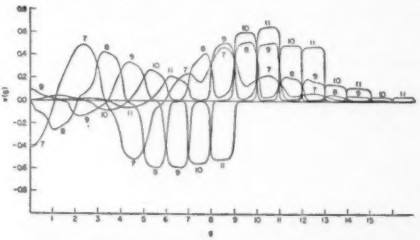

FIG. 5. Momentum eigenfunctions $v(g)$, for $s=100$, seventh to eleventh bands.

TABLE I—*Continued*.

g	Band 8	Band 9	Band 10	Band 11	Band 12	Band 13	Band 14
0.0	0.00000	0.09824	0.00000	−0.00710	0.00000		
0.5	−0.11098	0.04889	0.00749				
1.0	−0.26900	0.01637	0.03276	−0.00139	−0.00215		
1.5	−0.21239	−0.01961	0.02561				
2.0	−0.09420	−0.13661	0.01273	0.01468	−0.00094		
2.5	0.06384	−0.13019	−0.00242				
3.0	0.33931	−0.07138	−0.07742	0.00821	0.00839		
3.5	0.40063	0.00961	−0.08642				
4.0	0.24513	0.25980	−0.05053	−0.05114	0.00533		
4.5	−0.03259	0.31879	0.00100				
5.0	−0.38974	0.20069	0.20283	−0.03627	−0.03632		
5.5	−0.59244	−0.00523	0.25646				
6.0	−0.42605	−0.41961	0.16356	0.16377	−0.02681	−0.02681	
6.5	−0.00881	−0.59155	−0.00053				
7.0	0.16789	−0.41046	−0.40999	0.13491	0.13492	−0.02036	
7.5	0.36297	0.00014	−0.56603				
8.0	0.31824	0.30288	−0.38929	−0.38928	0.11286	0.11286	
8.5	0.03971	0.49995	0.00010				
9.0	0.33242	0.39026	0.38882	−0.36653	−0.36653	0.09566	
9.5	0.50210	0.00512	0.59488				
10.0	0.36167	0.35268	0.44725	0.44709	−0.34431	−0.34431	
10.5	0.02434	0.49954	0.00045				
11.0	0.14413	0.34758	0.34658	0.49028	0.49027	−0.32352	−0.32351
11.5	0.19492	0.00260	0.48034				
12.0	0.12938	0.12705	0.33159	0.33151	0.52354	0.52354	−0.30439
12.5	0.00680	0.16741	0.00020				
13.0	0.03346	0.10942	0.10919	0.31470	0.31471	0.54974	0.54974
13.5	0.04193	0.00064	0.14289				
14.0	0.02618	0.02581	0.09355	0.09354	0.29808	0.29808	0.57075
14.5	0.00117	0.03215	0.00004				
15.0	0.00500	0.01950	0.01955	0.08068	0.08068	0.28231	0.28231

of the function in going from a potential maximum to a potential minimum. Even in the 15th band, the energy ϵ is only about 28 units, while the top of the barrier is at 10 units, so that the kinetic energy varies from 28 units at the potential minimum to 18 units at the maximum. When we set up a WKB solution under these conditions, take account of the periodic change of amplitude and phase associated with the sinusoidal potential and expand the resulting wave function in Fourier series, we get in fact a good approximation to the exact momentum eigenfunction. There is then nothing mysterious about its departure from the free electron case; but we are put on our guard against thinking that we shall find a really free electron like case until the energy goes far above the top of the barrier.

There is a very informing way to plot the momentum eigenfunction, and that is to make a graphical test of the completeness relation given in Eq. (18). This relation tells us that if we square the v's associated with all the various energy bands, and sum them, the sum will equal unity for each value of p or of g. We demonstrate this in Fig. 7, where we plot $\sum(n)v_n^*(g)v_n(g)$ against g, for the various bands. We give first a curve for the first band; then for the first and second; then the first, second, and third; and so on. It is clear that the relation is verified (this gives a good check of the numerical calculations, checking all bands with a single operation). But there is much more information to be derived from this graph, which really contains within itself complete information about all the wave functions of all the energy bands of the problem (except that the sign of the wave function of course is not given, since Fig. 7 involves only the square of the wave function). Thus we see the great contrast in properties between the low levels, with their smooth momentum eigenfunctions, and the high levels, with their curious alternation of properties between successive integral ranges of g, but still with a certain orderliness which becomes more apparent in the figure than in the functions themselves. It is particularly interesting to see how, in the eighth and higher bands, the Fourier component begins to emerge which becomes the leading one in the free

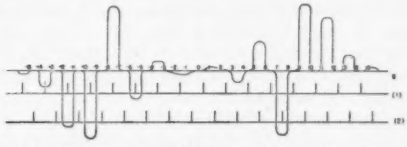

FIG. 6. Momentum eigenfunction for 10th band, $s=100$, with lattices of points (1) corresponding to $g_0=\frac{1}{2}$ and (2) corresponding to $g_0=-\frac{1}{2}$.

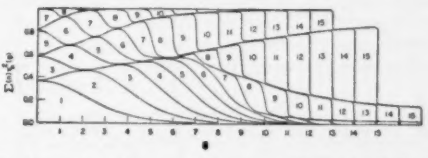

FIG. 7. Test of completeness relation, for $s=100$. Numbers indicate the bands fitting into each segment of the chart.

electron limit; that is, the component of the nth band in the range from $g=n-1$ to $g=n$, or the nth zone in momentum space. We note, as we have already pointed out, that even for the 15th band this component is still far from being the only one, though it is the largest.

It is also interesting in Fig. 7 to see the very complicated behavior in the intermediate range between the low and the high energies; and we cannot fail to realize that these intermediate states, the seventh and eighth bands in this case, represent precisely those bands which will be important in a real crystal, since they will represent the valence and conduction bands. Their properties are determined in a way by their being "squeezed in" between the very different patterns of the bound electrons and free electrons in Fig. 7. It is perhaps this observation—the remarkable complication of the wave functions for these bands near the top of the barrier—which is the most significant result of the present study. It is extraordinary that the energy levels, given in Fig. 3, can be so relatively simple, in spite of the complications of the wave functions. Certainly the fact that the energy of the conduction electrons in a metal varies in a simple fashion with the momentum, reminding us of a free electron case, is no reason for supposing that there is any corresponding simplicity in the wave functions.

A further use of Fig. 7 can perhaps suggest a rather powerful tool in considering the energy bands of a real crystal. Suppose we know the momentum eigenfunctions of some of the lower states—say the lowest six states in our present case. These represent bound states, and we could get a rather good approximation to their momentum eigenfunctions by actually using atomic functions, so that this represents a type of information which we could get in a corresponding case of a real crystal. Now we consider the next energy band, the seventh in our case. We have one specific piece of information: the component connected with any g value cannot be greater than the amount required to bring the sum of the $v^2(g)$'s for the g value up to unity. Thus for instance, in Fig. 7, we see that the component for $g=\frac{1}{2}$ could not be greater than approximately $(0.15)^{\frac{1}{2}}$. Such information could be very useful in actual cases. Thus it is well known that the wave functions in the conduction band for sodium correspond rather closely to a plane wave whose g value lies in the lowest Brillouin zone; the amplitude of this corresponds to more than $(0.90)^{\frac{1}{2}}$, and it is a result of this fact that there has been

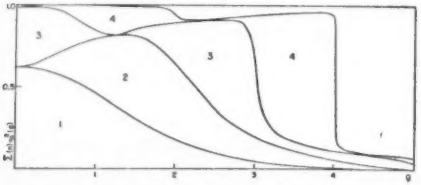

FIG. 8. Test of completeness relation, for $s=16$.

such a general assumption that the conduction electrons in a metal have wave functions like plane waves. This means, of course, that the momentum eigenfunctions of the bound electrons for sodium have a sum of $v^2(g)$ in the central Brillouin zone which is less than (0.10). We might now want to know whether a similar situation could hold in quite a different metal, say one in the iron group. We could throw light on this by finding the momentum eigenfunctions of the bound electrons, using an atomic approximation; squaring and summing, and seeing to what extent these filled the central zones of momentum space. The writer suspects that the case of the alkali metals will be found to be an exception.

It is worth while noticing, while we are considering the relation of Fig. 7 to a real crystal problem, that there is a very important difference between our Mathieu case and the case of a real crystal, in the matter of "filling up" the momentum space with the $v^2(g)$'s of the various bands. In a linear oscillator problem, the mean kinetic energy is half the total energy. Thus the lowest state has the lowest kinetic energy. Now the kinetic energy is of course merely the average of $p^2/2m$, weighted by the square of the momentum eigenfunction, so that this means that the states of low energy will have their momentum eigenfunctions concentrated in the zones of low g, successive bands coming at higher and higher g. This behavior is clear from Fig. 7. On the other hand, a tightly bound electron in an atom is in a potential similar to an inverse square field, in which the kinetic energy is the negative of the total energy, being large for the lowest energy level (which has a large negative value of energy) and decreasing as we go to higher energy levels. In other words, the momentum eigenfunction of the lowest state will extend out to high g values, and those of higher and higher bands will fill in at smaller and smaller momenta. The lowest kinetic energy of any energy bands will come approximately at the top of the barrier, or for the valence and conduction bands; it is for this reason that the $v(g)$ for the conduction band of sodium can lie largely in the central zone of momentum space. Then as we go to the higher free electron bands, of course the kinetic energy will increase again (these electrons are in a very different field from an inverse square field, so that there is nothing inconsistent in the kinetic and total energies increasing together), and the v's will lie further and further out. It is clear that, since the bound levels have already partly filled up the momentum space, the free electron wave functions cannot correspond to contributions of unity at any single momentum value, and hence cannot be really free electron like. This situation was pointed out in detail in reference 6, Secs. 21 and 22, but it is not generally recognized, and it seems worth while referring to it again here.

We have now considered the behavior of the momentum eigenfunction $v(p)$ or $v(g)$; let us ask what we can deduce about the nature of the Wannier function, its Fourier transform. We could get at this from our $v(g)$

only by making the Fourier analysis numerically, and this has not been done. We can make some deductions, however, fairly simply. In the first place, for the very tightly bound states, the Wannier function will be identical with the atomic function, a Hermite function. As the bands begin to broaden slightly, we can proceed as Wannier did in reference 8, to estimate the form of the function. The more interesting situation arises in the opposite limit, that of approximately but not completely free electrons, where the Wannier function has not been previously discussed. We have seen in this limit, for instance in Fig. 6, that $v(g)$ is approximately zero for one interval of unity along the g axis, approximately a constant in the next unit interval, zero along the next, another constant along the next, etc. If we assume that this approximate behavior is exact, then we can easily perform the Fourier transformation to determine the Wannier function analytically. Thus for instance let us consider an even momentum eigenfunction, which is equal to one constant, say $v(1/2)$, from $g=0$ to 1; zero from 1 to 2; another constant, say $v(5/2)$, from 2 to 3; zero from 3 to 4; and so on. The values for negative g's are the same. Then we can at once compute the Wannier function, by Eq. (23), or by the corresponding one-dimensional formula expressed in terms of our dimensionless variables, which is

$$a(w)=[(\pi)^{-\frac{1}{2}}/2]\int_{-\infty}^{\infty} v(g)\exp(igw)dg, \qquad (39)$$

where this a is normalized so that the integral of its square with respect to dw is equal to unity. If we substitute our assumption for v and carry out the integration, we find

$$a(w)=(\pi)^{-\frac{1}{2}}[(\sin\tfrac{1}{2}w)/(\tfrac{1}{2}w)][v(1/2)\cos w/2 + v(5/2)\cos(5w/2)+\cdots]. \qquad (40)$$

The term $v(1/2)\cos w/2+\cdots$ represents the real part of the wave function for $g=1/2$, and we see that it is to be multiplied by the function $(\sin\frac{1}{2}w)/(\frac{1}{2}w)$, equal to unity at $w=0$ but decreasing as w increases. The first zero of this function comes for $w=2\pi$, which we remember is two atomic distances away from $w=0$ (the lattice spacing in units of w equals π). In other words, $a(w)$ has the periodic oscillations of the actual wave function (which means that there are many oscillations in one lattice spacing, if we are dealing with a high energy), its amplitude shows the variation of the real wave function through the unit cell (having its maximum at the potential barriers, as we mentioned earlier), but superposed on this is the $\sin x/x$ type of function which makes the Wannier function gradually decrease as we go away from $w=0$. But we see that the function has considerable values not only in the cell at $w=0$, but also in the adjacent cells at $w=\pm\pi$. This slow falling off of the Wannier function for a free electron band is typical of situations we shall find in a number of other cases. We must realize, then, that though the Wannier

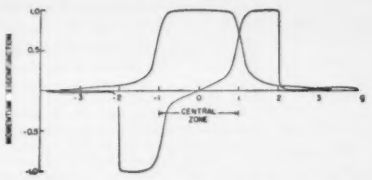

FIG. 9. Momentum eigenfunctions for two lowest bands, $s=1$.

functions have all the analytic properties mentioned earlier (orthogonality, usefulness in expressing the wave function by a Bloch-type sum, etc.), they are not always as concentrated in a single unit cell as has been generally assumed. A formula similar to (40) can be set up for momentum eigenfunctions which are odd functions of g. In this case it is interesting to note, as mentioned earlier, that in order to have the Wannier function real, the momentum eigenfunction $v(g)$ must be pure imaginary. We shall hence make this assumption in the future; it does not affect the results so far given, except that in Figs. 4 and 5 we must assume that we are plotting the odd momentum eigenfunctions divided by i.

We have now examined the case of $s=100$, considering the energy, momentum eigenfunctions, completeness relation, and Wannier functions. The cases of smaller s do not give us a great deal of new information, but they are interesting for comparison. In Fig. 8 we give a figure, like Fig. 7, for $s=16$, calculations from which these curves were plotted having been made at intervals of g 0.25 unit apart. We see that the lowest and second lowest bands have distributions much like the Hermite functions, as we expect, since they are bound states; the third is a transition type, and by the time we have reached the fourth band, it is very nearly free electron like, more so than even the 15th band for $s=100$. This situation is even more strikingly true for $s=1$. In Fig. 9 we give the momentum eigenfunctions for the two lowest states for $s=1$. (Calculations from which these curves were plotted were made at intervals of g 0.1 unit apart.) We see that even for these bands, the momentum eigenfunctions are almost free electron like; if they were exactly so, $v(g)$ for the lowest band would be equal to unity from $g=-1$ to $+1$, zero elsewhere, and for the second band it would be unity from $g=1$ to 2, -1 from -2 to -1, and zero elsewhere. And for the higher bands, the functions are very close to those for free electrons. We have given the momentum eigenfunctions themselves in Fig. 9, instead of their squares, as concerned in the test of the completeness relation, since the departures from the free electron case are more obvious in the functions themselves than in the squares.

4. THE EFFECT OF VARIOUS PERTURBATIONS ON THE ONE-DIMENSIONAL PROBLEM

Before we go on to consider the two- and three-dimensional cases, it is very much worth while to con-

TABLE II. Matrix components of sinusoidal perturbative energy, for free electron wave functions.

$0<g_0<1$ and $-1<g_0<0$: l and m both even, or l and m both odd:
$v_{lm}(g_0, n)=1$ if $2n=|m-l|$, unless $|m-l|=0$, when $v_{lm}(g_0, 0)=2$
$=0$ for other n's
$0<g_0<1$, l even, m odd: $v_{lm}(g_0, n)=i$ if $2n=m+l-1$; 0 for other n
l odd, m even: $v_{lm}(g_0, n)=-i$ if $2n=m+l-1$; 0 for other n
$-1<g_0<0$, one index even, other odd: conjugates of case $0<g_0<1$
$g_0=0$, l odd, m even, or vice versa: $v_{lm}(0, n)=0$
l and m both even: $v_{lm}(0, n)=1$ if $2n=|m-l|$, unless $|m-l|=0$, when $v_{lm}(0, 0)=2$
$v_{lm}(0, n)=-1$ if $2n=m+l$; $=0$ otherwise
l and m both odd: $v_{lm}(0, n)=1$ if $2n=|m-l|$, unless $|m-l|=0$, when $v_{lm}(0, 0)=2$
$v_{lm}(0, n)=1$ if $2n=m+l-2$; $=0$ otherwise
$g_0=1$, l odd, m even, or vice versa: $v_{lm}(1, n)=0$
l and m both even: $v_{lm}(1, n)=1$ if $2n=|m-l|$, unless $|m-l|=0$, when $v_{lm}(1, n)=2$
$v_{lm}(1, n)=-1$ if $2n=m+l-2$; $=0$ otherwise
l and m both odd: $v_{lm}(1, n)=1$ if $2n=|m-l|$, unless $|m-l|=0$, when $v_{lm}(1, n)=2$
$v_{lm}(1, n)=1$ if $2n=m+l$; $=0$ otherwise

sider the effect of certain small perturbations on the one-dimensional Mathieu problem. We have seen in Sec. 1 that a general one-dimensional potential would have Fourier components of wavelength Q_0, $2Q_0$, $\cdots$, but that the Mathieu case is that in which the amplitudes of all but one of these components were zero. We shall first consider the effect of adding a small Fourier component of wavelength nQ_0, where n is an integer [of course, if we are to retain a potential symmetrical in x, this implies setting up $W_n=W_{-n}\neq 0$, in the notation of Eq. (3)]. We must first find the nondiagonal matrix component of energy resulting from this perturbation, between any two unperturbed states. This is most conveniently handled in the momentum space; and for generality, let us consider the problem of the nondiagonal matrix component of an arbitrary Fourier component $W(\mathbf{P}_i)\exp[(-2\pi i/h)(\mathbf{P}_i\cdot\mathbf{r})]$ between two unperturbed wave functions expressed in the general form (16). We can show easily that there is no matrix component except between two wave functions u_l and u_m corresponding to the same lattice of points in p space (that is, corresponding to the same $\mathbf{p}_0$, if $\mathbf{p}_0$ is chosen to be in the central cell of momentum space). The matrix component between two such functions is then easily found to be

$$W(\mathbf{P}_i)\sum(\mathbf{P}_k)v_l^*(\mathbf{p}_0+\mathbf{P}_k)v_m(\mathbf{p}_0+\mathbf{P}_k+\mathbf{P}_i). \quad (41)$$

In our case of the one-dimensional problem with perturbative potential terms associated with W_n and W_{-n}, this nondiagonal component, expressed now in terms of our dimensionless variables, is

$$W_n\sum(k)v_l^*(g_0+2k)[v_m(g_0+2k+2n)+v_m(g_0+2k-2n)]. \quad (42)$$

We are interested, then, in the behavior of the sum

$$v_{lm}(g_0, n)=\sum(k)v_l^*(g_0+2k)[v_m(g_0+2k+2n)+v_m(g_0+2k-2n)], \quad (43)$$

where for simplicity we may take $-1\leq g_0\leq 1$.

As a first guide in our calculations, let us ask what this quantity, giving a matrix component of energy for a perturbative potential $2W\cos(2\pi nx/Q_0)$ for $W=1$, would equal for the case of really free electrons. We have already stated the nature of the free electron wave function. The function v_l is unity over the unit range of g from $l-1$ to l, and from $-(l-1)$ to $-l$, if l is odd, so that the wave function is even (bands are numbered upward from the lowest band, $l=1$). Just at $g=\pm(l-1)$, $\pm l$, the function must equal $2^{-\frac{1}{2}}$ in this case, to keep normalization; at these points, we are superposing traveling waves to form standing waves, or are at the edges of the band. The points $g=\pm(l-1)$ correspond to the lowest energy, $\pm l$ to the highest energy, in the band. Remembering that we are discussing odd l's, we see that the lowest energy of the band then corresponds to $g_0=0$, the highest energy to $g_0=1$. For even l, so that the wave function is odd, the v_l equals i (we remember that in this case v_l is imaginary, so as to yield a real Wannier function) from $l-1$ to l, $-i$ from $-(l-1)$ to $-l$, $2^{-\frac{1}{2}}i$ at $l-1$ and l, $-2^{-\frac{1}{2}}i$ at $-(l-1)$ and $-l$. Using these values and examining (43) with a little care, we find that $v_{lm}(g_0, n)$ takes on the values shown in Table II.

These values are somewhat complicated only on account of the way in which the momentum of the wave is expressed in terms of g_0 and an integer. We can explain them in words very simply. Except at the edge of a band, the wave function is a single wave, of the form $\exp(igw)$. If we wish to find the matrix component of a potential $\exp(\pm 2inw)$ between two waves with g's equal to g_l, g_m, we have to find the integral over w of $\exp i(-g_l+g_m\pm 2n)$, which is zero unless $2n=|g_l-g_m|$. At the edge of a band, however, we have standing waves of the form $2^{-\frac{1}{2}}[\exp(igw)\pm\exp(-igw)]$, so that we have an integral of a quantity like

$$\tfrac{1}{2}[\exp(-ig_lw)\pm\exp(ig_lw)]\times[\exp(-ig_mw)\pm\exp(ig_mw)]\exp(\pm 2inw),$$

which gives nonvanishing terms not only if $2n=|g_l-g_m|$, but also if $2n=|g_l+g_m|$. All the components in Table II fall into these simple categories.

It is now interesting to see to what extent the matrix components $v_{lm}(g_0, n)$ for the real wave functions agree with these free electron values. Accordingly we give,

in Table III, the components $v_{lm}(g_0, n)$ for the wave functions of the 9th and 10th bands, for the Mathieu case with $s=100$. Thus we have $v_{9,9}$, $v_{9,10}$, and $v_{10,10}$. We have computed these for $g_0=0$, $\frac{1}{2}$, and 1; but the behavior for all values of g_0 between 0 and 1 does not differ much from the values at $g_0=\frac{1}{2}$, the change of properties as we approach the edge of the band at $g_0=0$, 1 being quite sudden. Our rules of Table II would indicate that in this case if we had free electrons $v_{9,9}(g_0, n)$ should be 2 if $n=0$, for each g_0. There should be no further nonvanishing components except at the edge of the band, where at $g_0=0$ there should be a component equal to unity for $n=8$, and at $g_0=1$, where there should be a component of unity for $n=9$. Similarly $v_{10,10}(g_0, n)$ should be 2 if $n=0$ for each g_0, and in addition should have a value of -1 for $g_0=0$, $n=9$, and for $g_0=1$, $n=10$. The nondiagonal matrix component $v_{9,10}(g_0, n)$ should be $-i$ for $n=9$, zero for other n's, except at the edges of the band; it should be zero at both band edges. When we examine Table III, we see that the actual values are very far from these free electron cases. A few of the predictions of the free electron case must hold here too; thus for $n=0$ the result must come out the same, for then they depend only on the normalization of the wave function, and the vanishing of the nondiagonal component $v_{9,10}$ at the edges of the band follows from symmetry alone. (It is to be noted that this vanishing of the nondiagonal component holds only because one of our states has an even momentum eigenfunction, one an odd function; it would not occur if both had even eigenfunctions, or if both had odd functions.) But in all the cases where only one component would be different from zero in the free electron case, we actually find a wide range of components different from zero, and the one which would appear in the free electron case is not even the biggest component. This situation is, of course, a result of the fact that the individual wave functions have large contributions connected with many sinusoidal waves, as we have already pointed out.

The effect of perturbations is particularly interesting as far as it concerns the widening of gaps between bands; for here there has been widespread use,[12] particularly in the theory of alloys, of the assumption that a single gap was widened by the action of a single Fourier component of potential, as it would be for free electrons. Let us remind ourselves of how this would work out for the case we are considering, the 9th and 10th bands, if the wave functions were really free electron like. There would be a nondiagonal matrix component of energy coming from the perturbation $\cos 2nw$, with $n=9$. This would have a maximum effect as g approached the value 9, the boundary between the 9th and 10th zones in momentum space, at which the diagonal energies of the two states would become equal to each other. Just at this value $g=9$, the gap would appear, the perturbed wave functions being the sum and difference of the progressive waves, the gap width being proportional to the nondiagonal matrix component; the depression of the lower energy level and the elevation of the upper one, on account of the perturbation, would rapidly decrease as g departed from 9. If, as a matter of fact, the unperturbed wave functions were set up, as we have been doing it, to correspond to a standing wave just at the edge of the zones, the perturbation will not have to produce a linear combination of direct and reflected waves just at this point, since the linear combinations will already have been set up in the unperturbed wave functions. Hence the gap will be produced, just at $g=9$, by the diagonal, rather than the nondiagonal, matrix component of perturbative energy. As soon as g deviated from 9, however, the perturbation would produce linear combinations, so that the final result would be just as in the usual treatment of perturbations of sinusoidal wave functions by sinusoidal potentials. No matrix component of perturbative energy, except that for $n=9$, would be effective in setting up the gap at $g=9$.

We can now see how completely the situation is altered when we have the real wave functions, from the figures of Table III. The gap comes at $g_0=1$. Here $v_{9,9}(g_0, n)$ and $v_{10,10}(g_0, n)$ give a measure of the perturbation produced at the two edges of the gap by the diagonal matrix components of the various Fourier components of potential. We see that for all the larger n values, the two terms are almost equal and opposite. That is, each Fourier component pushes the energy at the two edges of the gap in opposite directions. As g_0 deviates slightly from unity, we have nondiagonal matrix components of energy; and we see from $v_{9,10}(g_0, n)$ for $g_0=\frac{1}{2}$ that these components are very nearly equal in absolute magnitude to the diagonal component for $g_0=1$, which is necessary in order to have a continuity in behavior between the edge of the gap, where our

TABLE III. Matrix components of sinusoidal perturbative potential, for Mathieu wave functions of 9th and 10th bands, $s=100$.

	$g_0=0$		$g_0=\frac{1}{2}$			$g_0=1$	
n	(9/9)	(10/10)	(9/9)	(9/10)	(10/10)	(9/9)	(10/10)
0	2.000	2.000	2.000	0.000	2.000	2.000	2.000
1	−0.516	−0.264	−0.386	−0.010i	−0.292	−0.392	−0.350
2	0.282	0.060	0.120	0.017i	0.066	0.064	0.112
3	−0.288	−0.016	−0.046	−0.051i	−0.020	0.018	−0.060
4	0.380	−0.010	0.024	0.116i	0.006	−0.100	0.120
5	−0.496	0.080	−0.008	−0.237i	0.002	0.228	−0.238
6	0.508	−0.166	0.002	0.421i		−0.416	0.424
7	−0.196	0.312		−0.521i		0.562	−0.554
8	−0.029	−0.532		0.383i		−0.396	0.380
9	0.240	0.496		0.188i		−0.180	0.186
10	0.360	0.056		−0.376i		0.380	−0.372
11	0.212	−0.460		−0.380i		0.380	−0.376
12	0.068	−0.364		−0.179i		0.180	−0.180
13	0.012	−0.148		−0.054i		0.056	−0.056
14		−0 042		−0.011i		0.012	−0.012
15		−0.008		−0.003i			

[12] H. Jones, Proc. Roy. Soc. (London) **144**, 225 (1934); L. Pauling and F. J. Ewing, Revs. Modern Phys. **20**, 112 (1948); and many other references.

wave functions represent standing waves, and different values of g_0, where they are approximately traveling waves. But the important fact is that almost any Fourier component of potential is effective in broadening the gap at $g=9$, not just the component $n=9$; and the interesting additional feature that some of the components are of one sign, some of the other, so that some components of potential can actually narrow the gaps, rather than broaden them.

There is, in other words, simply nothing like a one-to-one correspondence between Fourier components of potential and their effect on broadening the gaps between energy levels; and one must look with a great deal of reservation on such applications as those mentioned in reference 12. It is notable that the gap between the 9th and 10th bands, which we have used for illustration, is in a region of the energy *vs* g curve, shown in Fig. 3, where this curve resembles a free electron parabola very strongly, and the gap is very narrow; thus we might very easily be under the impression that a real free electron treatment was appropriate, whereas it obviously is not. It is interesting to point out another aspect of this situation, by which one Fourier component of potential can be effective in broadening other gaps, besides that which the free electron approximation would suggest. This aspect arises from our Mathieu problem itself. This is the problem in which there is only one Fourier component of potential, which on the free electron approximation would produce only an energy gap at $g=1$, between the first and second bands. On the other hand, as we see from Fig. 3, it has actually produced wide gaps between all the lower energy bands. If we try to explain the existence of these gaps from perturbation theory, we find that we must do it by using higher-order perturbations, the gap at $g=2$ coming from second-order perturbations, that at $g=3$ from third-order, and so on. The great width of the actual gaps shows the inappropriateness of perturbation method for handling the problem. This does not affect, however, the correctness of the application of perturbation theory which we are making in the present section, where we investigate the effect of an additional small perturbative potential of nature $\cos 2nw$, superposed on the large potential of form $\cos 2w$ already taken into account by our exact solution of the Mathieu problem

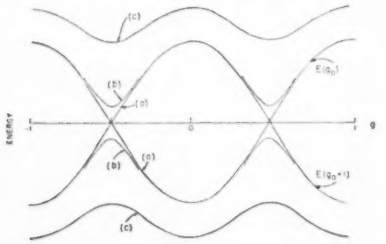

FIG. 10. Energy *versus* momentum for problem of band with perturbative potential of double periodicity, showing splitting of band. Unit cell in momentum space, unperturbed problem, extends from $g=-1$ to 1; for perturbed problem, from $g=-\frac{1}{2}$ to $\frac{1}{2}$. Curve (a), vanishing perturbation; (b), larger perturbation; (c), still larger perturbation.

The perturbation $\cos 2nw$ which we have discussed does not interfere with the periodicity of the structure, or the size of the unit cell. Another interesting type of perturbation, however, is that produced by a potential of for instance $\cos w$, which has a longer period (in this case 2π) than the unperturbed potential (with its period of π). Such a perturbative potential has the effect of producing an alternation in the depth of adjacent potential wells. It is this type of alternating potential which has been considered by the writer[13] in discussions of antiferromagnetism and order-disorder effects in certain alloys.

We easily find that such a perturbative potential has nondiagonal matrix components between two states of the same energy band, one with a given g_0, the other g_0 a unit greater. These nondiagonal components are more important than those between different energy bands. For a potential $2\cos w$, the nondiagonal matrix component of energy between these two states proves to be

$$\sum(k)v_l^*(g_0+2k)[v_l(g_0+2k+1)+v_l(g_0+2k-1)], \quad (44)$$

showing a close resemblance to Eq. (43). We can understand the situation better from Fig. 10. Here we plot the energy of the lth band as a function of g_0, in the central cell of momentum space, between $g_0=-1$ and 1. We also plot the energy, as a function of g_0+1. Then our rule states that there will be a nondiagonal matrix component of energy between states on the two curves lying vertically above each other. These nondiagonal components will cause the correct wave functions to be linear combinations of the two unperturbed functions, one of given g_0, the other of g_0+1. Just at $g_0=\pm\frac{1}{2}$, where the two curves cross, the unperturbed problem is degenerate, the perturbation will cause the levels to separate by amounts proportional to the nondiagonal matrix component, and the resulting wave functions will be the sum and difference of the unperturbed wave functions. As g_0 departs from $\pm\frac{1}{2}$, and the unperturbed energy levels deviate from each other, the situation will depend on the relative magitude of the nondiagonal matrix component of energy, and the separation of the unperturbed states; if the nondiagonal component is small compared to the separation of the unperturbed states, the displacements of the perturbed states, as seen from second-order perturbation theory, will be proportional to the square of the nondiagonal matrix components, divided by the difference of unperturbed energies. In Fig. 10(a), we show the unperturbed energy levels; in (b) the perturbed levels with a small perturbations; in (c) the perturbed levels with a

[13] J. C. Slater, Phys. Rev. **82**, 538 (1951); **84**, 179 (1951).

large perturbation. It is clear how the curves of Fig. 10 are to be interpreted. Once we have our perturbation $\cos w$, the perturbed problem really has a periodicity of 2π along w, rather than of π. Thus we should use a Brillouin zone half as great, the central zone extending from $g_0=-\frac{1}{2}$ to $\frac{1}{2}$ rather than from -1 to 1. The original energy band of the unperturbed problem has split into two, each holding one electron per unit cell of each spin; but since the unit cell is twice as great, the two bands taken together hold the same number of electrons per atom as the original unperturbed band. The net effect of the perturbation is to introduce a gap in the middle of the original band.

It is interesting to ask what happens to the perturbed wave functions as a result of this perturbation. If the perturbation is small—that is, if the separation of the unperturbed states is large compared to the nondiagonal matrix component—of course the effect is small; a little of one wave function is mixed in with the other. As the perturbation becomes large, however, the unperturbed wave functions are combined with almost the coefficients ± 1. In this case the combination becomes

$$\sum(k)\{v_l(g_0+2k)\exp[i(g_0+2k)w] \pm v_l(g_0+2k+1)\exp[i(g_0+2k+1)w]\}.$$

This can equally well be written

$$\sum(k)\{v_l(g_0+2k)\exp[i(g_0+2k)w] \pm(\tfrac{1}{2})[v_l(g_0+2k+1)\exp[i(g_0+2k+1)w] + v_l(g_0+2k-1)\exp[i(g_0+2k-1)w]]\},$$

since the latter two terms, when summed over k, are identical. It is now particularly interesting to consider how this behaves in the case of tightly-bound states. For this, we remember that $v_l(g)$ is a slowly varying function of g, not changing much in a unit interval along g. Thus we can approximately replace $v_l(g_0+2k\pm1)$ by $v_l(g_0+2k)$. If we do this, the function becomes

$$(1\pm\cos w)\sum(k)v_l(g_0+2k)\exp[i(g_0+2k)w]. \quad (45)$$

This is the wave function in the absence of perturbations, multiplied by the factor $1\pm\cos w$. If we take the $+$ sign, the function equals 2 when $w=0, 2\pi, \cdots$, and equals 0 when $w=\pi, 3\pi, \cdots$. That is, in this case, the wave function will correspond to having the wave functions on the atoms at $0, 2\pi, \cdots$, much as in the absence of perturbations, but to having the wave functions on the alternate atoms practically equal to zero. With the $-$ sign, the wave function is large on the intermediate atoms. The interpretation of the situation is simple. With a large nondiagonal matrix component of energy, the alternate potential minima are of quite different depths, as shown in Fig. 11(a). If we are dealing with tightly bound states, below the potential barrier, so that these states lie not far from the corresponding states of the isolated atoms, it is clear that the band will

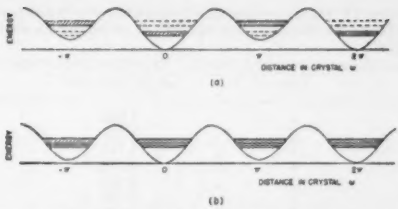

FIG. 11. Energy band split by an alternating component of potential. Curve (a), fairly large perturbation; dotted lines indicate region where the wave function is small. Curve (b), small perturbation, which merely introduces energy gaps.

split into two quite separate bands, one corresponding to a state where the wave function is large in one type of atom, the other where it is large in the others. It is this case which we have when the wave functions for all g_0's are the sums or differences of the unperturbed wave functions, as in (45). The other case, however, where this occurs only in a narrow range of g_0's about $g_0=\pm\frac{1}{2}$, is that in which the nondiagonal matrix component of energy is small compared to the band width; this will be the case in Fig. 11(b), where the difference in heights of the two types of minima is small compared to the width of the band. In this case most of the wave functions extend with approximately equal amplitudes into both types of atoms; it is only those in the immediate neighborhood of the gaps which are concentrated largely in one type of atom or the other (a concentration which is not easy to show in a diagram like Fig. 11(b)).

Now that we have considered the general nature of the perturbation produced by the potential $\cos w$, it is interesting to consider the nondiagonal matrix component (44) involved in the perturbation. If we were dealing with perfectly free electrons, we could show easily that this expression would be zero, except for the first band, for which it would be unity; no higher bands would be split by this perturbation. For contrast, we give in Table IV the values computed for $s=100$, for a series of bands. We see that for the bound states, the matrix component is between 1 and 2 (it would be just 2 if our approximation that $v_l(g_0+2k\pm1)$ equaled $v_l(g_0+2k)$ were justified, as we see from (44), using the fact that the wave functions are normalized). It begins to decrease rapidly as we get to the top of the barrier, and by the time we have gone several states above the barrier, it has become small. For the states near the top of the barrier, then, the component is not far from unity; and this shows us that, in a real crystal, we may well expect that this type of perturbation, applied to the valence or conduction band, may produce a splitting of the band, much as it would do in the lowest band with really free electrons.

It is now interesting to go further and ask about the behavior of the Wannier functions when we impose a perturbation of the type we have been considering on an

TABLE IV. Matrix components of sinusoidal perturbative potential 2 cos$w$, for Mathieu wave functions of various bands, $s=100$, for $g_0=\frac{1}{2}$.

Band	Matrix component
1	1.944
2	1.837
3	1.714
4	1.574
5	1.404
6	1.118
7	0.629
8	0.184
9	0.026

originally sinusoidal potential. Our approach is naturally to consider the momentum eigenfunction, and then to find the Wannier function by Fourier transformation. Let us first start with the unperturbed problem and ask what happens to the momentum eigenfunction when we describe the problem in terms of a unit cell twice as great (that is, of period 2π in w), and correspondingly a Brillouin zone half as great (extending from $g=-\frac{1}{2}$ to $\frac{1}{2}$). For definiteness, let us take the lowest band of the unperturbed problem, for $s=100$. Here the momentum eigenfunction for the unperturbed problem, as given in Fig. 4, is reproduced in Fig. 12(a). Next, in Fig. 12(b), we show the momentum eigenfunction of the lower half-band (in the sense of Fig. 10) arising from the single band of the unperturbed problem, when we change the cell size. We must now write our wave functions in terms of a sum over all g values differing by an integer, rather than all g values differing by an even integer. Yet the final wave function, of course, must be the same as in our original description. Thus for instance if g_0 is $\frac{1}{4}$, the components of the momentum eigenfunction at $1\frac{1}{4}, 3\frac{1}{4}, 5\frac{1}{4}, \cdots, -\frac{3}{4}, -2\frac{3}{4}, \cdots$, must all be zero; but those at $2\frac{1}{4}, 4\frac{1}{4}, \cdots, -1\frac{3}{4}, -3\frac{3}{4}, \cdots$, must have the same values as in the original description. A similar situation holds if g_0 is between 0 and $-\frac{1}{2}$, say $-\frac{1}{4}$. In other words, $v(g)$ must be just as in Fig. 12(a) for g in the range $-\frac{1}{2}$ to $\frac{1}{2}$, $1\frac{1}{2}$ to $2\frac{1}{2}$, $3\frac{1}{2}$, $\cdots$, and $-1\frac{1}{2}$ to $-2\frac{1}{2}$, $-3\frac{1}{2}$ to $-4\frac{1}{2}$, etc., but it must be zero in between; that is, it must be as in Fig. 12(b). For the upper half-band, the components in alternate unit intervals of g must be different from zero, as in Fig. 12(c).

We may now consider the Wannier function, obtained by Fourier transformation of the functions of Fig. 12. These functions may be obtained from the original momentum eigenfunction of Fig. 12(a), which we may call $v_0(g)$, by multiplying by a function which, in (b), equals 1 from $-\frac{1}{2}$ to $\frac{1}{2}$, $1\frac{1}{2}$ to $2\frac{1}{2}$, etc., and is zero between; or which, in (c), equals 1 from $\frac{1}{2}$ to $1\frac{1}{2}$, $2\frac{1}{2}$ to $3\frac{1}{2}$, etc., and is zero between. These step functions are easily expressed as Fourier series. Thus the function which is unity in the region $-\frac{1}{2}$ to $\frac{1}{2}$, $1\frac{1}{2}$ to $2\frac{1}{2}$, etc., zero between, is

$$f_1(g)=\sum(n=-\infty\cdots\infty)c_n\exp(\pi ing),$$

where

$$c_0=\tfrac{1}{2},\quad c_1=c_{-1}=1/\pi,\quad c_2=c_{-2}=0,$$
$$c_3=c_{-3}=-1/3\pi,\quad c_4=c_{-4}=0,\quad c_5=c_{-5}=1/5\pi,\cdots. \quad (46)$$

The corresponding function $f_2(g)$, equal to unity when g is between $\frac{1}{2}$ and $1\frac{1}{2}$, $2\frac{1}{2}$, and $3\frac{1}{2}$, etc., and zero between, is $1-f_1(g)$, or

$$f_2(g)=\sum(n)d_n\exp(\pi ing),\quad d_0=\tfrac{1}{2},$$
$$d_1=d_{-1}=-1/\pi,\quad d_3=d_{-3}=1/3\pi,\text{ etc.} \quad (47)$$

Thus the momentum eigenfunction given in Fig. 12(b) can be written as $v_0(g)f_1(g)$, and that in Fig. 12(c) as $v_0(g)f_2(g)$. It is now simple to substitute the expressions into the formula (23) for finding the Wannier function, or the corresponding formula (39) in terms of our dimensionless variables.

From Eq. (39), we have

$$a(w)=\tfrac{1}{2}\pi^{-1}\int_{-\infty}^{\infty}v(g)\exp(igw)dg.$$

When we substitute $v(g)=v_0(g)f_1(g)$ or $v_0(g)f_2(g)$, we have

$$a(w)=\sum(n)c_n\int_{-\infty}^{\infty}v_0(g)\exp[i(w+n\pi)g]dg$$

$$=\sum(n)c_n a_0(w+n\pi),\quad\text{or}\quad\sum(n)d_n a_0(w+n\pi), \quad (48)$$

where

$$a_0(w)=\tfrac{1}{2}\pi^{-1}\int_{-\infty}^{\infty}v_0(g)\exp(igw)dg. \quad (49)$$

That is, from (48), the Wannier function of the lower half-band, in the new description in terms of the doubled unit cell, consists of the original Wannier function a_0 located at the atom at the origin, with an amplitude $\frac{1}{2}$; but also similar Wannier functions with amplitudes $1/\pi$ located on the adjacent atoms at $\pm\pi$, functions with amplitudes $-1/3\pi$ at the atoms at $\pm3\pi$,

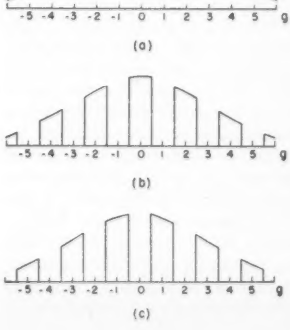

FIG. 12. Momentum eigenfunction of lowest band, $s=100$, for (a) original problem; (b) and (c), same problem expressed in terms of unit cell twice as great; (b), lower half-band, and (c), upper half-band.

and so on. A similar situation holds for the upper half-band. This composite Wannier function, in other words, extends out much further than the original Wannier function, and we note that this change has been brought about, not by a change in the physical situation, for the perturbation is still vanishingly small, but merely by a change in the method of description. This is an example of a situation that has not been sufficiently appreciated: the method of setting up the Wannier functions is not unique.

Now let us ask how these Wannier functions will change when the amplitude of the perturbative potential builds up from zero to a large value. First we consider the limiting case where the perturbation is so great that for all g values the perturbed wave functions are the sum and difference of the original wave functions, so that the perturbed momentum eigenfunctions are the sum and difference of the original momentum eigenfunctions. For the sum, the problem is simple. The sum of the functions shown in Figs. 12(b) and 12(c) is obviously the original function shown in Fig. 12(a); thus the corresponding Wannier function must be just the original Wannier functions located at the origin. This is also clear from Eq. (48), in which the sum of c_n and d_n equals unity for $n=0$, zero for any other n. But there is a difference between this problem and the unperturbed one, nevertheless. For now our unit cells are twice as great as before. Wannier functions are to be located only at the atoms at $w=0, \pm 2\pi, \pm 4\pi$, etc., in setting up the Bloch sum (20) and are to be omitted from the atoms at $w=\pm\pi, \pm 3\pi$, etc. This is the case shown in Fig. 11(a), where the potential minima at $w=0, \pm 2\pi, \pm 4\pi$, etc., are much lower than those at $\pm\pi, \pm 3\pi$, etc., and we are speaking of the wave functions which have their intensities located almost entirely in these lower potential wells. It is natural that the Wannier functions are concentrated about these potential wells in which the final wave function is large.

The situation is really not as simple as this, however, as we see when we consider the upper half-band. There the wave functions, and momentum eigenfunctions, in the limit of large perturbations, are the differences rather than the sums of the original functions. The momentum eigenfunction is then $v_0(g)$ multiplied by a function which is unity from $-\frac{1}{2}$ to $\frac{1}{2}$, -1 from $\frac{1}{2}$ to $1\frac{1}{2}$, 1 from $1\frac{1}{2}$ to $2\frac{1}{2}$, -1 from $2\frac{1}{2}$ to $3\frac{1}{2}$, etc. And the Wannier function is determined by the difference c_n-d_n in Eq. (48), and hence corresponds to nothing on the atom at $w=0$, functions of amplitude $2/\pi$ at $w=\pm\pi$, nothing at $w=\pm 2\pi$, functions of amplitude $-2/3\pi$ at $w=\pm 3\pi$, and so on. This is an unexpected situation, for physically we expect the wave functions in this case to be essentially like those in the lower half-band, only concentrated now on the atoms at odd multiples of π, rather than at even multiples, and we might suppose that the Wannier functions would be entirely concentrated at one atom at $w=\pi$. The reason why it is not is that we introduce at the outset the postulate that the Wannier functions were to be located at $w=0, \pm 2\pi$, etc., by our original equations (39) and (48). The Wannier functions which we have found, with contributions at $w=\pm\pi, \pm 3\pi$, etc., lead in fact to the same final wave functions, when we combine them into Bloch sums, as we should get if we had a Wannier function concentrated only on the atom at $w=\pi$, with a similar one on $w=3\pi, 5\pi$, etc.; this is shown in Appendix I. But the description is different, and this is another illustration of the fact that the Wannier function is not unique.

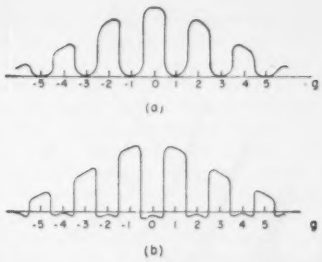

FIG. 13. Momentum eigenfunction of cases shown in Fig. 12(b) and Fig. 12(c), but for nonvanishing but small perturbative potential. (a), same case as Fig. 12(b); (b), same case as Fig. 12(c).

We have considered the Wannier function, for our problem of the perturbative potential $2W\cos w$, for two limiting cases: first, for infinitesimal W; next for very large W. Let us now ask qualitatively how they behave for intermediate W. It is clear in a general way what will happen: the Wannier function for the lower band, which has components at $w=0, \pm\pi, \pm 3\pi$, etc., when $W=0$, and which has only a component at $w=0$ when W is large, will naturally gradually lose the components at $\pm\pi, \pm 3\pi$, etc., as W increases. We can say something more than this, however, from our general knowledge of Fourier series, coupled with our knowledge of how the perturbation problem behaves. The rather slow falling off of the c_n's of Eq. (48) with increasing n is a result of the discontinuities of the step function given in Eq. (46); if the function were rounded off at the half-integral values of g, instead of being discontinuous, the c_n's would decrease more rapidly with n. But this is just what we are to expect as a result of our perturbations. With a relatively small value of W, we may expect Fig. 12(b) and (c) to be modified as indicated in Fig. 13 (which is not a result of quantitative calculation). The modification comes in, for small W, mostly near the half-integral values of g, resulting in each case in a decreasing of the amplitude of the function as given in Fig. 12, in the region where that function is different from zero, with a compensating build-up in the region where the function of Fig. 12 is equal to zero. Thus we may suppose that the Wannier function corresponding to the lower band begins to lose its contributions corresponding to large w values quite rapidly as W increases, the contributions from $w=\pm\pi$ persist-

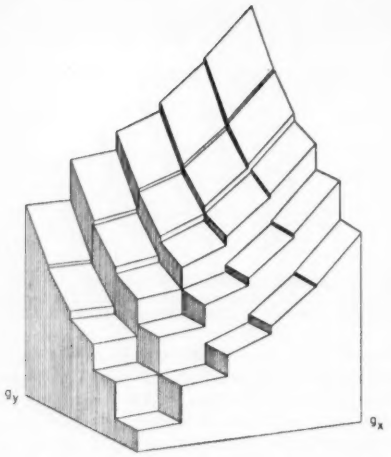

FIG. 14. Energy ϵ as function of components of momentum, g_x and g_y, in dimensionless units, for the case $s=16$.

ing until quite a large value of W is reached. For the upper band, on the other hand, where these contributions for large w's are present even for large W, the Wannier function will naturally be extended over many unit cells for any value of W.

5. THE UNPERTURBED MATHIEU PROBLEM IN TWO DIMENSIONS

The unperturbed Mathieu problem in two dimensions follows directly from the one-dimensional problem, and at first glance there seems to be very little about it which we have not already met in our one-dimensional problem; we find later, however, that certain degeneracies between energy levels, which would be removed by almost any sort of perturbation, really make an essentially new feature of the problem. First we consider the unperturbed case. The energy as a function of momentum is of course simply the sum of the energies of two one-dimensional problems. Thus if we let g_x, g_y be quantities like our earlier g, measuring momentum in dimensionless variables in the x and y direction, we can show the energy as a function of g_x and g_y by a surface. Such a surface, for the case $s=16$, is shown in Fig. 14. A section of this surface, but by a plane $g_x=$constant or $g_y=$constant, would be like Fig. 3, except that we show the case $s=16$, instead of $s=100$ as in Fig. 3. In Fig. 14, we have shown the energy in an extended momentum space, rather than showing all sheets of the energy surface in the central zone of momentum space, since this makes it easier to visualize the situation. We can also display the energy bands as a function of lattice spacing, as shown in Fig. 15. This can be computed directly from Fig. 1, the corresponding one-dimensional case, by simply adding the energies of two one-dimensional cases. We now observe the interesting fact that for small interatomic distances we no longer have any energy gaps; the bands overlap, as in a real crystalline conductor. As for the momentum eigenfunction, it simply is a function of g_x times a function of g_y, each being of the form discussed in Sec. 3.

The problem becomes more interesting, however, as we begin to consider the various energy bands, and their degeneracies, more in detail. Let us consider the limit of large interatomic distances. In this limit, the potential energy is proportional to r^2, where r is the distance from a lattice point, so that the solutions have the properties characteristic of the two-dimensional analog of the central field, and hence can be described by an azimuthal quantum number and a principal quantum number. We can also, of course, describe the solutions by the quantum numbers n_x and n_y associated with the one-dimensional linear oscillator problems in terms of which the two-dimensional linear oscillator can be expressed. At infinite separation, we have seen that the energy of the one-dimensional problem is $2n+1$, in units of $h\nu_0/2$, ν_0 being the oscillation frequency of the oscillator, and n taking on the values 0, 1, 2, $\cdots$. Thus the energy of the two-dimensional problem, at infinite separation, is $2(n_x+n_y)+2$. The atomic wave functions, which represent the real wave functions at infinite separation, are the products of Hermite functions, as given in Eq. (13), for x and y. Thus let us consider some of the lowest wave functions. Using Eq. (13), we have functions as given in Table V. We see that the ground state of the problem, with $n_x=0$, $n_y=0$, wave function $\exp(-r^2/2)$, has the properties of an s state, the wave function depending on r only. The next two functions, which can be written $\cos\theta[r\exp(-r^2/2)]$ and $\sin\theta[r\exp(-r^2/2)]$, where θ is the angle in a polar coordinate system where z_x, z_y are rectangular coordinates, are p-like functions, corresponding to the p_z and p_y type of atomic orbitals. Of the next three, the one with $n_x=1$, $n_y=1$, whose wave function can be written $\sin 2\theta[r^2\exp(-r^2/2)]$, is of a d type. The other two do not correspond to any definite azimuthal quantum number as they stand; but their sum and difference do. The sum is $-2(1-r^2)\exp(-r^2/2)$, an s-like function, which we might call $2s$, and the difference is $\cos 2\theta[2r^2\exp(-r^2/2)]$, the other function of the d type. We can make similar identification of the cases with higher n_x, n_y in terms of the quantum numbers of the

TABLE V. Unnormalized atomic wave functions for two-dimensional linear oscillator, for different quantum numbers n_x, n_y. Here $r^2=z_x^2+z_y^2$, $z=s^{\frac{1}{4}}w$.

n_x	n_y	ϵ	u
0	0	2	$\exp(-r^2/2)$
1	0	4	$z_x\exp(-r^2/2)$
0	1	4	$z_y\exp(-r^2/2)$
2	0	6	$(-1+2z_x^2)\exp(-r^2/2)$
0	2	6	$(-1+2z_y^2)\exp(-r^2/2)$
1	1	6	$2z_xz_y\exp(-r^2/2)$

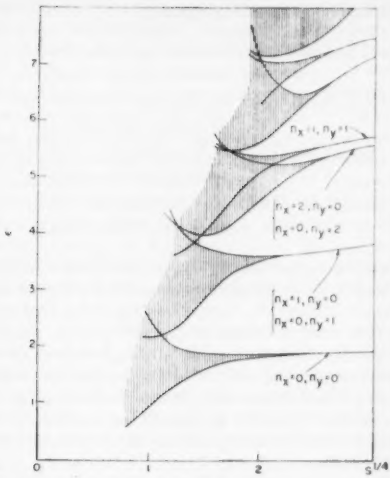

FIG. 15. Energy bands as functions of lattice spacing, two-dimensional Mathieu problem. Quantum numbers n_x, n_y are given as indicated in Table V.

central field problem. It is then convenient to denote the various bands, as we do in the crystal formed from real atoms, by the quantum numbers of the corresponding states in the separated atoms. Thus the band arising from $n_x=0$, $n_y=0$ can be considered to be the $1s$ band; that arising from $n_x=1$, $n_y=0$, and $n_y=1$, $n_x=0$ is the $2p$ band, showing the twofold degeneracy characteristic of a p state in a two-dimensional problem; that arising from the sum of $n_x=2$, $n_y=0$ and $n_x=0$, $n_y=2$ is the $2s$ band; that from the difference of these states and that from $n_x=1$, $n_y=1$ are the two components of the first d band, which we may call $3d$; like the p states, it shows only a twofold degeneracy in the two-dimensional problem. We observe that there is degeneracy between the $2s$ and $3d$, in this linear oscillator problem.

Now that we have looked at the behavior of our energy levels and wave functions at infinite separation, we can ask what happens to the states as the interatomic distance decreases. From Fig. 2, or Fig. 15, we know that the first effect is to displace each of the energy levels of the one-dimensional problem, before the band begins to broaden significantly. The displacement is greater, in the one-dimensional problem, the greater the value of n, but it is not a simple function of n. We then see that the displacement will be the same for the two p-like solutions $n_x=1$, $n_y=0$, and $n_x=0$, $n_y=1$, so that the degeneracy of these p states will not be removed by the effect of the "crystalline field" mentioned in Sec. 1. However, the displacement of the two states $n_x=2$, $n_y=0$, and $n_x=0$, $n_y=2$, will be different from that of the state $n_x=1$, $n_y=1$, so that the degeneracy of the two d-like states will be removed by the crystalline field, though the degeneracy between the one with wave function like $\cos 2\theta r^2 \exp(-r^2/2)$ and the $2s$-like function, will not be removed by this field. This removal of the degeneracy of the d states by the square, or cubic, crystalline field is entirely analogous to the corresponding situation in real three-dimensional crystals. The degeneracy between one of these d states and the s state is, however, peculiar to our special problem.

Let us now reduce the interatomic distance still more, to a point where the bands begin to broaden. Nothing remarkable happens to the $1s$-like band. The $2p$-like band, however, immediately involves us in a very interesting problem of degeneracy, the simplest case of the general problem of overlapping bands which one meets in real crystals. We can make this problem plain by drawing the surfaces giving energy ϵ as a function of momentum g_x and g_y, not as in Fig. 14, but in the central cell of momentum space. This is done for the two p-like states in Fig. 16. First, in Figs. 16(a) and (b), we draw separately the surfaces for the case $n_x=1$, $n_y=0$, and $n_x=0$, $n_y=1$. Then in Fig. 16(c) we superpose these two surfaces. It is clear from the figure that the two surfaces intersect along the 45° diagonals in the momentum space, given by $g_y=\pm g_x$. That is, at any point of these two diagonals, the two energy bands are degenerate with each other. This degeneracy, as we shall show later, is characteristic only of our specialized Mathieu problem. We shall see in the next section that if we introduce as perturbations the type of additional Fourier components of potential which would automatically be present in a real crystal, there will be nondiagonal matrix components of energy between the two states shown by the energy surfaces of Fig. 16, acting to repel the upper sheet from the lower; and this will cause the two degenerate states to separate along the 45° lines so that there will really be two energy surfaces, one lying above the other at every g value and formed by displacement of the upper surfaces of Fig. 16, and the other lying everywhere below. The only exceptions come at certain special symmetry points, namely, the center and corners of the cell in momentum space; at these points the nondiagonal matrix component of energy is automatically zero, by symmetry, and the two perturbed energy surfaces adhere to each other. These interesting facts, and their effect on the Wannier functions, will be taken up in the next section.

Similarly in Fig. 17 we show the three energy sur-

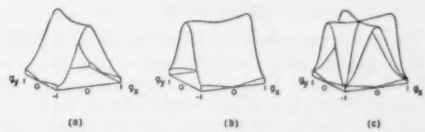

FIG. 16. Energy as a function of momentum, p-like states, two-dimensional Mathieu problem. (a) energy surface for case $n_x=1$, $n_y=0$; (b) for case $n_x=0$, $n_y=1$; (c) combination of cases (a) and (b), showing degeneracy, or intersection of surfaces, along diagonals $g_y=\pm g_x$.

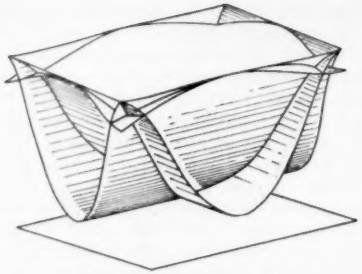

FIG. 17. Energy surfaces as function of momentum, for the states $n_x=2$, $n_y=0$; $n_x=0$, $n_y=2$; and $n_x=1$, $n_y=1$, for two-dimensional Mathieu problem.

faces for the states for $n_x=2$, $n_y=0$; $n_x=0$, $n_y=2$; and $n_x=1$, $n_y=1$, which are degenerate with respect to each other at infinity, at a smaller interatomic distance at which they are overlapping each other, but where they do not overlap any other band. The two states $n_x=2$, $n_y=0$, and $n_x=0$, $n_y=2$, have surfaces intersecting along the 45° diagonal, for the same symmetry reason found in the case of the p functions of Fig. 16. The remaining state, however, has an entirely different energy surface, which cuts the other two, but along lines in the momentum space which have no simple geometrical significance, and which vary with internuclear distance. Here as before when we investigate the nondiagonal matrix components of perturbative energy these components do not vanish for the type of perturbation found in a real crystal; in this case, unlike the preceding one, there are not even any special points at which symmetry demands that they vanish. Thus really the perturbed energy surfaces of all these three states will not cut each other, and we shall have three perturbed surfaces, one resembling the upper sheet of the surfaces on Fig. 17, for each g_x, g_y value, one resembling the middle sheet, one the lower sheet. Since the intersections are now partly along curves in momentum space with no simple geometrical description we see how the real energy surfaces in the perturbed problem can have great complication, even in this simple problem. We therefore pass on, in the next section, to a consideration of the effect of various perturbations on the two-dimensional Mathieu problem.

6. THE PERTURBED MATHIEU PROBLEM IN TWO DIMENSIONS

The type of perturbative potential which is consistent with a general cubic two-dimensional structure is a sum of terms like $W_{m_1m_2}\exp(\pm 2im_1w_x\pm 2im_2w_y)$. In the general case where m_1 and m_2 are different from each other, there are four such terms, and four others with m_1 and m_2 interchanged, and the combination possessing cubic symmetry is a sum of these eight terms. Then by methods like those used in deriving Eqs. (41) and (42) we find for the nondiagonal matrix component of this perturbative potential the quantity

$$\begin{aligned}W_{m_1m_2}\{&\sum(k_x)v_{n_x}{}^*(g_{0x}+2k_x)[v_{n_x}{}'(g_{0x}+2k_x+2m_1)\\&+v_{n_x}{}'(g_{0x}+2k_x-2m_1)]\\&\times\sum(k_y)v_{n_y}{}^*(g_{0y}+2k_y)[v_{n_y}{}'(g_{0y}+2k_y+2m_2)\\&+v_{n_y}{}'(g_{0y}+2k_y-2m_2)]\\&+\sum(k_x)v_{n_x}{}^*(g_{0x}+2k_x)[v_{n_x}{}'(g_{0x}+2k_x+2m_2)\\&+v_{n_x}{}'(g_{0x}+2k_x-2m_2)]\\&\times\sum(k_y)v_{n_y}{}^*(g_{0y}+2k_y)[v_{n_y}{}'(g_{0y}+2k_y+2m_1)\\&+v_{n_y}{}'(g_{0y}+2k_y-2m_1)]\}.\end{aligned}\tag{50}$$

This is the component between an initial wave function characterized by the momentum eigenfunction $v_{n_x}(g_x)$ along the x direction, $v_{n_y}(g_y)$ along y, and a final wave function with momentum eigenfunctions $v_{n_x}{}'(g_x)$, $v_{n_y}{}'(g_y)$. In other words, this nondiagonal matrix component can be built up out of the nondiagonal matrix components of the one-dimensional problem, which we have already discussed in Sec. 4. Let us then use the results of that section to discuss the effects to be expected here.

The general result of Sec. 4, and in particular of Table III, was that the matrix components of the type given in Eq. (43), out of which the expression (50) is built up, are different from zero for the actual wave functions for all values of the m's, and for all g_0's except $g_0=0$ and ± 1, corresponding to the edges of the bands in the one-dimensional case. At these special points, the nondiagonal matrix component of energy between a state with an even momentum eigenfunction and one with an odd eigenfunction must be zero; no such situation holds between two states with even eigenfunctions, or two states with odd eigenfunctions. We can then conclude that the type of perturbation potential of the sort considered in Eq. (50), provided both m_1 and m_2 are different from zero, will produce nonvanishing, nondiagonal matrix components between any two unperturbed wave functions, except in some cases on the lines $g_{0x}=0$, ± 1, and $g_{0y}=0$, ± 1 in momentum space. In a real crystal of two-dimensional cubic symmetry we may expect all components of the type $W_{m_1m_2}$ to be different from zero; thus certainly there will be perturbations which will cause intersecting energy surfaces derived from the Mathieu problem, of the type discussed in Sec. 5, to interact with each other as discussed in that section. If they intersect along the 45° diagonals, as discussed there, they will interact everywhere except at the center of the central zone in momentum space, $g_{0x}=g_{0y}=0$, and at the corners of the central cell, $g_{0x}=\pm 1$, $g_{0y}=\pm 1$. At those points, in case the momentum eigenfunctions have suitable symmetry, the nondiagonal matrix component of energy is zero, and the two energy surfaces will not repel each other at these points. There will, of course, be diagonal matrix components of perturbative energy as well as nondiagonal components, just as in Sec. 5, and they can also be found from Eq. (50), by setting $n_x'=n_x$, $n_y'=n_y$. We note,

however, that if we are considering the interaction of two states which intersect along the 45° diagonal on account of symmetry, such as the states $n_x=1$, $n_y=0$, and $n_x=0$, $n_y=1$, the diagonal components of energy of these two states, as computed by Eq. (50), will be equal by symmetry at the points on the 45° diagonal. Thus neither the diagonal nor the nondiagonal matrix component of energy will cause these states to separate from each other at the points $g_{0x}=g_{0y}=0$ or $g_{0x}=\pm 1$, $g_{0y}=\pm 1$, so that the energy surfaces of the two-dimensional cubic problem will show a degeneracy at these special points in the momentum space. This is the sort of result concerning the adhering of energy surfaces at special points in the momentum space which can also be proved by group theory.[14]

The type of perturbation which we have just discussed, which is present in a real cubic field but is absent in a separable problem like the Mathieu problem, produces profound changes in the energy surfaces, wave functions, and Wannier functions. Let us take the p-like functions as an example, those with $n_x=1$, $n_y=0$ and $n_x=0$, $n_y=1$. For our illustration, we shall choose a fairly large interatomic distance so that the band is only slightly broadened and the wave functions are almost atomic. We have already shown the energy surfaces, in Fig. 16. Let us now show the energy by a different graphical method, plotting energy contours in a two-dimensional momentum space. Such a plot, for a relatively small value of nondiagonal perturbative energy, is shown in Fig. 18. Here (a) shows the lower band, (b) the upper band. The method of calculating the energy contours is very simple: we merely use cosine-type functions for expressing the diagonal and nondiagonal matrix components of energy for the unperturbed functions and solve the quadratic secular equation between the two unperturbed states. Specifically, we take the diagonal energies to be $a\cos\pi g_x - b\cos\pi g_y$ and $a\cos\pi g_y - b\cos\pi g_x$ for the $n_x=1$, $n_y=0$ and $n_x=0$, $n_y=1$ states, respectively, and take the nondiagonal component to be $c\sin\pi g_x \sin\pi g_y$, where a, b, c are constants; these are the simplest functional forms which depend in the right way on the momentum. The general result is that the energy of the lower band is approximately equal to that of one of the unperturbed wave functions in half the unit cell in momentum space, enclosed between the 45° diagonals, but is approximately equal to that of the other in the other half of the unit cell, changing rapidly from the one to the other near the 45° diagonal. As a result of this, the analytic expression for energy as a function of momentum takes on a complicated form, expressible in terms of square roots, near the 45° diagonal, and hence at the center and corners of the unit cell. There are singularities in the energy at these points, of such a nature that the energy cannot be expanded in power series in the momentum.

[14] Bouckaert, Smoluchowski, and Wigner, Phys. Rev. **50**, 58 (1936).

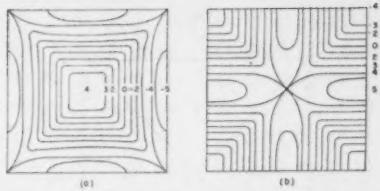

FIG. 18. Energy contours illustrating energy surfaces arising from p-like states, $n_x=1$, $n_y=0$, and $n_y=0$, $n_y=1$, for two-dimensional Mathieu problem. Energy contours are indicated in the unit cells in momentum space. Numbers on contours indicate energies, in arbitrary units, so that energy of 5 units is the highest in the composite energy band, −5 the lowest. Case (a), lower band; (b), upper band. These surfaces arise by letting a horizontal plane cut the surfaces of Fig. 16(a), modified by perturbations.

The maxima and minima of energy in the composite band, however, do not come at these points, but rather at the points $g_{0x}=0$, $g_{0y}=\pm 1$ and $g_{0x}=\pm 1$, $g_{0y}=0$; at these points the energy is a regular function of the momentum, though it is clear from Fig. 18 that it is a highly anisotropic function, varying much more strongly with g_y than with g_x, or vice versa. It is interesting that this rather complicated type of energy surface results from the very simplest case of overlapping energy bands which we can set up.

Now let us consider the momentum eigenfunctions and Wannier functions arising from these perturbed p-like states. We take first the case where the perturbation is nonvanishing, but of negligible magnitude. In Fig. 19 we show the unit cell in momentum space, divided into four regions, numbered 1, 2, 3, 4, by the diagonals. Then the wave function of the lowest band will be almost exactly that of the state $n_x=1$, $n_y=0$ through the regions 1 and 3 of the unit cell, and that of $n_x=0$, $n_y=1$ in regions 2 and 4. Closer examination shows that for the perturbed function to be continuous as we go across the diagonals, the wave function of the lowest band should actually be that of the state $n_x=1$, $n_y=0$ in region 1, but its negative in region 3; and similarly it should be that of $n_x=0$, $n_y=1$ in region 2, but its negative in region 4. We also find that to have the resulting Wannier function real, these values must be multiplied by i. In other words, the momentum eigenfunction is equal to that of the state $n_x=1$, $n_y=0$, multiplied by a function $f(g_x, g_y)$ which is i in region 1, 0 in region 2, $-i$ in region 3, 0 in region 4; plus that of the state $n_x=0$, $n_y=1$, multiplied by the same function $f(g_y, g_x)$. This function f can be expanded in Fourier series. It is easily shown that it is

$$f(g_x, g_y)=\sum(n, m)c_{nm}\exp[\pi i(ng_x+mg_y)], \quad (51)$$

where the quantities c_{nm} are given in Table VI.

In terms of this function, we can now set up the Wannier functions for the two bands. Let $v_0(g)$ be the momentum eigenfunction of the state $n=0$ of the one-dimensional problem, and $v_1(g)$ for the state $n=1$; $v_0(g)$ is a real even function of g, $v_1(g)$ an imaginary odd

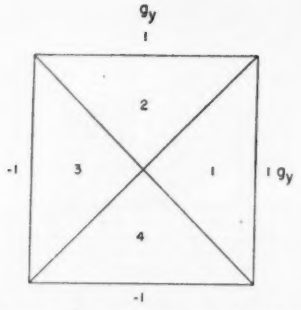

FIG. 19. Unit cell in momentum space, subdivided into regions 1, 2, 3, 4 in which momentum eigenfunction of p states has different behavior.

function. The one-dimensional Wannier function will be given in terms of the v's by Eq. (39), where we note that $a_0(w)$ will be a real even function of w, $a_1(w)$ a real odd function. Then if we set up the two-dimensional analog of Eq. (39) and determine the Wannier function of our lower p-band, we find that by methods like those used in deriving Eq. (48) it is

$$a(w_x, w_y)=\sum(n, m)[c_{nm}a_1(w_x+n\pi)a_0(w_y+m\pi) + c_{mn}a_0(w_x+n\pi)a_1(w_y+m\pi)], \quad (52)$$

while in a similar way for the upper band we have

$$a(w_x, w_y)=\sum(n, m)[c_{nm}a_0(w_x+n\pi)a_1(w_y+m\pi) - c_{mn}a_1(w_x+n\pi)a_0(w_y+m\pi)]. \quad (53)$$

We can now describe these results, both for the momentum eigenfunctions and the Wannier functions, in words. In the lower band, if we take the propagation vector in the central cell of momentum space, the wave function is made up largely of that type of p atomic function which points as closely as possible along the propagation vector, with its nodal plane as closely as possible perpendicular to that vector. In the upper band, we use the p function in each case which points as nearly as possible perpendicular to the propagation vector. The Wannier function, for the lower band, has no contribution at all on the atom for which it is being computed. It has contributions, however, on all atoms displaced from the central atom along the plus or minus x or y axes, or along the 45° diagonals. The contributions in each case fall off in magnitude inversely proportional to the distance from the central atom. For the atoms along the x direction, this contribution is like a Wannier function $a_1(w_x)a_0(w_y)$, a function with p_x-like symmetry; for those along the $-x$ direction, it is like $-a_1(w_x)a_0(w_y)$, the same thing but pointing the other way; along the y axis, it is like $a_1(w_y)a_0(w_x)$, a p_y-like function; and so on. Along the 45° diagonal, $w_x=w_y$, we have the combination $a_1(w_x)a_0(w_y)+a_0(w_x)a_1(w_y)$, which resembles a p-like function pointing along the same 45° direction; and so on. In other words, starting with original Wannier functions which have the symmetry properties of a vector, pointing along the x or y directions, we have constructed a function having a square symmetry, consisting of functions pointing out (or in) in a radial direction. We can indicate this schematically as in Fig. 20(a), where we represent a p-like Wannier function in a neighboring atom by a vector, pointing along the axis of the p-function. We indicate the amplitudes of the functions by the lengths of the vectors. We show in Fig. 20(a) the lower band, which we have described above, and in Fig. 20(b) the upper band.

As the strength of the perturbation is increased, and we approach the type of potential which we should find in a real cubic two-dimensional crystal, the situation just described changes quantitatively, but not qualitatively. The energy surfaces will still resemble those of Fig. 16 and Fig. 18, but more smoothed in the neighborhood of the 45° diagonals. The momentum eigenfunctions will still resemble the previous case qualitatively, but will simply change rapidly, rather than discontinuously, across the 45° diagonal. This will leave Wannier functions of the general type of Fig. 20, but falling off somewhat more rapidly as we go away from the central atom.

To set up these resulting Wannier functions, we may proceed along the lines already described. Our treatment is a little neater, however, if we prove an important general theorem about the Wannier functions of perturbed energy bands. Let us suppose that we have a set of unperturbed wave functions $u_{n,p}{}^0$, which for instance might be the functions determined from the unperturbed Mathieu problem. From these unperturbed wave functions we construct unperturbed Wannier functions $a_n{}^0(\mathbf{r}-\mathbf{Q}_i)$ by Eq. (21). Now we introduce a perturbation having the periodicity of the lattice; this might for instance be the perturbative potential having a nondiagonal matrix component like that given in Eq. (50). We assume that we solve the perturbation problem resulting from this potential and that the resulting wave functions $u_{n,p}$ are related to the unperturbed functions by the equations

$$u_{n,p}=\sum(m)s_{mn}(\mathbf{p})u_{m,p}{}^0, \quad (54)$$

where on account of the periodicity of the perturbing potential our sum involves only unperturbed wave

TABLE VI. $2\pi c_{mn}$, from Eq. (51).

m \ n	−4	−3	−2	−1	0	1	2	3	4
4	−1/4	0	0	0	0	0	0	0	1/4
3	0	−1/3	0	0	0	0	0	1/3	0
2	0	0	−1/2	0	0	0	1/2	0	0
1	0	0	0	−1	0	1	0	0	0
0	2/4	−2/3	2/2	−2	0	2	−2/2	2/3	−2/4
−1	0	0	0	−1	0	1	0	0	0
−2	0	0	−1/2	0	0	0	1/2	0	0
−3	0	−1/3	0	0	0	0	0	1/3	0
−4	−1/4	0	0	0	0	0	0	0	1/4

Note: The c_{mn}'s continue for greater n and m, in an obvious manner.

functions of the same p value. Now we wish to compute the perturbed Wannier functions. As a first step, we note that the s_{mn}'s are periodic functions of $\mathbf{p}$ in the reciprocal space, and hence can be expanded in the form

$$s_{mn}(\mathbf{p})=\sum(\mathbf{Q}_k)S_{mn}(\mathbf{Q}_k)\exp[(-2\pi i/h)(\mathbf{p}\cdot\mathbf{Q}_k)]. \quad (55)$$

When we insert (55) in (54), and use Eq. (21) to find the correct Wannier functions, we find at once

$$a_n(\mathbf{r}-\mathbf{Q}_j)=\sum(m,\mathbf{Q}_k)S_{mn}(\mathbf{Q}_k)a_m{}^0(\mathbf{r}-\mathbf{Q}_j-\mathbf{Q}_k). \quad (56)$$

This shows that the situation which we have encountered a number of times in the present work, by which the Wannier function of a perturbed problem is a sum of unperturbed Wannier functions located on different atoms, is a perfectly general situation; it also shows us directly how to find the coefficients of the expansion in series of unperturbed Wannier functions. The expansions (52) and (54) were special cases of this general theorem, though the notation was a little different. Unfortunately, in most actual cases the Fourier expansion (55) is too difficult to carry out analytically, as we were able to do in our special case in Table VI; but this does not diminish the validity of the general theorem (56), and the insight which it gives into the nature of the Wannier functions of overlapping bands.

The general nature of the problem of the d-like levels, and of the s-like band degenerate with them, as shown in Fig. 17, is not different in principle from the p bands which we have just considered. The interaction of the two states with $n_x=2$, $n_y=0$ and $n_x=0$, $n_y=2$ is very much like the problem of the p bands, except that symmetry no longer requires that the nondiagonal matrix component of a general cubic perturbation should vanish at the center and corners of the unit cell; it will be nonvanishing everywhere, so that the perturbed energy surfaces will not adhere to each other. Here in addition, however, as we pointed out in the preceding section, the band with $n_x=1$, $n_y=1$ overlaps these. We see from Eq. (50) that there will be nondiagonal matrix components of energy between these two states everywhere where they intersect each other, so that the perturbed energy surfaces will not intersect. The problem of the momentum eigenfunction and Wannier function are more difficult to handle here than in the earlier case, however, on account of the fact that the regions of momentum space where the different unperturbed wave functions are approximately correct are no longer bounded by lines as simple as the 45° diagonals. It would thus be a complicated procedure to find the Wannier functions; but the result would still be qualitatively much like that of Fig. 20, the Wannier function consisting of the Wannier functions of the unperturbed problems, suitably combined on atomic sites distributed at considerable distances from the place where the Wannier function is centered, with amplitudes falling off as we depart from that point. In all these cases, there is one general and interesting result to be noted: after we have applied the perturbations, the energy surfaces, momentum eigenfunctions, and Wannier functions all show a fourfold symmetry; rotation through 90° brings all these functions back to their original values. This is not true in general of the unperturbed solutions of the Mathieu problem.

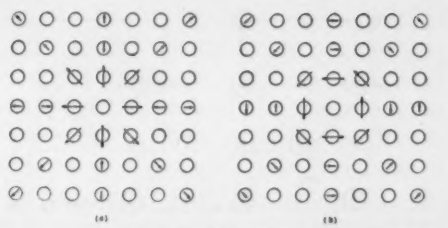

FIG. 20. Wannier function for lower (a) and upper (b) bands arising from degeneracy of two p states in two-dimensional Mathieu problem with small perturbations. The circles indicate atoms; the Wannier function is being computed for the central atom in each figure. They consist of p-like unperturbed Wannier functions on adjacent atoms, pointing in the direction of the arrows, and with amplitudes indicated schematically by the lengths of the arrows. There is no contribution in either case on the central atom itself.

There is another type of perturbative potential which is of interest in the two-dimensional case, in addition to those already considered. This is a term which would convert the problem from a two-dimensional analog to the simple cubic crystal, to the two-dimensional analog to the body-centered or face-centered cubic. In Fig. 21, we show the positions of the atoms in a two-dimensional square lattice. If we lowered the potential minima at the atoms surrounded by circles in Fig. 21, raised those not so surrounded, then the atoms of either type would form a two-dimensional face-centered structure, with twice the original lattice spacing in each direction. We can accomplish this by superposing a perturbative potential of the form made up by adding the four terms $W\exp(\pm iw_x\pm iw_y)$. This is a problem similar to the one-dimensional one considered in Sec. 4, where we took up the potential $W\cos w$. We shall not really achieve our face-centered structure unless the perturbative potential is great enough in magnitude so that it entirely splits the energy bands, as in Fig. 11(a), so that some bands consist of wave functions entirely concentrated around the atoms surrounded by circles in Fig. 21, other bands of wave functions concentrated around the remaining atoms, so that bands of either type can be considered as belonging to two interpenetrating face-centered lattices of different sorts of atoms. Let us consider what will happen to the energy surfaces, momentum eigenfunctions, and Wannier functions when such a perturbation is applied.

When we investigate the nondiagonal matrix components of energy arising from this perturbation, we find that we have such components between an original state characterized by values g_{0x}, g_{0y}, and states with $g_{0x}'=g_{0x}\pm1$, $g_{0y}'=g_{0y}\pm1$; the matrix component of this

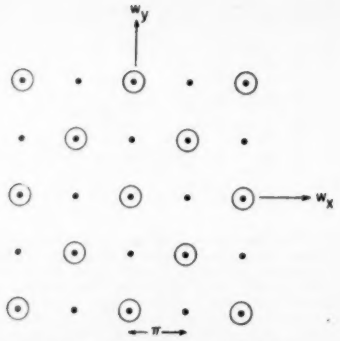

FIG. 21. Position of atoms in a two-dimensional square lattice, with modified potential lowering potential minima at those atoms indicated by circles, so that atoms of latter type lie on a two-dimensional analog to a face-centered cubic three-dimensional structure.

potential has the form

$$\sum(k_x)v_{n_x}^*(g_{0x}+2k_x)\times[v_{n_x}'(g_{0x}+2k_x+1)+v_{n_x}'(g_{0x}+2k_x-1)],$$

$$\sum(k_y)v_{n_y}^*(g_{0y}+2k_y)\times[v_{n_y}'(g_{0y}+2k_y+1)+v_{n_y}'(g_{0y}+2k_y-1)]. \quad (57)$$

We start by plotting the energy of the original simple cubic problem as a function of g_{0x}, g_{0y}. This energy is periodic, with a square unit cell which we may choose as extending from $g_{0x}=-1$ to 1, $g_{0y}=-1$ to 1. If we already have introduced the type of perturbation leading to a general simple cubic potential, as discussed earlier in this section, there will be a fourfold symmetry of energy in the square unit cell; it may be, for instance, that there will be an energy minimum at the center of the cell, maximum in the corners. Now let us repeat the same energy surface shifted along each axis by unit distance, so that the positions that were at the centers of the original unit cells will lie at the corners, and vice versa. Then we shall find that the two states represented by points vertically above each other on the two resulting sheets will have nondiagonal matrix components of energy between them, similar to the case of Fig. 10. As in that figure, the perturbations will have a maximum effect where the two energy surfaces intersect each other; and by symmetry, the intersection will occur along the diagonal lines drawn in Fig. 22(a). The nondiagonal matrix component of energy will be different from zero at each point of these lines, as we see from Eq. (57). Thus the two surfaces will split apart, resulting in an upper and lower sheet which nowhere touch each other. Furthermore, it is clear that the pattern found inside the shaded tilted square of Fig. 22(a) will repeat itself outside the square. This square, in other words, is a suitable unit cell in momentum space, for this perturbed problem; it is, in fact, precisely the central Brillouin zone, as defined in the usual way, for this face-centered lattice. If we ask what is the unit cell in coordinate space for which this is the unit cell in momentum space, we find the tilted square shown in Fig. 22(b), which is precisely the Wigner-Seitz cell for this problem. We note that this unit cell contains two of the original atoms per unit cell, one at the center, another at the corner (each of the four corners counts $\frac{1}{4}$ in this unit cell). The tilted unit cells of Fig. 22 are the natural ones to use for this problem, rather than those shown by dotted lines; the dotted unit cell in coordinate space, in Fig. 22(b), contains twice as many atoms as the Wigner-Seitz cell, that in Fig. 22(a) being correspondingly half as large as the Brillouin zone, and if we use them we run into complications regarding the momentum eigenfunction and Wannier function which do not correspond to any physical reality, but arise merely from using a unit cell twice as large as necessary.

We may now ask, following closely the model of Sec. 4, what is the effect of this perturbation on the momentum eigenfunction and the Wannier function. For a small perturbation, such as we should have if the two types of sites in Fig. 21 corresponded to only very slightly different potential wells, we must introduce the new unit cells in momentum space, corresponding to Fig. 22(a), but without making appreciable changes in the real wave functions. A given wave function will have a momentum eigenfunction which has a component in each of the square unit cells shown in Fig. 22(a); for instance, there may be a lattice of points consisting of g_0, as shown in Fig. 22(a), and corresponding points in each square unit cell. As in Sec. 4 and in Fig. 12, we may call the function made up by letting g_0 range through the square unit cell $v_0(g)$. But with our perturbed problem, we wish to use the shaded unit cell in Fig. 22(a) half as large as the original square one. We shall then have twice as many points in our momentum lattice as before; thus the point g_0' in Fig. 22(a) will correspond to g_0. But the real unperturbed wave function, which has a nonvanishing component $v_0(g_0)$, will have to be zero at the point g_0'. In other words, the $v(g)$ for this function, using our new unit cells, will equal $v_0(g)$ within the shaded part of the square unit cell in Fig. 22(a), but will be zero in the unshaded region. Thus its momentum eigenfunction will be $v_0(g)f_1(g)$, where $f_1(g)$ is unity in the shaded region of Fig. 22(a), zero in the unshaded region. Similarly for the upper band, the momentum eigenfunction will be $v_0(g)f_2(g)$, where $f_2(g)$ is zero where $f_1(g)$ is unity, and vice versa. We can now expand these functions $f_1(g)$ and $f_2(g)$ in Fourier series, as in Eqs. (46) and (47). We find that

$$f_1(g_x, g_y)=\sum(n, m)c_{nm}\exp[\pi i(ng_x+mg_y)],$$

where

$$c_{nm}=-\pi^{-2}[(-1)^n-(-1)^m]/(n^2-m^2) \quad \text{if} \quad n\neq m,$$
$$c_{nn}=0 \quad \text{if} \quad n\neq 0; \quad c_{00}=\tfrac{1}{2}. \quad (58)$$

For $f_2(g_x, g_y)$, the components are the negatives of the c_{nm}'s above, except c_{00}, which equals $\frac{1}{2}$. Thus when we set up the Wannier functions, corresponding to small perturbations, following the model of Eqs. (52) and (53), we find components in many cells of coordinate space, falling off slowly with the distance.

The case which we have considered is that of a vanishing perturbation. We have already noted, however, that we are interested in the case of a large perturbation; this is the case where the sites of the two sorts are entirely different, so that a wave function can be concentrated around sites of one type or the other. In such a case, as in Sec. 4, the correct wave function will consist approximately of the sums or differences of the two types of functions, and hence the Wannier functions will be the sum or difference of those indicated above. The sums correspond to the wave functions concentrated about the atoms at the centers of the tilted unit cells shown in Fig. 22(b), the differences to atoms at the corners of the cell. And now we see from Eq. (58) that the sums, but not the differences, of the Wannier functions are equivalent to Wannier functions of the unperturbed problem located at the origin. The differences, on the contrary, are distributed through many unit cells.

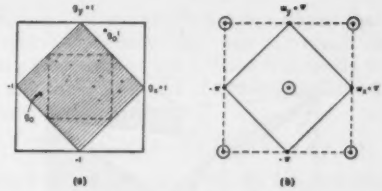

FIG. 22. Unit cells in momentum space (a) and coordinate space (b), for problem of square lattice perturbed to convert it to face-centered lattice. In (a), large square is original unit cell of unperturbed problem; shaded tilted square is central Brillouin zone for face-centered structure, corresponding to tilted square in (b), which is Wigner-Seitz cell; small square in (a) corresponds to large square in (b), square unit cell two atomic distances on a side.

7. THE THREE-DIMENSIONAL MATHIEU PROBLEM

The three-dimensional case resembles very strongly the two-dimensional one, which we have already treated in Secs. 5 and 6; for that reason our treatment of it will be very brief. The energy bands as functions of lattice spacing are very similar to those of Fig. 15. We can describe each energy band at large distances in terms of the quantum numbers of the spherically symmetrical field around a potential well, as in Table V. Thus the lowest level is an s-like level, with energy $\epsilon=3$. Next come three degenerate p-like levels, similar to the ordinary functions p_x, p_y, p_z, with $\epsilon=5$. Next, with $\epsilon=7$, there are six degenerate levels, coming from the quantum numbers n_x, n_y, n_z equal to the combinations (200), (020), (002), (011), (101), (110). From the first three, we can make linear combinations to form an s-like and two d-like functions, having symmetry like the functions $(x^2-y^2)f(r)$, and $(2z^2-x^2-y^2)f(r)$; the last three are d-like functions as they stand, with wave functions like $yzf(r)$, $zxf(r)$, $xyf(r)$. As the interatomic distance decreases, the crystalline field separates the latter three d states from the former two; but the degeneracy or hybridization between these two and the s-like state persists as long as we have the unperturbed Mathieu problem. As in the two-dimensional case, the really interesting problems arise from the degeneracies between the p and d bands, and the effect of perturbations on these degeneracies. The situation is so similar to that in the two-dimensional case that we can state the results in many cases in a qualitative form.

First, as in Sec. 6, let us consider those perturbations arising from a general simple cubic potential, but absent in the separable Mathieu problem. We consider first the p-like energy bands. We can no longer plot energy as a function of position in the unit cell of momentum space. We can, however, investigate the planes over which the energies of the unperturbed bands, formed from the functions of the type p_x, p_y, and p_z, will become equal to each other. Let us write things down analytically. We may let $\epsilon_0(g)$ be the energy of the one-dimensional problem for the first band, for $n=0$, as a function of g; $\epsilon_1(g)$ for the second band; and so on. Then the energy of the p_x function is $\epsilon_1(g_x)+\epsilon_0(g_y)+\epsilon_0(g_z)$; of the p_y, $\epsilon_0(g_x)+\epsilon_1(g_y)+\epsilon_0(g_z)$; and similarly for p_z. The function $\epsilon_0(g)$ has a minimum at $g=0$, maximum at $g=\pm 1$; $\epsilon_1(g)$ on the contrary has a maximum at $g=0$, minimum at $g=\pm 1$, and it varies much more with g than does $\epsilon_0(g)$. Clearly the energies of the p_x and p_y functions will be equal when $g_x=\pm g_y$ (the $\pm$ arising because the ϵ's are even functions of g), and so on. We then may subdivide the unit cube in momentum space (extending from $g_x=-1$ to 1, g_y from -1 to 1, etc.) by the planes $g_x=\pm g_y$, $g_y=\pm g_z$, $g_z=\pm g_x$. These planes are shown in Fig. 23. We may now examine the various segments of the cube, and ask which order the various energy surfaces lie in, in each segment. On a plane where two of the bands have the same energy, we may expect a general cubic perturbation to result in the bands separating from each other.

There are 24 equivalent prisms making up the cube, four extending out to each of the six faces of the cube. Let us consider the prism indicated by heavy lines in Fig. 23, bounded by the plane $g_x=1$, the planes $g_y=\pm g_z$, and the plane $g_x=g_y$, with $|g_x|>|g_y|>|g_z|$. Within this prism, the energy $\epsilon_1(g_x)+\epsilon_0(g_y)+\epsilon_0(g_z)$ will everywhere lie lowest; that $\epsilon_0(g_x)+\epsilon_1(g_y)+\epsilon_0(g_z)$ will be next; and $\epsilon_0(g_x)+\epsilon_0(g_y)+\epsilon_1(g_z)$ will lie highest. In Fig. 24(a), we show the way the lowest energy surfaces fit together in the various prisms, on the assumption that we have introduced slight perturbations of the cubic variety, to make the problem nondegenerate. For the lowest level, in other words, we have roughly cubical energy surfaces, rounded on the edges, and slightly concave. The

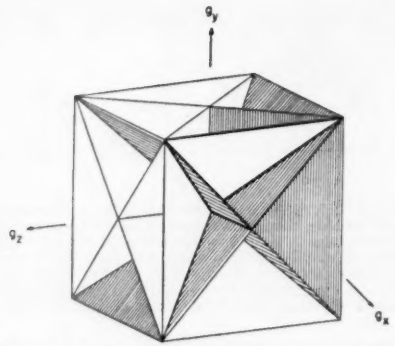

FIG. 23. Unit cube in momentum space, with planes $g_x = \pm g_y$, $g_y = \pm g_z$, $g_z = \pm g_x$, on which the various p-like wave functions are degenerate with each other in the three-dimensional Mathieu problem.

highest energy corresponds to the energy surface at the center of the cell, the lowest to the surface about the boundary. In Fig. 24(b) we show similarly the form of the energy surface for the middle energy band, and in Fig. 24(c) for the highest band; in each case the lowest energies correspond to the surfaces nearest the boundaries or corners of the cube, the highest to those nearest the center. The resemblance of these figures to the two-dimensional case of Fig. 18 is obvious. Here again, as in the two-dimensional case, we can show that the three sheets of the energy surface adhere at the center and the corners of the cube forming the unit cell in momentum space.

For the d-like states, with the s state degenerate with them, the problem as in the two-dimensional case is much more complicated. The three unperturbed states corresponding to n_x, n_y, n_z equal to (200), (020), (002), respectively, will have three surfaces which will intersect with each other, very much like the three p states, which we have discussed in Figs. 23 and 24, resulting in similar perturbed energy surfaces. Similarly the three states (011), (101), (110) will have a similar perturbation problem, with similar energy surfaces. But now we must consider the perturbations between these two sets of energy surfaces. The one set will be separated from the other by the effect of the crystalline field, and for large interatomic distance, the two sets of energy bands will not overlap. As the distance decreases, however, they will cut, and obviously the intersections of the surfaces will not be given by any simple considerations. As in the two-dimensional case, a general cubic perturbative potential will separate the surfaces at these intersections, so that the final perturbed surfaces will not cut each other, but the resulting forms will be very complicated.

We can next, as in two dimensions, introduce further perturbations designed to convert the problem from simple cubic to face-centered or body-centered cubic. The method of handling it is essentially just as in two dimensions. We set up a perturbative potential of the proper sort to depress those cubic lattice points forming the face-centered or body-centered cubic structure with respect to the remaining lattice points. We then find that we can carry out a construction, as in the one- and two-dimensional cases, by which we superpose energy surfaces with suitable displacements of ± 1 along g_x, g_y, and g_z, such that there are perturbations between the different sheets of the energy surface at the same points of momentum space. These perturbations will cause the energy surfaces to be pushed away from each other in the neighborhood of the intersections of these energy surfaces. But now we find that the planes on which the surfaces intersect, by symmetry, are precisely those planes bounding the central Brillouin zone for the appropriate type of structure. Thus we arrive at these Brillouin zones from the perturbation of the Mathieu problem, rather than by perturbation of a plane wave solution as is ordinarily done. Within the central Brillouin zone, the energy surfaces of the three p states, or of the six $d-s$ states, will not be unlike their values in the corresponding part of the unit cell of the simple cubic momentum space; but the energy will always have a vanishing normal derivative at the surface of the Brillouin zone.

As in one and two dimensions, we can also set up momentum eigenfunctions and Wannier functions for these more complicated three-dimensional cases; and as before, we shall find Wannier functions which generally are rather broadly extending out from one atom to another. Also as in two dimensions, the final Wannier functions will generally show the rotational symmetry of the lattice, as well the energy bands. It does not seem worth while, at present, to go more in detail into the nature of these functions. By the time we have introduced all the various perturbations which we have considered, we have departed so widely from the original Mathieu case that we really have a new problem, which could appropriately be considered separately, in a study of the actual behavior of the energy bands, momentum eigenfunctions, and Wannier functions of p and d bands in real crystals. It is hoped that this discussion of the Mathieu case, however, will be useful in pointing the way toward this more complicated future investigation.

APPENDIX 1

Let $a(w)$ be the original Wannier function of the unperturbed band. We have found that for the per-

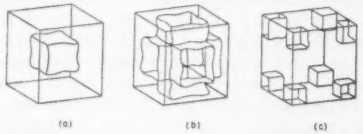

FIG. 24. Surfaces of constant energy, in momentum space, for (a) lowest band, (b) middle band, (c) highest band, resulting from removal of degeneracy between the overlapping p bands, in the three-dimensional Mathieu problem.

turbed upper half-band the Wannier function located at the atom at position $2n\pi$ may be written

$$a'(w-2n\pi)=(2/\pi)[a(w-2n\pi-\pi)+a(w-2n\pi+\pi)] -(2/3\pi)[a(w-2n\pi-3\pi)+a(w-2n\pi+3\pi)]\cdots.$$

We now wish to consider the sum $\sum(n)\exp(2\pi ing)\times a'(w-2n\pi)$, found by locating these Wannier functions on the atoms at positions $2n\pi$. When we insert $a'(w-2n\pi)$, as defined above, in this sum, we may rearrange the resulting double sum, so that it may be written

$$\sum(n)\exp[2\pi i(n+\tfrac{1}{2})g]a[w-2(n+\tfrac{1}{2})\pi] \times[(2/\pi)(\exp\pi ig+\exp-\pi ig) -(2/3\pi)(\exp 3\pi ig+\exp-3\pi ig)\cdots].$$

From Eqs. (46) and (47), however, we know that the function $(2/\pi)(\exp\pi ig+\exp-\pi ig)\cdots$ equals unity when g is between $-\frac{1}{2}$ and $\frac{1}{2}$, which includes the whole first unit cell of our lattice of double periodicity. Thus the wave function is

$$\sum(n)\exp[2\pi i(n+\tfrac{1}{2})g]a[w-2(n+\tfrac{1}{2})\pi],$$

just as if we had the original Wannier functions located at the points $\pm\pi$, $\pm 3\pi$, etc. Thus we verify the statement made in the text and show a simple example of a case where the identical wave functions can be expressed in terms of two types of Wannier functions, one, $a[w-2(n+\frac{1}{2})\pi]$, concentrated on a given atom, the other, $a'(w-2n\pi)$, extended over many atoms.

PHYSICAL REVIEW VOLUME 87, NUMBER 5 SEPTEMBER 1, 1952

Statistics of the Recombinations of Holes and Electrons

W. SHOCKLEY AND W. T. READ, JR.
Bell Telephone Laboratories, Murray Hill, New Jersey

(Received April 29, 1952)

The statistics of the recombination of holes and electrons in semiconductors is analyzed on the basis of a model in which the recombination occurs through the mechanism of trapping. A trap is assumed to have an energy level in the energy gap so that its charge may have either of two values differing by one electronic charge. The dependence of lifetime of injected carriers upon initial conductivity and upon injected carrier density is discussed.

SECTION 1. INTRODUCTION

IN connection with studies of transistor physics, the recombination of holes and electrons plays an important role. The lifetime of injected carriers in germanium has been found to be a structure sensitive property of the material. This suggests that the recombination process takes place through the medium of imperfections of some sort in the germanium crystal.[1] It is the purpose of this paper to investigate the mathematical consequences of a particular type of imperfection. We shall accordingly suppose that the crystal contains a density N_t of traps which contribute to the recombination process.

In Fig. 1 we illustrate the way in which holes and electrons may be recombined through the traps. The figure illustrates a trap which may exist in either of two states differing by one electronic unit of charge, being either negative or neutral; similar treatments may be applied to other possibilities, such as neutral or positive, or cases in which the charge changes between -1 and -2 units. If the trap is neutral it may capture an electron from the conduction band. The energy loss of the electron is then converted into heat or light or both depending upon the nature of the trapping process. It may also capture an electron from the valence band represented by part (d) of the figure, in which case it acquires a negative charge and leaves a hole in the valence band. Parts (b) and (c) represent the emission of an electron and the capture of a hole.

The effects which we shall consider in this study arise from the statistics of the processes shown in Fig. 1, and the limitation in rate is assumed to be due to the availability of electrons and holes to enter the traps. We shall neglect another possible limiting factor in the recombination process, the time of readjustment of the electron in the trap once it is trapped: Thus, the electron in part (a) of the figure might be trapped in an excited state in the trap and require some time before falling to the ground state. While the electron was in the excited state, the ability of the trap to emit an electron or to capture a hole would be different from the conditions represented in part (b) and (c) of the figure and there would, therefore, be a time lag before the trap reached its normal state. We shall assume that the readjustment time for a trapped electron is negligible compared to time required on the average for the trap to emit the electron or to capture a hole.

[1] See W. Shockley, *Electrons and Holes in Semiconductors* (D. van Nostrand Company, Inc., New York, 1950), p. 347. The methods of measuring lifetime and its role in transistor electronics are also discussed in this reference. This process of recombination has also been discussed by R. N. Hall, Phys. Rev. **83**, 228 (1951) and **87**, 387 (1952).

SECTION 2. THE BASIC FORMULATION FOR THE PROBLEM

In Table I we define most of the symbols used in the analysis.

Since the processes involved are governed by Fermi-Dirac statistics, we introduce the symbol f to represent the probability that a quantum state be occupied. f is a function of the energy level E of the quantum state and of the Fermi level F:

$$f=1/[1+\exp\{(E-F)/kT\}]. \tag{2.1}$$

We also introduce the symbol f_p to represent the probability that the state is empty or, in other words, occupied by a hole. (We use the symbol p for holes to be consistent with the notation for p-type semiconductors in which the carriers are positive; we similarly use the symbol n for electrons to be consistent with n-type.) The relation between f_p and f is

$$f_p=1-f=f\exp[(E-F)/kT]. \tag{2.2}$$

We shall first consider the electron capture process. The probability of electron capture will be dependent upon the initial quantum state of the electron. If we consider a unit volume of material, there will be a total number

$$N(E)dE \tag{2.3}$$

of quantum states in the energy range dE. We shall denote by $c_n(E)$ the average probability per unit time that an electron in the range dE be captured by an empty trap. If the speed of the electron is v and the cross section for capture by a trap is A, then we have

$$c_n(E)=\text{average of } vA \text{ for states of energy } E. \tag{2.4}$$

If the number of trapping centers per unit volume is N_t, then the rate of capture will evidently be

$$f_{pt}N_tc_n(E)f(E)N(E)dE, \tag{2.5}$$

where f_{pt} represents the probability that a trap is empty and thus capable of capturing an electron. $f(E)$ is the fraction of states of energy E that are occupied by electrons.

The probability that an electron be emitted from the trap into the band of energies in range dE will be proportional to the number of electrons in the traps times the probability that the states in range dE are empty. It can, therefore, be represented by the equation

$$f_tN_te_nf_p(E)N(E)dE, \tag{2.6}$$

where e_n is the emission constant corresponding to c_n.

We shall next make the assumption that the electrons in the conduction band are in thermal equilibrium among themselves. That is, we shall assume that the factors f and f_p are given by a Fermi-Dirac function of the form (2.1) or (2.2) with a suitable value of the Fermi level. This quasi-Fermi level,* or q.f.l., is denoted by F_n. The fraction of the traps which are occupied may also be described by a q.f.l. F_t for the traps. If the system is in thermal equilibrium then, of course, the relationship,

$$F_n=F_t \text{ for thermal equilibrium}, \tag{2.7}$$

must apply. For this case the principle of detail balancing requires that the rate of capture and the rate of emission of electrons must be equal. We shall next apply this consideration to determine the relationship between e_n and c_n.

The net rate of capture (i.e., capture minus emission) for the energy interval dE may be written in the form

$$dU_{en}=[f_{pt}f(E)-(e_n/c_n)f_tf_p(E)]N_tc_n(E)N(E)dE. \tag{2.8}$$

For thermal equilibrium the quantity in the square brackets must be zero and this leads to the result

$$e_n/c_n=\exp[(E_t-E)/kT]. \tag{2.9}$$

Inserting (2.9) in (2.8) we find that the square bracket depends only on F_n and F_t. The total rate of electron capture U_{en} is then obtained by integrating over dE:

$$U_{en}=[1-\exp\{(F_t-F_n)/kT\}]f_{pt}N_t \times\int_{E_c}^{\infty}f(E)N(E)c_n(E)dE, \tag{2.10}$$

where the integration extends from the bottom of the conduction band to all higher levels. When the system is in equilibrium the square bracket vanishes. On the other hand, if F_n is greater than F_t, then there is a higher density of electrons in the conduction band than is in keeping with the state of the traps and the exponential term is less than unity so that there is a net rate of capture.

An entirely similar expression may be derived for U_{ep}, the net rate of hole capture.

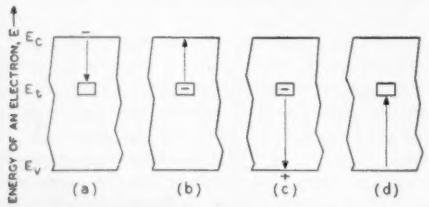

FIG. 1. The basic processes involved in recombination by trapping: (a) electron capture, (b) electron emission, (c) hole capture, (d) hole emission.

SECTION 3. APPLICATION TO THE CASE OF NONDEGENERATE SEMICONDUCTORS

We shall now adapt the expressions discussed above to the case of a semiconductor in which the electron and hole distributions are nondegenerate. For this case expression (2.10) derived in the preceding section may

* The quasi-Fermi level has been referred to as the chemical potential and as the "imref."

be rewritten in the form

$$U_{cn}=[1-\exp(F_t-F_n)/kT]f_{pt}nC_n, \quad (3.1)$$

where the new symbols are defined by the equations

$$n=N_c\exp(F_n-E_c)/kT, \quad (3.2)$$

$$N_c=\int_{E_c}^{\infty}[\exp(E_c-E)/kT]N(E)dE, \quad (3.3)$$

$$C_n=N_t\langle c_n\rangle, \quad (3.4)$$

$$\langle c_n\rangle=\int_{E_c}^{\infty}[\exp(E_c-E)/kT]c_n(E)N(E)dE\div N_c. \quad (3.5)$$

The quantity $\langle c_n\rangle$ is the average value of c_n over the states in the conduction band. It has the dimensions of cm^3/sec as may be seen from (2.4) and from the definition of $c_n(E)$. Due to the motion of the electrons in respect to the center, the center in effect sweeps out a volume $\langle c_n\rangle$ of space in unit time. Since N_t has the dimensions cm^{-3}, $C_n=N_t\langle c_n\rangle$ has the dimensions of sec^{-1}; it represents the fraction of space swept out per unit time. Thus C_n is simply the probability per unit time than an electron in the conduction band will be captured for the case in which the traps are all empty and, consequently, in a position to capture electrons. By a similar procedure, averaging over the valence band, we may define C_p, the probability per unit time that a hole will be captured if the traps are filled with electrons so that they are in a condition to capture holes.

For the case of nondegenerate statistics f_p is nearly unity for the states in the conduction band, and consequently the rate of emission (given in (2.6) before integration over dE) is a function of f_t alone. That the rate of emission is independent of F_n follows in (3.1) from the fact that the dependences upon F_n in the exponential and in n itself cancel. Thus, we find that

$$f_{pt}n\exp(F_t-F_n)/kT=f_tN_c\exp(E_t-E_c)/kT\equiv f_tn_1, \quad (3.6)$$

where

$$n_1=N_c\exp(E_t-E_c)/kT \quad (3.7)$$

is the number of electrons in the conduction band for the case in which the Fermi level falls at E_t.

Expressing the net rate of capture in terms of n_1, we obtain

$$U_{cn}=C_nf_{pt}n-C_nf_tn_1. \quad (3.8)$$

An entirely similar treatment may be carried out for holes leading to the equation

$$U_{cp}=C_pf_tp-C_pf_{pt}p_1. \quad (3.9)$$

SECTION 4. RATE OF RECOMBINATION FOR STEADY-STATE CONDITIONS

In this section we shall evaluate the rate of recombination for nonequilibrium conditions. We shall suppose that hole-electron pairs are being generated at a constant rate U by light or by some form of carrier injection. For steady-state conditions, the net rate of capture of electrons must be equal to that of holes. If the concentrations of holes and electrons are n and p, then the equality of rates leads to

$$C_n(1-f_t)n-C_nf_tn_1=C_pf_tp-C_p(1-f_t)p_1. \quad (4.1)$$

This equation may be solved for f_t, thus obtaining

$$f_t=(C_nn+C_pp_1)/[C_n(n+n_1)+C_p(p+p_1)], \quad (4.2)$$

and for f_{pt},

$$f_{pt}=1-f_t=(C_nn_1+C_pp)/[C_n(n+n_1)+C_p(p+p_1)]. \quad (4.3)$$

When these values are substituted into the rate expressions, the net rate of recombination is obtained:

$$U=C_nC_p(pn-p_1n_1)/[C_n(n+n_1)+C_p(p+p_1)]. \quad (4.4)$$

In this equation the product p_1n_1 is independent of the energy level E_t of the traps and has the value

$$p_1n_1=N_cN_p\exp(E_v-E_c)/kT=N_cN_p\exp(-E_G/kT)=n_i^2, \quad (4.5)$$

where n_i is the electron or hole concentration in an intrinsic sample, in which n and p are equal. For later use we shall introduce also an energy level corresponding to an intrinsic sample. This energy E_i is the energy at which the Fermi level would lie in an intrinsic sample. Its value is

$$E_i=\tfrac{1}{2}(E_c-E_v)+\tfrac{1}{2}kT\ln(N_v/N_c). \quad (4.6)$$

In the subsequent development we shall assume that

$$E_t>E_i, \quad (4.7)$$

so that

$$n_1>n_i>p_1. \quad (4.8)$$

The case of $E_t<E_i$ can be understood by reversing the roles of holes and electrons.

TABLE I. Symbols.

b	= ratio of electron to hole mobility
n	= density of electrons in conduction band
p	= density of holes in valence band
E_v	= energy of highest valence band level
E_c	= energy of lowest conduction band level
E_G	= energy gap $=E_c-E_v$
E_t	= effective energy level of traps (Appendix B)
F	= Fermi level for thermal equilibrium
F_n	= quasi-Fermi level (q.f.l.) for electrons
F_p	= q.f.l. for holes
F_t	= q.f.l. for traps
n_i	= density of electrons in an intrinsic specimen
N_t	= density of traps
$N(E)$	= density of energy levels per unit energy range
N_c	= effective density of levels for conduction band
N_v	= effective density of levels for valence band
f_t	= fraction of traps occupied by electrons
f_{pt}	= fraction of traps occupied by holes

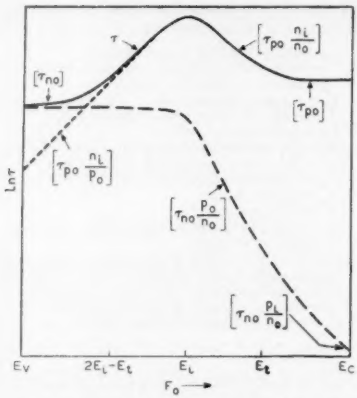

FIG. 2. Dependence of lifetime upon composition of the specimen. (The composition determines F_0, the Fermi level for equilibrium.) The solid curve gives total lifetime τ; the dashed curves give the two terms of which τ is the sum. The expressions in [ ] are approximations valid for the straight segments of the curves.

SECTION 5. EVALUATION OF THE LIFETIME FOR A SIMPLE CASE

In this section we shall consider how the lifetime of carriers depends upon the conductivity of a sample containing a fixed number of traps. We shall deal with the case of low disturbances in carrier density. In the next section we shall consider an extension of the reasoning to large disturbances in carrier densities. As a further simplification, we shall assume, in this section, that the majority carrier density under equilibrium conditions is large compared to the trap density so that we may neglect the change in charge density produced by changing concentrations in the traps. This condition is relaxed and a more general treatment carried out in the appendix. It is shown there that the simplified analysis of the present section is valid if any one of the four quantities n_0, p_0, n_1, p_1 is large compared to N_t. In this section, the deviations of electron and hole densities from their thermal equilibrium values, denoted by n_0 and p_0, must be equal so as to preserve electrical neutrality. If we let δn represent this deviation, then

$$n=n_0+\delta n, \quad p=p_0+\delta n. \tag{5.1}$$

In terms of this deviation and the corresponding rate of recombination U, we may define a lifetime τ by the equation

$$\tau \equiv \delta n/U. \tag{5.2}$$

From Eq. (4.4) we find that τ is given by

$$\begin{aligned}\tau&=(n_0+n_1+\delta n)/(n_0+p_0+\delta n)C_p\\&\quad+(p_0+p_1+\delta n)/(n_0+p_0+\delta n)C_n\\&=\tau_{p0}(n_0+n_1+\delta n)/(n_0+p_0+\delta n)\\&\quad+\tau_{n0}(p_0+p_1+\delta p)/(n_0+p_0+\delta n),\end{aligned} \tag{5.3}$$

where

$$\tau_{p0}\equiv 1/C_p, \quad \tau_{n0}\equiv 1/C_n. \tag{5.4}$$

The quantity τ_{p0} is the lifetime for holes injected into highly n-type specimens. For such specimens, the traps are filled so that the rate at which injected holes are captured and annihilated is simply C_p times the injected carrier density. The quantity τ_{n0} is similarly the lifetime of electrons in a highly p-type sample.

In the next section we shall consider the dependence of τ upon δn for large values of δn. For small values for δn the value of τ is simply

$$\tau=\tau_{p0}(n_0+n_1)/(n_0+p_0)+\tau_{n0}(p_0+p_1)/(n_0+p_0). \tag{5.5}$$

If it is assumed that the capture constants C_n and C_p are relatively insensitive to temperature, then the temperature dependence of τ can be predicted from the relatively simple dependencies of n_1, p_1, n_0, and p_0 upon temperature. Some observations by F. S. Goucher[2] and R. N. Hall[3] appear to be, in general, consistent with these predictions.

In Fig. 2 we represent in a qualitative fashion the dependence of τ upon the composition of the specimen.[4] The two terms in (5.5) of which τ is the sum are also plotted separately on the figure. The composition is represented by F_0 the Fermi level for thermal equilibrium conditions. Nondegenerate specimens correspond to values F_0 lying in the energy gap between E_v and E_c and an intrinsic sample corresponds to $F_0=E_i$. From the plot it is seen that there are four distinct regions to be considered for F_0. The behavior of τ in these regions may be understood by considering the following special cases.

In an n-type sample, where $F_0>E_i$, $n_0\gg p_0$, we have in accordance with approximation (4.8)

$$\begin{aligned}\tau&\doteq\tau_{p0}(1+n_1/n_0)\\&=\tau_{p0}[1+\exp(E_t-F_0)/kT],\end{aligned} \tag{5.6}$$

with a similar relation,

$$\begin{aligned}\tau&=\tau_{n0}+\tau_{p0}n_1/p_0\\&=\tau_{n0}+\tau_{p0}\exp(E_t+F_0-2E_i)/kT,\end{aligned} \tag{5.7}$$

for a p-type sample, $F_0<E_i$, $p_0\gg n_0$.

From (5.6) and (5.7) we see that, as F_0 increases from E_v to E_c, we can distinguish the four regions as follows:

(1) In a sufficiently strongly p-type that $F_0<2E_i-E_t$, $p_0\ll n_1$, τ is constant and equal to τ_{n0}. This corresponds to all the traps being empty and the number of holes being large enough that a hole will immediately recombine with every trapped electron.

(2) If the sample is somewhat less strongly p-type so

[2] Personal communication.
[3] R. N. Hall, personal communication.
[4] Data which is, in general, consistent with the trends indicated in Fig. 2 have been reported by R. N. Hall, Phys. Rev. **86**, 600T (1952) and **87**, 387 (1952).

that $F_0 > 2E_i - E_t$, $n_1 \gg p_0$, then τ increases with F_0

$$\tau = \tau_{p0} n_1/p_0 = \tau_{p0} \exp(F_0 - 2E_i + E_t)/kT. \quad (5.8)$$

In this case the traps are still mostly empty but there are not a sufficient number of holes to recombine with each trapped electron before the latter is re-emitted to the conduction band.

(3) In an n-type sample where $F_0 < E_t$, $n_0 \ll n_1$, τ decreases with F_0

$$\tau = \tau_{p0} n_1/n_0 = \tau_{p0} \exp(E_t - F_0)/kT. \quad (5.9)$$

Here the traps are still largely empty and the recombination is limited by the fact that an empty trap cannot capture a hole.

(4) Finally, in a sample sufficiently strongly n-type that $F_0 > E_t$, $n_0 \gg n_1$, the lifetime is again constant, now equal to τ_{p0}. This corresponds to full traps, all set to capture holes, and sufficient electrons that an electron recombines at once with every hole that is trapped.

It is interesting to note that if $\tau_{n0} = \tau_{p0}$, then τ is symmetrical in $F_0 - E_i$ so that the same behavior would arise for traps with energies lying at $E_t - E_i$ below E_i as for those lying at $E_t - E_i$ above E_i. This symmetry follows at once from (5.3) and thus applies to large as well as to small densities.

The exact position and value of the maximum value τ_m of τ will depend on the ratio τ_{n0}/τ_{p0}. Unless this differs by an order of magnitude from unity, the maximum will occur near intrinsic. For the case $\tau_{p0} = \tau_{n0}$, the maximum is seen from (5.5) to correspond to $F_0 = E_i$ so that

$$\begin{aligned} \tau_m &= \tau_{p0}[1 + (n_1 + p_1)/2n_i] \\ &= \tau_{p0}[1 + \cosh(E_t - E_i)/kT]. \end{aligned} \quad (5.10)$$

Thus the magnitude of the total possible variation of τ with composition is determined by the absolute difference in the energy level of the traps and the Fermi level for an intrinsic sample. For $E_t = E_i$, τ could vary by a factor of only 2.

SECTION 6. THE DEPENDENCE OF LIFETIME UPON CARRIER DENSITY

For large values of injected carrier densities, it is necessary to retain the δn terms of Eq. (5.3). If we denote by τ_0 the lifetime for vanishingly small values of δn as given by Eq. (5.5), then the value of τ for larger values of δn becomes

$$\begin{aligned} \tau = \tau_0\{1 + \delta n(\tau_{p0} + \tau_{n0})/[\tau_{p0}(n_0 + n_1) + \tau_{n0}(p_0 + p_1)]\} \\ \div \{1 + \delta n/(n_0 + p_0)\}. \end{aligned} \quad (6.1)$$

This expression is of the form

$$\tau = \tau_0(1 + a\delta n)/(1 + c\delta n), \quad (6.2)$$

from which it is seen that τ increases monotonically with δn if $a > c$ and decreases monotonically for $a < c$.

The limiting value for τ as δn approaches infinity is

$$\tau_\infty = \tau_{p0} + \tau_{n0}. \quad (6.3)$$

It is evident that if τ_0 is different from τ_∞, then there is a monotonic variation of τ from one to the other with increasing δn.

The variation δn can be deduced from the change in conductivity $\delta\sigma$ so that a comparison with experiment may be made in a relatively straight forward way. Thus for an n-type sample we have

$$\delta n/(n_0 + p_0) \doteq \delta n/n_0 \doteq \delta\sigma b/\sigma_0(1 + b), \quad (6.4)$$

where σ_0 is the equilibrium conductivity and b is the ratio of electron mobility to hole mobility. From Eq. (6.1) we then obtain

$$\begin{aligned} &\tau[1 + \delta\sigma b/\sigma_0(1 + b)]/\tau_0 \\ &= 1 + \delta n(\tau_{p0} + \tau_{n0})/[\tau_{p0}(n_0 + n_1) + \tau_{n0}(p_0 + p_1)]. \end{aligned} \quad (6.5)$$

For a strongly n-type sample, so that n_0 dominates the denominator in (6.5), the right side becomes approximately

$$1 + \delta\sigma b(\tau_{p0} + \tau_{n0})/\tau_{p0}\sigma_0(1 + b). \quad (6.6)$$

This relationship shows that if the left side of (6.5), which involves directly measurable quantities, is plotted as a function of $\delta\sigma$, the result should be a straight line. (It should be noted that if a number of different types of trapping centers are involved, the linear relationship between the left side of (6.5) and $\delta\sigma/\sigma_0$ will in general be modified.)

It should be noted that at high carrier densities the rate of recombination through traps is linear in the carrier density whereas any direct recombination would be quadratic. This is in agreement with the findings of R. N. Hall[8] for p-n junctions operating with high injected densities in the region of recombination.

SECTION 7. INTERPRETATION IN TERMS OF CAPTURE RESISTANCES

The behavior of the lifetime as a function of composition shown in Fig. 2 may be given a somewhat more physical interpretation with the aid of the concept of "recombination resistances." For this purpose we note that the quasi-Fermi levels are analogous to voltages and the U's to currents. We thus introduce

$$R_n = (F_n - F_t)/U_{cn} \doteq kT/f_p n_0 C_n, \quad (7.1)$$

$$R_p = (F_t - F_p)/U_{cp} \doteq kT/f_t p_0 C_p, \quad (7.2)$$

the approximations holding for differences in the F's small compared to kT. For the steady state the recombination currents are equal and we have

$$U(R_n + R_p) = (F_n - F_t) + (F_t - F_p) = F_n - F_p, \quad (7.3)$$

an equation analogous to that for resistances in series.

In Fig. 3, we plot R_n and R_p as functions of F_0. Evidently the recombination rate will be limited by the larger of the two. The sloping lines have a slope of $(1/kT)$. It is seen that if τ_{n0} and τ_{p0} are approximately

[8] R. N. Hall, Phys. Rev. **83**, 228 (1951).

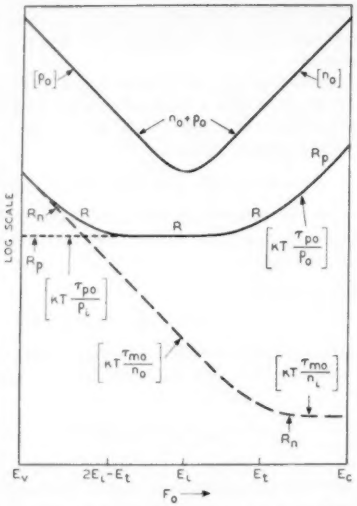

FIG. 3. Variation of recombination resistances with F_0. Solid curve represents total resistance $R=R_p+R_n$; dashed curves give R_p and R_n. Expressions in [ ] are approximations valid for the straight segments of the curves.

equal, recombination is limited by hole trapping for all specimens except those with $p_0>n_1$.

The sloping portions of the $\ln R$ *vs* F_0 plot correspond to constant lifetime. This result may be seen from the relationship between R and τ which is derived as follows:

$$\tau=\delta n/U=\delta nR/(F_n-F_p), \tag{7.4}$$

and

$$\delta(np)=n_i^2\{[\exp(F_n-F_p)/kT]-1\} \doteq n_i^2(F_n-F_p)/kT\doteq(n_0+p_0)\delta n, \tag{7.5}$$

so that

$$\tau=n_i^2R/kT(n_0+p_0). \tag{7.6}$$

On Fig. 3 we have also drawn $\ln(n_0+p_0)$; the straight line portions have slopes of $(1/kT)$, so that they cancel the slopes of $\ln R$ to give the constant lifetime portions of Fig. 2.

The effect of a number of different sorts of traps may be considered on the same basis. For each variety, the recombination is represented by a pair of resistances in series and these series pairs are combined in parallel for the entire system.

SECTION 8. RATE OF GENERATION IN SPACE-CHARGE REGIONS

If the minority carriers are swept out of an n-type specimen, so that

$$\delta n=-p_0 \quad \text{and} \quad p=0, \tag{8.1}$$

then from Eq. (4.4) the net rate of generation is

$$-U=C_nC_pn_i^2/[C_n(n_0+n_1-p_0)+C_pp_1], \tag{8.2}$$

corresponding to a lifetime of

$$\tau=\delta n/U=-p_0/U =\tau_{p0}(n_0+n_1-p_0)/n_0+\tau_{n0}p_1/n_0, \tag{8.3}$$

a result in agreement with (5.3). If the specimen is strongly n-type, p_0 and p_1 will be $\ll n_0$, and τ will be approximately

$$\tau_0\doteq\tau_{p0}(n_0+n_1)/n_0, \tag{8.4}$$

the value for very small disturbances. Hence the net rate of generation of minority carriers is represented by

$$-U=(p_0-p)/\tau_0. \tag{8.5}$$

This is the formula used, for example, in treating the reverse currents generated in the n-region of a p-n junction.

On the basis of the above reasoning, it would at first appear that the maximum rate at which hole-electron pairs could be generated in the n-type material would be given by (8.2), which is approximately equal to p_0/τ_0. Much greater values may occur in some cases, however; in particular, if the space-charge region in a p-n junction biased in the reverse direction penetrates the n-region, then both p and n may be much less than p_1. Under these conditions (4.4) reduces to

$$-U_{\text{sp.ch.}}=C_nC_pn_i^2/(C_nn_1+C_pp_1). \tag{8.6}$$

This corresponds to a "lifetime" defined as

$$\tau_{\text{sp.ch.}}=-p_0/U_{\text{sp.ch.}}=\tau_{p0}(n_1/n_0)+\tau_{p0}p_1/n_0. \tag{8.7}$$

This lifetime will be smaller that τ_0 for an n-type sample with $F_0>E_t$ approximately in the ratio.

$$\tau_{\text{sp.ch.}}/\tau_0=n_1/(n_1+n_0) \tag{8.8}$$

and the rate of generation of hole electron pairs will be greater in about the same ratio.

Hence the reverse current furnished by an element of volume of n-type material having $F_0>E_t$ will be increased by a factor

$$\tau_0/\tau_{\text{sp.ch.}}=\exp(F_0-E_t)kT \tag{8.9}$$

as it enters the space charge region. For $E_i<F_0<E_t$, on the other hand, the change is less than a factor of two.

For p-type samples, the value for the space-charge case

$$\tau_{\text{sp.ch.}}=-n_0/U_{\text{sp.ch.}}=\tau_{p0}n_1/p_0+\tau_{n0}p_1/p_0, \tag{8.10}$$

while

$$\tau_0=\tau_{p0}n_1/p_0+\tau_{n0}(p_0+p_1-n_0)/p_0. \tag{8.11}$$

It is again seen that $\tau_{\text{sp.ch.}}$ is less than τ_0 but the ratio does not become large until p_0 becomes greater than n_1 corresponding to

$$F_0<2E_i-E_t, \tag{8.12}$$

for which

$$\tau_0/\tau_{sp.ch.} \doteq (\tau_{n0}/\tau_{p0}) \exp(2E_i - E_i - F_0)/kT. \quad (8.13)$$

In strongly n-type or p-type material, the minority carrier density is small and, consequently, the generation of minority carriers is suppressed since the traps are generally in the state corresponding to the sign of the majority carriers. The large increases of hole-electron pair generation given in (8.9) and (8.13) in these cases result from removal of the majority carriers. Under these conditions the traps assume an average state given by (4.2) and (4.3) with

$$f_t = C_p p_1/(C_n n_1 + C_p p_1), \quad (8.14)$$

$$f_{pt} = C_n n_1/(C_n n_1 + C_p p_1), \quad (8.15)$$

and emit electrons and holes at the rates

$$C_n n_1 f_t = C_p p_1 f_{pt} = -U_{sp.ch.} \quad (8.16)$$

as given in Eq. (8.6).

APPENDIX A

In this appendix, we consider the general case where the density of traps is not small compared with the normal carrier density; δn and δp are then not necessarily equal, the difference being due to the deviation $N_t \delta f_t$ of the number of filled traps from the thermal equilibrium value.

We consider only the case where the disturbances in carrier density are small enough that only first-order terms in δn and δp need be considered. The recombination rates are then linear functions of δn and δp:

$$U_{cn} = A_{nn}\delta n + A_{np}\delta p, \quad U_{cp} = A_{pn}\delta n + A_{pp}\delta p, \quad (A1)$$

where the A's are constants which we shall evaluate [Eq. (A5)].

Equations (A1), together with the continuity equations, provide a set of linear partial differential equations from which the excess carrier densities δp and δn can be found for any set of boundary conditions. In this paper we are primarily concerned with the steady state, $U_{cn} = U_{cp} = U$, rather than with transient conditions. Since in general $\delta n \neq \delta p$, we have two lifetimes,

$$\begin{aligned} \tau_p &= \delta p/U = (A_{pp} - A_{np})/(A_{nn}A_{pp} - A_{np}A_{pn}), \\ \tau_n &= \delta n/U = (A_{nn} - A_{pn})/(A_{nn}A_{pp} - A_{np}A_{pn}). \end{aligned} \quad (A2)$$

In general $\tau_p \neq \tau_n$. For most purposes the lifetime of the minority carrier is of the most practical interest; we shall, therefore, find τ_p for an n-type specimen and τ_n for a p-type.

To begin we find the A's in Eq. (A1). From Eqs. (3.8) and (3.9) of the text, it is seen that small deviations δn, δp, δf_t from the equilibrium values n_0, p_0, f_t give recombination rates

$$\begin{aligned} U_{cn} &= C_n[(1-f_t)\delta n - (n_0+n_1)\delta f_t], \\ U_{cp} &= C_p[f_t \delta p + (p_0+p_1)\delta f_t]. \end{aligned} \quad (A3)$$

The relation between δf_t, δn, and δp comes from the requirement of electrical neutrality

$$\delta p - \delta n = N_t \delta f_t. \quad (A4)$$

Since f_t in (A3) refers to equilibrium, we have

$$f_t = \frac{1}{1+(n_1/n_0)} = 1 - \frac{1}{1+(p_1/p_0)}. \quad (A5)$$

Substituting (A4) and (A5) into (A3) gives (A1) with

$$\begin{aligned} A_{nn} &= C_n\left[\frac{n_1}{n_0+n_1} + \frac{n_0+n_1}{N_t}\right], \\ A_{np} &= -C_n\frac{n_0+n_1}{N_t}, \\ A_{pn} &= -C_p\frac{p_0+p_1}{N_t}, \\ A_{pp} &= C_p\left[\frac{p_1}{p_0+p_1} + \frac{p_0+p_1}{N_t}\right]. \end{aligned} \quad (A6)$$

Substituting (A5) into (A2) gives the lifetimes

$$\begin{aligned} \tau_p &= \frac{\tau_{n0}(p_0+p_1) + \tau_{p0}[n_0+n_1+N_t(1+n_0/n_1)^{-1}]}{n_0+p_0+N_t(1+n_0/n_1)^{-1}(1+n_1/n_0)^{-1}}, \\ \tau_n &= \frac{\tau_{p0}(n_0+n_1) + \tau_{n0}[p_0+p_1+N_t(1+p_0/p_1)^{-1}]}{n_0+p_0+N_t(1+p_0/p_1)^{-1}(1+p_1/p_0)^{-1}}. \end{aligned} \quad (A7)$$

The two expressions (A7) are symmetrical in n and p. It should be noted that $n_0/n_1 = p_1/p_0$, hence the denominators are the same in the two formulas.

For $N_t = 0$, the two equations (A7) both reduce to (5.5) of the text. At the other extreme, $N_t = \infty$, we have

$$\tau_p = \tau_{p0}(1+n_1/n_0), \quad (A8)$$

which is the same as (5.6) of the text for an n-type sample. Thus the lifetime of a hole in n-type material is correctly given by the simple theory except near intrinsic. For $N_t = \infty$, τ_n becomes

$$\tau_n = \tau_{n0}(1+p_1/p_0) = \tau_{n0}[1+\exp(F_0 - E_t)/kT]. \quad (A9)$$

Thus for $E_t > E_i$, $\tau_n = \tau_{n0}$ for all p-type samples when N_t is very large compared to both p_0 and n_1. The interpretation of (A8) is that $1+n_1/n$ is simply an alternative way of writing $1/f_t$. Hence $1/\tau_p$ is simply $1/\tau_{p0}$ times the probability that a trap be ready to capture a hole by being occupied by an electron. A similar interpretation applies to (A9).

We next consider the lifetime of the minority carrier for the four distinct regions discussed in Sec. 5 of the text.

In regions (3) and (4), n-type material, we have seen, [Eq. (A8)] that the formula for lifetime of a hole is independent of N_t. (The lifetime itself is, of course,

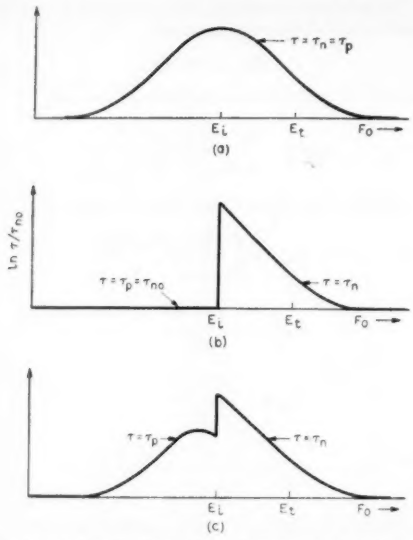

FIG. 4. Variation of lifetime of minority carrier with F_0: (a) $N_t=0$, (b) $N_t=$ infinity, (c) intermediate case.

inversely proportional to N_t since τ_{p0} is inversely proportional to N_t.) Likewise in region (1), $p_0 \gg n_1$, it is seen that $\tau_n=\tau_{n0}$. Hence, the analysis of the text correctly gives the lifetime of the minority carrier, except in region (2). The formula for lifetime of the majority carrier will depend on N_t over a wider range, but this is generally of less interest.

In region (2), $n_1 \gg p_0 \gg n_0$, we have from (A7)

$$\tau_n=\tau_{n0}+\tau_{p0}\frac{n_1}{p_0+(N_t p_1/p_0)}. \tag{A10}$$

There are three distinct sub cases under (A10) corresponding to different ranges of F_0.

(2a) When $n_1<p_0+N_t p_1/p_0$, then $\tau_n=\tau_{n0}$. Since in region (ii), $n_1 \gg p_0$, this requires $n_1<N_t p_1/p_0$. It will be convenient to express N_t in terms of an energy level E^*, such that $n_0=N_t$ when $F_0=E^*$. Also, for convenience, we take E_i as the zero of energy. Then, by definition,

$$N_t=n_i \exp(E^*/kT). \tag{A11}$$

Thus in terms of energies, we have $\tau_n=\tau_{n0}$ when

$$-E^*+2E_i<F_0<0. \tag{A12}$$

This case is only possible when there are enough traps that

$$E^*>2E_i. \tag{A13}$$

(2b) When $n_1>N_t p_1/p_0>p_0$ then $\tau=\tau_{p0}n_1 p_0/N_t p_1$. In terms of energies this corresponds to

$$\begin{aligned}&\tfrac{1}{2}(E_i-E^*)<F_0<2E_i-E^*,\\ &\tau_n=\tau_{p0}\exp[(2E_i-E^*-F_0)/kT].\end{aligned} \tag{A14}$$

In order for this case to be possible the number of traps must be such that

$$E_i<E^*<3E_i. \tag{A15}$$

(2c) When $p_0>N_t p_1/p_0$, $\tau_n=\tau_{p0}n_1/p$, which corresponds to

$$\begin{aligned}&-E_i<F_0<\tfrac{1}{2}(E_i-E^*),\\ &\tau_n=\tau_{p0}\exp[(E_i+F_0)/kT].\end{aligned} \tag{A16}$$

This case is possible only for

$$E^*<3E_i. \tag{A17}$$

In case (2c), τ_n is independent of E^* and therefore of N_t, and is the same as in the text.

It is seen that if $E^*<E_i$, $N_t<n_1$ then cases (2a) and (2b) are eliminated and, for all values of F_0 both positive and negative, the lifetime of the minority carrier is correctly given by the simplified formula (5.5) of the text. It is also readily verified from Eqs. (A7) that (5.5) of the text correctly gives $\tau_p=\tau_n$ when N_t is small compared with any one of the four quantities n_0, p_0, n_1, p_1.

As in the text the case $E_t<E_i$ can be understood by reversing the role of holes and electrons.

Figure 4 shows the variation of the lifetime of the minority carrier for $E_t>E_i=0$. For convenience τ_{p0} and τ_{n0} are taken equal. Due to the logarithmic functions involved, a considerable difference between τ_{p0} and τ_{n0} would be required to appreciably alter the curves.

APPENDIX B. EFFECT OF DEGENERACY OF THE STATES OF THE TRAPS

The quantity E_t used as the energy level for the traps is in fact an effective energy-level related to the energy-level E_t (true) by the equation

$$E_t=E_t(\text{true})+kT\ln(w_p/w), \tag{B1}$$

where w_p and w are the degeneracies of an empty and full trap, respectively. This result may be derived by noting that the probability factor for the electrons in traps is

$$w^{N_t f_t} w_p^{N_t f_{pt}} N_t!/(N_t f_t)!(N_t f_{pt})!. \tag{B2}$$

When the customary maximizing process for Fermi-Dirac statistics is carried out, the degeneracy factor in (B2) produces the effect of (B1), which may then be used in equations like (2.1) and (2.2). In case excited states in the empty and full traps make a significant contribution, then the ratio w_p/w should be replaced by a ratio of states-sums.

Cosine Interaction between Nucleons*

A. DE-SHALIT
Palmer Physical Laboratory, Princeton University, Princeton, New Jersey
(Received May 12, 1952)

Some properties of a nuclear interaction proportional to $(\mathbf{j}_1\cdot\mathbf{j}_2)$ are investigated. Although this interaction yields, qualitatively, reasonable results for even-even nuclei, it fails when applied to odd nuclei, the situation being similar to that in the long-range Majorana interaction.

THE regularities found among the lowest states of even-even nuclei have recently drawn some attention. It is now believed that these low states usually arise from an excitation of the ground-state configuration and one can try to predict their relative separation by using perturbation theory. For example, one can assume that the nucleons move in certain orbits determined by the strong central field of the nucleus and that the different states of the configuration considered are further split by a "weak" interaction between the nucleons.

As a possible expression for that weak interaction Peasle[1] suggested the consideration of $V_{12}=\sum a_m \cos^m(\mathbf{j}_1,\mathbf{j}_2)$, where $(\mathbf{j}_1,\mathbf{j}_2)$ is the angle between the two angular-momentum vectors of the interacting particles and a_m are constants. It is the purpose of this note to point out some further properties of that interaction for the special case $a_m=\delta(m, 1)$.

As $\cos(\mathbf{j}_1,\mathbf{j}_2)$ is proportional to the scalar product of the two angular momentum vectors $\mathbf{j}_1$ and $\mathbf{j}_2$, we shall put the interaction in the form

$$V=\sum f(r_{ik})(\mathbf{j}_i\cdot\mathbf{j}_k),$$

where a possible dependence on the distance between the particles was introduced through $f(r_{ik})$.

In the j-j coupling one uses the representation in which j_i^2, $J^2=(\sum\mathbf{j}_i)^2$ and $J_z=M$ are diagonal. In this representation $(\mathbf{j}_i\mathbf{j}_k)$ is diagonal too, and the average value of V in any state will therefore be given by

$$\langle V\rangle_{\alpha}=\sum\langle(fr_{ik})\rangle_{\alpha}\langle(\mathbf{j}_i\cdot\mathbf{j}_k)\rangle_{\alpha}.$$

For equivalent nucleons $(\mathbf{j}_1=\mathbf{j}_2=\cdots=\mathbf{j}_n=\mathbf{j})$ $\langle f(r_{ik})$ is independent of i and k and we denote it simply by f. We then find

$$\langle V\rangle_{\alpha}=f\sum\langle(\mathbf{j}_i\cdot\mathbf{j}_k)\rangle_{\alpha}=\tfrac{1}{2}f[J(J+1)-nj(j+1)],$$

where n is the number of equivalent nucleons.

We therefore see that under the above cosine interaction the lowest state will be that one which has the lowest allowed total spin. For even-even nuclei this checks nicely with the experimental results even in regard to the spin of the next excited state which predominantly has a spin of two units.[2] For odd nuclei, however, one does not obtain Mayer's empirical law $J=j$. This is closely connected with the failure to obtain that rule for the case of Majorana forces with an infinite range $[f(r_{ik})=\text{const}]$.[3] To see it we make use of the fact that in the representation considered here the average value of the intrinsic spin is given by[4]

$$\langle\mathbf{S}_i\rangle=\langle\mathbf{j}_i\rangle(\mathbf{S}_i\cdot\mathbf{j}_i)/[j_i(j_i+1)],$$

and further, following Racah,[3] we note that

$$(\mathbf{S}\mathbf{j})/[j(j+1)]=\epsilon/(2\mathbf{j}+1),$$

where $\epsilon=\pm1$ for $j=l\pm\frac{1}{2}$. We therefore get

$$\langle(\mathbf{j}_i\cdot\mathbf{j}_k)\rangle=\epsilon_i\epsilon_k(2l_i+1)(2l_k+1)\langle(\mathbf{S}_i\cdot\mathbf{S}_k)\rangle.$$

Thus, whereas for nonequivalent nucleons one may sometimes get opposite contributions to the interaction energy from the Majorana forces [which essentially depend on $(\mathbf{S}_i\cdot\mathbf{S}_k)$] and the cosine-interaction, for equivalent nucleons and infinite range they essentially behave in the same way $(\epsilon_i\cdot\epsilon_k=+1)$. For a finite range the nondiagonal elements of $(\mathbf{S}_i\cdot\mathbf{S}_k)$ start to play an important role, because then $f(r_{ik})$ can have nondiagonal elements and it is no longer true that the expectation value of $f(r_{ik})(\mathbf{S}_i\cdot\mathbf{S}_k)$ is the product of the corresponding expectation values. In fact one knows that as the δ-limit is approached the state with a total spin $J=j$ (for odd configurations) becomes the ground state and the state of minimum spin, which was the ground state in the infinite-range approximation, moves up.

Nuclear configurations probably overlap each other strongly in that sense that the energy separation between ground states of different configurations is often smaller than the corresponding quantity between states of the same configuration. As this generally leads to a strong configuration interaction, it is perhaps interesting to note that an infinite-range cosine interaction will yield a vanishing configuration interaction. This, however, may be considered a disadvantage rather than an advantage in view of relatively strong mixtures of certain configurations required to explain existing β-decay data.

* This work was supported by the AEC and the Higgins Scientific Trust Fund.

[1] Private communication to Professor J. Jensen.

[2] M. Goldhaber and A. W. Sunyar, Phys. Rev. 83, 906 (1951). A. de Shalit, thesis, Eidgenossische Technische Hochscule, Zürich, 1951.

[3] G. Racah, Phys. Rev. 78, 622 (1950).

[4] E. V. Condon and G. H. Shortley, *The Theory of Atomic Spectra* (Cambridge University Press, Cambridge, 1951), p. 64.

The Magnetic Properties of Superconducting Alloys of Indium and Thallium*

W. F. Love, E. Callen,† and F. C. Nix
Randal Morgan Laboratory, University of Pennsylvania, Philadelphia, Pennsylvania
(Received April 29, 1952)

Magnetization curves for spherical samples of a series of alloys in the solid solution range of thallium in indium have been measured as a function of temperature and composition, and critical field curves have been obtained. These alloys show a fairly strong Meissner effect, and the breadth of the transition region increases for increasing thallium content. Alloys of high thallium content were found to have magnetic properties strongly sensitive to mechanical shock while in the intermediate state.

I. INTRODUCTION

SUPERCONDUCTIVITY of alloys of the In-Tl system has been studied by Meissner, Franz, and Westerhoff[1] who made measurements of the resistivity as a function of temperature, and by Stout and Guttman[2] who have reported on the Meissner effect in these alloys. The purpose of the present investigation was to study the magnetic properties of superconducting solid solution alloys, for which the system In-Tl is rather convenient. The results of previous workers[3,4] have shown that thallium is soluble at room temperature in indium up to concentrations around 60 atomic percent thallium. Alloys with compositions ranging approximately from 15 to 25 atomic percent thallium can exist in two phases, a face-centered cubic structure stable at high temperatures, and a face-centered tetragonal structure stable at low temperatures. The transformation is a diffusionless one and is accompanied by a splitting up of an original crystal into a lamellar structure typical of the martersitic transformation in low carbon iron-carbon alloys.[4,5]

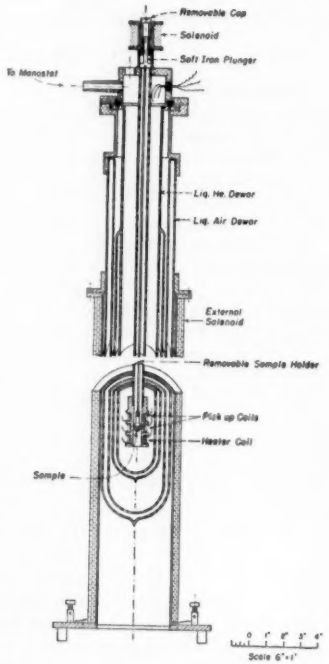

FIG. 1. Schematic diagram of measuring apparatus.

II. EXPERIMENTAL TECHNIQUE

1. Preparation of Samples

The indium used was obtained from the Idium Corporation of America and the thallium from the American Smelting and Refining Company. In both cases, the purity was given as 99.98 percent. The two components were weighed out carefully on an analytical balance and melted together in a closed graphite crucible over a Bunsen burner. The liquid metal was shaken vigorously to homogenize the melt and was then rapidly cooled by putting the crucible in running water. The resulting slug was placed in a graphite mold, remelted, and lowered through a single crystal vacuum furnace. The mold was made in two halves and shaped so that $\frac{1}{4}$-inch diameter spherical specimens could be obtained. The samples were kept in an annealing oven at 135°C for periods ranging from one day to several weeks. To check for homogeneity of

TABLE I. Results of chemical and analyses to check homogeneity of samples.

Atomic % Tl nominal value	Atomic % Tl from chemical analysis Sample No. 1	Sample No. 2
5	5.24	5.27
10	sample ruined	9.96
17	16.92	16.97
25	24.99	25.01
30	28.46	28.49
37	36.52	36.67

* This work was supported by the AEC.
† Now at the graduate school, Massachusetts Institute of Technology, Cambridge, Massachusetts.
[1] Meissner, Franz, and Westerhoff, Ann. Physik **13**, 505 (1932).
[2] J. W. Stout and L. Guttman, Phys. Rev. **79**, 396 (1950).
[3] S. Valentiner, Z. Metallkunde **32**, 244 (1940).
[4] L. Guttman, Trans. Am. Inst. Mining Met. Engrs. **188**, 1472 (1950).
[5] Bowles, Barrett, and Guttman, Trans. Am. Inst. Mining Met. Engrs. **188**, 1478 (1950).

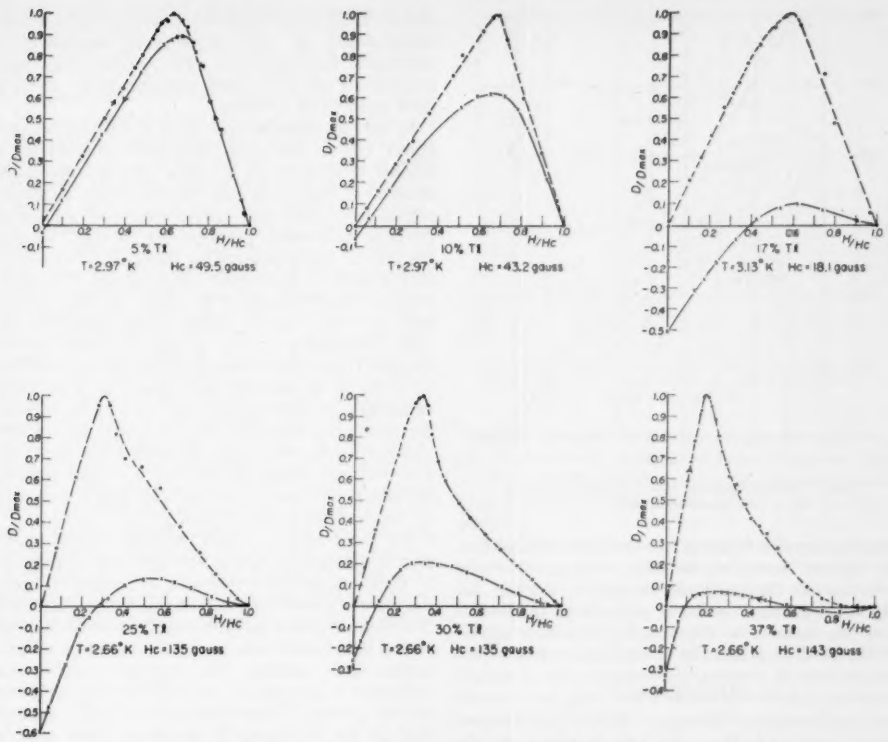

FIG. 2. Typical magnetization curves for a series of indium-thallium alloys.

composition, the spheres were cut in half transversely along the axis of growth after the measurements had been made and each half separately analyzed for its thallium content by a titration method due to Beale and co-workers.[6] The results are given in Table I. It can be seen from this table that segregation in these alloys is negligible.

2. Measuring Apparatus

The method of measurement is that originally used by Schoenberg.[7] A schematic diagram of the apparatus is shown in Fig. 1. The spherical sample is mounted at the end of a long glass tube and is placed at the center of the lower of a set of two identical pick-up coils, each consisting of 1000 turns of No. 40 Formex-coated copper wire. These coils are wound in opposition and connected in series. When the sample acquires a magnetic moment in the field of the external solenoid and is displaced sharply to the center of the other coil, the net flux change produces a ballistic throw of an external galvanameter proportional to its magnetic moment. The sample is displaced by the action of a solenoid on a soft iron plunger attached to the top of the glass rod. Samples can be exchanged during a single run by removing the top cap and pulling out the glass tube. The two pick-up coils are mounted on a Bakelite form attached to another larger glass tube. This tube has holes in its sides at frequent intervals in order to avoid the oscillations of the helium gas which occur in a closed tube terminated in a liquid helium bath. At the very bottom of the apparatus is placed a heater coil to produce thermal equilibrium in the bath. The pressure over the bath was maintained constant to 0.1 mm by means of a Cartesian manostat obtained from The Emil Greiner Company of New York. The pressure was measured with a Wallace and Tiernan absolute manometer.

III. EXPERIMENTAL RESULTS

A set of typical magnetization curves is shown in Fig. 2 for concentrations of Tl up to 37 atomic percent.

[6] Beale, Hutchison, and Chandlee, Ind. Eng. Chem., Anal. Edition **13**, 240 (1941).
[7] D. Shoenberg, Proc. Roy. Soc. (London) **A175**, 49 (1940).

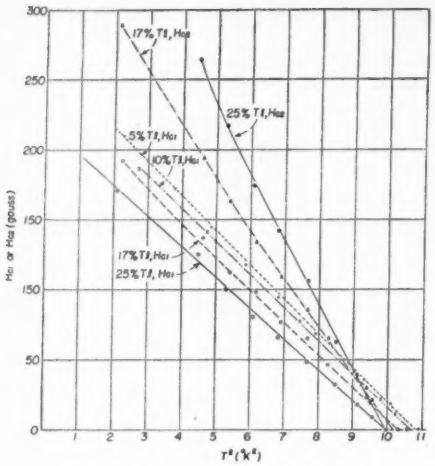

FIG. 3. Critical magnetic field curves for a series of indium-thallium alloys.

For purposes of comparison, the data have been plotted in "reduced" form, i.e., the ratio of the galvanometer deflection to the maximum deflection occurring for any field (D/D_{max}), which is proportional to the diamagnetic moment of the sample, is plotted against H/H_c, where H_c is taken to be the field at which superconductivity is completely destroyed. For a sample showing a perfect Meissner effect, this curve would increase linearly to a value of 1 at $H/H_c=\frac{2}{3}$ and decrease linearly to 0 at $H/H_c=1$ for both increasing and decreasing fields. Except for a small amount of frozen-in flux, this is seen to be the case for the 5 and 10 percent samples. However, an increasing breadth of transition is observed in the samples of higher Tl content. The abnormally large frozen-in flux in the 17 and 25 atomic percent samples is attributed to the presence of a polycrystalline structure caused by the cubic-to-tetragonal structure transformation that occurs in these two alloys.

The effect of grain structure on the magnetic properties was tested in a 10 atomic percent sample that was measured as a single crystal and then cold worked drastically to produce a polycrystalline specimen. It was found that the polycrystalline specimen showed about twice as much frozen-in flux as the single crystal, the breadth of transition remaining the same. It was also found that various heat treatments produced no appreciable difference in the superconductive properties of these alloys at low temperatures, i.e., a sample showed the same behavior whether it had been annealed for long or short periods of time, quenched or slowly cooled to room temperature. Of course, the possibility remains that there might be some influence due to the manner in which the sample is cooled to liquid helium temperatures. In these experiments, measurements were made on samples that were quenched from room temperature to liquid helium temperatures by lowering them rapidly into the bath.

By taking magnetization curves at different temperatures, critical field data have been obtained for a number of samples. In an alloy with an appreciable breadth of transition, one cannot define a unique critical field, since field penetration takes place over too large an interval. Consequently, in Fig. 3 we plot the field at which penetration starts (H_{c1}), as well as that at which it is complete (H_{c2}), against T^2 for four different concentrations of Tl. These two fields are the same for the 5 and 10 atomic percent samples, but differ considerably for the 17 and 25 atomic percent samples. It can be seen from the figure that both of these fields can be represented fairly closely by a parabolic variation with temperature. The slope of the straight line obtained is the same for each sample for the field at which penetration begins. In Table II are shown the values of the parameters H_0 and T_c which describe the variation of the two critical fields with temperature by means of the relation $H_c=H_0[1-(T^2/T_c^2)]$.

For the 5 and 10 atomic percent samples, which show a well-defined critical field and high reversibility in their magnetic transitions, it is possible to apply the thermodynamics of the pure superconducting state. The thermodynamic properties as determined from the critical field curves differ very little from those of pure indium. For example, the electronic specific heat coefficient γ is found to be 3.72×10^{-4} cal/mole deg^2 for the 5 percent Tl specimen and 3.67×10^{-4} cal/mole deg^2 for the 10 percent Tl specimen. These must be considered to be the same within the validity of the parabolic law. This result is to be expected since indium and thallium have the same valence, and consequently, the number of valence electrons remains unchanged as the concentration of thallium is increased. The only effects to be expected are those of a secondary nature such as variation of the lattice constant. The application of thermodynamics to the 17 and 25 atomic percent Tl samples is more doubtful because of the breadth of transition and lack of reversibility. However, by assuming that H_{c1} represents the true equilibrium field, the calculated electronic specific heat coefficients are 3.38×10^{-4} and 2.78×10^{-4} cal/mole deg^2, respectively, for the 17 and 25 atomic percent samples.

An interesting, but at the same time disturbing, aspect of the magnetic properties of these alloys was

TABLE II. Critical field data for indium-thallium alloys.

Atomic % Tl	H_{01}	H_{02}	T_c
5	263	263	3.30
10	257	257	3.25
17	242	390	3.21
25	216	500	3.16

brought about by the technique of measurement. It was found that, in those alloys that exhibit strong irreversibility and broad transitions, the magnetic moment is very sensitive to mechanical disturbances. Each measurement involved some mechanical jarring of the sample when it was displaced sharply. Figure 4 shows how this mechanical effect changes the magnetization curve for a 37 percent Tl specimen. The solid curve gives the galvanometer deflection as a function of applied field when only a single reading was taken. The dashed curve shows the "equilibrium" reading after the specimen has been displaced a number of times, i.e., the diamagnetic moment decreases with successive displacements in the intermediate state until a value is reached, after which it remains essentially constant with further jarring. It can be seen that the over-all effect of jarring the sample is to reduce the field at which penetration begins and to decrease the frozen-in flux by a considerable amount. Thus, you can get an apparently stronger Meissner effect by waiting for "mechanical" equilibrium to take place. No such effect as this was found in pure indium and only to a very small extent in the 5 and 10 atomic percent Tl specimens. This result cannot be attributed to time effects, since the magnetic moment remains constant for periods up to 30 minutes provided the sample has not been disturbed mechanically. It serves to emphasize the fact that a true state of thermodynamic equilibrium is difficult to achieve in alloys.

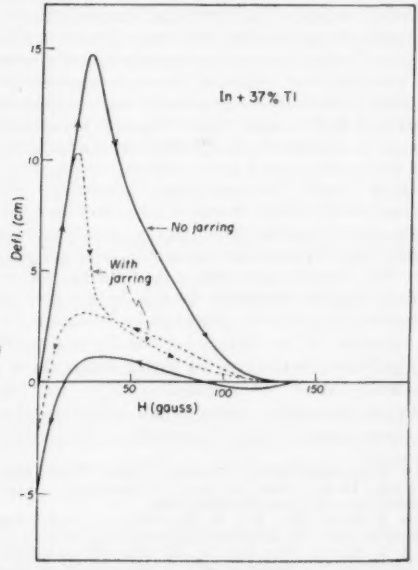

FIG. 4. Magnetization curves showing the effect of mechanical jarring on a 37 atomic percent thallium sample.

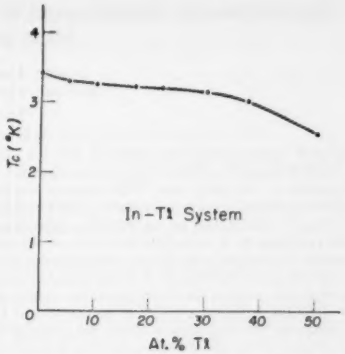

FIG. 5. Transition temperatures as a function of atomic percent of thallium.

Thus, it is difficult to make positive statements about the "fundamental" behavior of these alloys. Our data on magnetization curves and critical fields were taken by minimizing the mechanical influence on the specimens.

Transition temperatures were obtained for these alloys by measuring the temperature at which the first appreciable signs of diamagnetism occurred in a low field (2 gauss). The results are shown in Fig. 5. They are in essential agreement with the resistivity measurements of Meissner, Franz, and Westerhoff.[1]

IV. CONCLUSIONS

The results of these measurements show that homogeneous solid solution alloys of In-Tl approach the behavior of a pure metal more closely than has previously been found in other alloy systems. However, significant differences remain, the most important of which is the broad transition. It can be argued thermodynamically that a solid solution should either separate into its pure constituents or go over into an ordered structure at the absolute zero of temperature. The tendency to do either of these might set up microscopic strains within the material, which could cause the broadening effect actually observed in the superconductive transition. Another possible explanation is that these strains are produced in the lattice by the introduction of the larger thallium atoms. An x-ray investigation of these alloys at liquid helium temperatures is being undertaken in order to gain more insight into their structure at the temperature at which the measurements were taken. The existence of a mechanical effect further emphasizes the lack of thermodynamic equilibrium in these alloys.

The authors are indebted to Mr. F. Witt for assistance in taking data and to Mr. Elio Passaglia for carrying out the chemical analyses.

Electrodynamic Displacement of Atomic Energy Levels. III. The Hyperfine Structure of Positronium

ROBERT KARPLUS AND ABRAHAM KLEIN
Harvard University, Cambridge, Massachusetts

(Received May 13, 1952)

A functional integro-differential equation for the electron-positron Green's function is derived from a consideration of the effect of sources of the Dirac field. This equation contains an electron-positron interaction operator from which functional derivatives may be eliminated by an iteration procedure. The operator is evaluated so as to include the effects of one and two virtual quanta. It contains an interaction resulting from quantum exchange as well as one resulting from virtual annihilation of the pair. The wave functions of the electron-positron system are the solutions of the homogeneous equation related to the Green's function equation. The eigenvalues of the total energy of the system may be found by a four-dimensional perturbation technique. The system bound by the Coulomb interaction is here treated as the unperturbed situation. Numerical values for the spin-dependent change of the energy from the Coulomb value in the ground state are finally obtained accurate to order α relative to the hyperfine structure α^2 Ry. The result for the singlet-triplet energy difference is

$$\Delta W_{is} = \tfrac{1}{2}\alpha^2 \mathrm{Ry}_\infty[7/3-(32/9+2\ln 2)\alpha/\pi] = 2.0337\times 10^5 \text{ Mc/sec}.$$

Theory and experiment are in agreement.

I. INTRODUCTION

THE investigation to be described in this paper was suggested by the current theoretical interest in the quantum-mechanical two-body problem[1–3] and the recent accurate measurement of the ground state hyperfine structure of positronium.[4,5] The system composed of one electron and one positron in interaction is the simplest accessible to calculation because it is purely electrodynamic in nature. Moreover, the success of quantum electrodynamics in predicting with great accuracy the properties of a single particle in an external field indicates the absence of fundamental difficulties from the theory in the range of energies that are significant in positronium.

The discussion of the bound states of the electron-positron system is based upon a rigorous functional differential equation for the Green's function of that system, derived in Sec. II by the method described by Schwinger.[1] In order to obtain a useful approximate form of this equation (and of the associated homogeneous equation) we have iterated the implicitly defined interaction operator, in this way automatically generating to any required order the interaction kernel obtained from scattering considerations by Bethe and Salpeter.[3] In the present case we have included all interaction terms involving the emission and absorption of one or two quanta. The latter include self-energy and vacuum polarization corrections to one-photon exchange processes as well as two-photon exchange terms. The particle-antiparticle relationship of electron and positron is represented by terms describing one- and two-photon virtual annihilation of the pair.[6–8] In contrast to the case of scattering, only the irreducible[9] interactions appear explicitly.

Our subsequent concern is with the solution of the associated homogeneous equation. It should be emphasized at the outset that we shall be silent (out of ignorance) on the question of the fundamental interpretation of a wave function which refers to individual times for each of the particles. The possibility, nevertheless, of obtaining a solution to our problem entirely within the framework of the present formalism depends on two conditions. The first of these is that most of the binding is accounted for by the instantaneous Coulomb interaction. Salpeter[9] has shown that when the interaction is instantaneous, the wave equation can be rigorously reduced to one involving only equal times for the two particles. Moreover, the wave function for arbitrary individual time coordinates can be expressed in terms of that for equal times. This last circumstance can also be exploited in the development of a perturbation theory which yields the contribution to the energy levels of a small non-instantaneous interaction.[9] The relevant results of this treatment are given in Sec. III.

The second condition is that the free particle approximation for all intermediate states shall be an adequate one. The essential point here is that whether one derives an explicit interaction operator by the iteration procedure adopted in the present paper (tantamount to an expansion of the intrinsic nonlinearity in terms of free particle properties) or by a partial summation of a scattering kernel, the propagation which naturally enters in intermediate states is that of free particles. In the treatment of fine-structure effects, the contribu-

[1] J. Schwinger, Proc. Nat. Acad. Sci. US **37**, 452, 455 (1951).
[2] M. Gell-Mann and F. Low, Phys. Rev. **84**, 350 (1951).
[3] H. A. Bethe and E. E. Salpeter, Phys. Rev. **84**, 1232 (1951).
[4] M. Deutsch and S. C. Brown, Phys. Rev. **85**, 1047 (1952).
[5] M. Deutsch, latest result reported at the Washington Meeting of the American Physical Society, May, 1952. Phys. Rev. **87**, 212(T) (1952).
[6] J. Pirenne, Arch. sci. phys. et nat. **28**, 233 (1946); **29**, 121, 207, and 265 (1947).
[7] V. B. Berestetski and L. D. Landau, J. Exptl. Theoret. Phys. (U.S.S.R.) **19**, 673 (1949). See also V. B. Berestetski, J. Exptl. Theoret. Phys. (U.S.S.R.) **19**, 1130 (1949).
[8] R. A. Ferrell, Phys. Rev. **84**, 858 (1951) and Ph.D. thesis (Princeton, 1951). Dr. Ferrell kindly sent us a copy of his thesis.
[9] E. E. Salpeter, Phys. Rev. **87**, 328 (1952). We are indebted to Dr. Salpeter for making available to us a copy of his paper prior to publication. We have found his ideas very helpful in our work.

tion of nonrelativistic intermediate states, where the Coulomb binding cannot be ignored, must then be obtained in a manner reminiscent of the first treatments of the Lamb shift.[9] This will not be necessary in the present paper since we shall be concerned with the hyperfine (spin-spin) type of interaction to which only relativistic intermediate states contribute to the required precision.[10]

The practical goal of this work is to obtain the splitting of the singlet-triplet ground-state doublet of positronium correct to order α^3 Ry. Previous calculations,[6-8] accurate to order α^2 Ry, have included the lowest order contributions of the ordinary spin-spin coupling arising from the Breit[11] interaction (the analog of which in hydrogen is responsible for its hyperfine structure) and of the one-photon virtual annihilation force, characteristic of the system of particle-antiparticle. The expression for the energy shift given in Sec. III, Eq. (3.6) yields these again in lowest approximation and contains as well the matrix elements of all interactions which can contribute to the required accuracy.

Section IV is devoted to the detailed evaluation of all the matrix elements that may be looked upon as generalized Breit interactions because they depend purely on the exchange of photons between the two particles. In Sec. V we consider the annihilation interaction peculiar to the electron-positron system. Finally, the comparison with experiment is given in Sec. VI.

II. THE WAVE EQUATION

A discussion of the one-particle electron and positron Green's function associated with the vacuum state will serve as an introduction to this section. If the notation of reference 1 is extended to include the positron field variables $\psi'(x)$, $\bar{\psi}'(x)$, and their sources that are related to the electron variables $\psi(x)$, $\bar{\psi}(x)$, and their sources by the usual charge conjugating matrix C,

$$\begin{aligned} &C^{\dagger}C=1, \quad C=-\bar{C}, \quad C\tilde{\gamma}C^{-1}=-\gamma, \\ &\psi'=C\bar{\psi}, \quad \bar{\psi}'=C^{-1}\psi, \quad \eta'=C\bar{\eta}, \quad \bar{\eta}'=C^{-1}\eta, \end{aligned} \tag{2.1}$$

the Green's functions are defined by the vacuum expectation values

$$\delta_\eta\langle\psi(x)\rangle_0\big|_{\eta=0}=\int_{\sigma_2}^{\sigma_1} d^4x' G^-(x,x')\delta\eta(x') \tag{2.2a}$$

and

$$\delta_{\eta'}\langle\psi'(x)\rangle_0\big|_{\eta'=0}=\int_{\sigma_2}^{\sigma_1} d^4x' G^+(x,x')\delta\eta(x'), \tag{2.2b}$$

where $\delta\eta$ and $\delta\eta'$ are arbitrary variations of the electron and positron sources, respectively. The Green's functions can be expressed in terms of expectation values by

$$G^-(x,x')=i\langle(\psi(x)\bar{\psi}(x'))_+\rangle_0\epsilon(x,x') \tag{2.3a}$$

and

$$G^+(x,x')=i\langle(\psi'(x)\bar{\psi}'(x'))_+\rangle_0\epsilon(x,x') \tag{2.3b}$$

and satisfy the differential equations

$$[\gamma_\mu(-i\partial_\mu-eA_{+\mu}(x)+ie\delta/\delta J_\mu(x))+m] \times G^-(x,x')=\delta(x-x') \tag{2.4a}$$

and

$$[\gamma_\mu(-i\partial_\mu+eA_{+\mu}(x)-ie\delta/\delta J_\mu(x))+m] \times G^+(x,x')=\delta(x-x'), \tag{2.4b}$$

with the outgoing wave boundary condition. They are, of course, related by the matrix C:

$$G_{\alpha\beta}^+(x,x')=-C_{\alpha\alpha'}C^{-1}_{\beta\beta'}G_{\beta'\alpha'}^-(x',x). \tag{2.5}$$

We shall now introduce matrix notation for the combined particle coordinates and spinor indices, and the combined photon coordinates and vector indices. Because the formulas will get quite involved, the matrix indices will be expressed as arguments, by numbers for the particles and by ξ, ξ', $\cdots$ for the photons, and the summation convention will be understood. Functions of one coordinate are to be diagonal matrices; quantities affixed with only one matrix index are to be vectors with respect to that index. The arguments of the Dirac matrices will refer only to the vector and spinor indices of these quantities; they will be unit matrices in the coordinates. Similarly, functions of the coordinates alone must be understood as multiples of the Dirac unit matrix.

As an example, Eqs. (2.4) and (2.5) will be transcribed with the symbols $\mathfrak{F}^-$ and $\mathfrak{F}^+$ standing for the functional differential operators in Eq. (2.4):

$$\mathfrak{F}^-(12)G^-(23)=\delta(13); \tag{2.4'a}$$

$$\mathfrak{F}^+(12)G^+(23)=\delta(13); \tag{2.4'b}$$

$$G^+(12)=-C(11')C^{-1}(22')G^-(2'1'). \tag{2.5'}$$

If the mass operator $M(12)$ is defined in the usual way,

$$M^{\pm}(12)G^{\pm}(23)=\mathfrak{M}^{\pm}(12)G^{\pm}(23), \tag{2.6}$$

where $\mathfrak{M}$ is the functional differential operator

$$\mathfrak{M}^{\pm}(12)=m\delta(12)\mp ie\gamma(\xi,12)\delta/\delta J(\xi), \tag{2.7}$$

then the Green's function equations (2.4) can be written in terms of integro-differential operators F that are obtained from the $\mathfrak{F}$ by the replacement of $\mathfrak{M}$ by M.

A vertex operator $\Gamma(\xi,12)$ must now be defined for each Green's function,

$$\Gamma^+(\xi,12)=(\delta/\delta eA_+(\xi))(G^+(12))^{-1} =(\delta/\delta eA_+(\xi))F^+(12) \tag{2.8a}$$

and

$$\Gamma^-(\xi,12)=-(\delta/\delta eA_+(\xi))(G^-(12))^{-1} =-(\delta/\delta eA_+(\xi))F^-(12). \tag{2.8b}$$

In the absence of an external field these two quantities become equal because then the charge occurs always

[10] R. Karplus and A. Klein, Phys. Rev. **85**, 972 (1952).
[11] G. Breit, Phys. Rev. **34**, 553 (1929); **36**, 383 (1930); **39**, 616 (1932).

to an even power only, and the two differ just in the sign of the charge.

We now proceed to the two-particle system. The electron-positron Green's function for the vacuum state is defined by the relation

$$\delta_\psi\delta_{\psi'}\langle(\psi(x_1)\psi'(x_2))_+\rangle_0|_{\psi=\psi'=0}\epsilon(x_1,x_2)$$
$$=\int_{\sigma_2}^{\sigma_1}d^4x_1'\int_{\sigma_2}^{\sigma_1}d^4x_2'G^{-+}(x_1x_2,x_1'x_2')$$
$$\times\delta\eta(x_1')\delta\eta'(x_2'). \quad (2.9)$$

Evaluation of the variations with the help of Eq. (9), reference 1, leads to the explicit expression

$$G^{-+}(x_1x_2,x_1'x_2')$$
$$=\langle(\psi(x_1)\psi'(x_2)\bar\psi(x_1')\bar\psi'(x_2'))_+\rangle_0\epsilon$$
$$-\langle(\psi(x_1)\psi'(x_2))_+\rangle_0\epsilon(x_1,x_2)$$
$$\times\langle(\bar\psi(x_1')\bar\psi'(x_2'))_+\rangle_0\epsilon(x_1',x_2'). \quad (2.10)$$

As might be expected, this Green's function is related to a charge conjugate of the two-electron Green's function with arguments interchanged properly, by Eqs. (13, 20), reference 1:

$$G_{\alpha\beta\gamma\delta}^{-+}(x_1x_2,x_1'x_2')$$
$$=-C_{\beta\beta'}C^{-1}{}_{\delta\delta'}G_{\alpha\delta'\gamma\beta'}^{--}(x_1x_2',x_1'x_2)$$
$$-C_{\beta\beta'}C^{-1}{}_{\delta\delta'}G_{\alpha\beta'}^{-}(x_1x_2)G_{\delta'\gamma}^{-}(x_2'x_1'). \quad (2.11)$$

The antisymmetry of the two-electron Green's function assures that both direct and exchange processes are contained in the electron-positron Green's function; the second term merely corrects for the fact that the uncoupled electron-positron system cannot undergo an exchange process. In this case,

$$G_{\alpha\delta'\gamma\beta'}^{--}(x_1x_2',x_1'x_2)\to G_{\alpha\gamma}^{-}(x_1x_1')G_{\delta'\beta'}^{-}(x_2'x_2)$$
$$-G_{\alpha\beta'}^{-}(x_1x_2)G_{\delta'\gamma}^{-}(x_2'x_1'), \quad (2.12)$$

whence

$$G_{\alpha\beta\gamma\delta}^{-+}(x_1x_2,x_1'x_2')$$
$$\to-C_{\beta\beta'}C^{-1}{}_{\delta\delta'}G_{\alpha\gamma}^{-}(x_1x_1')G_{\delta'\beta'}^{-}(x_2'x_2)$$
$$=G_{\alpha\gamma}^{-}(x_1x_1')G_{\beta\delta}^{+}(x_2x_2'), \quad (2.13)$$

the proper description for noninteracting particles.

The differential equation for G^{-+} may be obtained with the help of that for G^{--}, Eq. (21), reference 1, and of Eq. (2.4′). They yield

$$\mathfrak{F}^{-}(11')G^{-+}(1'2,34)=\delta(13)G^{+}(24)$$
$$+ie\gamma(\xi,11')C(1'2')C^{-1}(44')$$
$$\times G^{+}(22')(\delta/\delta J(\xi))G^{-}(4'3) \quad (2.14)$$

and

$$F^{+}(22')\mathfrak{F}^{-}(11')G^{-+}(1'2',34)=\delta(13)\delta(24)$$
$$+ie\gamma(\xi,11')C(1'2)C^{-1}(44')(\delta/\delta J(\xi))G^{-}(4'3). \quad (2.15)$$

Finally, the equation may be written in the form

$$[F^{-}(11')F^{+}(22')-I(12,1'2')]G^{-+}(1'2',34)$$
$$=\delta(13)\delta(24), \quad (2.16)$$

where the interaction operator $I(1234)$ is defined by

$$I(12,1'2')G^{-+}(1'2',34)$$
$$=-F^{+}(22')[\mathfrak{M}^{-}(11')-M^{-}(11')]G^{-+}(1'2',34)$$
$$+ie\gamma(\xi,13')C(3'2)C^{-1}(44')(\delta/\delta J(\xi))G^{-}(4'3),$$
$$=-F^{-}(11')[\mathfrak{M}^{+}(22')-M^{+}(22')]G^{-+}(1'2',34)$$
$$-ie\gamma(\xi,22')C(2'1)C^{-1}(33')(\delta/\delta J(\xi))G^{+}(3'4). \quad (2.17)$$

The second expression arises when $\mathfrak{F}^{+}$ and then F^{-} are applied to the Green's function. These expressions must now be rearranged so as to yield the interaction operator explicitly as an integral operator up to the desired order of accuracy. In other words, the functional derivatives may occur only in terms that contribute negligibly to the effect that is being investigated. The subsequent operations will be directed at finding an expression that is suitable for the purposes of this paper. (For other effects, such as the Lamb shift in positronium, a different form of the interaction operator is necessary.)

With the help of the definition of the vertex operator, Eq. (2.8), the lowest order interaction may be separated as follows:

$$I(12,1'2')G^{-+}(1'2',34)$$
$$=ie^2\gamma(\xi,11')\mathcal{G}_{+}(\xi,\xi')\Gamma^{+}(\xi',22')G^{-+}(1'2',34)$$
$$-[\mathfrak{M}^{-}(11')-M^{-}(11')]F^{+}(22')G^{-+}(1'2',34)$$
$$+ie^2\gamma(\xi,13')C(3'2)\mathcal{G}_{+}(\xi,\xi')C^{-1}(2'4')$$
$$\times\Gamma^{-}(\xi',4'1')G^{-}(1'3)G^{+}(2'4). \quad (2.18)$$

The second term in Eq. (2.18) can be simplified by the use of Eqs. (2.16) and (2.6), whence it becomes

$$-ie^2\gamma(\xi,11')G^{-}(1'1'')[\delta/\delta eJ(\xi)]$$
$$\times I(1''2,3'4')G^{-+}(3'4',34). \quad (2.19)$$

The last term, finally, is brought into more useful form with the help of the identity

$$\mathcal{G}_{+}(\xi,\xi')C^{-1}(2'4')\Gamma^{-}(\xi',4'1')G^{-}(1'3)G^{+}(2'4)$$
$$=D_{+}(\xi,\xi')C^{-1}(2'4')\gamma(\xi',4'1')G^{-+}(1'2',34), \quad (2.20)$$

which may be verified by iteration of both sides. The interaction operator therefore is given by

$$I(12,34)=ie^2\gamma(\xi,13)\mathcal{G}_{+}(\xi,\xi')\Gamma^{+}(\xi',24)$$
$$+ie^2\gamma(\xi,11')C(1'2)D_{+}(\xi,\xi')C^{-1}(44')\gamma(\xi',4'3)$$
$$-ie^2\gamma(\xi,11')G(1'1'')[(\delta/\delta eJ(\xi))I(1''2,3'4')$$
$$\times G^{-+}(3'4',3''4'')][G^{-+}(3''4'',34)]^{-1}. \quad (2.21)$$

This, and a corresponding expression obtained from the alternative form of Eq. (2.17) correspond to Eq. (47), reference 1; the only difference lies in the second term above, which represents the interaction due to the virtual annihilation of the electron-positron pair. The last term contains the effects of higher order electrodynamic processes involving more than one virtual photon, such as multiple photon exchanges and the corrections that symmetrize the first term in the interaction so that it depends on the vertex operator of both the electron and the positron.

We are interested in the effects of one and two virtual quanta, terms of order e^4 in the interaction. For this reason, the functional derivative in Eq. (2.21) needs be evaluated only to the lowest order,

$$\begin{aligned}&[(\delta/\delta eJ(\xi))I(1''2,3'4')G^{+}(3'4',3''4'')]\\&\times[G^{+}(3''4'',34)]^{-1}\cong -I(1''2,3'4')\\&\times G^{+}(3'4',3''4'')[\delta/\delta eJ(\xi)]\\&\times[F^{-}(3''3)F^{+}(4''4)]\cong -ie^2[\gamma(\xi,1''3')\\&\times\gamma(\xi',24')+\gamma(\xi,1''2')C(2'2)C^{-1}(4''2'')\\&\times\gamma(\xi',2''3')]D_{+}(\xi,\xi')G^{-}(3'3'')G^{+}(4'4'')\\&\times D_{+}(\xi,\xi')[-F^{+}(4''4)\gamma(\xi',3''3)\\&\qquad+F^{-}(3''3)\gamma(\xi',4''4)]. \quad (2.22)\end{aligned}$$

When this expression is multiplied out, the first of the four terms is conveniently included in a symmetrical lowest order interaction, and the $(\pm)$ superscripts can be dropped in the limit of vanishing external field. This form of the approximate interaction operator,

$$\begin{aligned}&I(12,34)\cong ie^2\Gamma(\xi,13)\mathcal{G}_{+}(\xi,\xi')\Gamma(\xi',24)\\&\quad+ie^2\gamma(\xi,11')C(1'2)D_{+}(\xi,\xi')C^{-1}(44')\gamma(\xi',4'3)\\&\quad+(ie^2)^2\gamma(\xi,11')G(1'1'')\gamma(\xi,1''3)\gamma(\xi',24')\\&\quad\times G(4'4'')\gamma(\xi',4''4)D_{+}(\xi,\xi')D_{+}(\xi,\xi')\\&\quad+(ie^2)^2\gamma(\xi,11')G(1'1'')\gamma(\xi,1''2')C(2'2)D_{+}(\xi\xi')\\&\quad\times D_{+}(\xi,\xi')[C^{-1}(33')\gamma(\xi',3'4')G(4'4'')\gamma(\xi',4''4)\\&\qquad+C^{-1}(44')\gamma(\xi',4'3')G(3'3'')\gamma(\xi',3''3)], \quad (2.23)\end{aligned}$$

can be easily understood in terms of the equivalent Feynman diagram.

The wave functions $\psi(12)$ of the electron-positron system are solutions of the homogeneous equation,

$$[F^{-}(11')F^{+}(22')-I(12,1'2')]\psi(1'2')=0, \quad (2.24)$$

related to Eq. (2.16). It is important to realize that the operators $F(12)$ also contain electrodynamic corrections. These may be obtained from the corrections to the one-particle Green's function $G(12)$, of which $F(12)$ is the inverse.[12] For the nonrelativistic states in which we are interested, the operator $F(12)$ is a multiple of the Dirac operator $\bar{F}(12)$ that depends on the experimental mass m of the electron,

$$F^{\pm}(12)=(1-\alpha B/2\pi)^{-1}\bar{F}^{\pm}(12), \quad (2.25)$$

with

$$\bar{F}^{\pm}(x,x')=\delta(x-x')[\gamma_\mu(-i\partial_\mu'\pm eA_{+\mu}(x'))+m] \quad (2.26)$$

We may now introduce the interaction

$$\bar{I}(12,34)=(1-\alpha B/\pi)I(12,34), \quad (2.27)$$

which enters the equation of the usual form for the wave function,

$$[\bar{F}^{-}(11')\bar{F}^{+}(22')-\bar{I}(12,1'2')]\psi(1'2')=0. \quad (2.28)$$

To find the energy levels of the system, we seek solutions of the form

$$\psi(x_1x_2)=e^{iKX}\varphi_K(x); \quad X=\tfrac{1}{2}(x_1+x_2), \quad x=x_1-x_2, \quad (2.29)$$

that are eigenfunctions of the total momentum operator with eigenvalue K. This eigenvalue is the goal of the calculation. In the absence of an external field, the interaction operator conserves the total momentum, so that it is possible to write an equation for the function $\varphi_K(x)$ of the relative coordinate x,

$$[F_K(xx')-I_K(x,x')]\varphi_K(x')=0, \quad (2.30)$$

where

$$\begin{aligned}&e^{iKX}[F_K(xx')]_{\alpha\beta\gamma\delta}\\&=\int\bar{F}_{\alpha\gamma}(X+\tfrac{1}{2}x,X'+\tfrac{1}{2}x')\bar{F}_{\beta\delta}(X-\tfrac{1}{2}x,X'-\tfrac{1}{2}x')\\&\qquad\times e^{iK'X'}d^4X', \quad (2.31)\end{aligned}$$

and $I_K(x,x')$ is similarly related to $\bar{I}(1234)$. The Dirac indices in Eq. (2.30) are summed in the same way as those in Eq. (2.24); φ_K still has two sets of Dirac indices even through it has but one four-vector argument. To avoid complications in the notation, this matrix notation will be continued; where necessary, superscripts 1 and 2 will distinguish Dirac matrices that operate, respectively, on the first and second particle index of the wave function $\varphi_K(x)$.

Before we proceed to solve Eq. (2.30), we shall decompose the first two contributions to $\bar{I}(1234)$, Eqs. (2.23) and (2.27). With the help of the expressions[12]

$$\begin{aligned}&\Gamma_\mu(\xi,13)=\gamma_\mu(\xi,13)(1+\alpha B/2\pi)\\&\qquad+\bar{\Lambda}_\mu^{(3)}(1-\xi,\xi-3) \quad (2.32)\end{aligned}$$

and[12,13]

$$\begin{aligned}&\mathcal{G}_{+\mu\nu}(\xi,\xi')=(1+\alpha A/2\pi)D_{+}(\xi,\xi')\delta_{\mu\nu}\\&\qquad+\bar{D}_{+}^{(3)}(\xi,\xi')\delta_{\mu\nu}, \quad (2.33)\end{aligned}$$

[12] R. Karplus and N. M. Kroll, Phys. Rev. 77, 536 (1950).

[13] Note that

$$\mathcal{E}_{+}=\tfrac{1}{2}iD_F', \quad D_{+}=\tfrac{1}{2}iD_F, \quad \bar{D}_{+}^{(3)}=\tfrac{1}{2}i\bar{D}_F^{(3)}.$$

they become

$$4\pi i\alpha\gamma_\mu(\xi, 13)D_+(\xi, \xi')\gamma_\mu(\xi', 24)$$
$$+ie^2\gamma_\mu(\xi, 11')C(1'2)D_+(\xi\xi')C^{-1}(43')\gamma_\mu(\xi', 3'3)$$
$$\times(1-\alpha B/\pi)+4\pi i\alpha\gamma_\mu(\xi, 13)D_+(\xi, \xi')$$
$$\times\bar{\Lambda}_\mu^{(2)}(2-\xi', \xi'-4)+4\pi i\alpha\bar{\Lambda}_\mu^{(2)}(1-\xi, \xi-3)$$
$$\times D_+(\xi, \xi')\gamma_\mu(\xi', 24)+4\pi i\alpha\gamma_\mu(\xi, 13)$$
$$\bar{D}_+^{(2)}(\xi\xi')\gamma_\mu(\xi', 24), \quad (2.34)$$

up to terms involving two virtual photons. The experimental value of the fine structure constant α has been written to absorb the charge renormalization factor in Eq. (2.33),[12]

$$4\pi\alpha=e^2(1+\alpha A/2\pi)=4\pi/137.03\cdots. \quad (2.35)$$

III. PERTURBATION THEORY

Salpeter[9] has discussed a method for finding the eigenvalues of the total energy of a two-particle system described by an equation like Eq. (2.30) if the interaction function does not differ greatly from a local instantaneous interaction of the form

$$\delta(x-x')\delta(t)f(\mathbf{r}) \quad (x_\mu=\mathbf{r}, t; \quad i=1, 2, 3). \quad (3.1)$$

Such a term can indeed be separated from the center-of-mass transform of the first two contributions of Eq. (2.34), which may be written

$$I^C(x, x')+I_{K1}(x, x')=I^C(x, x')$$
$$+I_{K1B}(x, x')+I_{K1A}(x, x'), \quad (3.2)$$

where

$$I^C(x, x')=-i\alpha\delta(x-x')\gamma_0{}^1\gamma_0{}^2\delta(t)/r, \quad (3.3)$$

the Coulomb interaction, and

$$I_{K1B}=2i\alpha(2\pi)^{-3}\delta(x-x')$$
$$\times\int d^4k e^{ikx}\left[\frac{\boldsymbol{\gamma}^1\cdot\boldsymbol{\gamma}^2}{k_\mu{}^2}-\frac{\gamma_0{}^1\gamma_0{}^2k_0{}^2}{k_\nu{}^2k_\mu{}^2}\right], \quad (3.4)$$

$$I_{K1A}=ie^2(\gamma_\mu C)\delta(x)\delta(x')(C^{-1}\gamma_\mu)(1-\alpha B/\pi)/K_\nu{}^2. \quad (3.5)$$

These include the Breit[11] interaction, retardation effects, and the virtual annihilation exchange interaction. All the contributions derivable from Eqs. (2.23) and (2.34) that are not included in Eqs. (3.2–5) depend on the appearance of two virtual quanta. The two-quantum terms that are included in Eq. (2.34) will be denoted by $I_{K2B}^{(1)}$, while those that are explicit in Eq. (2.23) will be denoted by $I_{K2A}(x, x')$ or $I_{K2B}^{(2)}(x, x')$ depending on whether they are exchange or direct interactions.

The change in energy levels produced by the perturbations I_{K1} and I_{K2} acting on the electron-positron system bound by the Coulomb interaction Eq. (3.3) is then given to a sufficient approximation by[9]

$$\Delta E=-i\int d^4x d^4x'\bar{\varphi}_C(x)$$
$$\times\Big\{I_{K1}(x, x')+I_{K2A}(x, x')+I_{K2B}^{(1)}(x, x')$$
$$+I_{K2B}^{(2)}(x, x')+\int d^4x''d^4x'''I_{K1}(x, x'')$$
$$\times[F_K{}^C(x'', x''')]^{-1}I_{K1}(x''', x')\Big\}\varphi_C(x'), \quad (3.6)$$

measured in the reference frame in which the total spatial momentum vanishes,

$$K_\mu=(\mathbf{0}, K_0). \quad (3.7)$$

The function $\varphi_C(x)$ is the relativistic Coulomb wave function that is a good approximation to the actual wave function of the state whose energy level is sought. It is a solution of

$$[F_K{}^C(x, x')-I^C(x, x')]\varphi_C(x')=0, \quad (3.8)$$

whence

$$\Delta E=K_0-K_0{}^C. \quad (3.9)$$

The expression Eq. (3.6) is accurate to order α relative to the fine structure contribution I_{K1} and further presupposes that the intermediate states in the second-order perturbation term, the last in Eq. (3.6), can be replaced by free particle states. This is the case for the spin-spin interaction under investigation.

Before closing this section, we must briefly discuss the wave function $\varphi_C(x)$ that enters into Eq. (3.6). As is the case with the electrodynamic corrections to the magnetic interactions in hydrogen, the contributions to ΔE come mostly from the vicinity of the relative coordinate origin. The two-photon contributions, therefore, will be at most of the order $\alpha^2|\varphi_0(0)|^2$, where $\varphi_0(\mathbf{r})$ is the Pauli wave function for the ground state of positronium. Since this is the smallest magnitude that is being considered, contributions to these terms that are proportional to the relative momentum can be neglected. It therefore suffices to approximate $\bar{\varphi}_C(x)[\ ]\varphi_C(x')$ by the product of $|\varphi_0(0)|^2=(\frac{1}{2}\alpha m)^3/\pi$ and the appropriate spin matrix element, which will be denoted by $\langle\ \rangle$. In calculating the effect of I_{K1}, which contains contributions of order $\alpha|\varphi_0(0)|^2$ due to the exchange of one virtual photon, the relative momentum can no longer be neglected. Indeed, corrections of relative order α that arise from the large momentum components of the wave function must not be omitted. As Salpeter[9] has pointed out, an improvement over the Pauli wave functions is obtained when the integral equation,

$$\varphi_C(x)=-i\alpha\int[F_K{}^C(x, x')]^{-1}\varphi_C(\mathbf{r}', 0)d\mathbf{r}'/r', \quad (3.10)$$

is used for an iteration procedure based on the Pauli wave function,

$$\varphi_C(x)\cong -i\alpha\int[F_K C(x,x')]^{-1}\varphi_0(\mathbf{r}')d\mathbf{r}'/r'. \quad (3.11)$$

IV. THE DIRECT INTERACTION

We turn now to the evaluation of the matrix elements for the energy shift that was obtained in the previous section. We shall consider first the contributions ΔE_B of those terms which arise from direct interaction, namely, those in which an electron-positron pair is present in each intermediate state. According to Eq. (3.6) and the definition preceding this equation,

$$\Delta E_B=-i\int d^4x d^4x'\,\bar\varphi_C(x)I_{K1B}(x,x')\varphi_C(x')$$

$$-i|\,\varphi_0(0)|^2\int d^4x d^4x'\Big\langle I_{K2B}{}^{(2)}(x,x')$$

$$+\int d^4x''d^4x'''I_{K1B}(x,x'')$$

$$\times[F_K C(x'',x''')]^{-1}I_{K1B}(x''',x')\Big\rangle$$

$$-i|\,\varphi_0(0)|^2\int d^4x d^4x'\langle I_{K2B}{}^{(1)}(x,x')\rangle. \quad (4.1)$$

The one-photon part of the interaction,

$$\Delta E_{B1}=-i\int d^4x d^4x'\,\bar\varphi_C(x)I_{K1B}(x,x')\varphi_C(x')$$

$$=\frac{2\alpha}{(2\pi)^3}\int d^4x d^4k\,\bar\varphi_C(x)e^{ikx}$$

$$\times\left[\frac{\boldsymbol{\gamma}^1\cdot\boldsymbol{\gamma}^2}{k_\mu{}^2}-\frac{\gamma_0{}^1\gamma_0{}^2k_0{}^2}{k_t{}^2k_\mu{}^2}\right]\varphi_C(x), \quad (4.2)$$

presents the greatest complication because it contains the lowest order hyperfine structure as leading term. When the approximate Coulomb wave function evaluated in the appendix is inserted here, one obtains a spin matrix element and multiple momentum integral which is multiplied by the explicit factor $\alpha^3|\,\varphi_0(0)|^2$:

$$\Delta E_{B1}=\frac{8\alpha^3|\,\varphi_0(0)|^2}{(2\pi)^4m^2}\int d^4k d\mathbf{k}'d\mathbf{k}''dt e^{-ik_0t}$$

$$\times\frac{m^2}{(k'^2+\frac{1}{4}\alpha^2m^2)^2}\frac{m^2}{(k''^2+\frac{1}{4}\alpha^2m^2)^2}\delta(\mathbf{k}-\mathbf{k}'+\mathbf{k}'')$$

$$\times\left\langle F_{k'}(-t)\left[\frac{\boldsymbol{\gamma}^1\cdot\boldsymbol{\gamma}^2}{k_\mu{}^2}-\frac{\gamma_0{}^1\gamma_0{}^2k_0{}^2}{k_t{}^2k_\mu{}^2}\right]F_{k''}(t)\right\rangle. \quad (4.3)$$

The following observations can now be made about that part of the energy change which depends on the spin of both particles. Only large contributions of magnitude α^{-2} and α^{-1} will be important in the integral. It can be seen that only small values of the momenta k', $k''\lesssim\alpha m$ make such large contributions. The important region of integration, therefore, extends over small values of either or of both these momenta. When both momenta are large, k' and $k''\gtrsim m$, the integral becomes negligible for the purposes of the present calculation. A term proportional to k'^2 and k''^2 in the spin matrix element, for instance, is negligible because in its evaluation one may neglect $(\alpha m)^2$ compared to k'^2 and k''^2, so that the integral in Eq. (4.3) becomes effectively independent of α.[14] One may now see that the spin-dependent contribution of the retarded Coulomb interaction involves one of the $\boldsymbol{\alpha}^1\cdot\mathbf{k}'\boldsymbol{\alpha}^2\cdot\mathbf{k}'$ terms of both $F(t)$ operators and is therefore a negligible large momentum effect. The Breit interaction, of course, is important and contributes in conjunction with only one factor $\boldsymbol{\alpha}^1\cdot\mathbf{k}'\boldsymbol{\alpha}^2\cdot\mathbf{k}'$. Since corrections that involve an additional factor k''^2 are too small, one may use an approximate expression

$$F_k(t)\cong\tfrac{1}{2}(1+\boldsymbol{\alpha}^1\cdot\mathbf{k}/2m)(1-\boldsymbol{\alpha}^2\cdot\mathbf{k}/2m)$$

$$\times[(m/E)(e^{-i(E-m)|t|}+e^{-i(E+m)|t|})$$

$$+(e^{-i(E-m)|t|}-e^{-i(E+m)|t|})] \quad (4.4)$$

to evaluate ΔE_{B1}.

The spin matrix element has now become quite simple,

$$\langle(1+\boldsymbol{\alpha}^1\cdot\mathbf{k}'/2m)(1-\boldsymbol{\alpha}^2\cdot\mathbf{k}'/2m)$$

$$\times\boldsymbol{\alpha}^1\cdot\boldsymbol{\alpha}^2(1+\boldsymbol{\alpha}^1\cdot\mathbf{k}''/2m)(1-\boldsymbol{\alpha}^2\cdot\mathbf{k}''/2m)\rangle$$

$$\to\langle\boldsymbol{\sigma}^1\cdot\boldsymbol{\sigma}^2k^2-\boldsymbol{\sigma}^1\cdot\mathbf{k}\boldsymbol{\sigma}^2\cdot\mathbf{k}\rangle\to\tfrac{2}{3}\langle\boldsymbol{\sigma}^1\cdot\boldsymbol{\sigma}^2\rangle k^2, \quad (4.5)$$

since the δ-function implies that $\mathbf{k}'-\mathbf{k}''=\mathbf{k}$, and the integrand has the necessary spherical symmetry. The k_0 integration with the usual treatment of the poles yields

$$\int_{-\infty}^{\infty}e^{-ik_0t}dk_0(k^2-k_0{}^2-i\epsilon)^{-1}=\pi i k^{-1}e^{-ik|t|}(\epsilon>0). \quad (4.6)$$

The function of time in Eq. (4.3) is therefore even, so that the time integration may be carried out only over positive values if a factor of two is supplied. The integrals encountered are of the form

$$\int_0^{\infty}dt e^{-i(E'\pm m)t}e^{-ikt}e^{-i(E''\pm m)t}$$

$$=-i(k+E'+E''\pm m\pm m)^{-1}, \quad (4.7)$$

since the denominator never vanishes. The energy

[14] Detailed examination shows that the integral actually is proportional to $\log\alpha$ in this case. This dependence, however, is still negligible for our purposes.

change has now been reduced to

$$\Delta E_{B1}=\frac{4}{3}\langle\boldsymbol{\sigma}^1\cdot\boldsymbol{\sigma}^2\rangle\alpha^3(2\pi)^{-3}|\,\varphi_0(0)\,|^2$$
$$\times\int d\mathbf{k}d\mathbf{k}'d\mathbf{k}''\delta(\mathbf{k}-\mathbf{k}'+\mathbf{k}'')(k'^2+\tfrac{1}{4}\alpha^2m^2)^{-2}$$
$$\times(k''^2+\tfrac{1}{4}\alpha^2m^2)^{-2}\Big\{\frac{(E'+m)(E''+m)}{4E'E''}$$
$$\times\frac{k}{k+E'+E''-2m}+\frac{m^2-E'E''}{2E'E''}\,\frac{k}{k+E'+E''}$$
$$+\frac{(E'-m)(E''-m)}{4E'E''}\,\frac{k}{k+E'+E''+2m}\Big\}. \quad (4.8)$$

As it stands, the integral in Eq. (4.8) is quite difficult to carry out. We must remember, however, that at least one of the two variables k', k'' must be small compared to m, a fact which permits replacement of the corresponding kinetic energy by the rest energy. Furthermore, the occurrence of a factor $(E'-m)$ implies that the particular term contributes only for large $k'\sim m$, whence k'' must be small, and *vice versa*. In such a case, the small momentum may also be neglected in the argument of the δ-function. The remaining integration can then be carried out:

$$\Delta E_{B1}=\frac{4}{3}\langle\boldsymbol{\sigma}^1\cdot\boldsymbol{\sigma}^2\rangle\alpha^3(2\pi)^{-3}|\,\varphi_0(0)\,|^2$$
$$\times\int d\mathbf{k}d\mathbf{k}'d\mathbf{k}''\{(m^2/E'E'')\delta(\mathbf{k}+\mathbf{k}''-\mathbf{k}')$$
$$\times(k'^2+\tfrac{1}{4}\alpha^2m^2)^{-2}(k''^2+\tfrac{1}{4}\alpha^2m^2)^{-2}$$
$$+((k-E')/2mE'kk'^2)\delta(\mathbf{k}-\mathbf{k}')(k''^2+\tfrac{1}{4}\alpha^2m^2)^{-2}$$
$$+((k-E'')/2mE''kk''^2)\delta(\mathbf{k}+\mathbf{k}'')(k'^2+\tfrac{1}{4}\alpha^2m^2)^{-2}\}$$
$$=\frac{2\pi}{3}\langle\boldsymbol{\sigma}^1\cdot\boldsymbol{\sigma}^2\rangle\frac{\alpha}{m^2}|\,\varphi_0(0)\,|^2\Big\{1-\frac{4\alpha}{\pi}-\frac{2\alpha}{\pi}\ln\frac{m}{2k_m}\Big\}. \quad (4.9)$$

In the first term both k' and k'' are of the order αm, in the second $k'\sim m$, and in the third $k''\sim m$. A cutoff k_m has here been introduced as a lower limit on the final momentum integration. Its presence shows that some contributions of order $\alpha^2|\,\varphi_0(0)\,|^2$ to ΔE_{B1} do arise from small values of momentum, contrary to expectation. It will be seen, however, that the direct interaction $I_{K2B}^{(2)}$ and the second-order effect of I_{K1B} also contain contributions from small values of the momentum as represented by the appearance of $\ln(m/2k_m)$. Just as here, these are being treated incorrectly because of the assumption of free intermediate states that is implicit in the derivation of the interaction operator. The justification of this treatment lies in the fact that the sum of the direct interactions is independent of the cutoff; that a cutoff need not have been introduced at all if the terms had been grouped properly according to the photon momentum that makes the contribution rather than according to the physical process that is represented.

The evaluation of the remainder of Eq. (4.1) is relatively simple. The second line contributes

$$\Delta E_{B2}^{(2)}=-i|\,\varphi_0(0)\,|^2(4\pi i\alpha)^2$$
$$\times\int d^4xd^4x'e^{-iK^C(X-X')}d^4X'$$
$$\times\{\langle(\gamma_\mu{}^1G^1(X+\tfrac{1}{2}x,\,X'+\tfrac{1}{2}x')\gamma_\nu{}^1)$$
$$\times(\gamma_\nu{}^2G^2(X-\tfrac{1}{2}x,\,X'-\tfrac{1}{2}x')\gamma_\mu{}^2)\rangle$$
$$\times D_+(X-X'+\tfrac{1}{2}(x-x'))D_+(X'-X+\tfrac{1}{2}(x+x'))$$
$$+(2\pi)^{-8}\int d^4kd^4k'e^{ikx}e^{ik'x'}/k_\mu{}^2k_\mu{}'^2$$
$$\times\langle(\boldsymbol{\gamma}^1\cdot\boldsymbol{\gamma}^2-\gamma_0{}^1\gamma_0{}^2(k_0{}^2/k_i{}^2))G^1(X+\tfrac{1}{2}x,\,X'+\tfrac{1}{2}x')$$
$$\times G^2(X-\tfrac{1}{2}x,\,X'-\tfrac{1}{2}x')(\boldsymbol{\gamma}^1\cdot\boldsymbol{\gamma}^2-\gamma_0{}^1\gamma_0{}^2(k_0{}^2/k_i{}^2))\rangle, \quad (4.10)$$

an expression derived from Eqs. (2.23), (2.31), and (3.4). When Fourier transforms are introduced for the Green's functions, the energy may be written

$$\Delta E_{B2}^{(2)}=\frac{4\alpha^2}{(2\pi)^2}|\,\varphi_0(0)\,|^2\int d^4k(k_\mu{}^2)^{-2}$$
$$\times\Big\langle\Big(\gamma_\mu{}^1\frac{\boldsymbol{\gamma}^1(\frac{1}{2}K^C-k)-m}{E^2-(m-k_0)^2}\gamma_\nu{}^1\Big)$$
$$\times\Big(\gamma_\nu{}^2\frac{\boldsymbol{\gamma}^2(\frac{1}{2}K^C-k)-m}{E^2-(m-k_0)^2}\gamma_\mu{}^2\Big)$$
$$+(\boldsymbol{\gamma}^1\cdot\boldsymbol{\gamma}^2-\gamma_0{}^1\gamma_0{}^2k_0{}^2/k_i{}^2)\frac{\boldsymbol{\gamma}^1(\frac{1}{2}K^C-k)-m}{E^2-(m-k_0)^2}$$
$$\cdot\frac{\boldsymbol{\gamma}^2(\frac{1}{2}K^C+k)-m}{E^2-(m+k_0)^2}(\boldsymbol{\gamma}^1\cdot\boldsymbol{\gamma}^2-\gamma_0{}^1\gamma_0{}^2k_0{}^2/k_i{}^2)\Big\rangle, \quad (4.11)$$

where, as before,

$$E^2=k^2+m^2-i\epsilon\quad(\epsilon>0),\quad \tfrac{1}{2}K_0{}^C\simeq m \quad (4.12a)$$

and

$$k_\mu{}^2=k^2-k_0{}^2-i\epsilon \quad (4.12b)$$

define the treatment of the poles.

Explicit display of the spin matrix element and spherical averaging wisely precede the momentum

integration,

$$\Delta E_{B2}{}^{(2)}=(8\alpha^2/\pi)|\varphi_0(0)|^2\langle\boldsymbol{\sigma}^1\cdot\boldsymbol{\sigma}^2\rangle$$
$$\times\int_0^\infty k^2dk\int_{-\infty}^\infty dk_0(k_\mu{}^2)^{-2}$$
$$\times\{(k_0{}^2-\tfrac{2}{3}k^2)[E^2-(m-k_0)^2]^{-2}$$
$$+\tfrac{1}{3}k_0{}^2[E^2-(m-k_0)^2]^{-1}[E^2-(m+k_0)^2]^{-1}\}; \quad (4.13)$$

it depends on the identities

$$\gamma_i\gamma_j=-\delta_{ij}-i\sigma_{ij}; \quad \langle\sigma_{ij}{}^1\sigma_{ij}{}^2\rangle=2\langle\boldsymbol{\sigma}^1\cdot\boldsymbol{\sigma}^2\rangle. \quad (4.14)$$

The evaluation of the integrals is straightforward, except that the same cutoff k_m for small momentum values must be introduced. The result is

$$\Delta E_{B2}{}^{(2)}=\frac{2\pi}{3}\frac{\alpha}{m^2}\langle\boldsymbol{\sigma}^1\cdot\boldsymbol{\sigma}^2\rangle|\varphi_0(0)|^2\left\{\frac{5}{2}\frac{\alpha}{\pi}+\frac{2\alpha}{\pi}\ln\frac{m}{2k_m}\right\}, \quad (4.15)$$

and gives the total effect independent of k_m of processes where all quanta are exchanged between the two particles,

$$\Delta E_{B1}+\Delta E_{B2}{}^{(2)}=\frac{2\pi}{3}\frac{\alpha}{m^2}\langle\boldsymbol{\sigma}^1\cdot\boldsymbol{\sigma}^2\rangle|\varphi_0(0)|^2\left\{1-\frac{3}{2}\frac{\alpha}{\pi}\right\}. \quad (4.16)$$

The perturbation $\Delta E_{B2}{}^{(1)}$ includes effects of vacuum fluctuations on the exchange of a single quantum. The spin-dependent corrections to the vertex operator are contained in the anomalous-magnetic moment $(\alpha/2\pi)(e/2m)$ of each particle while the vacuum polarization has no effect on the singlet-triplet separation. The added contribution is therefore

$$\Delta E_{B2}{}^{(1)}=\frac{2\pi}{3}\frac{\alpha}{m^2}\langle\boldsymbol{\sigma}^1\cdot\boldsymbol{\sigma}^2\rangle|\varphi_0(0)|^2\{\alpha/\pi\}. \quad (4.17)$$

V. EXCHANGE INTERACTION

In this section we shall evaluate the matrix elements of the exchange energy, embracing all processes in which there is an intermediate state with no pairs present. The energy change, according to Eq. (3.6), is

$$\Delta E_A=-i\int d^4xd^4x'\,\bar{\varphi}_C(x)I_{K1A}(x,x')\varphi_C(x')(1-\alpha B/\pi)$$
$$-i|\varphi_0(0)|^2\int d^4xd^4x'\langle I_{K2A}(x,x')\rangle$$
$$-i|\varphi_0(0)|^2\int d^4xd^4x'd^4x''d^4x'''$$
$$\times\langle I_{K1A}(x,x'')[F_{KC}(x'',x''')]^{-1}I_{K1A}(x''',x')$$
$$+I_{K1B}(x,x'')[F_{KC}(x'',x''')]^{-1}I_{K1A}(x''',x')$$
$$+I_{K1A}(x,x'')[F_{KC}(x'',x''')]^{-1}I_{K1B}(x''',x')\rangle. \quad (5.1)$$

Consideration of the virtual two-quantum annihilation I_{K2A} and of the second-order single-quantum annihilation will be postponed to the end of this section. We only anticipate the result [see Appendix, Eq. (A.3)] that the latter will contribute a term that renormalizes the charge occurring in the first-order virtual annihilation from its uncorrected value e^2 to the measured value $4\pi\alpha$ [see Eq. (2.35)]; to the order considered in this paper, therefore, all quantities depend on α from here on.

The first one and last two terms in Eq. (5.1) present some complications since the quantity B is actually a divergent integral.[12] We expect that other divergent integrals will make the complete result finite, but we must exercise great care to obtain the correct finite result. For purposes of orientation it is instructive to consider briefly the matrix element in Eq. (5.1) for noninteracting, nonrelativistic initial and final states, because the high energy divergences may be expected to be the same in this simpler case as in the positronium atom. The wave function $\varphi_C(x)$ then represents the initial state plus a correction due to one Coulomb scattering, while $\int[F(x,x')]^{-1}I_{K1B}(x',x'')\varphi_0(0)d^4x'd^4x''$ represents the correction to the initial state due to the Breit interaction and retardation effects. The three terms we are now considering, therefore, comprise the matrix element of the virtual annihilation in the initial

FIG. 1. Feynman diagrams for virtual annihilation electron-positron scattering.

state plus a correction due to the four-dimensional interaction represented by one quantum exchange. The Feynman diagrams for these processes, Fig. 1, show that the electrodynamic corrections, Fig. 1b, 1c, are just the correction to the vertex operator, and therefore contain each a contribution $(\alpha/2\pi)B$ multiplying the basic interaction Fig. 1a.[12,15] To our order of accuracy, the divergent integrals disappear.

With this understanding we can attempt to evaluate the actual matrix element in Eq. (5.1). In order to keep track of the infinite quantities, it is very convenient to regulate the interaction brought about by photon II in Fig. 1 with a heavy photon of mass Λ.[16] The integral B can be evaluated to B_Λ,[12]

$$B_\Lambda=(i\pi^2)^{-1}\int_0^1 udu\int d^4k$$
$$\times\{(k^2+m^2u^2)^{-2}-(k^2+m^2u^2+\Lambda^2(1-u))^{-2}$$
$$-4m^2(1-u-\tfrac{1}{4}u^2)(k^2+m^2u^2)^{-3}\}$$
$$=\ln(\Lambda/m)+\tfrac{1}{4}-\ln(m/2k_m), \quad (5.2)$$

[15] J. C. Ward, Phys. Rev. **78**, 182 (1950).
[16] R. P. Feynman, Phys. Rev. **74**, 1430 (1948); W. Pauli and F. Villars, Revs. Modern Phys. **21**, 434 (1949).

where quantities depending inversely on Λ have been omitted and the low energy cutoff k_m has been introduced [see text following Eq. (4.9)].

The structure of the exchange interaction I_{K1A} implies that the energy change corresponding to Fig. 1 can be written

$$\Delta E_{A1}=-\pi\alpha m^{-2}\bar{\varphi}_A(0)_{\alpha\beta}(\gamma_j C)_{\alpha\beta}\times(C^{-1}\gamma_j)_{\beta'\alpha'}\varphi_A(0)_{\alpha'\beta'}, \quad (5.3)$$

where

$$\begin{aligned}(C^{-1}\gamma_j)_{\beta'\alpha'}\varphi_A(0)_{\alpha'\beta'}&=\mathrm{Tr}[C^{-1}\gamma_j\varphi_A(0)]\\&=[1-(\alpha/2\pi)B_\Lambda]2\alpha(2\pi)^{-2}\,\mathrm{Tr}\Big[\int d\mathbf{k}(m^2/E)\\&\times(k^2+\tfrac{1}{4}\alpha^2m^2)^{-2}\Big\{(1-\tilde{\boldsymbol{\gamma}}\cdot\mathbf{k}/2m)\\&\times C^{-1}\gamma_j(1+\boldsymbol{\gamma}\cdot\mathbf{k}/2m)+C^{-1}\gamma_j k^2/4m^2\Big\}\varphi_0(0)\\&+(i/2\pi)\int d^4k\{\tilde{\gamma}_i(m-\tilde{\gamma}(\tfrac{1}{2}K^C+k))\\&\times C^{-1}\gamma_j(m-\gamma(\tfrac{1}{2}K^C-k))\gamma_i-(k_0^2/k_i^2)\\&\times\tilde{\gamma}_0(m-\tilde{\gamma}(\tfrac{1}{2}K^C+k))C^{-1}\gamma_j(m-\gamma(\tfrac{1}{2}K^C-k))\gamma_0\}\\&\times[k_\mu^2]^{-1}[E^2-(m+k_0)^2]^{-1}[E^2-(m-k_0)^2]^{-1}\varphi_0(0)\\&-(i/2\pi)\int d^4k\{\tilde{\gamma}_\mu(m-\tilde{\gamma}(\tfrac{1}{2}K^C+k))\\&\times C^{-1}\gamma_j(m-\gamma(\tfrac{1}{2}K^C-k))\gamma_\mu\}[k_\mu^2+\Lambda^2]^{-1}\\&\times[E^2-(m+k_0)^2]^{-1}[E^2-(m-k_0)^2]^{-1}\varphi_0(0)\Big]. \quad (5.4)\end{aligned}$$

In writing the contribution of the regulating term, the last in Eq. (5.4), we have taken advantage of the fact that a very short range potential has no bound state so that the scattering picture described by Fig. 1 is applicable. The total energy has been approximated by $2m$ everywhere except in the correction to the Coulomb wave function, which comes from Eq. (A.9) evaluated at the origin. Only a space-like pair-producing Dirac matrix need be taken in Eq. (5.3). The trace is evaluated with the help of the facts that the Pauli wave function has only large components and that the charge-conjugating matrix C is an odd Dirac matrix. After integrating over k_0 with the usual treatment of the poles and after spherical averaging of the momentum integral, Eq. (5.4) becomes

$$\begin{aligned}&\mathrm{Tr}[C^{-1}\gamma_j\varphi_A(0)]\\&=[1-(\alpha/2\pi)B_\Lambda]\,\mathrm{Tr}[C^{-1}\gamma_j\varphi_0(0)](-\alpha/\pi m^2)\\&\times\int_0^\infty k^2dk\{-m^2E^{-1}(4k^2/3+2m^2)\\&\times(k^2+\tfrac{1}{4}\alpha^2m^2)^{-2}+\tfrac{1}{3}(E^{-1}-k^{-1})+m^2k^{-3}\\&-k^3(k^2+\Lambda^2-\Lambda^4/4m^2)^{-1}[-(m^2-\tfrac{1}{4}\Lambda^2)\\&\times E^{-1}(4k^2/3+2m^2)k^{-4}+\tfrac{1}{3}(E^{-1}-E'^{-1})\\&+(m^2-\tfrac{1}{2}\Lambda^2)k^{-2}E'^{-1}]\}. \quad (5.5)\end{aligned}$$

Here

$$E'=(k^2+\Lambda^2)^{\frac{1}{2}}, \quad (5.6)$$

in the second set of terms, which came from the regulating expression. One can observe that these reduce to the first set when $\Lambda=0$ if αm there is neglected with respect to k. The integrations are similar to the ones encountered in connection with Eq. (4.9) but made more complicated by the regulator. If one expands the result in powers of $(m/\Lambda)^2$ and keeps only the leading term, one obtains

$$\begin{aligned}&\mathrm{Tr}[C^{-1}\gamma_j\varphi_A(0)]\\&=[1-(\alpha/2\pi)B_\Lambda]\,\mathrm{Tr}[C^{-1}\gamma_j\varphi_0(0)]\\&\times\{1+(\alpha/2\pi)[\ln(\Lambda/m)]-4+\tfrac{1}{4}-\ln(m/2k_m)\}\\&=(1-2\alpha/\pi)\,\mathrm{Tr}[C^{-1}\gamma_j\varphi_0(0)], \quad (5.7)\end{aligned}$$

with B_Λ given by Eq. (5.2), whence

$$\Delta E_{A1}=-(\pi\alpha/m^2)(1-4\alpha/\pi)\times\mathrm{Tr}[\bar{\varphi}_0(0)\gamma_j C]\,\mathrm{Tr}[C^{-1}\gamma_j\varphi_0(0)], \quad (5.8)$$

because $\gamma_j C$ is a symmetrical matrix. When the usual representation of the charge conjugating matrix

$$C=C^{-1}=\gamma_0\gamma_2 \quad (5.9)$$

is inserted, the direct product of the Dirac matrices in Eq. (5.8) can be relabeled so that the operators refer to the spins of the individual particles:[6-8]

$$\begin{aligned}\bar{\varphi}_0(0)_{\alpha\beta}(\gamma_j C)_{\beta\alpha}(C^{-1}\gamma_j)_{\beta'\alpha'}\varphi_0(0)_{\alpha'\beta'}&\longrightarrow-\varphi_0^*(0)_{\alpha\beta}\\&\times[\tfrac{3}{2}\delta_{\alpha\alpha'}\delta_{\beta\beta'}+\tfrac{1}{2}\boldsymbol{\sigma}_{\alpha\alpha'}\cdot\boldsymbol{\sigma}_{\beta\beta'}]\varphi_0(0)_{\alpha'\beta'}\\&=-|\varphi_0(0)|^2\langle S^2\rangle, \quad (5.10)\end{aligned}$$

where S is the total spin of the system,

$$\mathbf{S}=\tfrac{1}{2}(\boldsymbol{\sigma}^1+\boldsymbol{\sigma}^2). \quad (5.11)$$

We then obtain the known effect of the virtual annihilation[6-8] plus a large correction of relative order α,

$$\Delta E_{A1}=(\pi\alpha/m^2)\langle S^2\rangle|\varphi_0(0)|^2\{1-4\alpha/\pi\}. \quad (5.12)$$

We now turn to the contribution of the second-order single quantum annihilation,

$$\Delta E_{A2}^{(1)}=i\pi^2\alpha^2m^{-4}\,\mathrm{Tr}[\varphi_0(0)\gamma_i C](C^{-1}\gamma_i)\times[F_{KC}(0,0)]^{-1}(\gamma_j C)\,\mathrm{Tr}[C^{-1}\gamma_j\varphi_0(0)], \quad (5.13)$$

with the spin sums as inferred from the derivation of this expression. In the appendix this effect is interpreted in terms of the polarization of the vacuum by the photon produced in the virtual annihilation. The evaluation given there together with Eq. (5.10) shows that the effect on the singlet-triplet splitting is[5]

$$\Delta E_{A2}^{(1)}=(\pi\alpha/m^2)\langle S^2\rangle|\,\varphi_0(0)\,|^2\{-8\alpha/9\pi\}, \quad (5.14)$$

since the renormalization constant A, Eq. (A.3) has been incorporated already.

The final item to be discussed in this section is the energy shift associated with two-quantum virtual annihilation given by

$$\begin{aligned}\Delta E_{A2}^{(2)}=&\frac{i\alpha^2}{\pi^2}|\,\varphi_0(0)\,|^2\\&\times[k_\rho{}^2(K^C-k)_\sigma{}^2[(\tfrac{1}{2}K^C-k)_\lambda{}^2+m^2]^2]^{-1}\\&\times\langle(\gamma_\mu[\gamma(\tfrac{1}{2}K^C-k)-m]\gamma_\sigma C)\\&\times(-C^{-1}\gamma_\mu[\gamma(\tfrac{1}{2}K^C-k)m]\gamma_\tau\\&\qquad+C^{-1}\gamma_\tau(\gamma(\tfrac{1}{2}K^C-k)-m]\gamma_\mu)\rangle, \quad (5.15)\end{aligned}$$

when Fourier representations are introduced for the Green's functions. The spin matrix elements of the two parentheses is to be taken as trace with the final and initial state wave functions, as in Eqs. (5.3) and (5.4). The momentum integration is simplified by the usual procedure of combining the three distinct denominators according to the formula

$$\begin{aligned}\int d^4k\,[k_\rho{}^2(K^C-k)_\sigma{}^2[(\tfrac{1}{2}K^C-k)_\lambda{}^2+m^2]^2]^{-1}&\\=6\int_0^1 x^2dx\int_0^1 ydy\int d^4k&\\\times[[k-\tfrac{1}{2}K^C(xy+2(1-x))]^2&\\+xm^2(xy^2-4(1-x)(1-y))-i\epsilon]^{-4}.&\quad (5.16)\end{aligned}$$

The displacement $k_0\to k_0+m(y+2(1-x))$ brings the denominator into the form

$$k^2+xm^2[x(2-y)^2-4(1-y)] \quad (5.17)$$

and leaves the numerator proportional to

$$\tfrac{1}{4}k_\lambda{}^2\langle(\gamma_\mu\gamma_\rho\gamma_\sigma C)(-C^{-1}\gamma_\mu\gamma_\rho\gamma_\sigma+C^{-1}\gamma_\sigma\gamma_\rho\gamma_\mu)\rangle \quad (5.18)$$

after hyperspherical averaging and the discarding of some terms whose dependence on the Dirac matrices prevents them from contributing. Since the wave functions in which the spin matrix elements are evaluated have only large components, Eq. (5.18) can be simplified to

$$-3k_\rho{}^2\langle(\gamma_0\gamma_5 C)(C^{-1}\gamma_0\gamma_5)\rangle=3k_\rho{}^2\langle(\gamma_2\gamma_5)(\gamma_2\gamma_5)\rangle, \quad (5.19)$$

where

$$\gamma_5=\gamma_1\gamma_2\gamma_3\gamma_0, \quad \gamma_5{}^2=-1. \quad (5.20)$$

Rearrangement of indices according to Eq. (5.10) finally produces the ordinary spin matrix element of a function of the total spin, Eq. (5.11),

$$3k_\rho{}^2\langle 2-S^2\rangle. \quad (5.21)$$

The momentum integration,

$$\int d^4k\,k_\rho{}^2[k_\nu{}^2+\Delta^2]^{-4}=i\pi^2/3\Delta^2, \quad (5.22)$$

brings the energy perturbation into the form

$$\begin{aligned}\Delta E_{A2}^{(3)}=&-6\alpha^2m^{-2}\langle 2-S^2\rangle|\,\varphi_0(0)\,|^2\\&\times\int_0^1 ydy\int_0^1 xdx[x(2-y)^2-4(1-y)-i\epsilon]^{-1}\\&=-(\alpha^2/m^2)\langle 2-S^2\rangle|\,\varphi_0(0)\,|^2(2-2\,\ln 2+\pi i). \quad (5.23)\end{aligned}$$

The real part of this expression corresponds to the energy change of the level while the imaginary part corresponds to the well-known[17] decay rate of the singlet state by two-photon annihilation,

$$\tau^{-1}=\alpha^3\,\mathrm{Ry}_\infty=0.804\times10^{10}\ \mathrm{sec}^{-1}. \quad (5.24)$$

The total contribution of the virtual annihilation interaction may be collected from Eqs. (5.12), (5.13), and (5.23),

$$\begin{aligned}\Delta E_A=(\pi\alpha/m^2)|\,\varphi_0(0)\,|^2\{\langle S^2\rangle(1-4\alpha/\pi-8\alpha/9\pi)&\\+2\langle S^2-2\rangle(1-\ln 2)\}.&\quad (5.25)\end{aligned}$$

VI. SUMMARY

The dependence of the 1^1S and 1^3S states in positronium on the spin of the system is obtained by the addition of Eqs. (4.16), (4.17), and (5.25):

$$\begin{aligned}\Delta E=(2\pi\alpha/m^2)|\,\varphi_0(0)\,|^2\{\tfrac{1}{3}\langle\sigma^1\cdot\sigma^2\rangle[1-\tfrac{1}{2}\alpha/\pi]&\\+\tfrac{1}{2}\langle S^2\rangle[1-(26/9+2\,\ln 2)\alpha/\pi]\}.&\end{aligned}$$

By taking the difference of the value of these operators in the singlet and triplet states, one arrives at the hyperfine splitting

$$\begin{aligned}\Delta W_{hs}&=(2\pi\alpha/m^2)|\,\varphi_0(0)\,|^2\{7/3-(32/9+2\,\ln 2)\alpha/\pi\}\\&=\tfrac{1}{2}\alpha^2\,\mathrm{Ry}_\infty\{7/3-(32/9+2\,\ln 2)\alpha/\pi\}\\&=2.0337\times10^5\ \mathrm{Mc/sec}.\end{aligned}$$

[17] J. A. Wheller, Ann. N. Y. Acad. Sci. **48**, 219 (1946).

The singlet state is the lower one. It can be seen that most of the rather large negative electrodynamic correction comes from the virtual annihilation interaction.

When the experiment of Deutsch and Brown[4] is interpreted on the basis of a Zeeman effect that depends on the total magnetic moment $(eh/2mc)(1+\alpha/2\pi)$ of each particle, the value of the separation obtained by them is[5]

$$\Delta W_{ts}=(2.035\pm0.003)10^5 \text{ Mc/sec.}$$

Theory and experiment are thus in satisfactory agreement.

We are grateful to V. F. Weisskopf for calling this problem to our attention. The authors are also indebted to the members of the Institute for Advanced Study, Princeton, for an informative discussion.

APPENDIX

The operator $[F^-(13)F^+(24)]^{-1}=G^-(13)G^+(24)$, the noninteracting two-particle Green's function, and its Fourier transforms appear so frequently that this appendix will be devoted to a discussion of some of its properties.

In connection with the second-order effect of the virtual annihilation, there appears the tensor

$$(C^{-1}\gamma_i)[F_K{}^C(0,0)]^{-1}(\gamma_j C)$$
$$=\int d^4X' e^{-iK(X-X')}(C^{-1}\gamma_i)_{\alpha\alpha'}G_{\alpha'\beta'}{}^-(X,X')$$
$$\times G_{\alpha\beta}{}^+(X,X')(\gamma_j C)_{\beta'\beta}=\int d^4X' e^{-iK(X-X')}$$
$$\times\mathrm{Tr}[\gamma_i G^-(X,X')\gamma_j G^-(X',X)], \quad \text{(A.1)}$$

by Eq. (2.5). This is, however, precisely the quantity that appears in the vacuum polarization tensor.[12] It is equal to

$$-\frac{i}{(4\pi)^2}(\delta_{ij}(K^C)^2-K_i{}^C K_j{}^C)$$
$$\times\left[2A+\int_0^1 dV\frac{V^2(1-\frac{1}{2}V^2)(K^C)^2}{m^2+\frac{1}{4}(K^C)^2(1-V^2)}\right]. \quad \text{(A.2)}$$

In the frame where $K_i{}^C=0$, $(K^C)^2\cong-4m^2$, the tensor becomes

$$\frac{im^2}{\pi\alpha}\delta_{ij}\left(\frac{\alpha}{2\pi}A-\frac{8}{9}\frac{\alpha}{\pi}\right). \quad \text{(A.3)}$$

The center-of-mass transform of the noninteracting Green's function appears in the integral equation (3.10). Its Fourier representation is

$$[F_K{}^C(x,x')]^{-1}=\frac{1}{(2\pi)^4}\int d^4k e^{ik(x-x')}$$
$$\times\frac{[m-\gamma^1(\frac{1}{2}K^C+k)][m-\gamma^2(\frac{1}{2}K^C-k)]}{[E^2-(\frac{1}{2}K_0{}^C+k_0)^2][E^2-(\frac{1}{2}K_0{}^C-k_0)^2]}, \quad \text{(A.4)}$$

when the center of mass is at rest. The quantity E^2 is defined by

$$E^2=k^2+m^2-i\epsilon, \quad \epsilon>0, \quad \text{(A.5)}$$

since Eq. (A.4) represents the noninteracting two-particle Green's function for outgoing waves. The integration over the fourth component of the momentum can be carried out with the help of the prescription Eq. (A.5). It gives the explicit function of the relative time coordinates,

$$[F_K{}^C(x,x')]^{-1}=i(2\pi)^{-3}\int d\mathbf{k}e^{i\mathbf{k}\cdot(\mathbf{r}-\mathbf{r}')}$$
$$\times(k^2+\tfrac{1}{4}\alpha^2m^2)F_k(t-t'), \quad \text{(A.6)}$$

where

$$F_k(t)=\frac{m}{2E}[e^{-i(E-m)|t|}+e^{-i(E+m)|t|}]$$
$$\times\left[\left(1+\frac{\boldsymbol{\alpha}^1\cdot\mathbf{k}}{2m}\right)\left(1-\frac{\boldsymbol{\alpha}^2\cdot\mathbf{k}}{2m}\right)+\frac{k^2}{4m^2}\right]$$
$$+\tfrac{1}{2}[e^{-i(E-m)|t|}-e^{-i(E+m)|t|}]$$
$$\times\left[\left(1+\frac{\boldsymbol{\alpha}^1\cdot\mathbf{k}}{2m}\right)\left(1-\frac{\boldsymbol{\alpha}^2\cdot\mathbf{k}}{2m}\right)\right.$$
$$\left.-\frac{k^2}{4m^2}\left(1+\frac{t}{|t|}\frac{\boldsymbol{\alpha}^1\cdot\mathbf{k}-\boldsymbol{\alpha}^2\cdot\mathbf{k}}{E}\right)\right], \quad \text{(A.7)}$$

and the total energy of the $1S$ state has been inserted,

$$K_0{}^C=2m-\tfrac{1}{2}\alpha^2m. \quad \text{(A.8)}$$

The wave function derived from Eq. (3.11) with the help of the operator just obtained is

$$\varphi_C(x)=(2\alpha/(2\pi)^2)\int d\mathbf{k}e^{i\mathbf{k}\cdot\mathbf{r}}m$$
$$\times(k^2+\tfrac{1}{4}\alpha^2m^2)^{-2}F_k(t)\varphi_0(0). \quad \text{(A.9)}$$

Promethium Isotopes*†

VERA KISTIAKOWSKY
Radiation Laboratory and Department of Chemistry, University of California, Berkeley, California
(Received March 25, 1952)

The half-lives and radiation characteristics of some promethium isotopes have been measured. Bombardments of isotopically enriched neodymium oxide samples by 8.9–32-Mev protons and of praseodymium oxide samples by 15–36-Mev helium ions were used to produce these nuclides. They were identified chemically and on the basis of relative yields. Nuclides studied: Pm^{141}, Pm^{142}, Pm^{143}, Pm^{144}, Pm^{148}, Pm^{149}, and Pm^{150}.

PROMETHIUM is one of the two medium-weight elements not found in nature, an absence that has been explained as arising from the fact that its most stable nuclides are 2–4 neutrons above the closed 82 neutron shell.[1,2] This work was undertaken to add to the knowledge concerning the radioactive characteristics of the promethium isotopes and thus to further substantiate the nuclear shell structure theory in this region.

PROCEDURE

The nuclides studied were produced by bombardment of isotopically enriched[3] neodymium oxides with 8.9-Mev protons from the 60-inch cyclotron, with 10-, 20- and 32-Mev protons from the linear accelerator, and by bombardment of praseodymium oxide with 15- to 36-Mev helium ions from the 60-inch cyclotron.

Since the number of radionuclides produced by the relatively low energy bombarding particles was limited, in general, chemical procedures were designed to isolate the rare earth elements as a group but not separate them from each other. The bombarded oxides were dissolved in nitric acid from which the rare earth fluoride was precipitated. This was dissolved; the hydroxide was precipitated and dissolved in concentrated hydrochloric acid, which was sucked through a column of anion exchange resin (Dowex A-1). The rare earth hydroxide was then prepared for counting samples. In those cases where complete chemical identification was desirable, rare earth separations were made using a cation exchange resin column (Dowex-50, citrate eluting solution of *p*H 3.5) at elevated temperatures as described by Thompson *et al.*[4]

The particle and electromagnetic radiation energies and the ratios of the various components of the decays were determined from aluminum, beryllium, and lead absorption data. When possible, positrons and negatrons were differentiated, and their approximate energies were determined using a 180° low resolution beta-ray spectrometer. The electromagnetic radiation of several samples was studied on a scintillation spectrometer, and the negatron spectra of Pm^{149} and Pm^{150} were examined on the double focusing beta-ray spectrometer described by O'Kelley.[5]

RESULTS

The bombardment of $(Nd^{142})_2O_3$ with 8.9–10.9-Mev protons and of $(Pr^{141})_6O_{11}$ with 15–36-Mev helium ions did not produce an observable Pm^{142} activity. If this nuclide undergoes a highly forbidden positron decay analogous to that[6] of La^{138}, which might be the case since both Pm^{142} and La^{138} have 81 neutrons, an activity with a very long half-life would be expected. The experiments limit the half-life to less than 2 minutes or more than 100 years.

The $(Nd^{142})_2O_3$ yielded a 20-minute half-life activity when bombarded with 20- and 32-Mev protons. This was assigned to Pm^{141} from the $Nd^{142}(p, 2n)$ reaction.

Wilkinson and Hicks[7] reported an isotope decaying by electron capture with 285-day half-life and another decaying by positron emission with 4-hour half-life produced by bombardment of $(Pr^{141})_6O_{11}$ with 18–35 Mev helium ions. These were assigned to Pm^{143} and Pm^{144}, respectively, on the basis of the variation of their formation cross sections with energy. The nuclide with 285-day half-life was identified chemically as an isotope of promethium. In the present work, the bombardments were repeated with similar results. It was shown chemically, however, that the 4-hour half-life probably does not belong to an isotope of praseodymium, neodymium, promethium, samarium, or europium. It does not arise from deuteron contamination of the beam, but may be due to an impurity in the sample. This seems unlikely since spectroscopic analysis could detect none.[8] Bombardments of $(Nd^{142})_2O_3$ and $(Nd^{144})_2O_3$

* This paper represents a summary of a thesis submitted in partial fulfillment of the requirements for the degree of Doctor of Philosophy. This has been published as University of California Radiation Laboratory Report No. 1629 (1952).

† This work was performed under the auspices of the AEC.

[1] L. Kowarski, Phys. Rev. **78**, 477 (1950).

[2] H. E. Suess, Phys. Rev. **81**, 1071 (1951).

[3] The percentage of the main constituent in each of the enriched fractions was as follows: $(Nd^{142})_2O_3$ (93.00), $(Nd^{143})_2O_3$ (83.93), $(Nd^{144})_2O_3$ (93.45), $(Nd^{145})_2O_3$ (78.60), $(Nd^{146})_2O_3$ (95.60), $(Nd^{148})_2O_3$ (89.85), and $(Nd^{150})_2O_3$ (94.76). Chemical purity >99 percent.

[4] Thompson, Ghiorso, and Seaborg, Phys. Rev. **80**, 781 (1950).

[5] G. D. O'Kelley, University of California Radiation Laboratory Declassified Report No. 1243 (1951).

[6] Pringle, Standil, and Roulston, Phys. Rev. **78**, 303 (1950).

[7] H. Hicks, University of California Radiation Laboratory Declassified Report No. 298 (1949); G. Wilkinson and H. Hicks, University of California Radiation Laboratory Declassified Report No. 751 (1950).

[8] Analysis by W. N. Tuttle, University of California Radiation Laboratory, Berkeley, California: As, Bi, Ce, Co, Cr, Dy, Er, Eu, Ho, La, Lu, Mn, Mo, Ni, Pb, Sb, Sn, Tb, Ti, V, Yb, Yt, and Zn not detected. Al, Ca, Fe, Mg, Nd, Sm, and Sc <0.1 percent.

TABLE I. Observed radioactive characteristics of promethium isotopes.

A	Type of radiation	Half-life	Energy of radiation (Mev) Particles	Electromagnetic	Produced by
141	β^+, γ	20±2 min	2.4–2.8 (spect.)		Nd^{142} $(p, 2n)$
142		<2 min >200 yr			
143 and 144	ϵ^-, γ K, L x-rays	200–400 days	0.6 (abs.)	0.9 (abs.) 0.17±0.02, 0.44±0.03 0.65±0.04 (spect.) K, L x-rays	Nd^{142} (p, n) Nd^{144} (p, n) Pr^{141} (α, n) Pr^{141} $(\alpha, 2n)$
146	β^- or ϵ^-, γ (?) K, L x-rays (?)	~1 yr	0.7 (abs.)	?	Nd^{146} (p, n)
148	β^-, γ K x-rays (?)	42±1 days	0.7 (92.6%) 2.7 (7.4%) (abs.)	~1.0 (abs.) K x-rays (?)	Nd^{148} $(p, 2n)$ or Nd^{148} (p, n)
149	β^-, γ K x-rays	54.4±1.1 hr	1.0 (abs.) 1.05±0.10 (spect.)	0.3–0.35 (spect.) (low intensity) K x-rays	Nd^{150} $(p, 2n)$
150	β^-, γ K x-rays (?)	161±1 min	2.01±0.03 (70±8%), 3.00±0.01 (30±8%) (spect.)	0.3, 1.4 (abs.) K x-rays	Nd^{150} (p, n)

separately with 8.9-Mev protons both yielded activities with half-lives of 200-400 days, consisting principally of electromagnetic radiation. These activities from the $(Pr^{141})_6O_{11}$, $(Nd^{142})_2O_3$, and $(Nd^{144})_2O_3$ bombardments were examined on a scintillation spectrometer. The conclusions drawn from these measurements were that Pm^{143} and Pm^{144} are probably very similar in their decay characteristics and that the activity observed from $(Pr^{141})_6O_{11}$ bombardments is probably a mixture due to both these nuclides. The possibility has not been ruled out that these two activities are independent isomers.

A particle emitting nuclide with a half-life of approximately one year was observed in high yield from $(Nd^{146})_2O_3$ and lower yields from $(Nd^{144})_2O_3$ and $(Nd^{143})_2O_3$ after 8.9-Mev proton bombardments; on the basis of yield considerations it was assigned to Pm^{146}.

Bombardment of $(Nd^{148})_2O_3$ with 8.9-Mev protons yielded the 42-day negatron emitter shown by Folger[9] to be an isotope of promethium, a long-lived nuclide emitting a 0.2-Mev negatron (probably the 3.7-year[10] Pm^{147}), and the 5.3-day[10] activity characteristic of Pm^{148}. Recently Long and Pool[11] reported a 48-day activity produced by 6-Mev protons on neodymium enriched in Nd^{148}. This is probably identical with the 42-day activity observed here, which thus belongs to an isomer of Pm^{148}.

Radionuclides with 161-minute and 54-hour half-lives were produced by the bombardment of $(Nd^{150})_2O_3$ with 8.9–9.9-Mev protons. On the basis of cross section considerations, they were assigned to Pm^{150} and Pm^{149}, respectively. The nuclide Pm^{149} has been reported[10] to have a half-life of 47–55 hours and to emit a 0.95–1.1-Mev negatron and a 0.2–0.25-Mev gamma-ray. The 161-minute activity assigned to Pm^{150} can probably be identified with a previously reported [10,11] 2.7-hour half-life activity. In the present experiments it was shown chemically to belong to an isotope of promethium.

The conclusions drawn are summarized in Table I.

I wish to express my gratitude to Dr. G. T. Seaborg under whose guidance this work was done. I wish to thank the Isotope Research and Development Division of the Y-12 Research Laboratory, Oak Ridge, Tennessee, for making available to me the enriched isotopes that made most of this work possible. I also wish to thank Dr. L. W. Alvarez, Mr. R. D. Watt, Mr. J. D. Gow, and the crew of the linear accelerator of the University of California Radiation Laboratory; and Dr. J. G. Hamilton, Mr. T. M. Putnam, Mr. G. B. Rossi, and the crew of the 60-inch cyclotron of Crocker Radiation Laboratory for their cooperation in making the bombardments.

[9] R. Folger and P. C. Stevenson, private communication (April, 1951).
[10] G. T. Seaborg and I. Perlman, Revs. Modern Phys. **20**, 585 (1948).
[11] J. K. Long and M. L. Pool, Phys. Rev. **85**, 137 (1952).

The Spectroscopy of the Solid State: Copper and Chromium*

E. M. GYORGY AND G. G. HARVEY
Research Laboratory of Electronics, Massachusetts Institute of Technology, Cambridge, Massachusetts
(Received May 14, 1952)

The M_{23} emission curves of copper and chromium have been obtained by using a vacuum recording spectrograph.

WE have obtained the M_{23} (valence to $3P_{\frac{1}{2}}$) emission curves of copper and chromium, using the spectrograph previously described.[1] We have made minor changes to facilitate focusing of the electron beam and to increase the power input into the evaporating furnace. Both curves have sharp emission edges and clearly show the M_{23} separation.

The chromium curve was taken with 600-volts bombarding voltage and 3-ma target current. The copper curve was taken with 500-volts bombarding voltage and 3-ma target current. The experimental curves are shown in Figs. 1 and 2. The range shown is from 40 to 160 counts per second. Both emission curves show satellites on the high energy side. In fact, at 700-volts bombarding voltage, the satellites completely obscure the emission edge. The curves were taken with the evaporation furnace running during the observation time, but even with this precaution, contamination (especially for chromium) was a serious problem. Therefore, the chromium curve had to be taken in a shorter time than was consistent with the response time of the counting-rate meter. As a result, the kink in the M_2 edge is due to the response time of the counting-rate meter and is not real. On curves where we only observed the high energy side, the inflection does not occur. In other respects, the chromium curve agrees with the curves taken with a slower speed of transversal over smaller energy ranges.

In Fig. 3 the experimental copper curve is plotted with the background eliminated and the ordinate divided by a factor proportional to the fourth power of the energy. The M_3 bands and M_2 bands are shown separated out by graphical means. The low energy end of the curve is not reliable, and this part of the curve

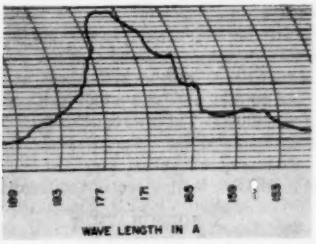

FIG. 1. Band emission curve of copper. $E_b = 500$ volts, $I_b = 3$ ma.

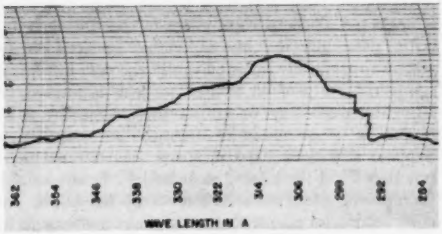

FIG. 2. Band emission curve of chromium. $E_b = 600$ volts, $I_b = 3$ ma.

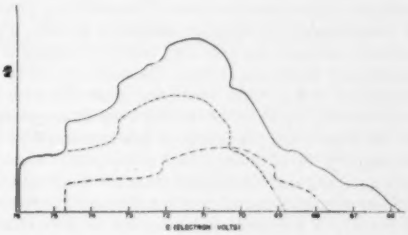

FIG. 3. Electron distribution in copper.

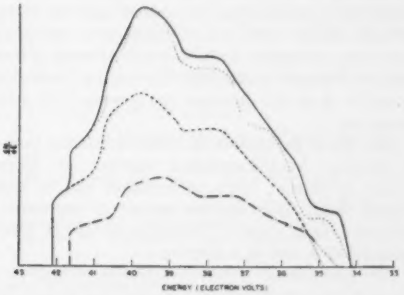

FIG. 4. Electron distribution in chromium.

* This work has been supported in part by the Signal Corps, Air Materiel Command, and ONR.
[1] Piore, Harvey, Gyorgy, and Kingston, Rev. Sci. Instr. 23, 8 (1952).

TABLE I. Summary of experimental results.

	Bandwidth (ev)	M_2 emission edge (ev)	M_{23} separation (ev)	Ratio of M_2 to M_3 intensities
Copper	7.1±0.5	75.9±0.2	1.2 ±0.1	0.51±0.03
Chromium	7.2±1.0	42.1±0.2	0.45±0.1	0.52±0.04

is emphasized by the E^4 factor. Therefore, the M_2 and M_3 bands were completed by the dotted lines at the low energy end, showing the probable position of the bottom of the Brillouin zone.

In order to minimize the effect of fluctuations, the average of experimental chromium curves is plotted modified by the E^4 factor in Fig. 4. The curve shown in Fig. 2 is shown (dotted) for comparison. M_2 and M_3 bands are completed by extrapolation.

The results are summarized in Table I.

PHYSICAL REVIEW VOLUME 87, NUMBER 5 SEPTEMBER 1, 1952

Elastic π-Carbon Scattering*

D. C. PEASLEE
Columbia University, New York, New York
(Received May 22, 1952)

Elastic scattering of 60-Mev π-mesons on carbon is analyzed to determine the following qualitative features of elementary π-nucleon scattering at this energy: p-wave scattering is predominant, with some s-wave interference at a relative phase that favors backscattering. The rather crude interpretation does not indicate d-wave scattering. Spin flip scattering is essentially absent from the C^{12} scattering. The Coulomb interference provides an absolute calibration, from which it is inferred that the p-wave "resonance" energy lies above 60 Mev.

1. INTRODUCTION AND SUMMARY

THE elastic scattering of 60-Mev π-mesons by carbon is analyzed to determine some qualitative features of the elementary π-nucleon scattering process. A second-order perturbation treatment is used, which takes into account the possibly "resonant" nature of the elementary scattering process. The final expressions are similar to a first-order scattering from C^{12} with the addition of a "form factor" arising from the asymmetry of the elementary scattering. A crude estimate of this asymmetry is obtained from comparison with the measured angular distribution from C^{12}. Because of the neglect of multiple scattering, the estimated asymmetry is actually a minimum estimate, and only qualitative conclusions can be drawn.

The qualitative conclusions are that for π-nucleon encounters at 60 Mev in the c.m. system (a) p-wave scattering is predominant, (b) some s-wave scattering is present, and (c) the relative phases of s- and p-wave scattering are such as to favor backscattering at the expense of forward scattering. The rather crude interpretation does not indicate the presence of d-wave scattering.

Spin flip of the nucleon in elastic scattering from C^{12} is forbidden by the exclusion principle. Its absence, within 20 percent limits, is indicated by the experimental data. This absence makes it impossible to determine from elastic C^{12} measurements the relative amounts of $p_{\frac{1}{2}}$ and $p_{\frac{3}{2}}$ scattering.

The pronounced Coulomb interference dip in the $C-\pi^+$ scattering at about 20° makes it possible to form some estimate of the absolute phases of the nuclear scattering amplitudes, since that of the Coulomb scattering is known. It is found that the p-wave scattering is compatible with a "resonance" at an energy higher than 60 Mev and with a half-width of the same order of magnitude. The s-wave scattering has rather little absorption and can be most satisfactorily represented in terms of a repulsive potential or possibly in terms of a far-away bound level of the meson.

2. FORMULATION

We wish to consider the scattering of π-mesons by an aggregation of nucleons, in particular C^{12}. The scattering is assumed to be the sum of single-nucleon scatterings alone; any scattering by multibody potentials is neglected. An important effect in the C^{12} scattering is the possibility that the individual nucleons do not scatter isotropically, as is generally the case if a quasi-compound state of an excited nucleon is formed.[1] A straightforward way to exhibit this anisotropy is by means of a second-order perturbation calculation. Suppose a nucleon fixed in space with internal wave function U_0 in the ground state and U_c in an unstable "compound" state of excitation energy $E_c-i\Gamma_c/2$. The cross section for elastic scattering of spinless mesons by a nucleon with initial spin $s_0=\frac{1}{2}$ is[2]

$$\sigma=\frac{\pi}{k^2}\frac{1}{(2s_0+1)}\sum_{m_i,m_f}\left|\left\langle m_i\left|\sum_c\frac{M_i{}^cM_f{}^{c*}}{E-E_c+i\Gamma_c/2}\right|m_f\right\rangle\right|^2, \quad (1)$$

* This work was performed under the research program of the AEC.

[1] K. A. Brueckner, Phys. Rev. 86, 106 (1952).
[2] H. A. Bethe and G. Placzek, Phys. Rev. 51, 450 (1937).

where m_i, m_f are the initial and final nucleon spin projections, and E is the kinetic plus rest mass energy of the meson. The matrix elements can be written symbolically as

$$M_{i,f}{}^{c}=N_E\int\int U_0(r')V(r-r')e^{i\mathbf{k}_i\cdot\mathbf{r}}U_c{}^*(r')dV'dV, \quad (2)$$

where $N_E=[(1/\pi)k^2(dk)/(dE)]^{\frac{1}{2}}$ is a normalization factor per unit energy for the meson plane wave.

The angular dependence of the scattering is associated with the l values of the incident and scattered mesons; because $s_0=\frac{1}{2}$, spin and parity conservation require that $l_i=l_f$. The differential scattering cross section is

$$\frac{d\sigma}{d\omega}=\frac{\pi}{k^2}\frac{1}{(2s_0+1)}\sum_{m_i,m_f=\pm\frac{1}{2}}|\langle m_i|\sum_j a_j\sum_{mj}C_{\frac{1}{2}lj}{}^{m_i(m_j)m_i}\times C_{jl\frac{1}{2}}{}^{m_j m_l m_f}(2l+1)^{\frac{1}{2}}Y_l{}^{m}(\mathbf{k}_i,\mathbf{k}_f)|m_f\rangle|^2, \quad (3)$$

where

$$a_j{}^{l}=\sum_{c(j,l)}\frac{M_i{}^{c}M_f{}^{c*}}{E-E_c+\frac{1}{2}i\Gamma_c}$$

is the sum over all levels with a given j and given parity, specified in this case by l. In view of the provisory nature of both measurement and calculation, we consider only three possibilities for l and j: $l=0$ and 1, $j=\frac{1}{2}$, $\frac{1}{2}$, $\frac{3}{2}$. Then, designating $m_i=m_f$ as "non-spin-flip" (nf) and $m_i=-m_f$ as "spin flip"(f), one has

$$\begin{aligned}d\sigma_{nf}&=(\pi/k^2)|a_{\frac{1}{2}}{}^{0}+(a_{\frac{1}{2}}{}^{1}+2a_{\frac{3}{2}}{}^{1})\cos\theta|^2d\omega/4\pi,\\ d\sigma_f&=(\pi/k^2)|(a_{\frac{3}{2}}{}^{1}-a_{\frac{1}{2}}{}^{1})\sin\theta|^2d\omega/4\pi.\end{aligned} \quad (4)$$

The use of perturbation theory to obtain the Breit-Wigner formula is, of course, unjustified for strong coupling. It has the remarkable feature, however, of leading to phenomenological results correct in every detail, as is known from nuclear reaction theory. The present calculation simply attempts to exploit this fortunate circumstance and obtain a first-order estimate of the π-carbon scattering. The perturbation treatment should be at least as valid for the motion of the struck nucleon in the C^{12} nucleus as for the π-nucleon collision, which occurs much more rapidly than the transfer of energy among nucleons. Crudely speaking, the "half-width" of the excited nucleon is on the order of a few hundred Mev, while the half-width corresponding to nucleon energy transfer in a nucleus is apparently on the order of a few Mev. Accordingly, the C^{12} nucleus is considered as a number of nucleons occupying independent orbits in a fictitious central potential. If there is one nucleon bound in a potential with wave functions ϕ_0, ϕ_n for the center-of-gravity motion, the argument of (1) becomes

$$\begin{aligned}&\sum_c\sum_n\frac{M_i{}^{c,n}M_f{}^{c,n*}}{E-E_c+\frac{1}{2}i\Gamma_c-E_n+\frac{1}{2}i\Gamma_n},\\ &M_{i,f}{}^{c,n}=M_{i,f}{}^{c}\int\phi_0(r)e^{i\mathbf{k}_{i,f}\cdot\mathbf{r}}\phi_n{}^*(r)dV.\end{aligned} \quad (5)$$

Now for all the lowest excited nuclear states E_n, $\Gamma_n \ll E_c$, Γ_c, so that the last two terms in the denominator of (5) may be neglected, and the sum over n evaluated by closure. Then (5) becomes, with $\Delta\mathbf{k}=\mathbf{k}_i-\mathbf{k}_f$,

$$\sum_{l,j}a_j{}^{l}\phi_0(r)e^{i\Delta\mathbf{k}\cdot\mathbf{r}}\phi_0{}^*(r)dV=\sum_{l,j}a_j{}^{l}\rho(\Delta k), \quad (6)$$

For the C^{12} nucleus with ground state wave function Φ_0 the corresponding expression for the cross section is

$$d\sigma=\frac{\pi}{k^2}\left|\int\Phi_0\sum_q a_q e^{i\Delta\mathbf{k}\cdot\mathbf{r}_q}\Phi_0{}^*\right|^2\frac{d\omega}{4\pi}, \quad (7)$$

where the sum extends over all nucleons. The amplitudes a_q have the forms given in (4) for (nf) and (f) scattering. The subscript q allows for the fact that the amplitudes for neutrons and protons have different magnitudes. In the single-nucleon approximation, the matrix element in (7) becomes $\sum_q a_q\rho_q(\Delta k)$, where ρ_q is the Fourier transform of the single-particle density as given in (6) and $\Delta k=2k\sin\frac{1}{2}\theta$ is the magnitude of $\Delta\mathbf{k}$. The expression (7) is equivalent to the first-order perturbation formula for x-ray scattering in which a_q is an intrinsic form factor for the elementary scattering process.

3. COMPARISON WITH EXPERIMENT

For elastic impacts on C^{12}, f scattering is forbidden by the exclusion principle. The nf scattering contains a coherent part of amplitude $b=\frac{1}{2}(a_q+a_n)$, and an incoherent part of amplitude $b'=\frac{1}{2}(a_p-a_n)$. Then

$$d\sigma_{nf}=\frac{\pi}{k^2}[|b^2|\,|\textstyle\sum_q\rho(\Delta k)|^2+|b'|^2\sum_q|\rho_q(\Delta k)|^2]\frac{d\omega}{4\pi}. \quad (8)$$

The quantities $|\sum_q\rho_q|^2$ and $\sum_q|\rho_q|^2$ are little known, but it seems reasonable to expect the first to be of order $A=12$ times as large as the second. If we furthermore assume[3] that all scattering occurs through a nucleon intermediate state of isotopic spin $T=\frac{3}{2}$, $|b'|=\frac{1}{2}|b|$. Hence to the crude order of accuracy maintained here, the incoherent term can be dropped from (8) in first approximation. Then only the average component, $\bar{\rho}(\Delta k)=(1/A)\sum_q\rho_q(\Delta k)$, is necessary. For $|\bar{\rho}(\Delta k)|^2$ we take the distributions inferred[4] from the production of π-mesons by protons on C^{12}, noting that the quantity written here as $|\bar{\rho}(\Delta k)|^2$ is written as $\rho(\mathbf{k})$ in reference 4 and is plotted in Fig. 1 of that reference.

From (8) and (4) the elastic scattering cross section is

$$d\sigma_{el}=(\pi/k^2)|b_{\frac{1}{2}}{}^{0}|^2(12)^2|\bar{\rho}(\Delta k)|^2\times[1+2\alpha\cos\delta\cos\theta+\alpha^2\cos^2\theta]d\omega/4\pi, \quad (9)$$

where $\alpha=|b_{\frac{1}{2}}{}^{1}+2b_{\frac{3}{2}}{}^{1}|/|b_{\frac{1}{2}}{}^{0}|$ and $\delta=(\delta_1-\delta_0)$ is the cor-

[3] Anderson, Fermi, Long, and Nagle, Phys. Rev. **85**, 936 (1952). If appreciable $T=\frac{1}{2}$ scattering occurs, the quantities b below will be replaced by more complicated averages of $T=\frac{3}{2}$ and $T=\frac{1}{2}$ scattering amplitudes for neutrons and protons. Qualitative conclusions should remain valid, however, as long as $T=\frac{3}{2}$ is the dominant scattering mode.

[4] E. M. Henley, Phys. Rev. **85**, 204 (1952).

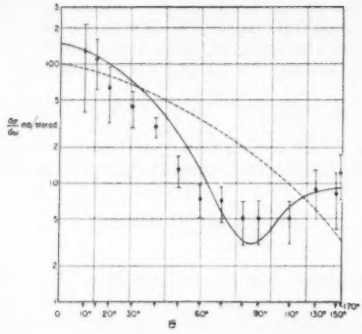

FIG. 1. Angular distribution of elastic π-carbon scattering. The solid circles give the average π^+ and π^- data of reference 5. The solid curve shows the fit of (9) with $\alpha=3$, $\cos\delta=-\frac{1}{2}$. The dashed curve is $|\tilde{\rho}(\Delta k)|^2$, relative scale only. The abscissa is linear in $\Delta k=2k\sin\frac{1}{2}\theta$.

responding relative phase of the two terms. The quantities α and $\cos\delta$ are fitted by comparison with the measurements[5] of $d\sigma_{el}/d\omega$ for 60-Mev π-mesons on C^{12}. To obtain a best fit, the experimental points are multiplied by the reciprocal of the angular factor in (9) and the resulting points compared with the smooth curve of the assumed $|\tilde{\rho}(\Delta k)|^2$. The choices indicated by this procedure are

$$\alpha\sim 3,\ \cos\delta\sim-\tfrac{1}{2}. \tag{10}$$

Figure 1 shows Eq. (9) with these parameters in comparison with the experimental points. The assumed shape of $|\tilde{\rho}(\Delta k)|^2$ is also shown. The values (10) are little better than order-of-magnitude precision, but it is very probable that α considerably exceeds unity and the $\cos\delta<0$. This implies that for the individual nucleon-meson scattering process p-wave scattering is predominant, but that s-wave scattering is also present with a phase such as to enhance backward scattering at the expense of forward scattering.

4. DISCUSSION

Major sources of error in the present treatment are neglect of absorption and of multiple scattering. The absorption may be specified[6] by a mean free path $\lambda\sim 3.5\times10^{-13}$ cm. A crude estimate of absorption effects is the following: for the incident meson wave $\mathbf{k}_i$ put $\mathbf{k}_i'=\mathbf{k}_i[1+i/2\lambda k]$, and for the final meson wave $\mathbf{k}_f$ put $\mathbf{k}_f'=\mathbf{k}_f[1-i/2\lambda k]$, so that $\Delta k'=\Delta k[1+i/\lambda k]$. Then $\Delta k'$ is substituted for Δk as the argument of $\tilde{\rho}$ in (9). The curve in Fig. 1 corresponds approximately to the choice $\tilde{\rho}(\Delta k)=\exp[-\alpha(\Delta k)^2]$ with $\alpha=0.77\times10^{-26}$ cm^2. Then

$$|\tilde{\rho}(\Delta k')|^2=|\tilde{\rho}(\Delta k)|^2\exp[0.25\sin^2\tfrac{1}{2}\theta]. \tag{11}$$

The inclusion of absorption therefore tends in first approximation to increase backscattering relative to forward scattering. In the present case this increase is a maximum of about 1.3, which is small in comparison with the uncertainty in the assumed shape of $\tilde{\rho}(\Delta k)$ and in the $\pi-C$ measurements. This suggests that the effects of absorption may safely be neglected here.

The effect of multiple scattering is always to smooth out the angular distribution. Hence neglect of multiple scattering means that the true π-nucleon angular distribution is somewhat more asymmetrical than here determined, and we are limited to qualitative conclusions on the basis of a minimum asymmetry. The assumed curve of $\tilde{\rho}(\Delta k)$ is based on experiments that also involve a certain amount of neglected multiple scattering. This curve therefore represents a sort of effective density component that contains some contribution from multiple scattering, and it does not seem worth while to attempt further corrections. The most important effect of multiple scattering is to make $\tilde{\rho}(0)<1$, so that only a minimum estimate of the absolute amplitude $|b_{\frac{1}{2}}^0|$ can be obtained. Inserting $1/k^2\approx18$ mb and $d\sigma(0)/d\omega=150$ mb/sterad in Eq. (9), one has $|b_{\frac{1}{2}}^0|>0.18$. If all scattering is assumed to pass through a nucleon state of isotopic spin $T=\frac{3}{2}$, the amplitude for $p-\pi^+$ scattering is $a_{\frac{1}{2}}^0=3/2b_{\frac{1}{2}}^0$. The corresponding cross sections for scattering of 70-Mev (60-Mev in c.m. system) π^+ mesons by protons without spin flip is $\sigma_{nf}>17$ mb. The measured value[3] of the total $p-\pi^+$ cross section at this energy is $\sigma\approx37$ mb, which suggests that $\sigma_f/\sigma_{nf}\lesssim1$. If the p-wave scattering is entirely $j=\frac{3}{2}$, the ratio expected with $\alpha=3$ is $\sigma_f/\sigma_{nf}=\frac{3}{8}$.

It is possible that the experimental points do not correspond to perfect elastic scattering but contain some admixture of slightly inelastic scattering. This scattering can involve spin flip, with

$$d\sigma_f=(\pi/k^2)|b_{\frac{1}{2}}^0|\,(12)^2|\tilde{\rho}(\Delta k)|^2[\gamma^2-\gamma^2\cos^2\theta]d\omega/4\pi, \tag{12}$$

where

$$\gamma=[|b_{\frac{1}{2}}^1-b_{\frac{1}{2}}^1|/|b_{\frac{1}{2}}^0|]\,|\rho'(\Delta k)/\tilde{\rho}(\Delta k)|, \tag{13}$$

and $|\rho'(\Delta k)|^2$ is an effective density for inelastic scattering, summed over the final states involved. As a crude approximation, we take $|\rho'(\Delta k)/\tilde{\rho}(\Delta k)|$ to be independent of Δk. Then if we add (12) and (9), condition (10) becomes

$$(\alpha^2-\gamma^2)/(1+\gamma^2)\approx9,\quad \gamma^2\lesssim\alpha^2/10. \tag{14}$$

Since $\int\sin^2\theta d\omega=2\int\cos^2\theta d\omega$, relation (14) implies that in the experimental points the amount of scattering with spin flip is less than $2(1/10)=\frac{1}{5}$ the amount of scattering without spin flip.

Because of the essential absence of spin-flip scattering, it is not possible to determine the relation between $b_{\frac{1}{2}}^1$ and $b_{\frac{1}{2}}^1$ separately from measurements on C^{12}. Only for the lightest targets like the proton or possibly the deuteron can elastic or almost elastic spin-flip scattering occur with appreciable probability. In π-proton scat-

[6] Byfield, Kessler, and Lederman, Phys. Rev. **86**, 17 (1952).
[6] Brueckner, Serber, and Watson, Phys. Rev. **84**, 258 (1951).

tering the measurement of maximum to minimum $d\sigma/d\omega$ at 180° and $\lesssim$90°, respectively, is a sensitive index of the relation between $a_{\frac{1}{2}}^1$ and $a_{\frac{3}{2}}^1$. For example, with the parameters of (10) the ratio $d\sigma_{\max}/d\sigma_{\min}\approx 17$ or ≈ 4 for the choices $a_{\frac{3}{2}}^1/a_{\frac{1}{2}}^1=1$ or 0.

The asymmetry of the form factor, which leads to a minimum in Fig. 1 around 80°, arises from the interference of an even-l wave with the dominant p-scattering. It is assumed above that the even-l interference is predominantly s-wave. The assumption of d-wave interference instead could only worsen the agreement with observation. The nf d-wave amplitude is $[\frac{3}{4}b_{\frac{3}{2}}+b_{\frac{1}{2}}]\times(3\cos^2\theta-1)$. A destructive interference of this factor with $\cos\theta$ in the 80° region implies considerably larger destructive interference at 180° and a corresponding constructive interference at 0°. This is just the opposite of the behavior of the p–s interference at 0° and 180°, which is in better agreement with experiment. Therefore the measurements in Fig. 1 suggest that the interference is mainly s-wave.

5. COULOMB SCATTERING INTERFERENCE

Coulomb scattering by the protons in C^{12} can be treated quite analogously to the nuclear scattering, except that it is no longer necessary to go so far as second-order perturbations. The first-order elastic scattering amplitude from a bound proton is proportional to

$$\int \phi_0(\mathbf{r}')e^{i\Delta\mathbf{k}\cdot\mathbf{r}}\frac{e^2}{|\mathbf{r}-\mathbf{r}'|}\phi_0(\mathbf{r}')dVdV'=\frac{4\pi e^2}{(\Delta k)^2}\rho(\Delta k). \quad (15)$$

To write the elementary cross section in a form corresponding to (4), we must include a Coulomb amplitude $a^c=2\eta/(1-\cos\theta)$ in the matrix element of (4), where $\eta=e^2/\hbar v=0.01$ for 60-Mev π-mesons. Now since $a_p{}^c=a^c$, $a_n{}^c=0$, one has $|b^c|=|b'^c|=|1/2a^c|$. Dropping the incoherent scattering as before, we have

$$d\sigma_{el}{}^c=\frac{\pi}{k^2}(12)^2|\tilde{\rho}(\Delta k)|^2 \times\left|(1+\alpha e^{i\delta}\cos\theta)Be^{i\beta}+\frac{\eta}{(1-\cos\theta)}\right|^2\frac{d\omega}{4\pi}, \quad (16)$$

where $b_{\frac{1}{2}}{}^0=Be^{i\beta}$.

The scattering of π^+ mesons shows a pronounced interference minimum in the neighborhood of $\theta=20°$. Since the Coulomb term in (16) is in this approximation entirely real, the minimum means that the real part of the matrix element of (16) vanishes at $\cos\theta\approx 0.94$, or

$$B[\cos\beta+2.9\cos(\beta+\delta)]+0.17\approx 0. \quad (17)$$

In order that the scattering amplitudes represent only elastic scattering and absorption but not creation of mesons, one must have $-\pi\leqslant\beta$, $(\beta+\delta)<0$. For $\cos\delta=-\frac{1}{2}$ and $B\geqslant 0.18$ there is only one such solution of (17):

$$\left.\begin{array}{l}\beta=-13°\text{ to }0°\\(\beta+\delta)\approx-133°\text{ to }-120°\end{array}\right\}\text{ as } B=0.18\text{ to }0.38. \quad (18)$$

The upper limit on B given by (18) is larger than that implied by the measured p–π^+ cross section.

The rough values (18) allow the following inferences: if the p-wave scattering is represented by a one-level resonance formula, $b^1=|M|^2/(E-E_c+\frac{1}{2}i\Gamma_c)$, the phase angle $(\beta+\delta)$ indicates that $E_\pi=60$ Mev is below the p-wave "resonance energy" E_c by an amount on the same order as the corresponding "half-width." This is not in disagreement with observation.[3] For the s-scattering the amplitude is small and has a relatively small imaginary part. This would suggest a "far-away" resonance level with $E_c\ll E_\pi$ and accordingly is probably better described by a simple repulsive potential.

As a final check on the internal consistency of this treatment, we may estimate the π^+ cross section at the Coulomb minimum, relative to the nuclear cross section at 0°. From (16) and (9) one has

$$\frac{[d\sigma^c(20°)]}{[d\sigma(0°)]}=\left|\frac{\tilde{\rho}(20°)}{\tilde{\rho}(0°)}\right|\frac{|\sin\beta+0.34\alpha\sin(\beta+\delta)|^2}{1+2\alpha\cos\delta+\alpha^2}\approx 0.1, \quad (19)$$

using the values $\beta\approx-13°$, $(\beta+\delta)\approx-133°$. Thus $(d\sigma^c)/(d\omega)\sim 15$ mb/sterad at the minimum, which is the measured value.[5] This must be regarded as only order-of-magnitude agreement, since angular resolution difficulties will tend always to make the measured minimum too high.

The author wishes to thank Professor R. Serber and Dr. T. A. Green for helpful criticism and suggestions.

The Absorption of a π^- Meson from the K-Shell of H^3†

SAUL A. BASRI
Department of Physics, Columbia University, New York, New York
(Received April 15, 1952)

The branching ratio R of the nonradiative to radiative absorption of a π^- meson by H^3 is calculated on the basis of a phenomenological pseudoscalar weak coupling theory. In order to make R independent of many unknown quantities, it is calculated by means of the formula $R=(R_n/R_\gamma)R_D$, where

$$R_n\equiv W(\pi^-+T\to 3N)/W(\pi^-+D\to 2N),\quad R_\gamma\equiv W(\pi^-+T\to 3N+\gamma)/W(\pi^-+D\to 2N+\gamma),$$

and R_D is the corresponding branching ratio in deuterium, whose experimental value is 2.36. Here W stands for the transition probability per unit time. Using the closure approximation, it is found that $R_\gamma=0.41$. The value of R_n is calculated by means of reasonable assumptions about the Fourier transforms of the initial and final state wave functions and is found to be 2.72. From these values it follows that $R=15.7$.

I. INTRODUCTION

THE investigation of the absorption of π^- mesons from the K-shells of hydrogen and deuterium[1,2] have shown that the π^- meson is either PS (spin zero and odd parity) or PV (spin one and even parity). Furthermore, it has been shown in a previous letter[3] that the branching ratio R of the nonradiative to radiative absorption of a π^- meson in tritium is practically zero for a PV π^- meson. In this paper, R is calculated for a PS π^- meson. It will be shown that $R_{PS}=15.7$ and that the neutrons emitted in the final state are fast ($\simeq$45 Mev) in the nonradiative absorption and relatively slow in the radiative absorption. It thus follows that the detection of any appreciable number of fast neutrons resulting from the absorption of slow π^- mesons in tritium would lend a very strong support to the symmetry hypothesis that the π^- meson is PS.

In order to make R independent of many unknown quantities, such as the wave function of a $3N$-system and coupling constants, it will be calculated by means of the following formula:

$$R(T)=[R_n/R_\gamma]R(D), \tag{1}$$

where

$$R_n\equiv\frac{W(\pi^-+T\to 3N)}{W(\pi^-+D\to 2N)}\equiv\frac{W_n(T)}{W_n(D)}, \tag{1a}$$

$$R_\gamma\equiv\frac{W(\pi^-+T\to 3N+\gamma)}{W(\pi^-+D\to 2N+\gamma)}\equiv\frac{W_\gamma(T)}{W_\gamma(D)}, \tag{1b}$$

and

$$R(D)\equiv W_n(D)/W_\gamma(D)=2.36^1 \tag{1c}$$

is an experimentally known quantity. Here W stands for the transition probability per unit time.

It should be mentioned that the reaction $\pi^-+T\to 3N+\pi^0$ is not energetically possible.

† This work has been done in partial fulfillment of the requirements for the Ph.D. degree at Columbia University, New York, New York.

[1] Panofsky, Aamodt, and Hadley, Phys. Rev. **81**, 565 (1951).
[2] R. E. Marshak, Revs. Modern Phys. **23**, 137 (1951).
[3] Messiah, Caianiello, and Basri, Phys. Rev. **83**, 652 (1951).

II. RADIATIVE ABSORPTION

The very sharp peak at 130 Mev, observed experimentally[1] in the γ-ray spectrum resulting from the reaction $\pi^-+D\to 2N+\gamma$, leads to the following two important conclusions:

(1) The photon takes up most of the available energy, which implies that the most probable energy of the neutrons in the final state is much smaller than the maximum value allowed by the conservation of energy.

(2) The neutrons interact strongly in the final state. The effect of this is to depress even more the average energy of the neutrons in the final state.

From this it follows that if we relax the restriction imposed by the conservation of energy and sum over all the energy states of the neutrons, the effect would be only to overestimate W_γ slightly.

The closure theorem may then be used and the result will be completely independent of any assumption about the final state wave function (about which very little is known).

Our method of calculation will, therefore, consist of assuming that

$$E_f-E_i=(cp-130)\text{ Mev},$$

where E_f and E_i are the total final and initial energies, respectively, and p is the momentum of the γ-ray.

For convenience, the units $\hbar=1$, $c=1$ will be used in all the following calculations.

According to the time dependent perturbation theory,

$$W_\gamma=2\pi\int\sum_f\langle|(\Psi_fH'\Psi_i)|^2\rangle_{sp}\delta(p-130)(2\pi)^{-3}d\mathbf{p}, \tag{2}$$

where Ψ_i and Ψ_f are the total initial and final state wave functions, respectively, H' is the perturbing potential and $\langle\ \rangle_{sp}$ indicates the operation of averaging over initial spin states and summing over final spin states and polarizations. By using the closure theorem, we get

$$\sum_f|(\Psi_fH'\Psi_i)|^2=\sum_f(\Psi_iH'^\dagger\Psi_f)(\Psi_fH'\Psi_i)=(\Psi_iH'^\dagger H'\Psi_i).$$

Substituting this value into (2) gives

$$W_\gamma=(2\pi)^{-2}\int\langle(\Psi_i H'^\dagger H'\Psi_i)\rangle_{\Omega}\delta(p-130)d\mathbf{p}. \quad (3)$$

The nonrelativistic limit of H may be written in the form[4]

$$H'=\alpha\textstyle\sum_\mu\mathcal{O}_\mu, \quad \mathcal{O}_\mu=\boldsymbol{\sigma}_\mu\cdot\boldsymbol{\epsilon}_\lambda p^{-\frac{1}{2}}e^{i\mathbf{p}\cdot\mathbf{x}_\mu}\tau_\mu^-, \quad (4)$$

where α is a constant, $\boldsymbol{\sigma}_\mu$ the Pauli spin operator associated with the μth nucleon, $\boldsymbol{\epsilon}_\lambda$ the unit polarization vector of the photon, $\mathbf{x}_\mu$ the coordinate of the μth nucleon, and τ_μ^- the isotopic variable operator which converts a proton into a neutron. Since (3) and (4) are applicable to both H^2 and H^3, the ratio R_γ defined in (1b) becomes

$$R_\gamma=\frac{\int\sum_{\mu,\nu}\langle(\Psi_{T,m}\mathcal{O}_\mu^\dagger\mathcal{O}_\nu\Psi_{T,m})\rangle_{\Omega}\delta(p-130)d\mathbf{p}}{\int\sum_{\mu,\nu}\langle(\Psi_{D,m}\mathcal{O}_\mu^\dagger\mathcal{O}_\nu\Psi_{D,m})\rangle_{\Omega}\delta(p-130)d\mathbf{p}}. \quad (5)$$

(A) Radiative Absorption in Deuterium

The H^2 ground state wave function may be written in the form

$$\Psi_{D,m}=\phi_D(r)\,{}^3\chi_m\,{}^1\tau_0, \quad (6)$$

where

$${}^3\chi_m=\begin{cases}{}^3\chi_1=(++),\\ {}^3\chi_0=2^{-\frac{1}{2}}[(+-)+(-+)]\\ {}^3\chi_{-1}=(--),\end{cases} \quad (6a)$$

is the triplet state spin function, and

$${}^1\tau_0=2^{-\frac{1}{2}}[(pn)-(np)] \quad (6b)$$

is the singlet isotopic variable eigenfunction.

From (4) and (6) it follows that

$$\mathfrak{M}_D(p_0)\equiv\int\sum_{\mu,\nu=1}^{2}\langle(\Psi_{D,m}\mathcal{O}_\mu^\dagger\mathcal{O}_\nu\Psi_{D,m})\rangle\delta(p-p_0)d\mathbf{p}$$
$$=8\pi p_0[1-\tfrac{1}{3}F_D(p_0)], \quad (7)$$

where

$$p_0=130/\hbar c=6.6\times10^{12}\ \text{cm}^{-1},$$

and

$$F_D(p_0)\equiv\int|\psi_D(r)|^2e^{i\mathbf{p}_0\cdot\mathbf{r}}d\mathbf{r}. \quad (8)$$

We may now evaluate F_D with the help of the wave function[5]

$$\psi_D(r)=(4\pi)^{-\frac{1}{2}}u(r)/r, \quad u(r)=N(e^{-\gamma r}-e^{-\beta r}),$$
$$N^2=8.70\times10^{-12}\ \text{cm}^{-1}, \quad \beta=11.4\times10^{-12}\ \text{cm}^{-1},$$
$$\gamma=2.30\times10^{-12}\ \text{cm}^{-1}. \quad (9)$$

We thus find

$$F_D(p_0)=0.44. \quad (10)$$

(B) Radiative Absorption in Tritium

The H^3 ground state wave function may be written in the form[2,6]

$$\Psi_{T,m}=\psi_T\phi_m, \quad \phi_m=2^{-\frac{1}{2}}({}^2\chi_m'\,{}^2\tau_{-\frac{1}{2}}-{}^2\chi_m\,{}^2\tau_{-\frac{1}{2}}'), \quad (11)$$

where

$$\begin{aligned}&{}^2\chi_{\frac{1}{2}}=2^{-\frac{1}{2}}[(++-)-(+-+)],\\ &{}^2\chi_{-\frac{1}{2}}=2^{-\frac{1}{2}}[(--+)-(-+-)],\\ &{}^2\chi_{\frac{1}{2}}'=6^{-\frac{1}{2}}[(++-)+(+-+)-2(-++)],\\ &{}^2\chi_{-\frac{1}{2}}'=6^{-\frac{1}{2}}[(--+)+(-+-)-2(+--)]\end{aligned} \quad (11a)$$

are the doublet spin eigenfunctions, and

$$\begin{aligned}&{}^2\tau_{-\frac{1}{2}}=2^{-\frac{1}{2}}[(nnp)-(npn)],\\ &{}^2\tau_{-\frac{1}{2}}'=6^{-\frac{1}{2}}[(nnp)+(npn)-2(pnn)]\end{aligned} \quad (11b)$$

are the isotopic variable eigenfunctions of He^3.

An explicit expression for the radial function ψ_T, which fits the binding energy of H^3 very well, has been obtained by Pease and Feshbach;[7] it is a ${}^2S_{\frac{1}{2}}$ space symmetric with about 2 percent ${}^4D_{\frac{1}{2}}$ admixture. The ${}^2S$ part may be written in the form

$$\psi_T=(175)^{-\frac{1}{2}}\sum_{r=1}^{2}A_r\exp[-\tfrac{1}{2}\lambda_r(x_{12}+x_{23}+x_{31})], \quad (11c)$$

where

$$x_{\mu\nu}\equiv|\mathbf{x}_\mu-\mathbf{x}_\nu|,$$

and

$$A_1=1.24, \quad A_2=3.35; \quad \lambda_1=0.9, \quad \lambda_2=1.7.$$

The unit of length is 1.184×10^{-13} cm.

From (4) and (11) it follows that

$$\mathfrak{M}_T(p_0)\equiv\int\sum_{\mu,\nu=1}^{3}\langle(\psi_{T,m}\mathcal{O}_\mu^\dagger\mathcal{O}_\nu\Psi_{T,m})\rangle\delta(p-p_0)d\mathbf{p}$$
$$=8\pi p_0[1-\tfrac{1}{3}F_T(p_0)], \quad (12)$$

where

$$F_T(p_0)\equiv\int|\psi_T|^2\textstyle\sum_{\mu>\nu}e^{i\mathbf{p}_0\cdot\mathbf{x}_{\mu\nu}}d\tau$$
$$=3\times0.65. \quad (13)$$

It now follows from (5), (7), (10), (12), and (13) that

$$R_\gamma=\frac{\mathfrak{M}_T(p_0)}{\mathfrak{M}_D(p_0)}=\frac{1-\frac{1}{3}F_T(p_0)}{1-\frac{1}{3}F_D(p_0)}=0.41. \quad (14)$$

III. NONRADIATIVE ABSORPTION

(A) Deuterium

The transition probability per unit time, for the reaction $\pi^-+D\to2N$, may be written in the form

$$W_n(D)=(4\pi)^{-1}MK_f\langle|(\Psi_{2N,m'}H'\Psi_{D,m})|^2\rangle_{\Omega}, \quad (15)$$

[4] S. Tamor, Phys. Rev. **82**, 38 (1951).
[5] J. F. Marshall and G. E. Guth, Phys. Rev. **78**, 738 (1950).
[6] F. Villars, Helv. Phys. Acta **20**, 480 (1947).
[7] R. L. Pease and H. Feshbach, Phys. Rev. **81**, 142 (1951).

where

$$K_f^2/M = \mu c^2 - |\text{B.E.}(\text{H}^2)| \simeq 138 \text{ Mev},$$
$$\Psi_{2N,m'} = \psi_{2N}(r)\, {}^3\chi_{m'} n(1) n(2) \tag{16}$$

is the final state $2N$ wave function, and

$$H' = \beta \sum_\mu \mathcal{O}_\mu', \quad \mathcal{O}_\mu' = \sigma_\mu \cdot \nabla_\mu \tau_\mu^- \tag{17}$$

is the nonrelativistic limit of the perturbing potential.[4]

If we substitute (6), (16), and (17) into (15) we get

$$W_n(D) = (\beta^2/3\pi) M K_f \textstyle\sum_i |I_i|^2, \tag{18}$$

where

$$I_i \equiv \int \psi_{2N}^*(r) \partial \psi_D(r)/\partial x_i d\mathbf{r} = i \int \phi_{2N}^*(K) \phi_D(K) K_i d\mathbf{K}. \tag{19}$$

Here, ϕ_{2N} and ϕ_D are the Fourier transforms of ψ_{2N} and ψ_D, respectively.

Since the energy available to the two neutrons in the final state is 138 Mev, it is clear that the high Fourier components of ψ_{2N} and ψ_D are the important ones. Therefore, wave functions which have been derived with the aid of low energy parameters cannot be used. However, it seems reasonable to assume that $\phi_{2N}(K)$ is peaked at $K = K_f$ and ϕ_D is peaked at $K = 0$. On the basis of this assumption the integral (19) breaks into two terms.

$$I_i = i\left[\phi_{2N}^*(0) \int \phi_D(K) K_i d\mathbf{K} + K_{fi} \phi_D(K_f) \int \phi_{2N}^*(K) d\mathbf{K}\right].$$

Since $\phi_D(K)$ is an even function of K, the first term vanishes and the result is

$$\textstyle\sum_i |I_i|^2 = (2\pi)^3 K_f^2 |\psi_{2N}(0)|^2 |\phi_D(K_f)|^2. \tag{20}$$

The quantity $|\phi_D(K_f)|^2$ may be evaluated from the wave equation

$$(-\nabla^2/M + V_D)\psi_D(r) = -\epsilon \psi_D(r)$$

and is found to be

$$(2\pi)^{\frac{1}{2}} \phi_D(K_f) = (E_f + \epsilon)^{-1} \int V_D(r) \psi_D(r) e^{-i\mathbf{K}_f \cdot \mathbf{r}} d\mathbf{r}.$$

The integral to the right is nothing but the high Fourier transform of $V_D \psi_D$. Since ψ_D is more or less constant about the origin whereas V_D is not, we may write approximately

$$\int V_D(r) \psi_D(r) e^{-i\mathbf{K}_f \cdot \mathbf{r}} d\mathbf{r} \simeq \psi_D(0) \mathcal{U}_D(K_f),$$

where

$$\mathcal{U}_D(K_f) \equiv \int V_D(r) e^{-i\mathbf{K}_f \cdot \mathbf{r}} d\mathbf{r} \tag{21}$$

is the high Fourier transform of V_D. Therefore,

$$(2\pi)^{\frac{1}{2}} \phi_D(K_f) \simeq -E_f^{-1} \psi_D(0) \mathcal{U}_D(K_f).$$

Substituting this value into (20), and then (20) into (18), we get

$$W_n(D) = (\beta^2/3\pi)(M K_f^3/E_f^2) \times |\psi_D(0)|^2 |\psi_{2N}(0)|^2 |\mathcal{U}_D(K_f)|^2. \tag{22}$$

(B) Tritium

In the reaction $\pi^- + T \to 3N$, under consideration, it seems reasonable to assume that the probability of a close collision of two nucleons in H^3 is much greater than that of a close collision of all three nucleons simultaneously. For this reason, we will assume that the proton shares the meson rest mass with only one of the neutrons in H^3. From this it follows that the final state will consist of two fast neutrons with equal and opposite momenta, in very much the same manner as in H^2, and one relatively slow neutron.

Since the low energy states of the slow neutron will be the most probable, it will be plausible to apply the closure approximation to the sum over these states just as in the case of the radiative absorption.

It can be easily shown from (11), (11a), and (11b) that

$$\Psi_{T,m} = 3^{-\frac{1}{2}} \psi_T [(pnn)\mathcal{U}(2,3)\mathcal{U}_m(1) + (npn)\mathcal{U}(3,1)\mathcal{U}_m(2) + (nnp)\mathcal{U}(1,2)\mathcal{U}_m(3)], \tag{23}$$

where

$$\mathcal{U}(\mu, \nu) \equiv 2^{-\frac{1}{2}} [\mathcal{U}_+(\mu)\mathcal{U}_-(\nu) - \mathcal{U}_+(\nu)\mathcal{U}_-(\mu)]$$

and $\mathcal{U}_\pm(\mu)$ are the spin eigenfunctions of the μth nucleon.

There are three independent final states, corresponding to the three possibilities that the slow neutron may be particle 1, 2, or 3. By symmetry, it is obvious that the contribution to the transition probability per unit time, $W_n(T)$, is the same in each and everyone of these cases. We may therefore consider only one of them, say the case where particle 3 is the slow neutron and particles 1 and 2 the fast neutrons, and then multiply $W_n(T)$ by 3. There are two terms in (23) that contribute to this case, corresponding to the two possibilities that either of neutrons 1 or 2 in the final state was initially a proton. These are given by the first two terms of (23).

Owing to the fact that ψ_T is symmetric,[3] the two nucleons absorbing the meson can only collide in states of even orbital momenta. In our calculation, we will consider only the S states. It is not obvious what the relative contribution of the D states is. Their neglect is partly justified by the fact that a close collision is more probable for states of lower angular momenta, and partly by the fact that not much can be gained by their inclusion since so little is known about tensor forces at high energies.

From this we see that the essential difference between the nonradiative absorption in H^2 and H^3 is that in H^3

the colliding nucleons may be in ^3S or ^1S states whereas in H^3 only the ^3S state comes in.

Since the π^- meson is PS (odd parity) the two fast neutrons in the final state will have to be in a ^3P state as in the case of H^3. This is a consequence of the fact that the markedly different energy of the slow neutron makes it distinguishable from the other two neutrons. It is, thus, no longer necessary to antisymmetrize the final state wave function with respect to all three neutrons, but only with respect to the two fast ones.

According to this, the final state wave function may be written in the form

$$\Psi_{2N}=\psi_{2N}(x_{12})\,{}^3\chi_m\psi_{\mathbf{K}_3}(\mathbf{x}_3)\mathcal{U}_n n(1)n(2)n(3), \quad (24)$$

where $\psi_{2N}\,{}^3\chi_m$ refer to the fast neutrons, $\psi_{\mathbf{K}_3}\mathcal{U}_n$ to the slow neutron, and $n(1)n(2)n(3)$ is the isotopic variable eigenfunctions of all three neutrons.

In terms of $^{1,3}\chi_m$ the initial state wave function (23) becomes, after omitting the last term,

$$\Psi_{T,\pm\frac{1}{2}}=(1/2\sqrt{3})[(pnn)\phi_\pm(2,3)+(npn)\phi_\pm(3,1)], \quad (25)$$

where

$$\phi_\pm(2,3)\equiv\pm\{{}^3\psi_T[\sqrt{2}\,{}^3\chi_{\pm1}\mathcal{U}_\mp-{}^3\chi_0\mathcal{U}_\pm] -{}^1\psi_T\,{}^1\chi_0\mathcal{U}_\pm\}, \quad (25a)$$

$$\phi_\pm(3,1)\equiv\mp\{{}^3\psi_T[\sqrt{2}\,{}^3\chi_{\pm1}\mathcal{U}_\mp-{}^3\chi_0\mathcal{U}_\pm] +{}^1\psi_T\,{}^1\chi_0\mathcal{U}_\pm\}. \quad (25b)$$

It is understood in these expressions that $^{1,3}\chi_m$ refers to nucleons 1 and 2, and $\mathcal{U}_n$ to nucleon 3.

Keeping in mind the above remarks, we get

$$W_n(T)=(3/4\pi)MK_f\int\langle|(\Psi_{2N,m}{}^*H'\Psi_{T,m})|^2\rangle_{\text{Av}}d\mathbf{K}_3.$$

After substituting (17), (24), and (25) into this expression and carrying the averaging and summation over spins, we get

$$W_n(T)=(\beta^2/4\pi)MK_f\int\sum_i[|{}^1I_i|^2+2|{}^3I_i|^2]d\mathbf{K}, \quad (26)$$

where

$${}^{1,3}I_i\equiv\int\psi_{2N}{}^*(x_{12})\psi_{\mathbf{K}_3}(\mathbf{x}_3) \times\{\partial[{}^{1,3}\psi_T(x_{12},\mathbf{x}_3)]/\partial x_i^{(1)}\}d\mathbf{x}_{12}d\mathbf{x}_3. \quad (27)$$

Here the quantities $^{1,3}\psi_T$ refer to the H^3 space wave function with nucleons 1 and 2 in $^{1,3}S$ states.

In terms of the Fourier transforms ϕ_{2N}, $\phi_{\mathbf{K}_3}$, and ϕ_T the integral (27) becomes

$${}^{1,3}I_i=i(2\pi)^{-\frac{1}{2}}\int d\mathbf{K}_3'\int d\mathbf{K}_{12}\phi_{2N}(K_{12})\,{}^{1,3}\phi_T(K_{12},\mathbf{K}_3') \times(K_{12}')_i\int\psi_{\mathbf{K}_3}(\mathbf{x}_3)e^{i(\mathbf{K}_3'\cdot\mathbf{x}_3}d\mathbf{x}_3.$$

As before, we will assume that $\phi_{2N}(K_{12})$ is peaked at $K_{12}=K_f$ and $^{1,3}\phi_T(K_{12},\mathbf{K}_3)$ is peaked at $K_{12}=0$. From this it follows, exactly as in the case of H^2, that

$$\sum_i|{}^{1,3}I_i|^2=K_f{}^3|\psi_{2N}(0)|^2 \times\left|\int d\mathbf{K}_3'\,{}^{1,3}\phi_T(K_f,\mathbf{K}_3')\int\psi_{\mathbf{K}_3}(\mathbf{x}_3)e^{i(\mathbf{K}_3'\cdot\mathbf{x}_3}dx_3\right|^2.$$

We may now use the closure theorem to sum over K_3:

$$\int d\mathbf{K}_3\sum_i|{}^{1,3}I_i|^2=(2\pi)^3K_f{}^3|\psi_{2N}(0)|^2 \times\int|{}^{1,3}\phi_T(K_f,\mathbf{K}_3)|^2d\mathbf{K}_3.$$

Substitute this expression into (26), and we find

$$W_n(T)=(\beta^2/4\pi)MK_f{}^3|\psi_{2N}(0)|^2({}^1\Lambda+2\,{}^3\Lambda), \quad (28)$$

where

$${}^{1,3}\Lambda=(2\pi)^3\int|{}^{1,3}\phi_T(K_f,\mathbf{K}_3)|^2d\mathbf{K}_3. \quad (28a)$$

As before, we may evaluate $^{1,3}\phi_T(K_f,\mathbf{K}_3)$ from the wave equation

$$[-(\nabla_{12}{}^2+\tfrac{3}{4}\nabla_3{}^2)/M+{}^{1,3}V_T+\epsilon]\psi_T(x_{12},\mathbf{x}_3)=0.$$

In this way, we find

$$-(2\pi)^3E_f\,{}^{1,3}\phi_T(K_f,\mathbf{K}_3)\simeq\int{}^{1,3}\psi_T(0,\mathbf{x}_3)e^{-i(\mathbf{K}_3\cdot\mathbf{x}_3}d\mathbf{x}_3 \times\int{}^{1,3}V_T(x_{12},\mathbf{x}_3)e^{-i(\mathbf{K}_f\cdot\mathbf{x}_{12}}d\mathbf{x}_{12}.$$

Assuming the existence of two-nucleon forces only, we may write

$$V_T(x_{12},\mathbf{x}_3)=V_{NP}(x_{12})+V_{NP}(x_{13})+V_{NN}(x_{23}).$$

Substituting this value into the above expression, and assuming that the Fourier transform of $V_{NP}(x_{12})$ is peaked about K_f whereas the Fourier transforms of $V_{NP}(x_{13})$ and $V_{NN}(x_{23})$ are peaked about $K\simeq0$, we get

$$-(2\pi)^3E_f\,{}^{1,3}\phi_T(K_f,\mathbf{K}_3) ={}^{1,3}\mathcal{U}_{NP}(K_f)\int{}^{1,3}\psi_T(0,\mathbf{x}_3)e^{-i(\mathbf{K}_3\cdot\mathbf{x}_3}d\mathbf{x}_3,$$

where

$${}^{1,3}\mathcal{U}_{NP}(K_f)=\int{}^{1,3}V_{NP}(x)e^{-i(\mathbf{K}_f\cdot\mathbf{x}}d\mathbf{x}. \quad (29)$$

After substitution of this value of ϕ_T into (28a) and then (28a) into (28), we find finally

$$W_n(T)=(\beta^2/4\pi)(MK_f{}^3/E_f{}^3)|\psi_{2N}(0)|^2 \times[{}^1P_T|{}^3\mathcal{U}_{NP}(K_f)|^2+2\,{}^3P_T|{}^3\mathcal{U}_{NP}(K_f)|^2], \quad (30)$$

where

$$^{1,3}P_T \equiv \int |{}^{1,3}\psi_T(0, \mathbf{x}_3)|^2 d\mathbf{x}_3 \tag{31}$$

is the probability density that nucleons 1 and 2 are at zero distance in a $^{1,3}S$ state in the H^3 nucleus.

(C) The Ratio R_n

Since $\mathcal{U}_D(K_f)$ is the high Fourier transform of the N–P potential in a ^3S state, we may set

$$|\mathcal{U}_D(K_f)|^2 = |{}^3\mathcal{U}_{NP}(K_f)|^2. \tag{32}$$

In analogy with (31) we write

$$P_D \equiv |\psi_D(0)|^2. \tag{33}$$

Substituting (32) and (33) into (22), we find finally from (22) and (30) that

$$R_n \equiv \frac{W_n(T)}{W_n(D)} = 2\left(\frac{3}{4}\frac{^3P_T}{P_D} + \frac{1}{4} \times \frac{3}{2}\frac{^1P_T}{P_D}\frac{|{}^1\mathcal{U}_{NP}(K_f)|^2}{|{}^3\mathcal{U}_{NP}(K_f)|^2}\right). \tag{34}$$

The factor 2 arises from the fact that there are 2 neutrons in the vicinity of the proton in H^3 as compared to 1 neutron in H^2. The factors $\frac{3}{4}$ and $\frac{1}{4}$ are, respectively, the statistical weights of the triplet and singlet states of the colliding nucleons in H^3. Finally the factor $\frac{3}{2}$ arises from the fact that the spin sum in the single state is $\frac{3}{2}$ times larger than that in the triplet state.

An n–p potential which has been derived from high energy n–p scattering experiments is given by[8]

$$-V_{NP}(x) = \tfrac{1}{2}(1+P_M)g^2 e^{-kr}/r = g^2 e^{-kr}/r \text{ for } S \text{ states},$$

where

$$g^2 = \begin{cases} 0.405 \text{ for triplet state} \\ 0.280 \text{ for singlet state} \end{cases}$$

and

$$1/k = 1.2 \times 10^{-13} \text{ cm}.$$

We thus find from these values and (29) that

$$|{}^1\mathcal{U}_{NP}(K_f)|^2 / |{}^3\mathcal{U}_{NP}(K_f)|^2 = (0.280/0.405)^2 \simeq \tfrac{1}{2}. \tag{35}$$

[8] Hadley, Kelly, Leith, Segrè, Wiegand, and York, Phys. Rev. 75, 351 (1949).

To evaluate $^{1,3}P_T/P_D$ properly, it is necessary to have H^2 and H^3 wave functions that are derived with the help of high energy parameters. Since such functions are not known, an estimate will be obtained from (9) and (11c). We thus find

$$^{1,3}P_T/P_D = 1.45. \tag{36}$$

Substituting (35) and (36) into (34), we find finally

$$R_n = 2.72. \tag{37}$$

IV. CONCLUSIONS

Summarizing, we have from (14) and (37)

$$R_\gamma = \frac{1-\frac{1}{2}F_T(k_0)}{1-\frac{1}{2}F_D(k_0)} = 0.41,$$

and

$$R_n = 2\frac{P_T}{P_D}\left[\frac{3}{4} + \frac{1}{4} \times \frac{3}{2}\frac{|{}^1\mathcal{U}_{NP}(K_f)|^2}{|{}^3\mathcal{U}_{NP}(K_f)|^2}\right] = 2.72.$$

Substituting these values into (1) we find

$$R(T) = W_n(T)/W_\gamma(T) = 15.7. \tag{38}$$

The quantities $F_T(k_0)$ and $F_D(k_0)$ depend on the low Fourier components of the H^2 and H^3 wave functions, which are well known. The contribution of tensor forces to R_γ is rather negligible. On the other hand, the ratio P_T/P_D occurring in R_n is very much dependent on the high Fourier components of the H^2 and H^3 wave functions. However, from the estimated radii of H^2 and H^3 it is felt that the value 1.45 found in (36) is not too unreasonable. Thus, any serious discrepancy of (38) with a future experimental value may indicate that the contribution of tensor forces at high energies, which has been neglected here, is appreciable after all.

In any case the detection of an appreciable number of fast neutrons would definitely rule out the slim possibility that the π^- meson is PV and would confirm the symmetry hypothesis that it is PS.

The author wishes to express his gratitude to Professors J. Steinberger and R. Serber for several valuable discussions and to Professor R. E. Marshak for suggesting the problem.

Selection Rules Imposed by Charge Conjugation and Charge Symmetry

A. PAIS AND R. JOST
Institute for Advanced Study, Princeton, New Jersey
(Received April 8, 1952)

It is found that the invariance with respect to charge conjugation and charge symmetry combined leads to selection rules, additional to those following from covariance and gauge invariance arguments. Besides rigorous selection rules which hold for certain processes involving neutral particles (mesons and photons) only, there exist weak selection rules according to which certain boson-boson transitions are less probable by a factor $e^2/\hbar c$ than the corresponding transitions in which an additional photon is emitted. The rules are stated in Sec. III, and some examples are given.

I. INTRODUCTION

THE existence of at least two bosons heavier than the π-meson ("heavy bosons") seems to be reasonably well established by recent cosmic-ray observations. They are: the τ-meson, a particle with unit charge decaying into three charged π-mesons;[1] and the "light V_0" particle, a neutral object presumably undergoing decay into a pair of oppositely charged π's.[2]

In the present unsatisfactory state of the theory of particles and fields, the safest way of approach to the study of the interrelations of these and other particles is surely to ask how much we can learn about, say, the decay of heavy bosons with as little use as is possible of field theoretical details. This means that in first instance one tries to find some order among various decay schemes by means of the sole use of conservation laws (of energy, momentum, angular momentum, and parity) and of additional invariance considerations, e.g., gauge invariance.

In quantum electrodynamics we have a further symmetry property at our disposal, namely, the one between positive and negative electric charges. It has been shown by Furry[3] that this symmetry can be expressed as an invariance property of the theory with respect to charge conjugation, a concept first introduced by Kramers.[4] Furry's theorem is very useful in two (obviously related) respects: first, it establishes certain absolute selection rules. Secondly, it implies that, in the calculation in some given order of perturbation theory of a matrix element for some particular process, certain "graphs" give no contribution. These are the well-known closed loops consisting of an odd number of electron lines (or charged boson lines).

In their analysis of the τ-meson decay, Fukuda and Miyamoto[5] found that certain graphs in the expansion of the S-matrix in meson theory give vanishing contributions as a result of the application of theorems, rather analogous to the Furry theorem, to a closed nucleon loop which represents the transitory nucleon pairs. Their results can be expressed as follows: Consider a graph consisting exclusively of a closed nucleon loop and of external boson lines.[6] Define the following three numbers characteristic of the graph:

$n(v)$: The total number of vector couplings operative in the vertices of the loop, irrespective of whether they involve scalar or vector mesons. (Note: if one kind of meson is coupled to nucleons in more than one way, like, for example, scalar mesons with scalar and vector coupling, it is here to be understood that one uses one coupling per vertex in one graph). $n(v)$ also comprises all electromagnetic vector couplings of the proton that may occur if external photons are involved.

$n(t)$: The total number of tensor couplings, irrespective of whether they refer to the tensor coupling of vector mesons or to the pseudo (=dual) tensor coupling of pseudovector mesons. $n(t)$ also comprises whatever electromagnetic couplings of nucleons of the Pauli-type that may occur.

$n(\tau_{(3)})$: The total number of neutral meson couplings involving $\tau_{(3)}$, the z component of the isotopic spin vector. (Note: if a certain neutral meson interaction is proportional to $\alpha+\beta\tau_{(3)}$, one has to take for the present purposes either the "α-part" or the "β-part" per vertex in one graph.)

Then the following theorems hold:

(I) If none of the external lines are photons, and if some of them are charged bosons, the graph gives no contribution if $n(v)+n(t)+n(\tau_{(3)})=$odd.

(II) If none of the external lines are photons or charged mesons, the graph gives no contribution if either $n(\tau_{(3)})=$odd, or, for even $n(\tau_{(3)})$, $n(v)+n(t)=$odd.

(III) If the external lines are exclusively photons and neutral mesons, the graph gives no contribution if $n(v)+n(t)=$odd.

The physical contents of these rules is of course intimately connected with the fact that nucleons with v or t coupling to an external field are subjected to a force equal and opposite to the one for antinucleons,

[1] C. F. Powell *et al.*, Phil. Mag. **42**, 1040 (1951).
[2] See references 2–11 in A. Pais, Phys. Rev. **86**, 663 (1952), for a list of the experimental papers on V-decay. More recently, another particle decaying into a pair of charged π-mesons has tentatively been identified by Danysz, Lock, and Yekutieli, Nature **169**, 364 (1952).
[3] W. H. Furry, Phys. Rev. **51**, 125 (1937).
[4] H. A. Kramers, Proc. K. Ned. Acad. Wet. **40**, 814 (1937).
[5] H. Fukuda and Y. Miyamoto, Progr. Theoret. Phys. **4**, 389 (1950). See also K. Nishijama, Progr. Theoret. Phys. **6**, 614 (1951) and A. Pais, reference 2, footnote 26.
[6] The usual couplings are considered in which one meson occurs per vertex.

while protons are acted on by a force opposite to that for neutrons in the case of a $\tau_{(3)}$ coupling. More formally, these theorems may be considered as consequences of two distinct symmetry properties of the theory:

(a) The symmetry with respect to an interchange of the nucleon and the antinucleon with all their attributes like electric charge and mesic coupling constants. This symmetry can be expressed by means of invariance for general charge conjugation (see Sec. III).

(b) The symmetry, apart from electromagnetic effects, with respect to the interchange of protons and neutrons (charge symmetry). This symmetry[7] can be expressed as the invariance with respect to a certain transformation in isotopic space.

It is the aim of this note to answer the question: under what circumstances of coupling and for what kinds of processes do the rules (I)–(III) represent absolute selection rules? Thus, we will be interested in a rigorous forbiddenness rather than in the vanishing of a matrix element to a given order, which in mesonic phenomena seems to be not a very useful statement anyhow. Following Furry's original procedure[8] we will give direct proofs based on the two mentioned invariance properties. Hence, the arguments will not explicitly refer to a power series expansion of the S-matrix.

In the next section the necessary formal properties of the charge conjugation and charge symmetry transformations are given. In Sec. III the selection rules are stated and a number of examples for specific processes is given. The main practical interest at present lies of course in the heavy boson decays.

II. FORMAL CONSIDERATIONS

A. Charge Conjugation

1. Fermions

Charge conjugation is defined independently of the representation chosen for the γ_μ in the Dirac equation[5]

$$[\gamma_\mu \partial/\partial x_\mu + m]\psi = 0, \tag{1}$$

but to fix ideas we take the γ_μ to be Hermitian. The adjoined equation to Eq. (1) is

$$(\partial/\partial x_\mu)\bar{\psi}\gamma_\mu - m\bar{\psi} = 0, \quad \bar{\psi} = \psi^\dagger \gamma_4. \tag{2}$$

The charge conjugate wave functions are obtained by adjoining in a Lorentz invariant way solutions of Eq. (1) to those of Eq. (2). One uses the following well-known procedure:[9] Define ψ^C and $\bar{\psi}^C$ by

$$\psi^C = C\bar{\psi}^T, \quad \bar{\psi}^C = (C^{-1}\psi)^T, \tag{3}$$

respectively, where the matrix C satisfies

$$C^{-1}\gamma_\mu C = -\gamma_\mu{}^T. \tag{4}$$

The $\gamma_\mu{}^T$ satisfy the same anticommutation relations as do the γ_μ, so C exists. As the γ_μ are Hermitian, C can be taken to be unitary

$$C^\dagger C = 1. \tag{5}$$

By comparing Eq. (4) with its transposed one finds that $C^T C^{-1}$ commutes with all γ_μ. Hence,

$$C^T C^{-1} = \beta \cdot 1,$$

where β is a number. β is independent of the choice of representation. Indeed, a change of representation of the γ_μ is expressed by

$$\gamma_\mu{}' = S^{-1}\gamma_\mu S, \tag{6}$$

and the corresponding transformation of C is (apart from an irrelevant phase factor)

$$C' = SCS^T, \tag{7}$$

whence $C'^T C'^{-1} = C^T C^{-1}$. Thus, β can be determined by explicitly constructing C in a special representation and one finds $\beta = -1$:

$$C^T C^{-1} = -1. \tag{8}$$

Considering Eq. (7) as the transformation of C under the proper Lorentz group (excluding reflections), for which S is uniquely determined, one has $C' = C$. There is a well-known arbitrariness in the choice of S for space-, time-, and space-time reflections. In the case of space reflections, one has, according to Eq. (7), $C' = C$, provided one chooses $S = i\gamma_4$.

If time reflections are involved, and one requires that, with $\psi' = S\psi$, also $\psi^{C'} = S\psi^C$ one has to replace Eq. (7) by $C' = -SCS^T$, due to $\bar{\psi}' = -S\bar{\psi}$. One can then again choose S such that $C' = C$, so that C may be considered as a scalar for the full Lorentz group. One has $S = \gamma_5\gamma_4$ (time-reflection); $S = i\gamma_4$ (space-time reflection).[10] However, it is not a physical requirement that C be a scalar; in particular the considerations of Sec. III are independent of the behavior of C under reflections.

Now let $\bar{\psi}\Omega\psi$ generally represent any of the five well-known covariant structures that can be formed by taking for Ω appropriate functions of the γ_μ; in obvious shorthand we denote them by s, v, t, pv, ps. According to Eqs. (3) and (8):

$$\bar{\psi}^C \Omega \psi^C = -\psi^T C^{-1} \Omega C \bar{\psi}^T.$$

Hence, using Eq. (4) and the anticommutation properties of ψ and $\bar{\psi}$:

$$\begin{aligned} \bar{\psi}^C \Omega \psi^C &= +\bar{\psi}\Omega\psi \text{ in the cases: } s, pv, ps, \\ &= -\bar{\psi}\Omega\psi \text{ in the cases: } v, t. \end{aligned} \tag{9}$$

(t denotes the tensor and the pseudotensor case as well.)[11] In Eq. (9) an infinite C-number (which can be

[7] The proton-neutron mass difference is neglected. The symmetry considered here should not be confused with charge independence, i.e., invariance with respect to all rotations in isotopic space.

[8] $\hbar = c = 1$; $x_\mu = x, y, z, it$.

[9] W. Pauli, Ann. Inst. H. Poincaré **6**, 109 (1936); J. Schwinger, Phys. Rev. **74**, 1439 (1948). T denotes transposition.

[10] This choice is due to G. Racah, Nuovo cimento **14**, 322 (1937). For the relevance of the choices of S in the case of more than one spinor field see C. N. Yang and J. Tiomno, Phys. Rev. **79**, 495 (1950).

[11] It has been suggested by Okayama [Phys. Rev. **75**, 308 (1949)] to use the difference in properties of s, pv, ps on the one

disposed of elegantly) has been dropped. The implications of the connections (9) for selection rules were first noted by Furry[12] in his original paper. They are occasionally rediscovered.[13]

Now let $S(x_\mu)$ represent any one of the S-functions representative for a spinor field:

$$S(x)=[\gamma_\mu\partial/\partial x_\mu-m]\Delta(x),$$

where Δ is either a solution of $(\Box-m^2)\Delta=0$ or of $(\Box-m^2)\Delta=-\delta(x)$. If $\Delta(-x)=\epsilon\Delta(x)$, $\epsilon=\pm1$, the corresponding S-function satisfies, according to Eq. (4),

$$[C^{-1}S(-x)C]^T=\epsilon S(x).$$

With the help of this relation one proves, in the interaction representation:

(1) The anticommutation relations are invariant under the C-transformation:

$$\{\psi_\alpha{}^C(x_\mu),\bar\psi_\beta{}^C(x_\mu')\}=\{\psi_\alpha(x_\mu),\bar\psi_\beta(x_\mu')\}.$$

(2) The invariance of the vacuum expectation value of any P-bracket. This follows directly from the invariance of the elementary P-bracket:

$$\langle P[\psi_\alpha{}^C(x),\bar\psi_\beta{}^C(x')]\rangle_{\text{vac}}=\langle P[\psi_\alpha(x),\bar\psi_\beta(x')]\rangle_{\text{vac}}.$$

Note that this invariance is true independent of whatever γ-matrices may occur within the general P-bracket.[14]

2. *Bosons.*

For a charged boson field ϕ the C-transformation is given by

$$\phi^C(x)=C\phi(x)=\phi^*(x), \tag{10a}$$

$$\phi^{C*}(x)=C\phi^*(x)=\phi(x), \tag{10b}$$

irrespective of the Lorentz transformation properties of ϕ. A neutral boson field remains unaffected. Again one verifies easily that, in the interaction representation, the commutation relations and vacuum expectation values are invariant for the C-transformation.

B. Charge Symmetry

Describing the proton-neutron in the usual way by an 8-component nucleon spinor ψ, the interchange of proton and neutron is expressed by[15]

$$\psi'=T\psi \qquad T\cong\begin{pmatrix}0&1\\1&0\end{pmatrix}.$$

If the nucleons are coupled to charged mesons ϕ, the role of positive and negative mesons has to be interchanged, so the "T-transformation" on ϕ is

$$\phi'=\phi^*, \qquad \phi^{*\prime}=\phi.$$

For neutral meson fields the transformation depends on whether the coupling to nucleons goes via $\tau_{(3)}$ or "1." Call the corresponding fields $\phi_{(3)}$ and $\phi_{(0)}$. In the first case proton and neutron have opposite mesic coupling,

$$\phi_{(3)}'=-\phi_{(3)}, \tag{11}$$

while

$$\phi_{(0)}'=\phi_{(0)}. \tag{12}$$

Comprising ϕ and $\phi_{(3)}$ to a vector $\phi_{(i)}=\phi$ in isotopic space we have

$$\phi'=T\phi \qquad T\cong\begin{pmatrix}1&&\\&-1&\\&&-1\end{pmatrix}.$$

The most general interaction invariant under T is of the form $a(\bar\psi\tau^+\psi+\phi^*\bar\psi\tau^-\psi)+b\phi_{(3)}\bar\psi\tau_{(3)}\psi+c\phi_{(0)}\bar\psi\psi$ with real a, b, c. Charge independence requires in addition $a=b$.

Commutation relations and vacuum expectation values are invariant under the T-transformation. We note that

$$CT\phi=\phi, CT\phi^*=\phi^*, CT\phi_{(3)}=-\phi_{(3)}, CT\phi_{(0)}=\phi_{(0)}. \tag{13}$$

In connection with a discussion of V-decay it has been suggested[3] that there may exist fermions with different mass than the nucleon but for the rest with analogous properties. Denoting the 8-component spinor for the ith kind of such particles by ψ_i, one can now consider interactions of the general type

$$G_{ij,k}[\bar\psi_i\tau^+\psi_j\phi_k+\bar\psi_j\tau^-\psi_i\phi_k{}^*],$$

where ϕ_k denotes charged mesons of the kind k. This interaction is charge symmetric if $G_{ij,k}=G_{ji,k}$. Neutral meson couplings of the kind

$$(\bar\psi_i\tau_{(3)}\psi_j+\bar\psi_j\tau_{(3)}\psi_i)\phi_{(3),k} \quad\text{or}\quad (\bar\psi_i\psi_j+\bar\psi_j\psi_i)\phi_{(0),k}$$

are automatically charge symmetric. Provided that the condition on $G_{ij,k}$ is satisfied, all considerations of the next section hold irrespective of the number of nucleon-like fermions.

III. SELECTION RULES

Consider a general system of nucleons, mesons, and photons in mutual interaction. The Lagrangian L of

---

hand and v, t on the other as a criterion for the exclusion of certain nucleon-meson interactions. This criterion, stated as a "conservation of mesic charge," would at present not seem applicable as it would in particular exclude the existence of any coupling between pseudoscalar mesons and nucleons.

[12] See reference 3, Eq. (18) where the connections are given for c-number spinors. The formal derivation was given earlier by W. Pauli, see, e.g., reference 9.

[13] See S. R. de Groot and H. A. Tolhoek, Physica **16**, 456 (1950); R. H. Good, Jr., Phys. Rev. **86**, 620 (1952).

[14] The conditions (5) and (8) which have to be satisfied by C still leave open the possibility of multiplying C with an arbitrary phase. It is irrelevant for what follows whether one wishes to assign to C a different phase for different spinor fields.

[15] If one wishes to consider this transformation as a representation in spin space of a rotation in a 3-space one would have to replace T by iT.

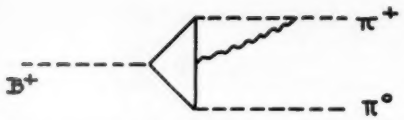

FIG. 1. Example of an allowed graph for transition (14).

this system remains unchanged if one applies C to all relevant operators in L and changes the sign of all coupling constants referring to v- and t-interactions [see Eq. (9)].

It is already clear from Sec. I that only then can we at all have selection rules if we assume: each scalar meson field that may occur is coupled to nucleons by either a scalar or a vector interaction (i.e., not by both simultaneously). Likewise a pv field may only have either pv or pt interaction. With this assumption (and only then) we may replace the prescription for the sign change of v- and t-coupling constants to a change in sign of the fields with v- and (or) t-interaction. We understand by invariance under general charge conjugation the invariance of L with respect to C and this change of sign of fields.

In addition, we shall assume L to be invariant with respect to T. This implies:

(1) Neutral fields transforming like Eqs. (11) and (12) are coupled to nucleons exclusively via $\tau_{(3)}$, 1, respectively.

(2) The electromagnetic field does not satisfy this requirement. Provisorily we omit it from our considerations. It is reincluded in subsection (b) below.

We now investigate various decay processes.

A. Boson-Boson Transitions (photons excluded)

Consider the S-matrix element for a given transition in which the fields representing the initial and the final particles are $\phi_a, \phi_b, \cdots \phi_n$. S is then generally of the form

$$S=\int d^4x_a \cdots d^4x_n \phi_a(x_a)\phi_b(x_b)\cdots\phi_n(x_n)K(x_a,\cdots,x_n),$$

where K is a complicated kernel involving implicitly the occurrence of all possible transitory nucleons and mesons. L is invariant under C and T and, thus, also under CT. S is also invariant under CT but, in general, not under C and T separately. For if in a process charged external bosons are involved, the application of C to S would lead us from the given process to one in which all these bosons now have opposite charge, i.e., we now have in general to do with another process. Thus we have further to distinguish two cases:

(α) *Transitions Involving Charged (External) Bosons.* These are forbidden if

$$n(\tau_{(3)})+n(v)+n(t)=\text{odd}. \qquad \text{(I)}$$

Proof: apply CT to S and denote this by priming all quantities:

$$S'=\int d^4x_a \cdots d^4x_n \phi_a'(x_a)\cdots\phi_n'(x_n)K'(x_a\cdots x_n).$$

Of course $S'=S$. Furthermore, $K'=K$ as all vacuum expectation values are invariant. Thus, according to Eqs. (9) and (13),

$$S'=(-1)^{n(\tau_{(3)})+n(v)+n(t)}S,$$

which proves (I).

Example: consider the process

$$B_v^+ \to \pi^+ + \pi^0, \qquad (14)$$

where B_v^+ is a positively charged vector meson with vector and/or tensor coupling. π^+, π^0 are the usual pseudoscalar mesons. Let π^0 be described by a $\phi_{(0)}$-field. Then process (14) is forbidden. Likewise

$$B_v^0 \to \pi^+ + \pi^- \qquad (15)$$

is forbidden if the B^0 field is of the $\phi_{(0)}$ type.

Note: the forbiddenness of processes (14) and (15) is a strict one only as long as the electromagnetic field is excluded. It will be discussed presently what happens if photons are also brought in.

(β) *Transitions Involving no Charged (External) Bosons.* Now besides (I) also

$$n(\tau_{(3)})=\text{odd is forbidden.}^{16} \qquad \text{(II)}$$

Hence from (I) and (II):

$$\text{if } n(\tau_{(3)})=\text{even}, \quad n(v)+n(t)=\text{odd is forbidden.} \qquad \text{(II')}$$

The proof is immediate from the application of T separately to S which is now legitimate.

Examples: the following two processes are forbidden

$$B^0{}_{\text{neut}(3)} \to 2\pi^0, \qquad (16)$$

$$B^0{}_{\text{neut}(3)} \to 2\pi^0. \qquad (17)$$

This is true whether π^0 is described by a $\phi_{(3)}$ or by a $\phi_{(0)}$ field.

B. Boson-Boson Transitions, Photons Included

Now only the C-invariance is strictly enforced. By the same argument as mentioned above, one can only expect rigorous selection rules if all external bosons

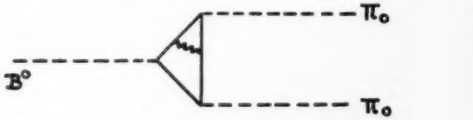

FIG. 2. Example of an allowed graph for transition (16).

[16] The formal generalization of (II) in the case of a charge independent theory is $n(\tau_{(3)})=\text{odd}$ is forbidden. This would apply to cases where the only external lines are $\phi_{(1)}$ and $\phi_{(0)}$, a situation which has no physical significance.

lines denote neutral mesons. One shows directly that, with this restriction,

$$n(v)+n(l)=\text{odd is forbidden.} \qquad \text{(III)}$$

Examples: (1) The 2 γ-decay of a neutral vector meson is rigorously forbidden, as first noted by Sakata and Tanikawa.[17]

(2) The 3γ-decay of a neutral pv meson with pv coupling is rigorously forbidden;[18] (the 2γ-decay is forbidden for parity reasons).

It is now also necessary to review the processes which according to (I) and (II) were strictly forbidden. To see what happens it is enough to consider the examples (14)–(17):

Transitions (14) and (15): These are now allowed as can be seen by inspection of a low order graph for process (14) drawn in Fig. 1. The waved line denotes a photon. When replacing B^+, π^0 by B^0, π^-, Fig. 1 also applies to Eq. (15).

Transition (16): Same situation, a representative graph is given in Fig. 2. Note that the internal nucleon lines here can only be protons.

Transition (17): This is still strictly forbidden as it falls under the jurisdiction of (III).

It should be noted that the internal photon line occurring in Figs. 1 and 2 makes the transition probabilities for processes (14), (15), and (16) proportional to at least the second power of $\alpha=1/137$. This means that

$$B_v^+\rightarrow\pi^++\pi^0+\gamma, \qquad (14')$$

$$B_v^0\rightarrow\pi^++\pi^-+\gamma, \qquad (15')$$

$$B^0{}_{\text{str}(3)}\rightarrow 2\pi^0+\gamma \qquad (16')$$

are more probable by a factor α than Eqs. (14), (15), and (16), respectively. It should be emphasized that this circumstance makes it indispensable to include such transitions as Eqs. (14′)–(16′) in the discussion of competing disintegration modes when studying V-decay. An example is given in reference 2, Sec. V.

Thus, for these processes the remarkable inversion occurs that the transition with an additional photon is favored to that without one. Hence, in as far as one can make qualitative statements concerning a theory fraught with divergences, one may say that for processes (14) and (15) a weak selection rule is still operative. This is true for any process to which (I) and (II) apply.

In a recent paper by one of us,[2] use was made of the Fukuda-Miyamoto theorems, mentioned in the introduction for the discussion of certain V-decay processes. It is easily seen that all processes which were found to be forbidden in low order are actually either strictly forbidden or else weakly forbidden in the sense just mentioned.

[17] S. Sakata and Y. Tanikawa, Phys. Rev. **57**, 548 (1940).

[18] In discussing the γ-decay of neutral mesons, R. Oehme, Z. Naturforsch **7a**, 55 (1952), reaches some conclusions which contradict the rigorous selection rule (III).

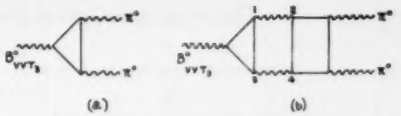

FIG. 3. Graphs referring to transition (17).

C. Boson-Fermion Transitions

We consider here decays in which electron-positron pairs may be created through electromagnetic interaction in addition to bosons. Always following the same reasoning it is readily seen that no rigorous selection rule is possible in this case. In fact, C inverts the charge of bosons *and* fermions, while T inverts the charge of bosons only. Therefore, the application of the CT-transformation to the S-matrix element for a process of the present type leads, in general, to the element for another process.

However, it is easy to see that in one instance a weak selection rule holds. This is for the case of a transition involving neutral bosons only plus a single electron-positron pair. One shows that now (III) is a weak selection rule, with the understanding that the pair counts as one v-interaction. Thus, for example, $\pi^0\rightarrow e^++e^-+\gamma$ ($\sim\alpha$ less probable than $\pi^0\rightarrow 2\gamma$) is more probable by a factor α than $\pi^0\rightarrow e^++e^-$, for a pseudoscalar meson. As was pointed out by Oehme[18] and by Fermi,[19] the latter process is not rigorously forbidden, however.

After this paper had been written, a survey article by L. Michel[20] came to our notice in which the rules (I)–(III) are also given for the restricted coupling scheme in which they are of absolute validity. Nevertheless, we believed it to be useful to give the present more comprehensive account in which no explicit study of graphs is necessary (see Fig. 3).[21]

[19] E. Fermi, Proc. Rochester Conference, 1952. The forbiddenness indicated by J. Steinberger, Phys. Rev. **76**, 1180 (1949), Table I, always refers to the lowest order in e.

[20] L. Michel, *Progress in Cosmic Ray Physics* (Interscience Publishers, Inc., New York, 1952), Chapter III. See especially pp. 142–144.

[21] Michel approaches the problem by attempting to locate in each graph a particular closed loop to which the Fukuda-Miyamoto theorems can be applied. This procedure suffices as one only allows *neutral* mesons to occur in intermediary states, and to this case Michel confines his attention. This method is not applicable in general, however, as it may lead to pitfalls of the following kind: Consider the graph in Fig. 3(a) for the process (17). Its contribution vanishes according to (II). Consider next the higher order graph drawn in Fig. 3(b), where 12 and 34 denote charged ps mesons. Now rule (I) has to be applied to the triangle as well as to the square, but neither yield a factor zero. The zero actually comes from the combination of the graph of Fig. 3(b) with one in which the charges along 12 and 34 have been interchanged. It is just for such reasons that we felt the need of a derivation in which no such subtleties are needed.

In reference 20, Tables II and III, some processes stated to be forbidden by Furry's theorem should be reinterpreted using the discussion on weak selection rules given above. In the present paper Fermi interactions have not been considered. A further selection rule pertaining to this case and of interest for processes like $\pi-\mu$ decay has been given by Michel, reference 20, p. 144. This is readily shown also to be a weak selection rule.

Electrical and Optical Properties of Rutile Single Crystals*

D. C. CRONEMEYER†
Laboratory for Insulation Research, Massachusetts Institute of Technology, Cambridge, Massachusetts
(Received January 9, 1952)

Clear, synthetic rutile (TiO_2) single crystals have been investigated by electrical and optical methods. It seems possible to correlate the high temperature conductivity ($E_G = 3.05$ ev) with the threshold of optical absorption at low temperatures (3.03 ev) and with the maximum of the photoconductivity (3.03–3.06 ev). This evidence indicates an energy gap *ca* 3.05 ev for rutile as an insulator.

Semiconducting rutile, prepared by hydrogen reduction at temperatures $\lesssim 800°C$, shows a blue color arising from an optical absorption maximum at *ca* 1.7μ (0.73 ev). Conductivity-temperature plots for slightly reduced specimens indicate an optical activation energy of 0.68 ev. A theoretical calculation for the ionization of the first electron from an oxygen vacancy indicates 0.74 ev as the expected value, in good agreement with the experimental results. At room temperature the mobility of electrons in slightly reduced single crystals is *ca* 10^{-4} m²/v-sec.

Strongly reduced rutile is opaque; a comparison of electron concentrations calculated from weight loss and Hall coefficient data shows that for samples in which the electron concentration is $10^{25}/m^3$, all contribute to conduction at room temperature.

INTRODUCTION

TWO major projects of the Laboratory for Insulation Research are concerned with long-range studies on (1) transition stages from insulators to semiconductors to metals, and (2) dielectrics of high dielectric constant, especially ferroelectrics. Rutile TiO_2 occupies a key position in both projects since it is a basic constituent of the ferroelectric titanates, and the series TiO_2-Ti_2O_3-TiO-Ti is an interesting oxide system in which a progressive transition from insulator to metal is accomplished by reduction.[1] Finally, TiO_2 itself has much higher dielectric constants and indices of refraction than most crystals and a large dielectric anisotropy.[2–5] Therefore, new information concerning the characteristic behavior of electrons in a medium of high electronic and atomic polarizability can be obtained.

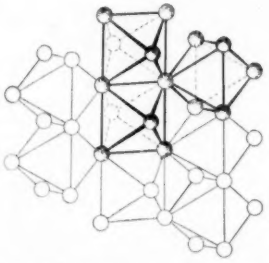

FIG. 1. Octahedra-packing diagram for rutile TiO_2.

The Laboratory has studied TiO_2 in some respects,[6–8] but its investigations until now have been limited to ceramic samples since the natural rutile crystals are usually impure. Recently, colorless large single crystals of synthetic rutile have been grown by the boule technique.[9] Therefore, the present research was undertaken to establish the fundamental electrical and optical properties of these crystals and the changes occuring upon reduction.

The rutile-TiO_2 crystal is composed of titanium and oxygen in their highest valence states $+4$ and -2, respectively. Titanium is a transition metal of the iron group, the normal atomic electronic configuration of which is $(4s)^2(3d)^2$ outside the argon core.[10] In the periodic system the place of titanium is just beyond the point in the iron transition group where the 4*s* shell is filled and it becomes easier to put the next electron into a 3*d* shell than into the 4*p* shell.[11] This fact might lead to an *s-p-d* hybridization resulting in a sixfold oxygen co-ordination, which may be described as the formation of a TiO_6 octahedron. Likewise, from the standpoint of a purely ionic structure, the radius ratio of Ti^{+4} to O^{-2} would lead one to expect a sixfold co-ordination of Ti with O.[12] In the rutile crystal each octahedron shares two of its edges with other octahedra while each of the remaining two free corners is shared with two other octahedra[13] (Fig. 1).

* Sponsored by the ONR, the Army Signal Corps, and the Air Force under ONR contract N5ori-07801.

† Present address, General Electric Company, Syracuse, New York.

[1] P. Ehrlich, Z. Elektrochem. **45**, 362 (1939).
[2] A. Schröder, Z. Krist. **67**, 485 (1928).
[3] T. Liebisch and H. Rubens, Sitzber. preuss. Akad. Wiss., Physik.-math. Kl. 211 (1921).
[4] W. Bärwald, Z. Krist. **7**, 168 (1883).
[5] C. W. Carstens, Z. Krist. **67**, 261 (1928).
[6] A. von Hippel *et al.*, "High Dielectric Constant Ceramics I and II," Lab. Ins. Res., N.D.R.C. Reports No. 300 (1944); 540 (1945).
[7] von Hippel, Breckenridge, Chesley, and Tisza, Ind. Eng. Chem. **38**, 1097 (1946).
[8] A. von Hippel, Revs. Modern Phys. **22**, 221 (1950).
[9] We are greatly indebted to Dr. C. H. Moore of the National Lead Company for the specimens used in this research.
[10] J. C. Slater, *Introduction to Chemical Physics* (McGraw-Hill Book Company, Inc., New York, 1939), p. 346.
[11] G. Herzberg, *Atomic Spectra and Atomic Structure* (Dover Publications, New York, 1944), p. 148.
[12] L. C. Pauling, *The Nature of the Chemical Bond* (Cornell University Press, Ithaca, 1948).
[13] R. W. G. Wyckoff, *Crystal Structures Handbook* (Interscience Publishing Company, New York, 1948).

This construction of the rutile crystal can be shown to be more stable than that of the other two modifications of TiO_2, brookite and anatase, where three and four edges of each octahedron are shared, respectively.[14] The density of the crystals,[2] anatase, brookite and rutile, progresses from 3.9 to 4.12 to 4.22 g/cm³ in accord with the fact that the dense rutile is the most stable form. The two other modifications are transformed into rutile upon heating near 1000°C. Within a TiO_6 group in rutile, the oxygen engaged in edge-sharing of this octahedron with two others have a bond distance of 1.89A from the central titanium ion, while the remaining two oxygens are found at the somewhat greater distance of 1.97A.

The assumption of completely ionic binding would make a regular octahedron the basic building block of TiO_2. With this assumption, Born and Bollnow[15] carried out a Madelung calculation for rutile which relates the electrostatic potential to the axial ratio c/a of the tetragonal unit cell. That analysis predicts an axial ratio c/a=0.721 for a maximum Madelung constant. In the actual crystal this would result in a too short O–O distance and the axial ratio[12] observed is c/a=0.644.

The failure of a purely ionic calculation to predict the correct c/a ratio and unequal Ti-O distances extends also to the magnitudes and temperature coefficients of the dielectric constants and refractive indices. It seems probable[16] that TiO_2 represents a transition between polar and nonpolar binding. Kirkwood[17] and Bartholomé[18] have made approximate calculations applying to such intermediate cases which show the change of dipole moment with internuclear separation. This change of dipole moment results in a negative temperature coefficient of the dielectric constant and refractive index.[2,6,19] Instead of visualizing octahedra, one may refer to chains of Ti-O-O-Ti-O-O-Ti ions,[20] alternate layers running perpendicular to one another throughout the crystal and oriented normal to the *c* axis. There is no tendency toward cleavage. The picture of Ti-O chains permits one to interpret the reststrahl vibrations as deformation and valence vibrations.[6] The Ti-O chains are so situated in the crystal that only a deformation vibration is excited by light with its *E* vector ∥ to the *c* axis (extraordinary ray), while light with its *E* vector ⊥ to the axis excites a combination of deformation and valence vibrations.[21] The optical dielectric constants[2] are: $(2.40)^2\perp$, $(2.57)^2\parallel$. Beyond the reststrahl region[3] the values of the dielectric constant at 300 μ approach those for static measurements,[3] namely 83 ⊥, 167 ∥ (Fig. 2).

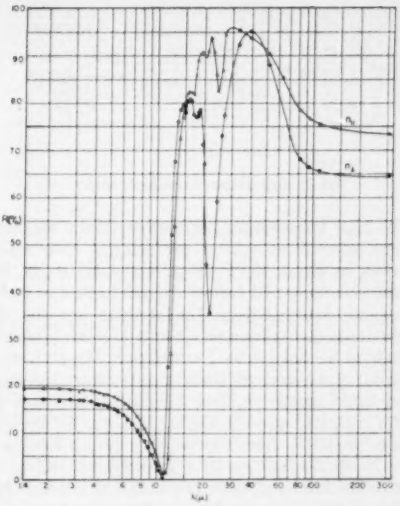

FIG. 2. Reflection coefficient in percent for rutile TiO_2 natural single crystals. Data from Liebisch and Rubens, reference 3.

THE INTRINSIC ELECTRICAL AND OPTICAL PROPERTIES OF RUTILE SINGLE CRYSTALS

Sample Preparation

Two samples of synthetic rutile were obtained in the form of boules, oriented by their x-ray Laue patterns, and sliced parallel and perpendicular to the *c* axis with a diamond wheel (accuracy *ca* 1°). After polishing, the first boule (*I*) showed several lineage flaws under the polarization microscope, with regions differing in extinction position by a degree or two. The second boule was a perfect single crystal with the exception of a small region on one face. Several prismatic bars *ca* 1×1×10 mm were cut from slices of boule *II* for the high temperature conductivity measurements; optical transmission measurements were made on polished plates.

High-Temperature Conductivity

Figure 3 shows one of the sample holders for high temperature conductivity measurements. Its construction has the advantage that the quartz holder extends outside the furnace into the room-temperature zone; hence the leakage is small and independent of the sample temperature. The temperature control of the furnace allowed maintenance of the temperature to *ca*±0.1° at 1000°C over long periods.

[14] L. Pauling, Z. Krist. **67**, 377 (1928).
[15] M. Born and O. F. Bollnow, Naturwiss. **13**, 559 (1925).
[16] A. Eucken and A. Büchner, Z. physik. Chem. **B27**, 321 (1934).
[17] J. G. Kirkwood, Physik. Z. **33**, 259 (1932).
[18] E. Bartholomé, Z. physik. Chem. **B23**, 131 (1933).
[19] E. Bretscher, Trans. Faraday Soc. **30**, 684 (1934).
[20] M. Born, *Dynamik der Kristallgitter* (Teubner, Leipzig, 1915); *Atomtheorie des festen Zustandes*, Encl. d. math. Wissenschaften V 3, 527 (1923); M. Born and M. Göppert-Mayer, *Dynamische Gittertheorie der Kristalle*, Handbuch der Physik **24**, 623 (1933).
[21] See also the case of UO_2 as discussed in P. Pringsheim, *Fluorescence and Phosphorescence* (Interscience Publishers, New York, 1949).

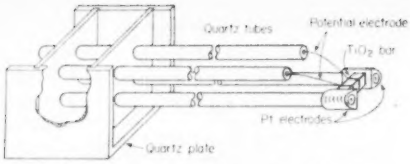

FIG. 3. High temperature sample holder.

The high temperature conductivity data for both crystal orientations fall on two straight lines which intersect at about 900°C (Figs. 4 and 5); about 200 points were measured for each characteristic to avoid ambiguous interpolation. The straight line for the conductivity $\perp$ to the c axis extends to lower temperatures than the line for the $\parallel$ orientation. The activation energies in ev derived from a Boltzmann equation $\sigma=\sigma_0\ e^{-\epsilon/kT}$ are: $\perp$, 1.53 at 350–850°C, 1.83 at 850–1400°C; $\parallel$, 1.53 at 500–950°C, 1.83 at 950–1400°C. Below *ca* 900°C the conductivity is field-strength sensitive for fields above 10^3 v/m (see insert of Fig. 4). The ac conductivity, measured at 100 cycles between 250° and 500°C checks the dc data almost exactly.

If the high temperature conductivity corresponds to an intrinsic electronic conduction, it follows from the band theory[22] that the actual gap width between the filled and the conduction band is twice the activation energy indicated on the previous $\log\sigma$ *vs* $1/T$ plot; i.e., $\sigma=\sigma_0 e^{-E_G/2kT}$. A tabulation of the constants σ_0 and E_G is given in Table I. A simple estimate of the values of σ_0 may be obtained by setting $\sigma_0=n_0eb$, where n_0 is the total number of valence electrons (4 per TiO_2), e is the electronic charge, and b the mobility in m^2/v-sec. Since the number of TiO_2's per m^3 is 3.18×10^{28}, $n_0=1.27\times10^{29}/m^3$. In general, the mobilities for electrons

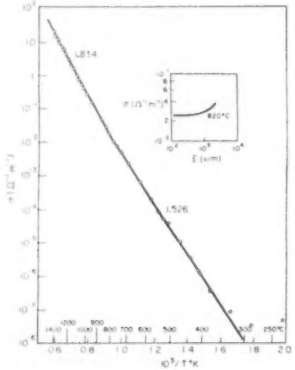

FIG. 4. High temperature conductivity-temperature plot for rutile $TiO_2\perp$ to c axis.

[22] A. H. Wilson, *Theory of Metals* (Cambridge University Press, Cambridge, 1936).

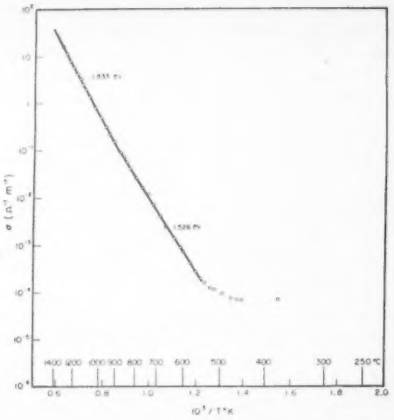

FIG. 5. High temperature conductivity-temperature plot for rutile $TiO_2\parallel$ to c axis.

in crystalline insulators at high temperatures are of the order of 10^3 to 10^5 m^2/v-sec (0.1 to 10 cm^2/v-sec); hence one obtains $\sigma_0=2\times10^5$ to 2×10^7 $\Omega^{-1}m^{-1}$ as the expected values in reasonable agreement with those of Table I.

That the conductivity is essentially electronic is evident from the fact that large currents can be passed for hours without destructive effect.

According to this interpretation of the high temperature conductivity, the optical eigenabsorption might be expected at 3.05 ev or 4070A.

The Optical Eigenabsorption and Associated Photoconductivity of Rutile

A quantitative study of the optical absorption edge of rutile single crystals requires index of refraction data near the edge for a calculation of the reflection loss. Such measurements were made on a small prism cut from a rutile single crystal (3 mm height, 3 mm face length, breaking angle 18°49′, c axis bisecting the base angle, and an a axis along the breaking edge). Figure 6 shows the results for the ordinary ray[23] in synthetic rutile as compared to the data of previous observers.[2,4] The refractive index measurements in the visible

TABLE I. Compilation of σ_0 and E_G values for rutile.

	$\sigma_0(\Omega^{-1}m^{-1})$	E_G(ev)	$\sigma_0(\Omega^{-1}m^{-1})$	E_G(ev)
($\parallel$)	4.59×10^5	3.05 (500–950°C)	8.38×10^6	3.67 (950–1400°C)
($\perp$)	2.76×10^5	3.05 (350–850°C)	6.82×10^6	3.67 (850–1400°C)
	$\frac{\sigma_{011}}{\sigma_{0\perp}}=1.66$		$\frac{\sigma_{011}}{\sigma_{0\perp}}=1.23$	

[23] The ordinary ray, often designated as n_0, is here indicated as n^* signifying that the E vector of the light is $\perp$ to the c axis of the crystal. Likewise, $n-$ denotes a wave with the E vector $\parallel$ to the c axis (the extraordinary ray).

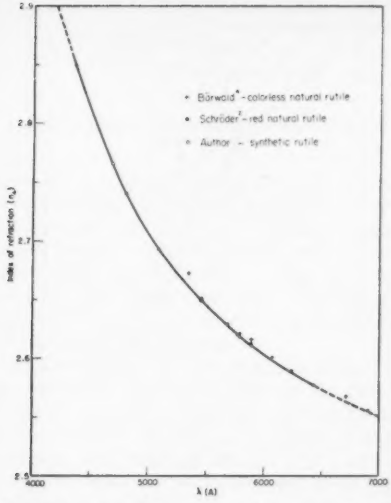

FIG. 6. Index of refraction, for the ordinary ray, of synthetic rutile TiO_2 compared with previous measurements for natural crystals.

region were extended into the infrared by calculation from reflection[8] and transmission curves (Fig. 7). Measurements of optical transmission in the visible range were made with a Cary recording spectrophotometer (Model 12-M, band width for the absorption edge, 5A).

A complete room-temperature transmission characteristic from 0.4 to 8μ is shown in Fig. 8. The infrared

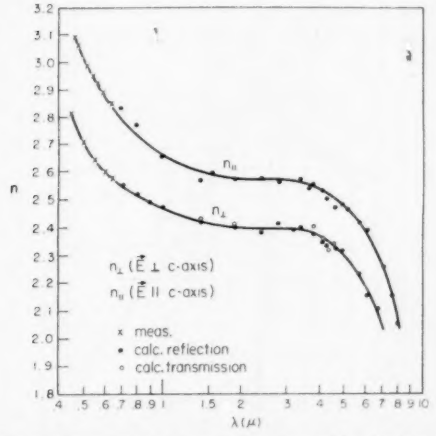

FIG. 7. Refractive index measurements extended by calculation from reflection (Liebisch and Rubens) and transmission.

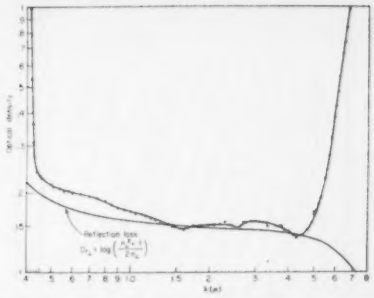

FIG. 8. Room-temperature optical transmission of 0.889-mm synthetic rutile plate cut normal to the optic axis.

transmission proves to be almost as large as the theoretical maximum calculated from refractive index data. The near-ultraviolet absorption edge appears quite sharp on this scale. Figure 9 shows the transmission in the visible region for a crystal cut parallel to the optic axis and measured with polarized light; the tail of the absorption appears considerably higher for the orientation ($\mathbf{E} \parallel c$) than the theoretical reflection loss justifies. This may be due to poor surface polish since plates having the optic axis in the plane are difficult to polish.

Thin film measurements have been made on evaporated layers of Ti formed on quartz after they were transformed to rutile by heating in air at 1000°C for several hours. The optical quality of such layers is so poor that curves are not given, but the room temperature maximum absorption is reached at 3.8 ev for an absorption coefficient of 5×10^7/m. The thickness determination from weighing and interference methods showed reasonable agreement.

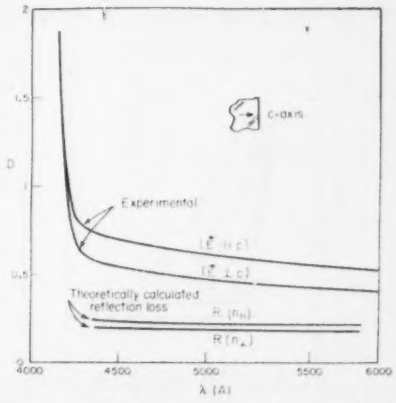

FIG. 9. Optical transmission of polarized light through 0.9-mm plate of synthetic rutile cut parallel to the optic axis.

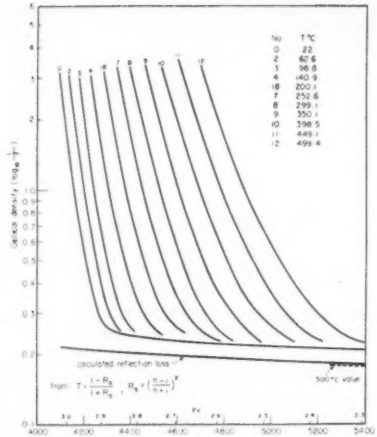

FIG. 10. Optical transmission (22–500°C) of 0.889-mm synthetic-rutile plate cut normal to the optic axis.

Reduction or oxidation affects the position of the optical absorption edge very little. Strong reduction moves the edge slightly to the red. Upon heating, the crystal turns greenish, then yellow and finally red at 800°C; the sequence is reversed upon cooling. The reason for this color change is evident from the optical density characteristics of Fig. 10. At 500°C the crystal is almost opaque to wavelengths shorter than green light, hence the crystal must appear amber by transmission.

The optical absorption edge sharpens toward low temperatures (Fig. 11) but exhibits, in addition, an unexpected shift toward longer wavelengths. To observe this behavior in more detail, measurements were carried out with higher resolution at temperatures

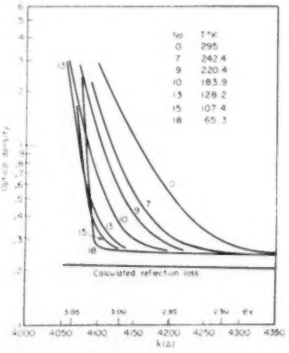

FIG. 11. Optical transmission (65–295°K) of 0.889-mm synthetic-rutile plate cut normal to the optic axis.

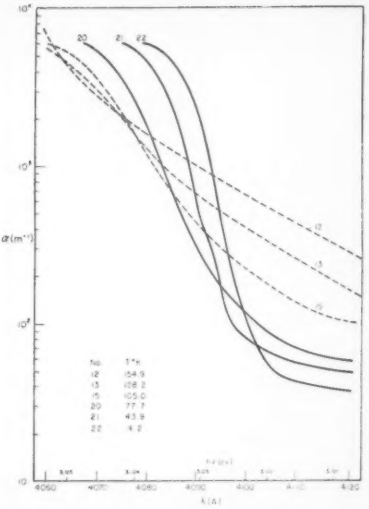

FIG. 12. Absorption coefficient of synthetic rutile TiO_2 normal to optic axis (derived from measurements on 0.889-mm plate).

between 65°K and the boiling point of liquid helium (4°K) (Fig. 12). It is seen that a secondary absorption separates from the fundamental absorption. Figure 13 combines measurements on two plates of different thickness in order to trace the characteristic into the region of high absorption.

The same crystal was clamped on a Vycor plate for photoconductivity measurements (Fig. 14). Graphite

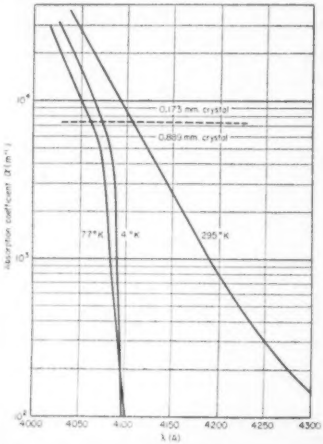

FIG. 13. Absorption coefficient (295–4°K) from a compilation of measurements on two crystals of synthetic rutile.

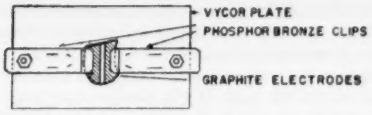

FIG. 14. Rutile crystal mounting for measurement of photoconductivity.

electrodes were applied to cover all of the face except for a central slit which exposed a single crystal region. The light, chopped at 60 cps, fell upon the sample through a quartz window. The data, corrected to constant incident energy, are shown in Fig. 15. Figure 16 shows the photocurrent for constant energy times quantum energy, i.e., the quantum yield, in arbitrary units, for several temperatures.

It may be noted that the maximum of the photoresponse moves toward shorter wavelengths with decreasing temperature paralleling the behavior of the optical absorption. At 100°K, a slight splitting into two peaks with a separation of about 0.1 ev is observed. A secondary maximum at 3.3 ev seems to be already in evidence at 230°K.

The long wavelength tail of the photoresponse has been measured to 1.2μ with modulated light (Fig. 17). There is some evidence that the response is still detectable to about 2μ, but these measurements were made uncertain by drift and long induction and decay times.

The optical band separation given by the edge of the eigenabsorption at low temperatures is 3.03 ev; from the high temperature conductivity it is 3.05 ev; and from the photoconductivity maximum it is 3.00 to 3.06 ev; an average value *ca* 3.05 ev is indicated.

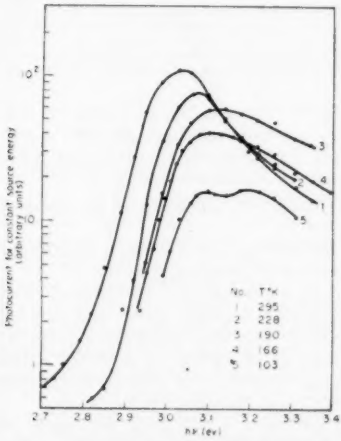

FIG. 15. Photocurrent response corrected to constant incident light intensity for rutile TiO_2.

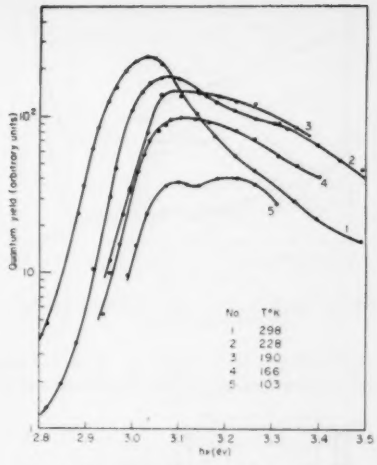

FIG. 16. Quantum yield *vs* $h\nu$ (ev) for rutile TiO_2.

OPTICAL ABSORPTION AND CONDUCTIVITY OF REDUCED SINGLE CRYSTALS

Slightly Reduced Crystals

Figure 18 compares the optical density expected from reflection loss only with the density actually measured on a clear crystal and on a slightly reduced crystal. In the nonreduced crystal the optical density in the visible range is already higher than the reflection loss; after traversing a broad maximum at *ca* 0.73μ, the discrepancy disappears at 1.5μ, and reappears with

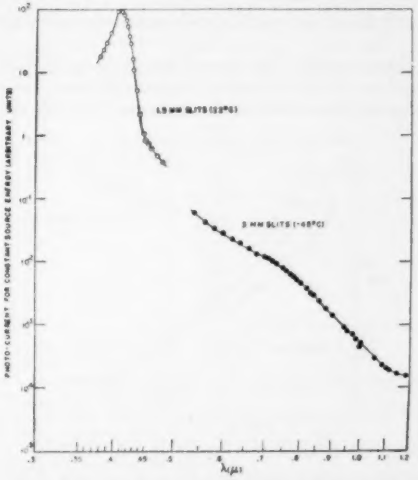

FIG. 17. Long wavelength photoresponse for rutile TiO_2.

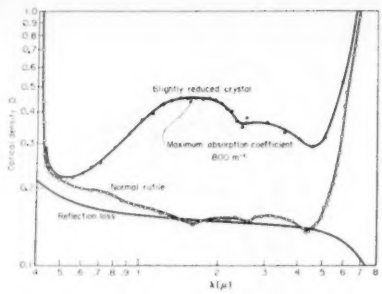

FIG. 18. Optical density *vs* wavelength for normal and slightly reduced rutile.

two slight maxima at 2.3 and 3.2μ. It is not certain that the minimum of optical density occurring at 2.55μ

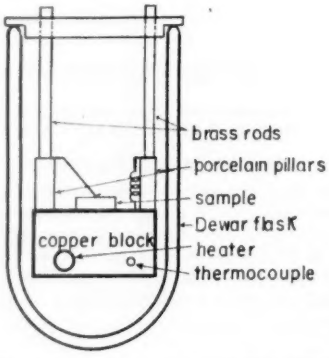

FIG. 19. Sample mounting for over-all conductivity measurement.

is characteristic of the crystal since this is the wavelength at which a change of infrared equipment had to be made. After reduction in hydrogen at 600°C until

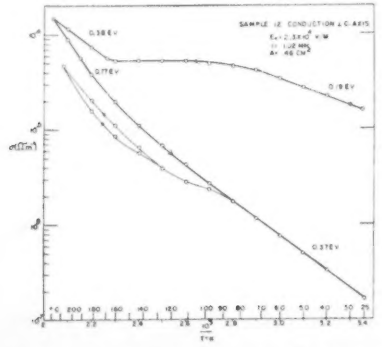

FIG. 20. Conductivity-temperature characteristic of rutile TiO_2.

a faint blue color was discernible a broad peak, with its maximum at 1.85μ, is observed. In the reduced crystal photoconduction was observable to at least 2μ by dc techniques but no response maximum was clearly discerned for the peak of the optical absorption.

To obtain the temperature dependence of the dark conductivity, gold electrodes were evaporated onto the samples. Since reduction increases the conductivity appreciably, a sample holder with thermostated silicone oil was used (Fig. 19) and the temperature taken to only *ca* 250°C. When a fairly low field was applied and

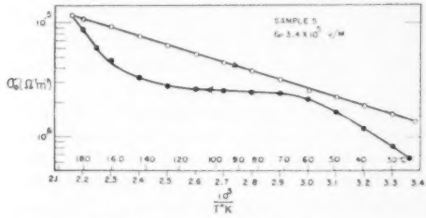

FIG. 21. Conductivity-temperature characteristic of rutile TiO_2.

the temperature raised, the $\log\sigma_0$ *vs* $1/T$ plot (Fig. 20) started at room temperature with a slope of 0.19 ev, leveled off at about 80°C, and at 160° rose again with a steeper slope. During cooling σ_0 followed an entirely different curve with a greater activation energy (0.37 ev). Upon repetition of the cycle (the lower loop in Fig. 20), the plateau of the curve almost disappeared, and the conductivity became nearly reproducible in subsequent warming and cooling cycles. For high field strength, on the other hand, the return trace was

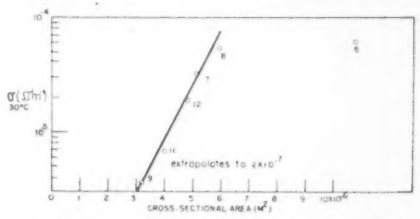

FIG. 22. Conductivity *vs* cross-sectional area for rutile TiO_2.

above the initial one and followed a straight line from 200°C to room temperature (Fig. 21).

Figure 22 shows that the initial over-all conductivities of a number of samples appear to depend upon the cross-sectional area. This might result from the increased effectiveness of oil cooling for a slender sample, but more likely indicates carrier injection with predominant recombination at the surface of the sample.

After cooling in a high field, the slightly reduced crystal bars sometimes showed a concentration of the blue color at the cathode probably caused by a migra-

tion of the color centers (oxygen defect) toward the negative electrode.

The conductivity values as reported above might be misleading since the voltage distribution within the sample is not specified. Therefore, a determination of this distribution $V(x)$ was made with a platinum probe which traversed the surface of optically polished TiO_2 bars (*ca* 1×1×10 mm). The probe potential with respect to both the anode and the cathode was determined with an electrometer in a null-type arrangement.

A typical $V_R(x)$ curve (Fig. 23) shows the field markedly distorted near the electrodes so that the net field in the central portion of the crystal (E) is appreciably smaller than the applied field strength (E_0). A variety of ratios of cathode- to anode-potential drops were obtained but all curves had the same general appearance. Figures 24(a) and (b) compare this true conductivity σ with the over-all conductivity σ_0 as

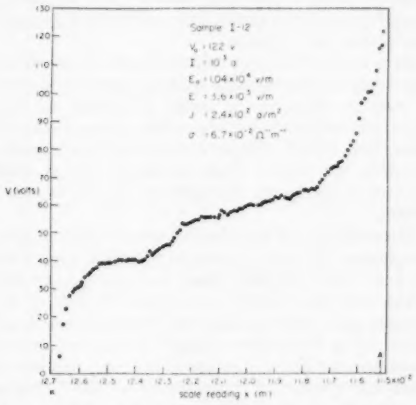

FIG. 23. Voltage-distribution curve illustrating the derivation of true conductivity σ compared with over-all conductivity σ_0.

a function of applied field and orientation. $V(x)$ curves taken for a constant applied voltage and variable temperature show that the field distortion disappears at about 90°C, and that above this temperature a slight distortion of the opposite character occurs.

Hall effect measurements were made using a sample holder, similar to that described by Hartmann,[24] with either a permanent magnet of 0.5 weber/m² or a Weiss magnet up to 1 weber/m² (10,000 gauss).

With a primary current of 800μ a parallel to the c axis of a crystal, measured in oil at room temperature, the characteristic of Fig. 25 was obtained. From the slope of the straight line ($V_H/B = 1.46\times10^{-3}$ [v-m²/weber]) we find the Hall constant $R = -2.26\times10^{-3}$ [m³/coulomb], hence a concentration of electrons 3.3×10^{21} m^{-3}. The conductivity was measured as σ

[24] W. Hartmann, Z. Physik **102**, 709 (1936).

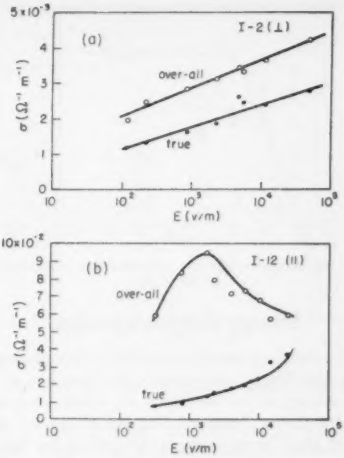

FIG. 24. True and over-all conductivity, σ and σ_0, for rutile crystals with the field (a) $\perp$ and (b) $\parallel$ to the c axis.

$= 5.63\times10^{-2}\ \Omega^{-1}\ m^{-2}$, hence the mobility b of the electrons is 1.1×10^{-4} m²/v-sec (or 1.1 cm²/v-sec).

It should be pointed out that this calculation is questionable since there are three possible orientations for Hall effect measurements in a tetragonal crystal, namely, (1) $I \parallel c$; (2) $I \perp c$, $B \perp c$; (3) $I \perp c$, $B \parallel c$. In bismuth single crystals, the Hall coefficients, and their temperature coefficients are different in all three directions.[25] There is also uncertainty regarding the interpretation of the Hall coefficients in an anisotropic crystal since the distribution of the energy surfaces within the Brillouin zone is required for a theoretical interpretation.[22,26–28] Unfortunately, time did not permit studying the directional Hall effect in rutile.

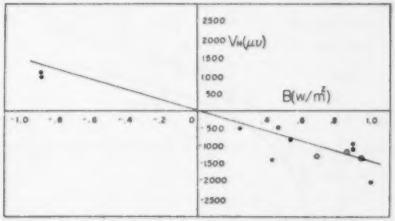

FIG. 25. Hall voltage *vs* magnetic induction ($I \parallel c$).

[25] A. F. Joffé, *The Physics of Crystals* (McGraw-Hill Book Company, Inc., New York, 1928).
[26] W. Shockley, *Electrons and Holes in Semiconductors* (D. Van Nostrand Company, Inc., New York, 1950), p. 334.
[27] W. Hume-Rothery, *Structure of Metals and Alloys* (Institute of Metals Monograph, London, 1936).
[28] N. F. Mott and H. Jones, *The Theory of the Properties of Metals and Alloys* (Clarendon Press, Oxford, 1936).

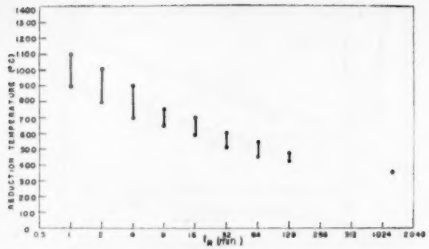

FIG. 26. Minimum time for uniform coloring of ceramic 10 mil sheet.

Strongly Reduced Ceramics

It is known that strong reduction of TiO_2 produces an *n*-type, blue-black, semiconductor which has an activation energy of *ca* 0.070 ev at room temperature in the 100 Ω^{-1} m^{-1} region.[6] This low activation energy indicates that, in this case, nearly all of the electrons are free to contribute to conduction at room temperature. The investigation of this conductivity region was made with ceramic samples.

Samples were reduced in a current of hydrogen in a controlled-temperature alundum furnace. The temperature of reduction was varied from 300° to 1150°C, and the depth of coloring noted after quenching to room temperature in nitrogen. Sheet samples[29] (10 mil) could be reduced uniformly at temperatures as low as 350°C (Fig. 26), although periods of the order of 24 hours were required; at 300°C, no observable reaction occurred in this length of time. In order to obtain uniformly reduced thin-sheet ceramic in times of the order of 5 minutes, it proved necessary to operate at temperatures above 700°C. For this reason most of the subsequent observations were carried out on materials reduced at 800°C in hydrogen.

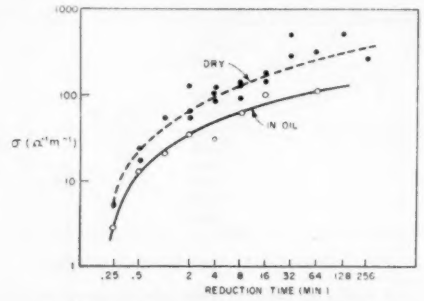

FIG. 27. Over-all conductivity *vs* reduction time for $\frac{1}{4}\times1\times0.01$ in. thin sheet samples.

[29] The samples were prepared from Tamco heavy grade rutile powder, partly in this Laboratory by J. Brownlow, and partly by courtesy of the Glenco Corporation, Metuchen, New Jersey.

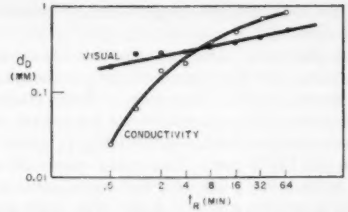

FIG. 28. "Diffusion distance" from visual observation of the "coloring distance" checked roughly by estimates from the over-all conductivity.

Nazu[30] has derived the chemical reaction constants for the reduction process $2TiO_2+H_2 \rightarrow Ti_2O_3+H_2O$ over the temperature range 775° to 1000°C. The free energy change accompanying this process is $\Delta G^0 = 4095 - 2.013T \log_{10}T - 3.86\times10^{-3}T^2 + 10.1T$. This equation predicts that ΔG^0 becomes zero at 324°C, a lower limit, which agrees fairly well with the experimental data just presented.

Some of the thin-sheet material showed a surprising anisotropy in reduction; the coloring appeared to move in from the edges of the sample as though the skin of the ceramic plate were impervious. At temperatures higher than 1100°C, a deposit of reduced TiO_2 is usually found on the furnace walls indicating that at these elevated temperatures the reduction process is rather violent.[6]

Measurements of the effective conductivity at room temperature for various times of reduction were made for $\frac{1}{4}$-in. cubes and 10-mil sheet ceramics. Copper electrodes were electroplated onto opposite ends of the samples after reduction and the resistance was determined by a Wheatstone bridge. These conductivity characteristics give a measure of the time required to reach the equilibrium concentration at 800°C. Figure 27 gives the conductivity characteristic for the sheet samples and Fig. 28 a comparison of a conductivity and visual penetration test on the cubes.

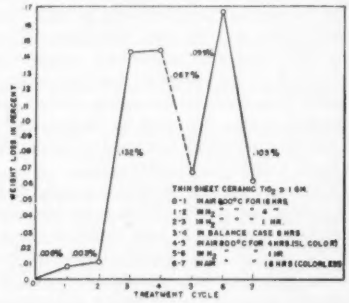

FIG. 29. Weight-loss experiment.

[30] N. Nazu, Science Repts Tôhoku Imp. Univ. 1, 25, 510 (1936).

To establish the amount of oxygen lost during the reduction process, a ceramic sheet sample (10 mil, *ca* 1 g) was subjected to reduction-oxidation cycles and the weight change measured with a microbalance. The sample was initially heated in air at 800°C until its weight showed no further change (Fig. 29, point 1). The subsequent reduction and oxidation cycles are noted in the figure; it may be seen that for a reduction time of one hour at 800°C, a reversible weight loss of 0.1 percent is attained. At 650°C the weight loss in one hour amounts to 0.01 percent. Since only oxygen is lost from the lattice in this type of treatment, one can derive a simple formula for the number of conduction electrons as a function of the fractional weight loss δ: $n=3.17\times10^{28}\delta$ electrons/m³ assuming that the loss of each oxygen atom leaves two electrons trapped

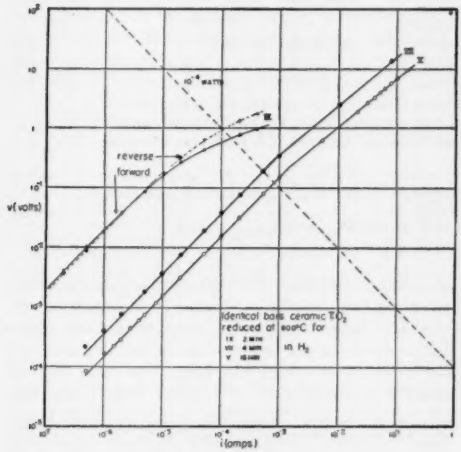

FIG. 30. Current-voltage curves for reduced ceramic bars.

at the resultant lattice vacancy. A weight loss of 0.1 percent should correspondingly release 3.17×10^{26} electrons/m³ for conduction. Near one percent oxygen loss, the lattice tends to break down and the corundum structure of Ti_2O_3 begins to appear. Nazu[30] finds it impossible to reduce the material below Ti_2O_3 by hydrogen treatment, so that a valence of three for the titanium is the lowest that need be considered in the discussion of reduced TiO_2.[31]

Typical current-voltage curves are shown in Fig. 30. The resistance proves ohmic up to an applied field strength of about 10 v/m (0.1 volt). The deviation from Ohm's law seems to be connected, not with a particular power input, but occurs rather above a certain voltage. The heating could be neglected below a power input of 0.02 watt as comparison of oil and air

[31] M. D. Earle, Phys. Rev. **61**, 56 (1942), assumes Ti^{+4}.

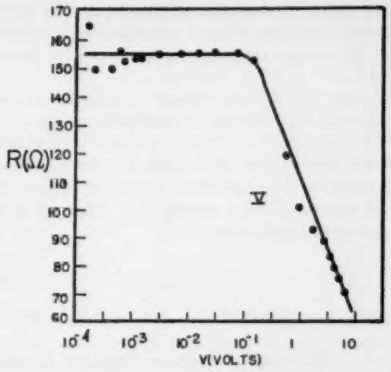

FIG. 31. Resistance as function of applied voltage.

cooling indicated, while the deviation from an ohmic behavior begins for a much smaller power input. Figure 31 gives a typical example of the rather sharp transition to a nonohmic behavior. This rapid change is tentatively identified with carrier injections; other evidence for this phenomenon has already been presented from photoconductivity and conductivity data.

The results of Hall-effect measurements, made with the arrangement previously used on a sheet sample reduced at 0.3 atmos hydrogen for 4 min at 800°C are shown in Fig. 32. One finds $V_H/B=8.88\times10^{-7}$ v-m²/weber for the Hall constant $R=5.55\times10^{-8}$ m³/coulomb, hence for the number n of charge carriers per unit volume, $(8/3\pi)(1/Re)=0.955\times10^{26}$ m^{-3}. From weight-loss experiments (1 hour reduction at 800°C gives 0.10 percent loss of weight corresponding to a conductivity

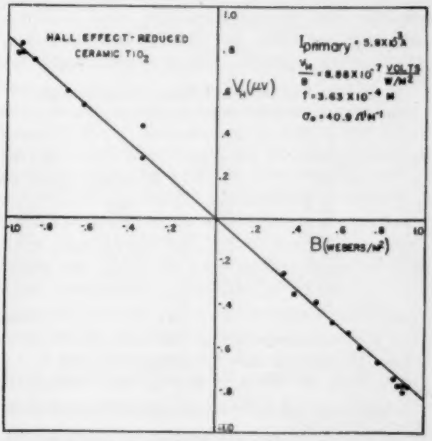

FIG. 32. Hall effect in reduced ceramic TiO_2.

of 112 $\Omega^{-1}m^{-1}$), the concentration 1.2×10^{26} m^{-3} is calculated, which is in good agreement with this Hall value. For other samples a similar agreement was obtained.

The very high conductivity of the reduced ceramics, and the fact that the Hall measurement indicates that all of the electrons are free to contribute to conduction at room temperature, show that, in strongly reduced TiO_2 samples, the activation energy has become very low in agreement with earlier data obtained during the war in this Laboratory.[6]

ACKNOWLEDGMENT

The author gratefully acknowledges the continuous advice and encouragement received from Professor A. von Hippel in the course of this research. He is also greatly indebted to M. A. Gilleo for his help in the optical and photoelectric investigation; to W. B. Westphal and the Dielectric Measurements Group for assistance with ac conductivity measurements; and to Professor R. C. Lord and Professor L. Harris for their kindness in determining the infrared absorption in one of the crystals.

PHYSICAL REVIEW VOLUME 87, NUMBER 5 SEPTEMBER 1, 1952

Thermal Neutron Capture Cross Section of A^{40} and Observation of A^{42}†

SEYMOUR KATCOFF
Chemistry Department, Brookhaven National Laboratory, Upton, New York
(Received May 16, 1952)

The thermal neutron absorption cross section of A^{40} was determined by measuring in calibrated proportional counters the amount of 110-min A^{41} produced from samples of argon irradiated in a neutron flux whose magnitude was measured by β-γ coincidence counting of gold monitors. The result was 0.53 ± 0.03 barn.

A^{42} was produced from A^{40} by two successive neutron captures and it was detected through its 12.5-hr K^{42} daughter. A lower limit of 3.5 years was set on its half-life. From this result the thermal neutron absorption cross section of A^{41} is calculated to be greater than 0.06 barn.

It was also shown that the thermal neutron absorption cross section of A^{38} is 0.8 ± 0.2 barn.

INTRODUCTION

THE thermal neutron cross section of A^{40} for the formation of 110-min A^{41} was measured by Kern[1] and by Wattenberg and West.[2] They found values of 1.24 barns and 0.72 barn, respectively. In both cases the activity was measured by placing the argon in a cell external to a Geiger counter. At about the same time the total neutron absorption cross section of argon was measured by the "danger coefficient" method[3] using cadmium wire of known length and diameter as standard. This value, which also measures an upper limit for the activation cross section of A^{40}, was 0.62 barn. In a similar experiment Colmer and Littler[4] used the pile oscillator at Harwell and obtained the same value, 0.62 ± 0.04 barn. The total thermal neutron cross section (absorption plus scattering) for argon was first determined by Carroll[5] from transmission measurements. He used a Rn-Be in paraffin source and an argon sample which transmitted 92 percent of the neutron beam. His value was 2.5 barns. Melkonian *et al.*,[6] employed the Columbia University slow neutron velocity spectrometer and a sample of argon which transmitted 79 percent of the beam at 0.025 ev. Their result for the total cross section was 1.4 barns. If one subtracts from this the thermal neutron scattering cross section of 0.80 ± 0.08 barn determined by Harris[7] one obtains 0.6 barn for the absorption cross section, in good agreement with the direct measurements.[3,4]

In the present work the thermal neutron activation cross section of A^{40} was determined by measuring the A^{41} activity within a proportional counter and measuring the neutron flux by coincidence counting of gold

TABLE I. Activity per cc as function of counter length.

Length of cathode (cm)	Total counter volume (cc)	Cathode volume (cc)	Activity at a given time (counts/min)	Activity per cc of cathode volume (counts/min)
7.0	31.8	19.0	3460	182
17.0	59.6	47.1	8400	178
29.7	98.5	85.0	15,700	185
29.8	101.6	87.6	16,000	183
45.2	137.7	125.7	23,700	189
75.8	222.2	211.0	38,600	183
Average				183±4

† Research carried out under the auspices of the AEC.

[1] B. D. Kern, unpublished Plutonium Project Report CP-772 (1943).

[2] A. Wattenberg and J. West, unpublished Plutonium Project Report CP-781 (1943).

[3] Lichtenberger, Fowler, and Wattenberg, unpublished Plutonium Project Report CP-781 (1943).

[4] F. C. W. Colmer and D. J. Littler, Proc. Phys. Soc. (London) **A63**, 1175 (1950).

[5] H. Carroll, Phys. Rev. **60**, 702 (1941).

[6] Melkonian, Rainwater, Havens, and Dunning, Phys. Rev. **73**, 1399 (1948).

[7] S. P. Harris, Phys. Rev. **80**, 20 (1950).

monitors. The result is 0.53±0.03 barn, considerably lower than previous direct determinations,[1,2] but consistent with the results of references 3 and 4, and of 6 combined with 7.

MEASUREMENT OF A^{40} CROSS SECTION

Small quartz ampules of measured volume (2 cc) were filled with pure argon at a carefully measured temperature (near 23°C) and pressure (near 500 mm Hg). These were irradiated in the Brookhaven pile for one minute with 10 mg gold monitors. Then each ampule was attached to a calibrated vacuum system and the irradiated argon was allowed to expand through a break-off seal into one or more glass bulbs. After allowing sufficient time for the pressure to equalize, additional carrier argon was added to one of these calibrated bulbs. It was mixed thoroughly with the irradiated argon by several cycles of cooling with liquid nitrogen and heating with a flame. When this gas was again at room temperature an aliquot was removed into a cylindrical proportional counter whose

TABLE II. Activity per cc as function of counter diameter.

Diameter of cathode (cm)	Counter gas cm argon	cm CH_4	Operating voltage	Total volume (cc)	Cathode volume (cc)	Activity at a given time (counts/min)	Activity per cc of cathode volume (counts/min)
1.9	0.6	76	3800	98.5	85.0	116	1.36
1.9	75	10	2300	101.6	87.6	114	1.30
2.7	75	10	2500	205	164	219	1.34
4.9	75	10	3050	667	544	723	1.33
6.8	75	10	3500	1250	1044	1380	1.32
8.7	75	10	3600	1990	1681	2220	1.32
Average							1.33±0.02

total volume and cathode volume had been measured previously. Methane was added to bring the total pressure up to one atmosphere.

The counting, which was done with proportional counters, was usually begun two hours after the irradiation and continued for about 3 half-lives. Coincidence loss corrections were negligible. When the background was subtracted, the decay was exponential with a half-life of 110±1 minutes for A^{41}, in good agreement with previous determinations. Two sets of experiments were done which indicated that the counting rate was actually equal to the disintegration rate of the A^{41} contained within the volume bounded by the counter cathode. In one series of experiments, the counter length was varied, and in the other series, the diameter was varied. The volumes were measured by passing in toluene from a buret. In each experiment, all the counters were opened to one manifold and filled with the irradiated argon at the same time. The data and results are shown in Tables I and II. All the counters of Table I have a diameter of 1.9 cm, a pressure of 16 cm of argon and 58 cm of methane, and they were

TABLE III. Thermal neutron absorption cross section of A^{40}.

No. of run	Thermal neutron flux (n/cm^2 sec)	Number of irradiated argon atoms in cathode volume	Activity at end of irradiation (disint/sec)	Thermal cross section of A^{40} (cm^2)
1	4.92×10^{12}	15.12×10^{18}	2409	0.514×10^{-24}
2	4.42	6.36	893	0.505
3	4.19	0.95	141	0.562
4	3.20	3.07	322	0.520
5	3.90	14.63	1908	0.531
6	3.76	5.21	674	0.546
7	3.84	4.70	614	0.540
Average				0.531±0.020

operated at 3600 volts (middle of 200-300 volt plateau); the counters of Table II are 30 cm long and they were filled with argon and methane as indicated in columns 2 and 3. It is seen from these results that the specific counting rate (activity per unit of cathode volume) for the 1.2-Mev β-rays of A^{41} is independent of counter length or counter diameter, within the experimental error of 2 percent. Bernstein and Ballentine[8] found similar results for the 0.155-Mev β-rays of C^{14}. Apparently the sensitive length of the counter is shorter than the cathode by a small amount which just compensates for the β-rays which enter the sensitive volume from the ends of the counter. This amounts to about one cm for the standard counters whose diameter is 19 mm.

The neutron flux in each irradiation was measured by making a determination of the absolute disintegration rate of the gold monitor by means of β-γ coincidence counting. The detectors were crystals of anthracene and of thallium activated NaI mounted on No. 5819 photomultiplier tubes. The random coincidence rate was measured by introducing a 1.3 μsec delay which is long compared to the 0.3 μsec resolving time. This was subtracted from the total coincidence rate to obtain the true rate. The counts recorded by the β-ray counter were reduced by 3 percent to correct for the γ-rays it records. Another small correction was applied for the effect of the 411-kev γ-rays which are converted 3 percent in the K shell and one percent in the L shell, the conversion electrons raising the counting rate in the β-ray counter by 4 percent. The γ-ray counter was covered with 600 mg/cm² of aluminum to remove the β-rays and the discriminator was set so that 2 percent of the counts were from the K x-rays. The disintegration rate A of the gold monitor was then determined from the formula, $A=C_\beta C_\gamma/1.02C_{\beta-\gamma}$, where C_β is the counting rate in the β-counter corrected for γ-rays, C_γ is the counting rate in the γ-counter, and $C_{\beta-\gamma}$ is the true coincidence rate. In one run the disintegration rate was also measured by comparing a small aliquot of the gold with a RaE standard by means

[8] W. Bernstein and R. Ballentine, Rev. Sci. Instr. **21**, 158 (1950).

of an end-window Geiger counter.[9] The results from both methods agreed within 4 percent.

By irradiating gold monitors in the same position in the pile both with and without cadmium shielding, it was found that 70±2 percent of the Au^{198} is produced by thermal neutrons. The thermal neutron flux was calculated using 0.70 of the observed Au^{198} disintegration rate, 64.5 hr for the Au^{198} half-life, and 95 barns for the Au^{197} cross section. No correction was made for the small branches to the 1.09-Mev level and to the ground state because these are completely negligible for the purpose of the present calculation. The flux for each run is listed in Table III. In one case, the flux was also determined from the amount of a fission product produced in a uranium monitor. A quantitative radiochemical analysis was done for 12.8-day Ba^{140}. Its activity was measured with an end-window Geiger tube whose efficiency was measured with a uranium "geometry" standard. The usual corrections were applied and the flux calculated from the Ba^{140} disintegration rate, the fission yield, the fission cross section of uranium, the weight of the monitor, and the irradiation time. The result was within 5 percent of that derived from the coincidence measurements on the gold monitor.

The observed A^{41} disintegration rate was decreased by 3 percent to correct for the activation produced by neutrons above the cadmium cutoff. This was determined from two special runs. The thermal neutron activation cross section of A^{40} calculated from each run is given in Table III. The average is 0.53±0.02 barn. The error indicated is the standard deviation for the seven values given in the table. In addition, the following uncertainties must be considered: 3 percent in the fraction of the Au^{198} activity that is produced by neutrons below the cadmium cutoff; 2 percent in the gold cross section; and one percent in the A^{41} half-life. The over-all standard deviation then becomes 6 percent and the value of the cross section is taken as 0.53±0.03 barn. The purity of the argon was kindly checked with a mass spectrometer by Dr. O. A. Schaeffer. About 0.7 percent of foreign gas (principally nitrogen) was found and the necessary correction was made.

A^{39}

In order to compare the above result with the neutron absorption cross section of natural argon as reported in the literature,[3,4] the other two stable isotopes must be considered. A^{36}, whose abundance is 0.337 percent, has an isotopic cross section of 6 barns,[10] thus contributing 0.02 barn to the total absorption. The sum for A^{36} and A^{40} (99.600 percent abundance) is 0.55±0.03 barn. Subtracting this from 0.62±0.04, the value of Colmer and Littler[4] for the total absorption cross section, one obtains 0.07±0.05 barn for the contribution of A^{38}. The upper value, 0.12 barn, specifies an upper limit of 190 barns for the isotopic absorption cross section of A^{38} whose natural abundance is only 0.063 percent.

A direct determination of this cross section by the activation method is not feasible because only a lower limit has been established[11] for the half-life of A^{39} (>15 years). Nevertheless, some A^{39} was prepared by irradiating 1.56 liters of argon in a quartz tube near the center of the Brookhaven pile for 12 days in a flux of 4×10^{12} neutrons/cm²/sec. A small aliquot was put into a cell with a mica window (5 mg/cm²) and counted with an end-window G-M tube about one year after the irradiation. The very soft radiations of 34-day A^{37} were completely absorbed by the windows. The A^{39} was identified by means of the characteristic absorption curve of its 0.565-Mev β-rays in aluminum. The total activity corrected for backscattering, absorption, aliquot, and counter efficiency was 7600 disintegrations/sec. By combining this value with the minimum half-life of 15 years, a lower limit of 0.05 barn can be placed on the cross section of A^{38}. By using the upper limit of 190 barns (calculated in the previous paragraph) an upper limit of 6×10^4 years can be set for the A^{39} half-life.

Note added in proof:—Very recently H. Zeldes *et al.*, Phys. Rev. **86,** 811 (1952), reported 265±30 years for the A^{39} half-life. Based on this value and the data given above, the thermal neutron absorption cross section of A^{38} is 0.8±0.2 barn.

A^{42}

Most of the 1.56-liter argon sample that had been irradiated for 12 days was used to investigate A^{42} which can be formed from A^{40} by two consecutive neutron captures. No attempt was made to detect the A^{42} radiations directly because of the greatly preponderant activity of A^{39}. Rather, the A^{42} was detected by successive extractions of its 12.5-hr K^{42} daughter. The first extraction was made two days after the end of the irradiation; growth times were varied from 4 hours to 131 days. Initial counting rates were about 12 counts/min above the background and the natural K^{40} activity. The decay curves corresponded to the known K^{42} half-life, 12.5 hours. In 13 extractions over a period of 400 days, the corrected activity of A^{42} showed no apparent decrease; consideration of the possible errors indicates that it could not have gone down by more than 20 percent. This sets a lower limit of 3.5 years on the half-life of A^{42} and a lower limit of 0.06 barn on the thermal neutron absorption cross section of 110-min A^{41}.

[9] B. P. Burtt, Nucleonics **5**, 28 (1949).
[10] G. E. McMurtrie and D. P. Crawford, Phys. Rev. **77**, 840 (1950).
[11] Brosi, Zeldes, and Ketelle, Phys. Rev. **79**, 902 (1950).

Correlation of Cosmic-Ray Ionization Measurements at High Altitudes, at Sea Level, and Neutron Intensities at Mountain Tops

H. V. NEHER*
California Institute of Technology, Pasadena, California

AND

S. E. FORBUSH
Carnegie Institution of Washington, Washington, D. C.

(Received May 19, 1952)

Although fluctuations in cosmic rays have been measured at sea level and high altitudes for a number of years, no serious attempt seems to have been made to correlate the two. As a result of a rather long series of balloon flights in the summer of 1951 it now becomes possible to correlate ionization measurements at high and low altitudes. Recent neutron intensity measurements during the same period by Simpson *et al.* permit a further comparison with this component. There seems to be a good correlation, during this period of observation, between the fluctuations as measured in (1) the ionization at 70,000 ft over North Dakota, (2) the meson component at Cheltenham, Maryland, (3) the meson component at the geomagnetic equator, and (4) the neutron component at mountain tops in Colorado and New Mexico.

IN a recent issue of this journal, Simpson *et al.*[1] reported a correlation of the fluctuations of neutron intensity, measured at three widely separated land stations. It is the purpose of this note to point out that correlations also exist between cosmic-ray intensity measurements at both high and low altitudes and the above neutron measurements.

In the summer of 1951 while these neutron measurements were being made, a group from the California Institute of Technology was making a series of balloon flights at Bismarck, North Dakota using ionization chambers. Also during this period, continuous measurements of cosmic-ray intensities were being made at Huancayo, Peru and at Cheltenham, Maryland by the Carnegie Institution of Washington. Plotted in Fig. 1 are the four sets of data. The neutron data were scaled from the curve given by Simpson *et al.*[1] for Climax, Colorado and are for the first 12-hour period of the respective days on which balloon flights were made. In three cases two flights were made on the same day at Bismarck, on July 27, August 6, and August 14. In such cases the trend of the neutron data at the particular times was taken, and what appeared to be a reasonable value was assigned. For the corresponding data at Cheltenham, the hourly values, corrected for bursts and barometric changes, for the 6 hours just before the balloon flights reached their maximum height and the 6 hours just afterward, are averaged. For the case of the data from Huancayo the daily mean values are plotted. Thus, the first point on July 18, is the mean for that day on 75° west meridian mean time. The points, for the respective times under consideration, are arbitrarily connected by straight lines in the figure. The balloon data at Bismarck are taken from the individual curves and are at 50 g cm^{-2} pressure or about 70,000 ft.

In Fig. 2 are shown the data for Cheltenham and Huancayo compared with the neutron measurements of Simpson *et al.*, for the three months of July, August, and September of 1951. The ionization data are daily averages, while the neutron measurements are for 12-hour periods.

These data show that, during this period of observation, there was a very good correlation in time of the fluctuations measured (1) in the total ionization due to cosmic rays at 70,000 ft elevation over North Dakota; (2) in the neutron intensity at 11,000 ft elevation at Climax, Colarado; (3) in the sea level ionization, of particles that can penetrate 12 cm of lead, at Cheltenham, Maryland; and (4) in the ionization at 11,000 ft elevation at Huancayo, Peru as measured by an instrument similar to the one at Cheltenham.

The approximate ratios of the relative fluctuations

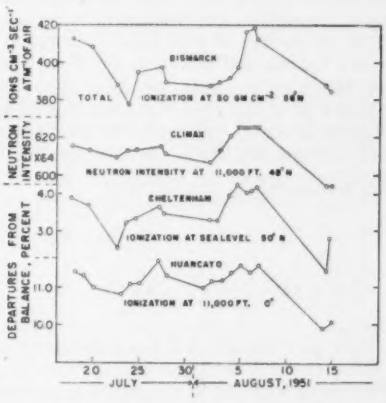

FIG. 1. Correlation between ionization measurements at high altitudes (about 70,000 ft), low altitudes, and neutron measurements at 11,000 ft.

* Assisted by the joint program of the ONR and AEC.

[1] Simpson, Fonger, and Wilcox, Phys. Rev. 85, 366 (1952).

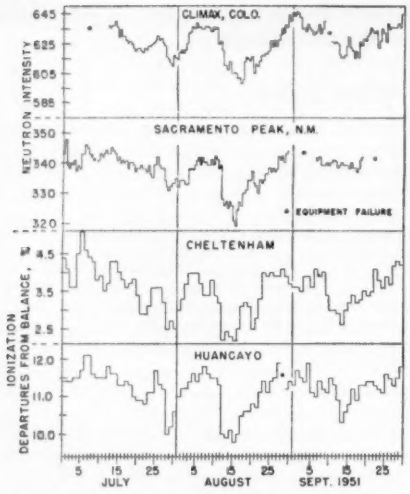

FIG. 2. Correlation between neutron measurements and ionization measurements at or near sea level.

as given in Fig. 1 are as follows: ionization at 70,000 ft to that at Cheltenham, 7:1; neutrons at 11,000 ft to ionization at Cheltenham, 3:1; ionization at Cheltenham to that at Huancayo, 1:1. A more detailed analysis[2] has shown that in the last case, the ratio between the fluctuations at Cheltenham and Huancayo is more nearly 1.1:1.

In addition to the above, two other pieces of experimental evidence are pertinent to the present discussion:

(1) A study of the differences in the balloon curves obtained at Bismarck during July and August, 1951 shows that there is a fairly wide distribution in the energy of the particles that fluctuate from day to day.

(2) In the summer of 1946 (data unpublished) an ionization chamber was sent up at Ft. Worth, Texas during the magnetic storm that followed the large flare of July 25 of that year. The percentage decrease in ionization compared with the normal value shown at 70,000 ft during this flight was approximately four times the decrease found in an unshielded ionization chamber at Mt. Wilson, California during the same period.

The manner in which the radiation responsible for these fluctuations is absorbed in the atmosphere is consistent with the fact that the fluctuations are also present at Huancayo, Peru. Since these fluctuations are also present at Thule, Greenland,[3] it is evident that they are world-wide and hence represent real changes in the total energy being brought into the earth by cosmic rays. The average energy of the particles must, however, be somewhat less than that for the total cosmic-ray particles since the fluctuations in ionization increase with altitude, and are less pronounced at the equator.

These changes do not appear to be of the same type that have been measured during sudden increases in cosmic-rays, such as occurred on November 19, 1949 and on July 25, 1946. This conclusion is borne out by (a) the small changes in neutron intensity, relative to those measured with ionization chambers shown in Fig. 1, as compared with the much larger relative change measured[4] during the increase of November 19, 1949; (b) the fact that on no occasion has as appreciable increase in cosmic rays been measured at Huancayo when these increases occurred at intermediate and higher latitudes, while the changes shown in Fig. 1 do occur also at the equator. On the contrary, we believe that these fluctuations are similar to those that have been correlated with magnetic disturbances[3,5] both of the long period type and the short period type such as that which occurred one day following the solar flare of July 25, 1946.

In conclusion we wish to thank the U. S. Weather Bureau and particularly Mr. F. J. Bavendick for their cooperation at Bismarck. We also wish to thank Dr. Vincent Peterson, Mr. Edward Stern, and Mr. Alan Johnston for their help in preparing the instruments, in carrying out the flights, and in reducing the data.

[2] S. E. Forbush, Phys. Rev. **54**, 975 (1938).

[3] Neher, Peterson, and Stern, Phys. Rev. **85**, 772 (1952).

[4] On this occasion the ratio of neutron increase to the increase in ionizing particles at Manchester, England was 60:1. See N. Adams, Phil. Mag. **41**, 503 (1950).

[5] S. E. Forbush, Internatl. Assoc. of Terrest. Mag. and Elec., Washington Assembly (September, 1939); also, S. E. Forbush and I. Lange, Phys. Rev. **76**, 1641 (1949).

The Influence of Multiple Scattering on the Angular Width of Čerenkov Radiation

K. G. DEDRICK
Stanford University, Stanford, California
(Received May 21, 1952)

One may measure the angle at which visible Čerenkov radiation appears from fast charged particles as they pass through a thin transparent plate. This angle is related to the velocity of the particle in a simple manner, and therefore offers a method of measuring the velocity. The angular width of the radiation is important in that it determines the resolution of the velocity measurement. This width contains contributions due to diffraction, energy loss of the charged particle, and multiple scattering. In this paper, the effects of multiple scattering and diffraction are considered in the following manner. The path of the particle through the transparent plate is considered to be a series of connected short straight-line segments. The radiation is calculated classically from this path, and with the aid of the results of multiple scattering theory, an ensemble average is taken over all possible paths. Two different methods are used in evaluating the radiation average. One is valid at viewing angles near the radiation maximum, and the other at viewing angles differing appreciably from the maximum. Curves are presented that give the radiation intensity as a function of the viewing angle for a variety of cases.

I. INTRODUCTION

THE Čerenkov radiation from a fast charged particle of speed v that passes through a thin transparent plate of refractive index n, appears mainly at an angle from the path of the particle given by $\theta_0 = \cos^{-1}[(1/n)\cdot(c/v)]$. If v/c is not too close to unity, measurement of θ_0 offers a convenient method for the determination of v/c, and hence, for a given rest mass, the momentum and energy of the particle. Recent experiments at Berkeley[1] with 340-Mev protons, indicate that this method is capable of high precision. It is then in order to calculate the effect of various factors on the resolution. An estimate of these factors is included in reference 1.

The natural diffraction width of the radiation is very small, being of the order of λ/L radians, where L is the thickness of the plate and λ is the wavelength of radiation viewed. One should also take into account the energy loss of the particle and the multiple scattering that occurs as the particle passes through the plate. The energy loss affects v/c in a direct and simple way. The multiple scattering changes the average direction of the particle and partially destroys the coherence of the radiation along the path. Only the effects of multiple scattering and diffraction will be considered here.

The problem then is to calculate the radiation from a charged particle moving with constant speed and undergoing multiple scattering in a thin transparent plate.

This problem may be attacked by classical radiation theory rather than by quantum radiation theory. A criterion for the validity of classical theory is that the dimension of the wave packet describing the charged particle be small compared with the reduced wavelength of the radiation emitted and remain small during the time t during which the radiation is emitted coherently. If the size of the wave packet at time t is Δx, then we have

$$\Delta x \sim \delta x + (\delta v)t,$$

where δx is the size of the packet at $t=0$. The time t may be taken as $\mathfrak{L}/v$, where $\mathfrak{L}$ is some length less than the thickness of the plate but substantially greater than the mean free path λ_0 of the charged particle between scattering events in the plate. A relation between δx and δv (the uncertainty in velocity of the charged particle) may be obtained as follows:

$$\delta p = m_0 \delta v/(1-v^2/c^2)^{\frac{1}{2}} \sim \hbar/\delta x.$$

Therefore,

$$\Delta x \sim \delta x + (\hbar/m_0 \delta x)(1-v^2/c^2)^{\frac{1}{2}}(\mathfrak{L}/v).$$

The minimum size of this packet is:

$$[(\hbar/m_0 v)(1-v^2/c^2)^{\frac{1}{2}}\mathfrak{L}]^{\frac{1}{2}}.$$

For an electron traversing a plate 1 mm thick and for $v \lesssim c$, we see that this is less than 10^{-6} cm, at least a factor of ten smaller than the reduced wavelength of visible radiation; it is even smaller for a proton.

II. THE RADIATION PROBLEM

(A) General

The power radiated from a classical system of currents can be calculated by evaluating the familiar retarded solution of the inhomogeneous electromagnetic wave equation. This retarded solution can be subjected to a Fourier analysis and the Fourier components of the power calculated. Such a development yields[2]

$$P_{\mathbf{k},\omega}(\mathbf{r}) = (nk^2/2\pi r^2 c) \times \left| \int J_{\perp \mathbf{k},\omega}(\mathbf{r}') \exp(-in\mathbf{k}\cdot\mathbf{r}')d\mathbf{r}' \right|^2. \quad (1)$$

The propagation vector $\mathbf{k}$ is directed along the line of observation and has a magnitude $2\pi/\lambda = \omega/c$. $J_{\perp \mathbf{k},\omega}(\mathbf{r}')$ is the Fourier component of that part of the current

[1] R. L. Mather, Phys. Rev. **84**, 181 (1951).

[2] L. I. Schiff, *Quantum Mechanics* (McGraw-Hill Book Company, Inc., New York, 1949), p. 264.

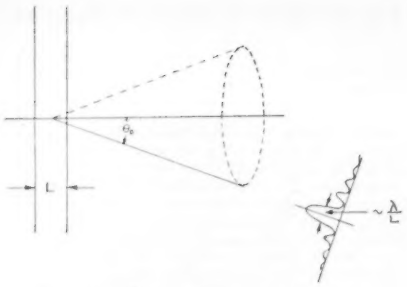

FIG. 1. The Čerenkov cone and the diffraction pattern given by Eq. (2).

that is perpendicular to **k**. n is the index of refraction of the medium in which the currents are located.

The simple case of a particle passing straight through a plate with an index of refraction n has been evaluated by many authors;[3] it yields a conical shell of light which has the path of the particle as an axis and a thickness given by a diffraction pattern (see Fig. 1). For $\lambda/L \ll 1$, the pattern is given very nearly by

$$L^2[\sin(\tfrac{1}{2}nkL\kappa \sin\theta_0)/(\tfrac{1}{2}nkL\kappa \sin\theta_0)]^2, \tag{2}$$

where $\kappa \equiv \theta - \theta_0$.

In the calculation of the radiation from a particle undergoing multiple scattering, the path is assumed to consits of many short straight segments. The integral in (1) is then seen to be a sum of integrals over all the segments of the path. Therefore, one must calculate

$$|\sum_{\nu=1}^{N} I_\nu|^2, \tag{3}$$

where I_ν is the contribution due to segment ν. The segment ν is of length l_ν, goes from x_ν, y_ν, z_ν, to $x_{\nu+1}, y_{\nu+1}, z_{\nu+1}$, and has polar angles θ_ν, ϕ_ν; the particle is at the point ν at the time t_ν. **k** has polar angles θ, ϕ (see Fig. 2). It is convenient to introduce Θ_ν, the angle between the path segment and **k**. From the geometry, it is seen that Θ_ν is related to θ, ϕ, etc., through $\cos\Theta_\nu = \cos\theta\cos\theta_\nu + \sin\theta\sin\theta_\nu\cos(\phi-\phi_\nu)$. From (1) we have

$$I_\nu = (e/2\pi)\sin\Theta_\nu \exp[i\omega t_\nu - ink(x_\nu \sin\theta\cos\phi + y_\nu \sin\theta\sin\phi + z_\nu\cos\theta)] \times \frac{\exp[i\omega l_\nu(1/v_\nu - n\cos\Theta_\nu/c)]-1}{i\omega(1/v_\nu - n\cos\Theta_\nu/c)}. \tag{4}$$

The angles θ_ν are the deviations of the path segments from the direction of the incident particle and are considered to be small. Consequently, we may take

$$\cos\Theta_\nu \cong \cos\theta + \alpha_\nu \sin\theta,$$
$$\sin\Theta_\nu \cong \sin\theta - \alpha_\nu\cos\theta, \ (\alpha_\nu \equiv \theta_\nu\cos\phi_\nu),$$

where, for convenience, we take $\phi = 0$, so that the direction of observation is in the x, z plane. Also, since the energy loss is neglected, we take $v_\nu = v$. The particle starts from the origin at time $t = 0$; therefore,

$$t_\nu = v^{-1}(l_0 + l_1 + l_2 + \cdots + l_{\nu-1}) \cong v^{-1}z_\nu.$$

With these approximations, (4) becomes

$$I_\nu \cong \frac{e(\sin\theta - \alpha_\nu\cos\theta)}{2\pi} \times \exp\left[i\omega z_\nu\left(\frac{1}{v} - \frac{n\cos\theta}{c}\right) - inkx_\nu\sin\theta\right] \times \frac{\exp[i\omega l_\nu(1/v - n\cos\theta/c) - inkl_\nu\alpha_\nu\sin\theta]-1}{i\omega(1/v - n\cos\theta/c) - ink\alpha_\nu\sin\theta}. \tag{5}$$

There are two different approaches to the evaluation of (3) by means of (5). One is an expansion valid near the radiation maximum. The other is an asymptotic expansion valid at viewing angles whose difference from the angle of the radiation maximum is much greater than the rms multiple scattering angle. The former will be treated first.

(B) The Solution Near the Radiation Maximum

It is convenient here to introduce $\kappa \equiv \theta - \theta_0$ where θ_0 is the angle of the radiation maximum (see Fig. 1). Under the small angle approximation for κ, (5) becomes

$$I_\nu \cong \frac{e\sin\theta_0}{2\pi}(1 + \kappa\cot\theta_0)\exp[ink\sin\theta_0(\kappa z_\nu - x_\nu)] \times \frac{\exp[ink\sin\theta_0(\kappa - \alpha_\nu)l_\nu]-1}{ink\sin\theta_0(\kappa - \alpha_\nu)}. \tag{6}$$

Here it is asked that $|(\kappa - \alpha_\nu)(l_\nu/\lambda)|$ be very much less than unity. This further limits the range of validity of this solution to small κ. Equation (6) can now be written approximately

$$I_\nu \cong \frac{e\sin\theta_0}{2\pi} l_\nu \exp[ink\sin\theta_0(\kappa z_\nu - x_\nu)]. \tag{7}$$

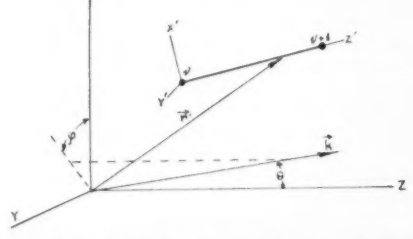

FIG. 2. The geometry involved in the development of the formula describing the radiation from a single path segment.

[3] I. Frank and I. Tamm, Compt. rend. acad. sci. U.R.S.S. **14**, 109 (1937). See also reference 2, p. 262.

Equation (3) may be written

$$\sum_{\nu=0}^{N-1}\sum_{\mu=0}^{N-1} I_\nu I_\mu^*. \tag{8}$$

Experimentally, one observes the radiation from a great number of particles. Therefore, one must calculate an ensemble average of (8) over all quantities which may be different for the paths of individual particles. This ensemble average may be computed by taking the averages of the individual terms $I_\nu I_\mu^*$ of (8) and then performing the summations indicated. With the aid of (7) we have

$$\langle I_\nu I_\mu^*\rangle_{Av}\left(\frac{e\sin\theta_0}{2\pi}\right)^{-1} \cong\langle l_\nu l_\mu \exp -iB[(x_\nu-x_\mu)+\kappa(z_\nu-z_\mu)]\rangle_{Av}, \tag{9}$$

where $B\equiv nk\sin\theta_0$. A change of variables will put this in a form that will allow the results of multiple scattering theory to be applied. From Fig. 3 it is clear that $x_\nu-x_\mu\cong\gamma_{\nu-\mu}+\alpha_\mu(z_\nu-z_\mu)$. With the aid of this, (9) becomes

$$\langle l_\nu l_\mu \exp -iB[\gamma_{\nu-\mu}+(\kappa+\alpha_\mu)(z_\nu-z_\mu)]\rangle_{Av}. \tag{10}$$

The average is computed by multiplying by the normalized distribution functions of all the variables represented in (10) and then integrating over the allowed ranges of the variables. We therefore multiply by $p_1(l_\nu)p_2(l_\mu)p_3(\alpha_\mu, z_\mu)p_4(z_\mu)p_5(\gamma_{\nu-\mu}, z_\nu-z_\mu)p_6(z_\nu-z_\mu)$. The combination p_3p_4 is the probability that after undergoing μ collisions, the particle makes an angle α_μ with the original path. The factor p_3 is the distribution function for α_μ given that the particle has traveled a distance z_μ; p_4 is the probability that the particle has indeed traveled a distance z_μ up to the μ^{th} collision. The combination p_5p_6 is to be interpreted in the same manner. At this point it is assumed that negligible error will occur if the result of averaging over z_μ, and also $z_\nu-z_\mu$, is to replace them by their mean values directly; i.e., replace z_μ by $\mu\lambda_0$ and $z_\nu-z_\mu$ by $(\nu-\mu)\lambda_0$,[4] where λ_0 is the mean free path of a particle in the transparent plate. $p_3(\alpha_\mu, \mu\lambda_0)$ is taken from the simplest multiple scattering theory and is[5]

$$A\pi^{-1}\mu^{-1}\exp[-(A^2\alpha_\mu^2/4\mu)].$$

Examination of Fig. 3 shows that we may also use this multiple scattering theory in developing $p_5(\gamma_{\nu-\mu}, (\nu-\mu)\lambda_0)$. This yields[6]

$$\frac{\sqrt{3}A}{2\pi^{\frac{1}{2}}\lambda_0(\nu-\mu)^{\frac{1}{2}}}\exp\left\{-\left[\frac{3A^2\gamma_{\nu-\mu}^2}{4\lambda_0^2(\nu-\mu)^3}\right]\right\}.$$

[4] In support of this assumption, it can be shown that although p_4 and p_6 are rather wide functions, their widths divided by their mean values become very small as the number of segments represented by them is taken larger. Therefore, it is felt justifiable to replace p_4 and p_6 by delta-functions centered about the mean values involved.

[5] See Appendix, Eq. (A2).

[6] See Appendix, Eq. (A3).

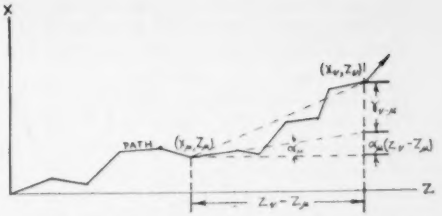

FIG. 3. Relations between variables characteristic of a give path.

$p_1(l_\nu)$ and $p_2(l_\mu)$ are $\lambda_0^{-1}\exp(-l_\nu/\lambda_0)$ and $\lambda_0^{-1}\exp(-l_\mu/\lambda_0)$, respectively.

Therefore, evaluation of (10) yields

$$\lambda_0^2\exp[-iB\lambda_0(\nu-\mu)\kappa - B^2\lambda_0^2A^{-2}(\nu-\mu)^2\{\mu+\tfrac{1}{3}(\nu-\mu)\}].$$

It is clear from this that

$$\langle I_\mu I_\nu^*\rangle_{Av}=\langle I_\nu I_\mu^*\rangle_{Av}^*.$$

Therefore,

$$\langle I_\nu I_\mu^*+I_\mu I_\nu^*\rangle_{Av}=(e\sin\theta_0/2\pi)^2 2\lambda_0^2\cos[B\lambda_0(\nu-\mu)\kappa] \times\exp[-B^2\lambda_0^2A^{-2}(\nu-\mu)^2\{\mu+\tfrac{1}{3}(\nu-\mu)\}]. \tag{11}$$

With the help of (11), a little consideration shows that the ensemble average of (8) may be written

$$2\lambda_0^2\left(\frac{e\sin\theta_0}{2\pi}\right)^2\sum_{l=0}^{N-1}\cos(B\lambda_0 l\kappa)\exp\left[-\left(\frac{B\lambda_0}{A}\right)^2\frac{l^3}{3}\right] \times\sum_{\mu=0}^{N-l-1}\exp\left[-\left(\frac{B\lambda_0}{A}\right)^2 l^2\mu\right], \tag{12}$$

where we have written: $l\equiv\nu-\mu$.

It will now be shown that the summations over l and μ may be approximated by integrals. The factor in (12) following the cosine, falls to e^{-1} for $l=(\sqrt{3}A/B\lambda_0)^{\frac{1}{2}}$. For this value of l, the exponent of the last factor in (12) is: $-(3B\lambda_0/A)^{\frac{1}{2}}\mu$. Here, the coefficient of μ can be seen to be small compared to unity in practical cases, so that the replacement of the sum over μ by an integral is justified. By a similar argument, one can show that the sum over l can also be replaced by an integral; the criteria in this case are that $B\lambda_0\kappa$ and $(B\lambda_0/\sqrt{3}A)^{\frac{1}{2}}$ both be small compared to unity. Equation (12) becomes:

$$2\lambda_0^2\left(\frac{e\sin\theta_0}{2\pi}\right)^2\int_{l=0}^{N-1}\cos(B\lambda_0 l\kappa)\exp\left[-\left(\frac{B\lambda_0}{A}\right)^2\frac{l^3}{3}\right] \times\int_{\mu=0}^{N-l-1}\exp\left[-\left(\frac{B\lambda_0}{A}\right)^2 l^2\mu\right]d\mu dl. \tag{13}$$

The integration over μ is elementary. It is convenient to express (13) in terms of some new variables. Let us

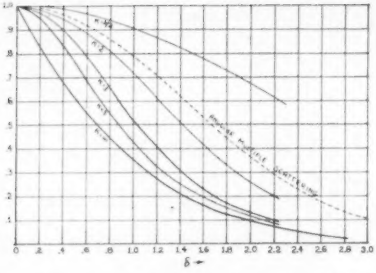

FIG. 4. Curves, normalized to unity at $\delta=0$, showing the angular shape of the radiation pattern. The abscissa is the difference between the viewing angle and the angle at which the radiation maximum appears, and it is measured in units of the rms multiple scattering which occurs in the plate. The dashed curve is a plot of the exponential of Eq. (A2) in the appendix, and shows the projected angular distribution of particles emerging from the plate. The curve for $K=\infty$ is the projected angular multiple scattering averaged over the thickness of the plate.

take:

$$u\equiv B\lambda_0 N^{\frac{1}{2}}l/A,$$
$$K\equiv(3B\lambda_0 N^{\frac{1}{2}}/A)^{\frac{1}{2}}=[(3BL/2^{\frac{1}{2}})((2N)^{\frac{1}{2}}/A)]^{\frac{1}{2}},$$
$$\delta\equiv A\kappa/N^{\frac{1}{2}}.$$

The rms value of the angular multiple scattering in the plate is $A^{-1}(2N)^{\frac{1}{2}}$. Therefore, it is seen that δ measures the viewing angle κ in terms of the rms multiple scattering. K is a constant characteristic of L/λ and the rms multiple scattering. In terms of these variables, (13) becomes

$$6\lambda_0{}^3\left(\frac{e\sin\theta_0}{2\pi}\right)^2\frac{N^2}{K^3}\int_0^{\frac{1}{2}K^3}\cos(\delta u)$$
$$\times\exp[-(u/K)^3]\frac{1-\exp[-u^2+3(u/K)^3]}{u^2}du. \quad (14)$$

The integral in (14) has been evaluated numerically for several values of K. The results, normalized[7] to unity are shown in Fig. 4. These curves are convenient for $K\gtrsim 1$, but for smaller K, it is best to express the results in terms of the variable $BN\lambda_0\kappa$ as is done in the elementary theory. [See Eq. (2).]

The case of very large K can be interpreted as the result of there being coherence only over a few adjoining segments. It is possible to arrive at the large K case in another manner. The power radiated by a few coherent adjoining segments can be found [by the simple theory Eq. (2)] to be proportional to Δz, the length of the group of segments. The radiation maximum due to this group of segments will appear at an angle differing from θ_0 by the projection of the average angle of the group of segments from the mean path, onto the plane determined by the line of observation and the mean path. Thus, to calculate the angular distribution of radiation from the entire plate, we multiply the power radiated from a group of segments, proportional to Δz, by the angular multiple scattering probability and sum over the thickness of the plate.

$$\sum_{r=0}^{L/\Delta z}\frac{A\lambda_0{}^{\frac{1}{2}}}{2\pi^{\frac{1}{2}}(r\Delta z)^{\frac{1}{2}}}\exp\left(-\frac{A^2\lambda_0\kappa^2}{4r\Delta z}\right)(\Delta z),$$

where $\kappa\equiv\theta-\theta_0$. In the limit of small Δz, we can replace $(r\Delta z)$ by z and

$$\sum_r(\cdots)\Delta z \text{ by } \int(\cdots)dz:$$

$$\int_0^{N\lambda_0}\frac{A\lambda_0{}^{\frac{1}{2}}}{2\pi^{\frac{1}{2}}z^{\frac{1}{2}}}\exp\left(-\frac{A^2\lambda_0\kappa^2}{4z}\right)dz$$
$$=(\lambda_0 N^{\frac{1}{2}}A/2\pi^{\frac{1}{2}})\tfrac{1}{2}\delta\int_{(\delta/2)^2}^{\infty}v^{-\frac{1}{2}}e^{-v}dv, \quad (15)$$

where δ is defined as before and $v\equiv 4z/(A^2\lambda_0\kappa^2)$. This integral is related to the incomplete gamma-function in a simple manner and may be expressed as a special case of the confluent hypergeometric series.[8] This series, multiplied by $(\delta/2)$, can be shown to be equal to the series expansion of

$$\frac{2}{\pi^{\frac{1}{2}}}\int_0^{\infty}\cos(\delta u)\frac{1-\exp(-u^2)}{u^2}du,$$

i.e., proportional to (14) for $K=\infty$. This serves as a check on (14). Another check on (14) is the case of no scattering. In this limit, the simple theory result, Eq. (2), is obtained.

(C) The Asymptotic Form

The radiation maximum occurs at a viewing angle θ_0 such that $\cos\theta_0=c/(nv)$. Since in this section we seek a solution away from this maximum, we may extract $(v^{-1}-nc^{-1}\cos\theta)$ from the denominator of (5) and expand the remaining factor in a power series, retaining only the first two terms. The limitation on the final result imposed by this approximation may be seen to restrict the result to values of κ much greater than any α_i that occurs, hence much greater than the angular rms scattering that occurs in the plate. As in the case of the solution near the radiation maximum, we note that the lateral deviation of a particle from its path between two collisions is small compared to a wavelength of the light observed. This allows us to replace $\exp(-inkl_r\alpha_r\sin\theta)$ by the first two terms of a power series expansion. With these two approximations, (5) becomes

$$I_r\cong(e\sin\theta/2\pi ia)\exp i(az_{r+1}-bx_r)$$
$$\times[(1-e^{-ial_r})(1+\alpha_r g)-ib\alpha_r l_r], \quad (16)$$

[7] In normalizing, we have divided by the value of the integral for $\delta=0$. These values are tabulated in Sec. (B) of the Appendix.

[8] E. T. Whittaker and G. N. Watson, *A Course of Modern Analysis* (The Macmillan Company, New York, 1946), p. 341.

where, for simplicity, we have introduced

$$a\equiv\omega[(1/v)-(n\cos\theta/c)],\qquad b\equiv\omega n\sin\theta/c,$$

$$g\equiv\frac{n-c\cos\theta/v}{c[(1/v)-(n\cos\theta/c)]\sin\theta}.$$

One may now use (16) to form

$$\sum_{\nu=0}^{N-1}I_\nu\cong(e\sin\theta/2\pi ia)\{-(1+\alpha_0 g)\exp[i(az_0-bx_0)]$$
$$-g\sum_{\nu=1}^{N-1}[\eta_\nu\exp\{i(az_\nu-bx_\nu)\}]$$
$$+(1+\alpha_{N-1}g)\exp\{i(az_N-bx_N)\}\}. \quad (17)$$

In forming this expression, it is necessary to interchange $\exp(-ib\alpha_\nu l_\nu)$ with $1-ib\alpha_\nu l_\nu$ occasionally, and also to neglect other terms of order α_ν^2 as compared with α_ν. Use has also be made of $z_{\nu+1}\cong z_\nu+l_\nu$ and $x_{\nu+1}\cong x_\nu+\alpha_\nu l_\nu$. The angle η_ν is defined as the projection of the angle of scattering of the charged particle at collision ν. This is clearly $\eta_\nu\equiv\alpha_\nu-\alpha_{\nu-1}$.

We are interested in the average of the absolute square of (17). In examining the square, we find many terms that are linear in any one particular η_i. The average of such terms will be zero, since the probability of any η_i (i.e., the projected cross section for a single collision) is an even function of η_i. We may take $\alpha_0=x_0=z_0=0$, since the particle is taken to be incident on the plate at the origin and directed along the z axis. The average of the square of (17) is then

$$\langle|\sum_{\nu=0}^{N-1}I_\nu|^2\rangle_{Av}=(e\sin\theta/2\pi a)^2\{\langle|(1+\alpha_{N-1})$$
$$\times\exp[i(az_N-bx_N)]-1|^2\rangle_{Av}+g^2\sum_{\nu=1}^{N-1}\langle\eta_\nu^2\rangle_{Av}\}$$
$$=2(e\sin\theta/2\pi a)^2\{1-\langle(1+g\alpha_{N-1})\cos(aL-bx_N)\rangle_{Av}$$
$$+g^2\langle\alpha_{N-1}^2\rangle_{Av}\}. \quad (18)$$

In obtaining (18), use has been made of $\langle\alpha_{N-1}\rangle_{Av}=0$, $z_N\equiv L$, and

$$\alpha_{N-1}\equiv\sum_{\nu=1}^{N-1}\eta_\nu.$$

The number of segments N is large, and hence, one may substitute α_N for α_{N-1} in (18). The averaging indicated in (18) is performed by utilizing the distribution function (A) and integrating over α_N and x_N. The result is

$$2\left(\frac{e\sin\theta}{2\pi a}\right)^2\left\{1-\left(\cos aL+\frac{gbN^2\lambda_0}{A^2}\sin aL\right)\right.$$
$$\left.\times\exp\left(-\frac{b^2\lambda_0^2N^3}{3A^2}\right)+\frac{2g^2N}{A^2}\right\}. \quad (19)$$

Equation (19) may be written in terms of K and δ. The limitation on this form being that κ should be small so that one may replace $\sin\kappa$ by κ, etc. This yields

$$2\left(\frac{e\sin\theta_0}{2\pi}\right)^2\frac{9L^2}{\delta^2K^6}\left\{1-\left[\cos\left(\frac{K^3\delta}{3}\right)+\frac{K^3}{3\delta}\sin\left(\frac{K^3\delta}{3}\right)\right]\right.$$
$$\left.\times\exp\left(-\frac{K^6}{27}\right)+\frac{2}{\delta^2}\right\}.$$

The exponential factor destroys the diffraction wiggles for large K.

The asymptotic solution was developed under the assumption that the viewing angle κ is large compared with the angular rms multiple scattering. In the limit of no scattering, the solution should be valid very near the radiation maximum. By allowing the scattering to go to zero in Eq. (19), i.e., by allowing NA^{-2} to go to zero, it can be seen that the result of the simple theory is obtained.

III. DISCUSSION OF RESULTS

The curves of Fig. 4 are the results of the calculation of the radiation near the usual maximum (see Sec. II-B). The asymptotic solution (Sec. II-C) is valid only for $\delta\gg1$ and, therefore, does not appear in Fig. 4. All the curves of Fig. 4 are symmetrical about the vertical axis. The abscissa δ is proportional to $\kappa\equiv\theta-\theta_0$, where θ is the viewing angle with respect to the direction of the path of the charged particle, and θ_0 is the viewing angle of the usual maximum. δ is related to κ through $\delta\equiv\kappa\sqrt{2}/\langle\langle\theta^2\rangle\rangle^{\frac{1}{2}}$, where $\langle\langle\theta^2\rangle\rangle^{\frac{1}{2}}$ is the rms multiple scattering angle that corresponds to the thickness of the plate. The dashed curve of Fig. 4 shows the projected angular distribution of particles emerging from the plate. This is the Gaussian from Eq. (A2) of the appendix.

The parameter K may be readily determined for a particular case in the following manner. First calculate the rms multiple scattering angle $\langle\langle\theta^2\rangle\rangle^{\frac{1}{2}}$. K is then obtained from

$$K\equiv[(6\pi/\sqrt{2})n\sin\theta_0(L/\lambda)\langle\langle\theta^2\rangle\rangle^{\frac{1}{2}}]^{\frac{1}{3}},$$

where L is the thickness of the plate, λ is the wavelength of the light observed, n is the refractive index of the plate, and θ_0 is the viewing angle at which the usual maximum occurs. As mentioned in the last paragraph of Sec. II-B, the angular distribution of radiation in the case of large K may be obtained by averaging the projected angular multiple scattering distribution function over the length of the path L. The results for large K will therefore fall within the dashed curve of Fig. 4. From the above definition of K, we may look on the curves for progressively smaller K as the radiation distribution if longer wavelength radiation is observed. The broadening is due to the effects of partial incoherence and, for sufficiently small K, due to the diffraction over the entire path length.

The author is indebted to Professor L. I. Schiff for suggesting this problem and for his very helpful aid and interest throughout the entire calculation.

APPENDIX

(A) Multiple Scattering Theory

Multiple scattering theories give the probability that a particle that has suffered a great number of collisions in a slab of material has a projected angle of emergence between θ and $\theta+d\theta$, and has been deviated from its original path by a distance between y and $y+dy$. The simplest of these theories make use of the fact that fast particles being scattered by the electric field of the nucleus are scattered predominantely forward. This allows approximations to be made that yield the distribution function originally due to Fermi[9]

$$F(z, y, \theta)=\frac{\sqrt{3}A^2\lambda_0}{2\pi z^2}\times\exp\left[-\frac{A^2\lambda_0}{z}\left\{\left(\theta-\frac{3y}{2z}\right)^2+\frac{3}{4}\left(\frac{y}{z}\right)^2\right\}\right], \quad \text{(A1)}$$

where z is defined as the thickness of the slab and is expressed in the same units as λ_0, the mean free path of a particle in the material. $A^2\lambda_0$ is a constant characteristic of the single scattering process and takes on slightly different values when one makes different assumptions regarding the screening of the Coulomb potential and uses different methods in calculating the single scattering cross section.[10] Equation (A1) may be integrated over y to form the distribution in θ alone. We then have

$$G(z, \theta)=\frac{A\lambda_0^{\frac{1}{2}}}{2\pi^{\frac{1}{2}}z^{\frac{1}{2}}}\exp\left[-\frac{A^2\lambda_0\theta^2}{4z}\right]. \quad \text{(A2)}$$

Alternatively, (A1) may be integrated over θ to yield the distribution in y.

$$H(z, y)=\frac{\sqrt{3}A\lambda_0^{\frac{1}{2}}}{2\pi^{\frac{1}{2}}z^{\frac{1}{2}}}\exp\left[-\frac{3A^2\lambda_0 y^2}{4z^3}\right]. \quad \text{(A3)}$$

(B) Normalizing Factors

The factors noted in reference 7 are the values of

$$\int_0^{\frac{1}{2}K^3}\left[\exp\left\{-\left(\frac{u}{K}\right)^3\right\}\right]\cdot\frac{1-\exp[-u^2+3(u/K)^3]}{u^2}du.$$

The values of these integrals are

K	∞	5	3	2	3/2
Value of the integral:	$\pi^{\frac{1}{2}}$	1.49	1.28	0.933	0.519.

[9] B. Rossi and K. Griesen, Revs. Modern Phys. **13**, 267 (1941).

[10] See reference 5 in W. T. Scott, Phys. Rev. **76**, 213 (1949).

Letters to the Editor

PUBLICATION of brief reports of important discoveries in physics may be secured by addressing them to this department. The closing date for this department is five weeks prior to the date of issue. No proof will be sent to the authors. The Board of Editors does not hold itself responsible for the opinions expressed by the correspondents. Communications should not exceed 600 words in length and should be submitted in duplicate.

Fusion as Hydrodynamic Instability in Thermal Wave Propagation

G. BONFIGLIOLI
Istituto Elettrotecnico Nazionale, Turin, Italy
(Received July 16, 1952)

THE writer and his associates recently attempted[1] to treat the fusion of metals (at least those with high crystalline symmetry) as being due to an instability of the atomic thermal vibrations.

The formulas obtained by them coincide basically with an old semi-empirical relation of Lindemann, that is easily transformable into the form:

$$KT_M = \sigma EV, \tag{1}$$

(K = Boltzmann's constant, T_M = melting point in °K, E = Young's modulus for polycrystalline quasi-isotropic material, V = atomic volume, σ = constant depending on lattice symmetry).

As is known, Lindemann's formula agrees well enough with experimental results; it is furthermore known that all kinetic theories of melting process give a relation of the same form (1).

This fact has been pointed out by Norzi,[2] who also deduced the same relation in a different manner.

Now, neglecting temporarily the main difficulty of the problem, that is, the "*a priori*" determination of the constant σ, and limiting the scope of this paper to setting forth the problem rather than to resolving it, we shall propose an interpretation of the melting process that gives immediately the fundamental relation (1) and that seems promising of interesting results.

An analogous criterion has been privately communicated to the writer by Norzi,[2] but the one proposed here seems less subject to criticism.

It is clear that the atomic vibrations responsible for the melting of a lattice are the high frequency ones—that is, those corresponding to wavelengths of the order of the period of the lattice (of the order of the atomic diameter, or the distance between nearest neighbors).

If equipartition for kinetic energy holds, as happens at high temperatures, then, remembering some results of the paper quoted,[1] one finds easily:

$$\omega A = (2kT/m)^{\frac{1}{2}}, \tag{2}$$

$$\omega = (Ed/m)^{\frac{1}{2}}. \tag{3}$$

($\omega = 2\pi$ times limiting frequency, A = rms value of the amplitude of atomic vibrations, m = mass of atom, d = atomic diameter).

Substituting the experimental data at high temperatures, these formulas—as well as direct x-ray measurements—show that $A/d \approx A/\lambda$ (where λ is the wavelength of the high frequency thermal waves) is not negligible compared to unity. This fact suggests that the propagation of thermal waves for temperatures approaching the melting point should be treated to a higher order approximation than is usual. This could be the method that has been applied by Hugoniot, Fubini-Ghiron *et al.*[4] for continuous media, giving rise to nonlinear equations for the propagation of finite amplitude acoustic waves. A result of these calculations seems to suggest a criterion that may be applied to the melting process.

As a matter of fact, the nonlinear propagation of an elastic wave of finite amplitude in a continuous, homogeneous, isotropic medium, at least in the adiabatic case, is characterized by the fact that a sinusoidal wave is being deformed during its motion, until—at a certain distance from its origin—the wave becomes discontinuous and the propagation laws change abruptly. If c is the propagation velocity ($\simeq$ sound velocity), the distance X from the origin of the wave, at which the discontinuity arises and the acoustic wave of amplitude A behaves as an explosion wave, is given to a good approximation by[5]

$$X = 2c^3/A\omega^2. \tag{4}$$

It is now evident that, if an assembly of sources of movement (the nodes of the lattice) is considered, the lattice will abruptly collapse when A is so large that X becomes of the order of the distance d between the sources (or, assuming $X = pd$, when p is near unity).

It is believed that it should be possible to interpret fusion by means of this mechanism.

Two remarks support this viewpoint: (a) If one puts:

$$c = (E/\rho)^{\frac{1}{2}}, \tag{5}$$

where ρ is the density, and

$$A = (2kT/Ed)^{\frac{1}{2}}, \tag{6}$$

one finds immediately that a formula like (1) holds for the melting point. (b) If one assumes for E the Young's modulus for a polycrystalline metal at normal temperature, that is, if one considers longitudinal waves, the agreement between the calculations and the experiments is fairly good for $p \simeq 10$, that is, not a too large number. But if, as seems justifiable, one takes into account the lowering of sound velocity at high temperature, and limits the consideration to transversal waves that travel at a lower speed, and to the crystallographic directions of minimum speed of these waves, the agreement becomes good for $p \simeq 1$.

As has been said, the problem is only set forth and is very far from resolved; but nevertheless there must be here something more than a mere coincidence; and this interpretation of fusion as hydrodynamic instability in the propagation of thermal waves of finite amplitude may give interesting results.

The stated criterion would perhaps be general and independent of the kind of chemical bond; and it would be very interesting—in order to test it—to obtain direct experimental data on the atomic vibration amplitudes and the elastic constants of some substances at temperatures near their melting point.

[1] Bonfiglioli, Ferro, and Montalenti, *Sur la théorie de la fusion des métaux*, presented at the "colloque sur les changements de phase" of the Société de Chimie Physique, Paris, June, 1952.
[2] L. Norzi, Atti accad. sci. Torino **84**, (1949–50).
[3] The suggested criterion was the following: the crystal melts when the maximum velocity of the vibrating atoms becomes comparable to the velocity of elastic waves through the crystal.
[4] H. Hugoniot, J. école polytech. **57**, 1 (1887); **58**, 1 (1889); E. Fubini-Ghiron, Alta Frequenzo, **4**, 530 (1935).
[5] See Fubini-Ghiron (reference 4).

The Mass of Cl^{39} and of A^{39}†

C. E. ANDERSON, G. W. WHEELER, AND W. W. WATSON
Yale University, New Haven, Connecticut
(Received July 10, 1952)

RECENTLY we have searched for the ground-state proton group from the nuclear reaction $A^{39}(d, p)A^{39}$, using argon analyzing 1.2 percent A^{36}, 1.2 percent A^{38}, and 97.6 percent A^{40}. We have not observed this group, but we would have if its Q value is greater than 5 Mev which would make its range longer than that of the first excited state proton group[1] from A^{37}. At shorter ranges weak proton groups from this argon gas target are obscured by the strong groups from A^{41} and A^{37}. We have also looked for gamma-rays in coincidence with the decay of A^{39} but could find none. Therefore, using the mass of K^{39} as 38.97606±3[2]

and E_{max} for the beta-decay of A^{39} as 0.565 ± 0.005 Mev,[a] one obtains 38.97667 ± 4 for the mass of A^{39}. This value for the mass of A^{39} yields a Q value for the $A^{38}(d, p)A^{39}$ reaction of 4.31 Mev, which we would not be able to observe.

From this mass of A^{39} we can calculate the mass of Cl^{39}, using the value of the total disintegration energy of $Cl^{39}-A^{39}$ as 3.31 ± 0.09 Mev.[4] This gives 38.98022 ± 13 for the mass of Cl^{39} which differs both from the value 38.97871 ± 10 given by Wilkinson and Carver[5] and also from that given by Haslam *et al.*,[4] 38.9826. If we were to start with Wilkinson and Carver's value for the mass of Cl^{39}, we obtain 38.97516 for the mass of A^{39}, and the Q value for the d, p reaction would be 5.92 Mev. Then we would have observed this proton group. Also this 38.97516 value for the mass of A^{39} is less than that of K^{39}, in contradiction to the observed β-decay. And, finally, the mass of Cl^{39} given by Haslam *et al.* leads to the prediction that the total disintegration energy for $A^{39}-K^{39}$ is 2.8 Mev, which is also in contradiction to the observed β-ray energy.

† Supported by the AEC.

[1] A. Zucker and W. W. Watson, Phys. Rev. **80**, 966 (1950).
[2] Collins, Nier, and Johnson, Phys. Rev. **84**, 717 (1951).
[3] Brosi, Zeldes, and Ketelle, Phys. Rev. **79**, 902 (1950).
[4] Haslam, Katz, Moody, and Skarsgard, Phys. Rev. **80**, 318 (1950).
[5] D. H. Wilkinson and J. H. Carver, Phys. Rev. **83**, 466 (1951).

Conservation Laws for Fields of Zero Rest Mass. I

JAMES A. MCLENNAN, JR.* AND PETER HAVAS
Department of Physics, Lehigh University, Bethlehem, Pennsylvania
(Received June 23, 1952)

IT is well known[1] that for any set of field equations which are derivable from a Lorentz-invariant variational principle, there exist laws of conservation of energy and momentum

$$\partial T_{\mu\nu}/\partial x_\mu=0, \tag{1}$$

where $T_{\mu\nu}$ can be chosen to be symmetric, and of angular momentum

$$\partial M_{\mu\nu\rho}/\partial x_\mu=0, \tag{2}$$

with

$$M_{\mu\nu\rho}=T_{\mu\nu}x_\rho-T_{\mu\rho}x_\nu. \tag{3}$$

It was found by Bessel-Hagen[2] that for the electromagnetic field there exist two additional conservation laws

$$\partial N_\mu/\partial x_\mu=0 \tag{4}$$

$$\partial R_{\mu\nu}/\partial x_\mu=0 \tag{5}$$

with

$$N_\mu=T_{\mu\nu}x^\nu \tag{6}$$

and

$$R_{\mu\nu}=2T_{\mu\rho}x^\rho x_\nu-T_{\mu\nu}x_\rho x^\rho. \tag{7}$$

It is easily shown that these laws hold because the symmetric energy-momentum tensor has zero trace. Their existence was shown by Bessel-Hagen to be connected with the fact that Maxwell's equations are invariant under the group of all conformal transformations in four dimensions, as found by Cunningham[3] and Bateman.[4]

Gårding[6] has given all those relativistically invariant sets of linear differential equations, homogeneous in the first partial derivatives of the unknowns u, which imply the equation

$$\partial^2 u/\partial x_\mu\partial x^\mu=0, \tag{8}$$

and which therefore appear to be suitable for a description of wave fields of zero rest mass. These equations include those proposed earlier by Dirac[6] and Fierz.[7]

We have found that all of Gårding's equations admit the conservation laws (4) and (5). The tensors N_μ and $R_{\mu\nu}$ have the form (6) and (7) respectively, due to the fact that symmetric energy-momentum tensors with zero trace can be constructed, except for those equations which are physically equivalent to the scalar wave equation. For this equation, however, the energy-momentum tensor has the form

$$T_{\mu\nu}=\frac{\partial u}{\partial x^\mu}\frac{\partial u}{\partial x^\nu}-\tfrac{1}{2}g_{\mu\nu}\frac{\partial u}{\partial x_\rho}\frac{\partial u}{\partial x^\rho}, \tag{9}$$

which has a nonzero trace. Nevertheless we still have the conservation laws (4) and (5), but N_μ and $R_{\mu\nu}$ are now given by

$$N_\mu=T_{\mu\nu}x^\nu+u\partial u/\partial x^\mu, \tag{10}$$

$$R_{\mu\nu}=2T_{\mu\rho}x^\rho x_\nu-T_{\mu\nu}x_\rho x^\rho-g_{\mu\nu}u^2+2u(\partial u/\partial x^\mu)x_\nu. \tag{11}$$

The existence of these conservation laws for wave equations for fields of zero rest mass is again connected with the invariance of these equations under the conformal group, as will be shown in a forthcoming paper. For non-zero rest mass the wave equation is known not to be conformally invariant[8] and no such additional conservation laws exist.

* AEC Predoctoral Fellow.
[1] See, e.g., W. Pauli, Revs. Modern Phys. **13**, 203 (1941).
[2] E. Bessel-Hagen, Math. Ann. **84**, 258 (1921).
[3] E. Cunningham, Proc. London Math. Soc. **8**, 77 (1910).
[4] H. Bateman, Proc. London Math. Soc. **8**, 223 (1910).
[5] L. Gårding, Proc. Cambridge Phil. Soc. **41**, 49 (1945).
[6] P. A. M. Dirac, Proc. Roy. Soc. (London) **A155**, 447 (1936).
[7] M. Fierz, Helv. Phys. Acta **12**, 3 (1939).
[8] W. Brittin, Phys. Rev. **87**, 197 (1952).

Conservation Laws for Fields of Zero Rest Mass. II

PETER HAVAS
Department of Physics, Lehigh University, Bethlehem, Pennsylvania
(Received June 23, 1952)

DETAILED conservation of energy and momentum for a point particle interacting with a field is expressed[1] in relativistic classical theory by

$$\frac{dP_\nu}{ds}+\frac{d}{ds}\int\frac{\partial T_{\mu\nu}}{\partial x_\mu}dx^0dx^1dx^2dx^3=0, \tag{1}$$

if the integral is extended over the neighborhood of the particle, and by vanishing of the integral if the region of integration does not include the particle. Here $T_{\mu\nu}$ is the energy-momentum tensor of the field, P_ν is a quantity depending on the variables at the position of the particle only, and s is the proper time of the particle. A similar equation expresses the conservation of angular momentum. It has been shown[1,2] that the integral appearing in Eq. (1) (or in similar laws for any other tensors of the field which are conserved) contains infinite terms which, however, can be compensated by similar terms in the quantities referring to the particle. It is, therefore, understood in the following that only the finite terms of the integrals are to be considered.

It was found by Bessel-Hagen[2] that the electromagnetic field admits two additional conservation laws, and it was shown in part I of this paper[4] that such additional conservation laws hold for all relativistically invariant wave equations for fields of zero rest mass.

The customary procedure for obtaining the equations of motion of point particles[1,2] is to start from the conservation laws for the field alone and to require such conservation laws [of the form of Eq. (1)] to persist in the presence of the particle as well. As the additional conservation laws mentioned above do not possess the same universal validity as those for energy-momentum and angular momentum (e.g., they do not hold for wave fields of non-zero rest mass), it does not appear to be justified physically to require their continued validity in the presence of sources of a field too. However, the question arises whether the equations found by requiring only the conservation of energy-momentum and angular momentum would admit any additional conservation laws.

The only equations of motion for particles interacting with fields of zero rest mass which have been obtained explicitly are those for an electromagnetic or a scalar field.[1,5] For point charges the equations of motion are

$$dP_\mu/ds=eG_{\mu\nu}v^\nu, \tag{2}$$

with

$$P_\mu = mv_\mu \tag{3}$$

for the electromagnetic field, and

$$dP_\mu/ds = -g\partial U/\partial x^\mu, \tag{4}$$

with

$$P_\mu = (m - gU)v_\mu \tag{5}$$

for the scalar field. Here m and v_μ are the mass and the four-velocity of the particle, e and g its coupling constants with the two fields, $G_{\mu\nu}$ is the electromagnetic field tensor and U the scalar field. $G_{\mu\nu}$ and U are to be taken as the total (external plus particle) field minus the particle's symmetric field.[1,5] If it is assumed that the field of the particle is wholly retarded, this equals the external field plus the radiation field; if it is assumed to be half-retarded, half-advanced, it is just the external field, and there is no radiation damping.[6] The following results are valid in either case.

It was found that the above equations of motion allow an additional conservation law, corresponding to the conservation law (4) of I,

$$\frac{dQ}{ds} + \frac{d}{ds}\int \frac{\partial N_\mu}{\partial x_\mu} dx^0 dx^1 dx^2 dx^3 = 0, \tag{6}$$

where

$$Q = P_\mu x^\mu - ms, \tag{7}$$

and P_μ is given by (3) and (5) respectively; N_μ is the vector defined by (I.6) and (I.10) respectively. A similar law exists for point charges which possess an intrinsic angular momentum, but no dipole moment. No law corresponding to the conservation law (5) of I exists.

Thus, the system of particle and field does not obey all the conservation laws obeyed by the field alone, for the equations considered. Conversely, if we require the system to possess all the conservation properties of the field, we will not obtain the above equations of motion, which are well verified for the electromagnetic case. Therefore, it appears that instead of basing the deduction of the equations of motion on the ambiguous information provided by the conservation laws for the field alone, it may be preferable to base it on other requirements. One possibility is provided by requiring the equations of the special theory of relativity to fit within the framework of general relativity.[7]

It is planned to publish a detailed account of this work shortly.

[1] P. A. M. Dirac, Proc. Roy. Soc. (London) **A167**, 148 (1938).
[2] H. J. Bhabha and Harish-Chandra, Proc. Roy. Soc. (London) **A183**, 134 (1944).
[3] E. Bessel-Hagen, Math. Ann. **84**, 258 (1921).
[4] J. A. McLennan, Jr. and P. Havas, preceding letter (referred to as I).
[5] Harish-Chandra, Proc. Roy. Soc. (London) **A185**, 269 (1946).
[6] P. Havas, Phys. Rev. **74**, 456 (1948); **87**, 309 (1952).
[7] J. Lubanski, Acta Phys. Polon. **6**, 356 (1937); L. Infeld and P. R. Wallace, Phys. Rev. **57**, 797 (1940).

The Coulomb Scattering of Deuterons*

J. B. FRENCH† AND M. L. GOLDBERGER‡
Department of Physics and Laboratory for Nuclear Science and Engineering, Massachusetts Institute of Technology, Cambridge, Massachusetts
(Received July 10, 1952)

DEVIATIONS from Rutherford scattering may be expected in the elastic scattering of deuterons by nuclei because (1) the deuteron is a loose structure with non-coincident centers of mass and charge and it may disintegrate on scattering, and (2) deuterons which penetrate through the barrier will encounter the nucleus and may initiate nuclear processes. We consider in this note the effects due to (1).

For scattering by a point Coulomb field, a simple Born approximation calculation gives for the ratio of the scattering to Rutherford scattering:

$$\frac{d\sigma}{d\sigma_R} = \left| \int d\mathbf{s}\chi_0^2(\mathbf{s}) \exp(\tfrac{1}{2}i\Delta\mathbf{k}\cdot\mathbf{s}) \right|^2 = S(\Delta\mathbf{k}). \tag{1}$$

Here $\mathbf{s} = \mathbf{r}_p - \mathbf{r}_n$, $\chi_0(\mathbf{s})$ is the deuteron space wave function and $\hbar\Delta\mathbf{k}$ the momentum transfer. $S(\Delta\mathbf{k})$ is then the deuteron form factor. It has the value unity for zero degree scattering but depresses the large angle scattering. For example, using the usual Hulthén wave function,

$$\chi_0(\mathbf{s}) = N[e^{-\alpha s} - e^{-\beta s}]/s, \quad \text{where} \quad \beta/\alpha = 7, \tag{2}$$

we have $S(180°) = 0.30$, for 4-Mev deuterons.

The use of the Born approximation is satisfactory only for $n = Ze^2/\hbar v \ll 1$. We make, therefore, a more accurate calculation and demonstrate thereby that the deuteron structure plays no part in the Coulomb scattering when $n \gg 1$.

With $\mathbf{k}_1$ = incident deuteron wave-vector, $\mathbf{R} = \frac{1}{2}(\mathbf{r}_n + \mathbf{r}_p)$, $V(s) = n - p$ potential, and ϵ = deuteron binding energy, we have

$$\left[\nabla_R^2 + k^2 - \frac{2kn}{R} + \nabla_s^2 + V(s) - \epsilon\right]\Psi(\mathbf{R}, \mathbf{s}) = 2kn\left[\frac{1}{|\mathbf{R} - \frac{1}{2}\mathbf{s}|} - \frac{1}{R}\right]\Psi(\mathbf{R}, \mathbf{s}). \tag{3}$$

We expand Ψ on the left-hand side by $\Psi = \Sigma\chi_n(\mathbf{s})\Omega_n(\mathbf{R})$, where the $\chi_n(\mathbf{s})$ are two-particle eigenfunctions, multiply through Eq. (3) by $\chi_0(\mathbf{s})$ and integrate over $\mathbf{s}$. Then, treating the right-hand side as a perturbation, we replace Ψ by $\chi_0(\mathbf{s})\psi_1(\mathbf{R})$, where ψ_1 is the Coulomb scattering wave function for the initial vector $\mathbf{k}_1$. We then have

$$\left[\nabla_R^2 + k^2 - \frac{2kn}{R}\right]\Omega_0(\mathbf{R}) = 2kn\int \chi_0^2(\mathbf{s})\left[\frac{1}{|\mathbf{R} - \frac{1}{2}\mathbf{s}|} - \frac{1}{R}\right]\chi_0(\mathbf{s})d\mathbf{s}\psi_1(\mathbf{R}), \tag{4}$$

and now $\Omega_0(\mathbf{R})$ is the wave function describing the elastic scattering. We note immediately that the inhomogeneous term becomes very small for high n. For, because of the spherical symmetry of the deuteron distribution, $[1/|\mathbf{R} - \frac{1}{2}\mathbf{s}| - 1/R] \equiv 0$ except for $R \leq \frac{1}{2}s$; i.e., it contributes only when the scattering center is inside the deuteron. For high Z such deep penetration is improbable [$\psi_1(\mathbf{R})$ is small for small R]. Thus in this case the correction to Rutherford scattering is negligible. (This is precisely analogous to the situation in zero-zero electromagnetic transitions without parity change, where one finds an oscillating electromagnetic field only inside the nucleus.)

The solution of (3) is found as in reference 1, proper attention being paid to the Coulomb phase factors. For the asymptotic Green's function we have

$$K(\mathbf{R}, \mathbf{r}) \underset{R\to\infty}{\longrightarrow} -\frac{1}{4\pi} e^{i(kR - n\ln 2kR)}\psi_2^+(\mathbf{r}), \tag{5}$$

where $\psi_2^+(\mathbf{r})$ is the Coulomb scattering wave function for incident wave vector $-\mathbf{k}_2 = -k\mathbf{R}/R$. Using this we find the amplitude for elastic deuteron scattering to be

$$f(\theta) = f^c(\theta) - \frac{nk}{2\pi}\int \psi_2^+(\mathbf{r})\left[\frac{1}{|\mathbf{r} - \frac{1}{2}\mathbf{s}|} - \frac{1}{r}\right]\psi_1(\mathbf{r})|\chi_0(\mathbf{s})|^2 d\mathbf{r}d\mathbf{s}, \tag{6}$$

where $f^c(\theta)$ is the usual Coulomb scattering amplitude. Using (2) we write the integral appearing in (6) as

$$-8\pi N^2\left[\int_{4\alpha}^{\infty} + \int_{4\beta}^{\infty} - 2\int_{4\rho}^{\infty}\right]\frac{d\gamma}{\gamma^2}\int d\mathbf{r}\psi_2^+(\mathbf{r})\psi_1(\mathbf{r})\frac{e^{-\gamma r}}{r},$$

where $2\rho = \alpha + \beta$. The $\mathbf{r}$ integration can now be done by a straightforward generalization of a method given by Sommerfeld[8] for the case $\gamma = 0$. Collecting the results, we have then

$$d\sigma/d\sigma_R = \Big|1 - 32\pi N^2 k^2 (2\pi n)(\rho^{2\pi n} - 1)^{-1} \sin^2\tfrac{1}{2}\theta \cdot \exp(in \ln \sin^2\tfrac{1}{2}\theta) \times \left[\int_{4\alpha}^{\infty} + \int_{4\beta}^{\infty} - 2\int_{4\rho}^{\infty}\right]\frac{d\gamma}{\gamma^2}(\gamma^2 - 2i\gamma k)^{2in}(\gamma^2 + 4k^2\sin^2\tfrac{1}{2}\theta)^{-2in-1} \times F\left(-in, -in, 1; -\frac{4k^2}{\gamma^2}\sin^2\tfrac{1}{2}\theta\right)\Big|^2. \tag{7}$$

For small n this reduces to the Born approximation result (1), but for large n it has the value unity for all angles. We have had occasion to evaluate this numerically for the case appropriate to 14-Mev deuterons on Al, for which $n=0.8$. We find, for example, at 140°, $d\sigma/d\sigma_R=0.67$ while the Born approximation result would be 0.11.

To summarize we would predict that, for deuteron energies below the barrier, the ratio $d\sigma/d\sigma_R$ would show for the cases where n is small a steady decrease as we move towards large angles. As n increases this decrease would become less marked, and finally for $n\gg1$ we would have simply Rutherford scattering. Not much data on Coulomb scattering seem to be available, though there is evidence that when $n\gg1$ the Coulomb scattering is simply Rutherford.[3]

* Assisted by the joint program of the ONR and AEC..
† Now at University of Rochester, Rochester, New York.
‡ Now at University of Chicago, Chicago, Illinois.
[1] N. F. Mott and H. S. W. Massey, *Theory of Atomic Collisions* (Oxford Press, London, 1949) second edition, chap. 6.
[2] A. Sommerfeld, *Wellenmechanik* (Frederic Ungar Publishing Company, New York, 1947), p. 502.
[3] The scattering of 4-Mev deuterons on Au has been measured by L. M. Goldman and is found to be Rutherford, private communication.

The Born Approximation Theory of (d,p) and (d,n) Reactions*

P. B. Daitch and J. B. French
University of Rochester, Rochester, New York
(Received July 11, 1952)

Butler[1] has given a theory for (d,p) and (d,n) reactions which has had remarkable success in explaining experimental results. The purpose of this note is to demonstrate that in all its essential features Butler's theory is equivalent to a Born approximation calculation. It is indeed clear that it should be, for Butler's theory everywhere ignores the reaction of the elastically and inelastically scattered particles as well as the scattering of the particle that is not captured; also his results are given in terms of the obvious momentum transfers of the problem. The Born approximation theory has already been given by Bhatia *et al.*,[2] but in their paper the connection with Butler's theory has not been made quite clear.

We write the case for (d,p) reactions. To avoid unessential complications we assume at first that the initial nucleus has spin 0 and that the neutron is captured under the influence of a potential $V(r_n)$ (assumed central) into the one-particle state with space dependence $\zeta_l^m(\mathbf{r})=R_l(r)Y_l^m$ with binding energy $\epsilon=\beta^2/2M$. Let the incident deuteron have wave vector $\mathbf{K}$ and the final proton have wave vector $\mathbf{k}$. Then ($\hbar=1$)

$$\frac{d\sigma}{d\omega}=\frac{M^2}{2\pi^2}\frac{k}{K}\frac{1}{3}\frac{j+\frac{1}{2}}{2l+1}\sum_{m_d,m_p,m_n,m}|\langle V\rangle|^2, \tag{1}$$

where $\langle V\rangle$ is the matrix element between the initial and final states and m_d, m_p, and m_n are the spin magnetic quantum numbers for the deuteron, proton, and neutron; m is the orbital magnetic quantum number for the captured neutron, and j is the final nuclear spin. The summation over spin quantum numbers gives simply a factor 3. The probability amplitude for finding a proton momentum $\mathbf{k}$ in the initial deuteron is

$$P(\mathbf{k}-\tfrac{1}{2}\mathbf{K})=\int\psi_d(\mathbf{s})\exp[i(\mathbf{k}-\tfrac{1}{2}\mathbf{K})\cdot\mathbf{s}]d\mathbf{s}$$
$$=4\pi N\left[\frac{1}{\alpha^2+(\mathbf{k}-\frac{1}{2}\mathbf{K})^2}-\frac{1}{\beta^2+(\mathbf{k}-\frac{1}{2}\mathbf{K})^2}\right], \tag{2}$$

where the last step follows on using for ψ_d the usual Hulthén wave function with constants N, α, β.

The momentum carried by the captured neutron is $\mathbf{q}=\mathbf{K}-\mathbf{k}$. The probability amplitude for capturing this neutron into the state $\zeta_l^m(\mathbf{r})$ is

$$\int\zeta_l^m(\mathbf{r})V(r)e^{i\mathbf{q}\cdot\mathbf{r}}d\tau=\delta_{m0}[4\pi(2l+1)]^{\frac{1}{2}}i^l\int_0^\infty R_l(r)V(r)j_l(qr)r^2dr$$
$$=-\delta_{m0}[4\pi(2l+1)]^{\frac{1}{2}}\frac{q^2+\beta^2}{2M}\int_0^\infty R_l(r)j_l(qr)r^2dr. \tag{3}$$

The second form follows by expanding $\exp(i\mathbf{q}\cdot\mathbf{r})$, and we get a nonvanishing result only for $m=0$ by taking the axis of quantization along $\mathbf{q}$. The third form follows by eliminating $V(r)$ by using the Schrödinger equation for $R_l(r)$. The matrix element is now given by the product of factors (2) and (3).

Bhatia *et al.*[2] approximate the radial integral by

$$\int R_l(r)V(r)j_l(qr)r^2dr=j_l(qR)\int R_l(r)V(r)r^2dr, \tag{4}$$

and now the proton angular distribution is given by $|P(\mathbf{k}-\frac{1}{2}\mathbf{K})\times j_l(qR)|^2$. The difficulty here is that there is no reason why R defined by (4) should be independent of q and therefore of angle.

To proceed differently, we use the third form of (3). If we assume, as Butler implicitly does, that we may neglect the contribution to the overlap integral from $r\leqslant r_0$ (where r_0 is greater than the nuclear radius) we can, by using the equations for $R_l(r)$ and $j_l(qr)$ along with Green's theorem, write

$$(q^2+\beta^2)\int R_l(r)j_l(qr)r^2dr$$
$$=R_l(r_0)r_0^2\left[\frac{\partial j_l(qr)}{\partial r}-\frac{1}{R_l(r)}\frac{\partial R_l(r)}{\partial r}j_l(qr)\right]_{r_0}, \tag{5}$$

where

$$\frac{1}{R_l(r)}\frac{\partial R_l(r)}{\partial r}=\frac{1}{h_l^{(1)}(i\beta r)}\frac{\partial h_l^{(1)}(i\beta r)}{\partial r} \tag{6}$$

is a number defined by the l value, binding energy and r_0. Using this, we have precisely Butler's form for the proton angular distribution. The magnitude is given here in terms of the value of the captured neutron wave function on the surface r_0.

If we do not care to omit the contribution to the overlap integral for $r\leqslant r_0$, we can define the quantity

$$\bar{V}(r_0)=-\int_0^{r_0}j_l(qr)R_l(r)V(r)r^2dr\Big/\int_0^{r_0}j_l(qr)R_l(r)r^2dr, \tag{7}$$

and then it is trivial to show that

$$\int_0^\infty R_l(r)j_l(qr)r^2dr=\left(1-\frac{q^2+\beta^2}{2M\bar{V}}\right)^{-1}\int_{r_0}^\infty R_l(r)j_l(qr)r^2dr. \tag{8}$$

In this case, the proton cross section contains also the angularly dependent factor $[1-(q^2+\beta^2)/2M\bar{V}]^{-2}$. It should be emphasized that the cross section is invariant to the choice of r_0 provided only that $r_0\geqslant r_{\text{nucleus}}$, but does of course depend on the value of the neutron potential.

Finally, we emphasize that application of the Born approximation in the low energy region is a very crude procedure. For example, the effects of scattering of the proton and deuteron are not at all small. We hope to report later some calculations of these effects.

If we take r_0 to be the nuclear radius and make the reasonable assumption that the neutron potential inside the nucleus is constant, then $\bar{V}$ is simply the potential depth. The extra factor will not disturb the most striking feature of Butler's angular distribution, namely, the angular position of the first maximum. It has a singularity at $q=(2M\bar{V}-\beta^2)^{\frac{1}{2}}$, but this simply removes one of the zeros of Butler's distribution. These zeros, in fact, occur when the neutron momentum transfer q equals an average wave number which a neutron could have when bound with binding energy $\epsilon=\beta^2/2M$ and orbital angular momentum l in a well of radius r_0. The extra factor above removes that zero which corresponds to the actual inside wave number of the captured neutron. Thus, for example, the formal Born approximation theory for a $2p$ state would not have the first zero of Butler's theory.

To treat the more general case where we impose no restrictions on the nature of the nuclear wave functions, we can define an "effective neutron wave function" by

$$\zeta_{l'l}{}^{M'M}(\mathbf{r}) = \int \Omega_{l'}{}^{M'}(\mathbf{x}, \mathbf{r})^* \Omega_l{}^{M}(\mathbf{x}) d\mathbf{x}, \tag{9}$$

where Ω's are the initial and final nuclear wave functions and $\mathbf{x}$ = coordinates of all initial nuclear particles. This can be expanded into a series containing all the l values compatible with the nuclear spins and parities, and the m summation can be easily performed. The only important point (as is clear from references 1 and 2) is that there is no interference between different l's.

* Work performed under the auspices of the AEC.
[1] S. T. Butler, Proc. Roy. Soc. (London) **208**, 559 (1951).
[2] Bhatia, Huang, Huby, and Newns, Phil. Mag. **43**, 485 (1952).

Half-Lives of Eu^{152}, Eu^{154}, and Sm^{151}

D. G. Karraker, R. J. Hayden and M. G. Inghram
Argonne National Laboratory, Chicago, Illinois
(Received July 10, 1952)

THE half-lives of Eu^{152}, Eu^{154}, and Sm^{151} have been measured directly by mass spectrometric methods. In each case, the half-life was determined by the change with time of the isotopic constitution of samples containing an appreciable percentage of the nuclide under investigation. For Eu^{152} and Eu^{154} the sample used for the determination of the half-lives was a normal europium sample irradiated in a pile. Data on this sample have been used previously for an indirect determination of the half-lives of Eu^{152} and Eu^{154}.[1]

The half-life of Sm^{151} was determined by the change in isotopic abundance of Sm^{151} in a sample of purified fission-produced samarium, used for a previous indirect determination of the half-life by Inghram, Hayden, and Hess.[2]

In every case, isotopic analysis was made on a 12-inch radius of curvature 60°-deflection mass spectrometer.[3] The europium sample was purified from its daughters by elution with pH 3.06 ammonium citrate from an ion exchange column filled with Dowex 50 resin. No further purification was made on the samarium. The data pertinent to the calculations and the results are given in Table I.

The errors quoted for the half-lives consider only the mean deviation of the isotopic determinations.

The value for the half-life of Sm^{151} is in fair agreement with the 122-year value determined indirectly by Inghram, Hayden, and Hess, but disagrees markedly with the 10^9-year half-life obtained by Marinsky.[4]

The serious discrepancy between the half-lives determined for Eu^{152} and Eu^{154} and the half-lives obtained by Hayden, Reynolds, and Ingham may be caused by an experimental error in the determination of the absolute amount of the gadolinium present after bombardment. The presence of a short-lived isomer of Eu^{154} would otherwise be necessary to explain the error in half-life of Eu^{154}. No such isomer is known.

The values for the branching ratios of the 9.2-hour Eu^{152}, the 13-year Eu^{152}, and the proportion of Eu^{151} capture that goes to each of the two Eu^{152} isomers, all measured indirectly by Hayden, Reynolds, and Ingham, are almost certainly in error since they involve the above determined half-lives. No statement about the correct values can be made without a repetition of their experiment.

TABLE I. Decay data.

	% decay	Decay period (yr)	Half-life (yr)
Eu^{152}	16.7±2.4	3.4	13±2
Eu^{154}	13.9±3.3	3.4	16±4
Sm^{151}	3.6±0.9	3.8	73^{+25}_{-14}

[1] Hayden, Reynolds, and Inghram, Phys. Rev. **75**, 1500 (1949).
[2] Inghram, Hayden, and Hess, Phys. Rev. **79**, 271 (1950).
[3] Inghram, Hess, and Hayden (to be published).
[4] Way, Fano, Scott, and Thew, *Nuclear Data*, National Bureau of Standards, Circular 499 (1950).

Fast Coincidences with Čerenkov Counters

Z. Bay,* *George Washington University, Washington, D. C.*
M. R. Cleland, *National Bureau of Standards, Washington, D. C.*
and
F. McLernon,* *George Washington University, Washington, D. C.*
(Received July 2, 1952)

THE duration of the light flash from a Čerenkov radiator is expected to be much shorter than that from a scintillation crystal. This letter reports an experiment performed at the National Bureau of Standards to study the resolving time limitations of Čerenkov counters[1] in preparation for coincidence experiments with high energy particles. The light was produced in Lucite radiators of two different types (A and B of Fig. 1), by secondary

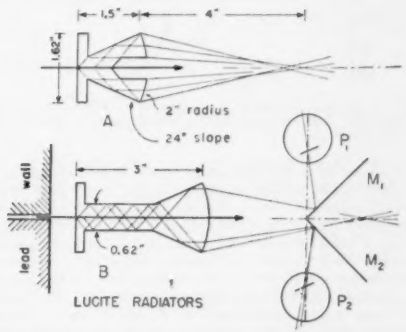

FIG. 1. Čerenkov radiator designs. Heavy arrow indicates direction of high energy electron. Thin lines show paths of optical radiation.

electrons in the x-ray beam of the 50-Mev betatron. The light was brought to an approximate focus by refraction at the spherical end surfaces of the radiators. At the focal point the duration of the light flash from radiator type B is expected to be about 1.5×10^{-10} second due to unequal light collection times. That from type A is expected to be much shorter as the optical path differences are just compensated by the transit time of the electron through the Lucite. However, imperfect focusing can produce path differences of about 3 millimeters and a pulse duration of about 10^{-11} second. The light beam is divided by the mirrors M_1 and M_2 so as to stimulate two 1P21 photomultipliers P_1 and P_2 in coincidence. One can expect to liberate about 6 photoelectrons from each photo-cathode per centimeter penetration of the electron.[2] The phototubes were operated at 1400 volts dc potential. The current pulses from the individual tubes were amplified by 200 megacycle band width distributed amplifiers (Hewlett Packard Model 460A) and brought out of the betatron room through 40 meters of *RG* 59/*U* cable. The coincidences vanish if a piece of black cloth is placed between the Lucite and the mirrors. Thus they are caused by optical radiation coming from the Lucite. The small solid angles (10^{-3} of 4π) subtended by the photo-cathodes inhibit detection of any weak isotropic radiation from the Lucite.

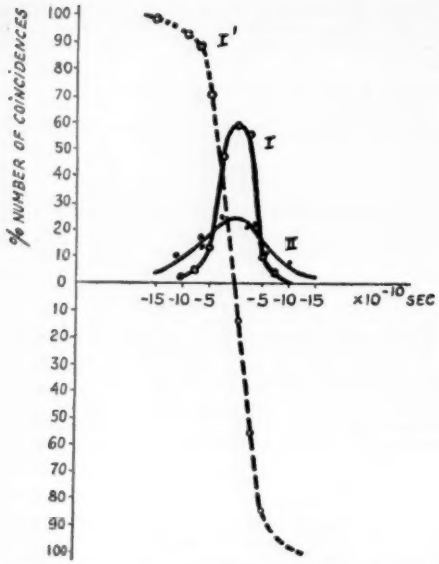

FIG. 2. Delayed coincidence curves obtained with Čerenkov counters. Curves I and I' obtained with radiator type *B*. Curve II obtained with radiator type *A*.

To obtain short resolving times in spite of the prolongation of the pulses in the multipliers, amplifiers, and long cables, the differential coincidence circuit was used.[3] This gives positive outputs if the pulse from P_1 is earlier than that from P_2 (counting rate $D_+(T)$, T being the delay cable in one channel) and negative outputs if P_1 is later than P_2 [counting rate $D_-(T)$]. A separate diode bridge coincidence circuit[4] (resolving time 5×10^{-9} second) was used to count the total number of coincidence [counting rate $C(T)$], and to gate (10^{-6} second) the D_+ and D_- scalars. Plotting $R=(C_{max}-D_+-D_-)/C_{max}$ *versus* T, we obtain the normalized coincidence curves I and II in Fig. 2. It has been shown[5] that the area of such delay curves gives the resolving time (2τ) of the equipment independently of random time delays between the pulses from the two counters. The width of the delay curves ($2\tau'$ = area divided by maximum value of R) measures a mean ($\bar{t}$) of the random time lags (t) which occur in the equipment including the counters. $\bar{t}$ for the separate channels is defined as follows:

$$\bar{t}=[(\tau'^2-\tau^2)/2]^{\frac{1}{2}}. \tag{1}$$

For Gaussian curves, which the data approximates, $\bar{t}$ and the root mean square time deviation, σ_{rms}, have the connection

$$\sigma_{rms}=(2/\pi)^{\frac{1}{2}}\bar{t}. \tag{2}$$

Curve I was taken with radiator type *B*. It gives $\tau=2.5\times10^{-10}$ second, $\tau'=4.4\times10^{-10}$ second, $\bar{t}=2.5\times10^{-10}$ second, and $\sigma_{rms}=2.0\times10^{-10}$ second. Plotting, instead, $S=(D_+-D_-)/C_{max}$ *versus* T we obtain the dotted curve I', whose slope is 15 percent per 10^{-10} second. Curve II was taken with radiator type A. It gives $\tau=1.9\times10^{-10}$ second, $\tau'=7.5\times10^{-10}$ second, $\bar{t}=5.1\times10^{-10}$ second and $\sigma_{rms}=4.0\times10^{-10}$ second.

The random time fluctuations (σ_{rms}) for Čerenkov counters are shorter in spite of the smaller number of photoelectrons than those presently found for scintillation counters. Since the fluctuations in the circuitry are smaller than 10^{-10} second (checked by branched pulses from one tube), the fluctuations observed here must occur mainly in the first stages of the photomultiplier tubes. This view can be further supported by the difference between curves I and II. The light collection time for curve II is certainly negligible, yet $\bar{t}$ is about 2 times larger than for curve I. This is to be expected from the threefold reduction in the number of photoelectrons produced at the photocathodes. At the present time it is possible to measure time intervals to within an error of 10^{-11} second with these techniques,[6] provided one can limit statistical counting errors to one percent.

* These authors' work supported by the ONR and AEC.

[1] J. Marshall, Phys. Rev. **81**, 275 (1951), Phys. Rev. **86**, 583 (1952); I. A. Getting, Phys. Rev. **71**, 123 (1947); R. H. Dicke, Phys. Rev. **71**, 737 (1947); R. W. Birge, Phys. Rev. **85**, 766 (1952).

[2] R. L. Mather, Phys. Rev. **84**, 181 (1951); J. Marshall, Phys. Rev. **86**, 685 (1952).

[3] Z. Bay, Phys. Rev. **83**, 242 (1951); Bay, Meijer, and Papp, Nucleonics **10**, 38 (1952).

[4] Z. Bay, Rev. Sci. Instr. **22**, 397 (1951).

[5] Z. Bay, Phys. Rev. **87**, 194 (1952).

[6] Bay, Meijer, and Papp, Phys. Rev. **82**, 754 (1951); Z. Bay, Phys. Rev. **77**, 419 (1950).

The Absolute Determination of Resonant Energies for Radiative Capture of Protons by Beryllium in the Energy Range Below 520 kev

S. E. HUNT
Research Laboratory, Associated Electrical Industries Limited, Aldermaston, Berkshire, England

(Received May 26, 1952)

THE electrostatic analyzer described previously[1] has been used to determine absolutely the proton energy for which resonances occur in the reaction $Be^9(p,\gamma)B^{10}$ in the energy range below 520 kev.

Thick target yield curves indicated that the yield below 200 kev was extremely small. The resonance postulated by Tangen[2] at about 150 kev therefore appears to be unlikely. The thick target curves could not be explained on the assumption of a single broad resonance at about 330 kev, since the yield continued to increase steeply up to 500 kev.

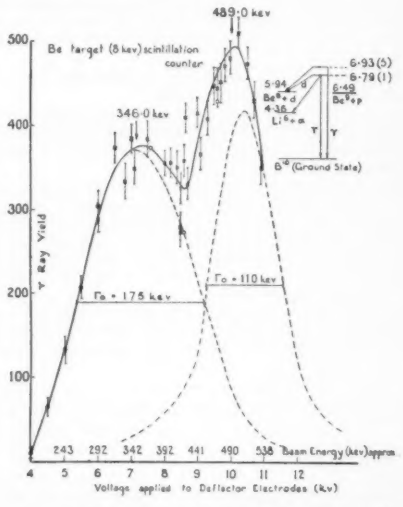

FIG. 1. Thin target (8-kev) yield curve for beryllium observed with a scintillation counter.

Tangen's tentative theory that the increased yield at higher energies was due to the increase in nonresonant radiation is not compatible with more recent work of Fowler, Lauritsen, and Lauritsen,[3] who found a $Be^9(p,\gamma)B^{10}$ resonance at 998 kev. This could be fitted closely to the Breit-Wigner formula even at the "tails," showing that nonresonant radiation at these energies was small. It follows that it must be even smaller in the energy range 400–500 kev.

In order to investigate this problem further, yield curves for thin targets of thickness in energy units between five and ten kev have been obtained. A typical curve is shown in Fig. 1. The efficiency of γ-detection has been increased by using a scintillation counter, and the targets were heated to 200°C and cold trapped. This has been found to be effective in eliminating carbon contamination.[1] The thin target yield curves were reproducible and had maxima at 341.8 ± 2.0 kev and 485.0 ± 3 kev. The rather large uncertainty was due to the great width of the resonances and consequent difficulty in determining precisely the points of maximum yield on the experimental curves.

The yield curve is thought to be due to two broad resonances incompletely resolved. Symmetrical curves obeying the Breit-Wigner formula and having maxima at 336.0 ± 2 kev and 492.0 ± 3 kev could be fitted closely to the experimental curve. The half-widths were 175 ± 5 kev and 110 ± 5 kev, respectively.

This corresponds to excited levels in the B^{10} nucleus at 6.79(1) Mev and 6.93(5) Mev, respectively. The figures in brackets lose their significance as absolute values because of the uncertainty in the Q value for the reaction (6.49 Mev).

Yield curves for this reaction have also been observed previously by Curran, Dee, and Petryilka.[4] They observed a highly asymmetric peak at about 350 kev and another at about 480 kev which they attributed to carbon contamination of the target. Tangen's value for the experimental peak was 330 ± 10 kev. This was reduced to 310 ± 10 kev by his corrections for the 150-kev resonance and the assumed increase in nonresonant radiation.

Thomas, Rubin, Fowler, and Lauritsen have investigated the $Be^9(p,d)Be^8$ and $Be^9(p,\alpha)Li^6$ yield curves. They observed resonant peaks at about 330 kev and 470 kev for the former reaction, and at 330 kev only for the latter. If it is assumed that the higher energy peak can be identified with the one observed in the present work, this would indicate that while the B^{10} level at 6.79(1) Mev is unstable both to α-particle and deuteron emission, α-particle emission is forbidden from the 6.93(5)-Mev level.

Walker[6] has observed γ-rays of energy 6.71 Mev from this reaction. The energy resolution of his spectrometer[7] was too low to separate γ-rays from the two levels suggested by the present work. Other investigations on the energy levels of this B^{10} nucleus have been reviewed by Hornyak *et al.*[8]

The author wishes to thank A. J. Salmon for his assistance in the design and operation of the scintillation counter.

He is also indebted to Dr. T. E. Allibone for permission to publish this letter.

[1] S. E. Hunt (to be published).
[2] R. Tangen, Kgl. Norske Videnskab. Selskabs, Skrifter, No. 1 (1946).
[3] Fowler, Lauritsen, and Lauritsen, Revs. Modern Phys. **20**, 236 (1948); W. A. Fowler and C. C. Lauritsen, Phys. Rev. **76**, 314 (1949).
[4] Curran, Dee, and Petryilka, Proc. Roy. Soc. (London) **169**, 269 (1939).
[5] Thomas, Rubin, Fowler, and Lauritsen, Phys. Rev. **75**, 1612 (1949).
[6] R. L. Walker, Phys. Rev. **79**, 172 (1950).
[7] R. L. Walker and B. D. McDaniel, Phys. Rev. **74**, 315 (1948).
[8] Hornyak, Lauritsen, Morrison, and Fowler, Revs. Modern Phys. **22**, 291 (1950).

Saturation Effect of Plastic Scintillators*

C. N. Chou
Department of Physics, University of Chicago, Chicago, Illinois
(Received June 23, 1952)

IT is known that for high energy losses the light output from a scintillating fluor is not proportional to the energy loss of the irradiating particle passing through it in the cases of organic crystals[1–7] and liquids,[8] and to a smaller extent, in the case of inorganic crystals.[9] Recently we made some measurements of this saturation effect in plastic scintillators and in phenylcyclohexane solution and in a NaI crystal making use of the negative pion beam and the outside proton beam of the Chicago cyclotron. The plastic samples were wrapped with 0.076-mm thick aluminum foil except for the end attached to a 5819 photomultiplier. Two scintillators were placed parallel to each other and perpendicular to the direction of the beam used. The output pulse of one phototube triggered the sweep of a synchroscope whose vertical plates were connected to the output of the second tube. The output pulse of the second tube was (a) observed visually and (b) recorded photographically with a specially designed camera. The two sets (a) and (b) of observations agreed within experimental errors. Absorbers of copper plates were placed between the scintillators to obtain particles of various energies. Calibration readings with Compton electrons of minimum ionization from the 1.3-Mev γ-rays of a Co^{60} source were intermittently made during the run. Figure 1 shows the variation of the light output from the scintillators *vs* energy loss. The phenylcyclohexane solution (containing 0.3 percent p-terphenyl and 0.001 percent diphenylhexatriene) was 3.4 cm in diameter and 3.4 cm in length. The NaI (Tl activated) crystal was 1.25-in. high, 2.25-in. wide and 0.5 in. in thickness. All the plastic samples were 1-in. square and 5-mm thick. The path length of the mesons and protons through the plastics was 0.5 mm. The specifications of the various plastics and the results obtained with the Co^{60} source and with the 5.3-Mev α-particles from a Po source are given in Table I.

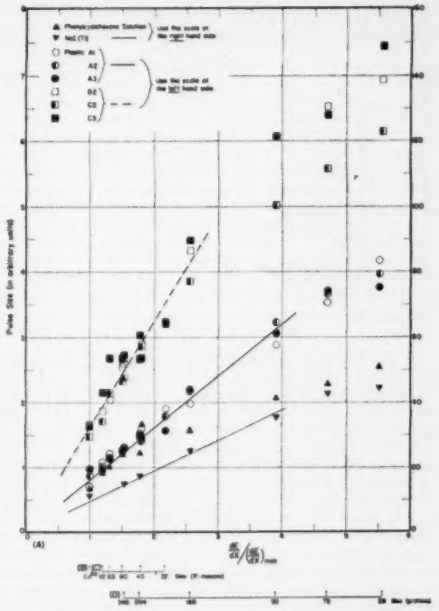

FIG. 1. Variation of light output from the scintillators with energy loss. The ordinate gives the pulse size (in arbitrary units) which is proportional to the light output. The abscissa gives the energy loss in the scintillators. The scale in row (A) represents the energy loss in units of the loss at minimum ionization. (B) refers to measurements with a Co^{60} source. Row (C) gives the energies of the pions in Mev corresponding to the energy losses represented in (A) and the scale in row (D) shows the proton energies corresponding to (A).

TABLE I. Pulse sizes (in the same arbitrary units as used in Fig. 1) from plastics irradiated with Co^{60} and Po sources.

Plastic scintillator	Specifications	Pulse size observed with Co^{60} source	Pulse size observed with Po source	Ratio of pulse size with Co^{60} to pulse size with Po
A1	2% anthracene in polystyrene	0.89	0.50	0.56
A2	3% anthracene in polystyrene	0.86	0.50	0.58
A3	5% anthracene in polystyrene	0.97	0.53	0.55
B2	2% p-terphenyl in polystyrene	1.65	0.82	0.50
C2	2% p-terphenyl +0.03% diphenyl-hexatriene in polystyrene	1.52	0.82	0.54
C3	4% p-terphenyl +0.03% diphenyl-hexatriene in polystyrene	2.05	1.05	0.51

We can make the following remarks concerning the experimental results shown in Fig. 1 and in Table I. Since it is known that in the case of small specimens being irradiated with electrons,[1] NaI(Tl) gives linear response at energy losses well beyond the range covered by the present experiment, the apparent deviation from linear response above about 4 times minimum ionization loss, as demonstrated in Fig. 1, is most probably due to the inhomogeneity of the proton beam and its straggling in passing through the copper absorbers and the geometrical arrangement adopted here. It is to be noted that the p-terphenyl in polystyrene plastic gives a reasonably linear response up to about 3 times minimum ionization loss, and the anthracene in polystyrene gives linear response up to at least 4 times minimum loss. The variation in concentration from 2–5 percent in the case of anthracene in polystyrene and from 2–4 percent in the case of p-terphenyl in polystyrene have within the experimental errors no significant effect on the saturation of these two scintillators. Also the addition of a small amount of diphenylhexatriene in the p-terphenyl in polystyrene did not show definite remarkable influence on the saturation effect observed. The results of Fig. 1 seem to indicate quite clearly that the plastic scintillators show less saturation than the liquid phenylcyclohexane solution. Table I shows that the results of the α-particle measurements regarding saturation support the conclusions drawn from the investigations with the mesons and protons.

The author wishes to express his sincere thanks to Professor Marcel Schein for the cordial hospitality in the Cosmic Ray Laboratory and for numerous valuable discussions and to Professor H. L. Anderson and the cyclotron group for facilities concerning the cyclotron measurements. He also thanks Theodore Bowen for his generous help in connection with the cyclotron measurements.

* Assisted by the joint program of the ONR and AEC.
[1] R. Hofstadter, Nucleonics **6**, 70 (1950).
[2] J. I. Hopkins, Phys. Rev. **77**, 406 (1950).
[3] J. B. Birks, Proc. Phys. Soc. (London) **A63**, 1294 (1950).
[4] W. J. Ramler and W. S. Freedman, Rev. Sci. Instr. **21**, 784 (1950).
[5] Franzen, Peelle, and Sherr, Phys. Rev. **79**, 742 (1950).
[6] Frey, Grim, Preston, and Gray, Phys. Rev. **82**, 372 (1951).
[7] Taylor, Jentschke, Remley, Eby, and Kruger, Phys. Rev. **84**, 1034 (1951).
[8] M. Furst and H. Kallman, Phys. Rev. **85**, 816 (1952).
[9] R. H. Lovberg, Phys. Rev. **84**, 852 (1951).

The Nature of the Saturation Effect of Fluorescent Scintillators*

C. N. CHOU
Department of Physics, University of Chicago, Chicago, Illinois
(Received June 23, 1952)

IT has been found that when a high energy particle passes through a scintillating organic crystal or liquid or a plastic scintillator, the fluorescent light output it produces is no longer proportional to its energy loss above a certain value of the loss.[1,2] The same kind of deviation from proportionality is less pronounced for scintillating inorganic crystals like NaI.[1,3] In the following we propose an interpretation of this phenomenon based on some general physical considerations. As an example, we consider first the case of plastic scintillators, for instance, polystyrene impregnated with a small amount of fluorescent substance like anthracene. For simplicity of argument, we shall consider the thickness of the scintillator unity. Let n_1 denote the number per cc, q_1 the quenching probability, and e_1 the probability of light emission of the molecules of the plastic substance excited by the passage of a high energy particle through the scintillator, and let n_2, q_2, and e_2 denote the same quantities for the excited molecules of the impregnated fluor. We shall denote the total number of molecules per cc available of the fluor as N_2 and assume that N_2 is always larger than n_1.

There is evidence that the irradiated energy is first absorbed by the molecules of the plastic substance and then transferred to the fluor.[4,5] According to recent results,[5] the mechanism of energy transfer is probably partly radiative and partly nonradiative. The probability of nonradiative transfer due to energy exchange through a sort of resonance is known to be proportional to the square of the concentration of the "dissolved" molecules.[6] One can set up for the change of n_1 and n_2 with time the following differential equations,

$$\frac{dn_1}{dt}=-T_1N_2\left(1-\frac{n_2}{N_2}\right)n_1-T_1'N_2^2\left(1-\frac{n_2}{N_2}\right)^2n_1-q_1n_1-e_1n_1, \quad (1)$$

$$\frac{dn_2}{dt}=T_1N_2\left(1-\frac{n_2}{N_2}\right)n_1+T_1'N_2^2\left(1-\frac{n_2}{N_2}\right)^2n_1-q_2n_2-e_2n_2, \quad (2)$$

where T_1 is the probability constant of the radiative transfer and T_1' that of the nonradiative transfer (assumed to be due to the above-mentioned mechanism of energy exchange). The initial condition for $t=0$, is given by $n_1=n_{10}$, where n_{10} is proportional to the energy lost by the irradiating particle. No attempt was made to find a complete solution of Eqs. (1) and (2). However, we make use of the fact mentioned above that the energy transfer from the plastic to the fluorescent molecules must be almost complete before the plastic itself emits an appreciable amount of light. Also we shall assume that $N_2\gg n_2$ for all times; then instead of (1) we solve the simplified equation.

$$dn_1/dt=-T_1N_2n_1-T_1'N_2^2n_1-q_1n_1,$$

and obtain the solution

$$n_1=n_{10}\exp[-(T_1N_2+T_1'N_2^2+q_1)t].$$

Similarly we shall solve (2) with its first two terms at the right-hand side omitted, and obtain

$$n_2=n_{20}\exp[-(q_2+e_2)t],$$

where n_{20} is the initial value of n_2, and is given approximately by

$$n_{20}\sim\int_0^\infty(T_1N_2+T_1'N_2^2)n_1dt=\frac{n_{10}(T_1N_2+T_1'N_2^2)}{T_1N_2+T_1'N_2^2+q_1}.$$

The light output observed should be given by

$$L=\int_0^\infty e_2n_2dt=\frac{e_2}{q_2+e_2}\frac{n_{10}(T_1N_2+T_1'N_2^2)}{T_1N_2+T_1'N_2^2+q_1}.$$

We further make the plausible assumption that

$$q_1=a+bn_{10}+cn_{10}^2, \quad (3)$$

(where a, b, and c are constants), to take into account the variation of the quenching effect with the various modes and degrees of excitations which in turn depend upon the initial energy loss of the irradiating particle. Then we obtain for the light output

$$L=\frac{n_{10}e_2}{q_2+e_2}\frac{T_1N_2+T_1'N_2^2}{T_1N_2+T_1'N_2^2+a+bn_{10}+cn_{10}^2}. \quad (4)$$

When the specific energy loss is small, i.e., $T_1N_2+T_1'N_2^2$

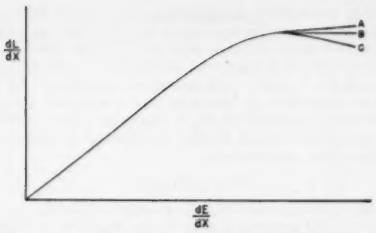

FIG. 1. Theoretical curves showing the variation of specific fluorescence vs specific energy loss in a fluorescent scintillator.

$\gg a+bn_{10}+cn_{10}^2$, we have

$$L_s \sim \frac{n_{10}e_2}{q_2+e_2}\left(1-\frac{a+bn_{10}+cn_{10}^2}{T_1N_2+T_1'N_2^2}\right). \quad (5)$$

When the specific energy loss is large, i.e., $T_1N_2+T_1'N_2^2 \ll a+bn_{10}+cn_{10}^2$, we have

$$L_s \sim \frac{n_{10}e_2}{q_2+e_2}\frac{T_1N_2+T_1'N_2^2}{a+bn_{10}+cn_{10}^2}\left(1-\frac{T_1N_2+T_1'N_2^2}{a+bn_{10}+cn_{10}^2}\right). \quad (6)$$

One can easily obtain similar results for other types of fluorescent scintillators, provided suitable similar general physical considerations are adopted. For example, for substances like anthracene or NaI(Tl) crystal, which absorb and emit the irradiated energy through the same kind of molecules, we obtain instead of (4) the expression

$$L=n_{10}e_1/(e_1+a+bn_{10}+cn_{10}^2), \quad (7)$$

with limiting cases similar to those given by (5) and (6).

The general feature of (4) or (7) is shown in Fig. 1. The three branches A, B, and C correspond respectively to the cases where the effect of the constants a or b or c respectively predominates the quenching factor q_1 as given by (3). In practical cases, it might not be easy to distinguish the cases A and B. Experimental curves like A and B have been reported[1,2] for organic and inorganic crystals being irradiated by electrons, γ-rays and heavy particles. An experimental curve like C has been reported for electrons passing through an anthracene crystal.[1] The theoretical curves derived above seem to be able to account for these experimental results satisfactorily.

The author wishes to express his sincere thanks to Professor Marcel Schein for his encouragement and valuable discussions.

* Assisted by the joint program of the ONR and AEC.

[1] Taylor, Jentschke, Remley, Eby, and Kruger, Phys. Rev. **84**, 1034 (1951).
[2] C. N. Chou [Phys. Rev. **87**, 903 (1952)] and the literature given there.
[3] R. H. Lovberg, Phys. Rev. **84**, 852 (9151).
[4] W. S. Koski, Phys. Rev. **82**, 230 (1951).
[5] W. L. Buck and R. K. Swank, Phys. Rev. **87**, 191 (1952), and private communication.
[6] T. Foerster, Ann. Physik **2**, 56 (1948).

Optical Polarization in Single Crystals of Tellurium*,†

J. J. LOFERSKI
University of Pennsylvania, Philadelphia, Pennsylvania
(Received June 17, 1952)

THE transmission of tellurium crystals has been observed in the infrared. Because of the hexagonal nature of the lattice, the transmission was measured as a function of the polarization of the incident radiation relative to the C-axis of the crystal. Recently, Moss has reported on the transmission of tellurium films and of a bulk sample, although he does not specify whether he had a single crystal.[1]

The crystals were obtained from the Anaconda Sales Company, which reported that the material was at least 99.8 percent pure, although subsequent spectroscopic tests failed to indicate any impurities.[2] The samples were prepared for investigation by polishing them according to metallographic techniques. Their resistivity as determined by probing the surface was about 0.3 ohm-cm at room temperature, at which temperature they were in the intrinsic range. A Beckman IR2 monochromator with rock salt optics was used with a Nernst glower to provide the monochromatic radiation, which was modulated at 10 cps. The emerging beam passed through the polarizer onto a mirror which formed an image of the exit slit on the sample, and the transmitted radiation was collected by a second mirror which formed an image on the exit slit on the sample, and the transmitted radiation was collected by a second mirror which formed an image on the target of a Perkin-Elmer radiation thermocouple, whence the ac signal was fed into a suitable amplifier. The transmission polarizer consisted of a set of unsupported films of amorphous selenium, and was constructed according to the method of Elliott *et al.*[3]

The transmission of a typical sample is shown in Fig. 1. It is to be noted that the position of the absorption edge as well as the amount of radiation transmitted at longer λ depends markedly on the polarization. By observing the transmission of a number of separate samples of different thicknesses, it is possible to determine the absorption constant as a function of λ and to get an approximate value of the index of refraction of the crystals. Typical results are shown in Fig. 2 for a few values of λ. For this purpose it is necessary to assume that the fraction of radiation transmitted is given by the expression

$$I/I_0=(1-R)^2e^{-kx},$$

where I and I_0 are the transmitted and incident radiation intensity, respectively, R is the reflection loss at a surface, k is the

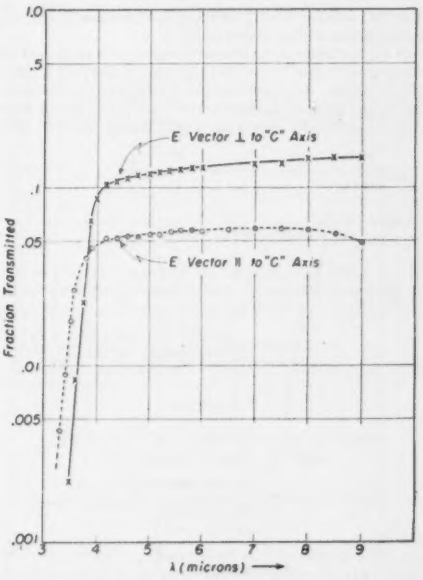

FIG. 1. Transmission of a Te crystal 0.063-cm thick, showing effect of polarizing the incident radiation.

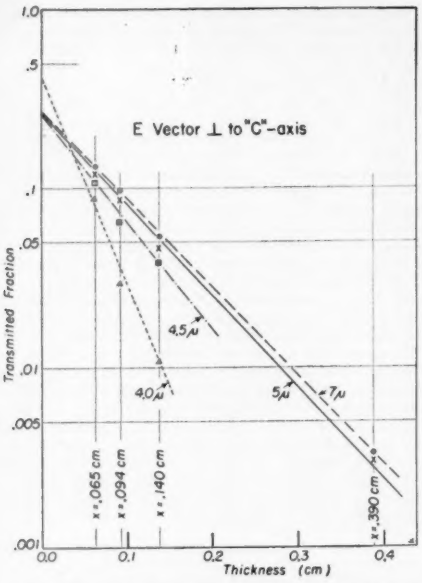

FIG. 2. Transmission of Te crystals as a function of thickness for a few values of λ.

absorption constant (cm^{-1}), and x is the thickness in cm. The resulting values of k are shown in Fig. 3.

The interpretation of these results suggests first of all that the increasing absorption beyond the edge toward shorter λ is due to electrons making the transition from the filled to the conduction band. If we locate the absorption edge which occurs for the larger value of λ at 3.6μ by associating it with the gap width as determined by conductivity measurements, i.e., 0.34 ev,[4] the criterion so established places the second edge at 3.3μ. This is an arbitrary method of locating the edge, since the values as determined by absorption and conductivity can be expected to agree only at low temperatures. Secondly, as in germanium and silicon,[5] the value of k as determined by assuming only free carrier absorption beyond the edge toward longer λ is smaller by a factor of 10^2 than the experimental values. Finally, the index of refraction, n, as computed from the expression

$$R=(n-1)^2/(n+1)^2,$$

is about 5.3±0.2 at 6μ, which is somewhat larger than the value found by Moss in tellurium films. It was impossible to detect any difference in the values of n for the two directions of polarization by this method. Preliminary measurements on prisms of crystalline tellurium yield values of n of this same magnitude.

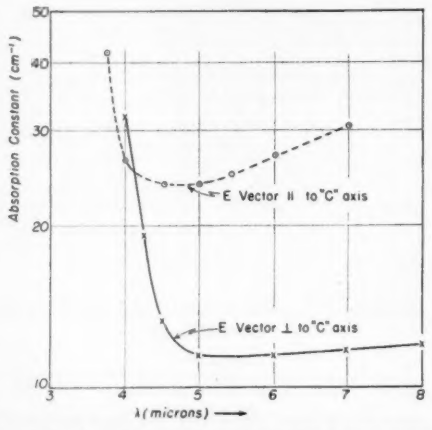

FIG. 3. Experimental values of the absorption constant of Te crystals as determined from the slopes of the lines in Fig. 2.

[a] Preliminary reports of this work were presented at the meetings of the American Physical Society on June 15, 1951 and March 21, 1952 [Phys. Rev. **83**, 876 (1951) and **86**, 652 (1952)].
[†] This work was supported by the ONR.
[1] T. S. Moss, Proc. Phys. Soc. (London) **B65**, 62 (1952).
[2] We wish to acknowledge the help of Dr. W. Scanlon, Naval Ordnance Laboratory, White Oaks, Maryland, who arranged for the analysis.
[3] Elliott, Ambrose, and Temple, J. Opt. Soc. Am. **38**, 212 (1948).
[4] V. E. Bottom, Science **115**, 570 (1952); T. Fukuroi, Sci. Repts. Research Inst. Tōkohu Univ. **A3**, 175 (1951).
[5] M. Becker and H. Fan, Phys. Rev. **76**, 1530 (1949).

Enhancement of the *F*- and *V*-Bands in Sodium Chloride Containing Calcium

H. W. ETZEL
Crystal Branch, Metallurgy Division, Naval Research Laboratory, Washington, D. C.
(Received July 18, 1952)

IT has been observed by Hummel[1] that the introduction of calcium as an impurity in KCl results in a γ-ray induced *F*-band absorption which is much greater than one observes for the "pure" alkali halide. Curves B, C, D, and E in Fig. 1 show this enhancement in x-rayed NaCl single crystals grown by the Kyropoulos method, which contain, respectively, 1, 5, 10, and 50×10^{-3} mol percent calcium added to the melt. Approximately one-tenth of the calcium concentration in the melt is present in the crystals. In the same figure is shown the *F*-band absorption for "pure" NaCl, curve A, and for two crystals, curves F and G, which contain additions of divalent cadmium rather than divalent calcium. To insure uniform coloration the crystals were cleaved to less than 0.36 mm in thickness. All crystals were x-rayed using molybdenum radiation at 40 kvp and 20 ma for one hour. After the first half-hour the crystals were rotated through 180°, and the second face was placed nearest the x-ray tube. The absorption measurements were made using a Beckman Model DU Quartz Spectrophotometer. All experimental work was carried out at room temperature.

It is interesting to note that the introduction of Cd^{++} to the lattice, and subsequent x-raying, do not produce the same striking enhancement of the *F*-band as does the incorporation of Ca^{++}. A difference in the behavior of Ca^{++} and Cd^{++} as impurities in NaCl is also observed in the work of Etzel and Maurer[2] and Bean and Maurer.[3] The former investigators found that in the neighborhood of 400°C the crystal shown in Fig. 1, curve F, has about one-third of the positive ion vacancies introduced by the Cd^{++} associated with this ion. At room temperature it is then likely that this association is complete. In contrast to this, Bean and Maurer find that no observable association occurs between the Ca^{++} and the positive ion vacancies.

The following mechanism is suggested to explain the enhancement of the *F*-band in the alkali halides containing ions of rare gas electronic structure as divalent impurities. When a Ca^{++}, for instance, is added to the NaCl lattice, one positive ion vacancy is also added to the lattice, at least to a first approximation. This occurs in order to maintain electrical neutrality within the crystal

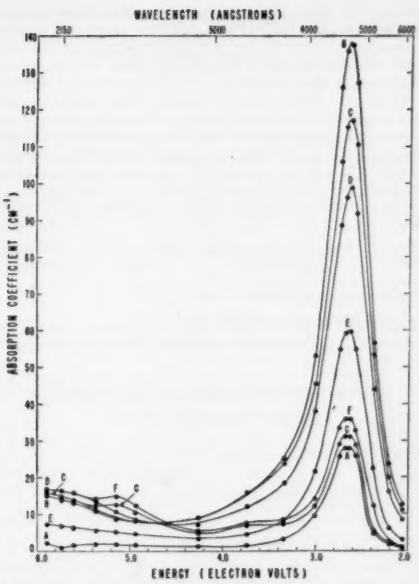

FIG. 1. Spectral absorption of x-rayed NaCl single crystals containing the following nominal mol ratios of impurities to Na in the melt: curve A: None; B: 0.005 Ca/Na; C: 0.001; D: 0.0005; E: 0.0001; F: 0.005 Cd/Na; G: 0.001.

since two Na^+ are replaced by each Ca^{++}. If the crystal is then x-rayed, the probability for the capture of holes by positive ion vacancies to form V-centers is greater than it would be in a "pure" crystal. As a result, the probability for the recombination of holes and electrons is reduced. The probability for the formation of F-centers is thereby increased since more electrons are free to be trapped by negative ion vacancies. If the F-band is enhanced, then an increase in the V-band absorption which occurs in the short wavelength ultraviolet region should also be observed. Figure 1 shows a three- to eightfold increase in the absorption in the neighborhood of 2100A for Ca^{++}-bearing crystals over that of "pure" NaCl. Irradiation into this band produces no observable emission, indicating these crystals are not radiophotoluminescent in this region. The same conditions do not exist in crystals containing Cd^{++} since the excess positive ion vacancies are bound to the Cd^{++} at room temperature and are not favorable traps for holes. Therefore, recombination of electrons and holes occurs with nearly the same probability as exists in a "pure" crystal, and the F-band is not significantly enhanced. Unfortunately NaCl containing Cd^{++} has radiophotoluminescent absorption bands at 2400A and 3400A; thus it is not possible to strengthen the explanation further by showing no enhancement of the V-band in the crystals containing Cd^{++}.

Further experiments are planned with Ca^{++} and Cd^{++} in NaCl and in other alkali halides. If the observed differences in the behavior of these ions in NaCl appear in other alkali halides, arguments[4] based on the *a priori* similarity of these ions may require modification.

The writer wishes to express his appreciation to Mr. R. D. Kirk for growing the single crystals used in this work.

[1] H. Hummel, thesis, Göttingen University (1950) (unpublished).
[2] H. W. Etzel and R. J. Maurer, J. Chem. Phys. **18**, 1003 (1950).
[3] C. Bean and R. J. Maurer, ONR Technical Report No. 4 (1952) (unpublished).
[4] F. Seitz, Phys. Rev. **83**, 134 (1951).

Threshold for (γ,p) Reaction in Be^9

B. L. TUCKER AND E. C. GREGG*
Case Institute of Technology, Cleveland, Ohio
(Received July 18, 1952)

ALTHOUGH the (γ,n) reaction in Be^9 is well known, only one paper[1] has established the existence of the $Be^9(\gamma,p)Li^8$ in beryllium. They identified a Li^8 beta-activity and made a rough estimate of 18 ± 1 Mev for the (γ,p) threshold.

The radioactive chain for $Be^9(\gamma,p)Li^8$ is:

$$Be^9+\gamma\rightarrow p+Li^8;\quad Li^8\rightarrow\beta+Be^8;\quad Be^8\rightarrow 2\alpha.$$

The 0.88-sec half-life beta-particles from Li^8 have a maximum energy of 13 Mev. The final α-particles have about 1.5 Mev each.

Possible alternative reactions from Be^9 in a betatron beam are: $Be^9(\gamma,n)2\alpha$, $Be^9(n,\alpha)He^6$, and $Be^9(\gamma,d)Li^7$. He^6 from the (n,α) reaction has a 0.86-sec beta-activity with a 3.5-Mev maximum energy. In spite of a low ($\sim$2.6 Mev)[2] threshold, the (n,α) probability is far below the (γ,p) because the neutron flux is far lower than the γ-intensity. There was no evidence of beta-activity below 16.9 Mev.

A large ($1\frac{1}{2}$ in.$\times$1 in.) NaI crystal was mounted in contact with a 5819 photomultiplier as shown in Fig. 1. The gate was off during the complete acceleration cycle of the betatron so that spurious γ-counts from the beam and the injection gun were avoided. The discriminator was set for the best ratio between background and true counts. The background remained high even during the dead time of the γ-beam, probably because iron, aluminum, and copper are all beta-active under γ-radiation of this energy.

Threshold determinations from seven sets of data for the (γ,p) reaction give 16.93 ± 0.15 Mev. An accurate mass difference calculation gives a theoretical value of 16.872 ± 0.008 Mev.[3] Graphical extrapolation of the seven curves agreed with calculations of the $N=k(E-E_0)^m$ type.

As a check against confusion of other beta-activities, the half-life was measured at 0.89 sec, and the beta-particles penetrated 0.39 in. of aluminum, indicating an energy above 6 Mev.

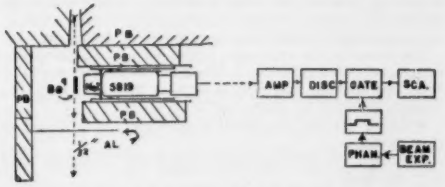

FIG. 1. Experimental arrangement.

A very rough estimate of the absolute cross section for (γ,p) indicates $\sim3\times10^{-28}$ cm^2 at 19 Mev. Further work is in progress to make an accurate determination of σ between 17 and 21 Mev.

* This work was done under the AEC.
[1] Ogle, Brown, and Conklin, Phys. Rev. **71**, 378 (1947).
[2] 2.6 Mev is the sum of the (γ,n) and (n,α) thresholds.
[3] D. M. Van Patter, Office of Naval Research Technical Report ONR-57 (1952) (unpublished).

Neutron Total Cross Section for Lead Between 37 and 156 Mev

A. E. TAYLOR AND E. WOOD
Atomic Energy Research Establishment, Harwell, Nr. Didcot, Berkshire, England
(Received July 14, 1952)

IN the course of an investigation into the variation of neutron total cross sections with energy for a number of elements, a dip has been found in the lead cross section at about 60 Mev. The neutrons used in this experiment were produced by proton bom-

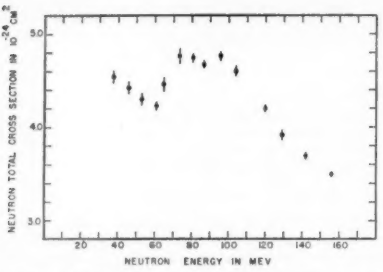

FIG. 1. The variation with energy of the neutron total cross section for lead. The cross sections have been corrected for forward scattering, and the errors shown are standard deviations based upon total counts.

bardment of internal targets in the 110-inch Harwell cyclotron, and were collimated by small diameter holes in the concrete shielding. The apparatus, neutron attenuators and geometrical layout were similar to those used in earlier measurements at this laboratory.[1] A triple coincidence proportional counter telescope was used to detect the protons recoiling from a polyethylene disk placed in the collimated neutron beam. By putting absorbers between the counters a lower energy limit was set for the detected recoil protons, and hence there was a lower energy limit to the neutrons used in the determination. The upper energy limit was governed by the position of the target in the cyclotron, the value of the magnetic field, and the threshold energy for production of neutrons by protons. It was therefore possible to use a small band of neutron energies in any measurement. Further, since the majority of the neutrons were detected as recoil protons coming from the hydrogen content of the polyethylene disk, the effective neutron energy could be calculated with an error dependent upon the accuracy of a range-energy relation. This error was estimated to be about 1 Mev at the lowest energies and about 3 Mev at the highest. The band of energies used varied from about 10 Mev at the lowest energy measured to about 20 Mev at the highest.

The values of the total cross section for lead at the various energies are presented in Fig. 1. The difference between the value at 81 Mev and the minimum value at 61 Mev is 10 times the standard deviation on either point.

A similar dip has been found in cadmium and in copper at lower energies.

The results for the whole investigation will be reported more fully elsewhere.

This letter is published with the permission of the Director, Atomic Energy Research Establishment, Harwell, Berkshire, England.

[1] Taylor, Pickavance, Cassels, and Randle, Phil. Mag. **42**, 20 (1951); **42**, 328 (1951); **42**, 751 (1951); **42**, 1336 (1951).

Size Effects in the Superconductivity of Cadmium

M. C. STEELE AND R. A. HEIN
Naval Research Laboratory, Washington, D. C.
(Received July 15, 1952)

AS part of a program to study electrical and magnetic properties of matter below 1°K, we have investigated the critical magnetic fields of various sized particles of superconducting cadmium. The experimental arrangement used for these measurements was similar to that of Daunt and Heer[1] except that we used a lead wire (0.025 cm in diameter and 50-cm long) as the heat switch. With such a switch it took from 40–60 minutes for the system to warm up from 0.1° to 1.2°K. To date we have obtained results for two different sizes of cadmium. Both specimens consisted of spheres of cadmium made by stirring the molten metal with a high boiling silicone oil.[2] The cadmium used for the preparation was spectroscopically pure material obtained from Johnson-Matthey. The pills were pressed into cylindrical form (diameter 1.75 cm, length about 2.2 cm) from a mixture of chromium potassium alum and the cadmium particles. Specifications are given below:

Pill No.	Cadmium particle size (radius in cm)	Wt. of cadmium (grams)	Wt. of salt (grams)
1	$2.2\text{-}3.1\times10^{-3}$	2.2	6.7
2	$6\text{-}12\times10^{-3}$	1.2	7.0

The critical fields, obtained from the warm up curves, are shown in Fig. 1. The dashed curve shows the results obtained by

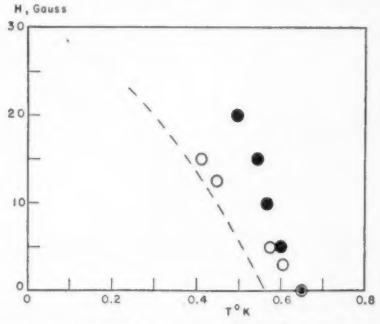

FIG. 1. Magnetic threshold for Cd as a function of temperature. ●—Pill No. 1; ○—Pill No. 2. Dashed curve shows data of Goodman and Mendoza.

Goodman and Mendoza[3] using another method and bulk cadmium. We obtained a zero field transition temperature of 0.65 ± 0.02°K for both specimens. This is somewhat higher than the value 0.56°K reported by the Cambridge workers. Since our experiments with superconducting zinc and ruthenium gave transition temperature in good agreement with other workers, we believe that this difference in T_c for cadmium is a real one. It may be associated in some way with our method of preparing the spheres. Aside from that factor the data reveals a definite increase in the critical fields for the smaller particles. If this is interpreted in light of the particle size becoming comparable to λ the penetration depth, one can estimate that $\lambda_0\sim10^{-4}$ cm for cadmium. This value is a factor of ten larger than penetration depths for such elements as indium, tin and lead.[4] It may be significant to note that the suggested large value of λ_0 for cadmium is qualitatively consistent with the empirical observation that λ_0 increases as T_c decreases.[4]

A detailed account of the work reported above, as well as experiments in progress at this date, will be given in subsequent publications.

[1] J. G. Daunt and C. V. Heer, Phys. Rev. **76**, 1324 (1949).
[2] M. C. Steele, Phys. Rev. **78**, 791 (1950).
[3] B. B. Goodman and E. Mendoza, Phil. Mag. **42**, 594 (1951).
[4] J. M. Lock, Proc. Roy. Soc. (London) **A208**, 391 (1951).

Proceedings of the American Physical Society

Minutes of the Meeting of the Division of Fluid Dynamics at Salt Lake City, Utah, June 25, 26, 27, 1952.

THE Division of Fluid Dynamics of the American Physical Society held its spring meeting at the University of Utah, Salt Lake City, at a three-day session on June 25, 26, and 27, 1952. The invited papers are listed below in the symposia program. There were thirty contributed papers, abstracts of which are contained below.

J. Howard McMillen, *Secretary*
U. S. Naval Ordnance Laboratory
White Oak, Maryland

Symposium on Explosion Phenomena (Henry Eyring presiding)

1. Flames and Detonations. J. O. Hirschfelder, *University of Wisconsin.*

2. Detonation Equation of State. M. A. Cook, *University of Utah.*

3. Fracturing Under Impulsive Loading. J. S. Rinehart, *NOTS, Inyokern.*

4. Damaging Air Shocks at Large Distances from Explosions. E. F. Cox, *Sandia Corporation, Albuquerque.*

Symposium on Shock Waves (J. H. McMillen presiding)

1. On Shock Wave Phenomena: Aerothermodynamic Interaction. R. J. Seeger, *National Science Foundation.*

2. Boundary Disturbances in High Explosive Shock Tubes. R. G. Shreffler, *Los Alamos.*

3. On Strong Shock Waves. E. L. Resle, Jr., H. Petschek, S. C. Lin, and A. Kantrowitz, *Cornell University.*

4. Shock Waves in Spark Discharges in Gases. R. G. Fowler, *University of Oklahoma.*

Symposium on Hydrodynamics and Jets (F. T. Rogers, Jr. presiding)

1. Hydrodynamical Theory of the Origin of Multiple Star Systems. R. W. Stewart and G. J. Odgers, *Pacific Naval Laboratory and Dominion Astrophysical Observatory, Victoria, B. C.*

2. Magnetohydrodynamics. W. M. Elsasser, *University of Utah.*

3. Structure of a Two-Dimensional Supersonic Jet. D. Bershader and D. C. Pack, *University of Maryland and University College, Dundee, Scotland.*

Special Evening Lecture

1. Research, Development, and Guided Missiles. R. E. Gibson, Director, *Applied Physics Laboratory, Johns Hopkins University, Silver Spring, Md.*

Contributed Papers (R. J. Seeger, L. B. Linford, and F. N. Frenkiel presiding)

1. An experimental Investigation of Spinning Detonation. Herbert T. Knight and Russell E. Duff, *Los Alamos Scientific Laboratory.*—Experimental work is reported which clarifies several features of the complex phenomenon of spinning detonation. The pitch-diameter ratio for spin in the carbon monoxide-oxygen system was found to be essentially independent of the initial percentage of carbon monoxide. The shape of the shock wave of a spinning detonation was determined by photographing the shock induced motion of a thin foil stretched across the detonation tube. The shock wave was found to be made up of at least two parts meeting at an angle near a diameter of the tube. During attempts to produce spinning detonation in large tubes it was found that wake confinement was essential to the propagation of this detonation. Finally, moving film photographs of a spinning detonation were taken through a slit perpendicular to the axis of the tube. These pictures showed a sinusoidal wave corresponding to a luminous disturbance moving around the tube at constant angular velocity. The nearly horizontal striations characteristic of the usual photographs of spinning detonation are produced by this disturbance passing a longitudinal slit on the detonation tube. In general the results of these experiments are in agreement with the hydrodynamic theory of spinning detonation proposed by Fay.

2. Measurement of Reaction Time in a Detonating Liquid. T. P. Cotter, *Los Alamos Scientific Laboratory.*—Detonation propagating through a homogeneous explosive consists of a strong shock followed by an induction period of comparatively slow reaction which culminates in a burst of vigorous reaction accompanied by thermal luminosity. The duration of the induction period is measured directly by observing the refraction of an inclined plane detonation wave through a thin plate of inert material which has been immersed in a transparent liquid explosive. A photograph of the steady-state refraction region showing both the deflection of the plate face by the shock and the onset of luminosity in the explosive is obtained by employing a rotating-mirror camera to hold the refraction region image stationary on the film for the appropriate exposure time. The perturbation of detonation by the plate can be corrected by choice of plate material and refraction angle and by extrapolation to zero plate thickness. The measured induction time of detonating nitromethane is roughly 0.1 microsecond. Induction times varying one hundred-fold about this value were produced following initiation by shocks of various strengths. Addition of sensitizer such as pyridine decreases the induction time markedly, but desensitizer such as benzene does not increase it.

3. Determination of Detonation Pressures From Flash Radiographs. J. N. Dewey, H. I. Breidenbach, Jr., and J. W. Gehring, Jr., *Aberdeen Proving Ground.*—The observation of shock and material velocities in a material in contact

with a steady state detonation gives a direct determination of the pressure on the surface of the material. When the detonation front in an explosive in contact with a metal is perpendicular to the metal surface, the compression of the metal results in an expansion of the detonation gases reducing the pressure on the metal surface below the detonation pressure. When the angle of incidence of the detonation on the metal, ϕ, is given by $\tan(\phi_o+\delta)=D\tan\phi/a_d$, where δ is the angle between the compressed and original metal surfaces, D is the detonation velocity, and a_d the velocity of sound behind the front, there is no rarefaction nor compression in the detonation gases at the surface of the metal and the pressure on the surface is the detonation pressure. Unfortunately, it is impossible to observe rarefactions small enough to permit accurate determination of a_d directly from a determination of ϕ_o. However, combination of the study of the effect of varying ϕ with observation of the shock fronts and mass velocity in the metal serves to determine both the detonation pressure and the properties of the metal under very high stresses. An approximate determination of the position of the shear front as well as the compression front is required for computation of the pressure. Another source of error is introduced by the small radius of curvature of the compression front in the metal directly behind the detonation front. Pressures and angles of the compression front at values of ϕ from O to those at which a shock forms have been determined using Pentolite and a magnesium alloy. A preliminary value of the detonation pressure slightly exceeds the computed, 2.1×10 in. dynes/cm^2, but this may result from an underestimate of the shear angle, which it is hoped to determine more precisely in other experiments.

4. Limiting Conditions for Jet Formation in High Velocity Collisions. J. M. WALSH, R. G. SHREFFLER AND F. J. WILLIG, *Los Alamos Scientific Laboratory.*—The high velocity collision of two solids is discussed as a problem in compressible fluid hydrodynamics. Such collisions may conveniently be divided into jetless and jet-forming categories. A theory is presented which describes flow in the collision region for the jetless case, and determines a critical collision angle (as a function of material velocities and equation-of-state properties of the materials) above which a jet must arise from the collision.

5. Jetless and Jet-Forming Collisions of Explosive-Driven Metal Plates. F. J. WILLIG, R. G. SHREFFLER, AND J. M. WALSH, *Los Alamos Scientific Laboratory.*—The experimental study of solid collisions utilizes metal plates driven by high explosives, the collision process being recorded with a high speed smear camera. Two experimental arrangements are used, and data for collisions employing Dural, mild steel, brass, and lead are presented. Jetless and jet-forming collisions are observed, and critical angles separating the two types are compared with theoretical predictions. Agreement seems satisfactory to indicate that the theory is valid.

6. Free Surface Properties of Explosive-Driven Metal Plates. W. E. DEAL AND R. G. SHREFFLER, *Los Almos Scientific Laboratory.*—A photographic method is presented for the determination of the free surface properties of metal plates moving at the extreme velocities obtained by high explosive acceleration. The determination of the free surface velocity of plane surfaces is emphasized. Specific results using brass plates driven by Composition *B* are cited. Photographic techniques and methods for reduction of data from the photographic record are described. The more qualtiative features of the free surface motion are mentioned and representative pictures from the cameras records are shown. An extension of the technique to the study of various free surface phenomena associated with both plane and curved surfaces is indicated.

7. Fast Metal Jets. F. J. WILLIG, *Los Alamos Scientific Laboratory*

8. Surface Motion Associated with Obliquely Incident Elastic Waves.* JOHN PEARSON AND JOHN S. RINEHART, *U. S. Naval Ordnance Test Station, Inyokern, China Lake, California.*—Well-known laws which govern the reflection of elastic waves that strike free surfaces obliquely are summarized. These are used to deduce particle motion at the free surface. A number of numerical computations are presented in the form of tables and graphs for the case of an incident longitudinal wave. Considerations indicate that, for oblique incidence, the particle motion at the surface will not, in general, be perpendicular to the surface. The data are expected to be of value in the solution of problems connected with impulsively loaded bodies such as metal-explosive systems.

* Work partially supported by the ONR.

9. Transient High Amplitude Waves Through Steel.* WILLIAM A. ALLEN, *Michelson Laboratory, U. S. Naval Ordnance Test Station, Inyokern, China Lake, California.*—An optical technique, reported in a previous paper[1] has been used to measure surface oscillations on a series of thick, circular steel plates while they deform under explosive attack. Analysis of many photographic records indicates the presence of elastic, plastic, and shear waves. The methods used in data analysis will be discussed briefly. Data will be presented on amplitude of oblique wave reflection from a free surface, particle velocities at a free surface, and attenuation of wave amplitude.

* Work supported by Armament and Mechanics Branches, ONR.
[1] W. A. Allen and C. L. McCrary, Phys. Rev. **85**, 769 (1952).

10. Numerical Solution of the Equations for a Discrete Model of a Spherical Blast. T. S. WALTON, *U. S. Naval Ordnance Laboratory.*—A sphere of perfect gas at uniformly high pressure and temperature is allowed to expand suddenly into a homogeneous atmosphere. The continuous distribution of matter is approximated by partitioning the medium with a set of expansible, concentric spherical shells in which all the inertia resides, each chamber being filled with an inertialess but otherwise perfect gas in thermodynamic equilibrium. To produce the required entropy changes wherever shocks develop, an artificial dissipative mechanism was introduced.[1] The system of differential-difference equations pertaining to this dynamical model was integrated on the IBM Card-Programmed Calculator, starting with an internal pressure of 12.82 atmospheres and an absolute temperature 3.24 times that of the surrounding atmosphere. Besides the outward-moving shock which originates at the gas-air interface, the computation revealed the presence of an inward-moving shock wave which follows behind the rarefaction wave and converges toward the center of the sphere with ever increasing pressure ratio. A minimum pressure of 0.008 atmosphere was computed at the center just before the arrival of the interior shock.

[1] J. von Neumann and R. D. Richtmyer, J. Appl. Phys. **21**, 232 (1950).

11. The Effect of Charge Radius on Detonation Velocity. R. B. PARLIN, C. J. THORNE, D. W. ROBINSON, *University of Utah.*—An analytic treatment of the effect of radial expansion on the velocity of propagation of a detonation wave in attempted. The resulting equations, together with auxiliary functions necessary for application to experimental data, are given. The approximations involved are discussed in terms of possible refinements in the treatment. Experimental data is applied to the results with reasonable consistency.

12. The Generation of Convection in a Planetary Atmosphere. JEAN I. KING, *University of Utah.* (Introduced by W. M. Elsasser).—A planetary atmosphere which absorbs partially in the infrared and is transparent in the visible and ultraviolet regions of the spectrum will, under radiative equilibrium, have a temperature decreasing monotonically with height. Such conditions prevail in the lowest 10 km of the terrestrial atmosphere and apparently on Mars. Equilibrium temperature distributions have been calculated for various line and band models of the absorption spectrum assuming the spectral lines are pressure-broadened. All the models show a steep temperature gradient near the lower boundary which is convectively unstable. Using these data, one can determine the height of this convective zone from a knowledge of the physical structure of the atmosphere. Results of this analysis shows that a planet with a completely quiescent atmosphere cannot exist.

13. On the Motion of Elliptical Vortices. HENRY C. ALBERTS, GEORGE A. COULTER, AND CHARLES M. WARDEN, *Aberdeen Proving Ground.*—When a shock wave is diffracted by an ½-in. slit, one of the phenomena observed is the formation of elliptical vortices at the exit of the slit. These vortices have been studied and the graphical solutions of their equations of motion as a function of the peak pressure of the incident wave are presented. An equation is derived to enable the growth of the vortex to be found as a function of time and the peak pressure of the incident wave.

14. Experimental Study of the Formation of a Vortex Ring.* F. K. ELDER, JR. AND N. DE HAAS, *Applied Physics Laboratory, The Johns Hopkins University, Silver Spring, Maryland.*—The formation of a vortex ring at the open end of a cylindrical shock tube at the emergence of the shock wave was investigated by means of spark schlieren photography, using an electronic timing control. The shock tube was of a conventional type, having a constant inner diameter of 3.375 inches. The expansion chamber, open to the atmosphere, was a little over seven times the length of the compression chamber, which was filled with superdry tank nitrogen. Vortex-ring formation was investigated at two values of compression-chamber (gauge) pressure: 10 and 40 pounds per square inch. At these pressures the air jet is subsonic, and the contact surface does not reach the open end of the tube. Measurements of position as a function of time indicate that in the first millisecond after shock emergence the vortex ring accelerates from zero axial velocity to about three-quarters the theoretical particle velocity of the mass flow following the initial plane shock. The diameter of the vortex ring increases nonlinearly with time and distance.

* This work was supported by the U. S. Navy, Bureau of Ordnance.

15. Compressible Laminar Boundary Layers.* S. H. CHRISTENSEN, *Georgia Institute of Technology.*—Assuming constant specific heat, unity Prandtl number and thermally insulated boundaries, the compressible laminar boundary-layer equations, under a Mises transformation and Mises independent variable, reduce to an equation analogous to the heat-conduction equation with variable "radiation" and "conductivity." A further change in independent variable removes the "radiation" term and the resulting equation is equivalent to the boundary-layer equations of an incompressible fluid having the same coordinate parallel to the surface as the compressible case, but a stretched normal coordinate, and variable viscosity which depends only upon the free-stream velocity. Further substitution of a stretched surface coordinate, related to the compressible coordinate by the free-stream velocity, results in the constant viscosity, incompressible boundary-layer equations. A similar transformation for the incompressible, constant viscosity case was found independently by Illingworth[1] and Stewartson,[2] using other methods of derivation. Variable viscosity method is simpler, however, and was applied to extend methods of Karman-Pohlhausen,[3] Goldstein[4] and Luckert[5] to the compressible case. Dimensionless curves of velocity and temperature profiles in the compressible wake behind an infinitely thin flat plate, from the trailing edge to two plate lengths down-stream, were obtained for free-stream Mach numbers of 0 to 10.

* Doctoral dissertation, Faculty of Arts and Sciences, Harvard University December 1, 1950.

[1] C. R. Illingworth, Proc. Roy. Soc. (London) **A199**, 533 (1949).
[2] K. Stewartson, Proc. Roy. Soc. (London) **A200**, 84 (1949).
[3] T. von Karman, Z.A.M.M. 1, 233 (1921). K. Pohlhausen, Z.A.M.M. 1, 252 (1921).
[4] S. Goldstein, Proc. Cambridge Phil. Soc. **26**, 1 (1930).
[5] H. J. Luckert, Schrift. d. Math. Seminars u.d. Inst. f.A. Math. d. Univ. Berlin 1, 245 (1933).

16. Turbulent Heat Transfer for Flow in a Channel. EUGENE N. PARKER, *University of Utah.*—The field equations describing the spectrum functions of a turbulent flow in a channel are set up and an approximate solution is obtained. From the resulting spectrum functions one computes the increase of the effective viscosity due to the turbulence, and the increased pressure gradient needed to maintain the laminar flow. The enhanced heat transfer with the walls of the channel is also computed, giving a relation between the increased effective thermal conductivity and the Reynold's number of the flow.

17. Effects of Damping Screens and Stream Contraction on Turbulence. MAURICE TUCKER, *NACA Cleveland.* (Introduced by J. C. Evvard).—An analysis is presented of the combined effect of cascaded damping screens followed by an axisymmetric stream contraction (or expansion) upon the intensities, macroscales, and one-dimensional spectra of a triple Fourier integral representation of a turbulence field convected by a main stream. The treatment is restricted to negligible turbulence decay and linearized by postulating small turbulence velocity fluctuations and absence of viscosity except as simulated by the idealized screen action. Compressibility of the main stream is allowed for during passage through the contraction. The density fluctuations ordinarily associated with turbulence are regarded as negligible. Numerical results for the longitudinal and lateral intensities, scales, and spectra of turbulence downstream of a screen-contraction configuration are obtained for the case of initial isotropic turbulence. The action of damping screens and contraction is to distort this initially isotropic field into a field of turbulence symmetric about the longitudinal direction with the lateral velocity fluctuations greater in magnitude than the longitudinal. The use of multiple screens tends to equalize the lateral and longitudinal fluctuations. Allowing for decay effects by an approximation strictly suitable only for isotropic turbulence, the predicted intensities show a fair agreement with the experimental data of Dryden and Schubauer.

18. Luminous Effects in the Shock Tube. R. N. HOLLYER, JR., A. C. HUNTING, OTTO LAPORTE, E. H. SCHWARCZ, AND E. B. TURNER, *University of Michigan.*—Recent experiments by R. W. Perry and A. Kantrowitz[1] on converging cylindrical shock waves and by R. G. Fowler, J. S. Goldstein and B. E. Clotfelter[2] on shock waves in electric discharge tubes have directed attention to luminous effects in shock tubes. Such effects have been observed with the University of Michigan shock tube (2×7-inch cross section) several times in the past and it was decided to investigate these effects in more detail. Considerable luminosity is observed visually behind the reflected shock in the following: N_2, He, A, air and at incident shock strengths as low as $\xi=0.1$ and up to $\xi=0.03$. The investigation is being continued in two directions: (a) by the use of a wave speed camera it has been definitely established

that the luminosity is in the extremely hot flow bounded by the reflected shock and later by the cold front, and (b) by spectrographic investigation using a two-prism glass spectrograph, identification of numerous lines between 6700A and 3500A is in progress.

[1] R. W. Perry and Arthur Kantrowitz, J. Appl. Phys. **22**, 878 (1951).
[2] R. G. Fowler, J. S. Goldstein, and B. E. Clotfelter, Phys. Rev. **82**, 879 (1951).

19. Observations on the Luminescence Accompanying Cone-Cylindrical and Spherical Missiles Traveling at High Speeds. J. ECKERMAN AND R. N. SCHWARTZ, *Naval Ordnance Laboratory, Silver Spring, Maryland.*—Open-shutter photographs and spectrograms have been obtained for 90° cone-cylindrical and spherical missles after traveling a path of from 50 to 100 calibers length in diatomic bromine and monatomic xenon. Observations were carried out with pressures varying from one to 200 mm of Hg. The missles had velocities of about 6000 ft/sec which gave a Mach number of 13 in bromine and 10 in xenon. An open-shutter camera using panchromatic film was focused on the missile path. The width of and intensity of the image increased in a regular manner with the density, reaching a maximum width of about one caliber. Information as to mechanism of light production was gained from density dependence of the luminosity. Although the cone-cylinders had a side and front survace area of about 2.8 times that of the spheres, about three times the gas pressure was required to produce the same light intensity. From the photographs and spectra taken, it was inferred that the major portion of the luminosity originated in the atmospheric gas. These studies were augmented by rotating mirror pictures.

20. Time-Resolved Spectroscopy of the Incandescence Associated with Ultra-Speed Pellets. EARLE B. MAYFIELD, *Michelson Laboratory, U. S. Naval Ordnance Test Station, Inyokern, China Lake, California.* (Introduced by J. S. Rinehart).—Further results of work reported at the December 27, 28, and 29, 1951 meeting of the American Physical Society at Berkeley[1] have been obtained. Small, aluminum pellets have been fired at velocities of 15,000 ft/sec in a vacuum as well as in air at atmospheric pressure, and in Oxygen and argon at atmospheric pressure. These pellets have also been fired together in a 4′ glass tube with the same gases and in vacuum. In air, AlO bands are formed about 150 μ sec behind the pellet; in oxygen they are formed immediately. In argon, the lines of both aluminum and argon are excited. The pellets emit a continuum after colliding which persists for about 25 μ sec. In this region the Al lines at λλ 3944 and 3961 were reversed for the case of oxygen.

[1] Phys. Rev. **85**, 769 (1952).

21. A Qualitative Comparison of Meteor and Fast-Particle Spectra.* WILLIAM C. WHITE AND RICHARD N. THOMAS, *University of Utah and Naval Ordnance Test Station.*—Meteors have kinetic energies ranging from 3 to 530 ev per atom (in a center-of-gravity system with an atmospheric atom), and a metallic line spectrum corresponding to excited levels ranging up to 9 ev. 5–6 km/sec fast particles have kinetic energies ranging from 0.66 to 2.6 ev, and a spectrum containing metallic lines corresponding to excited levels ranging up to 5.9 ev. The fast particles must produce a region of high kinetic temperature, while current thought holds that the majority of meteors do not. A comment is presented on the number of similarities in type spectra produced, and its interest in view of the above characteristics. The utility of such comparisons in studying the mechanism of production of such spectra by atom-atom collisions is discussed.

* Work supported by Armament and Mechanics Branches, ONR.

22. A Semi-Quantitative Interpretation of an Al Fast-Particle Spectrum.* RICHARD N. THOMAS AND WILLIAM C. WHITE, *University of Utah and Naval Ordnance Test Station.*—An interpretation of the 5 km/sec aluminum pellet time-resolved spectra reported by Allen, Mayfield, Rinehart, and White is presented. The differential appearance time of 3.1 ev Al lines (earlier) and AlO bands (later) suggests two alteratives for interpretation—as a pure rate process with appreciable activation time for the AlO or as a sequence of quasi-equilibrium states. Calculations under the two assumed mechanisms appear to favor the latter interpretation as the predominant factor, although some activation effect cannot be excluded. A phenomenological discussion based on the conditions determining the kinetic temperature along the pellet trail seems to offer promise both in interpreting the current—rather incomplete—observations and in providing predictions on the behavior at higher velocities.

* Work suported by Armament and Mechanics Branches, ONR.

23. The Interaction of Plane Shock Waves and Rough Surfaces. RUSSELL E. DUFF, *Los Alamos Scientific Laboratory.*—Shock retardation in nitrogen was measured in a shock tube for a series of two and three dimensionally rough surfaces at shock strengths from $\xi = 0.1$ to $\xi = 0.9$ to determine the effect of a rough surface on a shock wave. The approximation was made that the volume between the positions of the shock wave with and without the rough surface present multiplied by the specific energy behind the shock wave represented energy dissipated by the roughness. The space rate of energy dissipation is presented as a function of the average particle size of the rough surface. It is also shown that the curvature of the shock wave in the vicinity of the surface depends on the roughness of the surface, the length of roughness covered, and the shock strength. The hundreds of measurements of shock wave contours made in this investigation showed that there is a random fluctuation in the angle of incidence of the primary shock wave of 1/15°. This fluctuation is presumably caused by the details of the diaphragm rupture even though measurements were made 14 ft from the diaphragm in a 2-inch by 7-inch shock tube.

24. Effects of Curved Shock Waves in Pseudo-Stationary Flows. C. H. FLETCHER AND A. H. TAUB, *University of Illinois.*—Pseudo-stationary flows are those flows in which the flow variables (velocity, pressure, entropy, etc.) are functions of the independent variables x/t, y/t, z/t instead of the more usual x, y, z, and t. A necessary condition for pseudo-stationary flows is that the flow boundaries be describable in terms of the variables x/t, etc. in some inertial system for some choice of $t = 0$. In the case of the interaction of a plane shock wave traveling along a wall and meeting an angle in the wall, the physical boundaries satisfy the necessary condition above and experiments indicate that the shock boundaries do also. T. Y. Thomas[1] has studied the curvature of a stationary (two-dimensional) shock wave in a uniform flow and its relation to the curvature of the streamlines in the flow behind the curved shock. An analysis along similar lines has been carried out for pseudo-stationary shock waves. The resulting relations are identical in some respects with those obtained by Thomas. The influence of these considerations on the theory of regular (two shock) reflection and Mach (three shock) reflection is pointed out.

[1] T. Y. Thomas, J. Math. Phys. **28**, 91 (1949).

25. Reflection of Shock Waves as a Pseudo-Stationary Phenomenon. A. H. TAUB AND C. H. FLETCHER, *University of Illinois.*—The usual situation in the regular reflection of shock waves involves a reflected shock which is straight for

a portion of its length near the intersection with the incident shock and is curved at some distance from this point. The conditions at the point where the reflected shock ceases to be linear are investigated along the lines suggested in the preceding abstract. It is shown that a continuous wave must also appear at this point. The form of this wave is restricted by the pseudo-stationary character of the phenomenon. Analogous reasoning is applied to the case of Mach reflection of weak shock waves near glancing incidence. The case is examined in which the curved Mach shock joins the straight incident shock with a continuous tangent and the conditions on the curvature of the Mach shock are examined.

26. Experimental Study of Shock Refraction.* R. G. STONER, E. B. DAVIES, AND C. L. WOODBRIDGE, *The Pennsylvania State College.*—The interaction of plane shocks at a plane interface between two gases has been studied at angles of incidence, α, up to 70° and pressure ratios $\xi(=P_0/P)\geq 0.60$, using spark shadow photography. For certain ranges of α and ξ, a three-shock configuration[1,2] is observed. Application of oblique shock theory allows conditions behind the reflected and transmitted shocks to be calculated from their observed positions. Discrepancies in pressure and flow direction across the interface are attributable to the finite mass of the film which forms the interface. With air/CO_2, the reflected shock disappears when the angle of incidence approaches that for which the flow behind the incident shock becomes sonic. The situation is complicated by the catch-up of the signal from the corner, which is observed at about the same angle. With air/H_2, the three-shock configuration is replaced, beyond the angle for which the transmitted shock becomes normal to the interface, by a configuration similar to that previously described,[3] in which the transmitted wave runs ahead in the second medium and propagates a signal back into the first medium ahead of the incident shock.

* Supported by contract with ONR.
[1] A. H. Taub, Phys. Rev. **72**, 51 (1947).
[2] H. Polachek and R. J. Seeger, Phys. Rev. **84**, 922 (1951).
[3] R. G. Stoner and M. H. Glauberman, Phys. Rev. **76**, 882A (1949).

27. Measurement of Transient Flow Variables as a Function of Time.* C. W. CURTIS, R. J. EMRICH, AND J. E. MACK, *Lehigh University.*—Specification of a one-dimensional transient flow requires that the dependence of flow variables on both position and time be known. The required information can be obtained by recording changes in the flow either over the space of interest at successive times, or over the time of interest at successive positions. The chrono-interferometer to be described provides a record of the second type. The time interval over which this instrument can record is virtually unlimited, whereas the field of view of spatial interferometers is restricted by the size of available optical elements. Furthermore, since only small apertures are required, the chrono-interferometer is comparatively simple and inexpensive to construct. In the instrument constructed, the beam in one arm of a Michelson interferometer crosses a shock tube, and combines with the beam in the outside arm to give a single fringe in a $\frac{1}{8}$-in. diameter field. The resultant intensity is recorded photoelectrically on an oscillograph. The fringe count from the record yields an absolute measurement of the density change; fractional fringe shifts can be noted. The chrono-interferometer can be used to calibrate other devices recording in time such as piezoelectric and pressure bar gauges.

* Supported by the ONR.

28. On the Hydrodynamic Stability of Laminar Flame Fronts.* MARTIN LESSEN, *The Pennsylvania State College.*—In references 1 and 2, the stability of a laminar flame front to two-dimensional disturbances time variable is investigated. In reference 1, the flame front is considered as a discontinuity in velocity whereas in reference 2, a continuous distribution of velocity in the direction of flow is considered. In both works, the effect of energy dissipation is neglected. Both works conclude that the flow is unstable. In the present work, a dissipative flow is considered along with a three-dimensional disturbance. In a manner similar to that of reference 3, a transformation is found that transforms the three-dimensional disturbance equations to corresponding two-dimensional disturbance equations. The conclusions from the above are that if a minimum Reynolds number for stability of laminar flame fronts (based on flame front thickness) exists, it is the same for two and three dimensional disturbances. Hence, it is sufficient to consider only two-dimensional disturbances. It is also probable that such a minimum Reynolds number exists.

* This work was carried out at The Pennsylvania State College under ONR Contract NONR-656 (01).
[1] L. Landau, Acta Physicochim. U.R.S.S. **19**, 77 (1944).
[2] H. Einbinder, Phys. Rev. **75**, 1313 (1949).
[3] H. B. Squire, Proc. Roy. Soc. (London) **A142**, 621 (1933).

29. Compressible Fow of a Viscous Fluid in a Small Diameter Tube Closed at One End. J. M. KENDALL, *U. S. Naval Ordnance Laboratory.*—The basic nonlinear differential equation for a compressible viscous fluid flowing isothermally through a small diameter tube has been examined under the condition of nonslip. Under the assumption that the square of the pressure gradient is small compared to the rate of change of pressure gradient, the equation of pressure as a function of x and t takes on the form of the one-dimensional heat conduction equation (or also of the form of the voltage conduction in the long noninductive electric telegraph cable). Measurements were made of the pressure as a function of time at the end of a tube one and one-half millimeters inside diameter and fifteen-meters long as the pressure at the other end was suddenly changed by one quarter of a millimeter of Hg (10 percent change in initial pressure). The measured pressures as a function of time were in good agreement with those calculated using the solution of the corresponding problem of the temperature distribution in a bar.

30. Oscillations of the Gas Bubble Produced by an Underwater Explosion. L. C. BARRETT AND C. J. THORNE, *University of Utah.*—Under the usual assumptions, a derivation is given of the nonlinear differential equation governing the oscillations of the gas bubble produced by an underwater explosion. An integral solution of the equation is also obtained. Variations in the radius-time curve due to alterations in the gas constant γ are discussed, it being shown that neglecting the potential energy of the gas bubble leads to the same radius-time curve as that obtained by letting γ become infinite. This curve most nearly approximates the experimental data, over the contraction phase of the first cycle. A method of energy change is postulated which has the effect, on the integral solution of the differential equation, of replacing the constant coefficient appearing in the term representing the potential energy of the gas by a function of the radius, which, for a given γ can be numerically determined so that the experimental and theoretical curves coincide. A general procedure for determining the radius-time curve corresponding to any value of γ, or any temperature-independent equation of state, is also set forth, specific examples being carried through to illustrate the method.

THE AMERICAN INSTITUTE OF PHYSICS

AFFILIATED SOCIETIES

American Physical Society
KARL K. DARROW, Secretary, Columbia University, New York 27, New York

Optical Society of America
ARTHUR C. HARDY, Secretary, Massachusetts Institute of Technology, Cambridge 39, Massachusetts

Acoustical Society of America
WALLACE WATERFALL, Secretary, 57 East 55th Street, New York 22, New York

Society of Rheology
G. J. DEGUIRE, Secretary, Socony-Vacuum Laboratories, Paulsboro, Long Island, New York

American Association of Physics Teachers
R. F. PAUSHTER, Secretary, University of Illinois, Urbana, Illinois

AFFILIATED SOCIETIES

American Crystallographic Association
Electron Microscopy Society of America
Physical Society of the District of Columbia
Physics Club of Chicago
Physics Club of New York City
Cleveland Physics Society
Rhodes Club of the Tennessee Valley
Sigma Pi Sigma

ASSOCIATES

Over seventy industrial companies and other organizations which contribute to the support of the Institute

JOURNALS

The Physical Review
S. A. GOUDSMIT, Editor, Brookhaven National Laboratory, Upton, Long Island, New York

Reviews of Modern Physics
J. W. BUCHTA, Editor, University of Minnesota, Minneapolis 14, Minnesota

Journal of the Optical Society of America
WALLACE R. BRODE, Editor, National Bureau of Standards, Washington 25, D. C.

The Journal of the Acoustical Society of America
FLOYD A. FIRESTONE, Editor, 57 East 55th Street, New York 22, New York

American Journal of Physics
THOMAS H. OSGOOD, Editor, Michigan State College, East Lansing, Michigan

The Review of Scientific Instruments
GAYLORD P. HARNWELL, Editor, Research Laboratory of Physics, University of Pennsylvania, Philadelphia 4, Pennsylvania

The Journal of Chemical Physics
JOSEPH E. MAYER, Editor, Institute for Nuclear Studies, University of Chicago, Chicago 37, Illinois

Journal of Applied Physics
ELVEN G. FUBINI, Editor, Gas Turbine Laboratory, Case Institute of Technology, Cleveland 6, Ohio

Physics Today
GAYLORD P. HARNWELL, Editorial Director; JOSEPH A. BOYLE, Managing Editor, American Institute of Physics, 57 East 55th Street, New York 22, New York

OFFICERS

GAYLORD P. HARNWELL, Chairman
Massachusetts Institute of Technology

DONALD H. PORTER, Treasurer
Columbia University

GOVERNING BOARD

KARL K. DARROW
G. J. DEGUIRE
S. A. GOUDSMIT
G. W. HARTWIG
GAYLORD P. HARNWELL
P. V. HOYT
ROBERT KINGSTON
HUGH S. KNOWLES
C. C. LAURITSEN
F. W. LOOMIS
WILLIAM F. MEGGERS
GEORGE B. PEGRAM
I. I. RABI
DUANE ROLLER
FREDERICK SEITZ
FRANCIS G. SLACK
JOHN C. SLATER
RICHARD M. SUTTON
MARY W. ZABOLOTNY

Committee on Physics
KARL LARK-HOROVITZ

ADMINISTRATIVE STAFF

HENRY A. BARTON, Executive Secretary
WALLACE WATERFALL, Executive Secretary
THOMAS VICKERY, Advertising Manager
RUTH F. PEARSON, Publication Manager
BETTY H. CONNOR, Assistant Secretary
ELIZABETH S. NEILL, Circulation Manager
KATHRYN LEONARD, Assistant Treasurer

THE American Institute of Physics was founded in 1931 by [illegible] to the field of Physics. [illegible] into one organization [illegible] these functions of [illegible] which can best be carried on [illegible] unified Society. Its purpose [illegible] advancement and diffusion [illegible] and its applications [illegible] welfare. To this end [illegible] the world or the [illegible] journals listed on the [illegible] unite only as [illegible] object among all who [illegible] need it: physics; [illegible] direct services to [illegible] the public; and [illegible] governmental agencies, [illegible] institutions, education, [illegible] physical literature, [illegible] such manner as to [illegible] organization and [illegible] fullest of physics as a [illegible] and constructive human [illegible]

CONTENTS

The Physical Review — Second Series, Volume 94, No. 2

[illegible] — [illegible]

Letters to the Editor

Proceedings of the American Physical Society

Minutes of the Meeting of the Division of Fluid Dynamics, Salt Lake City, Utah, June 20–22, 1953

LANCASTER PRESS, INC., LANCASTER, PA.